

Bioanalysis

Series Editor: Tuan Vo-Dinh

Alice S. Pereira
Pedro Tavares
Paulo Limão-Vieira *Editors*

Radiation in Bioanalysis

Spectroscopic Techniques and
Theoretical Methods

 Springer

Bioanalysis

Advanced Materials, Methods, and Devices

Volume 8

Series Editor

Tuan Vo-Dinh, Fitzpatrick Institute for Photonics, Duke University, Durham,
NC, USA

More information about this series at <http://www.springer.com/series/8091>


Alice S. Pereira · Pedro Tavares ·
Paulo Limão-Vieira
Editors


Radiation in Bioanalysis


Spectroscopic Techniques and Theoretical
Methods

 Springer

Editors

Alice S. Pereira 
Molecular Biophysics Lab.,
UCIBIO/Requimte, Department
of Chemistry
Faculdade de Ciências e Tecnologia,
Universidade NOVA de Lisboa
Caparica, Portugal

Pedro Tavares 
Molecular Biophysics Lab.,
UCIBIO/Requimte, Department
of Chemistry
Faculdade de Ciências e Tecnologia,
Universidade NOVA de Lisboa
Caparica, Portugal

Paulo Limão-Vieira 
Atomic and Molecular Collisions
Laboratory, CEFITEC, Department
of Physics
Faculdade de Ciências e Tecnologia,
Universidade NOVA de Lisboa
Caparica, Portugal

ISSN 2364-1118

Bioanalysis

ISBN 978-3-030-28246-2

<https://doi.org/10.1007/978-3-030-28247-9>

ISSN 2364-1126 (electronic)

ISBN 978-3-030-28247-9 (eBook)

© Springer Nature Switzerland AG 2019

This work is subject to copyright. All rights are reserved by the Publisher, whether the whole or part of the material is concerned, specifically the rights of translation, reprinting, reuse of illustrations, recitation, broadcasting, reproduction on microfilms or in any other physical way, and transmission or information storage and retrieval, electronic adaptation, computer software, or by similar or dissimilar methodology now known or hereafter developed.

The use of general descriptive names, registered names, trademarks, service marks, etc. in this publication does not imply, even in the absence of a specific statement, that such names are exempt from the relevant protective laws and regulations and therefore free for general use.

The publisher, the authors and the editors are safe to assume that the advice and information in this book are believed to be true and accurate at the date of publication. Neither the publisher nor the authors or the editors give a warranty, expressed or implied, with respect to the material contained herein or for any errors or omissions that may have been made. The publisher remains neutral with regard to jurisdictional claims in published maps and institutional affiliations.

This Springer imprint is published by the registered company Springer Nature Switzerland AG
The registered company address is: Gewerbestrasse 11, 6330 Cham, Switzerland

Editorial

Radiation has been widely used to probe structure, redox properties, and reactivity of simple and complex biological molecules/systems. It is common for researchers with different biological, chemical, and physical backgrounds to face problems for which one or more spectroscopic techniques are usually applied for structural analysis.

Fundamentals and state-of-the-art spectroscopic techniques within the themes fully covered in the textbook are aimed to benefit students, scholars, and even professionals working alongside the experimental and theoretical perspectives related to the underlying and fundamental mechanisms of biological systems. The textbook is also intended to summarize some of the advances achieved in the application of different spectroscopic techniques for the analysis and characterization from small to large biological compounds and also as a function of the phase and stage of aggregation.

The proposed contents provide advanced training by putting together a set of different experts who are well versed in the development of bottom-up approaches on complementary fields, including atomic and molecular physics, radiation biology, biochemistry, and biophysics. Readers are exposed to cutting-edge theories and high-quality research methods, comprising an advanced and up-to-date skill-based training in Radiation in Bioanalysis—Spectroscopic Techniques and Theoretical Methods. However, the textbook contents are not exclusive to a particular specialization and serve as a tool to fulfill a gap that authors have identified to be urgent to contribute with their accumulated know-how.

An extensive first part addresses the physics of radiation and pertinent spectroscopic techniques used in the study of biomolecules. It comprises different investigation approaches including contributions on photon, electron, and ion interactions with biologically relevant molecules. Other methodologies include the use of X-ray interaction with matter. In the second part, the textbook presents examples of how those tools have been used and combined with other experimental and theoretical techniques, in particular charge transfer processes in key biological systems, rapid kinetics coupled to spectroscopy to assess the molecular mechanism of key biological catalyzed reactions, as well as a comprehensive application to clinical use of particle track simulations and dose planning.

Throughout this textbook, common keywords include: Biological spectroscopic tools, Molecular biophysics, Atomic and molecular collisions, Synchrotron radiation for biomolecules, Modeling radiation-induced processes, which by themselves are an indication of the diversity but complementary nature of the different themes that endorse this need to deliver such contribution.

The importance of bringing together expert contributors in the subjects covered in this textbook was made clear to us while devising and implementing the International Radiation Biology and Biophysics Doctoral Training Program (RaBBiT). It became obvious that students coming from different scientific backgrounds would greatly benefit from a concise and clear textbook that would provide the basic understanding of spectroscopic techniques and their application to biological systems while presenting them to meaningful uses of such techniques in their research work.

We acknowledge the Portuguese National Funding Agency *Fundação para a Ciência e a Tecnologia* FCT-MCTES through PD-F Radiation Biology and Biophysics Doctoral Training Program (RaBBiT, PD/00193/2012) and its affiliated research units on Applied Molecular Biosciences (UCIBIO) and Centre of Physics and Technological Research (CEFITEC) through their research schemes UID/Multi/04378/2019 (UCIBIO) and UID/FIS/00068/2019 (CEFITEC). The Research Grants POCTI/QUI/37413/2001, POCTI/QUI/47273/2002, POCI/QUI/57475/2004, PTDC/QUI/64248/2006, PTDC/QUI/67142/2006, PTDC/SAU-SAP/111482/2009, PTDC/BIA-PRO/111485/2009, PTDC/OCE-ETA/32567/2017, PTDC/FIS-AQM/31215/2017, and PTDC/FIS-AQM/31281/2017 from FCT-MCTES are also acknowledged.

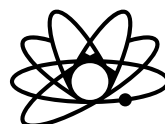
Within RaBBiT consortium, we fully acknowledge Universidade NOVA de Lisboa (PT), University of Innsbruck (AT), Queen's University Belfast (UK), Open University (UK), and Consejo Superior de Investigaciones Científicas, CSIC (ES) for their support over the last 8 years, which encouraged the need to publish this textbook.

Lisboa, Portugal
June 2019

Alice S. Pereira
masp@fct.unl.pt

Pedro Tavares
pabt@fct.unl.pt

Paulo Limão-Vieira
plimaovieira@fct.unl.pt



RABBIT^{PhD}

RADIATION BIOLOGY
& BIOPHYSICS

Contents

Part I Spectroscopic and Analyses Techniques

1 High-Resolution Electron Energy Loss Spectroscopy: Absolute Cross Section Measurements for Low Energy Electron Scattering from Biomolecules	3
V. Lemelin and L. Sanche	
2 Synchrotron Radiation UV-VUV Photoabsorption of Gas Phase Molecules	43
Denis Duflot, Søren Vrønning Hoffmann, Nykola C. Jones and Paulo Limão-Vieira	
3 Fluorescence Spectroscopy	83
Artur J. Moro and João Carlos Lima	
4 Raman Biospectroscopy and Imaging	111
Smilja Todorovic	
5 Circular Dichroism and Synchrotron Radiation Circular Dichroism Applications to Biomaterials	147
Rohanah Hussain, Tamás Jávorfí, Charlotte S. Hughes and Giuliano Siligardi	
6 Dynamic Light Scattering (DLS)	173
Sven Falke and Christian Betzel	
7 Pulsed Electron-Electron Double Resonance (PELDOR) and Electron Spin Echo Envelope Modulation (ESEEM) Spectroscopy in Bioanalysis	195
B. E. Bode and D. G. Norman	
8 Mössbauer Spectroscopy	213
João Carlos Waerenborgh, Pedro Tavares and Alice S. Pereira	

9	Principles of Nuclear Magnetic Resonance and Selected Biological Applications	245
	Carlos A. Salgueiro, Joana M. Dantas and Leonor Morgado	
10	Near Edge X-ray Absorption Fine Structure (NEXAFS) Spectroscopy of Molecules of Biological Interest: From Chemically Pure to Complex Samples	287
	G. Gerson B. de Souza and Joselaine C. Gonzalez	
11	Electron Impact Spectroscopy	313
	Alexander Dorn	
Part II Reaction Kinetics and Modelling		
12	Charge Transfer Processes in Key Biological Systems	329
	Filipe Ferreira da Silva, Mónica Mendes, Gustavo García and Paulo Limão-Vieira	
13	Fast Kinetics—Stopped-Flow and Rapid Freeze-Quench	349
	Pedro Tavares and Alice S. Pereira	
14	Radiobiological Effects Induced by X-ray (LINAC) Irradiation: Experiments and Modelling	367
	A. Traoré-Dubuis, L. Ellis-Gibbins, K. Krupa, A. I. Lozano, R. Colmenares, A. Muñoz, J. C. Oller, F. Blanco, A. García Grande, M. J. Coronado, S. Rosado, E. Ramil, L. Núñez, Paulo Limão-Vieira and G. García Gómez-Tejedor	

Part I
Spectroscopic and Analyses Techniques

Chapter 1

High-Resolution Electron Energy Loss Spectroscopy: Absolute Cross Section Measurements for Low Energy Electron Scattering from Biomolecules



V. Lemelin and L. Sanche

1.1 Introduction

1.1.1 General

The passage of high-energy particles or photons in biological matter produces copious numbers of secondary species along their tracks. It is well established that high-energy ionizing radiation (HEIR) deposits most of its energy in biological media via the secondary electrons it generates (Inokuti 1983; Pimblott et al. 1996; Boudaiffa et al. 2000; Pimblott and LaVerne 2007; Mucke et al. 2010; Duque et al. 2015). About 40,000 electrons per MeV of deposited energy (Pimblott and LaVerne 2007) are produced by single and multiple ionizations of biomolecules. Due to their abundance and their high reactivity, secondary electrons are considered as one of the most important species in radiobiology (Pimblott and LaVerne 2007; Mucke et al. 2010). The vast majority of these electrons have energies of less than 30 eV (Pimblott et al. 1996), the most probable energy being 9–10 eV (Pimblott and LaVerne 2007). These low-energy electrons (LEEs) interact with biological media by inelastic processes to vibrationally or electronically excite or ionize biomolecules. Subsequently, LEEs either recombine with ions or are thermalized by multiple processes such as intermolecular trapping, solvation, dissociative electron attachment (DEA) or resonance stabilisation. Ion-electron recombination and LEE inelastic scattering can create highly-reactive species including excited molecules, cations, anions and radicals. These species can damage cell components, change the biochemistry of the cell and create DNA damage. If DNA lesions are not repaired, they can lead to mutagenesis.

V. Lemelin · L. Sanche (✉)

Department of Nuclear Medicine and Radiobiology, Faculty of Medicine and Health Sciences, Université de Sherbrooke, 3001 12e Avenue Nord, Sherbrooke, QC, Canada
e-mail: leon.sanche@usherbrooke.ca

V. Lemelin

e-mail: vincent.lemelin@usherbrooke.ca

© Springer Nature Switzerland AG 2019

A. S. Pereira et al. (eds.), *Radiation in Bioanalysis*, Bioanalysis 8,
https://doi.org/10.1007/978-3-030-28247-9_1

nesis and lethality (Chiari et al. 2014). Moreover, it has been shown that LEEs even of sub-ionization energies can induce cluster DNA damage (Boudaïffa et al. 2000; Huels et al. 2003; Chen et al. 2016; Shao et al. 2017) and thus have the capacity to induce cell death.

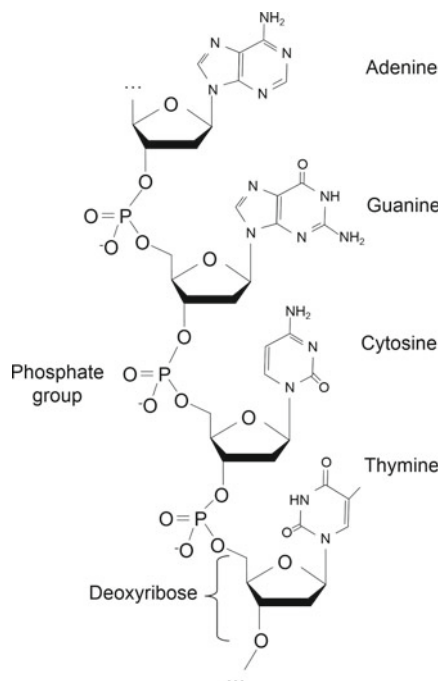
The primary objective of radiobiology is a complete understanding of the biological effects of HEIR. Since LEEs are one of the most abundant immediate species formed following irradiation, it is necessary to comprehend and model their interactions within biological media. Radiobiological models often rely on Monte Carlo (MC) simulations that can describe event-by-event modifications of the biological medium, predict the number of secondary species created and calculate the deposited energy after the passage of HEIR (Muñoz et al. 2008; Alloni et al. 2012; Liljequist et al. 2012; Sanz et al. 2012). These MC and track-structure calculations require a large number of parameters and values that are related to interaction probabilities, including cross sections (CSs). Because of the abundance and strong interactions of LEEs, MC simulations should incorporate as many CSs for their interactions with biological matter as possible (i.e., vibrational and electronic excitations, ionization, elastic scattering, DEA, etc.), to most accurately represent the biological effects of HEIR. Since biological media typically exist in a condensed phase, such CSs should be preferably measured in this phase.

In this chapter, we explain the use of high-resolution electron energy loss spectroscopy (HREELS), as a powerful experimental technique to study and measure absolute CSs for LEEs scattering from condensed molecules. We provide data on absolute CSs from the literature, which were derived from HREELS experiments with biologically relevant molecules, including those of the basic DNA constituents (Fig. 1.1). Even though this chapter is focused on CSs for dose calculations, particularly in localized radiotherapy, these values for LEEs induced processes are relevant to many other fields in which HEIR, and hence LEEs, play important roles. These include astrochemistry (Kaiser 2002; Holtom et al. 2005; Lafosse et al. 2006; Bennett and Kaiser 2007; Esmaili et al. 2017, 2018), planetary science (Lu and Sanche 2001; Samara et al. 2015), high-energy electron and extreme UV photon nanolithography (Wu et al. 2010), dosimetry for irradiation in space (Sridharan et al. 2015), plasma science (Lozano et al. 2017), biomedical imaging (Brix et al. 2005; Einstein et al. 2007; Eisenberg et al. 2011; Fazel et al. 2016) and radioprotection (Siragusa et al. 2017).

1.1.2 Radiotherapy Modalities and Low-Energy Electrons

The most important parameter to predict in any radiotherapy treatment is the energy deposited by HEIR per unit mass (i.e., absorbed dose (J/kg or Gy)). This parameter is crucial to maximise the damaging effects of HEIR to cancer cells, while minimizing them for healthy cells (Gaze 1996; Connell and Hellman 2009). Conventional radiotherapy modalities (e.g., external irradiation) deposit doses in macroscopic volumes (i.e., at organ and tissue level ($>\text{mm}^3$)). Radiobiological models presently used for

Fig. 1.1 Chemical structure of a short DNA strand including its four bases (Adapted from Lemelin et al. (2017), with the permission of AIP Publishing.)



these conventional treatments accurately predict the macroscopic doses (i.e., macrodosimetry) to be administered to patients. In conventional radiotherapy modalities, healthy cells are inevitably exposed to HEIR, thus increasing the risk of their death or of later secondary cancer development (Hall and Wu 2003). It is thus crucial to protect healthy cells from HEIR. Moreover, macro-dosimetric methods usually take into account only the primary particles (high-energy photons and particles) and their interactions with molecules of the biological media, particularly the water molecules (Meesungnoen et al. 2002; Emfietzoglou et al. 2005; Plante and Cucinotta 2009; Francis et al. 2011). Hence, while they can calculate the macroscopic dose, they do not consider the damage produced at the cellular and molecular levels by LEEs and other reactive species.

New radiotherapy modalities are being developed to selectively deliver a toxic dose exclusively to cancer cells, while preserving healthy cells (Gaze 1996; Seiwert et al. 2007; Reilly 2008; Connell and Hellman 2009; Chattopadhyay et al. 2010; Zalustky 2013; Sanche 2015; Hayes 2017; Rezaee et al. 2017). These new modalities focus on delivering localized nanoscopic or molecular doses using the reactivity of LEEs and/or other secondary species (Rezaee et al. 2017). Targeted radionuclide therapy (TRT) (Chattopadhyay et al. 2010; Hayes 2017) and concomitant chemoradiation therapy (CRT) (Seiwert et al. 2007) are two examples of these new improved modalities. The former uses radio-labeled molecules that localize preferentially in cancer cells and release, for example, Auger electrons (Zalustky 2013). Since the energy distribution of Auger electrons lies at low energy, they have short range

(~10–12 nm) and generate a large quantity of secondary LEEs in the vicinity of the cancer cell. These LEEs thus have the capacity to deposit most of their energy at the DNA level. Furthermore, the density of LEEs can be increased by combining targeted radionuclides with gold nanoparticles (GNPs) or by embedding radionuclides in gold nanocages (Sanche 2015). In these cases, the longer-range particles or photons emitted by the radionuclide strongly interact with the heavy metal, generating large quantities of LEEs. The incorporation of GNPs in TRT is an active field of research (Reilly 2008; Chattopadhyay et al. 2010; Hainfeld et al. 2010; Rezaee et al. 2017; Ghandi et al. 2018) and considerable efforts are being made to improve this new modality. Multiple studies (Hainfeld et al. 2004, 2008, 2010; Hyun Cho et al. 2005; Kong et al. 2008; Rahman et al. 2009; Lechtman et al. 2011; Chattopadhyay et al. 2013) have demonstrated dose and damage enhancements by GNPs in biological tissues, marking them promising tools for future radiotherapeutic treatments.

In cancer therapy, clinical protocols often combine chemotherapy, surgery and radiotherapy. CRT is the combination of chemotherapeutic agents (CAs) and radiotherapy, an approach that often enhances tumor treatment (Seiwert et al. 2007) since, when used in concomitance with HEIR, CAs can often radiosensitize cancer cells. It has been shown that CRT may rely, at least in part, on an increase in damage inflicted to the genome of the cancer cells due to the binding of the CA to DNA.

Conventional methods of estimating radiation doses for macroscopic volumes are obviously not suitable for predicting the subcellular radiobiological effectiveness of these new modalities. TRT and CRT require the details of energy deposition at the nanoscopic level to predict damages and radiobiological risks associated with locally delivered doses. Since these rely on the damages induced by secondary particles such as LEEs, TRT and CRT require new dosimetric models that can predict and calculate doses and damages at subcellular levels. Therefore, it is imperative to develop and improve nanodosimetric models for the continued development of these promising targeted radiotherapy modalities.

1.1.3 Monte Carlo Simulations and Nanodosimetry

MC simulations can predict damage to a biological medium and the deposited dose at nanoscopic scales, produced by primaries and secondary species, including LEEs (Rogers 2006; Nikjoo et al. 2016). Thus, TRT and CRT can benefit from the detailed description that MC simulations provide. However, for accuracy, MC codes must incorporate a panoply of CSs values for LEE interactions with the biological medium. MC simulations in water have received the most attention (Meesungnoen et al. 2002; Emfietzoglou et al. 2005; Plante and Cucinotta 2009; Francis et al. 2011) and CSs for LEEs interactions with water are incorporated in MC codes, such as Geant4-DNA simulation toolkit (Kyriakou et al. 2017), PENELOPE (Kyriakou et al. 2017) and TOPAS-nBio (McNamara et al. 2017). The general conclusion from these studies is that in MC simulations, LEEs interactions with water and biological medium play a

crucial role in describing the chemical and biophysical stages of radiation damage in cells.

Many parameters are user-defined in MC simulations, particularly in modelling radiation damage to DNA (Pater et al. 2014). For each relevant biomolecule present in cells and their nuclei, (e.g., water, DNA fundamentals units, amino acids, etc.), the various parameters needed for MC simulations include CSs for: total ionization, total excitation, total elastic scattering, partial ionization, electronic and vibrational excitation and phonon scattering of all particles involved in the energy deposition process. More specifically, MC simulations require such integral and differential CSs for all the relevant interaction mechanisms involving the fundamental units of DNA. Presently, there is a lack of information on these CSs for material relevant to radiation biology. There exist various experimental techniques to probe LEE-induced processes in biomolecules, including DNA, and measure corresponding CSs; these include X-ray photoelectron spectroscopy (XPS) (Klyachko et al. 1999), electron stimulated desorption (ESD) (Hervé Du Penhoat et al. 2001), electron transmission spectroscopy (ETS) (Burrow et al. 2008), coupled with chemical analysis of degradation products.

The next section focuses on HREELS, one of the most powerful tools to generate CSs for LEE-scattering from biomolecules. We will explain from basic principles, how this is possible and provide the most complete set of absolute CSs for condensed DNA constituents available.

1.2 Absolute Cross Sections Measurements with HREELS

1.2.1 Condensed Phase Scattering

At sufficiently high energy, the electron's wavelength is usually much smaller than the distance between biomolecules in cells. Accordingly, above about 100 eV, electrons interactions may begin to be approximated by collisions with individual targets for fairly disordered materials. Below this energy, the wavelength of a LEE may be comparable to intermolecular and interatomic distances, hence permitting simultaneous interactions with multiple targets (Bauer 1994). In fact, various quantum phenomena appear at low energies, such as diffraction of the electron's wave by the molecules of the solid (Zheng et al. 2006) and effects from the band structure of the molecular solid (Nagesha and Sanche 1998). Also, in condensed media, many excitation modes can be affected and new modes such as intermolecular vibrations or phonons are observed (Michaud et al. 2003). To take into account these latter processes and quantum phenomena, as well as to study biomolecules as close as possible to their biological environment, CSs should be preferably measured in condensed phase. This chapter focuses on the generation of absolute LEE-scattering CSs from off-specular HREELS data.

1.2.2 HREEL Spectroscopy

HREEL spectroscopy has been widely applied to many areas of surface and interface related research, e.g., to characterize substrates and adsorbates on surfaces. Multiple review articles exist on this technique (Ibach and Mills 1982; Bass and Sanche 1998; Lafosse and Azria 2011; Conrad and Kordesch 2017). As shown in this section, HREELS can also produce electron-scattering CSs for both gas and condensed phase molecules. For the latter, the majority of studies have focused on DNA constituents, such as the molecular moieties of its backbone (i.e., deoxyribose and phosphate group) and the bases (i.e., adenine, cytosine, thymine and guanine), as well as self-assembled monolayers (SAM) of DNA (Vilar et al. 2008).

Figure 1.2 represents a schematic diagram of a typical HREEL spectrometer for condensed-phase measurements. It consists of two hemispherical electrostatic deflectors; a monochromator and an analyzer (Michaud and Sanche 1984a). The monochromator produces monoenergetic electrons with energy ranging from 0 to 100 eV. In some HREELS systems, the monochromator and the analyzer can be rotated around the target. In this manner, it is possible to study the angular depen-

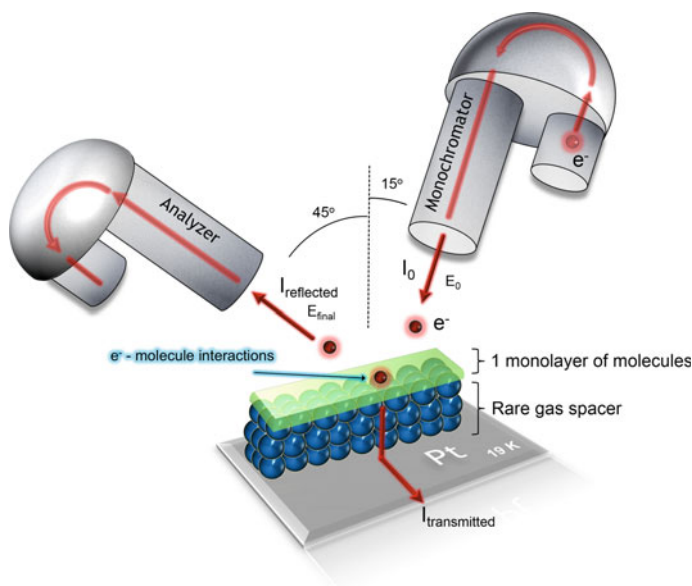


Fig. 1.2 Schematic representation of a High-Resolution Electron Energy Loss Spectrometer (HREELS) and solid phase target. The arrangement is composed of two electrostatic hemispheres: a monochromator and an analyzer. In this setup, monoenergetic electrons produced by the monochromator are incident at 15° from the normal of a platinum substrate surface, which is covered by a rare gas spacer layer held at 19 K. Biomolecules are condensed on the spacer layer. The analyzer measures the intensity of electrons inelastically scattered at 45° in the opposite azimuth. The total electron current transmitted through these layers can also be measured

dence of the electron scattering process with the condensed biomolecules. All the components are housed in an ultra-high vacuum chamber (UHV) where biomolecular films may be prepared by cryogenic condensation, as thin molecular solids. In the majority of such experiments, a metal substrate is cooled to temperatures between 15 and 100 K. First an inert rare gas spacer of several monolayer thickness (ML) is condensed on the metal surface. Afterwards, a monolayer or sub-monolayer of the biomolecular target is deposited. Spacer films of inert rare gas (usually Ar or Kr) reduce molecule-metal substrate interactions and image-charge polarization (Michaud and Sanche 1994). In the case of Ar films, the inert nature and large band gap ensure that electron scattering within the spacer layer is essentially elastic (Levesque et al. 2005a, b; Michaud et al. 2012) below the energy threshold of exciton creation (11.75 eV). These cryogenic conditions are needed in order to suppress the vibrational and phonon excitations of the molecular solid and the substrate, and to observe preferentially the interactions of electrons with molecules in their ground state. The resolution of the electron spectrometer can vary from 1 to 60 meV full width at half maximum (FWHM) depending on the incident current I_0 , the incident and scattered angle (θ_0 and θ_d , respectively) and on the optimization of the working conditions of the two hemispherical electrostatic deflectors.

1.2.2.1 Excitation Mechanisms

There exist two main classes of electron scattering with a medium or molecules: direct and resonant scattering. Direct scattering is mainly controlled by the exchange force and permanent and induced electrostatic potentials. The permanent or induced dipolar term is often the major contribution in the expansion of these potentials. It arises from long-range Coulombic interactions that operate at electron-molecule distances of between ~ 10 and 100 \AA (Lafosse and Azria 2011). Resonant scattering takes place on a much shorter range, at around $\sim 1\text{--}3 \text{ \AA}$ (Lafosse and Azria 2011). Contributions from each of these mechanisms in HREEL spectroscopy depends considerably on the experimental conditions; the incident energy E_0 , the incident (θ_0) and analyzing angle (θ_d). With dipolar scattering, the incident electron induces vibrational or electronic excitations via interaction with the dynamic dipole of the molecules or the solid. Since the electron interacts with a long-range Coulomb potential, it scatters with a small change in its wave vector ($\Delta k \ll k$) causing the electrons to scatter predominantly in the specular direction (Lafosse and Azria 2011). For the resonant mechanism, the vibrational or electronic excitations are induced via short-range interactions of the incoming electron with the atomic or molecular potential of the surface or near-surface components (Schulz 1976). With this type of interaction in a randomly oriented molecular film, the LEE wave vector experiences large momentum changes, with no particular backscattered direction being favored. Since dipolar (i.e., optical) selection rules no longer prevail in resonance scattering, multiple excitation losses are enhanced relative to dipolar scattering and electron resonances can be observed. These consist in the temporary capture of the incoming electron by a previously empty atomic or molecular orbital (Sanche and Schulz 1972) to form

a transient negative ion (TNI). There exist mainly two types of resonances: shape and core-excited resonance (Sanche and Schulz 1972; Schulz 1973). The shape or single particle resonance occurs usually at low energies (0–5 eV), when the incoming electron occupies a previously empty orbital of the molecule in its ground state (Caron and Sanche 2011). It is called “shape” resonance, because the electron is captured by the shape of the effective potential barrier created by the electron and the molecule (Schulz 1973). In a core-excited resonance, the capture of the incoming electron involves also electronic excitation of the target molecule (Schulz 1973). A core-excited resonance is also called a “two-electrons one-hole state”, since it involves the movement of an electron from a lower energy orbital to a higher one. In either type of resonances, the TNI is formed at a specific energy corresponding to that of the anion’s transient state involved. At resonance energies, CSs for electron interactions can be considerably enhanced.

During the life-time of the TNI, the nuclei may move apart from the equilibrium position due to the perturbation induced by the extra electron (Arumainayagam et al. 2010). The TNI has multiple outcomes or decay channels. In the autodetachment channel, this perturbation can result in a vibrationally excited neutral molecule (Arumainayagam et al. 2010). If the TNI is sufficiently long-lived and its inter-atomic potential energy surface is repulsive, the nuclei may move apart sufficiently for fragmentation of the anion, a process known as DEA, in which the electron is captured permanently by one fragment ($AB + e^- \rightarrow AB^- \rightarrow A^- + B$) (Sanche 2010).

TNIs are of considerable interest in radiobiology, since multiple studies have shown that the decay of these resonances can cause fragmentation of biomolecules including lethal DNA damages, particularly local multiply-damage sites (Boudaïffa et al. 2000; Sanche 2010; Chen et al. 2016; Shao et al. 2017). Thus, resonance scattering is probably one of the most relevant physical mechanisms to investigate in radiobiology.

1.2.2.2 Condensed-Phase HREELS and Scattering Models

In its condensed-phase version, HREELS allows the study of elastic scattering and energy losses by electrons scattered inside or at the surface of a solid. There exist principally two modes of measurement. It is possible to measure the magnitude of a given energy loss by sweeping the energy of both the monochromator and the analyzer, while maintaining a constant potential difference between them corresponding to the probed energy loss (Michaud et al. 1991; Lepage et al. 1998). The recorded current is termed an excitation function for the given energy-loss process (e.g., a vibration or an electronic mode). Excitation functions provide information on the energy dependence of interaction probabilities (Lepage et al. 1998), which are required to detect the presence of TNI at certain incident energies, but reliable absolute CSs cannot be extracted from such measurements (Allan 2007).

In the electron energy loss (EEL) modes of HREELS, spectra are recorded by sweeping the potential of the analyzer relative to the grounded target and keeping constant the potential of the monochromator or vice versa. When the incident electron

energy (E_0) is kept constant, the analyzer measures electrons that have experienced a range of energy losses. Absolute CSs are usually measured in this mode. An example of a vibrational HREEL spectrum is shown in Fig. 1.3.

The sample molecules can be condensed as a multilayer film or isolated on a rare gas spacer. To condense molecules on the substrate, there exist two alternative methods, which depend on the phase of the sample at ambient temperature (T) and pressure (P). For samples that are gases or liquids under ambient conditions, the vapor is introduced into a gas-handling manifold (Michaud and Sanche 1984a). Thereafter, a controlled quantity of vapor, determined by a pressure change in the manifold can be expanded into the UHV chamber and condensed onto a substrate. Alternatively, for samples that are solid at ambient temperature and pressure, a double-stage oven has been developed by Lévesque et al. (2003) for film deposition. In a secondary chamber, a crucible containing the sample in powder form, is heated up to the point of sublimation. Sublimated molecules escape the crucible via an aperture and condense upon a ceramic tip that is positioned beside the crucible. Thereafter, the tip is brought into the UHV analysis chamber and positioned in front of the metal surface, at a distance of 5 mm. The tip is then heated to desorb the molecules, which condense onto the cooled substrate (Levesque et al. 2003).

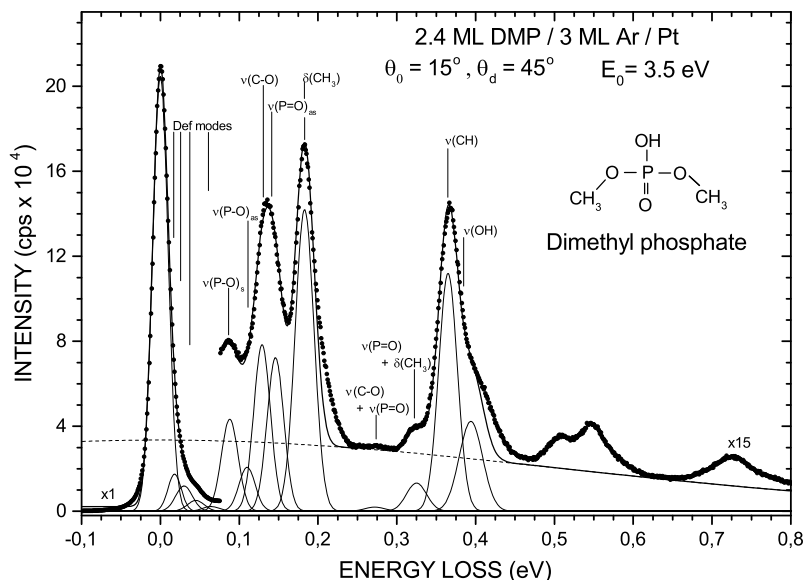


Fig. 1.3 A representative electron-energy-loss (EEL) spectrum recorded with 3.5-eV incident electrons on 2.4 monolayers (ML) of Dimethyl Phosphate (DMP) deposited on 3 ML of Ar. The thin solid line passing through the data points corresponds to the sum of Gaussian functions appearing at the bottom, which are associated with each vibrational peak. The dashed line accounts for the background current produced by the Ar and Pt substrates (Reproduced from Lemelin et al. (2017), with the permission of AIP Publishing.)

For extracting absolute CSs from LEE scattering data, two models have been developed to analyze results from either multilayer or (sub-) monolayer films. Dependent on film thickness, HREEL data are analyzed by a multiple scattering model (Michaud and Sanche 1987a; Michaud et al. 2003) or a single collision model (Levesque et al. 2005b; Bazin et al. 2010). In the latter, the elastically scattered current measured by the analyzer at an angle of θ_d , with respect to the surface normal, is assumed to have a diffuse reflectivity. Since this model only considers single collisions within a monolayer or submonolayer film, it can be shown that for an incident electron beam current I_0 of energy E_0 , with a near normal incidence θ_0 , the analyzer measures in the backscattered direction θ_d , a current of electrons with an energy E that have experienced an energy loss of $E - E_0$ into the film such that (Levesque et al. 2005b; Michaud et al. 2012):

$$I(\theta_d, E_0, E - E_0) \cong \frac{I_0(\theta_d, E_0)}{\cos\theta_0} \sigma_r(E_0, E - E_0) n_s \quad (1.1)$$

where $\sigma_r(E_0, E - E_0)$ is the CS for an electron of energy E_0 to deposit an energy $E - E_0$ in the film and be backscattered into the vacuum; n_s is the surface number density of the target molecules (related to the thickness of the film). The term $I_0(\theta_d, E_0)$ is defined as an effective incident electron current and can be considered as that fraction of the total incident electron current I_0 that would be backscattered in the direction of the analyzer at θ_d by a material with a diffuse elastic reflectivity of one. This latter experimental parameter allows the normalization of EEL spectra and permits the energy integral over an energy loss feature to be expressed in terms of an absolute reflectivity value (Levesque et al. 2005b). To determine this value experimentally, a technique, which uses the linear relationship between the reflected and transmitted current has been developed and is described in detail elsewhere (Levesque et al. 2005b; Michaud et al. 2012). Briefly, the value of $I_0(\theta_d, E_0)$ can be determined from the conversion law between the backscattered and transmitted current (Levesque et al. 2005b; Michaud et al. 2012) and by extrapolation to zero thickness from measurements taken over a range of film thicknesses. Hence, from n_s and $I_0(\theta_d, E_0)$ values, it is possible to normalize EEL spectra ($I(\theta_d, E_0, E - E_0)$) and extract integral CSs for inelastically scattered electrons. To determine the absolute CS values, multiple EEL spectra $I(\theta_d, E_0, E - E_0)$ are recorded at different E_0 . Subsequently, each energy-loss spectrum is fitted with multiple Gaussian functions to delimit the various excitation energy regions (vibrational and electronic excitations) (Levesque et al. 2005b; Michaud et al. 2012) as is illustrated in the representative EEL spectrum of Fig. 1.3 (the solid black line represents the fit from the sum of the Gaussians). Then, the absolute CS value $\sigma_{ri}(E_0, E - E_0)$, for a given excitation, is calculated using the area under the corresponding Gaussian function i with the amplitude of $a_i(E_0)$ and δ_i FWHM using:

$$\sigma_{ri}(E_0) = \frac{a_i(E_0) \delta_i \pi^{\frac{1}{2}}}{2(\ln 2)^{\frac{1}{2}}} \quad (1.2)$$

By varying E_0 , it is possible to obtain the energy dependence of the absolute CSs for each excitation. The energy and the δ_i assigned to each Gaussian must stay constant between spectra and only the amplitude $a_i(E_0)$ can vary in order to produce each fit. It is important to note that the CSs extracted with the single collision model are integral and absolute values, if the backscattered intensity is isotropic and the electron only experiences single collisions; this is the case for the results that are presented starting in Sect. 1.2.3.2. Under near normal electron incidence and with azimuthally disordered film conditions (Levesque et al. 2003, 2005a, b), multiple studies (Michaud and Sanche 1984b, 1987b; Lepage et al. 2000) have shown that the backscattered intensity can be considered isotropic for the systems used in the studies discussed here. By measuring EEL spectra in a fixed direction and by normalizing to the effective current $I_0(\theta_d, E_0)$, the single collision model (Eq. (1.1)) leads to CS values corresponding to electrons backscattered over the whole half-angular space (Levesque et al. 2005b). Thereby, the CSs presented in this chapter are considered to be integral and absolute values.

1.2.3 Absolute Cross Sections for Condensed Biomolecules

1.2.3.1 Amorphous Ice

One of the most important and abundant molecules in cells and biological tissues, is water. CSs for LEE scattering by water molecules have therefore been measured in the condensed phase (Michaud and Sanche 1987a, b; Bader et al. 1988; Michaud et al. 2003) and the values implemented into MC simulations (Meesungnoen et al. 2003, 2015; Uehara and Nikjoo 2006; Dingfelder et al. 2009; Plante and Cucinotta 2009; Plante 2011; Francis et al. 2011, 2012; Plante et al. 2012; Douglass et al. 2015). We present and discuss in this section the results of Michaud et al. (Michaud and Sanche 1987a, b; Michaud et al. 2003). These authors generated absolute integral CSs for elastic collisions, phonon excitations, vibrational and electronic excitations and ionization, in the range 1–100 eV from analysis of HREEL data (Michaud and Sanche 1987a, b; Michaud et al. 2003). The absolute inelastic scattering CSs for incident electrons below 30 eV lie within the range of $5.6\text{--}9.8 \times 10^{-17} \text{ cm}^2$ (Michaud and Sanche 1987a, b; Bader et al. 1988; Michaud et al. 2003). Since the electrons were incident on 30-ML films of water, a multiple-scattering analysis in a two-stream approximation was required to extract the CSs. The method is described by Michaud and Sanche (Michaud and Sanche 1987a). The energy-dependence of the elastic CS in the range 1–100 eV exhibits three broad structures at around 6.5, 14.5 and 40 eV as well as a small shoulder near 80 eV, as seen in Fig. 1.4a). These authors also measured the CSs for the translational phonon mode $\nu_{T''}$, the energy dependence of which exhibits a strong rise at low energy similar to the elastic CSs. The librational modes $\nu_{L'}$ and $\nu_{L''}$ have also been resolved and the 0–100 eV dependence of their CSs shows a rise at low energy (Fig. 1.4a)). Maxima around 8.5 and 7 eV are also observed for $\nu_{L'}$ and $\nu_{L''}$ respectively. At higher incident energy, librational CSs exhibit an oscillatory

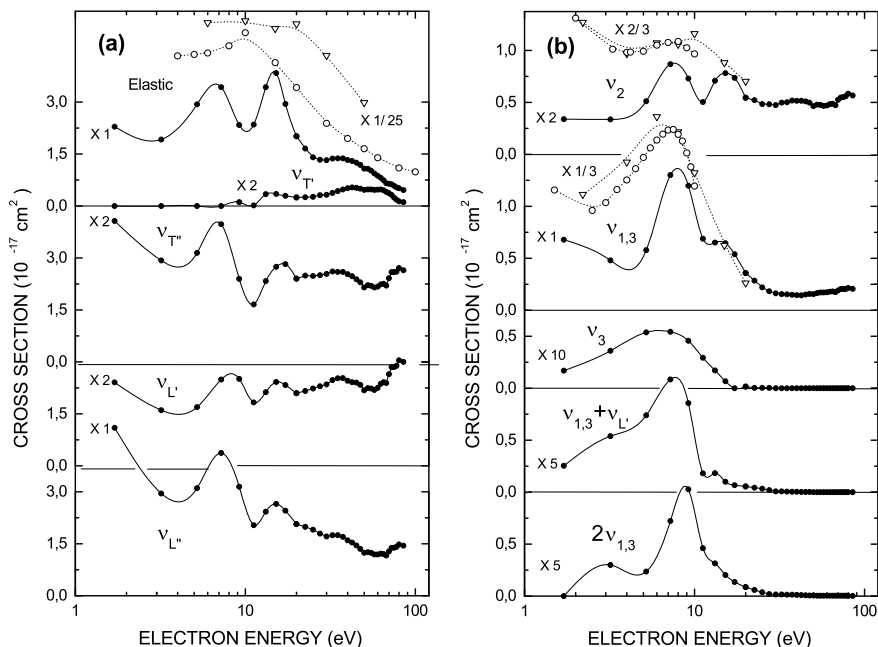


Fig. 1.4 Integral cross sections for **a** elastic scattering, translational ($v_{T'}$ and $v_{T''}$) and librational phonons modes ($v_{L'}$ and $v_{L''}$) and **b** vibrational modes v_2 , $v_{1,3}$, v_3 , $v_{1,3} + v_{L'}$ and $2v_{1,3}$ of amorphous ice extracted from multiple scattering analysis of electron energy loss spectra. The white dots and triangle are measured integral cross sections for electron scattering from water in the gas phase: **a** elastic CSs $\cdots\circ\cdots$ Danjo and Nishimura (1985); $\cdots\triangle\cdots$ Johnstone and Newell (1991) and **b** cross sections for the v_2 , $v_{1,3}$ modes; $\cdots\circ\cdots$ Seng and Linder (1976); $\cdots\triangle\cdots$ Shynstone and Newell (1988) (Reproduced with permission from Michaud et al. (2003), © 2018 Radiation Research Society.)

structure similar to that of the elastic CSs. The CSs for quasielastic scattering of electron in amorphous ice, represented as the sum of the CSs for elastic scattering and that for excitation of translational phonon modes ($v_{T'}$ and $v_{T''}$) is shown in Fig. 1.5.

From their analysis Michaud et al., also obtained the vibrational CSs shown in Fig. 1.4b) for the 1–100 eV energy range (Michaud et al. 2003). As seen, the vibrational mode $v_{1,3}$, v_2 , v_3 , $v_{1,3} + v_{L'}$ and $2v_{1,3}$ exhibits a strong enhancement around 8 eV. This maximum is due to decay of the transient 2B_2 anion state into these modes. The energy position of this resonance is higher than the same resonance in the gas phase (i.e., 6–8 eV), which is thought to be due to the presence of hydrogen bonding in condensed phase (Michaud et al. 2003).

The sum of the CSs for other inelastic processes associated with greater energy losses than vibrational excitation (i.e., dissociative attachment (DA), electronic and ionization) is shown in Fig. 1.6 in the 1–100 eV energy range. There is a small maximum around 5.2 eV, in the energy dependence of these CSs, ascribed to the formation

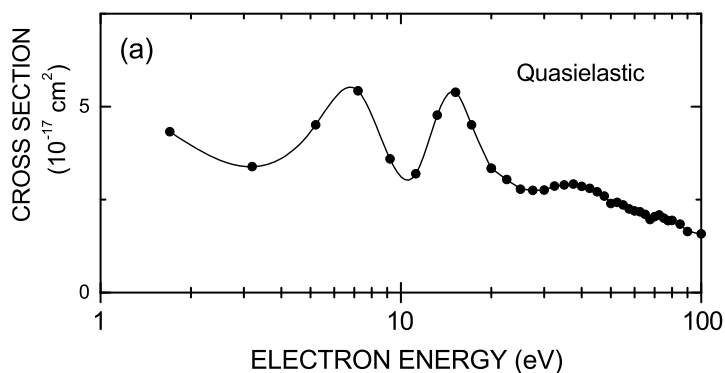


Fig. 1.5 Energy dependence of the integral cross sections of water given by the sum of the elastic and translational phonon $\nu_{T'}$ and $\nu_{T''}$ modes (Adapted from Michaud et al. (2003), © 2018 Radiation Research Society.)

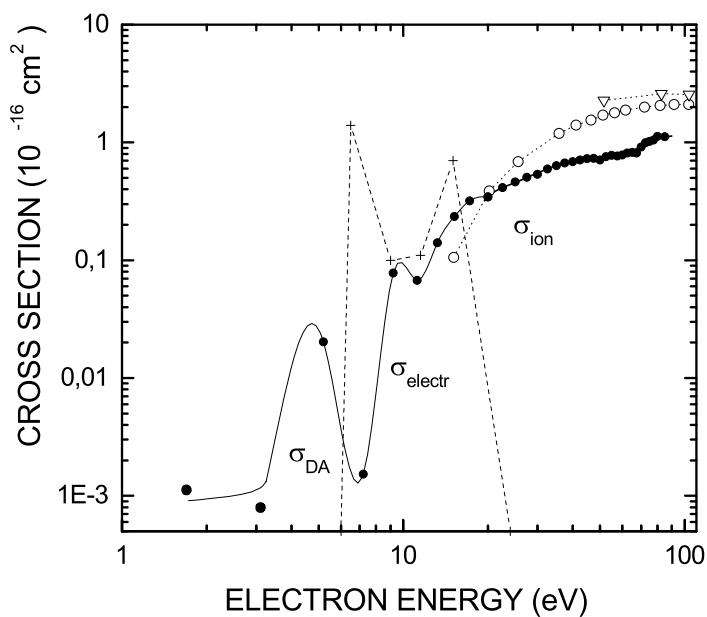


Fig. 1.6 Integral cross sections for dissociative electron attachment (DA), electronic excitation (electr) and ionization (ion) of amorphous ice (Reproduced from Michaud et al. (2003), © 2018 Radiation Research Society.)

of the 2B_1 transient negative ion state. Following this feature, there is a steady rise above 7.5 eV attributed to the electronic excitation and ionization processes.

Although the two-stream analysis of Michaud et al. considers electron scattering from individual isolated targets, the CSs derived from their work necessarily contains interference effects that modify the CS values. Since in amorphous ice, constructive or destructive interference is short range, the extracted values can be regarded as ensemble-averaged cross sections per scattering site, in the sense defined by Lekner and Cohen (Lekner 1967; Cohen and Lekner 1967) and Davis et al. (1971). Here, the scattering sites can be seen as those in the two-stream multiple scattering analysis. The extracted CSs include interference and screening effects originating from the surrounding molecules (Michaud and Sanche 1987a), which should be most pronounced in the elastic and quasi-elastic scattering CSs. In a first approximation, the ensemble-averaged integral quasideelastic scattering CS per scatterer can be expressed as

$$\sigma_{qe}(E_0) = \frac{m^2}{4\pi^2 h^4} \int_0^{2\pi} \int_0^\pi |V(K)|^2 S(K) \sin \theta d\theta d\varphi \quad (1.3)$$

where m is the reduced mass of the particle, $S(K)$ is the static structure factor of amorphous ice and $V(K)$ is the electron-molecule attraction potential. In the case of amorphous ice, the expression clearly shows that the gas-phase CSs are modulated by a structure factor taking into account short-range order diffraction. In fact, Michaud et al. have been able to correlate the results of Fig. 1.5 to the energy dependence of the structure factor (Michaud et al. 2003), showing that diffraction is occurring. Moreover, the structure factor decreases considerably with energy and, due to coherence, strongly reduces the quasi-elastic scattering CS below about 3 eV. In addition, Michaud et al. pointed out that a forward elastic scattering term is not contributing to the electron-beam attenuation in the two-stream analysis, which would make the derived elastic CSs, and thus the measured total CSs, smaller than they should be in amorphous ice. From this argument, Nikjoo et al. (2016) suggested to increase the published elastic CSs by factors derived from transport mean free paths, to produce values closer to those of the gas phase. Such factors are probably not needed for two reasons: (1) Eq. (1.3) can account for large reductions in the quasi-elastic CSs at low energies and (2) the higher momentum terms in the expansion of the scattered electron wavefunction are absent in the condensed phase due to the presence of neighboring molecules. This condition necessarily reduces the elastic and quasi-elastic scattering probabilities at each scattering site. Finally, we note that in similar investigations with disordered solid Xe films, the structure factor has been observed experimentally to reduce the gas-phase CS values by about an order of magnitude between 3 and 9 eV (Bader et al. 1982).

If CS values of amorphous ice are to be used for modelling liquid water, then they probably have to be increased to account for the reduction of coherence due

to enhancement of thermal phonon and vibrational excitation in the liquid phase, the different geometrical arrangement of the molecules and hydrogen bonding. A reasonable amplification factor of 2 was introduced empirically by Meesungnoen et al. (2002), when they applied the CSs of amorphous ice to their simulation of LEE elastic scattering in a water solution.

1.2.3.2 DNA Backbone: Deoxyribose and Phosphate Group

Figure 1.1 shows the structure of a DNA strand. The DNA backbone is comprised of two molecules: deoxyribose generally called the sugar group and the phosphate group. The most studied molecular analog of deoxyribose is tetrahydrofuran (THF— C_4H_8O) (Lepage et al. 1998; Antic et al. 1999, 2000; Breton et al. 2004; Bouchiha et al. 2006; Sulzer et al. 2006; Jäggle et al. 2006; Park et al. 2006). THF is a convenient model, since it represents the furyl ring at the center of the deoxyribose molecule, as seen in Fig. 1.7a). Lemelin et al. (2016b) measured absolute vibrational CSs for 1–19 eV electron scattering from THF using HREELS and the simple collision model described in Sect. 1.2.2.2. The vibrational CSs values were found to lie within the 10^{-17} cm² range. Figure 1.8 shows the energy dependence of the CSs. Highlighted in color are four features observed by the authors around 2.5, 4.5, 9.5 and 12.5 eV, which were all attributed to resonances. The maximum around 2.5 eV had not previously been predicted in theoretical calculations, but has been inferred in gas-phase studies (Allan 2007). Thus, its observation in this solid-phase study confirmed its existence and was attributed to the formation of a shape resonance. Considering the broadness of the other structures, the authors attributed these to shape or core-excited shape resonances. Pure core-excited resonances produce sharp features in scattering CSs; thus, they are rarely seen in vibrational CSs (Sanche and Schulz 1972). The three resonances at higher energy were also predicted or observed in other previous theoretical or experimental studies on LEEs interactions with THF (Lepage et al. 1998; Antic et al. 1999; Breton et al. 2004; Zecca et al. 2005; Trevisan et al. 2006; Winstead and McKoy 2006; Tonzani and Greene 2006; Allan 2007).

Absolute CSs were also measured for electronic excitations of THF by HREELS (Lemelin et al. 2016a). Spectra for energy losses between 6 and 11.5 eV were recorded

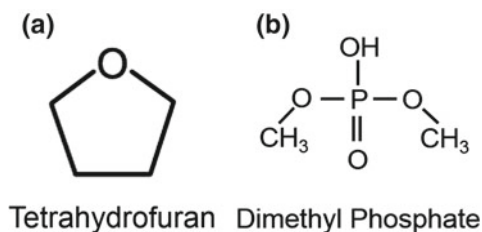


Fig. 1.7 Chemical structure of model molecules representing the sugar **a** Tetrahydrofuran (THF) and the phosphate group **b** Dimethyl Phosphate (DMP) of DNA

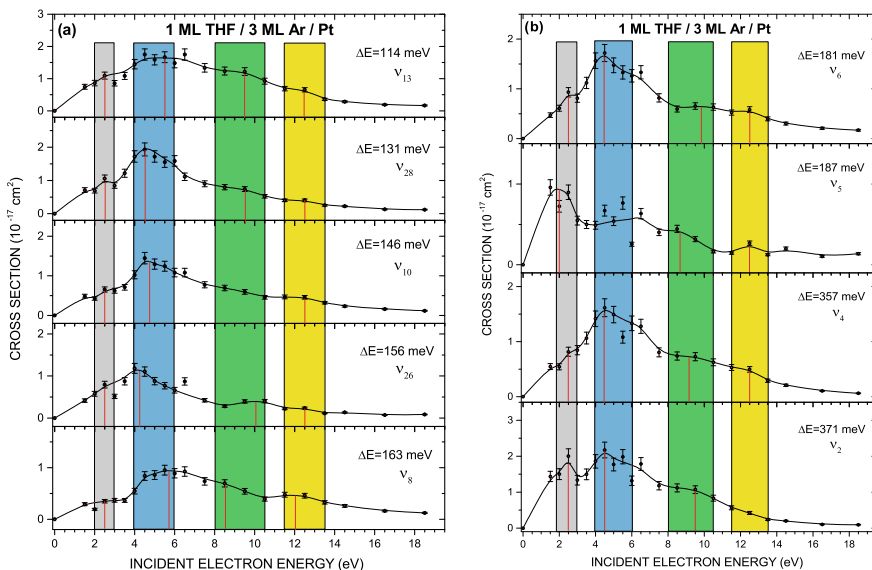


Fig. 1.8 Energy dependence of the absolute cross sections for various vibrational modes of tetrahydrofuran (THF) (Reproduced from Lemelin et al. (2016b), with the permission of AIP Publishing.)

for incident energies between 11 and 16 eV and a representative spectrum is shown in Fig. 1.9. Since unlike vibrational spectra, there were no readily identifiable energy loss peaks in the electronic spectra, fitting these latter with Gaussians functions to represent discrete electronic states, was unjustified. Instead, each spectrum was divided in five regions of 1 eV width and one remaining region of width 0.5 eV. Then, absolute CS values for each energy loss interval could be obtained from the area of the corresponding region using Eq. (1.1). The values of the CSs for each region lie within the 10^{-17} cm^2 range and are plotted as functions of E_0 in Fig. 1.10. No electron-resonance effects can be discerned in this figure. Furthermore, the CS values are lower than those measured for DNA bases or bases derivatives (see next subsection). These results are consistent with previous theoretical and experimental studies, which suggest that initial capture of an electron by DNA occurs on a base rather than on the backbone; subsequently, electron transfer to the backbone, can break a DNA strand (Barrios et al. 2002; Martin et al. 2004; Afatooni et al. 2006; Sanche 2010; Caron and Sanche 2011).

A useful model of the phosphate group of DNA is dimethyl phosphate (DMP) shown in Fig. 1.7b). DMP consists of a phosphate group linked to two CH_3 which is rather like the DNA phosphate group that is linked to a CH and a CH_2 . Absolute vibrational CSs have been measured for condensed DMP (Lemelin et al. 2017) using HREELS with the same technique and method described earlier (single collision treatment). They were acquired for electrons with incident energy of 1–18 eV. An example of EEL spectra of DMP is shown in Fig. 1.3. Each vibrational structure was identified and each spectrum was fitted to extract CSs. The energy dependence

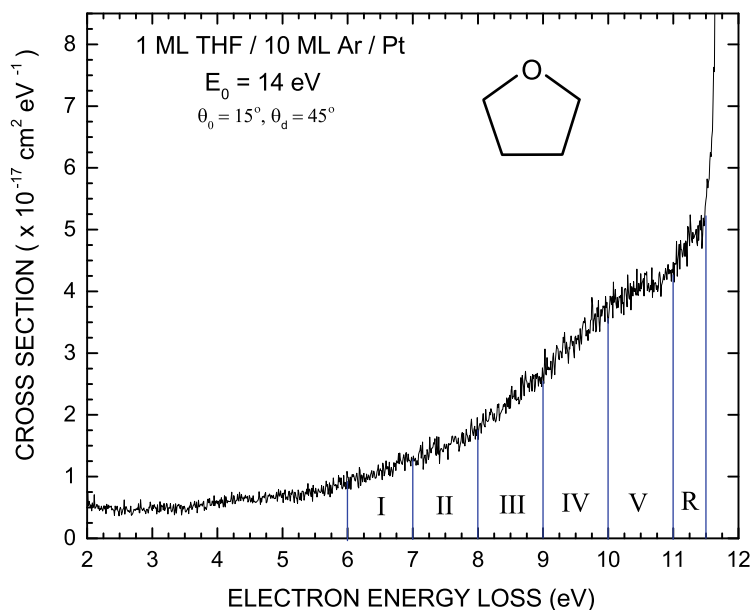


Fig. 1.9 EEL spectrum for electronic excitations of tetrahydrofuran recorded with incident electrons of 14 eV. No structure was clearly observed and fitting this spectrum with Gaussian distributions was not attempted. The spectrum is divided into 6 regions within which cross section values were extracted (Reproduced from Lemelin et al. (2016a), with the permission of AIP Publishing.)

of absolute vibrational CSs are presented in Fig. 1.11. It is possible to discern two strong electron resonances at low energies near 2 and 4 eV and two others of weaker magnitudes at higher energies near 7 and 12 eV. These structures can be compared to other resonances predicted or observed in prior theoretical and experimental studies with various phosphate group models (Pan and Sanche 2006; König et al. 2006; Aflatooni et al. 2006; Tonzani and Greene 2006; Burrow et al. 2008; Winstead and McKoy 2008; Bryjko et al. 2010; Bhaskaran and Sarma 2015). These resonances are likely pure shape resonances due to the broadness of the structures in the CS data.

1.2.3.3 DNA and RNA Bases Analogs

The DNA bases (or analogs) thymine, cytosine, adenine and pyrimidine have been studied with HREELS. Their absolute inelastic CSs, generated from the HREELS spectra, with the method described in Sect. 1.2.2.2 using the single collision model (Eq. (1.1)) are presented in this section.

Figure 1.12 shows the energy dependence of absolute vibrational CSs of condensed thymine for electrons with incident energies between 1 and 12 eV (Levesque et al. 2003). As seen, there is a common 2 eV wide structure around 4 eV for all of the vibrational modes of thymine. The maximum CS values is about $1.6 \times 10^{-16} \text{ cm}^2$

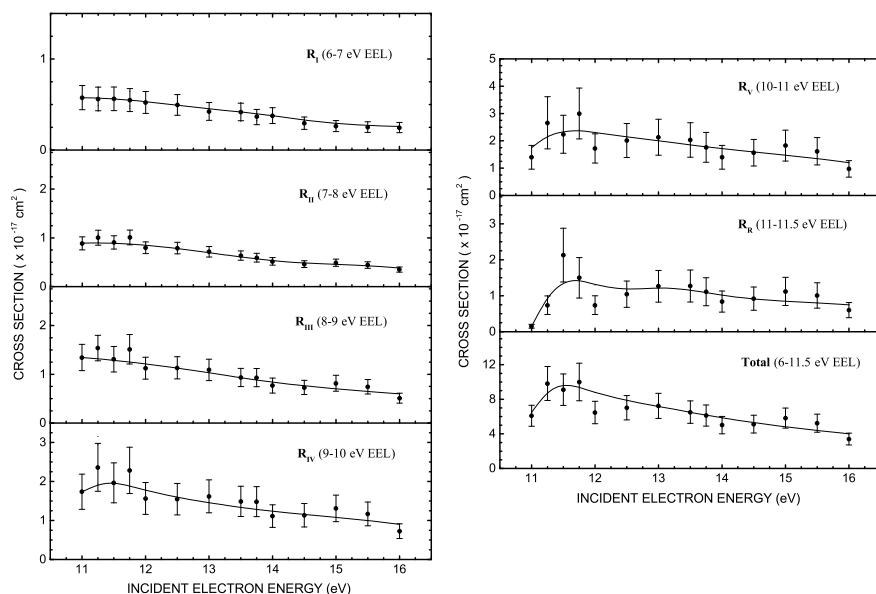


Fig. 1.10 Incident-electron-energy dependence of absolute cross sections for electronic excitations of THF in the 6 regions defined in the EEL spectrum of Fig. 1.9. The last graph represents the total cross section from the sum of energies losses from all regions (Reproduced from Lemelin et al. (2016a), with the permission of AIP Publishing.)

for the breathing mode (EEL of ~ 95 meV) at 4 eV and all the other CSs lie within the 10^{-17} cm² range. The feature at 4 eV is explained by the creation of a TNI by temporary trapping the incoming electron into the π^* orbital of thymine at 4.05 eV (Aflatooni et al. 1998) and its decay into vibrational excitations. The absolute CSs for electronic excitations of thymine have also been measured (Levesque et al. 2005a). The authors observed four electronic electron energy losses between 3.5 and 9 eV. The energy dependence of the absolute CSs associated with these modes are presented in Fig. 1.13. They observe two resonances: at low-energy around 5 eV with a CS of 2.9×10^{-17} cm² and at 8 eV with a maximum CS reaching 1.36×10^{-16} cm². These structures are related to the formation of TNIs and they correspond to the resonances at the same energies that have been reported in the O⁻ yield function from DEA to thymine in the gas phase (Huels et al. 1998). Thus, TNIs associated with the fragmentation of thymine can also decay into its electronic states.

In the case of cytosine (Michaud et al. 2012), absolute vibrational CSs have been reported for vibrational modes. The CS values are shown as a function of electron energy in Fig. 1.14, where four structures appear at 1.5, 3.5, 5.5 and 12 eV. These were also interpreted as arising from TNI formation by comparison with the features found in electron transmission spectra (Aflatooni et al. 1998) and DEA yield functions (Denifl et al. 2004; Aflatooni et al. 2006). The first two enhancements at 1.5 and 3.5 eV correspond to resonances found at 1.5 and 4.5 eV in gas-phase transmission

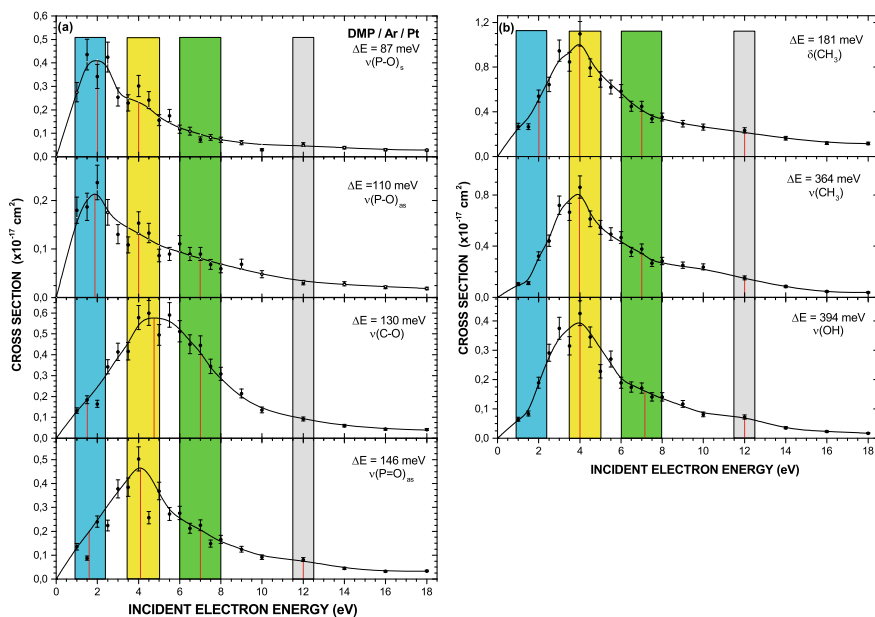
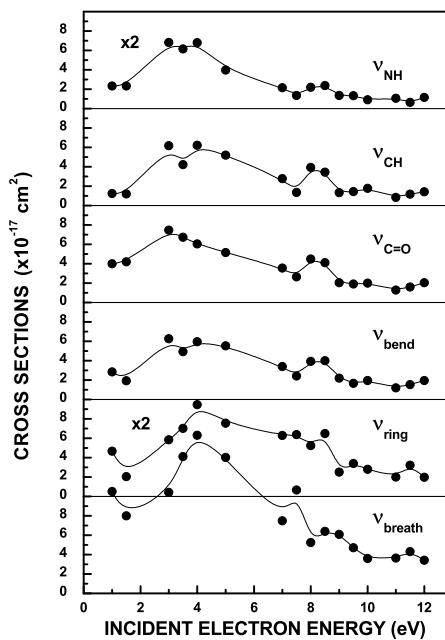


Fig. 1.11 Variation with electron collisional energy of the vibrational excitation cross sections of DMP (Reproduced from Lemelin et al. (2017), with the permission of AIP Publishing.)

Fig. 1.12 Absolute cross sections for different vibrational excitation modes of thymine as a function of electron incident energy (Reproduced with permission from Lévesque et al. (2003), with permission from Elsevier.)



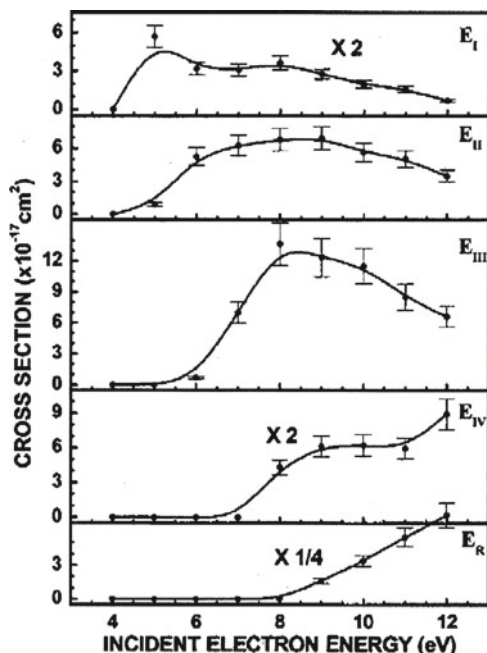


Fig. 1.13 Electron energy dependence of absolute cross sections for various electronic excitations (E_i) of thymine induce by 4–12 eV electron scattering (Reproduced from Lévesque et al. (2005a), with the permission of AIP Publishing.)

data. These resonances were ascribed to shape resonances. DEA studies on gas-phase cytosine also revealed three related resonances in the ranges of 1.5–2.1 eV, 5.2–6.8 eV, and 9.5–10.9 eV. It was then concluded that the TNIs responsible for these enhancements process have certain probabilities to decay into vibrational modes of cytosine. In addition, the absolute CSs for electronic excitations of cytosine have been measured (Bazin et al. 2010) for electron with energies between 5 and 18 eV. The authors observed eight electronic modes in HREEL spectra, from which they extracted the absolute CSs. They are all shown in Fig. 1.15. In the energy dependence of the CSs, they observe two resonances: a common maximum around 6 eV for the two lower excited states and another one near 10 eV. These TNIs correspond to the core-excited electron resonances found at the same energies (5.2–6.8 eV and 9.5–10.9 eV) in the gas-phase DEA channel (Denifl et al. 2004). The authors also measured the absolute CSs for four of the highest occupied orbitals of cytosine lying around 8.55, 9.21, 9.83 and 11.53 eV. The sum of their CSs are presented in Fig. 1.15 in the bottom right panel. This sum reaches a maximum of $8.1 \times 10^{-16} \text{ cm}^2$ for incident electrons of 13 eV. As it appears in this graph, the theoretical calculations for the total ionization CSs are smaller below 15 eV, than the experimental values for electronic excitation. This result illustrates the relative importance of TNIs and their decay into electronic excitation at low energy.

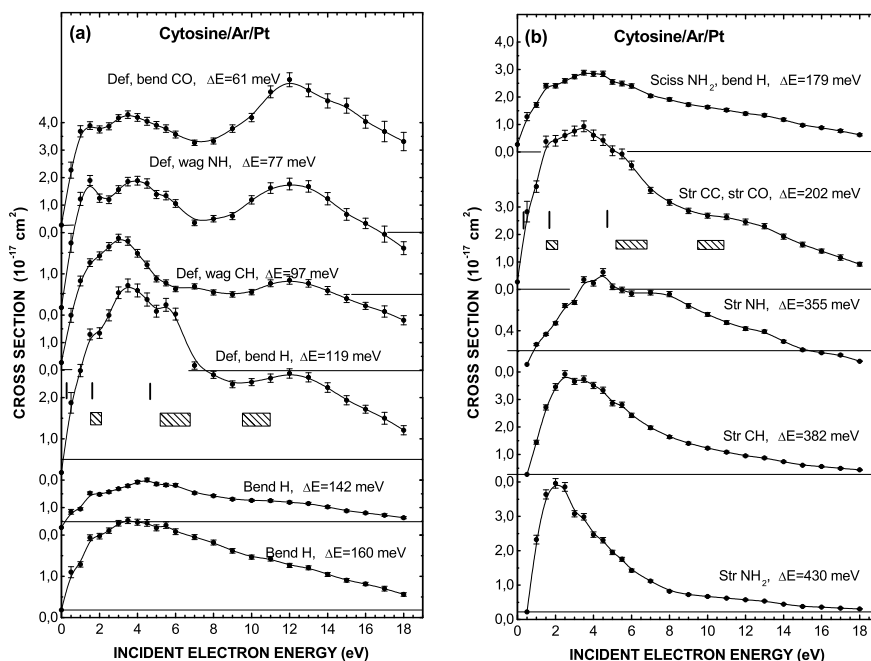


Fig. 1.14 Absolute cross sections for vibrational excitations of cytosine induced by 0.5–10 eV electron scattering (Reproduced from Michaud et al. (2012), with the permission of AIP Publishing.)

The base adenine is another important DNA constituent. Its vibrational excitation CSs measured (Panajotović et al. 2007) in the condensed phase by HREELS are shown in Fig. 1.16, where it is possible to observe a wide resonance for each vibrational mode in the range 3–5 eV. Also, a weak shoulder around 7 eV is present in the energy dependence of the vibrational absolute CSs for ring deformations and bending of hydrogen atoms. Shown in Fig. 1.17 is the energy dependence of the absolute CSs for electronic excitation by 8–12 eV electrons; a resonance can be seen around 10 eV in all decay channels.

The pyrimidine molecule has also been studied with HREELS in order to extract absolute vibrational and electronic excitation CSs (Levesque et al. 2005b). Pyrimidine is a relevant biomolecule or model to investigate its three nucleobases derivatives: cytosine, thymine and uracil. The energy dependence of the absolute vibrational CSs of pyrimidine is presented in Fig. 1.18 for five vibrational modes. As seen, the CSs exhibit a common 2 eV wide maximum in the 4–5 eV range. A shape resonance around 4 eV has been identified in electron transmission experiments of gas phase pyrimidine (Nenner and Schulz 1975) and compares well with energies of the structures in Fig. 1.18. In the ν_{9a} , ν_{18b} and ν_{CH} excitation modes, there is also a structure around 6 eV, which compares favorably with the energy of a resonance observed in the same transmission experiment (Nenner and Schulz 1975), as well as in the

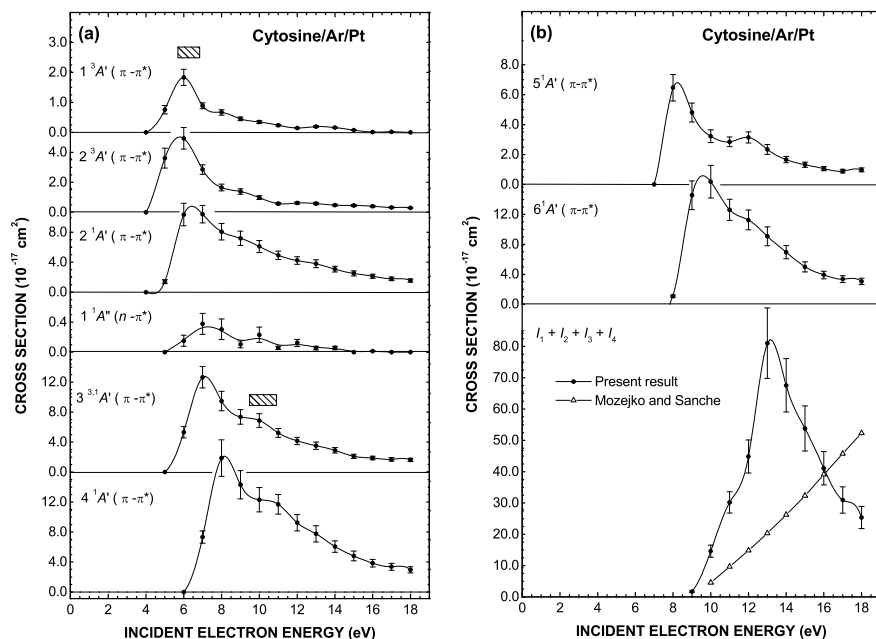


Fig. 1.15 Electron impact energy dependence of the cross sections to excite various electronic modes of cytosine within the range 4–15 eV (Reproduced from Bazin et al. (2010), with the permission of AIP Publishing.)

vibrational CSs of benzene (a closely related molecule to pyrimidine) found around 8 eV in the gas phase. This maximum has also been ascribed to the formation of a shape resonance (Burrow et al. 1987; Allan 1989; Arfa and Tronc 1990; Allan and Andric 1996). Finally, the numerical values of electronic excitation CSs of pyrimidine are presented in Table 1.1; there is no observable structure in energy dependence (Levesque et al. 2005b).

1.3 Nanodosimetry Using Absolute Cross Sections from HREELS Measurements

A simple application of LEE absolute CSs is presented in this section. This example demonstrates the relevance and potential for the determination of local doses by use of the absolute CSs values presented in the previous section. As mentioned in the introduction, new modalities such as TRT are currently being developed to target cancer cells with radiolabeled molecules and create local toxic and lethal doses to these cancer cells, while preserving healthy cells (Hayes 2017; Rezaee et al. 2017). TRT needs nanodosimetric modelling, which requires CSs (Itikawa and Mason 2005; Vinodkumar et al. 2006; Champion 2010; Anzai et al. 2012; Jones et al.

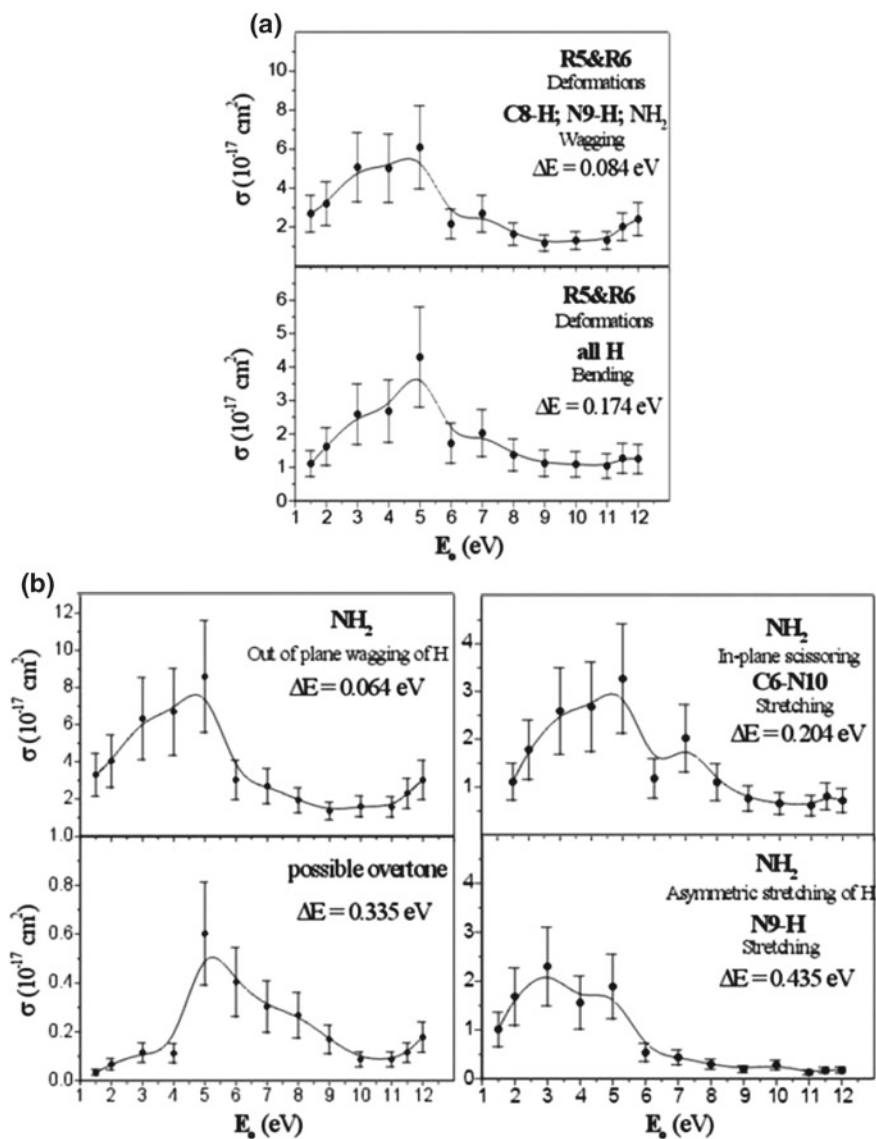


Fig. 1.16 Incident-electron-energy dependence of absolute cross sections for vibrational excitations of adenine within the range 1.5–12 eV. (Reproduced from Panajotović et al. (2007), with the permission of the Royal Society of Chemistry.)

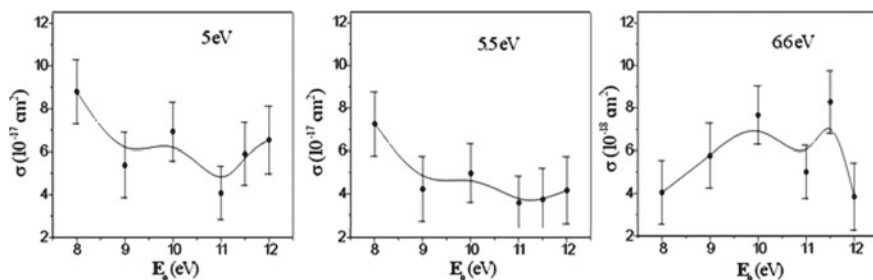
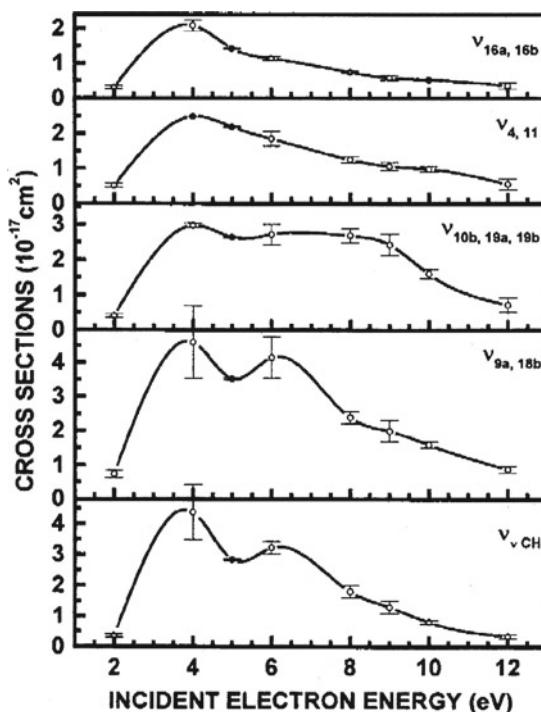


Fig. 1.17 Energy dependence of absolute cross sections for various electronic excitations of adenine induced by 8–12 eV electron scattering (Reproduced from Panajotović et al. (2007), with the permission of the Royal Society of Chemistry.)

Fig. 1.18 Absolute vibrational excitation cross sections of pyrimidine induced by electron scattering in the range 2–12 eV (Reproduced from Lévesque et al. (2005b), with the permission of AIP Publishing.)



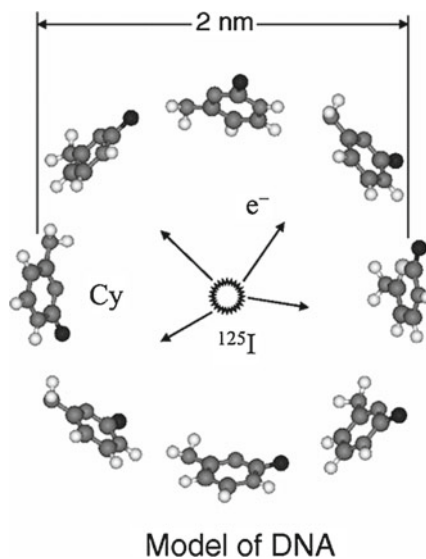
2012) to predict the energy deposited by LEEs and link that energy to radiobiological effectiveness (Nikjoo and Lindborg 2010).

An exclusive application of LEE absolute CSs was performed by Michaud et al. (2013). The goal was to present a simple method to assess the energy deposited near the site of a common targeting radioisotope (i.e., ^{125}I), using cytosine as a simple model for DNA. Figure 1.19 shows the geometry of a 1-nm-radius (R) cytosine shell with a ^{125}I nuclei lying at the center, which was used for calculations. The

Table 1.1 Cross sections (10^{-17} cm^2) at different incident energies E_0 (eV) for electrons exciting electronic states (E_i) of pyrimidine (Reproduced from Lévesque et al. (2005b), with the permission of AIP Publishing.)

E_0	Electronic modes				
	E_I	E_{II}	E_{III}	E_{IV}	E_R
E_0	σ				
6	3.1	1.3
8	4.8	6.6	9.9
10	2.5	3.5	11.0	...	6.6
12	0.82	1.2	3.8	6.0	12.9

Fig. 1.19 Model for calculating nanoscopic doses imparted by LEEs, emitted from a radionuclide, to nearby biomolecules. In this example, a one-nm-radius spherical shell of cytosine is irradiated by a ^{125}I nuclei at its center (Reproduced with permission from Michaud et al. (2013), Copyright 2018 by the American Physical Society.)



absolute vibrational, electronic and ionization CSs of cytosine were entered into these calculations to estimate the energy deposited by LEEs into the cytosine shell following the decay of a ^{125}I nuclei.

The authors based their estimate of deposited dose on the energy spectrum of Auger electrons $N(E_0)$ released by the decay of ^{125}I as shown in Table 1.2. To generate the dose absorbed by the cytosine shell on such a nanoscopic scale, they employed the MIRD schema and the following equation (Loevinger et al. 1991):

$$S_{k \leftarrow h} = \frac{1}{4\pi R^2 m_{cy}} \sum_{E_{0,i}} N(E_0) \sigma_i(E_0) \epsilon_i. \quad (1.4)$$

Here $S_{k \leftarrow h}$ is the absorbed dose of target region k produced by a unit nuclear decay in the source region h (i.e., at the center of the cytosine shell) and ϵ_i is the energy of the

Table 1.2 Frequency distribution $N(E_0)$ as a function of the energy in eV (E_0) of the Auger electrons for a single nuclear decay of a single ^{125}I atom (Reproduced with permission from Michaud et al. (2013), Copyright 2018 by the American Physical Society.)

E_0	$N(E_0)$																		
	2	0.3	0.08	0.5	0	0.15	0.1	0.2	0.1	0.1	0.07	0.08	0.1	0.15	0	0.07	0.1	0.04	0.04
	1	2	3	4	5	6	7	8	9	10	11	12	13	14	15	16	17	18	

excitation mode i of cytosine (i.e., vibrational, electronic excitation or ionization). $\sigma_i(E_0)$ is the integral CS to deposit energy ϵ_i into the excitations mode i and m_{cy} is the molecular mass of cytosine. The product $\sigma_i(E_0)\epsilon_i$ corresponds to the stopping CS (SCS) (Inokuti 1996). The SCSs can be calculated from the absolute CSs presented earlier in this chapter for cytosine; its energy dependence is presented in Fig. 1.20. The SCSs in this figure are divided in three categories for each type of excitations: vibrational, electronic and ionization. Using these SCSs as well as the frequency distribution of LEEs ($N(E_0)$) in Eq. (1.4), it is possible to calculate the dose absorbed by the cytosine shell for the decay of a ^{125}I at its center. The authors found that taking into account only the distribution of 0–18 eV electrons emanating from iodine, from a single decay of the isotope, 2.5, 31 and 45.5 kGy were absorbed by the shell due to vibrational and electronic excitations and ionization, respectively. Of course, the work of Michaud et al. only gives information on the energy deposited in the cytosine shell and does not correlate this quantity to possible damages made to the molecule in DNA, nor does it predicts the biological effects of this dose. Rather, this work provides an example of the nanodosimetry possible using absolute CSs and clearly demonstrates that, over a short range, LEEs can deposit an enormous dose.

The method was further elaborated by Rezaee et al. (2014), in a model of double-stranded DNA having the geometry shown in Fig. 1.19. These authors could correlate the absorbed dose deposited by LEEs to damage (Rezaee et al. 2014) in a 1 nm radius shell of double-stranded DNA with a ^{125}I nuclei at its center. They used all experimentally measured absolute CSs then available (supplemented with theoretical

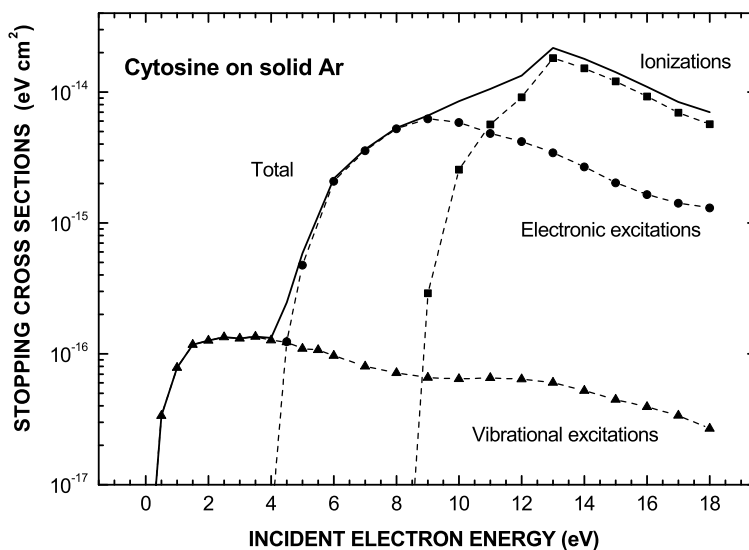


Fig. 1.20 Stopping cross sections for the vibrational and electronic excitations and ionizations of cytosine. These values were calculated from absolute cross sections of each process given in Figs. 1.14 and 1.15 (Reproduced with permission from Michaud et al. (2013), Copyright 2018 by the American Physical Society.)

data for unavailable CS) for DNA bases, THF and phosphate groups to model DNA strands of 8 nucleotides (4 base pairs). For a single decay of ^{125}I , the total dose absorbed by the 1 nm radius shell of hydrated and dry DNA was found to be about 272 and 205 kGy respectively, and resulted from the deposition of energy by LEEs via vibrational excitation, electronic excitation, and ionization. For hydrated DNA, the molecule was assumed to contain 20 water molecules per nucleotide. The energy range of LEEs considered was 5–18 eV.

In the same article, Rezaee et al. (2014) report damage CSs (DmCS) calculated from the energy dependence of the yields for the formation of SSBs and DSBs, which could be correlated to the efficiency of 5–18 eV Auger electrons (produced by the ^{125}I nuclei decay) to induce DNA strand breaks, in their 4-base DNA shell model. For a single nuclear decay of the radionuclide, the number of SSBs and DSBs induced by LEEs of energies between 5 and 18 eV was 0.5–0.02 respectively. This study amply demonstrated the short-range efficiency of LEEs in producing lethal cellular lesions. It also suggested that in nanometric volumes, the absorbed dose is no longer an appropriate physical parameter to represent biological effectiveness. In fact, the absorbed dose of LEEs in this study is 5 orders of magnitude larger than the dose absorbed in macro- and microscopic volumes, while the number of molecular lesions per unit dose is less than those in larger (macro- and microscopic) volumes (Goodhead 1994, 2006). However, the type of damage produced could have a greater impact at the biological level (e.g., cluster damages). In fact, since radiation interacts with matter in a stochastic way, a deterministic parameter like the absorbed dose has no meaning at the molecular level (Rezaee et al. 2014). For this reason, Rezaee et al. (2014) concluded that nanodosimetry and future radiotherapeutic modalities like TRT need to use both stopping and damage CSs, as biologically related physical parameters that can estimate the energy deposition and predict the damages at the nanometric level. Finally, these authors argued that their results illustrated how LEEs are as efficient as high-LET electrons and suggested that LEEs contribute considerably to the biological effects of radionuclides (Rezaee et al. 2014).

1.4 Future Trends

In Sect. 1.2.3, we presented absolute CSs for isolated fundamental units of DNA (i.e., each constituent was isolated from the others). When such species are combined into larger biomolecules, modifications of electron-molecule interactions are to be expected and thus also CSs values. Hence, the next logical step requires measurements of absolute CSs for LEEs scattering from larger biomolecules under more complex conditions. For example, it would be revealing to measure with HREELS the absolute CSs for a base linked to the deoxyribose (e.g., thymidine, cytidine, adenosine, etc.), and to compare the obtained CSs to those measured for each isolated constituent. It would give information on the effects of chemical bounding on the scattering process. Similarly, it would be interesting to investigate the effects of other molecules known to exist close to DNA in cells, for example water.

Rezaee et al. (2014) have previously discussed the effect of the presence of water molecules surrounding DNA. They refer to several studies (Rezaee et al. 2012; Boulanouar et al. 2013; Alizadeh and Sanche 2013), which have demonstrated that damage to DNA induced by LEEs is enhanced by the presence of water and oxygen. In recent years, a number of theoretical studies have incorporated additional water molecules into their calculations. For example, the review article of Kohanoff et al. (2017) discusses the effects microsolvation or solvation on electron-thymine interactions (Smyth and Kohanoff 2011; Smyth et al. 2014). It was shown (Smyth and Kohanoff 2011; Smyth et al. 2014) that as small a number as 5 water molecules linked to thymine by H-bonds, are sufficient to raise the energy required for dissociation of the molecule after the LEE attachment, relative to the gas phase. This phenomena has been observed experimentally with microhydrated uracil and thymine (Kočišek et al. 2016). One hypothesis to explain this result is that the DEA channel is suppressed due to the redistribution of internal energy (caging) by the fast energy transfer to solvent, which leads to the stabilization of the intact anion (Kočišek et al. 2016). Hence, it becomes crucial to study the effect of water on CSs for various DNA constituents by HREELS or other methods. Data obtained with biomolecules surrounded by water molecules will surely be more relevant and more representative of the biological reality.

In cells, DNA is also surrounded by and linked to proteins. Thus, the close proximity of proteins to DNA also provides an interest in studying experimentally, the variation in inelastic LEE-scattering CSs caused by protein constituents close to DNA, such as certain amino acids. Moreover, any estimate of the DNA damage produced would necessarily have to include that caused by the radiation-induced radicals in the amino acids. Thus, LEE-damage CSs are also needed for amino acids. CSs for gas-phase amino acids have already been reported (Scheer et al. 2007); Glycine has been the most studied amino acid (Gohlke et al. 2002; Ptasinska et al. 2003; Lafosse et al. 2006; Esmaili et al. 2017, 2018). However, the configuration of amino acids in biological media can differ considerably from that in the gas phase. Indeed, these molecules adopt the zwitterion configuration in the presence of water (McNaught 1997; Lafosse et al. 2006). This configuration is highly polarized and hence expected to induce significant changes to the gas-phase LEE CSs. Obviously, electron CSs for amino acid in the condensed phase are needed, particularly in the presence of water.

Ultimately, one would like to measure absolute LEE-CSs for an entire DNA strand with HREELS. This is not an easy task, but Vilar et al. (2008) were able to measure and identify sharp vibrational excitation in the HREEL spectra of well-organized self-assembled monolayers (SAM) of single DNA strand. However, no data treatment was attempted to extract either differential or absolute CSs from these measurements. To extract absolute CSs from HREEL data using the single collision model, molecules must be randomly oriented on an inert surface (as explained in Sect. 1.2.2.2), preferably as a single or sub-monolayer film, which is definitely not the case of a DNA SAM. Hence, with this configuration, it is not possible to extract absolute CSs for DNA from HREEL spectra with our present formulation

of scattering within molecular and atomic solids. With present HREEL systems, it is not possible to sublime DNA (under UHV) without breaking or damaging the molecule. In order to ultimately obtain condensed phase LEE-CSs for a DNA strand, more sophisticated methods of volatilisation must be implemented to create randomly oriented films of undamaged and condensed DNA strands. Laser-Induced Acoustic Desorption (LIAD) may be suitable for constructing such films, since it can sublime large neutral biomolecules into the gas phase without damage (Golovlev et al. 1997; Shea et al. 2007). This method consists of depositing a solution of sample molecules (e.g., oligonucleotides) on a thin titanium foil and introducing this latter into an UHV chamber, where its reverse side is irradiated with a pulsed ND:YAG laser (Bald et al. 2008). The acoustic waves generated by the short laser pulse, travel to the coated side of the titanium foil, leading to the soft desorption of neutral and intact complex biomolecules (Golovlev et al. 1997; Shea et al. 2007). Bald et al. (2008) used LIAD method to vaporize thymidine in order to measure anion yields from DEA to this molecule in the gas-phase. They showed that no fragmentation was induced by LIAD. Thus, LIAD may have the potential to vaporize oligonucleotides, which could then be condensed onto a substrate. If LIAD is incorporated into a HREELS system, it could provide a powerful instrument to measure absolute CSs for LEE scattering from DNA.

1.5 Conclusion

HREELS is a powerful tool for studying the interactions of LEEs with biomolecules. This type of spectroscopy permits the extraction of absolute CSs for LEE energy losses to phononic, vibrational and electronic excitations. These CSs are required in nanodosimetric models related to the interaction of LEEs with biological media, as presented in this chapter. Dosimetric modelling is particularly needed for clinical modalities, where radionuclides are injected directly into a tumour or intravenously with a carrier molecule capable of targeting cancer cells or/and their nucleus. In these cases, to deliver a toxic and lethal dose directly and almost exclusively to cancer cells, the energy imparted at the nanoscopic level by the secondary species (e.g., LEEs) must be estimated. In this chapter, we have presented absolute CSs for the scattering of LEEs from DNA fundamental units and water molecules in the condensed phase.

Apart from the measurements of absolute LEE CSs for DNA subunits by HREELS, CSs for lethal cellular damages such as cross links, SSBs, DSBs and other cluster lesions can be measured experimentally using other techniques. These include X-rays photoelectrons spectroscopy (Klyachko et al. 1999; Briggs and Seah 2003), electron stimulated desorption (Abdoul-carime et al. 2000; Dugal et al. 2000), atomic force microscopy (AFM) (Bald and Keller 2014; Keller et al. 2015; Rackwitz et al. 2016, 2017; Schürmann et al. 2017) and electrophoresis (Rezaee et al. 2012). The increased availability of such CSs implemented in MC simulations should help reaching a fundamental understanding of the consequences of the passage of radia-

tion into cells and knowing more precisely the energy deposited and damage induced at the molecular level in cells.

While the CSs presented here are of crucial importance for radiotherapy, they may also have a positive impact in other related fields. Indeed, these absolute CSs could be used in radioprotection to estimate the risk of any radiation source on human health. This includes estimating the energy deposited in modalities using ionizing radiation for imaging body structures, tissues and biochemical processes (e.g. X-ray radiography or positron emission tomography (Brix et al. 2005; Einstein et al. 2007; Eisenberg et al. 2011; Fazel et al. 2016)). CSs for LEE interactions with biomolecules are also of relevance to space radiobiology. Cosmic radiations are among the greatest obstacles to manned interplanetary missions and the assessment and prediction of doses absorbed by astronauts are based on dosimetric models, including track-structure Monte Carlo simulations (Nikjoo et al. 2006, 2016; Dingfelder 2006; Plante and Cucinotta 2009; Durante and Cucinotta 2011; Kennedy 2014; Durante 2014). Exposure to high-energy galactic cosmic rays in space corresponds to a low dose rate (Zeitlin et al. 2013; Hassler et al. 2014), making it difficult to determine the biological effects from this parameter alone (Cucinotta et al. 2011; Chancellor et al. 2014; Norbury et al. 2016; Slaba et al. 2016). LEE CSs values should aid in this fundamental comprehension, arising from models, to correlate the energy deposition at the nanoscopic level within cells to the biological effects of low-dose exposures.

References

- Abdoul-carime AH, Dugal P, Sanche L (2000) Damage induced by 1–30 eV electrons on thymine- and bromouracil-substituted oligonucleotides linked references are available on JSTOR for this article: damage Induced by 1–30 eV electrons on thymine- and bromouracil-substituted oligonucleotides. *Radiat Res Soc* 153:23–28
- Aflatooni K, Gallup GA, Burrow PD (1998) Electron attachment energies of the DNA bases. *J Phys Chem A* 102:6205–6207. <https://doi.org/10.1021/jp980865n>
- Aflatooni K, Scheer AM, Burrow PD (2006) Total dissociative electron attachment cross sections for molecular constituents of DNA. *J Chem Phys* 125:54301. <https://doi.org/10.1063/1.2229209>
- Alizadeh E, Sanche L (2013) Role of humidity and oxygen level on damage to DNA induced by soft X-rays and low-energy electrons. *J Phys Chem C* 117:22445–22453. <https://doi.org/10.1021/jp403350j>
- Allan M (1989) Study of triplet states and short-lived negative ions by means of electron impact spectroscopy. *J Electron Spectros Relat Phenomena* 48:219–351. [https://doi.org/10.1016/0368-2048\(89\)80018-0](https://doi.org/10.1016/0368-2048(89)80018-0)
- Allan M (2007) Absolute angle-differential elastic and vibrational excitation cross sections for electron collisions with tetrahydrofuran. *J Phys B: At Mol Opt Phys* 40:3531–3544. <https://doi.org/10.1088/0953-4075/40/17/020>
- Allan M, Andric L (1996) Σ^* resonances in electron impact-induced vibrational excitation of N-propane, cyclopropane, ethylene oxide, cyclopentane, and cyclohexane. *J Chem Phys* 105:3559–3568. <https://doi.org/10.1063/1.472819>
- Alloni D, Campa A, Friedland W et al (2012) Track structure, radiation quality and initial radiobiological events: considerations based on the PARTRAC code experience. *Int J Radiat Biol* 88:77–86. <https://doi.org/10.3109/09553002.2011.627976>

- Antic D, Parenteau L, Lepage M, Sanche L (1999) Low-energy electron damage to condensed-phase deoxyribose analogues investigated by electron stimulated desorption of H— and electron energy loss spectroscopy. *J Phys Chem B* 103:6611–6619. <https://doi.org/10.1021/jp990686l>
- Antic D, Parenteau L, Sanche L (2000) Electron-stimulated desorption of H— from condensed-phase deoxyribose analogues: dissociative electron attachment versus resonance decay into dipolar dissociation. *J Phys Chem B* 104:4711–4716. <https://doi.org/10.1021/jp000206m>
- Anzai K, Kato H, Hoshino M et al (2012) Cross section data sets for electron collisions with H₂, O₂, CO, CO₂, N₂O and H₂O. *Eur Phys J D* 66:36. <https://doi.org/10.1140/epjd/e2011-20630-1>
- Arfa MB, Tronc M (1990) Symmetry selection rules vs. vibronic coupling in resonant selective vibrational excitation of polyatomic molecules by electron impact. *J Electron Spectros Relat Phenomena* 50:117–128. [https://doi.org/10.1016/0368-2048\(90\)80013-Z](https://doi.org/10.1016/0368-2048(90)80013-Z)
- Arumainayagam CR, Lee HL, Nelson RB et al (2010) Low-energy electron-induced reactions in condensed matter. *Surf Sci Rep* 65:1–44. <https://doi.org/10.1016/j.surfrep.2009.09.001>
- Bader G, Perluzzo G, Caron LG, Sanche L (1982) Elastic and inelastic mean-free-path determination in solid xenon from electron transmission experiments. *Phys Rev B* 26:6019–6029. <https://doi.org/10.1103/physrevb.26.6019>
- Bader G, Chiasson J, Caron LG et al (1988) Absolute scattering probabilities for subexcitation electrons in condensed H₂O. *Radiat Res* 114:467–479. <https://doi.org/10.2307/3577118>
- Bald I, Keller A (2014) Molecular processes studied at a single-molecule level using DNA origami nanostructures and atomic force microscopy. *Molecules* 19:13803–13823. <https://doi.org/10.3390/molecules190913803>
- Bald I, Dąbkowska I, Illenberger E (2008) Probing biomolecules by laser-induced acoustic desorption: electrons at near zero electron volts trigger sugar-phosphate cleavage. *Angew Chemie Int Ed* 47:8518–8520. <https://doi.org/10.1002/anie.200803382>
- Barrios R, Skurski P, Simons J (2002) Mechanism for damage to DNA by low-energy electrons †. *J Phys Chem B* 106:7991–7994. <https://doi.org/10.1021/jp013861i>
- Bass AD, Sanche L (1998) Absolute and effective cross-sections for low-energy electron-scattering processes within condensed matter. *Radiat Environ Biophys* 37:243–257. <https://doi.org/10.1007/s004110050125>
- Bauer E (1994) Low energy electron microscopy. *Reports Prog Phys* 57:895–938
- Bazin M, Michaud M, Sanche L (2010) Absolute cross sections for electronic excitations of cytosine by low energy electron impact. *J Chem Phys* 133:155104. <https://doi.org/10.1063/1.3505301>
- Bennett CJ, Kaiser RI (2007) On the formation of glycolaldehyde (HCOCH₂OH) and methyl formate (HCOOCH₃) in interstellar ice analogs. *Astrophys J* 661:899–909. <https://doi.org/10.1086/516745>
- Bhaskaran R, Sarma M (2015) Low-energy electron interaction with the phosphate group in DNA molecule and the characteristics of single-strand break pathways. *J Phys Chem A* 119:10130–10136. <https://doi.org/10.1021/acs.jpca.5b08000>
- Bouchiha D, Gorfinkiel JD, Caron LG, Sanche L (2006) Low-energy electron collisions with tetrahydrofuran. *J Phys B: At Mol Opt Phys* 39:975–986. <https://doi.org/10.1088/0953-4075/39/4/021>
- Boudaïffa B, Cloutier P, Hunting D et al (2000) Resonant formation of DNA strand breaks by low-energy (3 to 20 eV) electrons. *Science* (80-) 287:1658–1660
- Boulanour O, Fromm M, Bass AD et al (2013) Absolute cross section for loss of supercoiled topology induced by 10 eV electrons in highly uniform/DNA/1,3-diaminopropane films deposited on highly ordered pyrolytic graphite. *J Chem Phys* 139:55104. <https://doi.org/10.1063/1.4817323>
- Breton S-P, Michaud M, Jäggle C et al (2004) Damage induced by low-energy electrons in solid films of tetrahydrofuran. *J Chem Phys* 121:11240. <https://doi.org/10.1063/1.1814632>
- Briggs D, Seah MP (2003) *Practical surface analysis: by auger and X-ray photoelectron spectroscopy*. Wiley
- Brix G, Lechel U, Glatting G et al (2005) Radiation exposure of patients undergoing whole-body dual-modality 18F-FDG PET/CT examinations. *J Nucl Med* 46:608–614

- Bryjko L, van Mourik T, Dora A, Tennyson J (2010) R-matrix calculation of low-energy electron collisions with phosphoric acid. *J Phys B: At Mol Opt Phys* 43:235203. <https://doi.org/10.1088/0953-4075/43/23/235203>
- Burrow PD, Michejda JA, Jordan KD (1987) Electron transmission study of the temporary negative ion states of selected benzenoid and conjugated aromatic hydrocarbons. *J Chem Phys* 86:9–24. <https://doi.org/10.1063/1.452598>
- Burrow PD, Gallup GA, Modelli A (2008) Are there π^* shape resonances in electron scattering from phosphate groups? *J Phys Chem A* 112:4106–4113. <https://doi.org/10.1021/jp7109143>
- Caron LG, Sanche L (2011) Theoretical studies of electron interactions with DNA and its subunits: from tetrahydrofuran to plasmid DNA. In: Carsky P, Curik R (eds) *Low-energy electron scattering from molecules*. CRC Press, Biomolecules and Surfaces, pp 161–230
- Champion C (2010) Electron impact ionization of liquid and gaseous water: a single-center partial-wave approach. *Phys Med Biol* 55:11–32. <https://doi.org/10.1088/0031-9155/55/1/002>
- Chancellor J, Scott G, Sutton J (2014) Space radiation: the number one risk to astronaut health beyond low earth orbit. *Life* 4:491–510. <https://doi.org/10.3390/life4030491>
- Chattopadhyay N, Cai Z, Pignol J-P et al (2010) Design and characterization of HER-2-targeted gold nanoparticles for enhanced X-radiation treatment of locally advanced breast cancer. *Mol Pharm* 7:2194–2206. <https://doi.org/10.1021/mp100207t>
- Chattopadhyay N, Cai Z, Kwon YL et al (2013) Molecularly targeted gold nanoparticles enhance the radiation response of breast cancer cells and tumor xenografts to X-radiation. *Breast Cancer Res Treat* 137:81–91. <https://doi.org/10.1007/s10549-012-2338-4>
- Chen W, Chen S, Dong Y et al (2016) Absolute cross-sections for DNA strand breaks and crosslinks induced by low energy electrons. *Phys Chem Chem Phys* 18:32762–32771. <https://doi.org/10.1039/c6cp05201k>
- Chiari L, Duque HV, Jones DB et al (2014) Differential cross sections for intermediate-energy electron scattering from α -tetrahydrofurfuryl alcohol: excitation of electronic-states. *J Chem Phys* 141:24301. <https://doi.org/10.1063/1.4885856>
- Cohen MH, Lekner J (1967) Theory of hot electrons in gases, liquids, and solids. *Phys Rev* 158:305–309. <https://doi.org/10.1103/physrev.158.305>
- Connell PP, Hellman S (2009) Advances in radiotherapy and implications for the next century: a historical perspective. *Cancer Res* 69:383–392. <https://doi.org/10.1158/0008-5472.can-07-6871>
- Conrad H, Kordesch ME (2017) High resolution electron energy loss spectroscopy, applications. In: Lindon JC, Tranter GE, Koppelaar DW (eds) *Encyclopedia of spectroscopy and spectrometry*, 2nd edn. Elsevier, Oxford, pp 47–57
- Cucinotta F, Kim M, Chappell L (2011) Space radiation cancer risk projections and uncertainties-2010. NASA Tech Pap 1–132
- Danjo A, Nishimura H (1985) Elastic scattering of electrons from H₂O molecule. *J Phys Soc Japan* 54:1224–1227. <https://doi.org/10.1143/jpsj.54.1224>
- Davis HT, Schmidt LD, Minday RM (1971) Kinetic theory of excess electrons in polyatomic gases, liquids, and solids. *Phys Rev A* 3:1027–1037. <https://doi.org/10.1103/physreva.3.1027>
- Denifl S, Ptasíńska S, Probst M et al (2004) Electron attachment to the gas-phase DNA bases cytosine and thymine. *J Phys Chem A* 108:6562–6569. <https://doi.org/10.1021/jp049394x>
- Dingfelder M (2006) Track structure: time evolution from physics to chemistry. *Radiat Prot Dosimetry* 122:16–21. <https://doi.org/10.1093/rpd/ncl494>
- Dingfelder M, Travia A, Mclawhorn RA et al (2009) Electron emission from foils and biological materials after proton impact. *Radiat Phys Chem Oxf Engl* 1993 77:1213–1217. <https://doi.org/10.1016/j.radphyschem.2008.05.046.electron>
- Douglass M, Penfold S, Bezak E (2015) Preliminary investigation of microdosimetric track structure physics models in Geant4-DNA and RITRACKS. *Comput Math Methods Med* 2015. <https://doi.org/10.1155/2015/968429>
- Dugal P-C, Abdoul-Carime H, Sanche L (2000) Mechanisms for low-energy (0.5–30 eV) electron-induced pyrimidine ring fragmentation within thymine- and halogen-substituted single strands of DNA. *J Phys Chem B* 104:5610–5617. <https://doi.org/10.1021/jp9938112>

- Duque HV, Do TPT, Lopes MCA et al (2015) The role of electron-impact vibrational excitation in electron transport through gaseous tetrahydrofuran. *J Chem Phys* 142:124307. <https://doi.org/10.1063/1.4915889>
- Durante M (2014) Space radiation protection: destination Mars. *Life Sci Sp Res* 1:2–9. <https://doi.org/10.1016/j.lssr.2014.01.002>
- Durante M, Cucinotta FA (2011) Physical basis of radiation protection in space travel. *Rev Mod Phys* 83:1245–1281. <https://doi.org/10.1103/revmodphys.83.1245>
- Einstein AJ, Moser KW, Thompson RC et al (2007) Radiation dose to patients from cardiac diagnostic imaging. *Circulation* 116:1290–1305
- Eisenberg MJ, Afilalo J, Lawler PR et al (2011) Cancer risk related to low-dose ionizing radiation from cardiac imaging in patients after acute myocardial infarction. *CMAJ* 183:430–436. <https://doi.org/10.1503/cmaj.100463>
- Emfietzoglou D, Cucinotta FA, Nikjoo H (2005) A complete dielectric response model for liquid water: a solution of the Bethe ridge problem. *Radiat Res* 164:202–211. <https://doi.org/10.1667/rr3399>
- Esmaili S, Bass AD, Cloutier P et al (2017) Synthesis of complex organic molecules in simulated methane rich astrophysical ices. *J Chem Phys* 147. <https://doi.org/10.1063/1.5003898>
- Esmaili S, Bass AD, Cloutier P et al (2018) Glycine formation in CO₂ : CH₄ : NH₃ ices induced by 0–70 eV electrons. 164702:0–8. <https://doi.org/10.1063/1.5021596>
- Fazel R, Krumholz HM, Wang Y et al (2016) Exposure to low-dose ionizing radiation from medical imaging procedures. *Emerg Nurse* 24:15. <https://doi.org/10.1056/nejmp1002530>
- Francis Z, Incerti S, Karamitros M et al (2011) Stopping power and ranges of electrons, protons and alpha particles in liquid water using the Geant4-DNA package. *Nucl Instrum Methods Phys Res Sect B Beam Interact with Mater Atoms* 269:2307–2311. <https://doi.org/10.1016/j.nimb.2011.02.031>
- Francis Z, Incerti S, Ivanchenko V et al (2012) Monte Carlo simulation of energy-deposit clustering for ions of the same LET in liquid water. *Phys Med Biol* 57:209–224. <https://doi.org/10.1088/0031-9155/57/1/209>
- Gaze MN (1996) The current status of targeted radiotherapy in clinical practice. *Phys Med Biol* 41:1895
- Ghandi K, Wang F, Landry C, Mehran Mostafavi (2018) Naked gold nanoparticles and hot electrons in water. *Sci Rep* 1–6. <https://doi.org/10.1038/s41598-018-25711-2>
- Gohlke S, Rosa A, Illenberger E et al (2002) Formation of anion fragments from gas-phase glycine by low energy (0–15 eV) electron impact. *J Chem Phys* 116:10164–10169. <https://doi.org/10.1063/1.1479348>
- Golovlev VV, Allman SL, Garrett WR, Chen CH (1997) Laser-induced acoustic desorption of electrons and ions. *Appl Phys Lett* 71:852–854. <https://doi.org/10.1063/1.119667>
- Goodhead DT (1994) Initial events in the cellular effects of ionizing radiations: clustered damage in DNA. *Int J Radiat Biol* 65:7–17. <https://doi.org/10.1080/09553009414550021>
- Goodhead DT (2006) Energy deposition stochasticity and track structure: what about the target? *Radiat Prot Dosimetry* 122:3–15. <https://doi.org/10.1093/rpd/nc1498>
- Hainfeld JF, Slatkin DN, Smilowitz HM (2004) The use of gold nanoparticles to enhance radiotherapy in mice. *Phys Med Biol* 49. <https://doi.org/10.1088/0031-9155/49/18/n03>
- Hainfeld JF, Dilmanian FA, Slatkin DN, Smilowitz HM (2008) Radiotherapy enhancement with gold nanoparticles. *J Pharm Pharmacol* 60:977–985. <https://doi.org/10.1211/jpp.60.8.0005>
- Hainfeld JF, Dilmanian FA, Zhong Z et al (2010) Gold nanoparticles enhance the radiation therapy of a murine squamous cell carcinoma. *Phys Med Biol* 55:3045–3059. <https://doi.org/10.1088/0031-9155/55/11/004>
- Hall EJ, Wu CS (2003) Radiation-induced second cancers: the impact of 3D-CRT and IMRT. *Int J Radiat Oncol Biol Phys* 56:83–88. [https://doi.org/10.1016/s0360-3016\(03\)00073-7](https://doi.org/10.1016/s0360-3016(03)00073-7)
- Hassler DM, Zeitlin C, Wimmer-Schweingruber RF et al (2014) Mars' surface radiation environment measured with the Mars Science Laboratory's Curiosity Rover. *Science* (80-) 343:1244797–1244797. <https://doi.org/10.1126/science.1244797>

- Hayes AC (2017) Applications of nuclear physics. *Reports Prog Phys* 80. <https://doi.org/10.1088/1361-6633/80/2/026301>
- Hervé Du Penhoat MA, Huels MA, Cloutier P et al (2001) Electron stimulated desorption of H- from thin films of thymine and uracil. *J Chem Phys* 114:5755–5764. <https://doi.org/10.1063/1.1349707>
- Holtom PD, Bennett CJ, Osamura Y et al (2005) A combined experimental and theoretical study on the formation of the amino acid glycine ($\text{NH}_2\text{CH}_2\text{COOH}$) and its isomer (CH_3NHCOOH) in extraterrestrial ices. *Astrophys J* 626:940–952. <https://doi.org/10.1086/430106>
- Huels MA, Hahndorf I, Illenberger E, Sanche L (1998) Resonant dissociation of DNA bases by subionization electrons resonant dissociation of DNA bases by subionization electrons. 108:1309. <https://doi.org/10.1063/1.475503>
- Huels MA, Boudaiffa B, Cloutier P et al (2003) Single, double, and multiple double strand breaks induced in DNA by 3–100 eV electrons. *J Am Chem Soc* 125:4467–4477
- Hyun Cho S, Jones BL, Krishnan S (2005) Physics in medicine & biology estimation of tumour dose enhancement due to gold nanoparticles during typical radiation treatments: a preliminary Monte Carlo study. The dosimetric feasibility of GNRT. *Sang Hyun Cho Phys Med Biol* 50. <https://doi.org/10.1088/0031-9155/50/15/n01>
- Ibach H, Mills DL (1982) *Electron energy loss spectroscopy and surface vibrations*. Academic, Elsevier Science, New York
- Inokuti M (1983) Radiation physics as basis of radiation chemistry and biology. In: *Applied atomic collision physics*. Academic Press, New-York, pp 179–236
- Inokuti M (1996) Remarks on stopping power: its connections with particle transport and with the electronic structure of matter. *Int J Quantum Chem* 57:173–182
- Itikawa Y, Mason N (2005) Cross sections for electron collisions with water molecules. *J Phys Chem Ref Data* 34:1–22. <https://doi.org/10.1063/1.1799251>
- Jäggle C, Swiderek P, Breton S-P et al (2006) Products and reaction sequences in tetrahydrofuran exposed to low-energy electrons. *J Phys Chem B* 110:12512–12522. <https://doi.org/10.1021/jp0614291>
- Johnstone WM, Newell WR (1991) Absolute vibrationally elastic cross sections for electrons scattered from water molecules between 6 eV and 50 eV. *J Phys B: At Mol Opt Phys* 24:3633–3643. <https://doi.org/10.1088/0953-4075/24/16/015>
- Jones DB, Bellm SM, Blanco F et al (2012) Differential cross sections for the electron impact excitation of pyrimidine. *J Chem Phys* 137:74304. <https://doi.org/10.1063/1.4743961>
- Kaiser RI (2002) Experimental investigation on the formation of carbon-bearing molecules in the interstellar medium via neutral-neutral reactions. *Chem Rev* 102:1309–1358. <https://doi.org/10.1021/cr970004v>
- Keller A, Rackwitz J, Cauët E et al (2015) Sequence dependence of electron-induced DNA strand breakage revealed by DNA nanoarrays. *Sci Rep* 4:7391. <https://doi.org/10.1038/srep07391>
- Kennedy AR (2014) Biological effects of space radiation and development of effective countermeasures. *Life Sci Space Res* 1:10–43. <https://doi.org/10.1016/j.lssr.2014.02.004>
- Klyachko DV, Huels MA, Sanche L, Sanche L (1999) Halogen anion formation in 5-halouracil films: X rays compared to subionization electrons. *Radiat Res* 151:177. <https://doi.org/10.2307/3579768>
- Kočišek J, Pysanenko A, Fárník M, Fedor J (2016) Microhydration prevents fragmentation of uracil and thymine by low-energy electrons. *J Phys Chem Lett* 7:3401–3405. <https://doi.org/10.1021/acs.jpcclett.6b01601>
- Kohanoff J, McAllister M, Tribello GA, Gu B (2017) Interactions between low energy electrons and DNA: a perspective from first-principles simulations. *J Phys: Condens Matter* 29:383001. <https://doi.org/10.1088/1361-648x/aa79e3>
- Kong T, Zeng J, Wang X et al (2008) Enhancement of radiation cytotoxicity in breast-cancer cells by localized attachment of gold nanoparticles. *Small* 4:1537–1543. <https://doi.org/10.1002/smll.200700794>

- König C, Kopyra J, Bald I, Illenberger E (2006) Dissociative electron attachment to phosphoric acid esters: the direct mechanism for single strand breaks in DNA. *Phys Rev Lett* 97:18105. <https://doi.org/10.1103/physrevlett.97.018105>
- Kyriakou I, Emfietzoglou D, Ivanchenko V et al (2017) Microdosimetry of electrons in liquid water using the low-energy models of Geant4. *J Appl Phys* 122. <https://doi.org/10.1063/1.4992076>
- Lafosse A, Azria R (2011) Low-energy electron scattering at surfaces. In: Čurík R, Čárský P (eds) *Low-energy electron scattering from molecules. CRC Press, Biomolecules and Surfaces*, pp 231–262
- Lafosse A, Bertin M, Domaracka A et al (2006) Reactivity induced at 25 K by low-energy electron irradiation of condensed NH₃–CH₃COOD (1: 1) mixture. *Phys Chem Chem Phys* 8:5564–5568. <https://doi.org/10.1039/b613479c>
- Lechtman E, Chattopadhyay N, Cai Z et al (2011) Implications on clinical scenario of gold nanoparticle radiosensitization in regards to photon energy. *Phys Med Biol* 56:4631–4647. <https://doi.org/10.1088/0031-9155/56/15/001>
- Lekner J (1967) Motion of electrons in liquid argon. *Phys Rev* 158:130–137. <https://doi.org/10.1103/physrev.158.130>
- Lemelin V, Bass AD, Cloutier P, Sanche L (2016a) Absolute cross sections for electronic excitation of condensed tetrahydrofuran (THF) by 11–16 eV electrons. *J Chem Phys* 145:174703. <https://doi.org/10.1063/1.4966650>
- Lemelin V, Bass AD, Cloutier P, Sanche L (2016b) Absolute vibrational cross sections for 1–19 eV electron scattering from condensed tetrahydrofuran (THF). *J Chem Phys* 144:74701. <https://doi.org/10.1063/1.4941377>
- Lemelin V, Bass AD, Wagner JR, Sanche L (2017) Absolute vibrational excitation cross sections for 1–18 eV electron scattering from condensed dimethyl phosphate (DMP). *J Chem Phys* 147:234305. <https://doi.org/10.1063/1.5008486>
- Lepage M, Letarte S, Michaud M et al (1998) Electron spectroscopy of resonance-enhanced vibrational excitations of gaseous and solid tetrahydrofuran. *J Chem Phys* 109:5980–5986. <https://doi.org/10.1063/1.477223>
- Lepage M, Michaud M, Sanche L (2000) Low-energy electron-energy-loss spectroscopy of condensed acetone: electronic transitions and resonance-enhanced vibrational excitations. *J Chem Phys* 112:6707–6715. <https://doi.org/10.1063/1.481245>
- Levesque PL, Michaud M, Sanche L (2003) Cross sections for low energy (1–12 eV) inelastic electron scattering from condensed thymine. *Nucl Instrum Methods Phys Res Sect B Beam Interact with Mater Atoms* 208:225–230. [https://doi.org/10.1016/s0168-583x\(03\)00661-x](https://doi.org/10.1016/s0168-583x(03)00661-x)
- Levesque PL, Michaud M, Cho W, Sanche L (2005a) Absolute electronic excitation cross sections for low-energy electron (5–12 eV) scattering from condensed thymine. *J Chem Phys* 122:224704. <https://doi.org/10.1063/1.1925610>
- Levesque PL, Michaud M, Sanche L (2005b) Absolute vibrational and electronic cross sections for low-energy electron (2–12 eV) scattering from condensed pyrimidine. *J Chem Phys* 122:94701. <https://doi.org/10.1063/1.1854121>
- Liljequist D, Liamsuwan T, Nikjoo H (2012) Elastic scattering cross section models used for Monte Carlo simulation of electron tracks in media of biological and medical interest. *Int J Radiat Biol* 88:29–37. <https://doi.org/10.3109/09553002.2011.584943>
- Loevinger R, Budinger TF, Watson EE (1991) *MIRD primer for absorbed dose calculations, revised edition*. The Society of Nuclear Medicine, Inc., New York
- Lozano AI, Krupa K, Ferreira da Silva F et al (2017) Low energy electron transport in furfural. *Eur Phys J D* 71:226. <https://doi.org/10.1140/epjd/e2017-80326-0>
- Lu QB, Sanche L (2001) Effects of cosmic rays on atmospheric chlorofluorocarbon dissociation and ozone depletion. *Phys Rev Lett* 87:78501-1–78501-4. <https://doi.org/10.1103/physrevlett.87.078501>
- Martin F, Burrow PD, Cai Z et al (2004) DNA strand breaks induced by 0–4 eV electrons: the role of shape resonances. *Phys Rev Lett* 93:68101. <https://doi.org/10.1103/physrevlett.93.068101>

- McNamara A, Geng C, Turner R et al (2017) Validation of the radiobiology toolkit TOPAS-nBio in simple DNA geometries. *Phys Med* 33:207–215. <https://doi.org/10.1016/j.ejmp.2016.12.010>
- McNaught AD (1997) Compendium of chemical terminology. Blackwell Science, Oxford
- Meesungnoen J, Jay-Gerin J-P, Filali-Mouhim A, Mankhetkorn S (2002) Low-energy electron penetration range in liquid water. *Radiat Res* 158:657–660. [https://doi.org/10.1667/0033-7587\(2002\)158%5b0657:leepri%5d2.0.co;2](https://doi.org/10.1667/0033-7587(2002)158%5b0657:leepri%5d2.0.co;2)
- Meesungnoen J, Filali-Mouhim A, Ayudhya NSN et al (2003) Multiple ionization effects on the yields of HO₂·/O₂·- and H₂O₂ produced in the radiolysis of liquid water with high-LET¹²C⁶⁺ ions: a Monte-Carlo simulation study. *Chem Phys Lett* 377:419–425. [https://doi.org/10.1016/s0009-2614\(03\)01101-1](https://doi.org/10.1016/s0009-2614(03)01101-1)
- Meesungnoen J, Sanguanmith S, Jay-Gerin JP (2015) Yields of H₂ and hydrated electrons in low-LET radiolysis of water determined by Monte Carlo track chemistry simulations using phenol/N₂O aqueous solutions up to 350 °C. *RSC Adv* 5:76813–76824. <https://doi.org/10.1039/c5ra15801j>
- Michaud M, Sanche L (1984a) Interaction of low-energy electrons (1–30 eV) with condensed molecules: II. Vibrational-librational excitation and shape resonances in thin N₂ and CO films. *Phys Rev B* 30:6078
- Michaud M, Sanche L (1984b) Interaction of low-energy electrons (1–30 eV) with condensed molecules: I. Multiple scattering theory. *Phys Rev B* 30:6067–6077
- Michaud M, Sanche L (1987a) Absolute vibrational excitation cross sections for slow-electron (1 > 18 eV) scattering in solid H₂O. *Phys Rev A* 36:4684–4699. <https://doi.org/10.1103/physreva.36.4684>
- Michaud M, Sanche L (1987b) Total cross sections for slow-electron (1–20 eV) scattering in solid H₂O. *Phys Rev A* 36:4672–4683. <https://doi.org/10.1103/physreva.36.4672>
- Michaud M, Sanche L (1994) Low-energy electron-energy-loss spectroscopy of solid films of argon: surface and bulk valence excitons. *Phys Rev B* 50:4725–4732
- Michaud M, Cloutier P, Sanche L (1991) Phonon excitations in low-energy-electron scattering from solid Ar, Kr, and Xe films: direct observation of conduction-band density of states. *Phys Rev B* 44:10485
- Michaud M, Wen A, Sanche L (2003) Cross sections for low-energy (1–100 eV) electron elastic and inelastic scattering in amorphous ice. *Radiat Res* 159:3–22. [https://doi.org/10.1667/0033-7587\(2003\)159%5b0003:csfee%5d2.0.co;2](https://doi.org/10.1667/0033-7587(2003)159%5b0003:csfee%5d2.0.co;2)
- Michaud M, Bazin M, Sanche L (2012) Absolute cross sections for vibrational excitations of cytosine by low energy electron impact. *J Chem Phys* 137:115103. <https://doi.org/10.1063/1.4752655>
- Michaud M, Bazin M, Sanche L (2013) Nanodosimetry of Auger electrons: a case study from the decay of ¹²⁵I and 0–18-eV electron stopping cross sections of cytosine. *Phys Rev E* 87:32701. <https://doi.org/10.1103/physreve.87.032701>
- Mucke M, Braune M, Barth S et al (2010) A hitherto unrecognized source of low-energy electrons in water. *Nat Phys* 6:143–146. <https://doi.org/10.1038/nphys1500>
- Muñoz A, Blanco F, Garcia G et al (2008) Single electron tracks in water vapour for energies below 100 eV. *Int J Mass Spectrom* 277:175–179. <https://doi.org/10.1016/j.ijms.2008.04.028>
- Nagesha K, Sanche L (1998) Effects of band structure on electron attachment to adsorbed molecules: cross section enhancements via coupling to image states. *Phys Rev Lett* 81:5892–5895. <https://doi.org/10.1103/physrevlett.81.5892>
- Nenner I, Schulz GJ (1975) Temporary negative ions and electron affinities of benzene and N-heterocyclic molecules: pyridine, pyridazine, pyrimidine, pyrazine, and s-triazine. *J Chem Phys* 62:1747–1758. <https://doi.org/10.1063/1.430700>
- Nikjoo H, Lindborg L (2010) RBE of low energy electrons and photons. *Phys Med Biol* 55:R65–R109. <https://doi.org/10.1088/0031-9155/55/10/r01>
- Nikjoo H, Uehara S, Emfietzoglou D, Cucinotta FA (2006) Track-structure codes in radiation research. *Radiat Meas* 41:1052–1074. <https://doi.org/10.1016/j.radmeas.2006.02.001>
- Nikjoo H, Emfietzoglou D, Liamsuwan T et al (2016) Radiation track, DNA damage and response—a review. *Rep Prog Phys* 79. <https://doi.org/10.1088/0034-4885/79/11/116601>

- Norbury JW, Schimmerling W, Slaba TC et al (2016) Galactic cosmic ray simulation at the NASA Space Radiation Laboratory. *Life Sci Sp Res* 8:38–51. <https://doi.org/10.1016/j.lssr.2016.02.001>
- Pan X, Sanche L (2006) Dissociative electron attachment to DNA basic constituents: the phosphate group. *Chem Phys Lett* 421:404–408. <https://doi.org/10.1016/j.cplett.2006.01.099>
- Panajotović R, Michaud M, Sanche L (2007) Cross sections for low-energy electron scattering from adenine in the condensed phase. *Phys Chem Chem Phys* 9:138–148. <https://doi.org/10.1039/b612700b>
- Park YS, Cho H, Parenteau L et al (2006) Cross sections for electron trapping by DNA and its component subunits I: Condensed tetrahydrofuran deposited on Kr. *J Chem Phys* 125:74714. <https://doi.org/10.1063/1.2229201>
- Pater P, Seuntjens J, El Naqa I, Bernal MA (2014) On the consistency of Monte Carlo track structure DNA damage simulations. *Med Phys* 41:121708. <https://doi.org/10.1118/1.4901555>
- Pimblott SM, LaVerne JA (2007) Production of low-energy electrons by ionizing radiation. *Radiat Phys Chem* 76:1244–1247. <https://doi.org/10.1016/j.radphyschem.2007.02.012>
- Pimblott SM, Laverne JA, Mozumder A (1996) Monte Carlo simulation of range and energy deposition by electrons in gaseous and liquid water. *J Phys Chem* 100:8595–8606
- Plante I (2011) A Monte-Carlo step-by-step simulation code of the non-homogeneous chemistry of the radiolysis of water and aqueous solutions-Part II: Calculation of radiolytic yields under different conditions of LET, pH, and temperature. *Radiat Environ Biophys* 50:405–415. <https://doi.org/10.1007/s00411-011-0368-7>
- Plante I, Cucinotta FA (2009) Cross sections for the interactions of 1 eV–100 MeV electrons in liquid water and application to Monte-Carlo simulation of HZE radiation tracks. *New J Phys* 11:63047. <https://doi.org/10.1088/1367-2630/11/6/063047>
- Plante I, Tippayamontri T, Autsavapromporn N et al (2012) Monte Carlo simulation of the radiolysis of the ceric sulfate dosimeter by low linear energy transfer radiation. *Can J Chem* 90:717–723. <https://doi.org/10.1139/v2012-052>
- Ptasinska S, Denifl S, Abedi A et al (2003) Dissociative electron attachment to gas-phase glycine. *Anal Bioanal Chem* 377:1115–1119. <https://doi.org/10.1007/s00216-003-2254-x>
- Rackwitz J, Kopyra J, Dąbkowska I et al (2016) Sensitizing DNA towards low-energy electrons with 2-fluoroadenine. *Angew Chemie Int Ed* 55:10248–10252. <https://doi.org/10.1002/anie.201603464>
- Rackwitz J, Ranković ML, Milosavljević AR, Bald I (2017) A novel setup for the determination of absolute cross sections for low-energy electron induced strand breaks in oligonucleotides—the effect of the radiosensitizer 5-fluorouracil*. *Eur Phys J D* 71:32. <https://doi.org/10.1140/epjd/e2016-70608-4>
- Rahman WN, Bishara N, Ackerly T et al (2009) Enhancement of radiation effects by gold nanoparticles for superficial radiation therapy. *Nanomed Nanotechnol Biol Med* 5:136–142. <https://doi.org/10.1016/j.nano.2009.01.014>
- Reilly RM (2008) Biopharmaceuticals as targeting vehicles for in situ radiotherapy of malignancies. In: *Modern biopharmaceuticals*. Wiley-Blackwell, pp 497–535
- Rezaee M, Cloutier P, Bass AD et al (2012) Absolute cross section for low-energy-electron damage to condensed macromolecules: a case study of DNA. *Phys Rev E* 86:31913. <https://doi.org/10.1103/physreve.86.031913>
- Rezaee M, Hunting DJ, Sanche L (2014) Correlation between energy deposition and molecular damage from Auger electrons: a case study of ultra-low energy (5–18 eV) electron interactions with DNA. *Med Phys* 41:72502. <https://doi.org/10.1118/1.4881329>
- Rezaee M, Hill RP, Jaffray DA (2017) The exploitation of low-energy electrons in cancer treatment. *Radiat Res* 188:123–143. <https://doi.org/10.1667/rr14727.1>
- Rogers DWO (2006) Fifty years of Monte Carlo simulations for medical physics. *Phys Med Biol* 51:R287–R301. <https://doi.org/10.1088/0031-9155/51/13/r17>
- Samara M, Michell RG, Redmon RJ (2015) Low-altitude satellite measurements of pulsating auroral electrons. *J Geophys Res A Sp Phys* 120:8111–8124. <https://doi.org/10.1002/2015ja021292>

- Sanche L (2010) Low-energy electron interaction with DNA: bond dissociation and formation of transient anions, radicals, and radical anions. In: Greenberg MM (ed) *Radical and radical ion reactivity in nucleic acid chemistry*, John Wiley, Wiley, Inc, pp 239–294
- Sanche L (2015) Cancer treatment: Low-energy electron therapy. *Nat Mater* 14:861–863. <https://doi.org/10.1038/nmat4333>
- Sanche L, Schulz GJ (1972) Electron transmission spectroscopy: core-excited resonances in diatomic molecules. *Phys Rev A* 6:69
- Sanz AG, Fuss MC, Muñoz A et al (2012) Modelling low energy electron and positron tracks for biomedical applications. *Int J Radiat Biol* 88:71–76. <https://doi.org/10.3109/09553002.2011.624151>
- Scheer AM, Mozejko P, Gallup GA, Burrow PD (2007) Total dissociative electron attachment cross sections of selected amino acids. *J Chem Phys* 126:174301. <https://doi.org/10.1063/1.2727460>
- Schulz GJ (1973) Resonances in electron impact on diatomic molecules. *Rev Mod Phys* 45:423
- Schulz GJ (1976) *Principles of Laser Plasmas*. Ed G Bekefi, J Wiley Adson 33
- Schürmann R, Tsering T, Tanzer K et al (2017) Resonant formation of strand breaks in sensitized oligonucleotides induced by low-energy electrons (0.5–9 eV). *Angew Chemie Int Ed* 56:10952–10955. <https://doi.org/10.1002/anie.201705504>
- Seiwert TY, Salama JK, Vokes EE (2007) The concurrent chemoradiation paradigm—general principles. *Nat Clin Pract Oncol* 4:86–100. <https://doi.org/10.1038/nclonc0714>
- Seng G, Linder F (1976) Vibrational excitation of polar molecules by electron impact II. Direct and resonant excitation in H₂O. *J Phys B Atom Molec Phys* 9:2539–2551
- Shao Y, Dong Y, Hunting D et al (2017) Unified mechanism for the generation of isolated and clustered DNA damages by a single low energy (5–10 eV) electron. *J Phys Chem C* 121:2466–2472. <https://doi.org/10.1021/acs.jpcc.6b12110>
- Shea RC, Petzold CJ, Liu J, Kenttämää HI (2007) Experimental investigations of the internal energy of molecules evaporated via laser-induced acoustic desorption into a Fourier transform ion cyclotron resonance mass spectrometer. *Anal Chem* 79:1825–1832. <https://doi.org/10.1021/ac061596x>
- Shyn TW, Cho SY, Cravens TE (1988) Vibrational-excitation cross sections of water molecules by electron impact. *Phys Rev A* 38:678–682. <https://doi.org/10.1103/physreva.38.678>
- Siragusa M, Baiocco G, Fredericia PM et al (2017) The COOLER code: a novel analytical approach to calculate subcellular energy deposition by internal electron emitters. *Radiat Res* 188:204–220. <https://doi.org/10.1667/rr14683.1>
- Slaba TC, Blattnig SR, Norbury JW et al (2016) Reference field specification and preliminary beam selection strategy for accelerator-based GCR simulation. *Life Sci Sp Res* 8:52–67. <https://doi.org/10.1016/j.lssr.2016.01.001>
- Smyth M, Kohanoff J (2011) Excess electron localization in solvated DNA bases. *Phys Rev Lett* 106:238108. <https://doi.org/10.1103/physrevlett.106.238108>
- Smyth M, Kohanoff J, Fabrikant II (2014) Electron-induced hydrogen loss in uracil in a water cluster environment. *J Chem Phys* 140:184313. <https://doi.org/10.1063/1.4874841>
- Sridharan DM, Chappell LJ, Whalen MK et al (2015) Defining the biological effectiveness of components of high-LET track structure. *Radiat Res* 184:105–119. <https://doi.org/10.1667/rr13684.1>
- Sulzer P, Ptasińska S, Zappa F et al (2006) Dissociative electron attachment to furan, tetrahydrofuran, and fructose. *J Chem Phys* 125:44304. <https://doi.org/10.1063/1.2222370>
- Tonzani S, Greene CH (2006) Radiation damage to DNA: electron scattering from the backbone subunits. *J Chem Phys* 125:94504. <https://doi.org/10.1063/1.2333455>
- Trevisan CS, Orel AE, Rescigno TN (2006) Elastic scattering of low-energy electrons by tetrahydrofuran. *J Phys B: At Mol Opt Phys* 39:L255–L260. <https://doi.org/10.1088/0953-4075/39/12/101>
- Uehara S, Nikjoo H (2006) Monte Carlo simulation of water radiolysis for low-energy charged particles. *J Radiat Res* 47:69–81. <https://doi.org/10.1269/jrr.47.69>

- Vilar MR, Do Rego AMB, Ferraria AM et al (2008) Interaction of self-assembled monolayers of DNA with electrons: HREELS and XPS studies. *J Phys Chem B* 112:6957–6964. <https://doi.org/10.1021/jp8008207>
- Vinodkumar M, Joshipura KN, Limbachiya C, Mason N (2006) Theoretical calculations of the total and ionization cross sections for electron impact on some simple biomolecules. *Phys Rev A* 74:22721. <https://doi.org/10.1103/physreva.74.022721>
- Winstead C, McKoy V (2006) Low-energy electron scattering by deoxyribose and related molecules. *J Chem Phys* 125:74302. <https://doi.org/10.1063/1.2263824>
- Winstead C, McKoy V (2008) Interaction of slow electrons with methyl phosphate esters. *Int J Mass Spectrom* 277:279–283. <https://doi.org/10.1016/j.ijms.2008.04.015>
- Wu C, Makiuchi Y, Chen C (2010) High-energy electron beam lithography for nanoscale fabrication. *Lithography*. <https://doi.org/10.5772/45639>
- Zalustky MR (2013) Radionuclide therapy. In: Vertes A, Nagy S, Klencsar Z et al (eds) *Handbook of nuclear chemistry*. Springer, Heidelberg, pp 2179–2203
- Zecca A, Perazzolli C, Brunger MJ (2005) Positron and electron scattering from tetrahydrofuran. *J Phys B: At Mol Opt Phys* 38:2079–2086. <https://doi.org/10.1088/0953-4075/38/13/002>
- Zeitlin C, Hassler DM, Cucinotta FA et al (2013) Measurements of energetic particle radiation in transit to Mars on the Mars Science Laboratory. *Science* (80–) 340:1080–1084. <https://doi.org/10.1126/science.1235989>
- Zheng Y, Wagner JR, Sanche L (2006) DNA damage induced by low-energy electrons: electron transfer and diffraction. *Phys Rev Lett* 96:208101. <https://doi.org/10.1103/physrevlett.96.208101>

Chapter 2

Synchrotron Radiation UV-VUV

Photoabsorption of Gas Phase Molecules



Denis Dufлот, Søren Vrønning Hoffmann, Nykola C. Jones
and Paulo Limão-Vieira

2.1 Introduction

The emission and use of synchrotron radiation (SR) are powerful tools for performing state-of-the-art research at the fundamental and applied levels, benefiting a diversity of research areas across medicine, molecular and cell biology, condensed matter physics, nanotechnology, cultural heritage, environmental science, atomic and molecular physics, among many others. The earliest record of synchrotron radiation dates back to the late 1940s, with cyclic electron synchrotron sources used to produce this light in the 1950s, before the presently known type of electron storage devices were established in the late 1960s. Since then, at least four generations of storage ring facilities have been built around the world where, briefly, the first was designed for high-energy physics research, followed by the second where the primary use was as a light source and the third in the early 1990s delivering lower electron beam emittance and higher brightness of the light. By this time these storage rings were equipped with undulators capable of delivering $\sim 10^4$ times higher brightness than that from

D. Dufлот (✉)

Université Lille, UMR 8523 - Physique des Lasers Atomes et Molécules, 59000 Lille, France
e-mail: denis.dufлот@univ-lille.fr

CNRS, UMR 8523, 59000 Lille, France

S. V. Hoffmann · N. C. Jones

ISA, Department of Physics and Astronomy, Aarhus University, Ny Munkegade 120, 8000
Aarhus C, Denmark
e-mail: vrønning@phys.au.dk

N. C. Jones

e-mail: nykj@phys.au.dk

P. Limão-Vieira

Atomic and Molecular Collisions Laboratory, CEFITEC, Department of Physics, Faculdade de
Ciências e Tecnologia, Universidade NOVA de Lisboa, 2829-516 Caparica, Portugal
e-mail: plimaovieira@fct.unl.pt

© Springer Nature Switzerland AG 2019

A. S. Pereira et al. (eds.), *Radiation in Bioanalysis*, Bioanalysis 8,
https://doi.org/10.1007/978-3-030-28247-9_2

second generation bending magnet sources. The newest fourth generation facilities are capable of delivering even higher brightness and also laser-like coherence by one or more orders of magnitude relative to the previous generation, and are much more attuned to rising research areas involving radiation wavelengths in the VUV to hard X-rays. During the last decade the international community has been deeply involved in the development and use of short wavelength free-electron lasers (FELs), which can generate shorter femtosecond pulses with full transverse coherence, providing optimal conditions to investigate at higher peak brightness key spectroscopic and structural features of inner shell atomic and molecular systems in macromolecular crystallography, soft condensed matter, imaging and microscopy, biological cryo-imaging, biological molecular systems, magnetic materials, structures and surfaces, just to mention a few.

SR is electromagnetic radiation emitted in a wide spectral region by charged particles (typically electrons) when travelling at speeds close to the speed of light and are forced to change direction by a magnetic field, resulting in coherent, intense, highly collimated and highly polarised radiation in the plane of the storage ring and can be used to achieve very high spectral resolution. This high intensity and broad spectral range, when combined with other properties such as high degree of polarization and collimation, makes SR well attuned to explore, as a function of the phase and stage of aggregation, key features in atomic, molecular and macromolecular systems. SR based research has seen a rapid growth since the inception of the earlier generations of SR light facilities. Nowadays the scientific community uses these modern sources, coupled with especially developed state-of-the art devices implemented in facilities worldwide, which are accessible for researchers from different backgrounds across the globe.

As most small molecules have their dominating chromophores in the VUV spectral region below the typical 190 nm lamp cut-off, the obvious choice of light source for photoabsorption spectroscopy is SR. The subsequent sections in this chapter describe how SR is used to probe the electronic structure of molecules in the VUV-visible region, through the measurement of gas phase photoabsorption spectra.

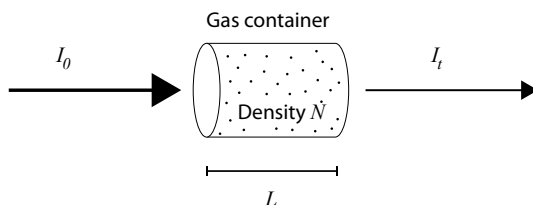
2.2 Photoabsorption Basics

2.2.1 *The Beer Lambert Law*

Consider light going through a sample under investigation, Fig. 2.1. Let the intensity of the light before the sample be denoted I_0 and the transmitted light intensity be denoted I_t .

For an absorbing sample, the transmitted intensity will be lower than the intensity before the sample, and the absorption, A , is defined as a dimensionless quantity given by

Fig. 2.1 Incoming light with intensity I_0 is absorbed by a gas of density N in a container of path length L . The transmitted intensity is given by I_t



$$A_e = \ln(I_0/I_t) \quad (2.1)$$

where \ln is the natural logarithm of base e . Often an alternative definition of the absorbance is encountered

$$A_{10} = \log(I_0/I_t) \quad (2.2)$$

where the \log denotes the logarithm of base 10. This definition is often used in analytical chemistry for absorbance measurements on liquids or aqueous solutions and in some cases on solids. In gas phase the definition based on the natural logarithm is the most commonly used, and is sometimes described as the Napierian absorbance, named after John Napier, the discoverer of logarithms. The two definitions are directly related and easily interconverted: from the two definitions of A_{10} and A_e we have

$$A_e = \ln(e^{A_e}) = \ln(I_0/I_t) = \ln(10^{A_{10}}) = A_{10} \ln(10) \quad (2.3)$$

and thus we have the simple conversion

$$A_e = \ln(10)A_{10} \quad (2.4)$$

In the remainder of the chapter, when not explicitly stated, we will only use the Napierian absorbance, and will simply refer to it as A , without any subscript.

The absorbance has a very important property: the absorbance is proportional to the density of the gas, N , and to the length of the sample, called the pathlength l .

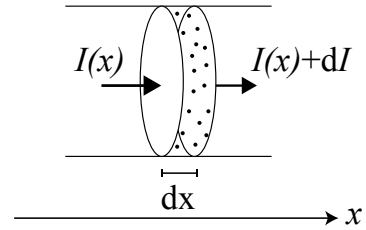
$$A = \sigma \cdot N \cdot l \quad (2.5)$$

This relation is known as the Beer-Lambert law.

2.2.2 Cross-Section

As the absorbance is dimensionless (absorbance units), N is the number of gas molecule per volume and l is a length, then the quantity σ has units of an area and is named the cross-section. This can be thought of as the effective area that the individual

Fig. 2.2 Elemental path length dx of a gas container subject to incident radiation of a particular intensity $I(x)$



molecule has for stopping (absorbing) light in the gas. In an absorbance measurement, the light is most often monochromatized and scanned over a range of wavelengths, so that the incoming and transmitted intensities, and thus the absorbance, are wavelength dependent. For wavelengths where the gas has a high absorbance the cross-section will also be high. This effective area is therefore not to be thought of as a constant disc size and the cross-section is wavelength dependent.

The origin of the Beer-Lambert law can be understood by considering a (infinitesimal) small section of the gas container with length dx at a point x along the pathlength direction, see Fig. 2.2.

The change in intensity, dI , over the length dx is proportional to the density of the gas, N , the length of the small section, dx , and the intensity at x , $I(x)$, with a proportionality factor σ .

$$dI = -\sigma \cdot N \cdot dx \cdot I(x) \quad (2.6)$$

The minus sign reflects that the intensity is decreasing as the light passes through the sample. As the intensity at the entrance and exit of the gas container are $I(x=0) = I_0$ and $I(x=l) = I_t$, then integrating Eq. 2.6 we get

$$\int_{I_0}^{I_t} \frac{1}{I} dI = \int_0^l (-\sigma N) dx = -\sigma n \int_0^l dx = -\sigma N l$$

Since the integral of $1/x$ is $\ln(x)$, we get

$$\ln(I_t) - \ln(I_0) = -\sigma \cdot N \cdot l$$

using

$$A = \ln(I_0/I_t) = \ln(I_0) - \ln(I_t) = -\{\ln(I_t) - \ln(I_0)\}$$

this simplifies directly to Beer-Lamberts law

$$A = \sigma \cdot N \cdot l \quad (2.7)$$

In analytical chemistry, where the base 10 logarithm is used in the definition of the absorbance, concentrations (c) in solutions are most often given in molar units, $[c] = \text{moles/litre} = \text{M}$, and the pathlength, l , is measured in cm. In this case, the Beer-Lambert law takes the form

$$A_{10} = \varepsilon \cdot c \cdot l \quad (2.8)$$

where the proportionality constant, ε , has units of $\text{M}^{-1} \text{cm}^{-1}$ and is denoted the molar extinction coefficient.

The SI units for the cross-section is square meters, $[\sigma] = \text{m}^2$. For gas phase molecular cross-sections the traditional unit is megabarn (Mb) and corresponds to $1 \text{ Mb} = 10^{-22} \text{ m}^2$. The Mb unit has the advantage that typical cross-sections in gas phase molecular photoabsorption are in the range of 0–100 Mb, a much easier range of numbers to remember in everyday laboratory work.

2.2.3 Absorption of Light and the Dipole Approximation

The absorption of light by a molecule is a highly quantum mechanical process. All the nuclei and electrons of the molecule interacts with each other. If the entire molecule is characterized by a wavefunction, this will depend on the nuclei (\mathbf{R}) and electrons (\mathbf{r}) coordinates, $\Psi(\mathbf{R}, \mathbf{r})$. In the Born-Oppenheimer approximation description of a molecule, the movements of the nuclei are considered so slow, compared to the electrons, that the wavefunction can be factorized into an electron part for fixed nuclear coordinates $\psi(\mathbf{r}, \mathbf{R})$ and a nuclear part $\Phi(\mathbf{R})$ for the nuclei moving in a time averaged electron field. This approximation is very useful, as it allows us to focus on the electrons and their states.

Consider two electronic states, 1 and 2, in a molecule with energies E_1 , E_2 and with corresponding wave functions ψ_1 and ψ_2 . These are solutions to the time-independent Schrödinger equation:

$$\hat{H} \psi_i = E_i \psi_i \quad (2.9)$$

where the Hamilton operator is given by a sum of the kinetic energy operator and the potential energy operator:

$$\hat{H} = \sum_i \frac{-\hbar^2}{2m_i} \nabla^2 + V \quad (2.10)$$

The potential contains the Coulomb interactions of all the charges of the molecule. None of these terms contain time dependence, but introducing the oscillating light field to the potential, $\hat{V}'(t)$, now necessitates solutions to the time-dependent Schrödinger equation:

$$\{\widehat{H} + \widehat{V}'(t)\}\Psi = i\hbar \frac{\partial \Psi}{\partial t} \quad (2.11)$$

The perturbation of the molecule via $\widehat{V}'(t)$ introduces coupling and thus possible transitions between the two states 1 and 2. Details on the calculations can be found in standard quantum mechanics textbooks (see e.g. Cantor and Schimmel 2001; Bransden and Joachain 1983; Weissbluth 1978). The main result is that the transition rate from state 1 to state 2 is proportional to the transition moment:

$$\mu_{12} = \int d\mathbf{r} \Psi_2^* e \mathbf{r} \Psi_1 = e \langle 2 | \mathbf{r} | 1 \rangle \quad (2.12)$$

where the last equal sign shows the short hand Bra-ket or Dirac notation for the integral. This is the dipole approximation arising from the fact that the radiation plane wave $\exp(i\mathbf{k} \cdot \mathbf{r})$ is approximated by the first Taylor expansion term $1 + i\mathbf{k} \cdot \mathbf{r}$, which is valid only if the wavelength of the light is much larger than the size of the molecule. More specifically μ is termed the *electric dipole transition moment*, as it is the first, and thus most important, term of a Multipole Expansion of the electrostatic potential. A physical interpretation of the dipole transition moment is that when a molecule absorbs a photon the excitation of the molecule must result in a net change of the molecules dipole moment or, in other words, a linear displacement of the charge in the molecule.

For a transition between states 1 and 2 in a molecule to be dipole allowed, μ must be non-zero. There are situations where $\mu = 0$, but an absorption is still found. This is a consequence of a non-zero element in higher orders of the multipole expansion, giving rise to e.g. a quadrupole transition. Such transitions typically have much lower cross-section than dipole allowed transitions.

Small isolated molecules usually belong to a specific symmetry group. The symmetry properties of these kinds of molecules are described in many textbooks (see e.g. Kettle 2007; Harris and Bertolucci 1978). As a consequence, some dipole transitions are forbidden due to the so-called selection rules. For example, in a diatomic molecule, the projection of the orbital angular momentum \mathbf{L} on the z axis is labelled Λ . This gives rise to the following dipole transition selection rule:

$$\Delta \Lambda = 0, \pm 1 \quad (2.13)$$

So, for example, a transition from a Σ state to a Σ or Π state is dipole allowed, whereas a Σ to Δ transition is dipole forbidden. Similarly, the total spin is conserved ($\Delta S = 0$).

When quantum chemical calculations on transition states are made on a molecule, the transition strength is often calculated in terms of the oscillator strength, f , a dimensional-less quantity which is proportional to the square of the transition moment $f \propto \mu^2$. Specifically, the oscillator strength is given by (Cantor and Schimmel 2001)

$$f = \frac{4\pi m_e \nu}{3e^2 \hbar} \mu^2 \quad (2.14)$$

where m_e is the mass of the electron, e is the electron charge and ν is the frequency of the light. The oscillator strength is directly related to the cross-section and can thus be used as a direct link between experiment and calculations. In practise, calculated transitions are given at a single energy, where real absorption features measured experimentally have a finite width. Therefore, the correct relation between the oscillator strength and the measured cross-section is given as an integral over the measured absorption feature:

$$f \propto \int dE \sigma(E) \quad (2.15)$$

More details on the practical aspects of quantum chemical calculations can be found in Sect. 2.4, Electronic structure methods.

2.2.4 Valence and Rydberg States

Typical transitions in a molecule, when probed with ultraviolet light, involves the valence electrons in the molecules. For example, a transition from the highest occupied molecular orbital (HOMO) to the lowest unoccupied molecular orbital (LUMO). When such a transition occurs to an unoccupied orbital with a size not much larger than the ground state, the transition state is denoted as a valence state. Valence transition states are the most prominent absorption features on a UV-VUV spectrum of a molecule.

Other transitions to orbitals which lie further away from the core of the molecule may be of Rydberg nature. Rydberg states occur when the excited electron in a single electron picture of the molecules lies far enough away from the rest of the molecule to be approximately close to a state in a hydrogen atom: a singly positively charged ionic core of the molecule interacts with a single electron. The Rydberg formula for the hydrogen atom is the basis for a description of Rydberg states:

$$E = -\frac{R}{n^2} \quad (2.16)$$

where R is the Rydberg constant (13.605 eV) and n is the principal quantum number. Here the zero-energy level is chosen to be the ionization limit. If we know the adiabatic ionization energy (IE) of the molecule under investigation, see Sect. 2.2.5 for more detail, the Rydberg states in the molecules can be described via

$$IE - E_m = -\frac{R}{(n^*)^2} = -\frac{R}{(n - \delta)^2} \quad (2.17)$$

where E_m is the absorption energy of the m th transition state. Here we have introduced the effective quantum number $n^* = n - \delta$, where δ is termed the quantum defect. The origin of the quantum defect is the discrepancy between the ideal hydrogen atom picture of the molecule and the real nature of a molecular orbital. Any orbital of an excited electron in a molecule will have overlap with the ionic core of the molecule. The extreme case is Rydberg s -states, which have significant overlap with the ionic core. Here the quantum defect can be as high as 1. Conversely, Rydberg f states have very little orbital overlap with the ionic core, and thus have a quantum defect very close to zero.

Typical quantum defects for s , p , d , and f Rydberg states are (Sandorfy 1981) $\delta \geq 0.75$, 0.4–0.6, 0.1–0.2 and 0.0–0.1, respectively. These quantum defect ranges can, together with the ionization energy, be used to identify Rydberg states in the absorption spectrum and assign them to their respective orbital angular momenta. Although there are certainly exceptions (e.g. Rydberg-valence mixed states), the Rydberg states are much less dominant in the absorption spectrum when compared to valence states. The Rydberg states might therefore be small features on a large valence state background. Thus, it can often be beneficial to subtract a number of Gaussian bands from the spectrum, as a crude representation of the valence states, and identify the Rydberg states from these regular residuals (Palmer et al. 2018). This is further described in the experimental Sect. 2.3.4 of this chapter.

2.2.5 Coupling to Photoelectron Spectroscopy (PES)

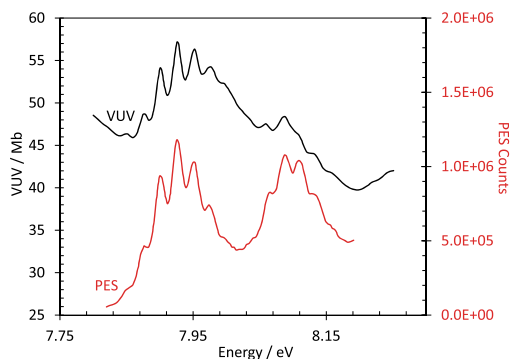
When the energy of the light is high enough to cause ionization of the molecule under investigation, a photoelectron is emitted and its kinetic energy (E_{kin}) may be analysed. This spectroscopy is called Photo-Electron Spectroscopy (PES). In contrast to photoabsorption, in PES the photon energy ($h\nu$) is constant. The kinetic energy of the emitted electron is scanned from close to zero up to the chosen photon energy and is converted into the binding energy (E_b) of the electron in the molecule.

$$E_b = h\nu - E_{kin} \quad (2.18)$$

The PES spectrum can be very rich in vibrational states and will also reflect not only the molecule's ionic ground state (\tilde{X}), but also higher ionic states (\tilde{A} , \tilde{B} , \tilde{C} , ...). The adiabatic ionization energy (IE) of the molecule is the lowest binding energy for a given ionic state.

The emitted electron moves in the potential of the ionic core of the molecule, and the electron/ionized molecule system can therefore be compared to Rydberg states in the photoabsorption spectrum. It may therefore be expected that the vibrational pattern in the PES spectrum is repeated in the Rydberg state of a photoabsorption spectrum. Note that, since there are several ionic states in the molecule, there are several IE's, one for each ionic state, the Rydberg series can converge to. The possible similarity of the vibrational pattern in the PES and Rydberg part of a photoabsorption

Fig. 2.3 VUV photoabsorption and PES spectra of C_6F_5I . The binding energy of the PES spectrum has been shifted down by 1.477 eV to match the vibrational features of the VUV spectrum. Adapted from Palmer et al. (2017)

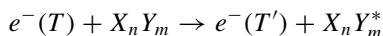


spectrum provides a good method for identifying Rydberg states. An example of a PES spectrum of C_6F_5I is shown as the red curve in Fig. 2.3 together with the black curve of the photoabsorption spectrum. The PES spectrum is shifted down in energy by 1.477 eV, so that the largest vibrational states in the two spectra are overlaid at 7.927 eV. The full analysis of the PES and VUV spectra of C_6F_5I have assigned this as an $n = 3$ d Rydberg state (Palmer et al. 2017).

However, some caution must be exerted when comparing PES spectra with sections of the photoabsorption spectrum to find possible Rydberg states. A replication of the vibrational pattern from the PES spectrum in the photoabsorption spectrum is by no means guaranteed. Often the comparison method works well for intermediate- n Rydberg states ($n > 4$), whereas for low n Rydberg states, the similarity can be much less obvious (Palmer et al. 2016a). Also, some ionic states have well defined vibrational structure, lending them to easy comparison with the photoabsorption spectrum, while others are broad bands, which in some cases stem from vibrational coupling from lower ionic states (see e.g. Palmer et al. 2015a).

2.2.6 Comparison to Electron Energy Loss Spectroscopy

Electron scattering spectroscopy can also be used to examine the electronic states of a molecule. Consider the scattering event of an electron with kinetic energy T , $e^-(T)$, on a molecule $X_n Y_m$:



which leaves the molecule in an excited state, $X_n Y_m^*$, by loss of the electron's kinetic energy to $T' < T$. The so-called Electron Energy Loss Spectroscopy (EELS) detects the lost electron energy, $E = T - T'$, after interaction of a beam of electrons with molecules, by recording the kinetic energy of the scattered electrons for a constant energy beam of electrons. EELS does not obey the strict selection rules of photoab-

sorption spectroscopy, and can e.g. probe dipole forbidden transitions as well as singlet-triplet transitions.

Under certain experimental conditions, the EELS spectrum can be put on a form that can be directly related to the cross-section measurements of a photoabsorption spectrum. This is possible when the incident electron energy is large compared to the energy loss, $T \gg E$, and the momentum transfer is small. Thus, the comparison is possible for a scattering geometry where the scattering angle is close to zero and the acceptance angle of the electron energy analyser is small, $\Delta\theta \sim 1^\circ$. Under these conditions, it can be shown that the scattering intensity spectrum, $I(E)$, can be related to the differential oscillator strength, $\partial f/\partial E$ given by (see e.g. Gingell et al. 1997; Huebner et al. 1973; or Inokuti 1971):

$$\frac{\partial f}{\partial E} \propto \frac{E \Delta\theta}{R \ln\left(1 + \left(\frac{\Delta\theta}{\gamma}\right)^2\right)} I(E) \quad (2.19)$$

where again the Rydberg constant is given by R and γ is given by

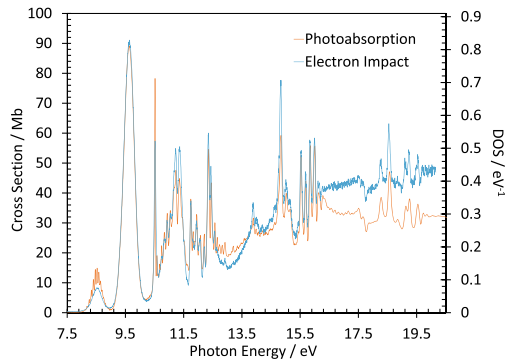
$$\gamma = \frac{(E/2T)^2}{1 - E/T} \quad (2.20)$$

In Sect. 2.2.2 we saw that the oscillator strength is proportional to the integral of the cross-section over energy, and thus the differential oscillator strength will be proportional to the cross-section. The exact expression, with the cross-section measured in Mb and the energy in eV, is given by (Giuliani et al. 1999)

$$\frac{\partial f}{\partial E} [\text{eV}^{-1}] = \frac{\sigma(E) [\text{Mb}]}{109.75} \quad (2.21)$$

An example of a comparison between an EELS and a photoabsorption spectrum for nitrous oxide is shown in Fig. 2.4. There is a clear agreement between the shapes of the two spectra. The figure highlights one typical limitation of using EELS to study

Fig. 2.4 Photo-absorption cross section and EELS differential oscillator strength for nitrous oxide (Jones 2000)



the electronic states of a molecule: notice the state near 8.5 eV. The photoabsorption spectrum shows a rich set of vibrational states, where this is not visible in the EELS spectrum. This is the result of an electron energy width of up to 50 meV in the EELS experiment, whereas most photoabsorption measurements can be done with photon resolutions in the order of a few meV. On the other hand, a clear strength of EELS over photoabsorption lies in the available energy range. Optical windows like MgF₂ or LiF used in the typical gas cell for photoabsorption measurements, limits the upper energy to about 10–11 eV, where EELS often is measured to at least twice this energy, thus extending the energy levels probed in the molecule.

2.3 Experimental Set-Up

As we have seen in the previous section, in order to measure absolute photoabsorption cross-sections, σ , the quantities that need to be measured are the intensity of light, I , passing through a cell of known length, l , with (I_t) and without (I_0) a gas of known number density, N .

$$\sigma = \ln\left(\frac{I_0}{I_t}\right) \frac{1}{Nl} \quad (2.22)$$

This section will present the experimental elements required to produce and accurately determine these parameters.

2.3.1 A Source of VUV-Visible Light

For accurate determination of gas phase photoabsorption cross-sections a stable, continuous light source over a large wavelength range, from the visible to vacuum—UV (VUV < 200 nm) region, is required.

Gas discharge lamps, where an electric discharge is passed through a plasma containing a gas, are a commonly used source of UV-visible light. Collisions between ions and neutral atoms in the plasma lead to the emission of light, the output spectrum of which is characteristic of the gas. Typical gases used in such lamps are deuterium, halogens, noble gases, or mixtures of noble gases with other substances such as mercury or sodium. Figure 2.5a shows a comparison of the emission of some of these lamps, which reveals that they are able to produce light over a wide wavelength range with high intensity. However, some limitations of these lamps are also obvious from this figure. The emission characteristic of a gas is not always continuous, many having sharp features with large variations in intensity, and most do not emit light below 200 nm (i.e. above 6.2 eV). One exception, a deuterium lamp, emits continuously to down 180 nm, with a more discrete spectrum down to 115 nm (Fig. 2.5b), but has no emission above 400 nm. The stability of the output intensity of these lamps is highly

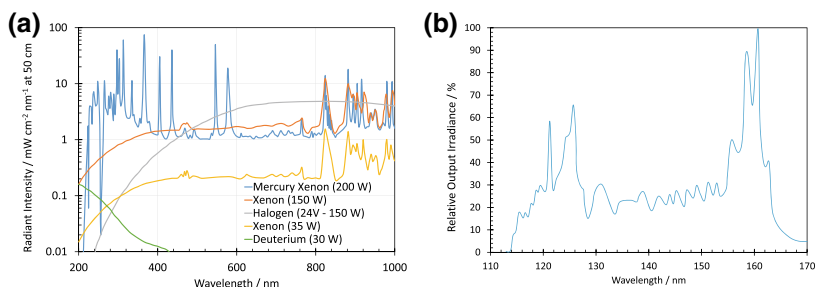


Fig. 2.5 **a** A comparison of output from discharge lamps (reproduced from https://www.photonics.com/Articles/A_Guide_to_Selecting_Lamps/a44487). **b** The discrete emission spectrum of a deuterium below 200 nm (reproduced from <https://www.hi-techlamps.com/hamamatsu-11835-water-cooled-type-deuterium-lamp/>)

dependent on many factors, such as temperature of the lamp and the stability of the power supply; their lifetime is also limited due to gradual erosion of the cathode in the lamp.

An ideal source of VUV-visible light is a synchrotron radiation (SR) light source. One such source is the third-generation light source, ASTRID2, at Aarhus University in Denmark and the remainder of this experimental section will focus on the light it produces and how it is monochromatized and used in photoabsorption experiments on the AU-UV beam line.

The ASTRID2 synchrotron light source (Fig. 2.6) is a 45.7 m circumference ring, maintained under ultra-high vacuum (UHV), where electrons are stored at an energy of 580 MeV. The properties of these relativistic electrons are such that electromagnetic radiation is emitted tangentially to their orbit as they pass through each of the 12 dipole bending magnets (red magnets in Fig. 2.6); this radiation is essentially continuous, covering a broad range of the electromagnetic spectrum from the IR to X-rays (red curve Fig. 2.7). The light produced is naturally collimated with

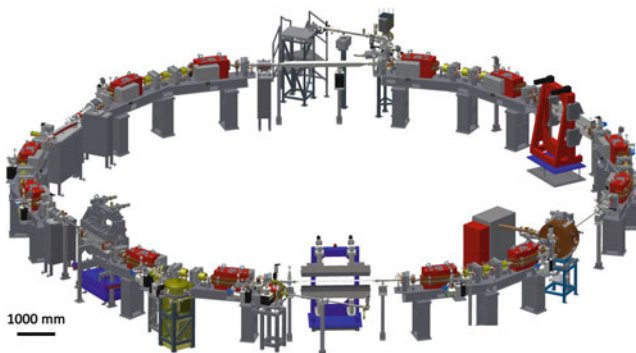


Fig. 2.6 The ASTRID2 synchrotron light source at Aarhus University, Denmark

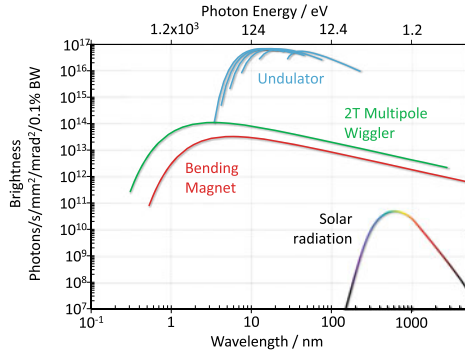


Fig. 2.7 Brightness of the photons produced in ASTRID2 over a range of wavelengths. The AU-UV beam line uses light from a dipole bending magnet (red curve). An undulator insertion device can produce photons with many times higher intensity in the UV-VUV region (blue curves), while a multipole wiggler is used to enhance the production of photons at higher energies, into the soft X-ray region (green curve)

a high degree of polarisation and with high brilliance due to the small size of the electron beam.

2.3.2 The AU-UV Beam Line

For this SR light to be useful in measuring photoabsorption (PA) cross-sections, it needs to be monochromatized. The AU-UV beam line accepts light from a dipole bending magnet in ASTRID2 and is transported under UHV to a monochromator using a series of mirrors, which also serve to focus the light (Fig. 2.8). The beam line was originally commissioned on the ASTRID storage ring in 2000 (Eden et al. 2006), then transferred and upgraded to use the new ASTRID2 facility in 2013 (Palmer et al. 2015b).

In the monochromator, light is directed through an entrance slit (ENS) onto a diffraction grating, a polished surface with parallel equidistant grooves. The grooves

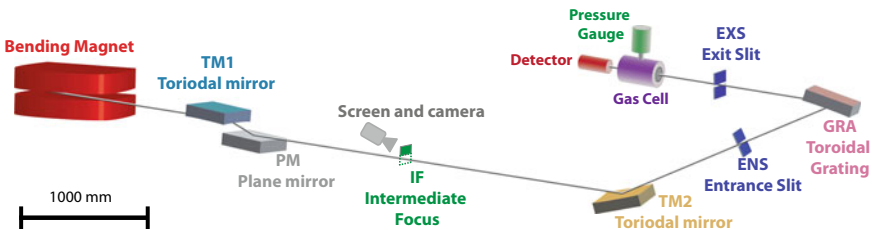


Fig. 2.8 Schematic overview of the AU-UV beam line on ASTRID2

Table 2.1 Grating parameters for the AU-UV beam line

Grating	Range (nm)	Range (eV)	Line density (Lines/mm)	d (m)	Resolution (nm)
HEG	100–340	12.4–3.65	2000	5×10^{-7}	0.08
LEG	160–700	7.75–1.8	1000	1×10^{-6}	0.16

reflect the incident light directed onto it such that light of differing wavelengths are diffracted according to the equation:

$$d \sin \theta_n = n\lambda \quad (2.23)$$

where λ is the wavelength of the diffracted light, d is the groove separation and n is the order of the diffracted light. The grating operates at near normal incidence and is rotated to change the incident angle and thus also the wavelength of light which is diffracted and passes through the exit slit (EXS) of the monochromator. There are two toroidal gratings in the AU-UV monochromator, a high energy (HEG) and low energy (LEG) grating, together producing a beam of monochromatized light covering the wavelength range 100–700 nm (12.4–1.8 eV). The parameters of the gratings are summarised in Table 2.1.

The focal distance of the grating changes according to the wavelength of the diffracted light, varying by some cm over the full wavelength range. Therefore, it is necessary to move the exit slit along the beam path in order to maintain focus on the EXS and have maximum photon intensity and best resolution at each wavelength.

The resolution of the resulting photon beam is also dependent upon the groove separation, d , and the size of the entrance and exit slits. The highest resolution possible, 0.08 nm, is obtained using the HEG with entrance and exit slits of 100 μm ; this corresponds to 7, 3 and 1 meV at the high, mid and low energy over which the HEG produces photons. Due to the larger value of d for the LEG the wavelength resolution is twice that of the HEG, however this gives a higher flux. The flux of photons produced by the beam line with 100 μm slits measured with an AXUV100G photodiode is shown in Fig. 2.9.

The monochromatized light exits the EXS and passes through a MgF_2 window at the end of the beam line for use in experiments.

2.3.3 The Gas Phase Photoabsorption Apparatus

The PA gas cell is mounted directly onto the end of the AU-UV beam line and essentially consists of a stainless-steel tube enclosed at each end with MgF_2 windows (Fig. 2.10), pumping, a sample inlet, a pressure gauge and a detector. The path length between the two windows, l , is 15.5 cm. The gas cell is evacuated and kept at high vacuum using a turbo pump, which is important to remove possible contaminants.

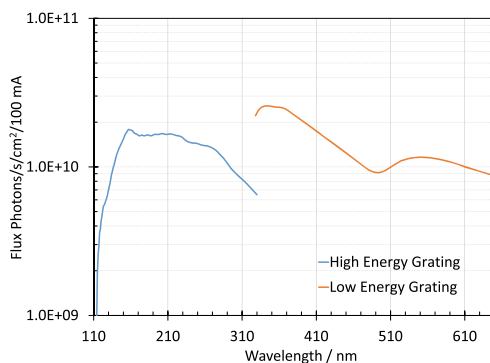


Fig. 2.9 Photo flux produced by the AU-UV beam line using the HEG and LEG with the entrance and exits slits at $100\ \mu\text{m}$

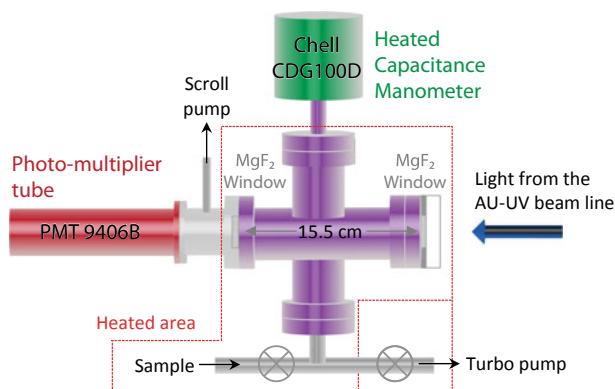


Fig. 2.10 Schematic of the photoabsorption gas cell used on the AU-UV beam line

2.3.3.1 Measurement of the Transmitted Light

The light passing through the gas cell is measured using a photo-multiplier tube (PMT); this is a vacuum tube containing dynodes which emit electrons as light hits them. Several stages of these dynodes within the tube allow the amplification of even the smallest flux of incident light, making them an extremely sensitive detector across the VUV to IR region. The Electron Tubes PMT (9406B) used here is fitted with an MgF_2 window and is optimised for use in the VUV-UV region. A high voltage is applied to the detector to accelerate the electrons between the dynodes, thus amplifying the signal; the output electron current is further amplified and converted into a voltage using a transimpedance amplifier. This voltage is then recorded in the experiment as the measurement of light intensity passing through the gas cell.

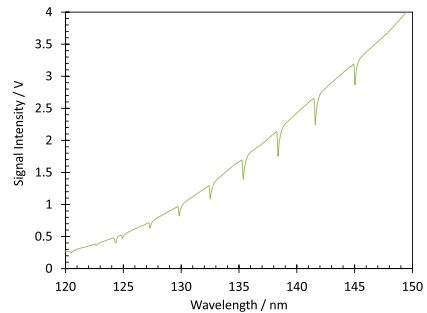
The stored electron beam in the ASTRID2 ring slowly decays with time, as the electrons lose energy or collisions occur within the beam, consequently so does

the photon intensity reaching the gas cell. To compensate for this loss, electrons are periodically injected into ASTRID2, which operates in so-called “top-up” mode, with the ring current typically varying by $\sim 2\%$ as a nominal 180 mA of stored current is maintained. An accurate measurement of the ring current is constantly monitored and the detector signal is normalised to compensate for this small change in intensity, therefore the effects of the decaying beam and injections are not observed in the final data.

After the exit MgF_2 window a small section before the detector is differentially pumped with a scroll pump in order to remove air and water which would otherwise absorb all light below 170 nm, however this section serves an additional purpose. The monochromator also produces unwanted higher orders of light, that is in Eq. 2.23 where $n > 1$. This means that, for example, when the required first order light at 300 nm is selected, 2nd order light with a wavelength of 150 nm also passes through the gas cell and is recorded by the detector. The MgF_2 windows absorb all light below 115 nm (above 10.8 eV) and therefore prevents 2nd order light up to 230 nm, but in order to accurately measure cross-sections at higher wavelengths the section between the cell and the detector is vented to allow air (mostly via O_2) to absorb 2nd order light up to 340 nm. When measurements to even higher wavelengths are required, a 310 nm or higher cut-off filter is placed between the gas cell and detector.

In order to confirm the wavelength of the photons produced, measurements of some well-known species with sharp features are taken and compared with peak positions from the literature. When using the HEG, in the low wavelength region the weak electric-dipole forbidden transitions in the $\tilde{a}^1\Pi_g - \tilde{X}^1\Sigma_g^+$ Lyman-Birge-Hopfield system can be observed (Lofthus and Krupenie 1977) with a high pressure $\gg 1$ Torr of high purity nitrogen, Fig. 2.11. At higher wavelengths, two regions of the sulphur dioxide spectrum (Wu et al. 2000; Vandaele et al. 1994) with distinctive vibrational progressions are measured, Fig. 2.12. These measurements allow the calibration of the photon wavelength to better than 0.05 nm across the full wavelength range.

Fig. 2.11 Nitrogen absorption in the $\tilde{a}^1\Pi_g - \tilde{X}^1\Sigma_g^+$ Lyman-Birge-Hopfield System. An electric dipole forbidden transition, therefore absorption is weak (Eden et al. 2006)



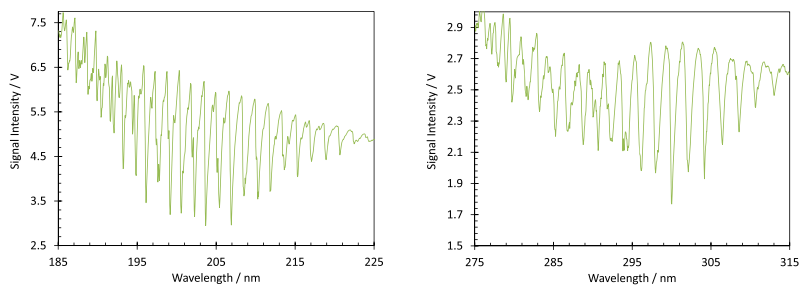


Fig. 2.12 Sulphur dioxide (SO_2) absorption peaks used to calibrate the wavelength of the photons and compared with (Wu et al. 2000) (185–225 nm) and (Vandaele et al. 1994) (275–315 nm)

2.3.3.2 Sample Preparation and Pressure Measurement

A liquid or solid sample, with as high a purity as possible, is placed into a pear shaped glass flask and attached to the gas cell via a valve. The air in the flask needs to be pumped away, and to avoid pumping the sample away the freeze-pump-thaw (FPT) technique is used. This involves cooling the sample in the flask with liquid nitrogen and pumping on the sample at this low temperature. If the sample is liquid at room temperature, then air will be trapped as it cools and solidifies and bubbles will be evident as the sample warms to room temperature. The FPT cycle is repeated until bubbles are no longer seen as the liquid sample thaws.

Some samples have a low vapour pressure at room temperature, so in order to increase the pressure for improved signal to noise ratio in the cross-section measurements, the gas cell and sample holder can be moderately heated up to a maximum of 80 °C.

Many liquid and solid samples have water as a contaminant. Due to the high vapour pressure of water (23.8 Torr @ 25 °C) it can be easily observed in a PA spectrum if it is present. If the vapour pressure of the desired sample is low, then the contamination may be removed (or just reduced) through pumping on the sample at room temperature (or a slightly elevated temperature). This is not always possible, therefore other methods of sample purification may be required.

The spectrum of water is well known (Fig. 2.13a) (Mota et al. 2005), with several sharp features with high cross-section at low wavelengths, so it may be easily identified. It is useful to compare all newly recorded spectra with that of water to check for sample contamination and to also compare with the spectrum of air (Fig. 2.13b) to ensure that none remains in the sample container, or indeed, that there are no leaks in the gas line.

The sample pressure in the gas cell is measured using a 1 Torr heated capacitance manometer (Chell CDG100D). In this type of gauge the capacitance between an electrode and a thin diaphragm exposed to the gas is measured. The distance, and hence capacitance, between them changes as the pressure of gas exerts force on and mechanically alters the diaphragm. The advantage of using this type of gauge is that it relies only upon a physical change in the diaphragm, and is therefore independent of

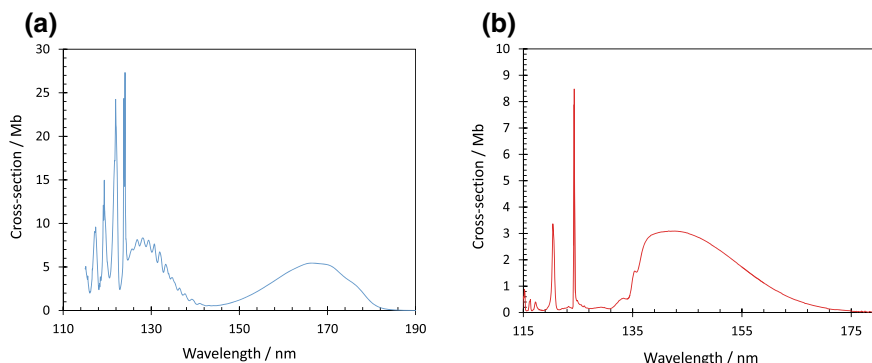


Fig. 2.13 **a** Photoabsorption spectrum of water. The most common contaminant observed in samples. **b** Spectrum of air, with oxygen absorption dominating the spectrum. The absolute cross-sections of pure O_2 and water are well known, and can be used to confirm that pressures are being measured correctly in the system

the gas being measured. The gauge is maintained at $100\text{ }^\circ\text{C}$ in order to prevent sample condensation within the gauge and therefore inaccuracies in pressure measurement. A 1 Torr full range gauge is the most suited for gas phase PA measurements in the VUV region, where typical sample pressures of 1 Torr, 0.1 Torr and 0.01 Torr can be used to accurately measure cross-sections of 1, 10 and 100 Mb respectively. The pressure measured by the gauge is given as voltage output in the range 0–10 V, with mV accuracy, where 10 V indicates a pressure of 1 Torr; this voltage is recorded during measurements and converted into the corresponding pressure and then number density, N , for calculation of the absolute cross-sections.

2.3.3.3 Acquisition of Data

The software for controlling the monochromator and recording the signals required for the calculation of cross-sections has been developed in-house. After selection of a wavelength range and step size, the scan proceeds to record the selected wavelength, light intensity, pressure and ring current for each step in the scan. The dwell time at each point is usually set to 2 s, but can be varied if required. To avoid measurement at the same time as an injection of electrons into the storage ring, which may cause disturbance to the light beam, the scanning programme pauses for 3 s before and after an injection.

A scan is first taken with an evacuated cell to give measurements of I_0 , then sample is added to the cell and two I_t scans recorded, finally the cell is evacuated again and the I_0 scan is repeated. A single scan with 200 wavelength steps takes about 10 min to measure. The final calculations are then carried out using averages of the four scans. This method of measurement has several benefits including:

- Measuring I_0 before and after I_t allows any long-term light intensity changes to be accounted for, for example changes due to the temperature stability of the beam line optics.
- Repeating the I_t scan gives a longer integration time at each point and therefore reduces the uncertainty and noise in the final spectrum.
- Comparing the two I_t scans will confirm whether or not the sample is stable over the timescale of the measurements. Degradation of the gas can occur, for example from contact with metal surfaces or due to photo-degradation during measurements.

With a new sample, a set of I_0 and I_t scans are first recorded over a broad range (110–220 nm) with 1 nm steps, which gives an overview of the spectrum, then afterwards overlapping sections with small step size are measured. In this way the ranges and smaller step sizes can be selected according to the level of fine structure and the variation in cross-section across the small section. A final spectrum is obtained through concatenation of the small sections, demonstrated in Fig. 2.14 for the spectrum of ammonia (Limão-Vieira et al. 2019).

Here all sections below 170 nm were measured with 0.02 nm steps to allow the sharp features to be well defined (the region below 145 nm is highlighted in the inset), while above 170 nm a step size of only 0.05 nm was required. The green dots are the result of the initial broad 1 nm step scan. Pressures used for measurement of this spectrum ranged from 0.03 to 0.5 Torr.

It is important to ensure that the pressure used for measurement is appropriate for the cross-sections. The incident light is normally attenuated linearly with pressure and the final calculated cross-section should be independent of the sample pressure used for measurement. However, this is not the case for very high or low pressures. If too high pressure is used then line saturation can occur, where the incident light is attenuated so much that the shape and cross-section of features will be altered (Fig. 2.15). Too little pressure, with low attenuation below 10%, can also lead to inaccurate measurements, with higher levels of noise in the resulting spectrum. Usually a sample pressure is chosen to give a maximum 40–50% attenuation of the incident light, this is enough to bring out low cross-section fine structure, but not so high that line saturation occurs.

Fig. 2.14 Spectrum of ammonia measured in small sections, represented by the various colours, to optimise pressure and step size. The green dots are the values measured in the initial 1 nm step broad scan

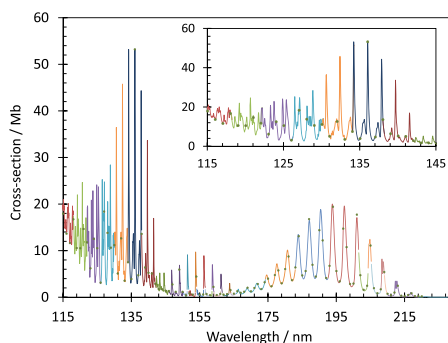
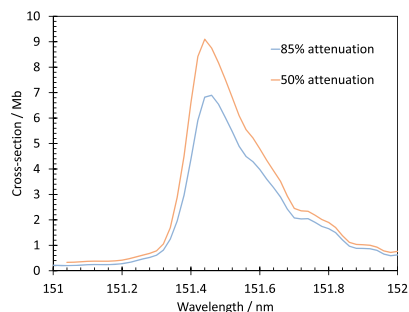


Fig. 2.15 Effect of over attenuation of the incident light on measurement of absolute cross-sections when using too high sample pressure



When adding a sample to the gas cell for measurement, ideally both valves to the sample and the pump can be closed with measurements carried out on a static, stable gas pressure throughout the scan. In reality this is not always possible, with considerable changes in pressure sometimes occurring, which depend on the nature of the sample and any possible contaminants. For example, the sample may condense on the surfaces of the cell, giving significant changes in pressure during the course of a scan, and if there is water contamination in the sample then highly unstable pressures can be seen. These problems can usually be overcome by allowing a small flow of sample through the cell, maintaining a reasonably stable pressure throughout a scan, leaving the valves to the sample and pump slightly open. As long as the pressure is recorded at each point in the spectrum, these pressure changes should not adversely affect the resulting spectrum. The exception to this is where there is significant water (or another) contamination in a sample; if the contaminant pressure increases while the sample pressure remains the same during the course of a scan then the spectrum will have the wrong shape, even in regions where no absorption of the contaminant occurs.

2.3.3.4 Errors Associated with Measurement

To confirm that the measurement of absolute cross-sections in the setup is correct, the spectrum of a well-known species is measured and compared with literature values. The Schuman–Rünge (6.9–9.5 eV) absorption band of O_2 is a good candidate due to the broad unstructured nature of the band (Fig. 2.13b), which minimises the effect of differences in energy resolution (Watanabe 1958). Statistical errors are typically less than $\pm 1\%$ and are associated with errors in the pressure measurement. The error on the absolute cross-section can be estimated on the basis of the partial errors for each of the factors in Eq. 2.24, derived from the substitution of the number density in Eq. 2.22.

$$\sigma = \ln\left(\frac{I_0}{I_t}\right) \frac{1}{Nl} = \ln\left(\frac{I_0}{I_t}\right) \frac{kT}{Pl} \quad (2.24)$$

where k is the Boltzmann constant, T is the temperature at which the spectrum was measured and P the measured pressure in mbar, giving an error of:

$$\begin{aligned} \Delta\sigma &= \sqrt{\left(\frac{\delta\sigma}{\delta T}\Delta T\right)^2 + \left(\frac{\delta\sigma}{\delta P}\Delta P\right)^2 + \left(\frac{\delta\sigma}{\delta l}\Delta l\right)^2 + \left(\frac{\delta\sigma}{\delta I_0}\Delta I_0\right)^2 + \left(\frac{\delta\sigma}{\delta I_t}\Delta I_t\right)^2} \\ &= \sqrt{\left(\left|\frac{k}{Pl}\ln\frac{I_0}{I_t}\right|\Delta T\right)^2 + \left(\left|\frac{kT}{P^2l}\ln\frac{I_0}{I_t}\right|\Delta P\right)^2 + \left(\left|\frac{kT}{Pl^2}\ln\frac{I_0}{I_t}\right|\Delta l\right)^2 + \left(\left|\frac{kT}{PlI_0}\right|\Delta I_0\right)^2 + \left(\left|\frac{kT}{PlI_t}\right|\Delta I_t\right)^2} \end{aligned} \quad (2.25)$$

Unless heating is required for improved vapour pressure of the sample, spectra are taken at room temperature with the laboratory maintained at 298 K. When there is heating on the cell, the temperature is accurately regulated with PID control; in either scenario the maximum error on the gas temperature is estimated to be ± 1 K. The error on the absorption path length is considered to be ± 1 mm. The random error on the pressure is estimated to be $\pm 1\%$ on the basis of fluctuations in the pressure gauge reading over a short period of time. Allowing for a systematic error associated with the purity of the gas sample, a total error of $\pm 3\%$ in the pressure is assumed. Absolute measurements for the incident beam are not required to evaluate the error on the cross-section as the terms in Eqs. 2.24 and 2.25 include intensity ratios only. The errors on I_t and I_0 are estimated as one half of the mean difference between the photomultiplier current measurements at a specific energy.

The combined error calculated using Eq. 2.25 for the present cross-sections averages at $\pm 5\%$, in agreement with the estimation made by Giuliani et al. (2003). Only when absorption by the sample is very weak ($I_0 \sim I_t$), does the calculated error increase significantly as a percentage of the measured cross-section. If we assume that $\Delta I_0 \approx \Delta I_t$ when $I_0 \approx I_t$, Eq. 2.25 simplifies to Eq. 2.26:

$$I_0 \approx I_t, \Delta I_0 \approx \Delta I_t \Rightarrow \Delta\sigma \approx \frac{(\sqrt{2})kT\Delta I_0}{PlI_0} \quad (2.26)$$

The approximate error on the cross-section measurement for $I_0 \approx I_t$ is therefore inversely proportional to the sample pressure (and the path length). This means that with the 1 Torr pressure gauge used for these experiments, it is not possible to obtain high accuracy of very low cross-sections (< 0.1 Mb). However, the apparent level of noise in the measured cross-section is generally a reliable indication of the error associated with very weak features.

2.3.4 Subtraction Methods for Rydberg and Vibrational State Analysis

A final VUV spectrum can exhibit significant structure, containing both broad valence states and fine structure due to vibrational or Rydberg states. Some of this fine

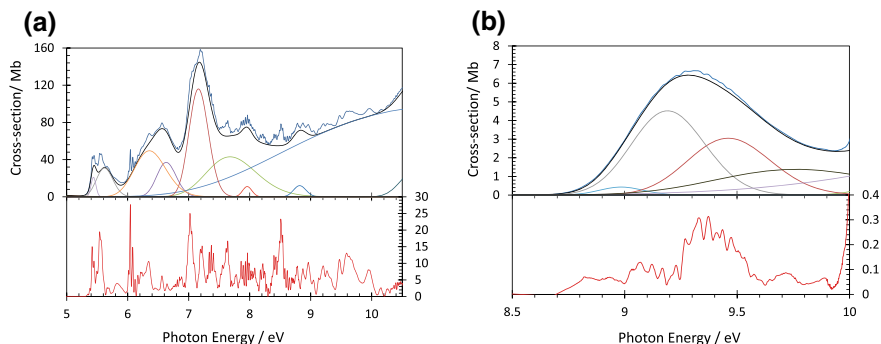


Fig. 2.16 Background subtraction of **a** the iodobenzene VUV spectrum. **b** A portion of the difluoromethane spectrum, after which fine structure can be more easily identified (the red “residual” spectra underneath). The original VUV spectra are in blue, and the underlying background which is subtracted is black. The individual Gaussian peaks making up the background are also shown

structure can appear as very small peaks on top of a broader large cross-section feature, making characterisation of these peaks difficult. In order to help identify these and other structures in the VUV spectrum, it is sometimes useful to subtract a smooth underlying “background”. This can be achieved through the calculation of a series of Gaussian peaks, the sum is a smooth curve which once subtracted from the VUV spectrum leaves a “residual” spectrum which highlights finer structure. The spectra for iodobenzene (Jones 2000) and difluoromethane (Harris and Bertolucci 1978) in Fig. 2.16 have been treated in this way. In particular, it can be seen from the treatment of the difluoromethane spectrum that this technique can help elucidate even small (0.1 Mb) structures.

It is important to note that the calculated Gaussian peaks used in this procedure are not representative of calculated valence or other bands for the molecule, simply created “by eye” in order to create a smooth underlying curve for subtraction.

2.3.5 Other SR Photo-absorption Beam Lines (Overview)

There are few beam lines world-wide which now measure the PA of species in this way, although there are many which produce VUV-UV light which could be used for this purpose. A list of some VUV beamlines used for PA measurements, past and present, are given in Table 2.2, those known to still be active are indicated with *.

Many PA experiments, such as that on the AU-UV beam line, are limited by the cut-off of windows used to enclose the gas cell. MgF_2 limits measurements to wavelengths above 115 nm; LiF can be used instead to reach 105 nm, however it is hygroscopic and is less durable than MgF_2 . There are PA setups that are not restricted in their measurements by optical crystals, which may be achieved through a variety of methods.

Table 2.2 A list of VUV beam lines where photoabsorption measurements have been carried out

Name	Facility	Country	WL range/nm
*AU-UV (UV1)	ASTRID2 (ASTRID)	Denmark	115–700
*HRVUV	Indus-1	India	105–300
*Photophysics	Indus-1	India	110–350
3.1	SRS, Daresbury	UK	30–300
3.2	SRS, Daresbury	UK	35–250
Beamline U11	Brookhaven	US	41–413
BL04B	SRRC	Taiwan	30–300
1 m-NIM-2	BESSY I	Germany	50–210
U125-2 NIM	BESSY II	Germany	35–310

For example, at BESSYI/II a differentially pumped section containing a microchannel plate separated the UHV beam line and the PA gas cell. While at beam line 3.1 at the SRS in Daresbury, the monochromatized light was directed through a differentially pumped capillary into the gas cell; highly efficient differential pumping is required in both cases in order to protect the beam line optics from the gases under investigation in the cell. These methods have the advantage of only being limited by the wavelength of photons that the monochromator can produce. Alternatively, a foil window can be used to separate the beam line UHV from the gas cell, a material such as aluminium with a thickness of only 0.15 μm can be used which allows transmission of light down to ~ 20 nm.

As all of these methods allow transmission of lower wavelength photons, it becomes necessary to ensure that artefacts are not produced in the resulting spectra due to higher orders of light. This can be achieved either through the use of cut-off filters or through the design of a monochromator preventing the transmission of higher order light. Other considerations for the windowless systems are the path length over which the light interacts with the gas, and any pressure gradients that may occur within the cell. If there is no longer a window to define the entrance of the gas cell, the path length is dependent upon how far the gas extends into the capillary, and pressure gradients may arise due to pumping of the gas through the capillary or microchannel plate. These will both affect the accuracy of final calculated absolute cross-sections.

The PA spectrum of N_2O , shown in Fig. 2.4, was taken on beam line 3.1 at the SRS in Daresbury, using a combination of an enclosed cell and a windowless capillary system. In this way the path length for the windowless measurements could be defined through comparison with those recorded in the enclosed cell at energies below the window cut-off.

PMTs are not able to directly measure VUV light at lower wavelengths as their entrance windows prevent its transmission, however a window coated with sodium salicylate on the exit of the cell converts the VUV light to visible, which can then be

detected by the PMT. The efficiency of this conversion is almost constant between 30 and 200 nm.

2.4 Electronic Structure Methods

Thanks to the recent progress in computer simulations of the electronic structure of molecular systems, the assignment of experimentally observed UV spectra is now possible for compounds containing a rather large number of electrons. In the following, we give a short summary of the methods, which have been employed to interpret the spectra mentioned in this chapter.

2.4.1 Short Introduction to *Ab Initio* Methods

The calculation of electronic excitation spectra requires that the time-independent Schrödinger equation is solved (within the Born-Oppenheimer approximation) not only for the ground state but also for as many excited states as possible. This directly gives the transitions energies. The oscillators strengths are usually calculated within the electric dipolar approximation, using the length gauge (cf. Eq. 2.14). It should be noted that obtaining Generalized Oscillator Strengths (i.e. non-dipolar) for comparison with Electron Energy Loss spectroscopy is much more difficult.

Due to the impossibility of exactly treating the electron-electron Coulomb repulsion, approximations are needed. In the Hartree-Fock model (HF) (Szabo and Ostlund 1996), each individual electron, i , is submitted to the mean field interaction created by all the other electrons. This means that the molecular Hamiltonian may be approximated by a sum of so-called mono-electronic Hamiltonian \hat{h}_i :

$$\hat{h}_i \phi_i = \varepsilon_i \phi_i \quad (2.27)$$

Thus, each electron occupies a single molecular orbital (MO) ϕ_i of energy ε_i and the total energy is the sum of all the mono-electronic energies, obtained after minimizing the total energy using the variational method. Because the Hartree-Fock Hamiltonian depends on the (unknown a priori) ϕ_i , a self-consistent procedure is used, hence the name SCF (Self-Consistent Field) for this method. Moreover, to satisfy Pauli's principle, the total wavefunction is expressed as a Slater determinant of the MO's.

For isolated molecular systems, the electronic wave function is usually obtained in the context of Linear Combination of Atomic Orbitals (LCAO) where MO's ϕ_i are obtained by combining nuclei-centred atomic orbitals χ_m (see also the next subsection):

$$\phi_i = \sum_{\{m\}=1}^M C_{im} \chi_m \quad (2.28)$$

The size of this basis set M is an important parameter to judge the quality of a calculation: due to the variational principle, a larger basis set always improves the energy.

Despite its ability to predict reasonable properties of molecules (geometries, infrared frequencies), the HF method cannot reproduce correctly the dissociation energy of a simple molecule like H_2 (Szabo and Ostlund 1996). This is due to the missing electronic correlation, which basically means that the HF electronic cloud is too compact. Moreover, electronic excited states are not available. Post-Hartree-Fock methods allow to correct these defaults and try to evaluate the missing correlation energy. They can be summarized in four main classes.

(a) *Perturbation theory*

In many cases, the single Slater determinant optimized at HF level is a good approximation of the exact wavefunction. This means that correlation effects are small (typically 1% of the HF energy) and can be treated using standard perturbation theory (Szabo and Ostlund 1996). In the molecular context, the most widely used variant is the Møller-Plesset method (MP) (Møller and Plesset 1934) where the HF Hamiltonian is the zeroth-order term. In principle, there is an infinite number of terms in the perturbation series which should be evaluated, but for computational reasons in practice only the second order term is included, leading to the widely known MP2 method. MP2 calculations improve HF results but it should, however, be kept in mind that the convergence of the series is not guaranteed and that this method is not variational. Moreover, excited states are not available.

(b) *Configuration interaction and multi-configurational methods*

Even at equilibrium distance, the HF approximation fails because the “true” wavefunction cannot be described accurately by a single Slater determinant. This is especially true for excited states, even for atoms. The logical improvement is to describe the wavefunction by a linear combination of determinants, created by promoting electrons from the $(n/2)$ occupied to the $(M - n/2)$ virtual (unoccupied) MO's obtained at the HF level:

$$|\Phi_{FCI}\rangle = c_0|\Phi_{HF}\rangle + \sum_S c_S|\Phi_S\rangle + \sum_D c_D|\Phi_D\rangle + \sum_T c_T|\Phi_T\rangle + \dots \quad (2.29)$$

where S stands for Single, D for Double, T for Triple excitation and so on. This so-called Full Configuration Interaction (FCI) also allows electronic excited states to be obtained. In practice, the size of the matrix to be diagonalized is too large and the excitation level has to be truncated to single and double for example (SDCI). But this leads to the so-called size-consistency problem: it can be shown that in SDCI; the energy of N non-interacting identical molecules is proportional to \sqrt{N} instead of N (Szabo and Ostlund 1996).

Nowadays, most CI calculations are used in a slightly different manner, in the so called multi-configurational methods. First, in order to lower the variational energy, both the weights of the atomic orbitals (AO) in the MO's (Eq. 2.28) AND the weights of the Slater determinants (Eq. 2.29) are optimized at the same time. Then Full CI is carried out but in a limited orbital space usually containing bonding, antibonding, non-bonding (and possibly Rydberg) MO's of interest. This leads to the so-called CASSCF (Complete Active Space Self-Consistent Field) method (Roos 2005). The remaining correlation energy implying excitation of electrons outside the active space is then evaluated either perturbatively (CASPT2 method (Roos 2008)), implemented in the MOLCAS code (Francesco et al. 2016) or variationally (MRCI (Werner and Knowles 1998)), implemented in the MOLPRO code (Werner et al. 2019).

Multi-configurational methods are very versatile methods allowing the description of every possible situation in a molecular system (Szalay et al. 2012): correct dissociation curves, electronic excited states of valence, Rydberg, mixed or charge transfer character. However, the size of the active space computationally accessible is relatively small.

(c) *Coupled Cluster theory*

Coupled Cluster methods (Crawford and Schaefer 2000) (CC) are the preferred choice when the HF determinant is a good approximation of the wavefunction. Although they are not variational (nor perturbational), they are size-consistent and give the same energy when the HF MO's are rotated. The main idea is to rewrite the CI wavefunction using an exponential operator. For example, in a CCD (Double) calculation:

$$|\Phi_{\text{CCD}}\rangle = e^{\widehat{T}_2}|\Phi_{\text{HF}}\rangle = \left[1 + \widehat{T}_2 + \frac{\widehat{T}_2^2}{2!} + \frac{\widehat{T}_2^3}{3!} + \dots \right] |\Phi_{\text{HF}}\rangle \quad (2.30)$$

where \widehat{T}_2 is an operator creating a double excitation from the occupied to the unoccupied MO's. Equation 4.1.4 shows that the CCD wavefunction contains not only double but also quadruple, sextuple ... excitations, which removes the size-consistency issue. As in a FCI calculation, the computational cost is increasing rapidly with the basis set size, so the most widely used method for ground state is the CCSD(T) method where triplet excitations are in fact treated by perturbation. Since CCSD(T) is basically a ground state method, for excited states the theoretical formulation is based on the Equation of Motion (EOM) leading to the EOM-CCSD method (Pielia 2007).

(d) *Density Functional Theory*

During the 1990s, Density Functional Theory (DFT) which was mostly used in solid state physics, has emerged as a very economical way to tackle the problem of electron correlation. This led to the possibility to calculate systems whose size was too large for standard ab initio methods. The main idea of DFT is to re-express the molecular Hamiltonian as a function of the total electronic density ρ . Hohenberg

and Kohn (1964) proved that there is a bijective relation between the exact density of a molecule and all its properties. Their second theorem states that ρ obeys the variational principle. However, these theorems say nothing about how to find ρ (and are in fact limited to the ground state). Kohn and Sham (1965) also rewrote the formalism in a LCAO way so that basically the cost of a DFT calculation is close to that of a HF one, with the benefit of including correlation effects, albeit in an approximate way.

Although DFT is an exact theory in principle, its practical implementation has a semi-empirical character, and is illustrated by the huge number of exchange-correlation functionals that are continuously proposed (Ruzsinszky and Perdew 2011). At the present time, there is no universal functional allowing the description of all the sought properties of a molecular system and the choice of a functional is a difficult task (Mardirossian and Head-Gordon 2017). For excited states, the theory is based on Time Dependent DFT (TDDFT) (Dreuw and Head-Gordon 2005; Goerigk and Grimme 2010). The choice of the functional is also crucial for excited states, due to the inability of some functionals to accurately describe Rydberg or charge transfer states (Mewes et al. 2018). Recent benchmark calculations (Laurent and Denis 2013) show that transition energies are not necessarily the best criterion for choosing a functional. In particular, even though this energy is correct, the nature of the MO's involved in the transition may be wrong (Prlj et al. 2015).

2.4.2 Atomic Basis Sets

In the context of the LCAO method, atomic basis sets are employed as the building blocks of molecular orbitals (MO's). Physically, the radial part of atomic orbitals should have the form of an exponential:

$$\text{STO}(n, \zeta) \sim r^{n-1} e^{(-\zeta r)} \quad (2.31)$$

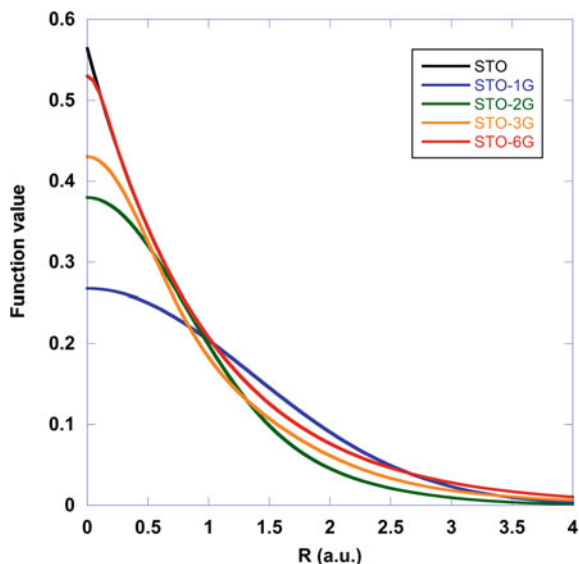
These functions are called Slater type orbitals (STO's). For reasons of computational efficiency, since the 1950s, Gaussian type orbitals (GTO's) are preferred to STO's for molecules:

$$G(\ell, \alpha) \sim r^\ell e^{(-\alpha r^2)} \quad (2.32)$$

However, a single Gaussian function does not have the correct shape of a STO at the origin (where the nucleus lies) and at long distance. Thus, a STO is modelled by a sum of a rather limited number of Gaussian functions, called contractions, as depicted in Fig. 2.17. As can be seen in this figure, a sum of properly chosen 6 gaussians is enough to reproduce the exponential behaviour of the STO wavefunction with acceptable accuracy.

For questions of “variational flexibility”, each atomic shell $s, p, d \dots$ is described by more than one STO, each one of them being a contraction of GTO's. So modern

Fig. 2.17 Normalized STO ($\zeta = 1.0$) fitted by 1, 2, 3 and 6 GTO's by maximizing the overlap. R is the distance from the nucleus in atomic units



basis sets are “multiple ζ ”: single, double, triple ... ζ basis sets. Moreover, so-called polarization functions (such as p functions for hydrogen, d functions for C, N, O) are necessary to improve the description of the electronic cloud. A large number of AO basis sets are available.¹ Among them, the “correlation-consistent” family proposed by Dunning is one of the most popular (Dunning 1989). They are labelled as cc-pVXZ, X being a cardinal number for the quality of the basis set. For example, the cc-pVTZ designates a triple- ζ basis set. However, these are not sufficient for the description of Rydberg excited states of isolated molecules, since they are designed for the valence region of the electronic cloud. Dunning has proposed “augmented” basis sets, labelled aug-cc-pVXZ but it should be noticed that the additional functions are meant to describe anionic states rather than highly diffuse states. For this reason, the basis set has to be supplemented by additional more diffuse functions. For C, N or O, the first Rydberg exponents ($n = 3$ and $n = 4$) are taken from (Dunning and Hay 1977). For the next exponents, we use the “universal” half-integer formula from Kaufmann et al. (1989)

$$\alpha(n, \ell) = \left(\frac{1}{2n}\right)^2 \frac{1}{(a_\ell n + b_\ell)^2} \quad (2.33)$$

Table 2.3 summarizes the exponents used for C, N, O and F.

¹see <https://bse.pnl.gov/bse/portal>.

Table 2.3 Rydberg exponents for main group atoms

n	s	p	d
3.0	0.005858	0.009988	0.014204
3.5	0.003346	0.005693	0.008077
4.0	0.002048	0.003476	0.004927
4.5	0.001324	0.002242	0.003175
5.0	0.000893	0.001511	0.002137
5.5	0.000624	0.001055	0.001491
6.0	0.000450	0.000759	0.001072

2.4.3 Assignment of Experimental Spectra

At the end of an ab initio calculation, we obtain a “stick” spectrum consisting of theoretical transition energies and oscillator strengths f , as shown in Fig. 2.18. However, the nature of the transitions (valence or Rydberg) has to be checked carefully. Several criteria are used:

- Calculations of the so-called Natural Orbitals (Löwdin and Shull 1956) and visual inspection of the mono-occupied ones. In some cases, the MO has a mixed valence-Rydberg character, such as a $3s/\sigma^*(C-H)$ found in many organic molecules. Sometimes, the excited state corresponds to a doubly excited state.
- Pure Rydberg transitions have very similar transition energies and much lower oscillator strengths. Because they correspond to an electron orbiting far away from the molecule, the corresponding electronic density should also be much diffuse than for a valence transition. A very useful parameter is the mean value of r^2 : $\langle r^2 \rangle$ in atomic units. Table 2.4 shows typical values taken from Nunes et al. (2010).

Fig. 2.18 Comparison between calculated and measured spectra for $c\text{-C}_5\text{F}_8$ (adapted from Limão-Vieira et al. 2008)

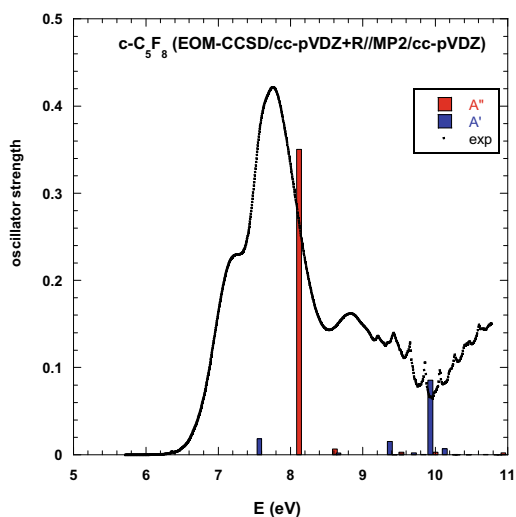


Table 2.4 Calculated selected transitions for methyl formate (Nunes et al. 2010)

State	E (eV)	f	$\langle r^2 \rangle$	Main character
$\tilde{X}^{-1}A'$	–	–	53	
$^1A''$	5.892	0.00131	53	$13a'$ (HOMO) \rightarrow LUMO
$^1A'$	7.946	0.00437	84	$13a'$ (HOMO) \rightarrow $3s\sigma/\sigma^*(CH)$
$^1A'$	8.206	0.15297	66	$3a''$ (HOMO-1) \rightarrow LUMO
$^1A''$	8.429	0.00915	88	$3a''$ (HOMO-1) \rightarrow $3s\sigma/\sigma^*(CH_3)$
$^1A'$	10.679	0.00221	1465	$13a'$ (HOMO) \rightarrow $6s\sigma$
$^1A'$	10.695	0.00238	1136	$13a'$ (HOMO) \rightarrow $6p\sigma$

Figure 2.18 shows an example of the comparison between a calculated stick spectrum and a measured one. The fact that the maxima of the bands do not correspond to the sticks maybe be due to either the accuracy of the calculations and/or vibrational effects which shift the 0–0 peak in the experiment. However, calculations are able to confirm if an observed band is due to a single intense transition for example.

2.4.4 Photoelectron Spectra

The calculation of photoelectron spectra (PES) is in principle very similar to that of UV spectra, with the important difference that the excited molecule has lost one electron. A first estimation of ionization energies IE's is provided by the well-known Koopmans' theorem (Koopmans 1934), which states that the mono-electronic energies of the MO's at the end of a Hartree-Fock calculation is equal to the experimental (vertical) ionization energy (IE):

$$IE_i = -\varepsilon_i$$

However, this approximation neglects the relaxation and correlation differences between the neutral and ionized electronic clouds. This requires specific techniques for solving the Schrödinger equation, based on Green functions methods, which eliminate the inconsistencies due to the different number of electrons (Danovich 2011). Among these, OVGf (Ortiz et al. 1997) and P3 (Ortiz 2005), implemented in the Gaussian code (Frisch et al. 2016), give reasonable values for ionization energies. The calculation of intensities is a more difficult task since the outgoing electron wavefunction is more like a plane wave than a localized orbital.

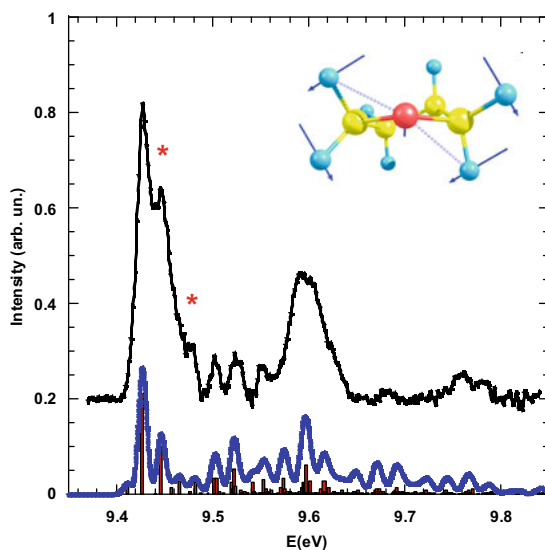
2.4.5 Vibrational Fine Structure

In some cases, especially for PES spectra with well separated bands, vibrational fine structure features can be observed in the experimental spectra (see Fig. 2.19). For a molecule containing N atoms, there are $3N-6$ degrees of freedom and therefore the number of vibrational modes increases rapidly with the size of the molecule. This can render the identification of vibrational peaks difficult. Again, theoretical calculations can provide useful information for the interpretation of observed structures.

For this, it is necessary to obtain the vibration frequencies not only for the ground state of the molecule, but also for each of the excited/ionized state. However, in most cases, the harmonic approximation is used for the calculation of these frequencies. This is done by calculating the second derivative of the electronic energy with respect to the coordinates of the atoms in the molecule. The result is a matrix called Hessian which has to be diagonalized. The eigenvalues, properly weighted by the reduced masses of the atoms, give the harmonic frequencies and the eigenfunctions show the nature of the mode (Harris and Bertolucci 1978). Armed with the frequencies of the ground and excited, the vibrational spectrum can be obtained via the evaluation of the Franck-Condon factors. While this is an easy task for a diatomic molecule (including anharmonicity), this becomes tedious as soon as the number of degrees of freedom increases. Codes such as eZspectrum (Koziol et al. 2009) greatly simplify this task by reading the outputs of common ab initio codes.

Here we give an example of how these calculations can help to assign vibrational fine features. In gas phase, the first band of the UV spectrum of tetrahydrofuran (THF) shows the presence of two conformers of C_2 and C_s symmetry (Giuliani et al. 2009).

Fig. 2.19 Comparison between calculated (black and red) and measured (blue) vibrational structure in THF Photoelectron spectrum (adapted from Dampc et al. 2009). The inset shows the nature of the mode responsible for the features labelled with a star in the spectrum



In the PES spectrum (see Fig. 2.19), the first band displays fine features due to the stable C_2 conformer superimposed with a broad band due to the C_s one (Dampc et al. 2009). This is due to the fact that the C_s ionic form is not stable (Park et al. 2017). By removing this continuum, the C_2 contribution can be isolated (Fig. 2.19). Most of the vibrational bands can be assigned but there remain two features separated by 21 meV (stars in Fig. 2.19). As shown in this figure, by performing frequency calculations at MP2/aug-cc-pVTZ level combined with eZspectrum calculations, it is possible to reproduce the observed spectrum with an excellent agreement and identify the mode responsible for the unknown features, which is calculated at 27 meV. These calculations include both hot and combinations bands for a total of about 3.4 billion.

2.5 Investigated Classes of Molecules

Since the UV photoabsorption beam line at Aarhus University was commissioned in 2000, an international consortium involving research groups from Denmark, England, Portugal, Belgium and France have collaborated to bring together experimental and theoretical expertise to deliver high-resolution VUV spectra and assignment of the most relevant photoabsorption features. The initial focus was related to concern about the prospects of anthropogenic climate change as a consequence of the constant emission into the atmosphere of pollutants, especially those arising from anthropogenic and biogenic emissions (including Volatile Organic Compounds, VOC) and the plasma-processing industries. The biogenic emissions we have concentrated on are VOCs found principally in forests. Indeed, forest VOC emissions are larger than all man-made VOC emissions combined. Estimation of biogenic emissions is therefore critical to assessing regional atmospheric chemistry processes which cause tropospheric ozone, since research has shown that VOC emissions lead to the formation of NO_x , a critical source precursor of tropospheric ozone. The subsequent reaction of ozone with VOCs may then cause particulate formation leading to the characteristic haze seen over rich deciduous forests.

As part of a major international research programme (including partners from Japanese industry) we have carried out an extensive study of the physical and chemical properties of feed stock gases currently used in the plasma industry and investigated alternative compounds for the development of so called 'green technology'. The photolysis of such compounds by sunlight is an essential part of these studies since the lifetime of these compounds in the terrestrial atmosphere is dominated by solar photolysis. Using the UV beam line at Aarhus University we have recorded the first VUV absorption spectra of alternative species such as CF_3I , C_2F_4 , SF_5CF_3 and most recently the cyclic compounds C_4F_8 and C_5F_8 . We have also extended these studies to $CHClF_2$ and $CHClF_4$, both of which have been suggested as replacements for C_2ClF_5 that is currently used with SF_6 for dry etching. These two gases, though similar to C_2ClF_5 , contain reactive hydrogen sites and may therefore be expected to be broken down in the atmosphere by reactions with OH radicals. It is necessary to record VUV photoabsorption spectra of these species in order to determine the

electronic state spectroscopy, the dissociation pathways and compare UV photolysis rates to those induced by OH reactions as sink mechanisms in the terrestrial troposphere.

The role of radiation induced damage on biomolecular systems is also another relevant topic with only a few studies concerning the UV-visible spectroscopy of such biomolecules and therefore little or no information on their electronic state spectroscopy that can lead to molecular dissociation (either by photon or electron impact). The electronic state spectroscopy of several biomolecules has been investigated in order to understand the structural and chemical modification of these systems during irradiation. This can provide information about the molecular pathways that lead from initial deposition of radiative energy to the formation of irreversible biomaterial damage. Most biomolecules are solid at room temperature and so it is hard to produce them in a gaseous phase for spectroscopic analysis, therefore development of an absorption cell with an oven-based apparatus to vaporize such compounds is required.

With the present configuration of the absorption gas-cell on the Aarhus University UV beam line, a wide range of molecules have been investigated, with the VUV photoabsorption spectra of over 200 molecules recorded. A list of molecules, including some biomolecular compounds and those of atmospheric interest, where the spectra have been analysed and published, is shown in Table 2.5.

An important source of photoabsorption spectra online is the MPI-Mainz UV/VIS Spectral Atlas of Gaseous Molecules of Atmospheric Interest [<http://www.atmosphere.mpg.de>] and the Science-SoftCon UV/Vis⁺ Spectra Data Base (UV/Vis⁺ Photochemistry Database) [<http://www.science-softcon.de/>].

2.5.1 An Example of a Series of Photoabsorption Spectra: Substituted Benzenes

Presented in this section is an example of a set of five related molecules, benzene and its mono-substituted halobenzenes (Fig. 2.20), which have been thoroughly investigated by VUV photoabsorption and complementary experimental and theoretical methods (Refs: Palmer et al. 2015a, b, 2016a, b). These spectra show the significant range in cross-sections that may be obtained in this VUV region of the spectrum, ranging from <1 to >400 Mb. The high-resolution achieved at the AU-UV beam line ($\Delta\lambda = 0.08$ nm) allows the identification of key absorption features which are signatures of valence and Rydberg transitions, both rich in vibrational excitation of particular active modes. Assignment of the features was aided by comprehensive Franck-Condon analyses of the photoabsorption spectra together with photoelectron spectroscopy revealing the nature of those bands (hot and cold), allowing vibronic transitions in both ionic and electronically excited states to be identified.

Table 2.5 A list of molecules for which VUV photoabsorption spectrum recorded on the Aarhus University UV beam line has been analysed and published

(-)- α pinene	Carbonyl sulphide	Isoxazole
(-)- β pinene	Chlorobenzene	Limonene
1,1-difluoroethylene	Chloromethane	Methyl formate
1,4-Pentadiene	Chlorotrifluoromethane	Methyl iodide
1-Methyl-1,2,4-triazole	Dichlorodifluoromethane	Octafluorocyclopentene
1-Methyl tetrazole	Difluorochloromethane	p-Benzoquinone
2,4-Difluorotoluene	Difluoromethane	Perfluorocyclobutane
2,6-Difluorotoluene	Dimethyl sulphide	Phenol
2H-1,2,3-triazole	DMSO	Propionic acid
2-Methyl tetrazole	Ethyl acetate	Pyridine-N-oxide
2-Methylfuran	Ethyl formate	Pyrimidine
2-Tetrahydrofurfuryl alcohol	Fluorobenzene	Quinoline
2-Vinylfuran	Furfural	Sevoflurane
Acetaldehyde	Furfuryl alcohol	Tetrachloroethylene
Acetic acid	Halothane	Tetrafluoroethylene
Acetone	Hexafluorobenzene	Tetrahydrofuran
Acetonitrile	Hexafluoropropene	Thiophene
Acrylic acid	Iodobenzene	Toluene
Acrylonitrile	Iodopentafluorobenzene	Trifluoriodomethane
Bromobenzene	Isobutyl acetate	Trifluoromethyl sulphur pentafluoride
Bromopentafluorobenzene	Isobutyl formate	Valeric acid
Bromopyruvic acid	Isoflurane	Vinyl chloride
Bromotrifluoromethane	Isoprene	Water
Butyric acid	Isoquinoline	

2.6 Outlook

High-resolution VUV photoabsorption in the 110–330 nm wavelength region using synchrotron radiation as a light source is an excellent tool to investigate the electronic state spectroscopy of key selected molecular targets. This information together with complementary experimental techniques such as High Resolution Electron Energy Loss Spectroscopy (HREELS) and Photoelectron Spectroscopy, together with state-of-the-art *ab initio* calculations at different levels of theory, provide an excellent tool to comprehensively assess the role of such electronic states.

Absolute photoabsorption data can be used as a reference for measurements of local abundances based on UV spectroscopy in many different environments including:

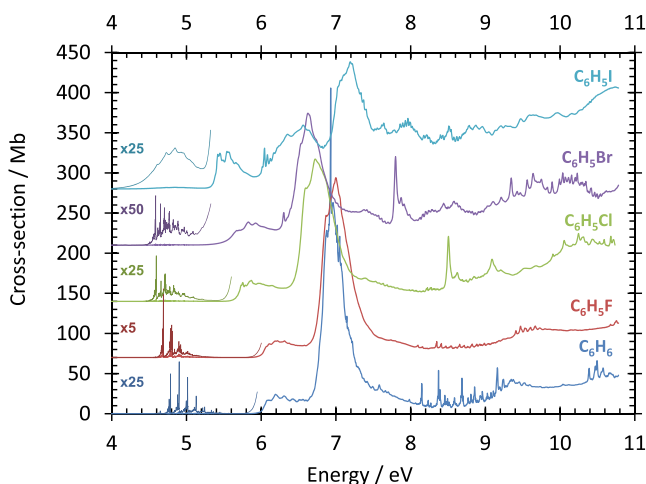


Fig. 2.20 Photoabsorption spectra of benzene and the mono-substituted halobenzenes, all measured on the AU-UV beam line, with the low energy regions highlighted through scaling by the amount indicated. The full spectra have not been scaled only offset, in order to improve visibility (Refs: Palmer et al. 2015a, b, 2016a, b)

- atmospheric chemistry—accurate absorption cross section values, as well as a comprehensive description of the electronic states of atmospheric relevant compounds, are needed as part of a wider research programme aimed at understanding the spectroscopy of these compounds and their role as trace gases in atmospheric chemical and physical reactions. The absolute photoabsorption cross sections are used to calculate photolysis rates at 0–50 km altitude in the Earth’s atmosphere.
- radiation biology—quantifying the risk from radiation damage and modelling the effect of radiation on cellular material requires a detailed understanding of the underlying interactions between the primary radiation (e.g. UV photons, X-rays etc.) and biomolecules (e.g. the nucleic and amino acids, sugars) as an important route to understand the effects of direct energy deposition by radiation.
- astro-chemistry—detailed knowledge of the nature of the electronically excited states by experimental and theoretical methods are also demanded to assess the nature of the excited states from which estimates of neutral dissociation cross sections can be obtained from electron energy loss spectroscopy.

The need to understand how the chemical compounds that we use in our daily life, as well as in industry, affects our atmosphere and our biology requires a continuous effort in their study. Thus, despite the large number of molecules already investigated at the ASTRID2 UV beam line, and other SR facilities, the endeavour continues: careful measurement and detailed analysis of VUV spectra of important classes of molecules is still expected to continue in the foreseeable future.

Acknowledgements The research has been supported by the project CALIPSOplus under the Grant Agreement 730872 from the EU Framework Programme for Research and Innovation HORIZON 2020. The research has also received funding from the European Community's Seventh Framework Programme (FP7/2007-2013) CALIPSO under grant agreement n° 312284 and i3-ELISA under grant agreement n° 226716. In addition, funding has been received from the I3 Integrated Activity on Synchrotron and Free Electron Laser Science (IA-SFS), contract number RII3-CT-2004-506008 under the Research Infrastructure Action of the FP6 EC programme 'Structuring the European Research Area'.

ASTRID2 and the upgraded UV beam line was funded by the National Programme for Research Infrastructures, the Danish Agency for Science, Technology and Innovation.

Support from the CaPPA project (Chemical and Physical Properties of the Atmosphere) funded by the French National Research Agency (ANR) through the PIA (Programme d'Investissement d'Avenir) under Contract No. ANR-10-LABX-005. Région Hauts de France and the Ministère de l'Enseignement Supérieur et de la Recherche (CPER Climibio) and the European Fund for Regional Economic Development for their financial support. This work was performed using HPC resources from GENCI-TGCC (Grant No. 2019-A0010806820). The Centre de Ressources Informatiques (CRI) of the Université of Lille also provided computing time.

The Portuguese National Funding Agency FCT-MCTES through Research Grants UID/FIS/00068/2013 and UID/FIS/00068/2019 (CEFITEC, Centre of Physics and Technological Research), PTDC/FIS-AQM/31215/2017 and PTDC/FIS-AQM/31281/2017. This work was also supported by Radiation Biology and Biophysics Doctoral Training Programme (RaBBiT, PD/00193/2012); UID/Multi/04378/ 2013 (UCIBIO).

EU COST Actions: P9-Radiation Damage in Bio-molecular Systems, CM0601-Electron Controlled Chemical Lithography, CM0805-The Chemical Cosmos; Understanding Chemistry in Astronomical Environments, MP1002-Nano-scale insights in ion beam cancer therapy, CM1301-Chemistry for Electron-Induced Nanolithography and CM1401-Our Astro-Chemical History.

The Brazilian Agency *Conselho Nacional de Desenvolvimento Científico e Tecnológico* (CNPq) and the Science Without Borders Programme.

Finally, we are indebted to former colleagues Dr. Marie-Jeanne Hubin-Franskin (Université de Liège, Belgium), and Prof. Jacques Delwiche (Université de Liège, Belgium) and Prof. Nigel Mason (Open University, UK), with whom we have had fruitful scientific collaborations over the last 20 years.

References

- Bransden BH, Joachain CJ (1983) Physics of atoms and molecules. Longman Scientific & Technical, Essex, UK
- Cantor CR, Schimmel PR (2001) Techniques for the study of biological structure and function. W.H. Freeman and Company, New York, USA
- Crawford DT, Schaefer III HF (2000) An introduction to coupled cluster theory for computational chemists. In: Lipkowitz KB, Boyd DB (eds) Reviews in computational chemistry. Wiley-VCH Inc., pp 33–136. <https://doi.org/10.1002/9780470125915.ch2>
- Dampc M, Mielewska B, Siggel-King MRF, King GC, Zubek M (2009) Threshold photoelectron spectra of tetrahydrofuran over the energy range 9–29 eV. Chem Phys 359:77–81
- Danovich D (2011) Green's function methods for calculating ionization potentials, electron affinities, and excitation energies. WIREs Comput Mol Sci 1:377–387
- Dreuw A, Head-Gordon M (2005) Single-reference ab initio methods for the calculation of excited states of large molecules. Chem Rev 105:4009–4037
- Dunning TH Jr (1989) Gaussian basis sets for use in correlated molecular calculations. I. The atoms boron through neon and hydrogen. J Chem Phys 90:1007–1023

- Dunning TH Jr, Hay PJ (1977) Gaussian basis sets for molecular calculations. In: Schaefer HF III (ed) *Modern theoretical chemistry*. Plenum Press, New York
- Eden S, Plimao-Vieira P, Hoffmann SV, Mason NJ (2006) VUV photoabsorption in CF₃X (X = Cl, Br, I) fluoro-alkanes. *Chem Phys* 323:313–333. <https://doi.org/10.1016/j.chemphys.2005.09.040>
- Francesco A et al (2016) Molcas 8: new capabilities for multiconfigurational quantum chemical calculations across the periodic table. *J Comput Chem* 37:506–541
- Frisch MJ et al (2016) Gaussian 16 Rev. B.01
- Gingell JM, Mason NJ, Zhao H, Walker IC, Siggel MRF (1997) VUV-optical absorption and electron-energy-loss spectroscopy of formamide. *Chem Phys* 220:191–205
- Giuliani A, Motte-Tollet F, Delwiche J, Heinesch J, Mason NJ, Gingell JM, Walker IC, Jones NC, Hubin-Franskin M-J (1999) Electronic excitation and oscillator strength of ethyl iodide by VUV photoabsorption and electron energy loss spectroscopy. *J Chem Phys* 110:10307. <https://doi.org/10.1063/1.478964>
- Giuliani A, Delwiche J, Hoffmann SV, Limao-Vieira P, Mason NJ, Hubin-Franskin M-J (2003) 2-methyl furan: an experimental study of the excited electronic levels by electron energy loss spectroscopy, vacuum ultraviolet photoabsorption and photoelectron spectroscopy. *J Chem Phys* 119:3670
- Giuliani A, Limão-Vieira P, Dufлот D, Milosavljevic AR, Marinkovic BP, Hoffmann SV, Mason N, Delwiche J, Hubin-Franskin M-J (2009) Electronic states of neutral and ionized tetrahydrofuran studied by VUV spectroscopy and ab initio calculations. *Eur Phys J D At Mol Opt Plasma Phys* 51:97–108
- Goerigk L, Grimme S (2010) Assessment of TD-DFT methods and of various spin scaled CIS(D) and CC2 versions for the treatment of low-lying valence excitations of large organic dyes. *J Chem Phys* 132:184103–184109
- Harris DC, Bertolucci MD (1978) *Symmetry and spectroscopy: an introduction to vibrational and electronic spectroscopy*. Oxford University Press Inc., New York
- Hohenberg P, Kohn W (1964) Inhomogeneous electron gas. *Phys Rev* 136:B864
- Huebner RH, Celotta RJ, Mielczarek SR, Kuyatt CE (1973) *J Chem Phys* 59:5434
- Inokuti M (1971) Inelastic collisions of fast charged particles with atoms and molecules—the Bethe theory revisited. *Rev Mod Phys* 43:297
- Jones NC (2000) *Spectroscopy and dissociation dynamics of simple polyatomic molecules*. PhD thesis, UCL, University of London, UK
- Kaufmann K, Baumeister W, Jungen M (1989) Universal Gaussian basis sets for an optimum representation of Rydberg and continuum wavefunctions. *J Phys B At Mol Opt Phys* 22:2223
- Kettle SFA (2007) *Symmetry and structure: readable group theory for chemists*, 3rd edn. Wiley, Chichester, UK
- Kohn W, Sham LJ (1965) Self-consistent equations including exchange and correlation effects. *Phys Rev* 140:A1133–A1138
- Koopmans T (1934) Über die Zuordnung von Wellenfunktionen und Eigenwerten zu den Einzelnen Elektronen Eines Atoms. *Physica* 1:104–113
- Koziol L, Mozhayskiy VA, Braams BJ, Bowman JM, Krylov AI (2009) Ab initio calculation of the photoelectron spectra of the hydroxycarbene diradicals. *J Phys Chem A* 113:7802–7809
- Laurent A, Jacquemin D (2013) TD-DFT benchmarks: a review. *Int J Quantum Chem* 113:2019–2039
- Limão-Vieira P, Dufлот D, Giuliani A, Vasekova E, Lourenço JMC, Santos PM, Hoffmann SV, Mason NJ, Delwiche J, Hubin-Franskin M-J (2008) Electronic state spectroscopy of c-C₅F₈ explored by photoabsorption, electron impact, photoelectron spectroscopies and ab initio calculations. *J Phys Chem A* 112:2782–2793
- Limão-Vieira P, Jones NC, Hoffmann SV, Dufлот D, Mendes M, Ferreira da Silva F, Hoshino M, Tanaka H (2019) Manuscript in preparation
- Lofthus A, Krupenie PH (1977) The spectrum of molecular nitrogen. *J Phys Chem Ref Data* 6:113–307. <https://doi.org/10.1063/1.555546>

- Löwdin P-O, Shull H (1956) Natural orbitals in the quantum theory of two-electron systems. *Phys Rev* 101:1730–1739
- Mardirossian N, Head-Gordon M (2017) Thirty years of density functional theory in computational chemistry: an overview and extensive assessment of 200 density functionals. *Mol Phys* 115:2315–2372
- Mewes SA, Plasser F, Krylov A, Dreuw A (2018) Benchmarking excited-state calculations using exciton properties. *J Chem Theory Comput* 14:710–725
- Møller C, Plesset MS (1934) Note on an approximation treatment for many-electron systems. *Phys Rev* 46:618–622
- Mota R, Parafita R, Giuliani A, Hubin-Franskin M-J, Lourenco JMC, Garcia G, Hoffmann SV, Mason NJ, Ribeiro PA, Raposo M, Limao-Vieira P (2005) Water VUV electronic state spectroscopy by synchrotron radiation. *Chem Phys Lett* 416:152–159. <https://doi.org/10.1016/j.cplett.2005.09.073>
- Nunes Y, Martins G, Mason NJ, Dufflot D, Hoffmann SV, Delwiche J, Hubin-Franskin M-J, Limão-Vieira P (2010) Electronic state spectroscopy of methyl formate probed by high resolution VUV photoabsorption, He(I) photoelectron spectroscopy and ab initio calculations. *Phys Chem Chem Phys* 12:15734–15743
- Ortiz JV (2005) An efficient, renormalized self-energy for calculating the electron binding energies of closed-shell molecules and anions. *Int J Quantum Chem* 105:803–808
- Ortiz JV, Zakrzewski VG, Dolgounitcheva O (1997) One-electron pictures of electronic structure: propagator calculations on photoelectron spectra of aromatic molecules. In: Calais J-L, Kryachko E (eds) *Conceptual perspectives in quantum chemistry*. Springer, Netherlands, pp 465–517. https://doi.org/10.1007/978-94-011-5572-4_13
- Palmer MH, Ridley T, Hoffmann SV, Jones NC, Coreno M, de Simone M, Grazioli C, Zhang T, Biczysko M, Baiardi A, Peterson KA (2015a) Interpretation of the photoelectron, ultra-violet, and vacuum ultraviolet photoabsorption spectra of bromobenzene by ab initio configuration interaction and DFT computations. *J Chem Phys* 143:164303. <https://doi.org/10.1063/1.4933419>
- Palmer MH, Ridley T, Hoffmann SV, Jones NC, Coreno M, De Simone M, Grazioli C, Biczysko M, Baiardi A, Limao-Vieira P (2015b) Interpretation of the vacuum ultraviolet photoabsorption spectrum of iodobenzene by ab initio computations. *J Chem Phys* 142:132302
- Palmer MH, Ridley T, Hoffmann SV, Jones NC, Coreno M, de Simone M, Grazioli C, Zhang T, Biczysko M, Baiardi A, Peterson KA (2016a) Combined theoretical and experimental study of the valence, Rydberg and ionic states of chlorobenzene. *J Chem Phys* 144:124302. <https://doi.org/10.1063/1.4944078>
- Palmer MH, Ridley T, Hoffmann SV, Jones NC, Coreno M, De Simone M, Grazioli C, Zhang T, Biczysko M, Baiardi A, Peterson KA (2016b) Combined theoretical and experimental study of the valence, Rydberg and ionic states of fluorobenzene. *J Chem Phys* 144:204305
- Palmer MH, Hoffmann SV, Jones NC, Coreno M, De Simone M, Grazioli C, Peterson K, Baiardi A, Zhang T, Biczysko M (2017) A combined theoretical and experimental study of the valence and Rydberg states of iodopentafluorobenzene. *J Chem Phys* 146:174301
- Palmer MH, Hoffmann SV, Jones NC, Coreno M, de Simone M, Grazioli C (2018) The valence and Rydberg states of difluoromethane: a combined experimental vacuum ultraviolet spectrum absorption and theoretical study by ab initio configuration interaction and density functional computations. *J Chem Phys* 148:214304. <https://doi.org/10.1063/1.5030657>
- Park SM, Lee YR, Kang DW, Kim HL, Kwon CH (2017) Conformational structures of the tetrahydrofuran cation determined using one-photon mass-analyzed threshold ionization spectroscopy. *Phys Chem Chem Phys* 19:30362–30369
- Piela L (2007) Correlation of the electronic motions. In: Piela L (ed) *Ideas of quantum chemistry*, 2nd ed. Elsevier, pp 498–566. <https://doi.org/10.1016/b978-044452227-6/50011-9>
- Prlj A, Curchod BFE, Fabrizio A, Floryan L, Corminboeuf C (2015) Qualitatively in-correct features in the TDDFT spectrum of thiophene-based compounds. *J Phys Chem Lett* 6:13–21

- Roos BO (2005) Multiconfigurational quantum chemistry. In: Dykstra CE, Frenking G, Kim KS, Scuseria GE (eds) *Theory and applications of computational chemistry*. Elsevier, pp 725–764. <https://doi.org/10.1016/b978-044451719-7/50068-8>
- Roos BO (2008) Multiconfigurational quantum chemistry for ground and excited states. In: Shukla, MK, Leszczynski J (eds) *Radiation induced molecular phenomena in nucleic acids: a comprehensive theoretical and experimental analysis*. Springer, Netherlands, pp 125–156. https://doi.org/10.1007/978-1-4020-8184-2_5
- Ruzsinszky A, Perdew JP (2011) Twelve outstanding problems in ground-state density functional theory: a bouquet of puzzles. *Comput Theor Chem* 963:2–6
- Sandorfy C (1981) Rydberg states in chemistry. *Int J Quantum Chem* 19:1147
- Szabo A, Ostlund NS (1996) *Modern quantum chemistry: introduction to advanced electronic structure theory*. Dover Publications Inc
- Szalay PG, Müller T, Gidofalvi G, Lischka H, Shepard R (2012) Multiconfiguration self-consistent field and multireference configuration interaction methods and applications. *Chem Rev* 112:108–181
- Vandaele AC, Simon PC, Guilmot MM, Carleer RC (1994) SO₂ absorption cross section measurement in the UV using a Fourier transform spectrometer. *J Geophys Res* 99:25599–25605. <https://doi.org/10.1029/94jd02187>
- Watanabe K (1958) Ultraviolet absorption processes in the upper atmosphere. *Adv Geophys* 5:153–221
- Weissbluth M (1978) *Atoms and molecules*. Academic Press Inc., San Diego, USA
- Werner H, Knowles PJ (1998) An efficient internally contracted multiconfiguration–reference configuration interaction method. *J Chem Phys* 89:5803–5814
- Werner H-J, Knowles PJ, Knizia G, Manby FR, Schütz M, Celani P, Györfy W, Kats D, Korona T, Lindh R, Mitrushenkov A, Rauhut G, Shamasundar KR, Adler TB, Amos RD, Bennie SJ, Bernhardsson A, Berning A, Cooper DL, Deegan MJO, Dobbyn AJ, Eckert F, Goll E, Hampel C, Hesselmann A, Hetzer G, Hrenar T, Jansen G, Köppl C, Lee SJR, Liu Y, Lloyd AW, Ma Q, Mata RA, May AJ, McNicholas SJ, Meyer W, Miller III TF, Mura ME, Nicklass A, O’Neill DP, Palmieri P, Peng D, Pflüger K, Pitzer R, Reiher M, Shiozaki T, Stoll H, Stone AJ, Tarroni R, Thorsteinsson T, Wang M, Welborn M (2019) MOLPRO, version 2019.1, a package of ab initio programs. <http://www.molpro.net>
- Wu CYR, Yang BW, Chen FZ, Judge DL, Caldwell J, Trafton LM (2000) Measurements of high-, room-, and low-temperature photoabsorption cross sections of SO₂ in the 2080- to 2950-Å region, with application to Io. *Icarus* 145:289–296. <https://doi.org/10.1006/icar.1999.6322>

Chapter 3

Fluorescence Spectroscopy



Artur J. Moro and João Carlos Lima

3.1 General Considerations

“Measuring the fluorescence of a sample” refers in common terms to measuring the emission of light emitted by substances following excitation by light. The term comprises both fluorescence and phosphorescence (emission from spin allowed or spin forbidden transitions, respectively) and relates more to the nature of the equipment used: the spectrofluorometer. “Measuring the photoluminescence of a sample” is a more accurate description of the general phenomenon of light emission upon photoexcitation and distinguishes it from electroluminescence and chemiluminescence (light emission after electrical excitation, LEDs, or chemical excitation, fireflies).

When electromagnetic radiation and atomic or molecular systems interact, there are three distinct processes which are relevant to luminescence: absorption, stimulated emission and spontaneous emission, theoretically treated by Einstein (1916) and exemplified in Fig. 3.1 for a system involving two states. In absorption, a photon interacts with the system in a low energy state, 1, and transforms it into a higher energy state, 2. The rate of this process will depend on the concentration of molecules in state 1 (N_1) and the density of photons, ρ , as in a second-order kinetic process:

$$\frac{dN_1}{dt} = B_{12}N_1\rho \quad (3.1)$$

where B_{12} is a proportionality constant. The corresponding process with molecules in state 2, have a rate:

A. J. Moro · J. C. Lima (✉)
LAQV/Requimte, Department of Chemistry, Faculdade de Ciências e Tecnologia, Universidade NOVA de Lisboa, 2829-516 Caparica, Portugal
e-mail: lima@fct.unl.pt

A. J. Moro
e-mail: ajm12769@fct.unl.pt

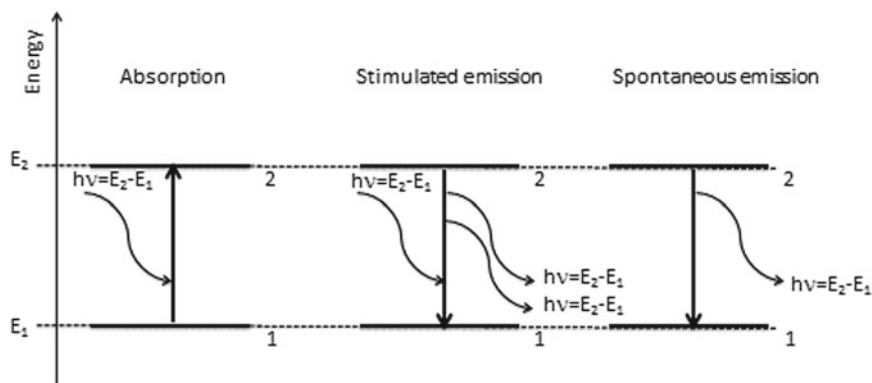


Fig. 3.1 The processes of absorption, stimulated emission and spontaneous emission observed upon interaction of electromagnetic radiation with atoms or molecules; in the case of molecules the emitted photons have energy $h\nu \leq E_2 - E_1$ due to vibrational energy loss

$$\frac{dN_2}{dt} = B_{21}N_2\rho \quad (3.2)$$

This is termed stimulated emission, since it is a process in which the state 1 returns to the state 2 (losing energy through emitted photons), but whose rate depends on the density of photons irradiating the sample, ρ . Stimulated emission is responsible for lasing, and according to the microscopic reversibility principle $B_{21} = B_{12}$. For electronic transitions and under thermal equilibrium, the Boltzmann distribution shows that the concentration of state 1 is much higher than the concentration of state 2 ($h\nu \gg k_bT$). Consequently, stimulated emission is negligible in luminescence spectroscopy conditions and only becomes important if a population inversion can be achieved (e.g. under laser excitation).

Since stimulated emission normally has a negligible probability and the equilibrium must be maintained, a further process is necessary for conversion of state 2 to state 1 (remember that 1 is thermodynamically more stable than 2). This process is termed spontaneous emission which corresponds to the normal emission processes of fluorescence and phosphorescence. Spontaneous emission of fluorescence occurs within a few nanoseconds after formation of the excited state, while spontaneous emission by phosphorescence may persist for milliseconds or even seconds.

Spontaneous emission is a random process, such that for a statistical ensemble of molecules it will follow first-order kinetics and it is independent of the photon density:

$$\frac{dN_2}{dt} = A_{21}N_2\rho \quad (3.3)$$

The proportionality constants B_{12} ($=B_{21}$) and A_{21} are termed the Einstein coefficients (Hilborn 1982).

There are a variety of terms commonly used to describe the strength or probability of absorption, i.e., the ‘allowedness’ or ‘forbiddenness’ of the transition. The molar absorption (extinction) coefficient, the Einstein coefficients and the absorption cross-section are commonly used measures of transition probability. Both B_{12} and A_{21} can be related to experimental properties for the absorption and emission of light.

The integrated absorption coefficient, i.e., the area of the absorption peak is related to the B_{12} Einstein coefficient for spontaneous absorption by:

$$\int_0^{\infty} \varepsilon(\tilde{\nu}) d\tilde{\nu} = \frac{B_{12} h \tilde{\nu} N_A}{\ln 10} \quad (3.4)$$

where N_A is Avogadro’s number. Additionally, absorption and emission probabilities are theoretically related by:

$$A_{21} = \left(\frac{8\pi h \nu_{12}^3}{c^3} \right) B_{12} \quad (3.5)$$

where ν_{12} is the frequency of the radiation corresponding to the transition between states 1 and 2, c is the velocity of light and h is Planck’s constant.

3.1.1 Excited State Deactivation Pathways for Molecules

In molecules, additionally to the radiative transitions described above, a set of non-radiative pathways related with vibrational dumping are available, which are generally grouped in the classification of internal conversion, taking place without the emission of a photon. The unimolecular processes available to excited state relaxation are summarized in Fig. 3.2. Fluorescence and phosphorescence, both radiative processes, involve emission of photons either from spin allowed (for example singlet to singlet such as in $S_1 \rightarrow S_0$ transition) or spin forbidden (for example singlet to triplet such as in the $T_1 \rightarrow S_0$ transition) transitions, where singlet and triplet correspond to the spin multiplicity of the system ($2S+1$) for a given value of spin, S .

In molecular spectroscopy, molecules absorb a photon (are excited) to an electronic excited state and lose the excess of energy through non-radiative relaxation (internal conversion, IC) to the lowest excited electronic state, S_1 . From the relaxed S_1 state, the internal conversion to the ground state, S_0 , is slow enough to allow efficient competition from the radiative (emission) pathway to the ground state (10^{-12} to 10^{-9} s). The fact that the energy difference between states S_1 and S_0 is larger than between S_2 and S_1 and the internal conversion is faster for smaller energy differences is known as the energy gap law. A consequence of this is the very well known Kasha’s rule which states that, regardless of which electronic state is excited (e.g. S_2), the emission always occur from the lowest excited state (S_1) (Kasha 1950).

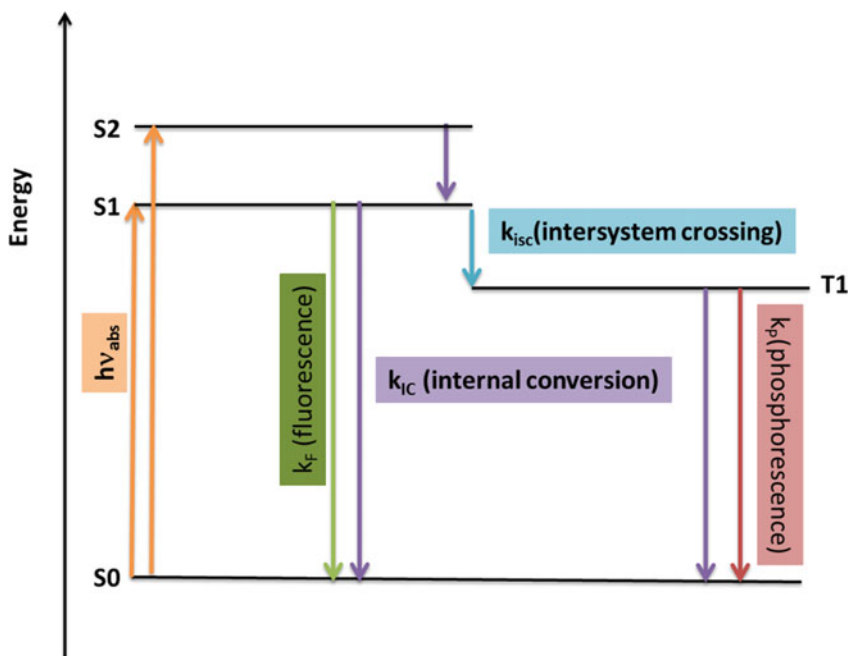


Fig. 3.2 Jablonski diagram summarizing the deactivation following excitation

An alternative route for deactivation of S1 is the non-radiative singlet to triplet conversion, named intersystem crossing (ISC) (Rohatgi-Mukherjee 1986). The importance of this process, that can occur in time scales ranging from picoseconds to hundreds of nanoseconds, strongly depends on the energy proximity of singlet and triplet states of adequate (different) symmetry, and on the presence of heavy atoms (e.g. metals) which strongly favor intersystem crossing (Kasha 1952; Medinger and Wilkinson 1965).

The molecule can also emit a photon from the radiative T1- \rightarrow S0 transition, a phenomenon known as phosphorescence. However, since this transition is forbidden (the electron undergoes change in spin) it takes much longer times to occur than the correspondent S1- \rightarrow S0 transition, typically microseconds to seconds. For that reason i.e. slow rate of emission, most of the systems do not show phosphorescence at room temperature, since the internal conversion (vibrational relaxation) is faster. Rigid matrices (frozen solutions, glasses, polymers, etc.) are used to observe phosphorescence. Molecules with long lifetimes (either singlets with forbidden transitions to the ground state or triplets) are highly sensitive to the oxygen present in the dispersion media, and the luminescence is strongly quenched unless the system is degassed. Systems with short lifetimes (strongly allowed transitions) are unaffected by oxygen. The reason for that is that oxygen must diffuse to a collisional distance of the molecules, and the shorter the excited state life time, the lowest the probability of such encounters.

3.1.2 Quantum Yields

Three states play a dominant role in the luminescence of organic molecules in solution. They are the ground state, the lowest triplet state, and the lowest excited singlet state. In condensed media, vibrational relaxation is usually so fast that excited molecules quickly relax to one of the two excited states. For such systems, a three-state model, with the transitions between the states governed by first-order competing kinetics, forms an adequate framework to understand much of the data on unimolecular decays from the excited states.

In particular, radiative and radiationless transitions between these two excited states and the ground state (see Fig. 3.2) delimit the extent to which luminescence processes can occur. For singlet luminescence i.e. fluorescence, the quantum yield, φ_F , in the absence of external quenchers can be written in terms of the fundamental kinetic parameters as:

$$\varphi_F = \frac{k_F}{k_F + k_{IC} + k_{ISC}} \quad (3.6)$$

where k_F is the first-order rate constant for singlet emission, k_{IC} is the first-order rate constant for internal conversion and k_{ISC} is the first-order rate constant for intersystem crossing. Thus, in order to see fluorescence, k_F must be competitive with other decay channels of the lowest excited singlet state. Triplet luminescence, phosphorescence, is limited both by analogous processes (competition between k_p and k_{IC} in the ratio $k_p/(k_p + k_{IC})$) and also by the triplet formation quantum yield, φ_{ISC} .

$$\varphi_P = \varphi_{ISC} \cdot \frac{k_p}{k_p + k_{IC}} = \frac{k_{ISC}}{k_F + k_{IC} + k_{ISC}} \cdot \frac{k_p}{k_p + k_{IC}} \quad (3.7)$$

The fluorescence quantum yield, φ_F , and the triplet quantum yield, φ_{ISC} (also called intersystem crossing quantum yield) are related by the condition in the absence of external quenchers:

$$\varphi_F + \varphi_{ISC} + \varphi_{IC} = 1$$

or, when in the presence of an external quencher, by the relation:

$$\varphi_F + \varphi_{ISC} + \varphi_{IC} + \varphi_q = 1$$

The last two quantum yields are the internal conversion and the quenching quantum yields, respectively. Since φ_{ISC} is often small due to the large singlet-triplet energy gaps, the sum of φ_F and φ_{IC} is often close to one when there is no quenching.

Experimentally, the determination of the fluorescence quantum yield can be performed in two methods, described below.

Relative method

Measuring the fluorescence quantum yield of an unknown sample can be done by comparing its emission against a reference with a known quantum yield (Resch-Genger and Rurack 2013), according to equation

$$\varphi = \varphi_{ref} \frac{I_S}{I_{ref}} \frac{(1 - 10^{A_{ref}})}{(1 - 10^{A_S})} \frac{n_S^2}{n_{ref}^2} \quad (3.8)$$

where φ , I , A and n represent fluorescence quantum yield, emission intensity, absorption value (at the excitation wavelength) and refractive index, of either sample (S) or reference (ref), respectively.

In this method, the choice of the reference is crucial to minimize the error and there are several criteria for this selection process:

1. The maximum absorption wavelength should be as close as possible to that of the sample. Additionally, the selected wavelength of excitation should be in an “flat” area of the absorption spectrum, so that the absorption values have minimal variation over the selected excitation window (which is dependent on the slit width).
2. The emission spectral range must be the same for sample and reference. Special caution should be taken in terms of Stokes’ shift, to ensure that all the emitted light is recorded. Furthermore, the shape of the emission bands of sample and reference should as similar as possible.

Selection of reference can be done by consulting the literature (Murov et al. 1993) or a spectra database (<https://omlc.org/spectra/PhotochemCAD/index.html>). Experimentally, the user starts by acquiring an absorption and an emission spectrum of the sample. Afterwards, upon defining the excitation wavelength, a solution of the reference (preferably in the same solvent) is prepared and its absorption value at the excitation wavelength is adjusted to match that of the sample solution. Finally, the emission spectrum of the reference is acquired in the exact same conditions as the sample. The integral of the spectra of sample and reference are then used for the quantum yield determination, through the above mentioned equation.

Absolute method

An alternative to the relative method is to use an integration sphere, which allows for determining the fluorescent quantum yield in a direct and absolute way (Hanssen 2001; Leyre 2014). The integration sphere is an accessory (typically purchased as an “extra”), composed of a barium sulphate, a material which capable of reflecting any incident light. The excitation light itself is used as a background signal to determine the amount of light absorbed by the sample, using the difference between the excitation light reaching the detector in the absence and presence of the sample.

Spectra have to be recorded in three geometries (Fig. 3.3):

- (a) With no sample present;
- (b) With sample present but off-beam, in a position where the sample is not excited with direct light;

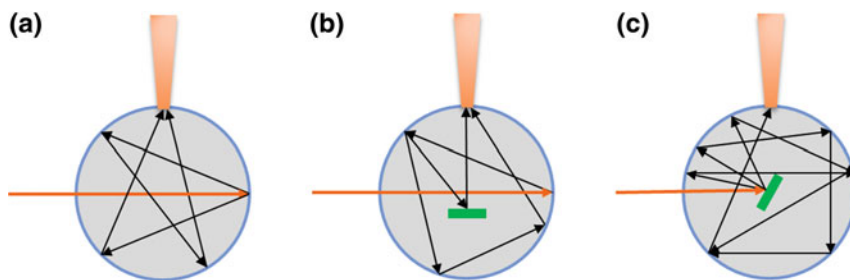


Fig. 3.3 Schematic of measurements using an integration sphere: **a** no sample; **b** sample *off-beam*; and **c** sample *in-beam*

(c) With sample present and in-beam.

For spectrum acquisition, two spectral windows must be covered:

- (L) Emission spectrum of the excitation light. For example, if we excite our sample at 320 nm, the spectrum will be recorded in the range 300–340 nm;
- (E) Emission spectrum of the sample, at the same excitation wavelength as for (L). In this example, we would acquire above 340 nm.

The measurements comprise a total of 6 spectra. The fraction of absorbed light can be determined as

$$A = \left(1 - \frac{L_c}{L_b}\right) \quad (3.9)$$

where L_c and L_b represent the integral of the emission of the excitation light upon direct (*in-beam*) and indirect (*off-beam*) excitation of the sample, respectively.

The observed quantum yield is therefore given by the following equation:

$$\phi_F = \frac{E_c - (1 - A)E_b}{L_a A} \quad (3.10)$$

where E_c and E_b represent the integrals of emission of the sample *in-beam* and *off-beam*, respectively, while L_a represents the integral of the excitation light with no sample in the sphere.

Although this methodology can be used for any type of sample, it is particularly relevant for the luminescent quantum yield determination of solids or films. Particular experimental care has to be taken when collecting the emission of the excitation light, namely by adding neutral density filters (ND) that block part of the excitation light, preventing photodamage to the detector. The absorption of ND must then be included as a correction of the L spectra.

3.1.3 Excited State Lifetimes

Lifetimes of the two excited states (i.e. singlet and triplet) are also related with the rate constants of the different deactivation processes. The overall fluorescence lifetime is the reciprocal of the decay rate constant of the excited singlet state which in the three state model (in the absence of external quenchers) is given by

$$k_S = \frac{1}{\tau_S} = k_F + k_{IC} + k_{ISC} \quad (3.11)$$

and the natural radiative rate constant from the excited singlet, k_F , can be calculated from

$$k_F = \frac{\varphi_F}{\tau_S} \quad (3.12)$$

Similarly the triplet lifetime is the reciprocal of the total decay rate constant for all processes out of the triplet state. The triplet lifetimes are usually several orders of magnitude longer than those of the singlet which makes triplet states susceptible to bimolecular quenching with impurities, cell walls, self-quenching with ground state species, or even weak reactions with solvents.

3.1.4 Stern-Volmer Analysis and Quenching Mechanisms

A dynamic (or Stern-Volmer) quenching process is defined as one which competes with the spontaneous emission process and thereby shortens the lifetime of the emitting molecule. Basically, these quenching reactions are energy transfer, proton transfer or electron transfer processes (Balzani et al. 2014), or in some cases transient dimer or complex formation in the excited state may be involved [excimer (Birks 1975) or exciplex (Förster 1975) formation]. These excited dimer or complex may or may not emit their own characteristic emission which is likely to be different from that of the original molecule.

In solution, possibility of weak complex formation in the ground state is also present. This may cause immediate loss of electronic energy and is called static quenching. Since there is no competition with emission processes, the lifetime is not affected. Ground state complex formation reduces fluorescence intensity by competing with the uncomplexed molecules for the absorption of the incident radiation. This is called the inner filter effect, similar to the presence of other added absorbing molecules.

Under steady illumination, the rate of formation of an excited molecule A^* is equal to its rate of deactivation and the concentration $[A^*]$ remains constant (steady state condition):

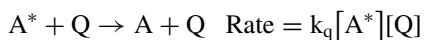
$$\frac{d[A^*]}{dt} = 0$$

The concentration of A^* in the absence of any bimolecular quenching step is given by:

$$[A^*]^0 = \frac{I_a}{k_f + k_{ic} + k_{isc}} = \frac{I_a}{k_f + k_{nr}} \quad (3.13)$$

where I_a , is the rate of light absorption or the rate of formation of the excited molecule, k_f is the rate constant for fluorescence and k_{nr} , the sum of rate constants for all the unimolecular non-radiative deactivating steps, such as internal conversion k_{ic} and intersystem crossing k_{isc} , which originate from this excited state.

If another molecule Q is added to the solution which quenches the fluorescence by a bimolecular quenching step, then



The concentration of the light emitting molecule $[A^*]$ in presence of the quencher is given as

$$[A^*] = \frac{I_a}{k_f + k_{nr} + k_q[Q]} \quad (3.14)$$

If $[A^*]^0$ and $[A^*]$ are light emitting molecule concentrations in absence and in presence of the quencher, the respective quantum yields are:

$$\varphi_f^0 = \frac{k_f[A^*]^0}{I_a} = \frac{k_f}{k_f + k_{nr}} \quad (3.15)$$

and

$$\varphi_f = \frac{k_f[A^*]}{I_a} = \frac{k_f}{k_f + k_{nr} + k_q[Q]} \quad (3.16)$$

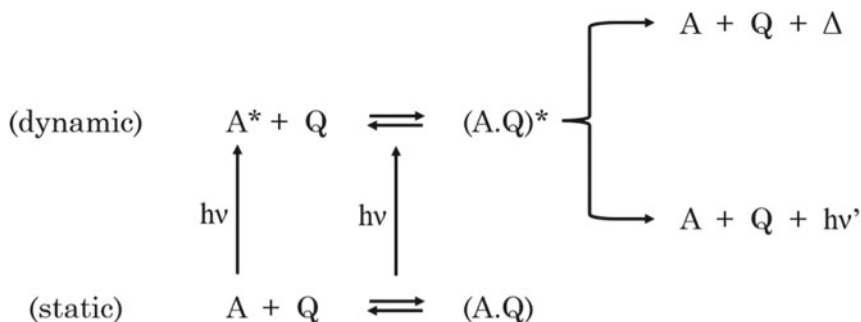
The ratio of the two yields is

$$\frac{\varphi_f^0}{\varphi_f} = \frac{k_f + k_{nr} + k_q[Q]}{k_f + k_{nr}} = 1 + \frac{k_q[Q]}{k_f + k_{nr}} = 1 + k_q\tau[Q] = 1 + K_{SV}[Q] \quad (3.17)$$

This expression is known as the Stern-Volmer equation and K_{SV} as Stern-Volmer constant. K_{SV} is the ratio of bimolecular quenching constant to unimolecular decay constant and has the dimension of $L \text{ mol}^{-1}$. It implies a competition between the two decay pathways and has the character of an equilibrium constant. The Stern-Volmer expression is linear in quencher concentration and K_{SV} is obtained as the slope of

the plot of $\frac{\phi_f^0}{\phi_f}$ versus $[Q]$. Here, τ is the actual lifetime of the light emitting molecule in absence of bimolecular quenching and is measured independently. Then from the knowledge of K_{SV} , the rate constant k_q , for the bimolecular quenching step can be determined.

Deviations from Stern-Volmer relationship may arise if static quenching is present. The simultaneous presence of dynamic and static quenching may be summarized in the scheme below:



If K_0 is the molar equilibrium constant for the formation of the complex in the ground state

$$K_0 = \frac{[AQ]}{[A][Q]} \quad (3.18)$$

then the fraction α , of incident light absorbed by the complex AQ is given by

$$\alpha = \frac{\varepsilon' K_0 [Q]}{\varepsilon + \varepsilon' K_0 [Q]} \quad (3.19)$$

where ε and ε' are the molar extinction coefficients of A and AQ, respectively at the wavelength of excitation.

If the complex is nonfluorescent, only the fraction $(1 - \alpha)$ is effectively used for fluorescence emission and for small α , and $\varepsilon = \varepsilon'$,

$$\frac{F_0 - F}{F} = (K_{SV} + K_0)[Q] + K_{SV} K_0 [Q]^2 \quad (3.20)$$

where F_0 , and F are fluorescence intensities in absence and in presence of quencher, respectively. Another way to represent the dependence on $[Q]$ is:

$$\frac{\left(\frac{F_0 - F}{F}\right)}{[Q]} = (K_{SV} + K_0) + K_{SV} K_0 [Q] \quad (3.21)$$

In this expression, the quantity on the left is the apparent quenching constant and varies linearly with $[Q]$, with a slope given by the product of collisional (K_{SV}) and static (K_0) quenching constants, which is identical to the equilibrium constant. The intercept corresponds to the sum of the two. The expression becomes more elaborate if the ground state complex also emits after excitation or fluorescent complexes are formed in the excited state (exciplex formation and emission).

3.1.5 Concentration Quenching and Excimer Formation

The fluorescence intensity F per unit volume is proportional to the fraction of light absorption, I_a , per unit volume per unit time.

$$F = \varphi_f I_a = \varphi_f I_0 (1 - e^{-2.3\epsilon l C}) \quad (3.22)$$

where φ_f is the proportionality constant termed quantum yield of fluorescence, I_0 the incident light flux, ϵ the molar absorptivity of the light absorbing molecule, l the path length of light in the sample and C the concentration of the light absorbing molecule. In an actual experiment, a factor G , which expresses the effect of geometry of the experimental setup on the measurements of fluorescence and absorption intensities must be considered. For dilute solutions, the term inside the bracket can be expanded. If identical experimental conditions are maintained, fluorescence intensities and concentrations are linearly related according to the expression:

$$F = \varphi_f I_0 2.3\epsilon l C \quad (3.23)$$

On the other hand, at high concentrations where all the incident light is completely absorbed, the exponential term becomes negligible and $F = \varphi_f I_0$. The fluorescence intensity should remain constant for any further increase in concentration, but for many compounds, the intensity starts decreasing after reaching a critical concentration even if geometrical effects are avoided in the experimental setup. The quantum yield, which is expected to be independent of concentration, starts decreasing as the concentration increases. The decrease is due to the quenching of fluorescence by molecules of the same kind and is known as **concentration quenching**. It follows the Stern-Volmer equation, with $[Q]$ representing the concentration of the light emitting molecule itself. In some cases, simultaneously with the quenching of the normal fluorescence a new structureless emission band appears at about 6000 cm^{-1} to the red side of the monomer fluorescence spectrum (Fig. 3.4). This phenomenon was first observed in pyrene solution by Förster and Kasper (1955) and was explained as due to transient complex formation between the ground and the excited state molecules since the absorption spectrum was not modified by the increase in concentration (Stevens 1961; Birks 1963). These short-lived excited state dimers are called excimers to differentiate them from electronically excited dimeric ground state species. The excimers dissociate when they return to the ground state by emis-

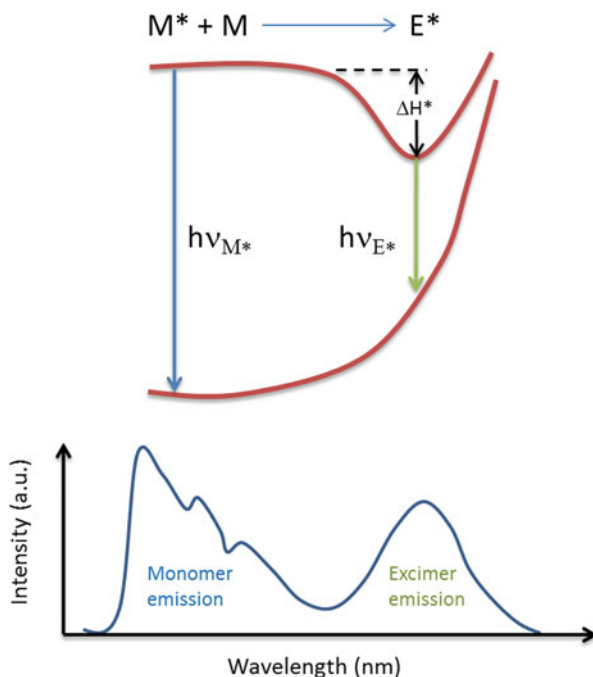


Fig. 3.4 Monomer and excimer emission and potential energy scheme for monomer and excimer

sion, giving rise to a structureless envelope for the emission spectrum. This shows that the ground state potential energy surface must be repulsive (Fig. 3.4).

Excimer emission is often observed from planar molecules when the two component molecules are placed in parallel configuration. The conditions are that (i) the two planar molecules approach within a distance of 0.35 nm of each other, (ii) that the concentration is high enough for interaction to occur within the excited lifetime, and (iii) that the interaction energy between an excited and a normal molecule is attractive such that the excimer binding energy— ΔH^* is greater than the thermal energy.

If flat molecules form a part of properly oriented molecular system, red-shifted structureless band due to excimer may appear even at low concentrations. Emission from the biopolymer deoxyribonucleic acid (DNA) is due to excimer formation between the constituent bases (Eisinger et al. 1966).

Physical quenching by foreign added substances generally occur by two broad based mechanisms:

- (a) Charge transfer mechanism (Leonhardt and Weller 1963; Ware and Richter 1968);
- (b) Energy transfer mechanism (Förster 1948; Dexter 1953).

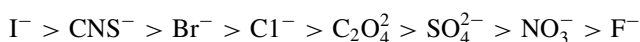
3.1.6 Charge Transfer Mechanism: Exciplex Formation and Decay

The formation of excimers between ground and excited states of similar molecules has already been discussed. When two dissimilar molecules collide, attractive tendencies are usually greater, depending on polarity and polarizability properties. Interaction involves some degree of charge transfer, and the frequently formed complexes between excited fluorescent **molecules** and added foreign molecules are called **exciplexes** (Förster 1975). Absorption spectra remain unchanged, in contrast to ground state interactions, because of the short life of the complexes. Molecules with heavy atoms act as quenchers of singlet excited state emission by an exciplex mechanism that facilitate change of electron spin because. In this case exciplex dissociation occurs via triplet formation. In the absence of the heavy atom effect exciplex lifetimes may be long enough for them to decay through light emission. More commonly, however, dissociation occurs via an ion-pair complex, as was first suggested by Weiss. Solvation is an important factor affecting such reactions and the exciplex lifetime. The solvent-shared ion-pair character of the exciplex increases with the increase in solvent dielectric Constant and ionization potential of the donor and electron affinity of the acceptor. The free energy change, ΔG , involved in the actual electron transfer can be calculated according to the expression

$$\Delta G = \left[E_{ox}(D) - E_{red}(A) - \frac{e^2}{\epsilon \cdot d} \right] - \Delta E_{00} \quad (3.24)$$

where $E_{ox}(D)$ and $E_{red}(A)$ are, respectively the oxidation and reduction potentials of donor and acceptor, and the last term inside the brackets is the free energy change gained by bringing two radical ions to a distance d in the solvent of dielectric constant ϵ . ΔE_{00} is the electronic excitation energy. If fast proton transfer follows electron transfer the quenching may be said to involve H-atom transfer.

The fluorescence of a number of dyes is quenched by ions in the order:



This correlates with the increasing ionization potential which shows that the fluorescence quenching efficiency of these ions is related to the ease of charge transfer from the ion. The quenching effects can be produced by solvents in absence of any other added quenchers. Polar solvents in particular may be involved interactions of the charge transfer type.

One of the most important and persistent quenchers in solution is dissolved oxygen. Electronically excited organic molecules are often deactivated by one or two collisions with molecular oxygen. In some cases, the substrates are oxidized whereas in others no permanent chemical change is observed. The high quenching efficiency is due to its paramagnetic property. The same is true for NO. They act by promoting intersystem crossing rates ($S_1 \rightarrow T_1$ and $T_1 \rightarrow S_0$). Two types of perturbation mecha-

nisms are operative here: (i) charge-transfer interaction and (ii) spin-orbit interaction which mixes the singlet and triplet characters.

3.1.7 Energy Transfer Mechanisms

Electronic energy transfer mechanism has become one of the most useful processes in photochemistry. It allows photosensitization of physical and chemical changes in the acceptor molecule by the electronically excited donor molecule.

The electronically excited D^* (donor) is initially formed by direct light absorption. This can transfer the electronic energy to a suitable molecule A (acceptor) resulting in simultaneous quenching of D^* and electronic excitation of A to A^* . The transfer occurs before D^* is able to radiate and hence it is known as *nonradiative transfer of excitation energy*.

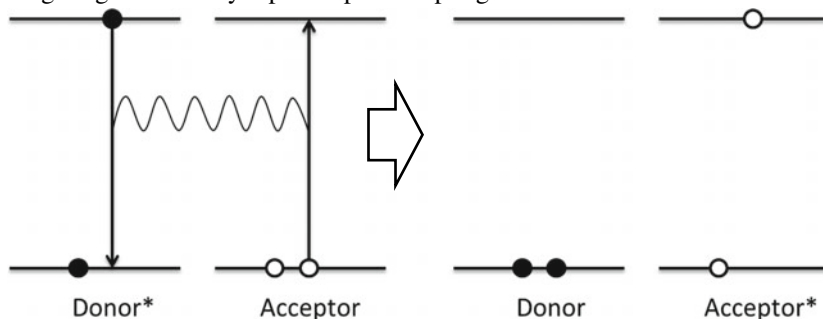
The A^* molecule, thus excited indirectly, can undergo various photophysical and photochemical processes. Such processes are *photosensitized reactions*. In these reactions, the initial light absorbing species remains unchanged. One of the most important sensitized photochemical reactions is photosynthesis by plants. The green chlorophyll molecules of the leaves are the light absorbing molecules. They initiate reaction between CO_2 and H_2O to produce carbohydrates as the stable products. Examples of many such sensitized photoprocesses are observed in photobiology and photochemistry. Photosensitized oxidation of proteins and nucleic acids is termed *photodynamic action*.

The *nonradiative energy transfer* must be differentiated from *radiative transfer* which involves the *trivial* process of emission by the donor and subsequent absorption of the emitted photon by the acceptor: It is called *trivial* because it does not require any energetic interaction between the donor and the acceptor. It is merely reabsorption of fluorescence radiation in accordance with Beer's Law and shows r^{-2} dependence on donor-acceptor distance. Although called trivial, it causes radiation imprisonment and can be important factor to be considered in fluorescence measurements. It may introduce error and distort emission spectrum absorbing only that portion which overlaps its absorption spectrum. It is particularly troublesome in studies on concentration quenching.

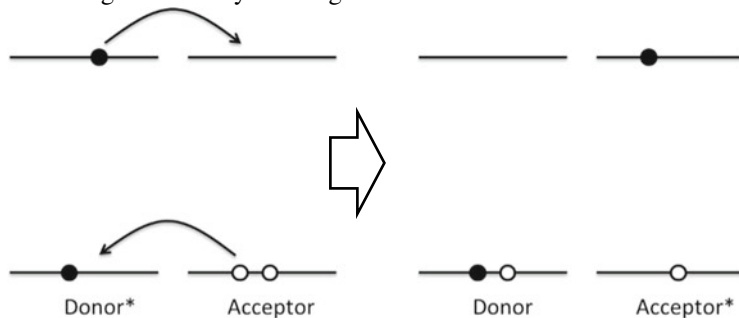
For quenching by energy transfer mechanism, the quencher must have suitable energy levels, singlet or triplet, near or below the energy level of the donor molecule. Such a transfer has the greatest probability if there is an approximate resonance between the donor and the acceptor energy levels.

In general, two different types of mechanisms are postulated for the nonradiative energy transfer phenomenon:

(a) long range transfer by dipole-dipole coupling interactions²⁰



(b) short range transfer by exchange interactions²¹



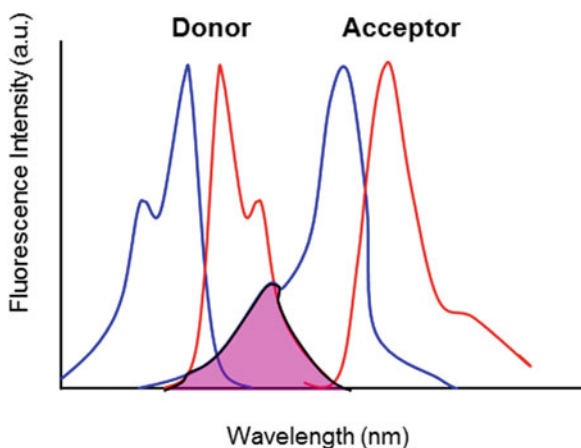
Long Range Transfer by Dipole-Dipole Coupling

The long range transfer by dipole-dipole coupling interactions is better known as Fluorescence Resonance Energy Transfer (FRET) and is a physical phenomenon used more and more in biomedical research (Valeur and Berberan-Santos 2012). FRET relies on the distance-dependent transfer of energy from a donor molecule to an acceptor molecule. Due to its sensitivity to distance, FRET has been used to investigate molecular interactions. FRET is a radiationless transmission of energy from the donor molecule to the acceptor molecule where the donor molecule is the light absorbing molecule that initially absorbs the light energy and the acceptor is the light absorbing molecule to which the energy is subsequently transferred. This resonance interaction occurs over greater than interatomic distances without any molecular collision. The transfer of energy leads to a reduction in the donor's fluorescence intensity and excited state lifetime, and an increase in the acceptor's emission intensity. A pair of molecules that interact in such a manner that FRET occurs is often referred to as a donor/acceptor pair.

While there are many factors that influence FRET, the primary conditions that need to be met in order for FRET to occur are relatively few. The donor and acceptor molecules must be in close proximity to one another (typically 10–100 Å). The absorption or excitation spectrum of the acceptor must overlap the fluorescence emission spectrum of the donor (Fig. 3.5).

The degree to which they overlap is referred to as the spectral overlap integral (**J**). The donor and acceptor transition dipole orientations must be approximately

Fig. 3.5 Schematic representation of the spectral overlap integral (pink region) between absorption (blue lines) and emission (red lines) of donor and acceptor



parallel. Assuming that the donor acceptor pairs are compatible the most critical element necessary for FRET to occur is close proximity of the pairs. The efficiency of the process (E_{FRET}) depends on the inverse sixth-distance between donor and acceptor:

$$E_{FRET} = \frac{R_0^6}{(R_0^6 + r^6)} \quad (3.25)$$

where R_0 is the distance at which half the energy is transferred and r is the actual distance between donor and acceptor. The distance at which energy transfer is 50% efficient is referred to as the Förster radius (R_0) (Schaufele 2005). The magnitude of the R_0 is dependent on the spectral properties of the donor and the acceptor. Förster distances ranging from 20 to 90 Å are most useful for studies of biological macromolecules. These distances are comparable to the diameters of many proteins, the thickness of biological membranes, and the distances between sites on multi-subunit proteins. Any process that affects the energy transfer rate allows the process to be quantified. As a result, FRET is often referred to as a spectroscopic ruler. Note that the Förster distance (R_0) is dependent on a number of factors, including the fluorescence quantum yield of the donor in the absence of acceptor (φ_d), the refractive index of the solution (n), the relative dipole angular orientation of the molecules (k^2), and the spectral overlap integral of the donor and acceptor (J):

$$R_0 = 9.78 \times 10^3 (n^{-4} \varphi_d k^2 J)^{1/6} \quad (3.26)$$

In general the donor and acceptor molecules are different, in which case FRET can be detected by the appearance of fluorescence of the acceptor or by quenching of donor fluorescence. The donor probe is always a fluorescent molecule.

The detection and quantitation of FRET can certainly be accomplished in a number of different ways. Because FRET can result in both a decrease in fluorescence of the

donor molecule as well as an increase in fluorescence of the acceptor, a ratio metric determination of the two signals can be made. The advantage of this method is that a measure of interaction can be made that is independent of the absolute concentration of the sensor. Because not all acceptor moieties are fluorescent, they can be used as a means to quench fluorescence. In these instances, those interactions that result in a fluorescent donor molecule coming in close proximity to such a molecule would result in a loss of signal. Inversely, reactions that remove the proximity of a fluorescent donor and a quencher would result in an increase in fluorescence.

Genetically encoded fluorescent dyes, such as Green Fluorescent Protein (GFP) and related molecules blue, cyan, yellow and red have provided the ability to perform FRET *in vitro*, particularly in living cells (Periasamy 2001; Nguyen and Daugherty 2005). These proteins form FRET pairs with each other as well as with conventional dyes. They can be attached to other proteins genetically or covalently yet still retain their fluorescent capability (Rizzuto et al. 1995). These dyes have the utility of being genetic elements that can be linked with other genes to form chimeric proteins (Chalfie et al. 1994). These chimeric proteins contain a GFP (or related fluorescent protein element) and a putative binding domain. With different chimeric proteins (one donor and one acceptor) protein-protein interactions can be investigated. Only when the donor/acceptor pairs interacted through protein-protein interactions would FRET result (Fig. 3.6).

In Fig. 3.6, protein-protein interactions bring Blue fluorescent protein and Green fluorescent proteins to close proximity and excitation of blue fluorescent protein results in the emission of fluorescence by Green fluorescent protein through FRET.

Organic dyes (e.g. Cy3, Cy5, Cy5.5 and Cy7), which emit in the red range (>550 nm), offer a number of advantages (Shindy 2017). Their emission range is such that background fluorescence is often reduced. Additionally large distances (>100 Å) can be measured as a result of the high extinction coefficients and good quantum yields. Even donor-acceptor pairs with separated emission spectra (i.e. low overlap integral) result in acceptable Förster distances. For example, Cy3, which emits maximally at 570 nm and Cy5, which emits at 670 nm, have a Förster distance >50 Å. Large separation between pairs allows the measurement of acceptor emission as a result of FRET without interference from donor emission. In addition

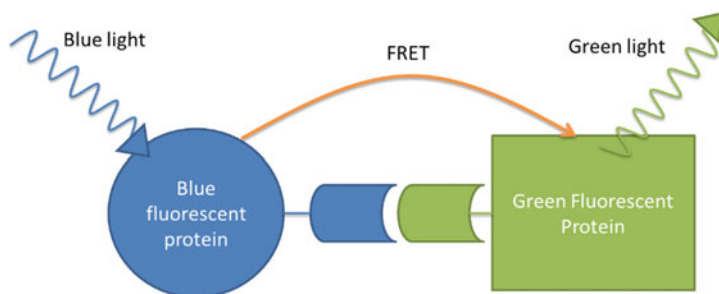


Fig. 3.6 Schematic representation of the interaction of two different fluorescent protein chimeras

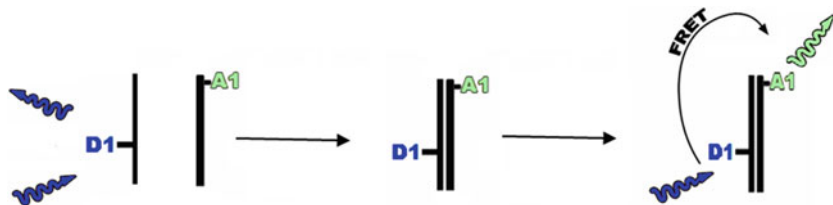


Fig. 3.7 Schematic representation of FRET occurring between donor and acceptor fluorescent dyes when labeled oligonucleotides are annealed

these molecules can be linked directly to specific locations in synthetically produced nucleic acids, allowing FRET to be used to assess nucleic acid annealing (Didenko 2001).

In the example depicted in Fig. 3.7, two complementary RNA oligonucleotides are labeled with Cy3 and Cy5 respectively. When these labeled molecules are not annealed, excitation of an RNA oligonucleotide labeled with Cy3 with light at 540 nm results only in the emission of light by Cy3 at 590 nm, while the complementary RNA-oligo labeled with Cy5 does not emit any light at 590 nm or its true emission wavelength of 680 nm. However, when the two oligonucleotides are allowed to anneal, the close proximity of the molecules allows for FRET transfer to occur. This results in the emission of light at 680 nm when the annealed molecule is excited with 540 nm light. Note that not all of the emission of Cy3 at 590 nm is lost, but a significant portion is.

Short Range Transfer by Exchange Interaction

The exchange interaction is a quantum mechanical effect and arises because of the symmetry requirement of electronic wave functions with respect to exchange of space and spin coordinates of any two electrons in the donor-acceptor complex. It is the same kind of interaction which causes singlet-triplet splitting. The characteristic features of the exchange interaction energy are:

- (i) the electrostatic interaction between the charge clouds will be large only when there is a spatial overlap of the donor and the acceptor wave functions, i.e. when the two actually collide, in kinetic sense. Therefore, it can only be a short range phenomenon. No transfer outside the boundaries of the molecule is expected by this mechanism. The transfer occurs at diffusion-controlled rate.
- (ii) the magnitude of the exchange interaction is not related to the oscillator strengths of the transitions in the donor and the acceptor. For forbidden transitions like singlet to triplet, exchange interactions will be predominant at short distances. But if the transitions are allowed dipole-dipole interactions may take over.

Intermolecular energy transfer from the *triplet* of the donor to the *triplet* of the acceptor was first established by Terenin and Ermofaev in 1952. They demonstrated photosensitized phosphorescence emission from naphthalene in rigid glassy medium at 77 K using 365 nm radiation in the presence of suitable donor (Terenin and Ermofaev 1956). They chose donors whose triplet energy E_{TD} was higher than the triplet

of naphthalene E_{TA} but where singlet energy of the donor E_{SD} was less than the singlet energy of naphthalene E_{SA} . Benzophenone was found to possess the criteria for a suitable donor sensitizer. For this molecule, the intersystem crossing occurs with unit efficiency. Under the experimental setup, no phosphorescence from naphthalene was observed in absence of benzophenone. The critical separation distance calculated from the quenching data was found to be 13\AA which is of the same order as the van der Waals separation. The critical separation distance remained unchanged when halogen substituted naphthalenes were used. No increase in transfer efficiency is a clear indication of the lack of dependence on the oscillator strength, so the short range exchange mechanism is in action here. Bimolecular rate constants for triplet-triplet energy transfers can be measured in fluid solutions from quenching data. The effectiveness of an energy transfer quencher is determined mainly by the position of its lower triplet level and not by its molecular structure.

In practical application, both singlet-singlet and triplet-triplet transfers can be arranged in suitable donor-acceptor systems so chosen as to provide conveniently located energy levels. Aromatic carbonyl compounds are, good sensitizers of triplet state because of small singlet-triplet splitting. On the other hand, aromatic hydrocarbons and olefins have convenient singlet-triplet levels to act as good triplet quenchers or acceptors.

3.2 Experimental Aspects of Fluorescence Spectroscopy

Although having experienced a boom in its usage by the general scientific community, fluorescence measurements are not as easy and straightforward as one may assume at first glance. The following sections will account on some of the most common considerations for acquiring reliable experimental luminescence spectra.

3.2.1 *The Spectrofluorometer*

Fluorescence spectroscopy is regarded upon as an extremely sensitive technique which explains its widespread use, particularly for applications in Biochemistry, Biology and Materials Science.

In a Physical-Chemistry lab, standard luminescence measurements are performed using a spectrofluorometer (Fig. 3.8). These next paragraphs describe the chronological pathway of light through each of the working parts of a standard spectrofluorometer, to yield a luminescence spectrum.

The light source

The first law of Photochemistry states that light must be absorbed in order for photochemistry to occur. As such, each spectrofluorometer must be equipped with a light source, without whom one cannot perform an emission spectrum. The choice of

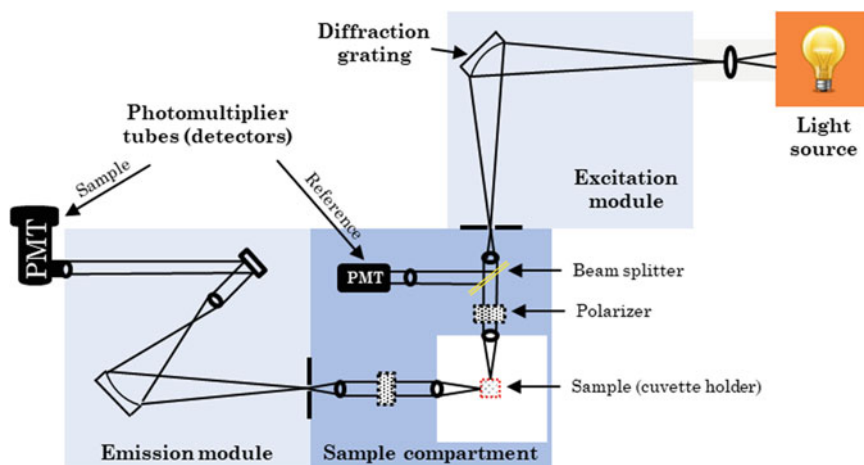


Fig. 3.8 Schematic representation of the components of a standard spectrofluorometer

light source is crucial, as we must guarantee that it can irradiate a strong enough light (excitation) at the wavelength at which our sample absorbs.

Standard apparatuses are equipped with a white light of high power, typically a Xe arc lamp of 450 W, which provides continuous irradiation throughout the whole UV-Vis range, roughly 250–700 nm (Fig. 3.9), extending in some cases up to 1100 nm.

Some spectrofluorometers are equipped with pulsed light sources instead of continuous light, consuming lower power (30–60 W) and generating less heat. A natural consequence is loss of light output when compared to a 450 W Xe arc lamp. Given that

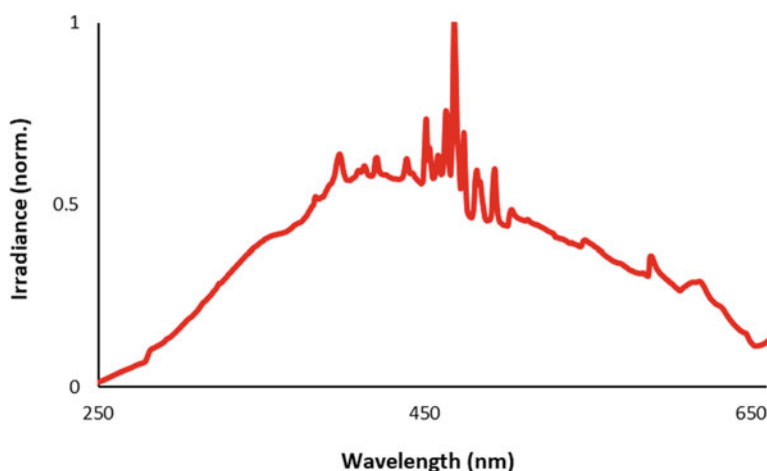


Fig. 3.9 The spectrum of a 450 W Xe arc lamp. The irradiance profile indicates the wavelength range where the lamp can be used for exciting samples

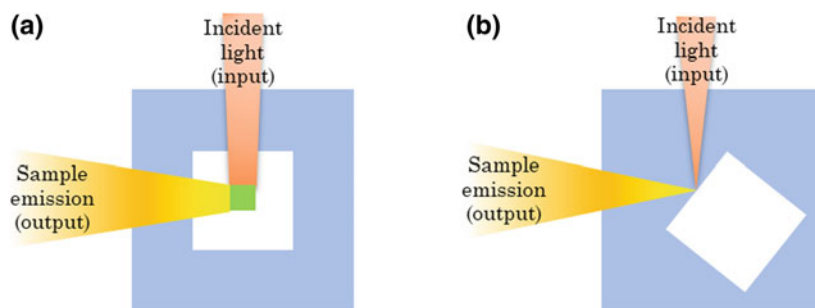


Fig. 3.10 Two geometries for acquiring emission spectra: **a** *right-angle*, and **b** *front-face* modes

pulsed light sources have time-dependent output, one has to ensure that the lamp's decay profile is compatible with the sample's luminescence lifetime and quantum yield. These light sources are commonly found in fluorimeters at laboratories for biological applications, particularly in analysis of screening plates, since most of the experiments at these facilities are based on well-defined and characterized fluorescent probes.

Excitation monochromator

The light from the lamp is channeled and monochromated before reaching the sample using a diffraction grating, which allows to select the wavelength with which we are exciting our sample. The standard experiment is performed primarily by exciting the sample at its maximum absorption wavelength, which will maximize the number of photons in the excited state and by consequence provide the strongest light output from the sample. For cases where the Stokes' shift is relatively small (<30 nm), we can shift slightly the excitation to lower wavelengths, to allow us to acquire the full emission spectrum. Nevertheless, we must guarantee that the resulting emission corresponds to the same electronic transition. The excitation monochromator module is essential from acquiring excitation spectra (see section below).

Sample holder

Traditionally, sample compartments/holders are adapted for measuring dilute solutions of a given sample in quartz cuvettes. Presently, sample holders can be customized to measure any sample, including solid powders and thin films.

The traditional geometry for receiving emitted light from the sample is at a right-angle conformation, i.e. fluorescence emission is detected at a 90° angle from the excitation beam (Fig. 3.10a). In some cases, an alternative geometry, front-face illumination, can be used (Fig. 3.10b). This latter configuration can be particularly useful for minimizing undesired interferences such as light scattering and inner-filter effects (see section below for details).

Emission monochromator

In exactly the same way as its excitation counterpart, the emission monochromator consists of a diffraction grating that discriminates the amount of light emitted by the sample at each wavelength, which is then reflected to the detector to measure the amount of emitted photons.

The detector

The vast majority of spectrofluorometers uses Photo-Multiplier Tubes (PMTs) for detecting light coming from the sample. PMTs act as a source for current, which is directly proportional to the number of incident photons. A PMT consists of a photocathode and a series of dynodes. Both the photocathode and the dynode are maintained at negative potential, and this potential is sequentially decreased until zero, when it reaches the anode. For each single photon hitting the photocathode, one electron is ejected from its surface. The potential difference between the photocathode and the first dynode causes the electron to accelerate and hit this dynode, promoting the release of 5–20 electrons, depending on the applied potential difference. This process is iteratively repeated until a current pulse generated by all the electrons finally reaches the anode. The sensitivity of PMTs can be increased to detect lower emitting samples by increasing its voltage, which amplifies the number of electrons reaching the anode. However, caution has to be taken not to overflow the photocathode with high light intensity, which may result in irreparable damage to the PMT, causing an increase in its dark current (the current in the absence of incident light), and consequently lowering its sensitivity.

3.2.2 Acquisition of Spectra

This section is a summarized guided tour on a typical sequence of experiments in a fluorometer when measuring a sample for the first time. However, we would like to stress out the importance of reading the section “Troubleshooting” before rushing off to start your fluorescence spectroscopy experience.

Having said that, the first experiment to perform is ALWAYS an emission spectrum. In an emission spectrum, we excite our sample at a fixed wavelength, and measure how much light is coming from our sample at longer wavelengths. The choice of excitation wavelength is of key importance, since we want our sample to emit as much light as possible to increase the signal-to-noise ratio. Therefore, a key aspect in fluorescence spectroscopy is that, prior to acquiring the spectrum of a sample on a fluorometer, it is imperative to have previously acquired the absorption spectrum of that same sample.

Emission spectrum acquisition must start 10–20 nm after the excitation wavelength, depending on the slit width (e.g. when exciting at 400 nm, acquisition should start at 410–420 nm). For some experiments, the excitation wavelength may be included in the spectral window (e.g. quantum yield determination using the abso-

lute method, see section below). In these specific cases, attenuation filters must be added, since the high intensity of the excitation light may photodamage the detector.

Upon obtaining the emission spectrum, the first question the user must make is: how can I be sure that this emission comes from my sample?

The simplest way is to record what is known as “excitation spectrum”, i.e., we excite our sample at different wavelengths and monitor the emission from our sample at a fixed wavelength. For example, if your first emission spectrum reaches its maximum intensity at 450 nm, you will now look exclusively to this wavelength and excite your sample over a range of shorter wavelengths (e.g. 250–430 nm). The resulting excitation spectrum will tell you which exciting wavelength enables you to achieve the strongest emission intensity at 450 nm. In an ideal case, i.e. when you have a very clean and pure sample, the excitation spectrum overlaps with your sample’s absorption spectrum, since the highest emission intensity is achieved when more photons are absorbed. When this is not the case, a thorough analysis on the origin of the emission bands has to be performed, cross-checking with the absorption spectrum. The possible presence of strongly emitting contaminants is the most common occurrence for this observation.

Nowadays, software programs developed for fluorescence spectroscopy include the possibility of performing 3-D spectra, i.e. a combination of excitation and emission spectra to yield a 3-D map on the emission of the sample. However, this experiment is only recommended if one makes sure that no overlap exists between the excitation and emission spectra, and that the emission maximum intensity does not overflow the detector with light.

Fluorometers can also be used for monitoring single wavelength emission over time. Nevertheless, this requires the user to have already a solid picture of the emission (and absorption/excitation) profile of his/her sample. It is also possible to record full spectra over time, although, as in any kinetic experiment, one must take into account both the time required for spectral acquisition, as well as the “dead” time between experiments.

3.2.3 *Troubleshooting*

Fluorescence spectroscopy, unlike absorption spectroscopy, is a technique which aims to collect light coming from your sample, perpendicularly (or *quasi*) to the excitation light. One of its main advantages, i.e. high sensitivity, can also be regarded as one of its drawbacks, since it is much more prone to external stimuli, and also to interferences. This section includes the most commonly observed undesired interferences in fluorescence spectroscopy which, if not prevented, can lead to gross misinterpretation of the results. As such, we strongly advise any new user of this technique to pay particular attention to the following troubleshooting occurrences.

Inner-filter effect (into the sample and from the bulk of the sample)

Any fluorometer manufacturer has written in the operations manual that a sample should be as dilute as possible, to minimize what is known as *inner-filter effect*, i.e. where the sample itself acts as a filter.

As sample concentration increases, more molecules are absorbing in the light pathway, which may prevent light from reaching the solution bulk (excitation inner-filter effect). Additionally, if there is a significant overlap between absorption and emission of the sample, emitted light coming out from the bulk can also be absorbed by surrounding molecules in the ground state (self-absorption or emission inner-filter effect). This results in loss of linearity (proportionality) between concentration and light output. The best (and essential!) way to understand and prevent this effect when studying new molecules is to record the emission of a sample at increasing concentrations. This will immediately let us know the linear concentration range up to which no inner-filter effect takes place. For the most common cases, in which the user is measuring a solution in a 10×10 mm quartz cuvette, samples should have absorption values of 0.05–0.15 at its excitation maximum. For cases where the samples have to be measured in their “concentrated” form, or for samples presenting a high degree of turbidity (e.g. suspensions of particles, *front-face* geometry should be used (see Fig. 3.10b).

Second Order Diffractions

This is undoubtedly one of the most common “rookie” mistakes from those who are using fluorescence spectroscopy for the first time. Typically, we want to have a spectral acquisition as wide as possible to make sure we get the full picture on the emission of our sample. However, when we reach the double (or multiples) of the excitation wavelength, we observe a sharp and intense peak, which most likely will “blind” your detector with light, risking permanent photodamage.

These peaks which, more often than one would think, are mistaken for sample emission, arise from high-order diffraction phenomena. This observation occurs because the monochromators are equipped with diffraction gratings which transmit not only first order diffractions (i.e. the selected excitation wavelength), but also diffract light at twice (and thrice, etc.) the excitation wavelength. For example, when we excite a sample at 350 nm, a second-order diffraction peak will appear at 700 nm. A way to eliminate second-order diffractions is by limiting the spectral window. If a significant difference in wavelength exists between the beginning of the spectral acquisition and the excitation wavelength, an appropriate *cut-off* filter (also known as *long-pass* filter) can be used to prevent excitation light (and its high-order diffractions) from reaching the detector.

Raman scattering from solvent

Another common effect which can be observed especially when measuring very low fluorescent samples, is the appearance of sharp peaks in the middle of an emission band. In most of the cases, particularly when measuring organic fluorophores that should have relatively wide emission bands, these peaks represent Raman scattering from solvent molecules and not from the sample. All solvents present Raman scattering peaks, which are dependent of the excitation light wavenumber (see Table 3.1).

Table 3.1 Raman peaks from commonly used spectroscopy solvents

Solvent	Raman scattering peak (nm)			
	λ_{Exc} 313 nm	λ_{Exc} 366 nm	λ_{Exc} 405 nm	λ_{Exc} 436 nm
Water	350	418	469	511
Acetonitrile	340	406	457	504
Cyclohexane	344	409	458	499
Chloroform	346	411	461	502

Therefore, in order to unequivocally assign a given peak to Raman scattering from the solvent, the user can change slightly shift the excitation wavelength (± 10 nm, where the difference from wavenumber to wavelength is negligible). If the peak shifts in the same manner, it is positively identified as Raman scattering from the solvent.

Removal of these peaks can be done by (1) shifting the excitation to higher wavelengths so that the Raman peaks no longer appear in the output spectrum (be mindful that you should ensure that your sample is still being excited!), or by (2) recording the emission spectrum of your solvent alone in the exact same conditions as your sample spectrum, and then subtracting it mathematically. Due to the error associated with the latter method, the former option is recommended.

3.2.4 Fluorescence Versus Phosphorescence

As mentioned in the section above, essentially two types of emission can be detected with a fluorescence spectrometer: fluorescence and phosphorescence. Therefore, the question remains on how to distinguish which of these are we observed while acquiring an emission spectrum. Experimentally, there are two parameters that can be generically used to discriminate between fluorescence and phosphorescence: (1) the presence (or absence) of oxygen and (2) the luminescence lifetime.

The influence of oxygen on triplet emission arises from the fact that molecular oxygen is intrinsically in a triplet state, thus being able to quench the phosphorescence of surrounding triplets by inducing inter-system crossing. This quenching process is dependent essentially on the concentration and diffusion of oxygen molecules within a solvent. As such, a very straightforward method for assessing the nature of any observed emission is to remove any dissolved oxygen by degassing the solution in a high-vacuum system through several freeze-pump-thaw cycles, and re-acquiring the emission spectrum in the exact same conditions. If an increase in the emission is observed, it is most likely phosphorescence. An alternative to high-vacuum degassing is by bubbling the solution with Argon gas. Although faster, it is much less efficient and thus, if no change is observed in the emission, the user will remain in doubt whether the emission is really fluorescence, or the oxygen removal was not sufficient to remove all dissolved oxygen from the solvent. Additional care must be taken when using this latter method because of solvent volatility, since evaporation from

the solvent will also induce emission increase (since the concentration becomes higher).

Another method for determining the nature of the transition is by measuring its luminescence lifetime. Typically, emissive singlet states decay much faster than triplet states. Therefore, measuring the lifetime of any observed emission will provide a strong indication of the type of transition involved. Nevertheless, if one measures an emission lifetime in the order of 10^9 to 10^6 , it does not become unequivocal on the type of luminescence observed.

3.2.5 *Low Temperature Luminescence*

According to the Jablonsky diagram (see Fig. 3.2), deactivation of an excited chemical species can occur either radiatively or non-radiatively. The non-radiative pathways in organic fluorophores consist mainly on the loss of energy in the form of heat through vibrations, which is transferred to the surrounding solvent molecules. For many applications, particularly regarding those involving solid state devices (OLED displays, testing strips, thin films), it becomes particularly important to understand how these luminescent systems behave in the solid state, i.e. where no energy is lost by vibrations, and to determine the contribution of singlet and triplet emission in the overall luminescence. A straightforward method to understand the contribution of each of the radiative pathways to the emission in these conditions is to dissolve the sample in an organic solvent, inserting it in a quartz tube (typically an EPR or NMR tube, just make sure that it is transparent to the excitation wavelength) and then freezing it in a Dewar container under liquid nitrogen (77 K). For most fluorimeters, an additional sample compartment can be mounted for this purpose. Particular attention (in addition to the general precautions when handling liquid nitrogen) should be taken with respect to solvent selection. Organic solvents that generate good/clear glass states are highly desirable to minimize the appearance of peaks from light scattering that may arise from “cracks” in the glass phase (Scott and Allison 1962). Furthermore, measurements at 77 K of aqueous samples present a significant risk of tube rupture upon freezing, due to the expansion of water when fusing to ice, in addition of light scattering contaminations. Therefore, we recommend that tentative approximations to aqueous media should be performed as an alternative (e.g. using methanol).

References

- Balzani V, Ceroni P, Juris A (2014) Photochemistry and photophysics: concepts, research, applications. Wiley-VCH Verlag GmbH, Weinheim, pp 103–124
- Birks JB (1975) Excimers. Rep Prog Phys 38:903–974

- Birks JB, Christophorou LG (1963) Excimer fluorescence spectra of pyrene derivatives. *Spectrochim Acta* 19:401–410
- Chalfie M, Tu Y, Euskirchen G, Ward WW, Prasher DC (1994) Green fluorescent protein as a marker for gene expression. *Science* 263:802–805
- Dexter DL (1953) A theory of sensitized luminescence in solids. *J Chem Phys* 21:836–850
- Didenko VV (2001) DNA probes using fluorescence resonance energy transfer (FRET): designs and applications. *Biotechniques* 31:1106–1121
- Einstein A (1916) Strahlungs-Emission und -Absorption nach der Quantentheorie. *Verh Dtsch Phys Ges* 18:318–323
- Eisinger J, Gueron M, Shulman RG, Yamane T (1966) Excimer fluorescence of dinucleotides, polynucleotides, and DNA. *Proc Natl Acad Sci USA* 55:1015–1020
- Förster T (1948) Intermolecular energy migration and fluorescence. *Ann Phys* 2:55–75
- Förster T (1975) Excimers and exciplexes. In: Gordon M, Ware WR (eds) *The exciplex*. Academic Press Inc., London, pp 1–21
- Förster T, Kasper K (1955) Ein Konzentrationsumschlag der Fluoreszenz des Pyrens. *Z Elektrochem* 59:976–980
- Hanssen L (2001) Integrating-sphere system and method for absolute measurement of transmittance, reflectance, and absorptance of specular samples. *Appl Opt* 40:3196–3204
- Hilborn RC (1982) Einstein coefficients, cross sections, f values, dipole moments, and all that. *Am J Phys* 50:982–986
- Kasha M (1950) Characterization of electronic transitions in complex molecules. *Discuss Faraday Soc* 9:14–19
- Kasha M (1952) Collisional perturbation of spin-orbital coupling and the mechanism of fluorescence quenching. A visual demonstration of the perturbation. *J Chem Phys* 20:71
- Leonhardt H, Weller A (1963) Elektronenübertragungsreaktionen des angeregten Perylens. *Ber Bunsenges Physik Chem* 67:791–795
- Leyre S, Coutino-Gonzalez E, Joos JJ, Ryckaert J, Meuret Y, Poelman D, Smet PF, Durinck G, Hofkens J, Deconinck G, Hanselaer P (2014) Absolute determination of photoluminescence quantum efficiency using an integrating sphere setup. *Rev Sci Instrum* 85:123115
- Medinger T, Wilkinson F (1965) Mechanism of fluorescence quenching in solution. *Trans Faraday Soc* 61:620–630
- Murov SL, Carmichael I, Hug GL (1993) *Handbook of photochemistry*, 2nd edn. CRC Press, New York
- Nguyen AW, Daugherty PS (2005) Evolutionary optimization of fluorescent proteins for intracellular FRET. *Nat Biotechnol* 23:355–360
- Periasamy A (2001) Fluorescence resonance energy transfer microscopy: a mini review. *J Biomed Opt* 6:287–291
- Resch-Genger U, Rurack K (2013) Determination of the photoluminescence quantum yield of dilute dye solutions (IUPAC Technical Report). *Pure Appl Chem* 85:2005–2013
- Rizzuto R, Brini M, Pizzo P, Murgia M, Pozzan T (1995) Chimeric green fluorescent protein as a tool for visualizing subcellular organelles in living cells. *Curr Biol* 5:635–642
- Rohatgi-Mukherjee KK (1986) *Fundamentals of photochemistry*, pp 126–160
- Schaufele F, Demarco I, Day RN (2005) FRET imaging in the wide-field microscope. In: Periasamy A, Day RN (eds) *Molecular imaging: FRET microscopy and spectroscopy*. Oxford University Press, Oxford, pp 72–94
- Scott DR, Allison JB (1962) Solvent glasses for low temperature spectroscopic studies. *J Phys Chem* 66:561–562
- Shindy HA (2017) *Fundamentals in the chemistry of cyanine dyes: a review*. *Dyes Pigm* 145:505–513
- Stevens B (1961) Evidence for the photo-association of aromatic hydrocarbons in fluid media. *Nature* 192:725–727
- Terenin A, Ermolaev V (1956) Sensitized phosphorescence in organic solutions at low temperature: energy transfer between triplet states. *Trans Faraday Soc* 52:1042–1052

- Valeur B, Berberan-Santos M (2012) Excitation energy transfer. *Molecular fluorescence: principles and applications*, 2nd edn. Wiley-VCH, Weinheim, pp 213–261
- Ware WR, Richter HP (1968) Fluorescence quenching via charge transfer: the perylene-N, N-dimethylaniline system. *J. Chem. Phys.* 48:1595–1601

Chapter 4

Raman Biospectroscopy and Imaging



Smilja Todorovic

Abbreviations

A	Adenine
Ab	Antibody
AFM	Atomic Force Microscopy
BCA	Basic component analysis
C	Cytosine
CcO	Cytochrome c oxidase
Cys	Cysteine
cyt c	Cytochrome c
CCD	Charge coupled device
CV	Crystal violet
CVa	Crystal violet acetate
DET	Direct Electron Transfer
DPA	Dipicolinic acid
DyP	Dye decolorizing peroxidase
E^0	Midpoint redox potential
EndoIII	Endonuclease III
ET	Electron Transfer
FT	Fourier Transform
G	Guanine
Hb	Hemoglobin
HCO	Heme copper oxidase
HPV	Human papilloma virus
HRP	Horse radish peroxidase

S. Todorovic (✉)

Raman Biospectroscopy Laboratory, Instituto de Tecnologia Química e Biológica António Xavier ITQB-NOVA, Universidade NOVA de Lisboa, 2780-157 Oeiras, Portugal
e-mail: smilja@itqb.unl.pt

HS	High spin
k_{ET}	Electron transfer rate constant
LDA	Linear discriminant analysis
LMCT	Ligand to metal charge transfer
LS	Low spin
Mb	Myoglobin
MBA	4-mercaptobenzoic acid
MNP	Magnetic nanoparticle
NiR	Nitrite reductase
NP	Nanoparticle
P450	Cytochrome P450
PCA	Principal component analysis
Phe	Phenylalanine
PLS-DA	Partial least squares-discriminant analysis
PSII	Photosystem II
QS	Quantum spin state admixture
RR	Resonance Raman
RS	Raman spectroscopy
SAM	Self assembled monolayer
<i>SAM</i>	S-Adenosyl methionine
SER(S)	Surface Enhanced Raman (spectroscopy)
SERR(S)	Surface Enhanced resonance Raman (spectroscopy)
SESORS	Surface-enhanced spatially offset Raman spectroscopy
SHE	Standard hydrogen electrode
T	Thymine
TERRS	Tip Enhanced resonance Raman spectroscopy
TERS	Tip Enhanced Raman spectroscopy
TR	Time resolved
TRS	Transmission Raman Spectroscopy
Tyr	Tyrosine
U	Uracil
UVRR	Ultraviolet resonance Raman

4.1 Introduction

Raman spectroscopy is a light scattering technique which, like IR, probes vibrational levels of a molecule; the spectra are therefore molecule-specific and represent its vibrational fingerprint (Siebert and Hildebrandt 2008). It is named after Indian physicist C. V. Raman who was awarded the Nobel Prize ‘for his work on the scattering of light and for the discovery of the effect named after him’ in 1930 (Raman and Krishnan 1928). Raman spectroscopy and more recently Raman imaging have been increasingly popular in life sciences and biomedicine, due to the non-destructive and

non-invasive nature and the possibility of studying biological samples in physiological conditions. The intrinsically low efficiency of the scattering process, nevertheless, results in poor sensitivity of Raman spectroscopy. This major drawback can be overcome by surface enhancement of the signal by the use of metallic substrates with plasmonic properties, which upon modification can also increase the selectivity of Raman spectra. Integration with other techniques like AFM, can increase spatial resolution of Raman based-imaging, or like electrochemistry, can provide sensitive and selective spectro-electrochemical information (Bailo and Deckert 2008; Schmid et al. 2013; Todorovic and Murgida 2016; Reguera et al. 2017). Recent advancements in engineering of novel plasmonic nano-materials for surface enhancement of Raman signal, together with technical developments in the design of new instruments with high throughput optics and improved detection sensitivity, place nowadays Raman spectroscopy and imaging in forefront of methods capable of providing molecular details on biological samples in vivo (Qian and Nie 2008; Vo-Dinh et al. 2015; Lane et al. 2015a, b; Heraud et al. 2017). Reports on novel analytical, pharmaceutical, forensic, biochemical, environmental and medical applications emerge on a regular basis (Qian and Nie 2008; Bailo and Deckert 2008; Guerrini and Graham 2012; Schlucker 2014; Cialla et al. 2014; Kong et al. 2015; Lane et al. 2015a, b; Cialla-May et al. 2017).

Raman-based approaches represent particularly powerful tools for diverse bioanalytical and biomedical applications as well as for fundamental biosciences. These include (i) *detection* and *identification* of biological species (e.g. metabolites, small bioactive molecules, DNA/RNA, proteins, antibodies and receptors, viruses, cancerous cells and bacteria) in food and clinical samples (Craig et al. 2013; Old et al. 2014; Pahlow et al. 2015; Frost et al. 2017), (ii) *2D mapping* and *3D imaging* of cells and tissues (Heraud et al. 2017) and (iii) *structure-function* correlated *studies* of (metallo)proteins (Murgida and Hildebrandt 2008; Todorovic and Murgida 2016). In special focus are biomedical applications which take advantage of the capacity of Raman spectroscopy to identify molecular changes in tissues, indicative of e.g. different types of cancer, or to specifically and selectively detect biomarkers of cancer, asthma, inflammation, malaria, etc. (Ngo et al. 2014; Kong et al. 2015). Raman spectroscopy can provide molecular information with high chemical specificity without damaging the cells or disturbing their biological activity, which is often the case when fluorescent labels or other contrast agents are used. For these reasons intensive ongoing efforts aim to establish Raman based clinical spectroscopy as a label-free diagnostic tool for remote, real-time, in vivo medical diagnosis based on fiber optics Raman probes (Mohs et al. 2010; Iping Petterson et al. 2016; Matousek and Stone 2016; Ember et al. 2017).

The Raman effect accounts for a change in monochromatic light frequency upon inelastic scattering from a molecule. The energy change (note that the terms ‘energy’ and ‘frequency’ are equivalent and are commonly inter-changed in ‘Raman jargon’) corresponds to a transition between discrete vibrational energy levels of the molecule. In the case of small molecules, Raman spectra provide information on their structures. The measured frequencies are sensitive to bond strength, number of atoms, their geometries, coordination and molecular environment, being therefore unique

for the given molecule (hence the term ‘Raman fingerprint’ of a molecule) (Siebert and Hildebrandt 2008). However, in the case of large biomolecules, the spectra consist of numerous overlapping bands, originating from all Raman active modes of the molecule, therefore lacking the selectivity. The selectivity, together with sensitivity of Raman spectroscopy (often referred to as normal or conventional Raman, hereafter referred to as RS) can be significantly increased through resonance enhancement (resonance Raman spectroscopy, RR) for molecules that possess chromophoric cofactors; in this case only signal of the chromophore becomes enhanced (Siebert and Hildebrandt 2008). Selectivity and sensitivity of RS can also be increased through surface enhancement of the Raman signal (i.e. Surface Enhanced Raman spectroscopy, SERS, and Tip Enhanced Raman Spectroscopy, TERS) of any molecule that is found in the close proximity of a plasmonic metal substrate, such as a nanoparticle (NP). Moreover, SER and RR can combine to give origin to surface enhanced resonance Raman spectroscopy (SERRS), which probes only chromophores of the molecules attached to plasmonic nanostructures, enhancing their signal by several orders of magnitude (Siebert and Hildebrandt 2008).

The type of information that can be extracted from Raman spectra of a biological sample critically depends on its complexity (i.e. small biomolecule, protein, protein complex, organelle, cell or tissue) and the adopted experimental approach (i.e. RS, RR, SERS, SERRS or TERS), which can probe either specific or all Raman active bonds in the sample molecules. For instance, in the case of tissues, conventional Raman spectra reveal an average contribution of all Raman active modes in the sample (i.e. from proteins, lipids, polysaccharides, nucleic acids) and typically require chemometrics analysis for extraction of the relevant information (Hobro et al. 2016). The spectra of the same tissue, obtained by SERS employing NPs decorated with specific antibodies, can provide ultrasensitive and selective detection of specific target molecules, like disease biomarkers, and their localization within the tissue (Schlucker 2014; Vo-Dinh et al. 2015). Raman spectra of metalloenzymes consist mainly of overlapping amide bands with additional contributions from several specific amino acid residues. On the other hand, very fine structural details on metal active sites of these molecules and even their short-living catalytic intermediates, can be revealed by RR (Siebert and Hildebrandt 2008). Furthermore, selective probing of structure, conformation and thermodynamic and kinetic properties of heme proteins that are attached to plasmonic silver electrodes can be achieved by SERRS, providing unmatched information on their functional properties (Todorovic and Murgida 2016).

In the first part of this chapter, we provide an introduction to very basic experimental aspects of conventional Raman and advanced Raman spectroscopies (the term that we adopted for RR, SERS, SERRS, TERS and imaging techniques), which are crucial for understanding of different applications, their potentials and challenges. Then we present an overview of the current state of the art in the analysis of biomacromolecules and identification and differentiation of cells by RS, studies of proteins by RR, detection of molecules and disease biomarkers by SERS and studies of immobilized metalloproteins by SERRS. Finally, we demonstrate the potential of Raman-based imaging of cells and tissues, such as label-free chemical imaging

and SERS-based imaging for localization of targeted molecules. We conclude with examples of TERS, which combines topographic and spectroscopic information on the nanometer scale even for weakly scattering and small biological molecules, and a brief outlook.

4.2 Methodology

4.2.1 Raman Spectroscopy (RS)

When a sample is excited with highly monochromatic laser light of frequency ν_0 , it mainly passes through the sample unaltered. Only a small fraction of the incoming photons emerges with a different energy, due to inelastic scattering from the sample molecules; the frequency shift of the scattered radiation is $\nu_0 \pm \nu_m$. The so called Stokes-shifted Raman scattering of $(\nu_0 - \nu_m)$ frequency is measured in most of the Raman based techniques. It results from energy transfer from the incident photon (ν_0) to the molecule in an amount that equals a quantum of vibrational energy (ν_m) and thereby produces a vibrationally excited molecule and scattered radiation of higher wavelength (lower energy) than the incident laser (Siebert and Hildebrandt 2008). The Raman spectrum is represented as a plot of intensity (arbitrary units, a. u.) versus frequency of Raman scattered photons (cm^{-1}). Each band typically originates from a specific Raman active molecular vibration for which, according to the selection rules, the incident light induces a change in polarizability. The scattering process nevertheless has an inherently low quantum yield ($<10^{-9}$), which imposes low sensitivity as a major drawback of conventional RS (Siebert and Hildebrandt 2008). Thus, especially in the case of biological samples, fluorescence from the target molecule or from impurities may completely override Raman scattering.

4.2.2 Advanced Raman Spectroscopy

4.2.2.1 Resonance Raman (RR) Spectroscopy

If a molecule possesses a chromophore that has an electronic transition in resonance with the energy of the excitation laser, the quantum yield of the scattering process increases by several orders of magnitude, Fig. 4.1a. Under these conditions, the so-called resonance Raman signal can reach enhancements of 10^3 to 10^5 , but only for the vibrational modes originating from the chromophore, regardless of the size of the molecule. RR therefore increases both sensitivity and selectivity, as it probes only the light absorbing part of the molecule. It can be employed in static and time resolved (TR) mode; the latter allows monitoring of short living processes in biomolecules, like formation of transient catalytic intermediates (Siebert and Hildebrandt 2008).

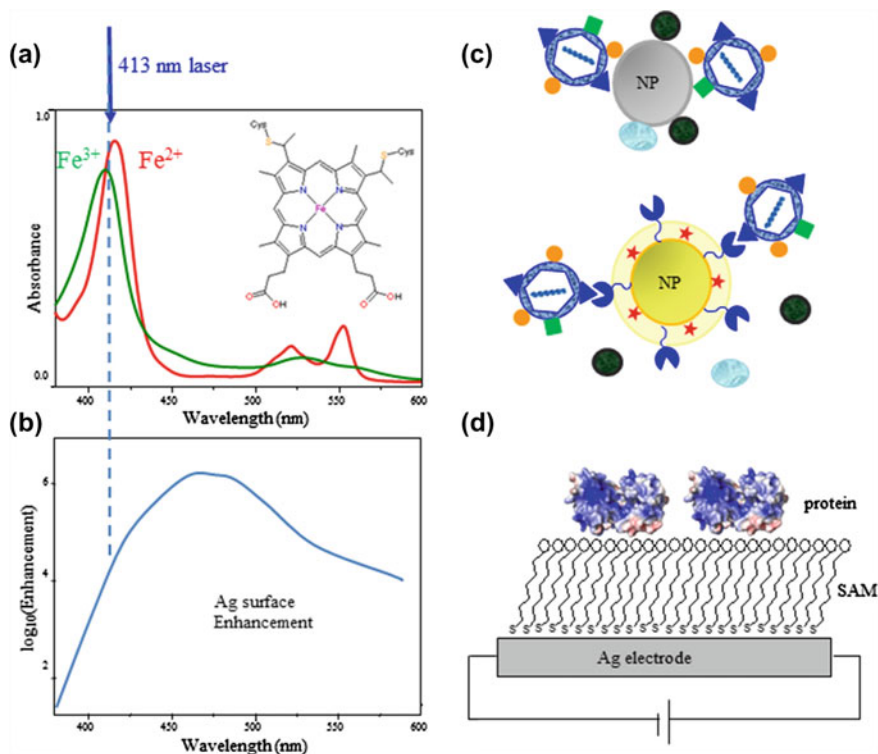


Fig. 4.1 Schematic representation of RR and SE(R)R enhancements and SER substrates. **a** RR enhancement for a heme protein excited into Soret band with 413 nm laser, **b** SER enhancement for Ag substrate and 413 nm excitation, **(a, b)** RR + SER = SERR enhancements for a heme protein attached to Ag substrate excited into Soret band; **c** metallic NP SER substrates. Top, 'bare' NP for direct attachment of the analyte (e.g. virus particle, carrying structural proteins represented as orange spheres and green squares, and antigens, represented as blue triangles), other molecules from the sample mixture (represented as brown spheres and light blue ellipsoids) also readily bind to bare NPs. Bottom, functionalized NP for indirect detection of the analyte (e.g. virus particle), decorated with Raman tags (red star) and antibodies (blue 'packman'), which ensure specific binding of the target only via antibody-antigen interaction. **d** Modified nanostructured bulk Ag electrode coated with SAM for biocompatible protein immobilization

4.2.2.2 Surface Enhanced Raman Spectroscopy (SERS)

If a molecule is located in the vicinity of a plasmonic structure, the resonant interaction of the laser light with the surface plasmons of the substrate can lead to an enhancement of the signal by >5 orders of magnitude, Fig. 4.1b (Siebert and Hildebrandt 2008; Todorovic and Murgida 2016). The created localized enhanced electric field is constrained to only few nanometers from the surface of the nanostructure, which results in an increased intensity of the Raman bands of the molecules located in that region.

The most commonly used SER-active metals are Ag and Au, which need to be excited with lasers of wavelengths above ca 320 and 570 nm, respectively (Todorovic and Murgida 2016). These plasmonic nanostructures, also called SER substrates, can be in solution or solid state. They can consist of monomers, dimers or aggregates of NPs in solution, Fig. 4.1c or rely on 2D arrays and films composed of collection of NPs. The SER substrate can also be a bulk plasmonic metal functioning as an electrode Fig. 4.1d. Regardless of the type of the used platform, the molecule of interest (i.e. analyte) can be attached directly to a ‘bare’ or to a functionalized SER-active surface, Fig. 4.1c. The functionalized substrates carry Raman labels and recognition moieties for specific interaction with the analyte molecules on the surface, Fig. 4.1c, bottom (Schlucker 2014). Note that term ‘bare’ typically refers to electrolyte ion protected substrates, which are not decorated with specific groups. These two types of substrates give origin to distinct, direct and indirect methods for SER-based detection and imaging of biological samples (vide infra). The indirect methods take advantage of specific interaction between the targeted molecule and recognition group (also known as a ‘capture group’) and rely on the SER signal of the Raman reporter molecule (also known as Raman label, tag or dye), which is simultaneously conjugated to the substrate Fig. 4.1c, bottom. The direct methods are based on the SER spectra of the analyte molecules.

In the case of TERS, the surface enhancement of Raman signal comes from an atomic force microscopy (AFM) metal tip. The tip is illuminated by the laser which simultaneously excites Raman spectra and localized surface plasmons at the tip apex, resulting in the enhanced field at molecules found at close vicinity (few nm) of the tip (Bailo and Deckert 2008).

4.2.2.3 Surface Enhanced Resonance Raman Spectroscopy (SERRS)

Combined, RR and SER give origin to SERR spectroscopy, which sensitively and selectively probes only chromophores of molecules that are attached to nanostructured substrates. In this case the energy of excitation laser has to match simultaneously that of the surface plasmons (SER condition) and that of the electronic transition (RR condition) (Siebert and Hildebrandt 2008). This is the case of heme proteins attached to plasmonic Ag substrates and probed with ca. 410 nm excitation, Fig. 4.1a, b. The metal that gives rise to the surface enhancement can at the same time serve as an electrode, allowing for coupling of SERR spectroscopy with electrochemistry, Fig. 4.1d. The so-called SERR spectro-electrochemistry provides information on the nature of redox active species and on potential dependent redox processes of the immobilized species (Todorovic and Murgida 2016). It is particularly informative in the studies of heme proteins, which have distinct (SE)RR fingerprints in oxidized (Fe^{3+}) and reduced (Fe^{2+}) states, allowing for monitoring redox transitions of the immobilized protein. The nanostructured electrodes are typically modified by thin organic films that provide biocompatible or biomimetic interfaces (Murgida and Hildebrandt 2008). The most frequently used coatings are bifunctional alkanethiols that form self-assembled monolayers (SAMs) by covalent binding to the metal via the

thiol group. The other SAM head-group defines the interface for protein attachment, which depending on its surface charge distribution, can be achieved via electrostatic, hydrophobic or polar interactions, via cross-linking or direct coordination (Murgida and Hildebrandt 2008). SERR spectro-electrochemistry can be performed in the TR mode to probe the dynamics of processes in the micro- to milli-second range, triggered by a rapid potential jump (Murgida and Hildebrandt 2001, 2004).

4.2.2.4 Raman Imaging

Raman images can be reconstituted from Raman, SE(R)R or TER spectra, collected by point-by-point acquisition from a surface (or other focal plane) of the sample (vide infra). Scanning is achieved by moving the sample in x and y direction using a sensitive xyz stage that positions it in a defined step size, or by galvanometric mirrors, which move the laser across the chosen area of the static sample (Abramczyk and Brozek-Pluska 2013). A 2D Raman image therefore provides mapping of the surface or other focal plane of the sample. The in-depth discrimination is achieved by successive changes of the focal plane of the sample (note that photons from outside focal plane will not be detected); a series of confocal images at successive planes along z axis can be used to generate 3D Raman images. Typically, the lateral resolution is in Raman imaging restricted by the Abbe diffraction limit, while the axial resolution reaches few μm . TER imaging provides resolution beyond the diffraction limit; the spatial resolution, defined by the size of the tip apex radius, is typically 20–30 nm or even lower in the case of NP modified tips (Deckert-Gaudig et al. 2012; Schmid et al. 2013; Verma 2016).

4.2.3 Raman Instrument

Basic components of Raman set-up are: (i) a laser excitation source, (ii) optical element(s) for focusing incoming and collecting scattered light, (iii) a spectrometer and (iv) a detector. (i) The laser excitation source emits light of desired frequency; Ar^+ and Kr^+ ion lasers are used for visible range, He–Ne and He–Cd gas lasers for near UV-visible range, while tunable lasers based on organic dyes and diode solid-state lasers cover a spectral range from the UV to the near IR. The Raman signal intensity is proportional to $1/\lambda_{\text{exc}}^4$ (or more precisely to $(\nu_0 \pm \nu_m)^4$), therefore, lower the laser wavelength, higher the sensitivity. The choice of laser line can nevertheless be restricted by resonance condition in RR, SER and SERR experiments (vide supra), or when fluorescence needs to be avoided; the latter can often be achieved by using longer (>600 nm) wavelengths. Moreover, λ_{exc} and its intensity should be carefully considered when studying biological samples, due to possible laser induced damage related to photochemical reactions initiated by the laser. (ii) The optical element focuses the laser beam onto the sample and collects the radiation scattered back from the illuminated spot. It is nowadays typically a confocal microscope with high optical

throughput. Only photons generated inside the focal plane of the sample will reach the detector; different focal planes can be selected by adjusting the pinhole placed in front of the spectrometer. (iii) The spectrometer rejects elastically scattered (so-called Rayleigh scattering) radiation and spectrally resolves the inelastically scattered light. This can be achieved by single stage spectrographs, equipped with holographic notch or edge filters or double/triple stage spectrographs. The spectrometers are typically dispersive, with exception of interferometric FT Raman instruments. (iv) The detector is most commonly a charge-coupled device (CCD) (Siebert and Hildebrandt 2008).

4.3 Applications

4.3.1 Raman Spectroscopy for Bioanalysis

4.3.1.1 RS of Biomacromolecules

RS can be used to identify and structurally characterize major cellular macromolecules *in vitro* and *in vivo*.

Proteins. The most distinguished Raman bands of proteins are due to the peptide bonds, i.e. the amide I (1600–1700 cm^{-1}), originating mainly from C=O stretching, amide II (1480–1580 cm^{-1}) and amide III (1230–1300 cm^{-1}), which are both associated with C–N stretching coupled to N–H bending (Niaura 2014). The frequencies of these bands are sensitive to protein secondary structural elements; predominantly α -helical structures show amide I and amide III bands at 1655–1662 cm^{-1} and 1264–1272 cm^{-1} and β -sheet structures at 1672–1674 cm^{-1} and 1227–1250 cm^{-1} (Rygula et al. 2013). RS can also probe several specific amino acids, such as Trp, Tyr, Phe and Cys. The characteristic bands are: Trp doublet at 1340/1360 cm^{-1} , Phe ring breathing mode at 1004 cm^{-1} , Tyr band at 1270 cm^{-1} and doublet at 833/860 cm^{-1} . Sulfur-containing amino acid residues also show specific bands at 510–750 cm^{-1} and at 2530–2580 cm^{-1} ; the latter are S–H stretching modes, which are sensitive to H bonding.

Nucleic acids. The most characteristic bands of DNA and RNA are ring breathing modes at approximately 680 cm^{-1} (G), 730 cm^{-1} (A), 740–785 cm^{-1} (C, T, U), 1087–1100 cm^{-1} (PO_2^- symmetric stretching). Several pronounced bands are found at higher frequencies: 1230–1250 cm^{-1} (C, T, U), 1290–1380 cm^{-1} (A, C, T), 1530–1590 cm^{-1} (A, C, G) and 1655 cm^{-1} (T) (Benevides et al. 2005; Niaura 2014). RS can provide information about the conformations of the sugar–phosphate backbone of nucleic acids, and also about the constituent nucleosides, such as hydrogen-bonding or interactions between bases (base stacking) and with other molecules, like proteins, drugs and metal ions (Benevides et al. 2005).

Other biomolecules. RS of lipids reveals mainly C–H stretching (2800–3000 cm^{-1}) and C–C skeletal (1000–1200 cm^{-1}) modes that are sensitive to inter- and intra-

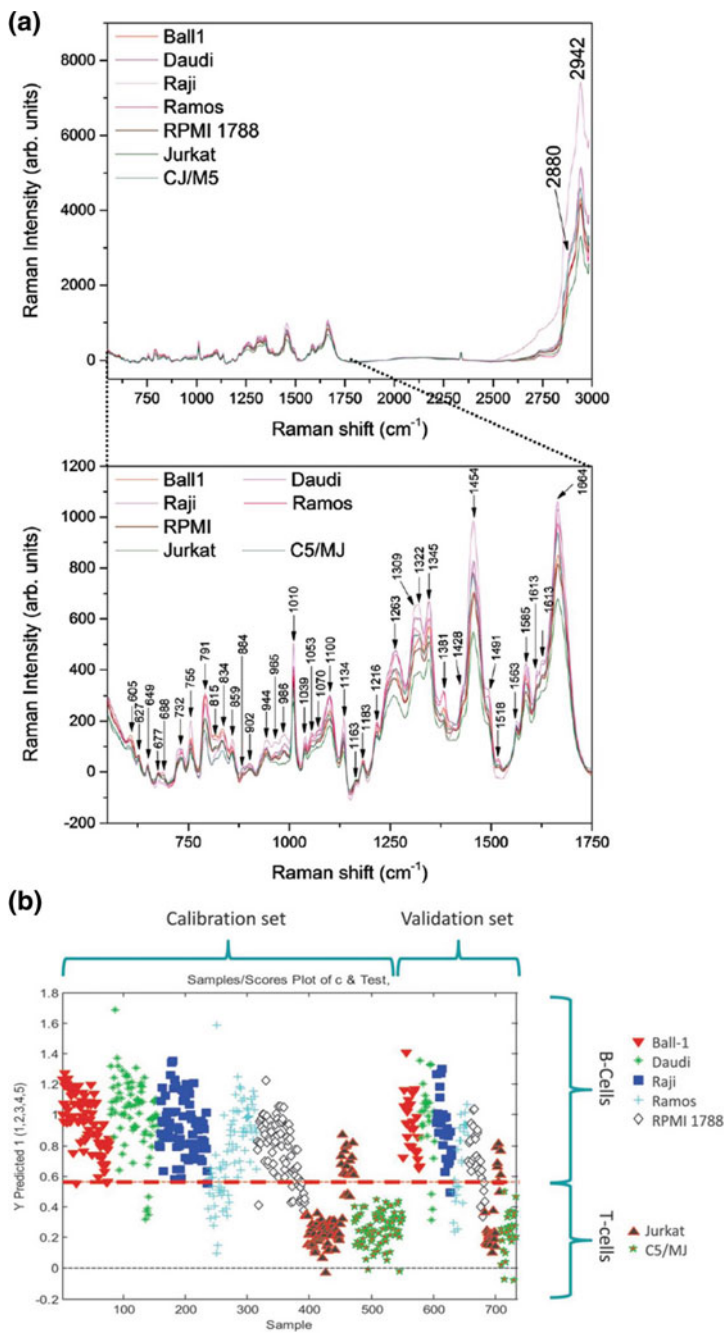
molecular interactions, in addition to non-specific CH_2 deformations at around 1440 cm^{-1} (Niaura 2014). RS can also be used for identification and in some cases quantification of small biomolecules, like glucose, urea, cholesterol and analogues, triglycerides, etc. in biofluids and other samples (Todorovic and Murgida 2016). The analysis is particularly straightforward when the molecule possesses a Raman active group with isolated, well resolved characteristic bands, which can be used as markers (e.g. glucose at 1125 cm^{-1} , collagen fibers at 950 cm^{-1} , dipicolinic acid (DPA) at 1016 and 1395 cm^{-1} , ergosterol at 1602 cm^{-1} etc.).

4.3.1.2 Identification and Differentiation of Cells by RS

RS can provide information on physical and chemical properties of cells *in vitro* and *in vivo*, without a necessity for their labeling or devitalizing. The spectra of cells are dominated by vibrational bands of proteins and nucleic acids, and in some cases membrane lipids. RS has a capacity to discriminate between different cell groups, such as tumor and normal, dead and alive, proliferating and non-proliferating cells, Fig. 4.2 (Short et al. 2005). The differences in most of the cases originate from variations of lipids, proteins, DNA and RNA, which are due to distinct biochemical activities. These molecules have Raman signatures (*vide supra*) that contribute to the most prominent Raman spectral features observed in cells, at $2800\text{--}3100\text{ cm}^{-1}$ (CH_3 and CH_2 stretching in carbohydrates, lipids, proteins), $1655\text{--}1665\text{ cm}^{-1}$ (amide I), $1575\text{--}1590\text{ cm}^{-1}$ (G, A), $1440\text{--}1460\text{ cm}^{-1}$ (CH_2 deformation in lipids, proteins, carbohydrates), $1230\text{--}1300\text{ cm}^{-1}$ (amide III), 1004 cm^{-1} (Phe), $650\text{--}850\text{ cm}^{-1}$ (nucleic acids and Tyr), which often allow for a quantitative description of relative alterations in cells and nuclei (Notingher et al. 2002; Short et al. 2005). The changes in Raman spectra can be deduced directly from the band ratios or upon treatment of experimental spectra by statistical or fitting tools, such as e.g. principal component analysis (PCA), linear discriminant analysis (LDA), PCA combined with cluster analysis for cell classification, and basic component analysis (BCA), among others (Frost et al. 2017). The scores from PCA (or other type of data analysis) can reveal differences between groups of cells and successfully classify e.g. normal versus malignant cells.

Application of RS for early detection of cancer, based on differentiation between normal and malignant tissues in *in-vivo* and *ex vivo* samples, represents a remarkably active field of research (Frost et al. 2017). RS coupled to partial least squares-discriminant analysis (PLS-DA) of spectra can discriminate between morphologically identical B and T lymphocytes. They have very subtle biochemical differences (and very similar Raman spectra, Fig. 4.2a), but quite distinct roles in adaptive immune response (Hobro et al. 2016). Nevertheless, the PLS-DA scores clearly demonstrate that it is possible to differentiate between B- and T-type cells and even among individual B-cell and T-cell lines, Fig. 4.2b.

RS can also sensitively discriminate between cells and nuclei from cultures of non-proliferating, proliferating and tumorigenic proliferating cells in mammalian cell cultures (Short et al. 2005), which is of a crucial importance for Raman detection of rapidly dividing populations of cancer cells *in vivo*. The observed alterations



◀**Fig. 4.2** Raman spectra of B and T lymphocyte cell lines and their PLS-DA scores plot. **a** Upper panel, 550–3000 cm^{-1} range and lower panel 550–1750 cm^{-1} range of the spectra. B-cell lines (Ball-1, Daudi, Raji, Ramos and RPMI 1788) are shown in shades of red and pink, T-cell lines (Jurkat and C5/MJ) are shown in green. **b** PLS-DA scores plot for B- and T-cell line discrimination. Each cell line is denoted by different symbols as shown in the figure key. The red dashed line represents a dividing line between the B- and T-cell spectra. Reproduced from Hobro et al. (2016) with permission from The Royal Society of Chemistry via Copyright Clearance Center

could be assigned to specific biochemical changes. It was furthermore demonstrated that variations between populations of actively dividing and quiescent cells also need to be considered. Another interesting example represents a recent study of single mycobacteria cells (Stockel et al. 2017). In combination with data analysis supported by a large reference database of Raman spectra, RS revealed that it is possible to identify mycobacteria at the species level. It was feasible to identify *Mycobacterium tuberculosis* strains as the main cause of pulmonary tuberculosis and to differentiate between pathogenic and commensal non-tuberculous mycobacteria. This finding revealed the potential of RS as a first-line tool for the confirmation of a tuberculosis diagnosis. Importantly, individual intact cells were used in the study, demonstrating that the time-consuming pre-cultivation of the bacteria could be omitted in the procedure, which represents a major advantage specifically in the case of slow growing bacteria (Stockel et al. 2017).

4.3.2 Resonance Raman Spectroscopy of Biomolecules Containing Metal or Organic Chromophores

4.3.2.1 RR Spectroscopy of Metalloproteins

RR spectroscopy is an indispensable tool for elucidation of structure–function relationship in heme, iron–sulfur, diiron and copper containing metalloproteins, since it specifically probes the respective metal sites, which are often the active centers in enzymes or have other functional roles (Spiro and Li 1988). Moreover, if the studied metalloprotein possesses multiple chromophores with distinct electronic transitions, RR offers a unique possibility to selectively excite, identify and characterize individual centers by matching the excitation laser wavelength with the respective electronic transition of each chromophore.

Heme proteins. RR has provided a wealth of structural and functional details on diverse heme proteins, including hemoglobin (Hb) (Egawa and Yeh 2005), myoglobin (Mb) (Spiro and Li 1988), heme sensory proteins (Catarino et al. 2010), cytochromes (e.g. cyt *c*) (Spiro and Li 1988), peroxidases (Smulevich et al. 2005; Sezer et al. 2012, 2013) and other oxido-reductases (Siebert and Hildebrandt 2008; Spiro and Li 1988). The most informative are the RR spectra obtained upon excitation into Soret band ($\lambda_{\text{exc}} \sim 400 \text{ nm}$), originating from $\pi\text{-}\pi^*$ electronic transitions of the porphyrin; note

that RR can also be excited into heme Q bands found above 500 nm, using higher excitation wavelength (Kranich et al. 2008).

In the high-frequency (1300–1700 cm^{-1}) region, RR spectra display ‘so-called’ core-size marker bands, designated as ν_4 , ν_3 , ν_2 and ν_{10} , which originate from complex vibrations of porphyrin macrocycle, and which are sensitive to the redox and spin state and coordination pattern of the heme iron, Fig. 4.3 (Murgida and Hildebrandt 2004; Siebert and Hildebrandt 2008; Sezer et al. 2012). These parameters govern reactivity, molecular interactions and redox behavior of heme proteins and enzymes that are essential for understanding their mechanistic properties. For instance, reduction of a ferric to ferrous heme is associated with a $\sim 10 \text{ cm}^{-1}$ downshift of most of the RR marker bands, particularly ν_4 and ν_3 (Spiro and Li 1988; Siebert and Hildebrandt 2008). The conversion from a five-coordinated high spin (5cHS) to a six-coordinated low spin (6cLS) heme, which may be indicative of substrate or inhibitor binding, causes an upshift of e.g. ν_3 and ν_2 . In the low-frequency (200–600 cm^{-1}) region,

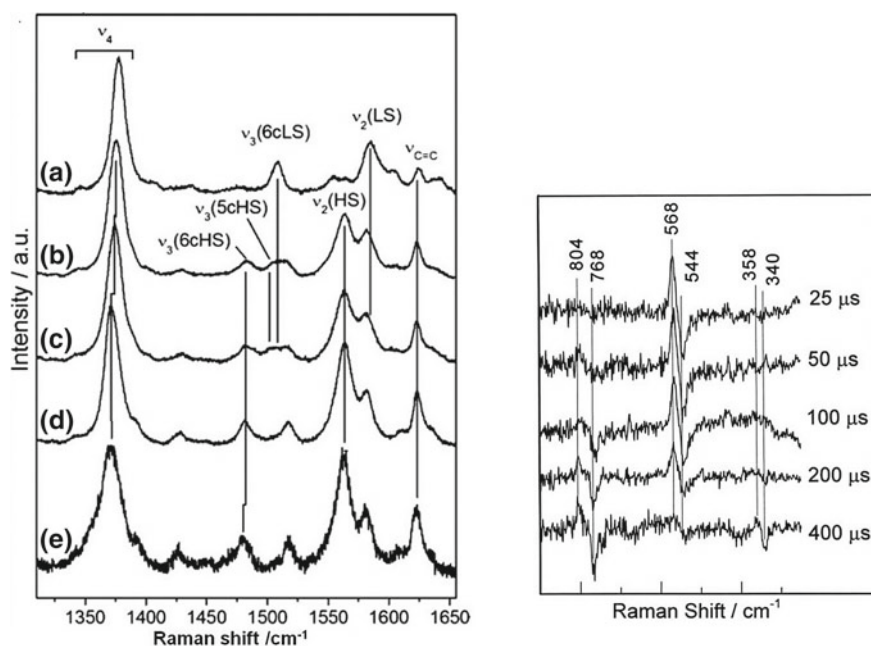


Fig. 4.3 RR spectra of heme proteins. Left, high frequency region of RR spectra of ferric DyP peroxidase: DyP–imidazole complex (a) and DyP measured at pH 10.0 (b), 7.6 (c), and 5.0 (d) and in the crystal state (e). Adapted with permission from Sezer et al. (2013). Copyright 2013 American Chemical Society. Right, low frequency region of RR spectra of cytochrome c oxidase reaction with O_2 . Difference RR spectra at the indicated times after initiation of the reaction were obtained by subtracting the spectra recorded with $^{18}\text{O}_2$ as a substrate from those obtained with $^{16}\text{O}_2$. All porphyrin vibrations cancel in the difference spectra, whereas vibrations of bound oxygen appear as derivative-shaped features. Reprinted from Rousseau and Han (2002). Copyright 2002 with permission from Elsevier

RR spectra contain heme Fe-axial ligand stretching and bending modes, allowing for identification of the physiological ligand, or monitoring of substrate binding and formation of transient catalytic intermediate species, Fig. 4.3 (Spiro and Li 1988; Rousseau and Han 2002). To that end, RR has provided unmatched information on heme group structure, geometry, and binding of small diatomic ligands, such as CO, NO, CN⁻, O₂, which can act as substrates or inhibitors of functionally distinct heme proteins (Spiro and Li 1988). RR helped characterize oxy- and deoxy-forms of Hb and Mb, allosteric R → T transitions in Hb, and physiological ligands of periplasmic heme sensory domains in chemotaxis bacteria (Spiro and Li 1988; Catarino et al. 2010). Furthermore, RR frequencies of Fe-(CO) and FeC-O stretching modes of heme-CO adducts are sensitive to immediate molecular environment and can be explored as indirect local probes of the heme pocket (Spiro and Li 1988; Siebert and Hildebrandt 2008).

RR has played a particularly important role in understanding conformational states of cyt *c*, which govern its physiological function (Capdevila et al. 2015a). Namely, RR can distinguish with superior sensitivity between the native His/Met ligated 6cLS state of cyt *c*, which it adopts when it shuttles electrons between respiratory chain complexes, and 5cHS state, in which cyt *c* acquires peroxidase activity, becomes the key component of mitochondrial apoptotic pathways and therefore responsible for cell death. The identification of these distinct spin states of cyt *c* under physiological conditions is crucial for understanding and the control of apoptosis (Capdevila et al. 2015b). Extensive RR studies of numerous enzymes from the diverse superfamily of heme peroxidases provided deep understanding of their active site architecture; the presence of an extensive network of H-bonds coupling the distal and proximal sides of the active site was shown to play a critical role in the heme ligation, ligand binding and reactivity of these enzymes (Smulevich et al. 2005). Recently RR revealed structural details on active sites of novel dye decolorizing-type peroxidases (DyPs), which are particularly interesting due to their capacity to efficiently degrade inert molecules, including numerous industrially and environmentally relevant dyes, such as anthraquinone-based and azo dyes (Sezer et al. 2012, 2013). Unlike the well-known HRP, some DyPs are of bacterial origin and can therefore be produced in large yield and easily genetically modified, which represents a big advantage for their biotechnological applications. A comparative study of several DyPs allowed correlating the heme coordination pattern with the respective catalytic efficiencies, revealing the structural basis for significantly different activities of enzymes from different subfamilies. In particular, the relative ratio between the 6cLS and 5cHS species (the former of which is catalytically incompetent) that is easily accessible from RR spectra (Fig. 4.3, left panel) could be directly correlated with catalytic efficiency of native DyPs and their variants (Sezer et al. 2012, 2013).

RR has been an essential tool for assessment of structural and mechanistic properties of multi-hemic oxidoreductases, often at the level of individual heme groups (Gennis 1989; Rousseau and Han 2002; Siebert and Hildebrandt 2008). This is a highly challenging task for other spectroscopic methods; UV-Vis spectroscopy is insufficiently sensitive, while EPR suffers from the presence of EPR silent states (e.g. Fe²⁺) and generally hard to interpret overlapping spectra of multiple hemes.

On this note, RR has played a crucial role in disentangling the active site structures and catalytic mechanisms of diverse heme copper oxygen reductases (HCOs). These enzymes catalyze one of the most fundamental processes in life, the reduction of molecular oxygen to water, employing the catalytic 5cHS heme and one or more 6cLS heme groups (Proshlyakov et al. 1998; Rousseau and Han 2002). The catalytic cycle starts by binding of molecular oxygen to the reduced HCO and proceeds through formation of several short living intermediates. The nature and formation kinetics of the catalytic intermediates could be assessed from low-frequency TR RR spectra (Fig. 4.3, right panel), which contributed to overall description and understanding of mechanistic properties of HCOs (Rousseau and Han 2002). Note that HCOs also possess one or more copper atoms, which are not observable in RR spectra obtained with Soret band excitation. RR also provided unprecedented details on functional properties of cyt *c*: nitrite reductase (NiR) that catalyzes the 6-electron reduction of nitrite to ammonia (Martins et al. 2010). The enzyme houses an impressive total of 28 heme groups in the biological unit, 22 of which are in 6cLS state and 6 in 5cHS state. The HS and LS hemes could be distinguished in RR spectra, revealing that the nitrite substrate binding to the catalytic 5cHS hemes induces a transition to the LS configuration. This implies that heterolytic N–O bond cleavage is favored, which is essential for elucidating the subsequent steps of the NiR catalytic cycle.

Fe–S proteins. RR spectra, obtained upon excitation into S → Fe charge transfer electronic transition band (a ligand-to-metal charge transfer transition) are sensitive to Fe–S cluster type, geometry and nature of the ligands. RR provided a wealth of information on Fe–S proteins, which carry out diverse cellular processes, including electron transfer (ET), DNA repair, biogenesis of Fe–S clusters and other cofactors, substrate binding and activation, S-donation and catalysis (Todorovic and Teixeira 2018). These proteins can incorporate one or more of the common 2Fe–2S, 3Fe–4S and 4Fe–4S clusters, each of which has a distinct RR fingerprint, or more complex heteronuclear centers.

In majority of the cases only one, typically oxidized state (i.e. $[\text{Fe}(\text{Cys})_4]^{3+}$, $[2\text{Fe}-2\text{S}]^{2+}$, $[3\text{Fe}-4\text{S}]^{1+}$, $[4\text{Fe}-4\text{S}]^{2+}$) is RR active. The bridging (Fe–S)^b and terminal (Fe–S)^f vibrational modes that involve inorganic and cysteinyl sulfur ligands, respectively, can be distinguished in the spectra, Fig. 4.4 (Todorovic and Teixeira 2018). These bands can therefore serve as sensitive internal probes for monitoring dynamic processes and interactions in proteins that involve the cluster, such as cluster inter-conversion, biogenesis, disassembly and catalysis. To that end, RR has played a crucial part in identification of the key players of complex enzymatic Fe–S cluster assembly machinery, and in disentangling of the dynamics of cluster formation and transfer. It was demonstrated based on distinct RR fingerprints, that the assembly of 4Fe–4S center in scaffold protein IscU accounts for initial formation of a product containing one $[2\text{Fe}-2\text{S}]^{2+}$ cluster, and then two of them, which subsequently become fully converted into one 4Fe–4S cluster (Johnson et al. 2005). RR played an important role in investigations of Fe–S proteins involved in substrate binding and catalysis, such as radical-SAM enzymes and aconitases, in which the cluster typically has a non-all-cysteinyl coordination to allow for substrate binding (Honar-

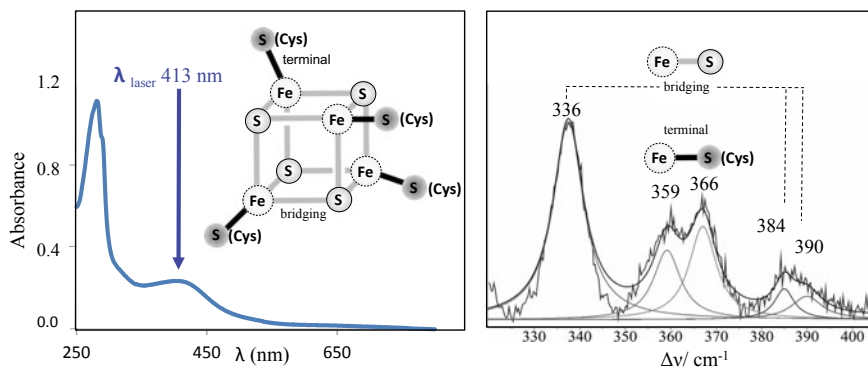


Fig. 4.4 Schematic representation of $[4\text{Fe-4S}]^{2+}$ cluster in a Fe-S protein and its spectra. Left, UV-Vis spectrum and right, RR spectrum of $[4\text{Fe-4S}]^{2+}$ cluster containing protein, measured with 413 nm excitation; bridging $[\text{Fe-S}]^b$ and terminal $[\text{Fe-S}]^t$ vibrational modes, obtained upon spectral deconvolution are designated

mand Ebrahimi et al. 2018). The incomplete coordination, nevertheless, makes these clusters particularly prone to degradation, which led to conflicting reports about the physiologically relevant cluster type. RR spectroscopy provided direct evidence that the relevant form is the $[4\text{Fe-4S}]^{2+}$ form, and not $[2\text{Fe-2S}]^{2+}$ or $[3\text{Fe-4S}]^{1+}$ as also suggested (Todorovic and Teixeira 2018).

Cu proteins. RR spectra of blue copper redox proteins like azurins, plastocyanins and laccases, excited into the characteristic intense S (p) \rightarrow Cu ($d_{x^2-y^2}$) charge transfer band at around 600 nm, selectively probe cupric (Cu^{2+}) Type 1 site (Chen et al. 2010). The cuprous (Cu^{1+}) state is RR silent. The spectra obtained with 568 nm or 647 nm excitation, consist of several commonly broadened and overlapping features in the low-frequency ($200\text{--}500\text{ cm}^{-1}$) region, originating from coupling of the Cu-S(Cys) stretch with the cystein S-C_b-C_a(Cys) bending modes. The bands can be analyzed in terms of relative contributions of the Cu-S stretching coordinate, the frequency of which is inversely proportional to the Cu-S bond length in the T1 site and can be furthermore correlated to its redox potential (E^0). RR studies of laccases from diverse sources and their rationally designed variants provided structural basis for understanding of the variation of E^0 , which is essential for evaluation of the potential of these enzymes for biotechnological applications (Chen et al. 2010). Namely, due to the capacity to oxidize a wide range of phenolic substrates with concomitant reduction of oxygen to water, these enzymes represent particularly promising biocatalysts in wood and textile treatment and environmental applications. It is noteworthy that in addition to T1 center, laccases possess a trinuclear Cu site (where the reduction of oxygen to water takes place) that is RR silent, therefore RR probes selectively the T1 site, at which the oxidizing substrate binds (Chen et al. 2010).

4.3.2.2 RR Spectroscopy of Biomolecules with Non-metallic Chromophores

Visible excitation of RR spectra of non-metallic chromophores, such as flavins (Benecky et al. 1997), visual pigments like rhodopsin, photosynthetic pigments (Tschirner et al. 2009) and photoreceptors (Gall et al. 2015) provides sensitive information on their respective structures and molecular environments. Particularly interesting are RR spectra of pigments bound to photosynthetic complexes, like chlorophyll and carotenoids, since they can reveal structural details that govern their functional physico-chemical properties. For instance, RR and TR RR spectra can report on conformations and interactions of these molecules, as well as on their excited states (e.g. carotenoid S_1 state), which are of primary interest in photosynthesis (Gall et al. 2015).

RR spectra of carotenoid molecules display four main groups of well resolved bands in the $900\text{--}1550\text{ cm}^{-1}$ region. The frequency of the intense band at $\sim 1520\text{ cm}^{-1}$, which originates from two overlapping C=C stretching modes, reflects the extent of conjugation (i.e. chain length), allowing for identification of the pigment type (Gall et al. 2015). It was demonstrated on PSII reaction center that it was possible to identify, *in vitro* and *in vivo*, different simultaneously present carotenoids, and in some cases even selectively excite individual ones. The other carotenoid bands can be found at 1150 cm^{-1} (C–C skeleton mode), 1000 cm^{-1} (in-plane rocking mode of the methyl groups) and 950 cm^{-1} (C–H out-of-plane wagging mode coupled to C=C torsions) (Gall et al. 2015).

RR spectra of chlorophyll contain bands in three different spectral windows; modes in the low frequency ($200\text{--}500\text{ cm}^{-1}$) region involve the central Mg ion, those in the mid-frequency ($900\text{--}1600\text{ cm}^{-1}$) region are sensitive to the conformation of the conjugated macrocycle, while the high-frequency ($1620\text{--}1710\text{ cm}^{-1}$) region contains stretching modes of the conjugated vinyl and carbonyl groups (Gall et al. 2015). Static and TR RR spectra of biological sensory photoreceptor phytochrome, obtained with (pre)resonance (1064 nm) excitation, provided selective characterization of the open-chain tetrapyrrole cofactor, its structural changes and conformations adopted along the photoinduced processes in physiologically active and inactive states (von Stetten et al. 2008; Velazquez Escobar et al. 2015).

UVRR spectra obtained employing excitation with UV light ($180\text{--}260\text{ nm}$), can selectively probe aromatic amino acids and amide bonds in proteins and peptides, as well as nucleic acid components (Ashton et al. 2015). The UVRR bands of the protein amide chromophore are selectively enhanced using $\sim 200\text{ nm}$ excitation. The band frequencies strongly depend on the polypeptide backbone dihedral angles, therefore providing information on the protein secondary structure. UVRR allows for elucidation of specific aspects of protein architecture that drive structure—(mis)function correlation, such as the dynamic evolution of secondary structural elements during unfolding of proteins and formation of protein fibrils (Oladepo et al. 2012; Handen and Lednev 2016; Jakubek et al. 2018). UVRR can also selectively enhance aromatic amino acid side chains, like phenylalanine (195 nm excitation) and tyrosine and tryptophan (230 nm excitation), revealing information about their local

environment and protein tertiary structure. Moreover, UVRR can provide spectral fingerprints of nucleosides, like adenosine and guanine, which possess characteristic bands at ~ 1340 and 1480 cm^{-1} , respectively, allowing for a sensitive detection of DNA and RNA in cells. This has inspired numerous applications, including real time on-line monitoring of nucleic acids in mammalian cell culture media throughout a bioprocess (Benevides et al. 2005; Ashton et al. 2015).

4.3.3 *Surface Enhanced (Resonance) Raman Spectroscopy of Biomolecules*

SE(R)R-based methods show exceptional sensitivity that allows for studies of biomolecules even at the single-molecule level (Xu et al. 1999; Qian and Nie 2008). Roughly speaking, plasmonic metal SER substrates can be NP-based (e.g. NPs, their aggregates, arrays, films, etc., vide supra) or bulk, and furthermore 'bare' or functionalized (Schlucker 2009; Guerrini and Graham 2012; Lane et al. 2015a; Reguera et al. 2017). Among the vast range of applications of SER(R)S, we will highlight here those that rely on the use of (i) NPs for detection of biomolecules (often referred to as bionanosensors in the literature) and (ii) bulk nanostructured electrodes for immobilization of proteins. The former reveal a perspective of becoming faster, more sensitive and multiplexing alternatives to conventional immunological and spectroscopic methods for detection of biomarkers in medical diagnosis and environmental monitoring (Cialla et al. 2014; Lane et al. 2015a; Cialla-May et al. 2017). The latter offer unique advantages in fundamental spectro-electrochemical investigations of mechanistic properties of metalloenzymes and their functioning in direct electron transfer (DET)-based 3rd generation bio-electrocatalysts and biosensors (Todorovic and Murgida 2016).

4.3.3.1 **Direct and Indirect Detection of Biomolecules, SERS Nanosensing**

Direct (label-free or intrinsic) SERS detection of biomolecules relies on measurement of Raman spectra of the targeted species upon spontaneous adsorption onto a plasmonic substrate, Fig. 4.1c, top. The spectra contain information on the nature and structural properties of the molecule through its SERS fingerprint, due to direct attachment to 'bare' substrates (note that SER and RS fingerprints of a molecule may differ owing to surface enhancement selection rules). The molecular specificity of SERS, combined with a simple sample preparation, makes the direct detection of biomacromolecules (e.g. proteins, lipids, short DNA strands), small metabolites and even cells and microorganisms (Stockel et al. 2016), fast and feasible and hence particularly relevant for medical diagnosis and food contamination investigations

(Guerrini et al. 2015). These include detection of: amyloid- β peptide aggregates, which are characteristic for Alzheimer's disease, small, specific DNA sequences of pathogens, metabolites, disease biomarkers and neurotransmitters, such as glucose, dopamine, insulin, serotonin and glutathione (Ciolla et al. 2014; Kadam et al. 2014; Lane et al. 2015a; Stockel et al. 2016). A proof-of-concept for a SERS-based device for direct detection of glucose has been reported and tested on a rat model (Yuen et al. 2010). Also, it has been shown that detection and identification of microorganisms, including pathogen bacteria, viruses and spores can effectively be achieved by SERS (Alexander and Le 2007; Wang et al. 2010; Huang et al. 2011). In these cases PCA of SER spectra is typically required for differentiation of cells. Some systems represent exceptions; spores, for instance, possess a unique chemical marker, DPA, that allows for their sensitive detection and quantification by SERS, which is particularly relevant for spores that can be used as bioweapons.

The drawbacks of direct SERS detection are its (i) limited sensitivity and selectivity, especially in the case of complex multicomponent samples and low analyte concentrations, and (ii) poor reproducibility due to non-specific nature of NP-biomolecule interactions. Significant research efforts have been dedicated to overcoming these issues; the use of iodide-modified Ag NPs resulted in reproducible SERS signals that provided identification of DNA with single-base sensitivity and observation of hybridization events (Xu et al. 2015).

Indirect (dye-labeled, extrinsic or tagging) SERS detection of bioanalytes relies on measurement of the signal of a selected Raman label (also called Raman tag or dye) attached to a plasmonic nanostructure (e.g. NP, solid platform or a chip), which simultaneously carries a receptor (or a capture group) that ensures specific binding of the target (e.g. biomolecule or whole cell, such as bacterial pathogen or virus), Fig. 4.1c bottom panel (Schlucker 2009; Guerrini and Graham 2012; Lane et al. 2015a). The signal of the Raman tag changes in a defined manner upon capture of the desired analyte, due to alterations of its molecular environment. The indirect SERS biosensors are rapid, sensitive, and capable of simultaneous detection of multiple analytes (Kearns et al. 2017). The specificity is typically achieved through antibody/antigen recognition in the case of proteins and hybridization of complementary sequences in the case of DNA/RNA (Barrett et al. 2011; Kadam et al. 2014). The method is indirect since one monitors the signal of the Raman tag and not the SER spectrum of targeted molecule as in the direct detection. It is more selective than the direct method, due to the presence of the recognition moiety for the specific target, and more sensitive owing to measurement of typically strong and well resolved Raman bands of the label; by choosing the Raman label that is resonant with the excitation laser, further increase of the sensitivity of the indirect detection can be achieved through SERRS (Stokes et al. 2008; Stevenson et al. 2009). However, the indirect detection does not provide structural information about the target, since it does not measure its SER spectral fingerprint.

The indirect SERS detection of biomolecules shows unprecedented potential due to the advancements in design, synthesis and fabrication of substrates, which allow for tailoring of sophisticated structures with desired plasmonic and surface modification characteristics (Guerrini and Graham 2012; Lane et al. 2015a; Reguera et al.

2017). Continuous efforts to develop new applications and further improve sensitivity, selectivity and reproducibility envisage, in particular, in vivo analysis. The most promising are platforms capable of simultaneous detection of several biomolecules or bacteria (so-called multiplexing), which can be achieved by associating a unique Raman label with NPs carrying a particular capture group, Fig. 4.5 (Kearns et al. 2017). Such SERS bionanosensor of bacterial pathogens, which is relevant for food and water safety and health, was recently reported employing a sandwich SERS assay and AgNPs. The NPs carrying pathogen specific antibodies and distinct Raman tags were combined with functionalized SER active magnetic NPs, enabling simultaneous capture and isolation of *E. coli*, MRSA and *Salmonella* species through magnetic separation, Fig. 4.5 (Kearns et al. 2017).

Other biomedical applications of indirect SERS detection include detection of biomarkers of prostate, breast and pancreatic cancer, markers for the diagnosis of infection and inflammation, as well as DNA immunoassay for indirect DNA detection through hybridization (Schlucker 2009, 2014; Lane et al. 2015a; Todorovic and Murgida 2016).

4.3.3.2 SERRS of Immobilized Metalloproteins

SERRS studies of metalloproteins in the vast majority of cases refer to heme proteins, for which SER and RR conditions become simultaneously fulfilled upon attachment to plasmonic Ag substrates for surface enhancement and excitation into the Soret electronic absorption band of the protoporphyrin (e.g. 413 nm) that ensures RR enhancement, Fig. 4.1a, b (Siebert and Hildebrandt 2008; Todorovic and Murgida 2016). Analogous to RR spectra of heme proteins in solution, SERR spectra selectively probe spin, coordination and oxidation state of the heme group, but in this case, of the immobilized molecules (Murgida and Hildebrandt 2001, 2004). SERRS offers a unique advantage of probing the structural features of metalloproteins which exert their function in the immobilized state, at natural interfaces (e.g. membrane heme proteins) or at electrode interfaces (e.g. enzyme-based 3rd generation bioelectronic devices). Furthermore, it was recently demonstrated that SERRS can be regarded as an alternative to RR spectroscopy for characterization of catalytic intermediates in heme peroxidases (i.e. Compound I), which is of particular interest when fluorescence impedes RR measurements in solution (Todorovic et al. 2015). As further advantages, SERRS requires only small (sub-micromolar) amounts of protein, the detection of intermediates is possible at ambient temperature and is applicable to the EPR-silent species.

If the plasmonic substrate is bulk Ag that simultaneously functions as an electrode, Fig. 4.1d, potential-dependent processes can be monitored by SERR electrochemistry. Such a potentiometric titration of immobilized monohemic subunit of *cbb*₃-type HCO is represented in Fig. 4.6. The potential dependent SERR spectra obtained at selected poised electrode potentials show particularly evident changes of the ν_4 band, found at $\sim 1360\text{ cm}^{-1}$ for ferrous and $\sim 1370\text{ cm}^{-1}$ for ferric species (Todorovic et al. 2008). The analysis of these spectra can, like electro-

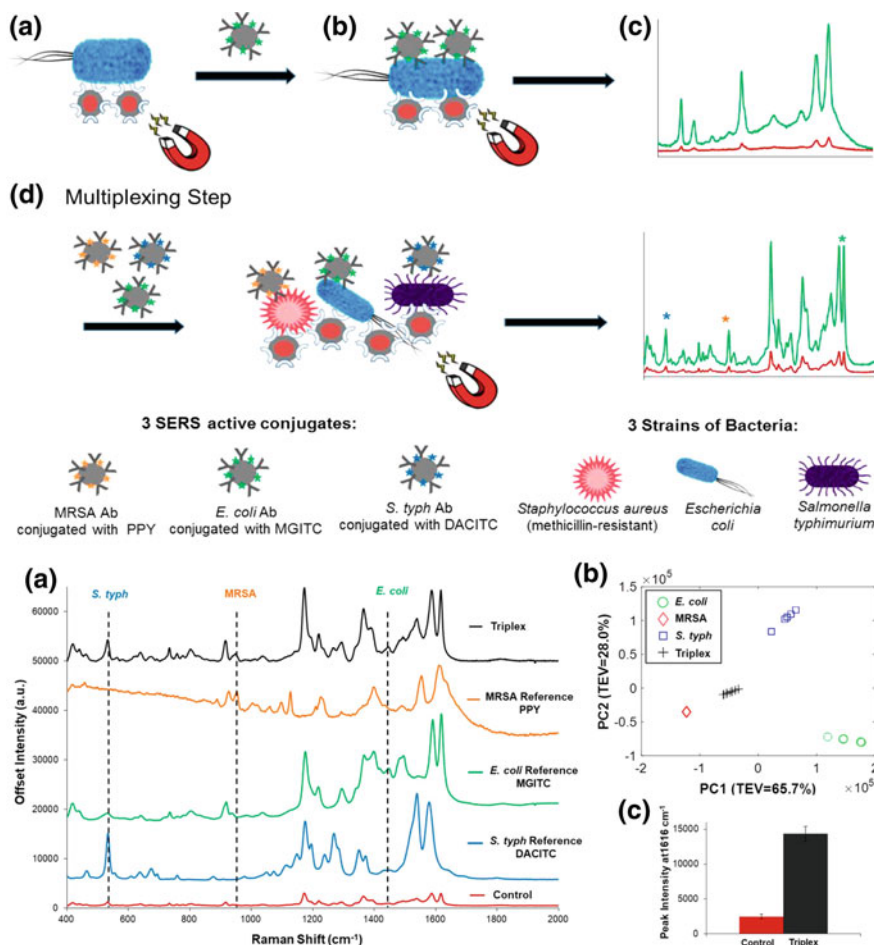
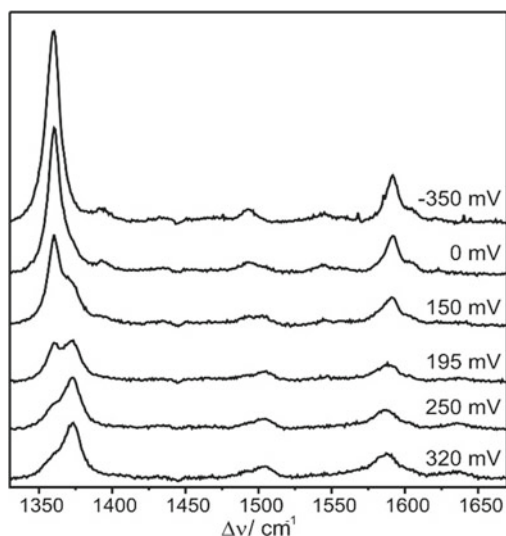


Fig. 4.5 Indirect detection of bacteria by SERS. Top panel, Schematic illustrating of indirect detection of bacteria via single and multiplex detection assays. **a** Functionalized magnetic NPs (Ag@MNPs) that bind to bacteria and the presence of the magnet allow for magnetic separation of the bacteria from the sample matrix. **b** SER active AgNPs, functionalized with a biorecognition molecule (Ab) and a unique SER reporter are added. The mixture is shaken, magnet applied, sample collected and the unbound mixture removed. **c** The sample is re-suspended in water and measured (green SER spectrum). When no target is present, the functionalized AgNPs are washed away, as they do not bind to bacteria, traces of signal is obtained (red SER spectrum). **d** Multiplexing detection of 3 bacterial pathogens: 3 types of AgNP are employed, each of which is functionalized with a different Raman reporter and an antibody (which is specific for a bacterial pathogen); each SER spectrum contains characteristic peaks from the specific Raman reporter. Bottom panel, SER spectra obtained from the detection of three bacterial pathogens simultaneously (black), each pathogen separately (blue, *S. typh*; green, *E. coli*; orange, MRSA) and a control sample (red). The vertical lines show peaks that are unique to each Raman reporter. **b** PCA scores plot showing the relationship between the multiplex spectra and each of the three single pathogen spectra. **c** Comparative peak intensities at 1616 cm^{-1} for assay and control. Reprinted with permission from Kearns et al. (2017). Copyright 2017 American Chemical Society

Fig. 4.6 Potential-dependent SERR spectra of mono-hemic subunit of *cbb3*-type HCO, immobilized on plasmonic SAM coated Ag electrodes and measured with 413 nm excitation, at indicated poised potentials. Adapted with permission from Todorovic et al. (2008). Copyright 2008 American Chemical Society



chemical methods, reveal thermodynamic and kinetic properties (i.e. E^0 , k_{ET}) of the immobilized protein. Namely, relative amounts of oxidized and reduced species present at each potential can be derived by deconvolution of SERR spectra and further used for construction of Nernst plot and determination of E^0 , Fig. 4.7; k_{ET} can be obtained from TR SERRS measurements (Murgida and Hildebrandt 2008). Importantly, unlike electrochemical methods, SERRS concomitantly probes the nature and structural features of the immobilized molecules, revealing whether they retained the native solution structure or underwent structural alterations upon immobilization. SERR spectro-electrochemistry has provided a wealth of information on biological ET, structural/functional properties of membrane heme proteins and immobilized enzymes that function as biocatalysts in bioelectronic devices (Todorovic et al. 2005, 2006, 2012; Murgida and Hildebrandt 2008; Sezer et al. 2010, 2012, 2013, 2015; Silveira et al. 2015, 2017; Molinas et al. 2011; Todorovic and Murgida 2016).

In particular, SERRS studies of cyt *c*, immobilized under different orientations and variable electric fields that the protein senses at electrode interface, highly contributed to our understanding of kinetics, dynamics and thermodynamics of heterogeneous ET (Murgida and Hildebrandt 2001, 2004, 2008). SERR spectro-electrochemistry provided novel insights into mechanistic features of complex membrane metalloenzymes (Todorovic et al. 2005, 2008, 2012; Sezer et al. 2010, 2015; Molinas et al. 2011; Silveira et al. 2015). Namely, these enzymes exert their functions under (i) restricted mobility, (ii) directionalized ET, (iii) effects of interfacial electric fields (i.e. membrane potential) and (iv) hydrophobic environment, which all can be mimicked in SERRS experiments. It is noteworthy that these conditions cannot be simultaneously reproduced by any other spectroscopic method. Moreover, the biocompatible metal electrode can play a role of artificial redox partner, supplying (or withdrawing) electrons required for the catalysis and/or carry co-immobilized natural redox partner

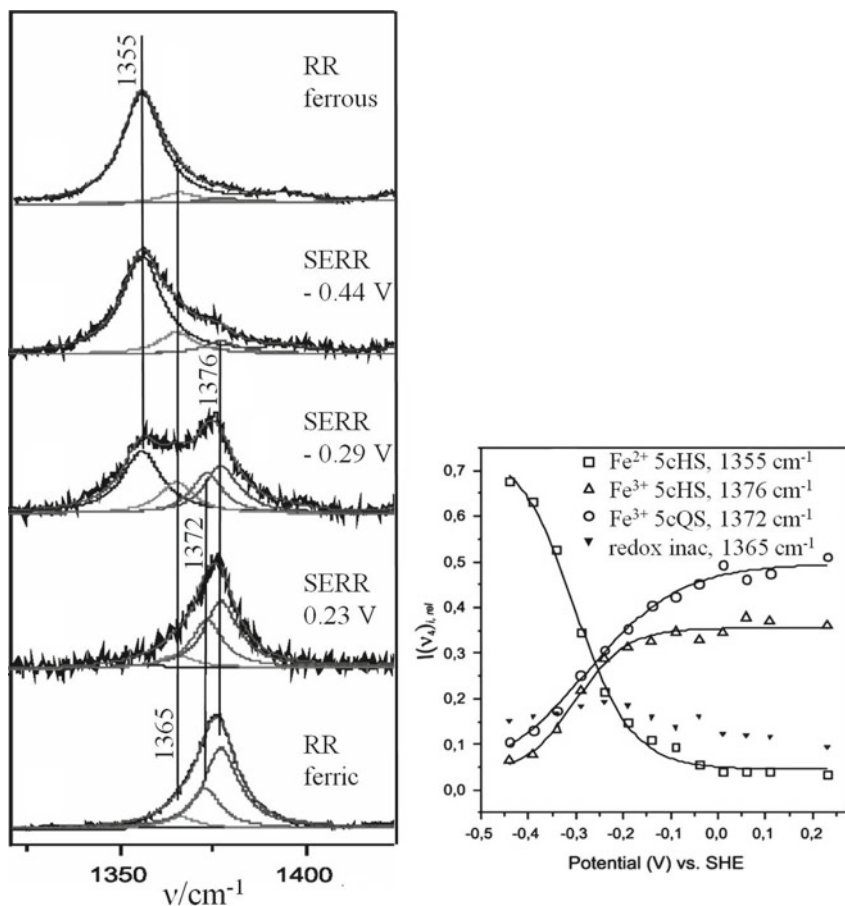


Fig. 4.7 RR and SERR spectra of DyP peroxidase and redox behaviour of the identified spin populations. Left, the ν_4 region of RR spectra of ferric (bottom) and ferrous (top) DyP in solution, and SERR spectra of DyP immobilized on SAM-coated Ag electrodes at indicated poised potentials. Experimental and overall simulated spectra are depicted together with the individual spin populations, 5cHS (ferric at 1376 cm^{-1} and ferrous at 1355 cm^{-1}), ferric 5cQS (1372 cm^{-1}), and the redox-inactive species (1365 cm^{-1}). Right, potential dependence of relative SERR contributions $[I(\nu_4)_{i,rel}]$ of different species as obtained from component analysis. Hollow squares: ferrous 5cHS, hollow triangles: ferric 5cHS and hollow circles: ferric 5cQS species; solid triangles: redox-inactive species. The solid lines are fits of sigmoid functions to the data. The respective output fit parameters: redox midpoint potential, E^0 , and number of transferred electrons. Reproduced from Sezer et al. (2012) with permission from The Royal Society of Chemistry

or substrate of the studied enzyme (Silveira et al. 2015). Under these conditions, structural and thermodynamic properties of HS and LS heme groups in multihemic membrane complexes, which typically have distinct roles in the complex, can be monitored independently via characteristic SERR bands. To that end, SERRS provided valuable insights into mechanistic properties of several HCOs and NiRs, disclosing e.g. the respective electron flow pathways in these enzymes (Todorovic et al. 2005, 2008, 2012; Molinas et al. 2011; Sezer et al. 2015; Silveira et al. 2015).

SERR spectro-electrochemistry is also a particularly powerful tool for investigations of redox metalloenzymes that are potentially interesting for development of biotechnological devices. Namely, wiring of metalloenzymes to conductive supports represents a crucial step in the construction of the 3rd generation (bio)catalytic and sensoric devices, which rely on DET between the immobilized enzyme and the electrode. The enzyme ensures high specificity for the targeted molecule (i.e. enzyme's substrate) and the electrode controllable electron source for the catalytic reaction (Todorovic and Murgida 2016). The critical point in the construction of these devices is the immobilization of the enzyme under preservation of its structural, thermodynamic and catalytic properties, and SERRS represent the only available method that can provide in situ information on these parameters, allowing for prediction of the enzyme efficiency in actual devices. It has been used to explore the potential of NiRs for the construction of electrochemical nitrite biosensors (Silveira et al. 2015), cellobiose dehydrogenase as anode catalyst in biofuel cells (Sezer et al. 2010), peroxidases and cyt *c*-derived micro and (pseudo)peroxidases for biosensing of H₂O₂ (Sezer et al. 2012, 2013; Capdevila et al. 2015b; Silveira et al. 2017), cytochromes P450 (P450) for biodegradation or bioelectrosynthesis of inert molecules (Todorovic et al. 2006), among other examples. P450 has been regarded as promising biocatalyst owing to important monooxygenation reactions that it catalyzes. However, its catalytic efficiency in solution could not be translated to immobilized state, which caused the failure of numerous trials to use this enzyme in biotechnological applications. SERRS provided insights into the origin of anomalous behavior of P450, demonstrating that upon immobilization it becomes converted into an inactive form, which has a very distinct (SE)RR fingerprint (Todorovic et al. 2006). The structural integrity of DyP peroxidases on the other hand could be preserved upon immobilization. A comparison of RR spectra of the protein in solution and SERR spectra of the immobilized protein revealed that no alterations occurred upon its attachment to modified electrodes, Fig. 4.7 (Sezer et al. 2012). The electrocatalytic activity in the presence of H₂O₂ and preservation of thermodynamic properties in the immobilized state, were nevertheless found to be case dependent, as DyPs from different sources behaved differently (Sezer et al. 2012, 2013). Some, but not all DyPs therefore represent promising candidates for the use in construction of biosensors for detection of H₂O₂ and/or biocatalysts for degradation of inert organic substrates.

The first SERR spectra of a non-hemic protein were reported only recently for a [4Fe-4S]²⁺ cluster containing DNA repair enzyme, endonuclease III. The enzyme was immobilized on electrodes coated with undamaged- and damaged-DNA terminated SAMs, the latter of which represents the enzymes' substrate. The nature of the redox active species was unambiguously identified for the first time, providing spec-

troscopically based evidence for establishment of a complete mechanistic model of DNA glycosylases (Moe et al. 2015).

4.3.4 Raman Imaging of Cells and Tissues

Raman imaging of organelles, cells and tissues is becoming a powerful alternative to commonly employed bio-imaging techniques (Abramczyk and Brozek-Pluska 2013; Palonpon et al. 2013; Iacono et al. 2014; Lee et al. 2014; Xiao et al. 2014; Harmsen et al. 2015; Kann et al. 2015; Chen et al. 2016; Noothalapati et al. 2016; Bodelon et al. 2017; Heraud et al. 2017; Lohumi et al. 2017; Manciu et al. 2017; Navas-Moreno et al. 2017). It does not require external labeling of molecules like fluorescence microscopy, and in some cases (e.g. TERS imaging, vide infra) can achieve much higher resolution. In analogy with detection of biomolecules, Raman imaging can be label-free or ‘direct’ (also known as chemical imaging); the images are in this case derived from Raman fingerprint spectra of the molecular constituents of the sample, thus providing simultaneous visualization of distribution e.g. lipids, proteins, nucleic acids, biological chromophores, etc. Alternatively, Raman imaging can be based on SERS. In this case, it employs functionalized NPs that carry Raman tags and capture groups; the image is reconstructed from the SER(R)S spectra of the tag, revealing the localization of the targeted molecules.

4.3.4.1 Label-Free or Chemical Imaging of Cells

Raman label-free or chemical imaging provides simultaneous spectral and spatial information about all Raman active chemical species in the sample (Heraud et al. 2017). The sample is screened through point-by-point acquisition of Raman spectra from a focal plane and the image is reconstructed from the spatial distribution of selected Raman band(s). In this manner identification of the specific chemical species can be achieved and their distribution/localization can be visualized as a 2D map or 3D image. The spatial resolution is diffraction limited to 200–500 nm for the most commonly used lasers in Raman biospectroscopy. The images can be constructed directly from Raman bands, or from features derived by spectral processing, analogous to that described in RS identification of biomolecules (vide supra).

Raman chemical imaging has been emerging as a valuable tool in medicine and bio-sciences. The label-free cellular imaging can provide information on sample composition and localization of molecules of interest, and, furthermore, on dynamic processes that account for biochemical changes in the samples, which are e.g. drug-induced, indicative of pathologies, etc. Chemical imaging can provide visualization of differences between tumor cells and healthy tissue, offering a possibility of faster diagnosis of tumors than histopathology, without a necessity for tissue sectioning or staining; this is particularly relevant for determining tumor margins during cancer surgery (Kong et al. 2013). Raman imaging has been successful in detection of brain,

breast and lung cancer, and bone and skin diseases, among other pathologies (Kong et al. 2013, 2015; Manciu et al. 2017).

Label-free Raman imaging was employed to disclose the distribution of glucans, lipids and proteins in yeast cells and spores, based on images derived from representative Raman bands, Fig. 4.8. Furthermore, it could successfully discriminate between structurally similar cell wall components, like α - and β -glucans (Noothalapati et al. 2016). Importantly, chemical imaging can also probe distribution of small molecules which cannot be labeled or visualized by other imaging approaches; such an example is DPA, which plays a crucial role in spore germination. Raman chemical imaging also provided important fundamental insights into plant cells, contributing to our understanding of the distribution of polysaccharides, lignin and cellulose and in situ detection of carotenoids. It is paving the way to become a routine tool for fruit quality control (Lohumi et al. 2017).

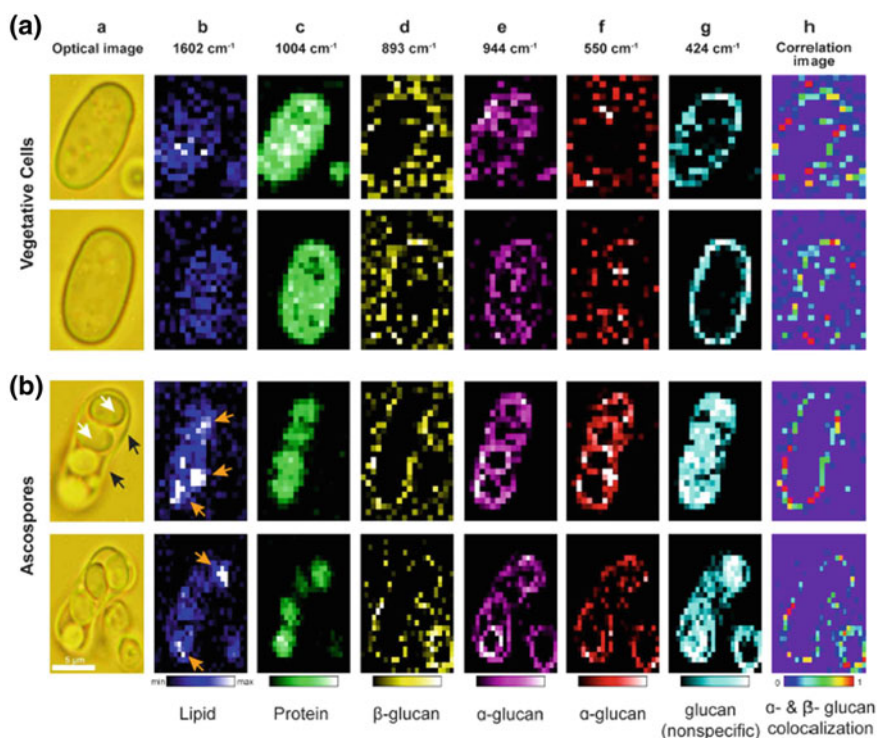


Fig. 4.8 Raman imaging of *Schizosaccharomyces pombe* vegetative cells (A) and spores (B). **a** Bright field optical images. Scale bar measures 5 μ m; white arrows indicate spores and black arrows indicate ascus wall. **(b–f)** Raman images constructed for **b** lipids using 1602 cm⁻¹ (arrows indicate lipid accumulation), **c** proteins using 1004 cm⁻¹, **d** β -glucans using 893 cm⁻¹, **e** α -glucans using 944 cm⁻¹ and **f** 550 cm⁻¹ and **g** both glucan anomers using skeletal vibrations at 424 cm⁻¹. **h** Correlation images based on **d** and **e** showing co-localization of α - and β -glucans only in the spore containing sac (ascus). Reproduced from Noothalapati et al. (2016) licensed under CC BY 4.0

The main obstacles that impede wider applications of label-free Raman imaging are related to interference of fluorescence, commonly present in biological samples, and low intensity of Raman signal. The former can often be avoided by the use of laser wavelength which does not excite fluorescence. The latter can be overcome by higher laser powers and/or longer accumulation times, which nevertheless have to be set as a compromise between the laser and signal intensity in order to avoid possible laser induced damage of the sample.

4.3.4.2 SER-Based Imaging of Cells

The sensitivity and selectivity of Raman imaging can be improved by using functionalized NPs for surface enhancement of the signal and molecular recognition of the target species (Schlucker 2009). SER imaging employing NPs can reveal details on the sub-cellular and higher level structures. It can be used for discrimination of bacterial cells, cancer cells and for in vivo applications (Zavaleta et al. 2009; Abramczyk and Brozek-Pluska 2013; Kang et al. 2015; Chen et al. 2016; Bodelon et al. 2017).

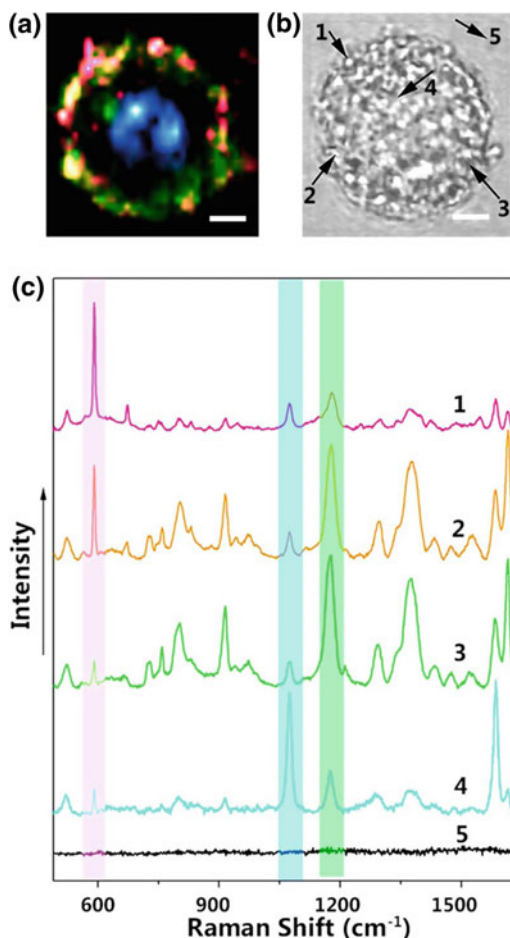
In analogy with indirect SER(R)S detection of biomolecules (*vide supra*), NPs for indirect SER-based imaging are decorated with Raman tags and recognition groups and often with other functionalities (Schlucker 2009, 2014; Guerrini and Graham 2012). Due to the presence of the capture group, NPs selectively interact with the targeted molecules in the sample. This specific interaction is most commonly achieved via DNA hybridization of complementary sequence or antibody–antigen recognition (Harmsen et al. 2015). The signal of the Raman tag is then measured across the sample area and the image is reconstructed from its spatial distribution. However, as stated for the indirect detection (*vide supra*), the chemical nature of the target has to be pre-defined by the choice of recognition moiety, while the structural information, which can be achieved by label free imaging, is in this case lost.

This method is nevertheless highly versatile and specific, owing to the high level of sophistication that can be achieved in the design of NPs (Lane et al. 2015a; Reguera et al. 2017). NPs can simultaneously carry multiple functionalities, like cell penetrating peptides, mitochondria or nucleus targeting peptides, in addition to Raman tags and antibodies for antigen recognition, which allows for targeting of distinct organelles in the cellular environment (Kang et al. 2015). This approach was successfully applied to discriminate between human oral cancer HCS-3 and HeLa cells (Chen et al. 2016). As depicted in Fig. 4.9, different Raman dyes are used to decorate membrane and nucleus targeting NPs, providing visualization of both.

However, NP internalization and trafficking by cells may pose some restrictions on their use in live-cell imaging applications, as demonstrated for NPs targeting breast cancer cell surface biomarkers (Navas-Moreno et al. 2017). To that end, active research efforts have been dedicated to understanding cytotoxicity and long-term fate of NPs in complex physiological environments, which will ultimately decide the perspectives of NP based SER imaging for in vivo clinical applications (Lane et al. 2015b).

Fig. 4.9 Multi-targeting SER imaging of a HeLa cell treated with crystal violet acetate (CVa), crystal violet (CV), and 4-mercaptobenzoic acid (MBA) dye coated NPs.

a Overlap of SER images of CVa- (red) and CV-coated NPs (green), which are membrane targeting, and MBA-coated NPs (blue), which are nucleus targeting. **b** The bright-field image of the investigated HeLa cell. **c** SER spectra obtained from different positions in the cell (marked in panel B by arrows). The Raman intensities at 595, 1078, and 1175 cm^{-1} revealed the relative amount of CVa-coated, MBA-coated and CV-coated NPs at the corresponding positions, respectively (scale bar, 4 μm). Reproduced from Chen et al. (2016) licensed under CC BY 4.0



4.3.4.3 TERS Imaging of Cells

TERS takes advantage of the near-field enhancement generated by laser excitation of surface plasmons, resulting in a strong electromagnetic field centered at the laser-irradiated apex of metal AFM tip (Schmid et al. 2013). It can provide molecular information of the sample at the nanoscale, offering a unique way to characterize and visualize the sample through spectra or images reconstructed from the spectra. TERS chemical images of a sample surface thus couple morphological and chemical information provided by AFM and Raman techniques. TERS can achieve an exceptionally high spatial resolution of the image, which is by far beyond Abbe's diffraction limit that restricts resolution to $\sim\lambda/2$ in Raman imaging. In the case of TERS tip apex modified with NP, resolution can even reach values below 10 nm (Lipiec et al. 2014).

Although still somewhat challenging in the case of biological samples, TERS is capable of successfully combining topographic and spectroscopic information on e.g. DNA/RNA (Najjar et al. 2014), proteins (Yeo et al. 2008), lipids (Opilik et al. 2011), cell membranes and walls, mitochondria, bacteria, viruses, and even weakly scattering small biological molecules (Pahlow et al. 2012). TER spectra are typically measured, and TERS images or maps are therefore reconstructed, from a defined area of interest of the sample, which is selected from the AFM image. This is demonstrated in Fig. 4.10 for a single spore. In this case the TERS maps were constructed from the intensity of the Tyr (830 cm^{-1}) / protein (1570 cm^{-1}) and glycans/carbohydrates (930 cm^{-1}) bands, providing a visualization of their distribution at the selected area of the spore surface (Rusciano et al. 2014).

It is noteworthy that, side by side with imaging, the superior sensitivity and ultra-high resolution of TERS, make it a powerful spectroscopic tool. On that note, TER spectra have revealed molecular information on the level of a single nucleotide, allowing for label-free sequencing, monitoring of DNA hybridization and detecting

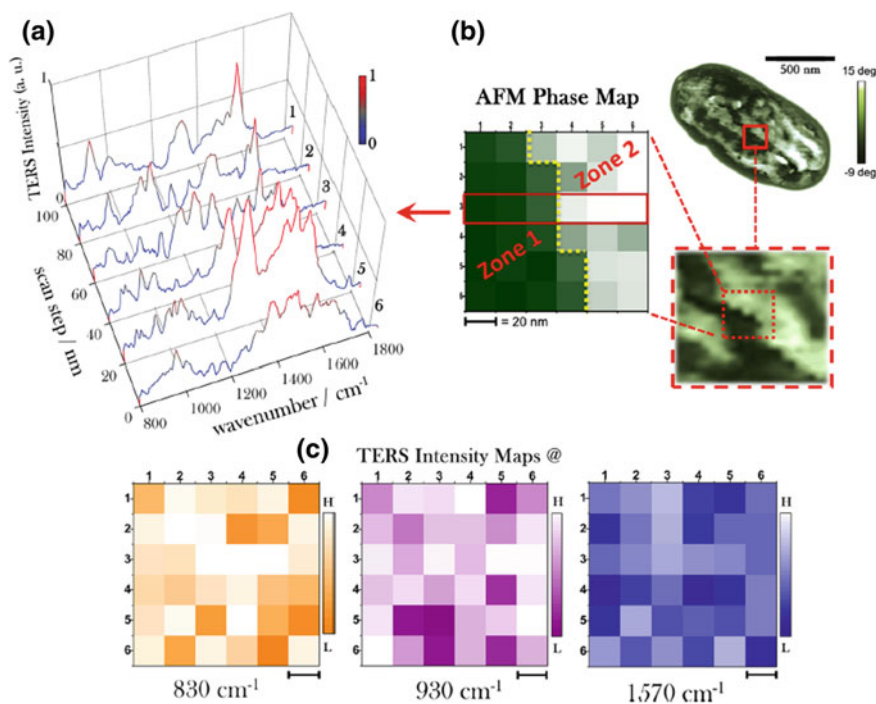


Fig. 4.10 TER spectra and maps of *Bacillus subtilis* spore ridge. **a** The spectra are acquired with 20 nm step along the horizontal line highlighted by the red rectangle in the phase map zoom of panel **(b)**. **b** AFM phase map and detailed zoom of a selected spore region across a spore ridge. **c** TERS maps were obtained from the intensity of Raman peaks at 830 cm^{-1} (Tyr), 930 cm^{-1} (glycans/carbohydrates), and 1570 cm^{-1} (proteins). Scale bar = 20 nm. Reprinted with permission from Rusciano et al. (2014). Copyright 2014 American Chemical Society

of DNA damages (Lipiec et al. 2014). It was possible employing resonance Raman conditions (therefore TERRS) to discriminate between HS and LS cyt *c* in ferric and ferrous states, and disclose the spatial distribution of different subpopulations across the mitochondrion (Bohme et al. 2011). Furthermore, it was demonstrated that TERS can be considered as a highly promising approach for quick and label free identification of pathogens. Due to distinct surface composition, single bacterial cells and virus particles could be easily discriminated based on their TERS spectral features (Olschewski et al. 2015).

4.4 Outlook

Raman spectroscopy has experienced a ‘quantum jump’ upon invention and appearance of affordable lasers in the second half of the last century. The following big events that gave a head start to Raman-based applications were the discovery of SER(R)S almost four decades ago and the first demonstration of TER effect, accomplished in 2000. Ever since, the progress in the development of diverse applications of Raman spectroscopies has been exponential, particularly in biological, biophysical and biomedical fields. One can highlight the progress in SER-based bionanosensing and imaging, which take advantage of the continuously improving design of plasmonic substrates. It envisages production of sensitive and reproducible SE(R)RS substrates with better enhancement properties, stability and specificity, and smart stimuli responsive NPs for reliable *in vivo* applications as the ultimate goal. In parallel, exploiting of alternative materials as efficient plasmonic substrates for UV–SE(R)RS, such as metals (e.g. Al, Rh, Ga, In, Sn and Ru) (McMahon et al. 2013), metal oxides and graphene (Ling et al. 2010; Li et al. 2012), may offer new possibilities particularly for biophysical and bioanalytical applications. Similarly, advances in design and fabrication of high quality TERS tips will govern further optimization of the technique, which is necessary for reliable studies of liquid and soft biological samples. Other frontlines include biomedical applications, such as development of new technical and methodological solutions, like handheld spectroscopic devices for intraoperative cancer detection, or SESORS (Stone et al. 2011) and TRS (Ghita et al. 2018) (Surface-Enhanced Spatially Offset Raman Spectroscopy and Transmission Raman Spectroscopy, respectively) for improvement of tissue penetration depth limits of Raman signals and chemical specific detection within a large sampling volume. Taken together, although nowadays indispensable in fundamental biosciences and applied bioanalysis, Raman scattering techniques await bigger protagonism outside research labs, among non-spectroscopists and clinicians as users.

Acknowledgements This work was financially supported by: Project LISBOA-01-0145-FEDER-007660 (Microbiologia Molecular, Estrutural e Celular) funded by FEDER funds through COMPETE2020 - Programa Operacional Competitividade e Internacionalização (POCI) and by national funds through FCT - Fundação para a Ciência e a Tecnologia, FCT grant PTDC/BTM-SAL/29507/2017 awarded to S.T., and European Union’s Horizon 2020 research and innovation programme under grant agreement No 810856.

References

- Abramczyk H, Brozek-Pluska B (2013) Raman imaging in biochemical and biomedical applications. Diagnosis and treatment of breast cancer. *Chem Rev* 113:5766–5781
- Alexander TA, Le DM (2007) Characterization of a commercialized SERS-active substrate and its application to the identification of intact *Bacillus* endospores. *Appl Opt* 46:3878–3890
- Ashton L, Hogwood CEM, Tait AS et al (2015) UV resonance Raman spectroscopy: a process analytical tool for host cell DNA and RNA dynamics in mammalian cell lines. *J Chem Technol Biotechnol* 90:237–243
- Bailo E, Deckert V (2008) Tip enhanced Raman scattering. *Chem Soc Rev* 37:921–930
- Barrett L, Dougan JA, Faulds K et al (2011) Stable dye-labelled oligonucleotide-nanoparticle conjugates for nucleic acid detection. *Nanoscale* 3:3221–3227
- Benecky M, Li TJ, Schmidt J et al (1997) Resonance Raman study of flavins and the flavoprotein fatty acyl coenzyme A dehydrogenase. *Biochemistry* 18:3471–3476
- Benevides JM, Overman SA, Thomas G Jr (2005) Raman, polarized Raman and ultraviolet resonance Raman spectroscopy of nucleic acids and their complexes. *J Raman Spectrosc* 36:279–299
- Bodelon G, Montes-Garcia V, Costas C et al (2017) Imaging bacterial interspecies chemical interactions by surface-enhanced Raman scattering. *ACS Nano* 11:4631–4640
- Bohme R, Mkandawire M, Krause-Buchholz U et al (2011) Characterizing cytochrome *c* states—TERS studies of whole mitochondria. *Chem Comm* 47:11453–11455
- Capdevila DA, Marmisolle WA, Tomasina F et al (2015a) Specific methionine oxidation of cytochrome *c* in complexes with zwitterionic lipids by hydrogen peroxide: potential implications for apoptosis. *Chem Sci* 6:705–713
- Capdevila DA, Oviedo Rouco S, Tomasina F et al (2015b) Active site structure and peroxidase activity of oxidatively modified cytochrome *c* species in complexes with cardiolipin. *Biochemistry* 54:7491–7504
- Catarino T, Pessanha M, de Candia A et al (2010) Probing the chemotaxis periplasmic sensor domains from *Geobacter sulfurreducens* by combined resonance Raman and molecular dynamic approaches: NO and CO sensing. *J Phys Chem B* 114:11251–11260
- Chen Z, Durao P, Silva CS et al (2010) The role of Glu498 in the dioxygen reactivity of CotA-laccase from *Bacillus subtilis*. *Dalton Trans* 39:2875–2882
- Chen Y, Bai X, Su L et al (2016) Combined labeled and label-free SERS probes for triplex three-dimensional cellular imaging. *Sci Rep*. <https://doi.org/10.1038/srep19173>
- Cialla D, Pollok S, Steinbrucker C et al (2014) SERS-based detection of biomolecules. *Nanophot* 3:383–411
- Cialla-May D, Zheng XS, Weber K et al (2017) Recent progress in surface-enhanced Raman spectroscopy for biological and biomedical applications: from cells to clinics. *Chem Soc Rev* 46:3945–3961
- Craig AP, Franca AS, Irudayaraj J (2013) Surface-enhanced Raman spectroscopy applied to food safety. *Annu Rev Food Sci Technol* 4:369–380
- Deckert-Gaudig T, Bohme R, Freier E et al (2012) Nanoscale distinction of membrane patches: a TERS study of *Halobacterium salinarum*. *J Biophoton* 5:582–591
- Egawa T, Yeh S-R (2005) Structural and functional properties of hemoglobins from unicellular organisms as revealed by resonance Raman spectroscopy. *J Inorg Biochem* 99:72–96
- Ember KJJ, Hoeve MA, McAughtrie S et al (2017) Raman spectroscopy and regenerative medicine: a review. *Npj Regener Med*. <https://doi.org/10.1038/s41536-017-0014-3>
- Frost J, Ludeman L, Hillaby K et al (2017) Raman spectroscopy and multivariate analysis for the non-invasive diagnosis of clinically inconclusive vulval lichen sclerosus. *Analyst* 142:1200–1206
- Gall A, Pascal AA, Robert B (2015) Vibrational techniques applied to photosynthesis: resonance Raman and fluorescence line-narrowing. *Biochim Biophys Acta (BBA)* 1847:12–18
- Gennis RB (1989) *Biomembranes: molecular structure and function*. Springer, New York

- Ghita A, Matousek P, Stone N (2018) High sensitivity non-invasive detection of calcifications deep inside biological tissue using transmission Raman spectroscopy. *J Biophoton*. <https://doi.org/10.1002/jbio.201600260>
- Guerrini L, Graham D (2012) Molecularly-mediated assemblies of plasmonic nanoparticles for surface-enhanced Raman spectroscopy applications. *Chem Soc Rev* 41:7085–7107
- Guerrini L, Krpetic Z, van Lierop D et al (2015) Direct surface-enhanced Raman scattering analysis of DNA duplexes. *Angew Chem Int Ed* 54:1144–1148
- Handen JD, Lednev IK (2016) Deep UV resonance Raman spectroscopy for characterizing amyloid aggregation. In: Eliezer D (ed) *Protein amyloid aggregation*. Methods in molecular biology, vol 1345. Humana Press, New York
- Harmsen S, Huang R, Wall MA et al (2015) Surface-enhanced resonance Raman scattering nanostars for high-precision cancer imaging. *Sci Transl Med*. <https://doi.org/10.1126/scitranslmed.3010633>
- Heraud P, Marzec KM, Zhang Q-H et al (2017) Label-free in vivo Raman microspectroscopic imaging of the macromolecular architecture of oocytes. *Scientific Rep*. <https://doi.org/10.1038/s41598-017-08973-0>
- Hobro A, Kumagai Y, Akira S et al (2016) Raman spectroscopy as a tool for label-free lymphocyte cell line discrimination. *Analyst* 141:3756–3764
- Honarmand Ebrahimi K, Silveira CM, Todorovic S (2018) Evidence for the synthesis of an unusual high spin ($S = 7/2$) [Cu–3Fe–4S] cluster in the radical-SAM enzyme RSAD2 (viperin). *Chem Comm* 54:8614–8617
- Huang JY, Zong C, Xu LJ et al (2011) Clean and modified substrates for direct detection of living cells by surface-enhanced Raman spectroscopy. *Chem Commun* 47:5738–5740
- Iacono P, Karabeber H, Kircher MF (2014) All-in-one nanoparticle coating for multiplexed SE(R)RS biomedical imaging. *Angew Chem Int Ed* 53:11756–11761
- Iping Petterson IP, Stone N, Day JD et al (2016) Developing fibre optic Raman probes for applications in clinical spectroscopy. *Chem Soc Rev* 45:1919–1934
- Jakubek RS, Handen JD, White SE et al (2018) Ultraviolet resonance Raman spectroscopic markers for protein structure and dynamics. *Trends Anal Chem* 103:223–229
- Johnson DC, Dean DR, Smith AD et al (2005) Structure, function, and formation of biological iron-sulfur clusters. *Annu Rev Biochem* 74:274–281
- Kadam US, Schulz B, Irudayaraj J (2014) Detection and quantification of alternative splice sites in Arabidopsis genes AtDCL2 and AtPTB2 with highly sensitive surface enhanced Raman spectroscopy (SERS) and gold nanoprobe. *FEBS Lett* 588:1637–1643
- Kang JW, So PTC, Dasari RR et al (2015) High resolution live cell Raman imaging using subcellular organelle-targeting SERS-sensitive gold nanoparticles with highly narrow intra-nanogap. *Nano Lett* 15:1766–1772
- Kann B, Offerhaus HL, Windbergs M et al (2015) Raman microscopy for cellular investigations: from single cell imaging to drug carrier uptake visualization. *Adv Drug Del Rev* 89:71–90
- Kearns H, Goodacre R, Jamieson LE et al (2017) SERS detection of multiple antimicrobial-resistant pathogens using nanosensors. *Anal Chem* 89:12666–12673
- Kong K, Rowlands CJ, Varma S et al (2013) Diagnosis of tumors during tissue-conserving surgery with integrated autofluorescence and Raman scattering microscopy. *Proc Natl Acad Sci USA* 110:15189–15194
- Kong K, Kendall C, Stone N et al (2015) Raman spectroscopy for medical diagnostics, from *in-vitro* biofluid assays to *in-vivo* cancer detection. *Adv Drug Del Rev* 89:121–134
- Kranich A, Ly HK, Hildebrandt P et al (2008) Direct observation of the gating step in protein electron transfer: electric-field-controlled protein dynamics. *J Am Chem Soc* 130:9844–9848
- Lane LA, Qian X, Nie S (2015a) SERS Nanoparticles in medicine: from label-free detection to spectroscopic tagging. *Chem Rev* 115:10489–10529
- Lane LA, Qian X, Smith A et al (2015b) Physical chemistry of nanomedicine: understanding the complex behaviors of nanoparticles in vivo. *Annu Rev Phys Chem* 66:521–547
- Lee S, Chon H, Lee J et al (2014) Rapid and sensitive phenotypic marker detection of breast cancer cells using surface-enhanced Raman scattering (SERS) imaging. *Biosens Bioelectron* 51:238–243

- Li L, Hutter T, Finnemore ASS et al (2012) Metal oxide nanoparticle mediated enhanced Raman scattering and its use in direct monitoring of interfacial chemical reactions. *Nano Lett* 12:4242–4246
- Ling X, Xie L, Fang Y et al (2010) Can graphene be used as a substrate for Raman enhancement? *Nano Lett* 10:553–561
- Lipiec E, Sekine R, Bielecki J et al (2014) Molecular characterization of DNA double strand breaks with tip-enhanced Raman scattering. *Angew Chem Int Ed* 53:169–172
- Lohumi S, Kim MS, Qin J et al (2017) Raman imaging from microscopy to macroscopy: quality and safety control of biological materials. *Trends Anal Chem* 93:183–198
- Manciu FS, Ciubuc JD, Parra K et al (2017) Label-free Raman imaging to monitor breast tumor signatures. *Tech Cancer Res Treat* 16:461–469
- Martins G, Rodrigues L, Cunha FM et al (2010) Substrate binding to a nitrite reductase induces a spin transition. *J Phys Chem B* 114:5563–5566
- Matousek P, Stone N (2016) Development of deep subsurface Raman spectroscopy for medical diagnosis and disease monitoring. *Chem Soc Rev* 45:1794–1802
- McMahon JM, Schatz GC, Gray SK (2013) Plasmonics in the ultraviolet with the poor metals Al, Ga, In, Sn, Tl, Pb and Bi. *Phys Chem Chem Phys* 15:5415–5423
- Moe E, Sezer M, Hildebrandt P et al (2015) Surface enhanced vibrational spectroscopic evidence for an alternative DNA-independent redox activation of endonuclease III. *Chem Comm* 51:3255–327
- Mohs AM, Mancini MC, Singhal S et al (2010) Hand-held spectroscopic device for in vivo and intraoperative tumor detection: contrast enhancement, detection sensitivity, and tissue penetration. *Anal Chem* 82:9058–9065
- Molinas MF, de Candia A, Szajman SH et al (2011) Electron transfer dynamics of *Rhodothermus marinus caa3* cytochrome *c* domains on biomimetic films. *Phys Chem Chem Phys* 13:18088–18098
- Murgida DH, Hildebrandt P (2001) Active-site structure and dynamics of cytochrome *c* immobilized on self-assembled monolayers: a time-resolved surface enhanced resonance Raman spectroscopic study. *Angew Chem Int Ed* 40:728–731
- Murgida DH, Hildebrandt P (2004) Electron-transfer processes of cytochrome *c* at interfaces. New insights by surface-enhanced resonance Raman spectroscopy. *Acc Chem Res* 37:854–861
- Murgida DH, Hildebrandt P (2008) Disentangling interfacial redox processes of proteins by SERR spectroscopy. *Chem Soc Rev* 37:937–945
- Najjar S, Talaga D, Schu L et al (2014) Tip-enhanced Raman spectroscopy of combed double-stranded DNA bundles. *J Phys Chem C* 118:1174–1181
- Navas-Moreno M, Mehrpouyan M, Chernenko T et al (2017) Nanoparticles for live cell microscopy: a surface-enhanced Raman scattering perspective. *Sci Rep.* <https://doi.org/10.1038/s41598-017-04066-0>
- Ngo HT, Wang HN, Burke T et al (2014) Multiplex detection of disease biomarkers using SERS molecular sentinel-on-chip. *Anal Bioanal Chem* 406:3335–3344
- Niaura G (2014) Raman spectroscopy in analysis of biomolecules. In: *Encyclopedia of analytical chemistry*, Online. Wiley, pp 1–34
- Noothalapati H, Sasaki T, Kaino T et al (2016) Label-free chemical imaging of fungal spore walls by Raman microscopy and multivariate curve resolution analysis. *Sci Rep.* <https://doi.org/10.1038/srep27789>
- Nottinger I, Verrier S, Romanska H et al (2002) *In situ* characterisation of living cells by Raman spectroscopy. *Spectroscopy* 16:43–51
- Oladepo SA, Xiong K, Hong Z et al (2012) UV resonance Raman investigations of peptide and protein structure and dynamics. *Chem Rev* 112:2604–2628
- Old OJ, Fullwood LM, Scott R et al (2014) Vibrational spectroscopy for cancer diagnostics. *Anal Meth* 6:3901–3917
- Olschewski K, Kammer E, Stockel S et al (2015) A manual and an automatic TERS based virus discrimination. *Nanoscale* 7:4545–4552

- Opilik L, Bauer T, Schmid T et al (2011) Nanoscale chemical imaging of segregated lipid domains using tip-enhanced Raman spectroscopy. *Phys Chem Chem Phys* 13:9978–9981
- Pahlow S, Marz A, Seise B et al (2012) Bioanalytical application of surface- and tip-enhanced Raman spectroscopy. *Eng Life Sci* 12:131–143
- Pahlow S, Meisel S, Cialla-May D et al (2015) Isolation and identification of bacteria by means of Raman spectroscopy. *Adv Drug Del Rev* 89:105–120
- Palonpon AF, Ando J, Yamakoshi H et al (2013) Raman and SERS microscopy for molecular imaging of live cells. *Nat Prot* 8:677–692
- Proshlyakov DA, Pressler MA, Babcock GT (1998) Dioxygen activation and bond cleavage by mixed-valence cytochrome *c* oxidase. *Proc Natl Acad Sci USA* 95:8020–8025
- Qian X, Nie S (2008) Single-molecule and single-nanoparticle SERS: from fundamental mechanisms to biomedical applications. *Chem Soc Rev* 37:912–920
- Raman CV, Krishnan KS (1928) A new type of secondary radiation. *Nature* 121:501–502
- Reguera J, Langer JD, Jimenez de Aberasturi D et al (2017) Anisotropic metal nanoparticles for surface enhanced Raman scattering. *Chem Soc Rev* 46:3866–3885
- Rousseau DL, Han S (2002) Time-resolved resonance Raman spectroscopy of intermediates in cytochrome *c* oxidase. In: *Methods in enzymology*, vol 354. Elsevier Science, pp 351–368
- Rusciano G, Zito G, Isticato R et al (2014) Nanoscale chemical imaging of *Bacillus subtilis* spores by combining tip-enhanced Raman scattering and advanced statistical tools. *ACS Nano* 8:12300–12309
- Rygula A, Majzner K, Marzec KM et al (2013) Raman spectroscopy of proteins: a review. *J Raman Spectrosc* 44:1061–1076
- Schlucker S (2009) SERS microscopy: nanoparticle probes and biomedical applications. *Chem Phys Chem* 10:1344–1354
- Schlucker S (2014) Surface-enhanced Raman spectroscopy: concepts and chemical applications. *Angew Chem Int Ed* 53:4756–4795
- Schmid T, Opilik L, Blum C et al (2013) Nanoscale chemical imaging using tip-enhanced Raman spectroscopy: a critical review. *Angew Chem Int Ed* 52:5940–5954
- Sezer M, Spricigo R, Utesch T et al (2010) Redox properties and catalytic activity of surface-bound human sulfite oxidase studied by a combined surface enhanced resonance Raman spectroscopic and electrochemical approach. *Phys Chem Chem Phys* 12:7894–7903
- Sezer M, Genebra T, Mendes S et al (2012) A DyP-type peroxidase at a bio-compatible interface: structural and mechanistic insights. *Soft Matter* 8:10314–10321
- Sezer M, Santos A, Kielb P et al (2013) Distinct structural and redox properties of the heme active site in bacterial dye decolorizing peroxidase-type peroxidases from two subfamilies: resonance Raman and electrochemical study. *Biochemistry* 52:3074–3084
- Sezer M, Kielb P, Kuhlmann U et al (2015) Surface enhanced resonance Raman spectroscopy reveals potential induced redox and conformational changes of cytochrome *c* oxidase on electrodes. *J Phys Chem B* 119:9586–9591
- Short KW, Carpenter S, Freyer JP et al (2005) Raman spectroscopy detects biochemical changes due to proliferation in mammalian cell cultures. *Biophys J* 88:4274–4288
- Siebert F, Hildebrandt P (2008) *Vibrational spectroscopy in life science*. Wiley VCH, Weinheim
- Silveira CM, Quintas PO, Moura I et al (2015) SERR spectroelectrochemical study of cytochrome *cd₁* nitrite reductase co-immobilized with physiological redox partner cytochrome *c₅₅₂* on bio-compatible metal electrodes. *PlosOne*. <https://doi.org/10.1371/journal.pone.0129940>
- Silveira CM, Castro MA, Damas JM et al (2017) Structure, electrocatalysis and dynamics of immobilized cytochrome PccH and its microperoxidase. *Phys Chem Chem Phys* 19:8908–8918
- Smulevich G, Feis A, Howes BD (2005) Fifteen years of Raman spectroscopy of engineered heme containing peroxidases: what have we learned? *Acc Chem Res* 38:433–440
- Spiro TG, Li X-Y (1988) Resonance Raman spectroscopy of metalloproteins. In: Spiro TG (ed) *Biological applications of Raman spectroscopy*, vol 3. Wiley, New York, pp 1–95
- Stevenson R, Ingram A, Leung H et al (2009) Quantitative SERRS immunoassay for the detection of human PSA. *Analyst* 134:842–844

- Stockel S, Kirchhoff J, Neugebauer UJ et al (2016) The application of Raman spectroscopy for the detection and identification of microorganisms. *J Raman Spectrosc* 47:89–109
- Stockel S, Meisel S, Lorenz B et al (2017) Raman spectroscopic identification of *Mycobacterium tuberculosis*. *J Photonics* 10:727–734
- Stokes R, Dougan J, Graham D (2008) Dip-pen nanolithography and SERRS as synergic techniques. *Chem Commun* 5734–5736
- Stone N, Kerssens M, Lloyd GR et al (2011) Surface enhanced spatially offset Raman spectroscopic (SESORS) imaging—the next dimension. *Chem Sci* 2:776–780
- Todorovic S, Murgida DH (2016) Surface-enhanced Raman scattering of biological materials. In: *Encyclopedia of analytical chemistry*, online. Wiley, pp 1–29
- Todorovic S, Teixeira M (2018) Resonance Raman spectroscopy of Fe–S proteins and their redox properties. *J Biol Inorg Chem* 23:647–661
- Todorovic S, Pereira MM, Bandejas TM et al (2005) Midpoint potentials of hemes a and a_3 in the quinol oxidase from *Acidianus ambivalens* are inverted. *J Am Chem Soc* 127:13561–13566
- Todorovic S, Jung C, Hildebrandt P et al (2006) Conformational transitions and redox potential shifts of cytochrome P450 induced by immobilization. *J Biol Inorg Chem* 11:119–127
- Todorovic S, Verissimo A, Wisitruangsakul et al (2008) SERR-spectroelectrochemical study of a cbb3 oxygen reductase in a biomimetic construct. *J Phys Chem B* 112:16952–16959
- Todorovic S, Rodrigues ML, Matos D et al (2012) Redox properties of lysine- and methionine-coordinated hemes ensure downhill electron transfer in NrfH₂A₄ nitrite reductase. *J Phys Chem B* 116:5637–5643
- Todorovic S, Hildebrandt P, Martins LO (2015) Surface enhanced resonance Raman detection of a catalytic intermediate of DyP-type peroxidase. *Phys Chem Chem Phys* 17:11954–11957
- Tschirner N, Schenderlein M, Brose K et al (2009) Resonance Raman spectra of beta-carotene in solution and in photosystems revisited: an experimental and theoretical study. *Phys Chem Chem Phys* 11:11471–11478
- Velazquez Escobar F, Piwowarski P, Salewski J et al (2015) A protonation-coupled feedback mechanism controls the signaling process in bathy phytochromes. *Nat Chem* 7:423–430
- Verma P (2016) Tip-enhanced Raman spectroscopy: technique and recent advances. *Chem Soc Rev* 117:6447–6466
- Vo-Dinh T, Liu Y, Fales AM et al (2015) SERS nanosensors and nanoreporters: golden opportunities in biomedical applications. *WIREs Nanomed Nanobiotechnol* 7:17–33
- von Stetten D, Gunther M, Scheerer P et al (2008) Chromophore heterogeneity and photoconversion in phytochrome crystals and solution studied by resonance Raman spectroscopy. *Angew Chem Int Ed* 47:4753–4755
- Wang Y, Ravindranath S, Irudayaraj J (2010) Separation and detection of multiple pathogens in a food matrix by magnetic SERS nanoprobe. *Anal Bioanal Chem* 399:1271–1278
- Xiao L, Harihar S, Welch DR et al (2014) Imaging of epidermal growth factor receptor on single breast cancer cells using surface-enhanced Raman spectroscopy. *Anal Chim Acta* 843:73–82
- Xu H, Bjerneld EJ, Kall M et al (1999) Spectroscopy of single hemoglobin molecules by surface enhanced Raman scattering. *Phys Rev Lett* 83:4357–4360
- Xu LJ, Lei ZC, Li J et al (2015) Label-free surface-enhanced Raman spectroscopy detection of DNA with single-base sensitivity. *J Am Chem Soc* 137:5149–5154
- Yeo BS, Madler S, Schmid T et al (2008) Tip-enhanced Raman spectroscopy can see more: the case of cytochrome *c*. *J Phys Chem C* 112:4867–4873
- Yuen JM, Shah NC, Walsh JT et al (2010) Transcutaneous glucose sensing by surface-enhanced spatially offset Raman spectroscopy in a rat model. *Anal Chem* 82:8382–8385
- Zavaleta CL, Smith BR, Walton I et al (2009) Multiplexed imaging of surface enhanced Raman scattering nanotags in living mice using noninvasive Raman spectroscopy. *Proc Natl Acad Sci USA* 106:13511–13516

Chapter 5

Circular Dichroism and Synchrotron Radiation Circular Dichroism

Applications to Biomaterials



Rohanah Hussain, Tamás Jávorfí, Charlotte S. Hughes
and Giuliano Siligardi

5.1 Introduction

Circular dichroism is the differential absorption of left and right circularly polarized light (CPL) of chiral molecules. Molecules that do not superimpose their mirror images are chiral like L and D amino acids, of which the L enantiomers are the building blocks of proteins and analogously D-deoxyribose for DNA.

The first golden rule to measure a good signal-to-noise CD/SRCD spectrum is to know the spectral range and how much the chromophore/s of the chiral molecule absorbs light. For peptides/proteins, the chromophores are the amide bonds and the amino acid residues that absorb in the far-UV region (180–250 nm), the aromatic side-chains and the dihedral angle of the disulphide bonds in the near-UV region (250–320 nm), and prosthetic groups like flavonoids, carotenoids and beams in the visible regions (400–800 nm) (reviewed in Fasman 1996; Berova et al. 2000; Siligardi and Hussain 1998). For nucleic acids, the chromophores are the aromatic bases that absorb in the far- and near-UV regions (Fasman 1996; Berova et al. 2000). Similarly, for chiral small organic molecules and drugs, aromatic rings and/or conjugated double bonds moieties are often the chromophores to be dealt with (Fasman 1996; Berova et al. 2000; Siligardi and Hussain 1998).

For biopolymers, CD/SRCD spectroscopy is not only sensitive to the absolute configuration of the stereoisomers building blocks but also to their conformation and more importantly to the conformational behaviour as a function of environment such as concentration, solvent composition, temperature, ionic strength, pH, detergents,

R. Hussain (✉) · T. Jávorfí · C. S. Hughes · G. Siligardi
Diamond Light Source, Harwell Science and Innovation Campus,
Chilton, Didcot OX11 0DE, UK
e-mail: rohanah.hussain@diamond.ac.uk

G. Siligardi
e-mail: giuliano.siligardi@diamond.ac.uk

precipitants, ligand interactions, UV irradiation and any other perturbing condition (Siligardi and Hussain 2010; Hussain and Siligardi 2016; Hussain et al. 2016).

A modern CD spectropolarimeter operating in the UV-visible spectral region consists of a light source, typically a Xe lamp for bench top CD instruments (Applied Photophysics (UK), Jasco (Japan) and Olis (USA)) or a synchrotron light source for beamlines for synchrotron radiation circular dichroism (SRCD) (see Appendix 1) (Hussain et al. 2011, 2012), a monochromator, a photo-elastic modulator (PEM) to generate the left and right circularly polarised modulated light at 50 kHz, a sample compartment and a light sensitive detector (typically a photomultiplier tube (PMT) or recently an avalanche photo diode (APD) (Fig. 5.1).

CD/SRCD spectroscopy is an important technique to study the conformational behaviour of chiral molecules as a function of their environment. The strength of CD/SRCD spectroscopy lies in its ability to characterise the conformational properties of a chiral systems characterising how do they behaves under a variety of conditions in both solution and solid state. This properties are of particular interest because from the analysis of the data under dynamic conditions CD/SRCD spec-

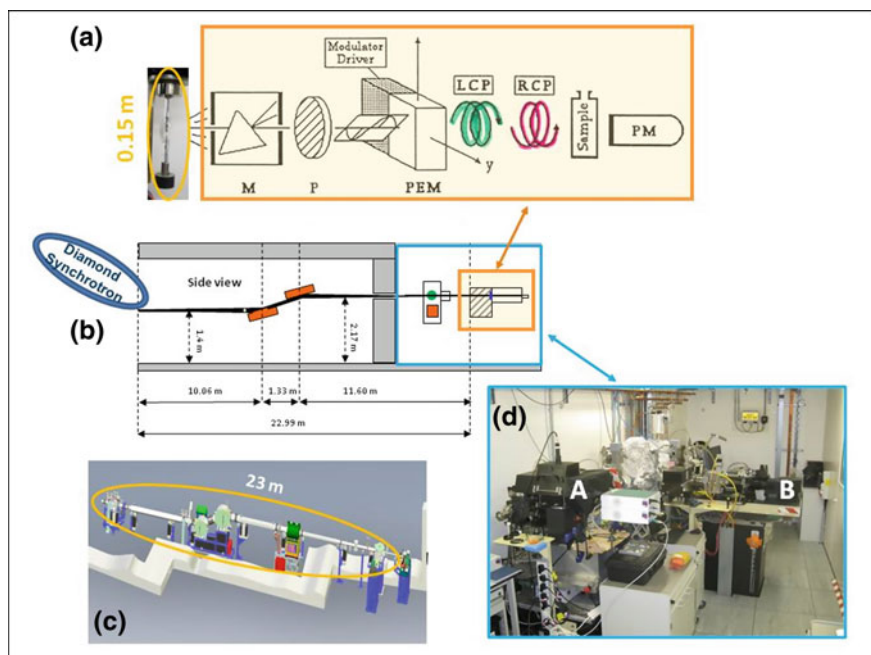


Fig. 5.1 **a** Scheme of bench-top CD instrument layout: from left: Xe lamp (a 150 W lamp is about 15 cm long), M: monochromator, P: Polariser Rochon Prism, PEM: photo elastic modulator that generates left (green) and right (red) modulated circular polarised light at 50 kHz, sample, PM: PMT or APD detector. **b** Diamond synchrotron ring, front end with silicon mirror M1 and M2 to focus light source of bending magnet to entrance slit of monochromator M followed by all the components described in (a) and represented as a orange rectangle. **c** Cartoon of the B23 components and **d** photo of the B23 experimental room with the two stations A and B

troscopy can help to build a preliminary molecular model guiding the design of subsequent experiments using other biophysical techniques (e.g. SAXS, SANS or NMR) to ratify such a model and apply it for predictive purposes.

For systems that cannot be crystallised, such as natively disordered proteins, membrane proteins and protein-protein complexes, CD/SRCD spectroscopy can provide valuable information to assist, together with the data from other biophysical techniques, the construction of a 3D model of the system investigated.

5.2 B23 Beamline for Synchrotron Radiation Circular Dichroism (SRCD)

5.2.1 B23 Higher Photon Flux

Diamond Light Source B23 SRCD provides two main advantages over conventional benchtop CD instruments and other beamlines for SRCD: a higher photon flux and a highly collimated micro beamlight. The high photon-flux enables measurements in the vacuum UV (VUV) and far-UV regions, especially of samples with high salt concentration (up to 500 mM NaCl often used in protein samples) otherwise unattainable with bespoke bench top CD instruments. Figure 5.2 summarizes the benefits of the extended wavelength range offered using B23 beamline. The yellow bar illustrates the cut-off region not accessible with bench-top CD instruments but accessible with B23 that increases the spectral. For small organic molecules, though the improvement might be modest, it can still make the difference as in this example it enabled the measurement of an extra band that was essential for the ab initio calculations of the correct absolute configuration (Berova et al. 2000) (Fig. 5.2c). For bio-macromolecules, like nucleic acids (Fig. 5.2a) or proteins (Fig. 5.2b), it can reveal more conformational features (Fig. 5.2a) or less distorted one (Fig. 5.2b) enabling a more accurate estimation of secondary structure content.

The High photon flux of SRCD beamlines have been known to denature protein in solutions and potentially causing misinterpretation of the estimated secondary structure content (Fasman 1996; Sreerama and Woody 2004; Provencher and Glockner 1981). However, this effect has been exploited by development at B23 a novel assay that uses the rate of protein denaturation to assess the relative photostability of proteins with and without ligands, excipients, detergents, formulating agents, precipitants that was used as a qualitative ligand binding interactions assay in particular for molecules devoid or with negligible UV absorption (Hussain et al. 2012; Siligardi and Hussain 2015). Figure 5.3 summarizes a typical experiment, which is a simple experiment consisting of 30 consecutive repeated scanned measurements carried out to identify not only the best stabilising formulation C but also the effect of different formulation on the content of secondary structure estimation (SSE) of antibodies to be used as biopharmaceuticals.

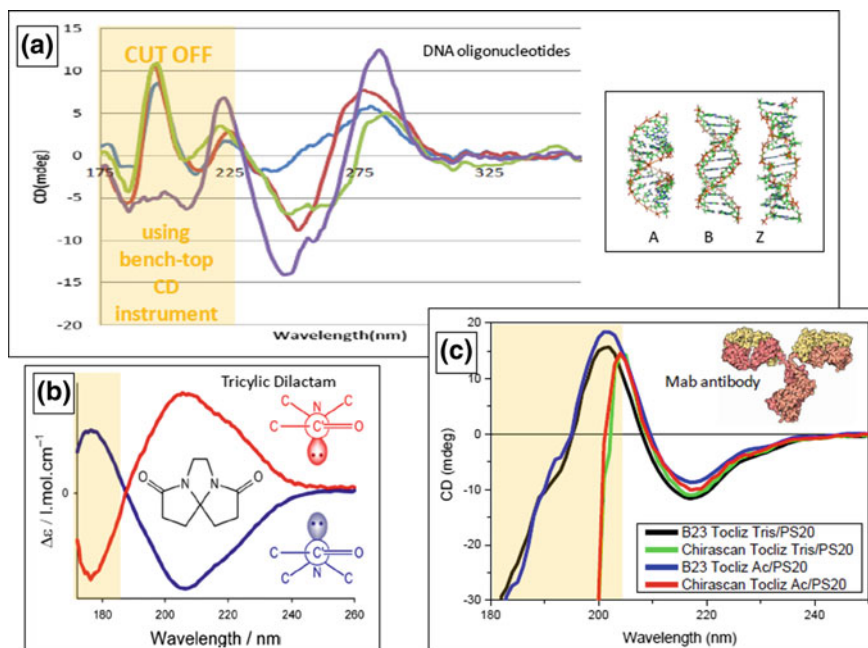


Fig. 5.2 Advantages of B23 versus bench-top CD instruments: higher photon-flux. I—**a** Cut off regions observed for DNA oligonucleotides in 100 mM NaCl using Chirascan Plus versus B23. **b** Cut-off for Mab monoclonal antibodies in different formulations. **c** Cut-off for chiral small organic molecules (tricyclic dilactam) (Pazderková et al. 2014)

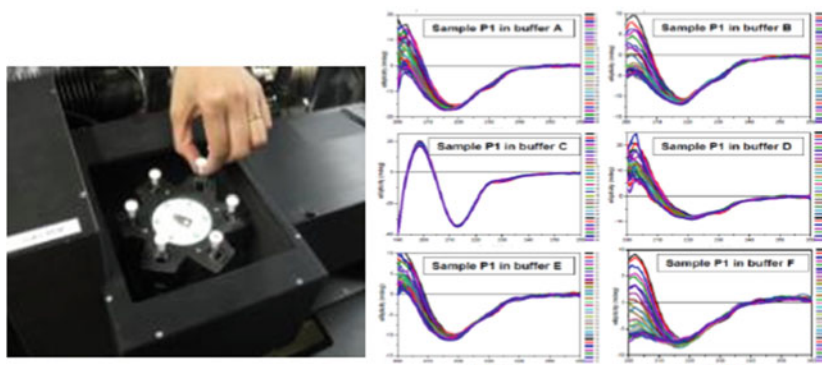


Fig. 5.3 Advantages of B23 versus bench-top CD instruments: (1) higher photon-flux. Example of the novel B23 protein UV denaturation assay applied a Mab antibody in different formulations that reveal different rates of protein denaturation induced by the UV high photon-flux of the synchrotron beamline on scanning the spectra in the 180–250 nm region. Formulation C prevented the Mab antibody to denature by UV irradiation compared to the other five formulations (redrawn from Siligardi and Hussain 2015)

It is important to note that the use of the 6-cell turret is very convenient overnight in particular for long experiments such as the UV-denaturation assays and temperature studies experiments that taking 2–3 h per experiment will be conducted efficiently in one go via script program for a total time of 12–18 h.

5.2.2 Protein UV-Denaturation Assay

The exploitation of the high photon flux of B23, about 1×10^{12} photon s^{-1} at 200 nm has led the development of the novel UV protein denaturation assay to rapidly assessing the photostability of proteins by scanning consecutive repeated SRCD spectra. For a protein under a variety of conditions such as in different formulations, in the presence of ligands or in comparison with mutants, the difference in spectral changes that analysed in terms of content of elements of secondary structure reveals an increased rate of unordered structure at the expenses of the other ordered structures α -helices, β -strands and β -turns has been used as a relative measure of protein photostability. The UV-denaturation assay can also be used to determine unambiguously binding interactions of ligand devoid or with negligible UV absorption, such as lipids or carbohydrates and sometimes even when no detectable changes in thermal stability are observed. The use of this assay to assess protein photostability and qualitatively ligand binding interactions has been applied in several studies (Hussain et al. 2012; Siligardi and Hussain 2015).

5.3 B23 Highly Collimated Microbeam

5.3.1 Use of Small Aperture 10 cm Pathlength Cuvette

The highly collimated microbeam focused at the sample (Fig. 5.4) enables CD measurements using small aperture cuvettes with small volume capacity (20 μ l for 1 cm cell to 780 μ l for 10 cm cell (Fig. 5.5)) which is essential for the measurements of samples that are difficult to produce in large quantities. These conditions that can span from measuring a small sample volume in capillary cells to small spots or larger sample areas led the development at B23 of novel sample compartments.

The microbeam enabled also the use of a rotating holder for cylindrical cuvettes of 16 mm internal diameter (Fig. 5.6) eliminating the protein UV denaturation effect induced by the high radiation power of B23 when conducting repeated consecutive scanned SRCD spectra.

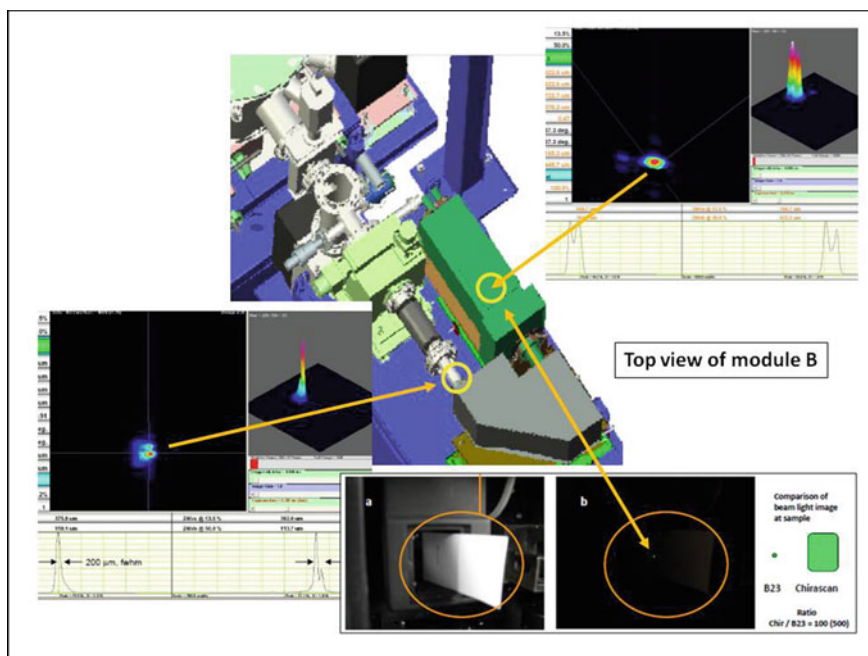


Fig. 5.4 Advantages of B23 versus bench-top CD instruments: (2) highly collimated microbeam. Cartoon of modular components of end station module B: (2) Subtractive double grating monochromator purged with nitrogen gas; (3) Rochon prism, (4) PEM; (5) Sample compartment, the yellow circle indicate the Peltier sample holder of which top view is illustrated in (a) where a piece of white paper is inserted instead of the cuvette cell to view in the dark the beam spot size (b). On the bottom right is represented the relative beamsizes of incident light at sample of B23 compared to that of a bespoke bench-top CD instrument. The spot size generated with B23 can be 100–400 times smaller than commercial bench-top CD instruments depending on the sample being in or out the focal plane

The incorporation of a temperature controlled XY motorised Linkam stage has enabled measurements from cryogenic ($-170\text{ }^{\circ}\text{C}$) to high temperature ($+350\text{ }^{\circ}\text{C}$) (Figs. 5.7 and 5.8).

A large motorised XY stage enables the measurements microfluidic lab-on-a-chip (Fig. 5.9) and the use of 96- and/or 384-well plates (Figs. 5.10, 5.11 and 5.12) for high-throughput CD (HTCD) screening (Siligardi and Hussain 2015; Hussain and Siligardi 2016; Hussain et al. 2016).

All these applications are unattainable with bench-top CD instruments and other SRCD beamlines.

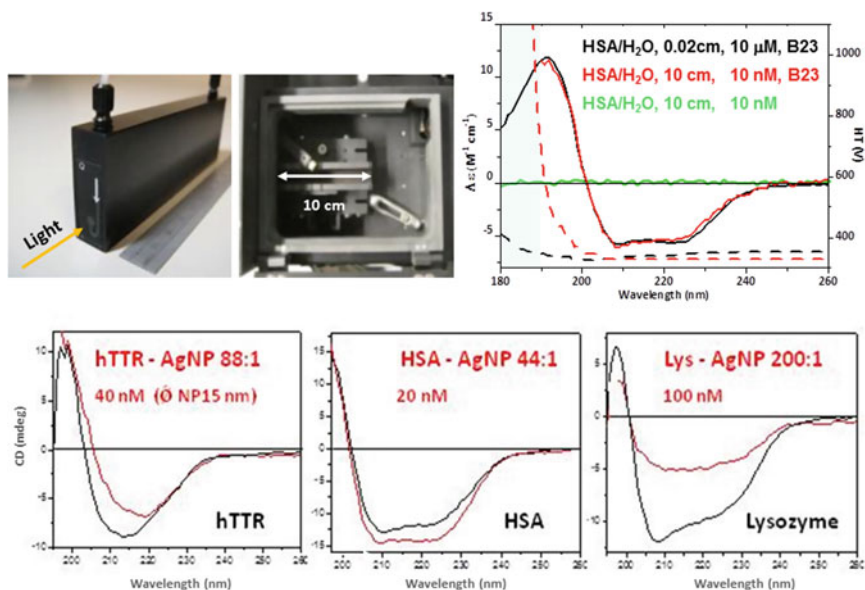


Fig. 5.5 (Top left) 10 cm pathlength cell with 3 mm aperture with volume capacity of 800 μl . (Top middle) Top view of the open sample chamber of module B with cell holder for 10 cm cell. (Top right) Unsmoothed CD spectra (solid lines) and detector high-tension (HT) spectra (dashed line) of 10 μM aqueous HSAff solution (red spectrum measured with cylindrical cell of 0.02 cm pathlength using B23 and 10 nM aqueous HSAff solution (black spectrum measured with 10 cm cell using B23, and green spectrum measured using a bench-top CD instrument. Note that, for the green spectrum, the lack of the CD features of HSA protein observed with B23 (black and red) are due to light depolarisation of the reflected highly divergent light beam of the Chirascan CD instrument. Bottom) SRCD spectra of hTTR, HSA and Lysozyme protein with (red) and without (black) silver nanoparticles of average 15 nm diameter (redrawn from Laera et al. 2011)

5.3.2 Small Aperture Long Pathlength Ultralow Concentration (nanoMolar) Measurement

A small aperture 10 cm cuvette pathlength with low volume capacity of 0.8 ml was first used in 2015 to assess whether the conformation of proteins adsorbed on nanoparticle was significantly affected, which could potentially trigger immunogenic responses on nanoparticles uptaken in living cells.

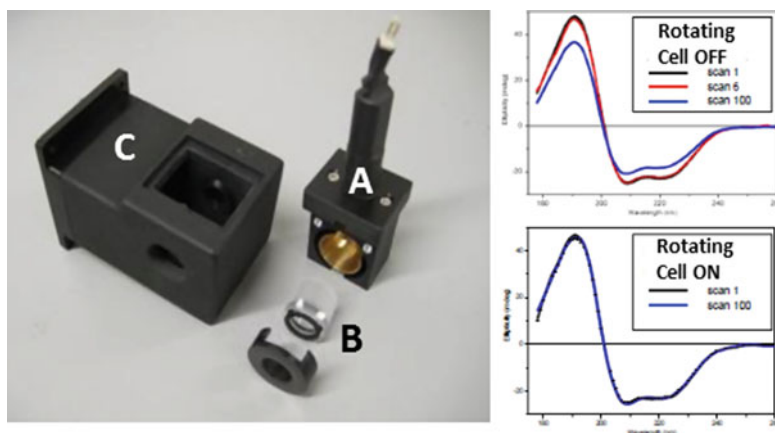


Fig. 5.6 (Left) Assembly of the rotating cell holder. **A** Rotating cell holder for cylindrical cells. **B** Recommended cylindrical cells of 0.02 cm and 0.05 cm pathlengths. The rotating cell holder can be used with the Peltier stage (**C**) for thermal studies in the 5–95 °C temperature range. (Right) 100 repeated consecutive SRCD spectra of human serum albumin essentially fatty acid free (HSAff) with rotating cell OFF (top) or ON (bottom). Using the rotating cell on ON there were no detectable UV denaturation effects

The CD spectrum measured with benchtop CD instrument (Fig. 5.5, green line) showed no detectable signal due to depolarisation of the highly divergent light beam of the CD instrument bouncing inside the 10 cm cuvette cancelling the differential absorption between left and right circularly polarized light. This, however, was not the case when using the highly collimated microbeam of B23. For human serum albumin (HSA), the SRCD spectrum of 10 nM solution measured in 10 cm pathlength (Fig. 5.5, red) was superimposable to that of 10 μ M concentration in 0.02 cm pathlength (Fig. 5.5, black) indicating that no conformational changes were observed. These experiments conducted with proteins in the presence and absence of various nanoparticle made of different metals and materials revealed that conformational changes were revealed with Silver but not gold nanoparticles (Fig. 5.5, bottom) (Laera et al. 2011). Since then, this method have been optimised and applied to sample concentrations as little as few nM.

As large variety of nanomaterials are present in many health and consumer products from nanomedicines, toothpastes, cosmetic products, paints, aerosols, and food excipients it is important to assess the risk of increased nanotoxicology.

5.3.3 *Rotating Cell Holder to Make Protein UV Denaturation Negligible*

The photon flux at the sample can be reduced by reducing the slitwidths of B23 double grating subtractive monochromators of stations A and B. However, for week

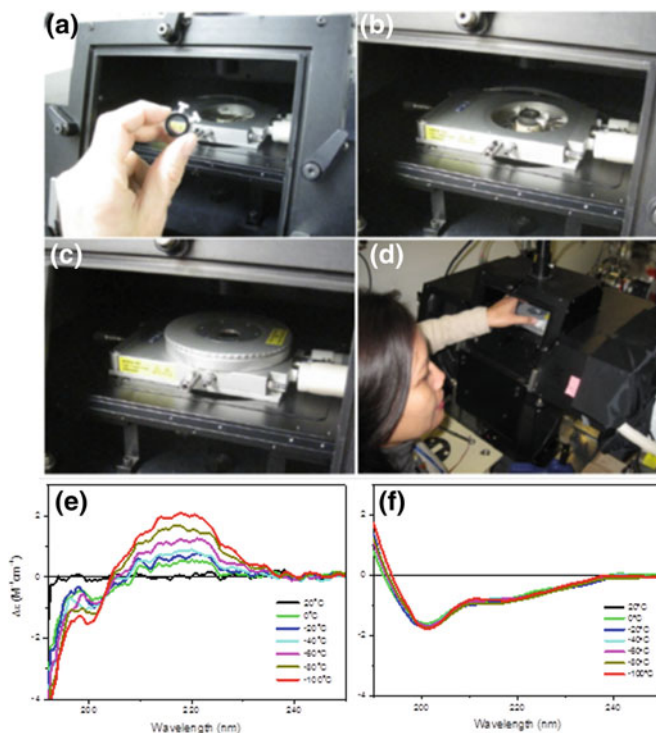


Fig. 5.7 First use of the Linkam stage for low temperature SRCD measurements of peptides in a cryogenic solvent mixture to determine the most thermodynamic stable conformation (a–d). Preliminary far-UV CD spectra of antimicrobial peptide (e) and PKC pseudo-substrate analogue (f) in antifreeze solvent mixture ethanediol-water (2:1 v/v)

CD signals the drawback is a poor signal-to-noise ratio of the measurement. A unique solution developed for B23 is the use of the rotating cell holder (Fig. 5.6) that allows the SRCD measurements to be carried out also at variable temperatures eliminating the UV-denaturation effects without the need of reducing the photon flux hence retaining the quality of signal-to-noise ratio. Another important use of the rotating cell holder is the ability to measure CD of protein suspensions that otherwise will precipitate by gravity to the bottom of the cuvette distorting the spectral shape.

5.3.4 Cryogenic and High Temperature Studies

One exploitation of B23 highly collimated microbeam is illustrated in Fig. 5.7 that enables the use of the temperature controlled Linkam stage that can operate between -170 and $+350$ °C. The Linkam stage (Linkam Scientific Instruments, UK) is held on the large motorised X-Y stage inside the novel vertical sample compartment of

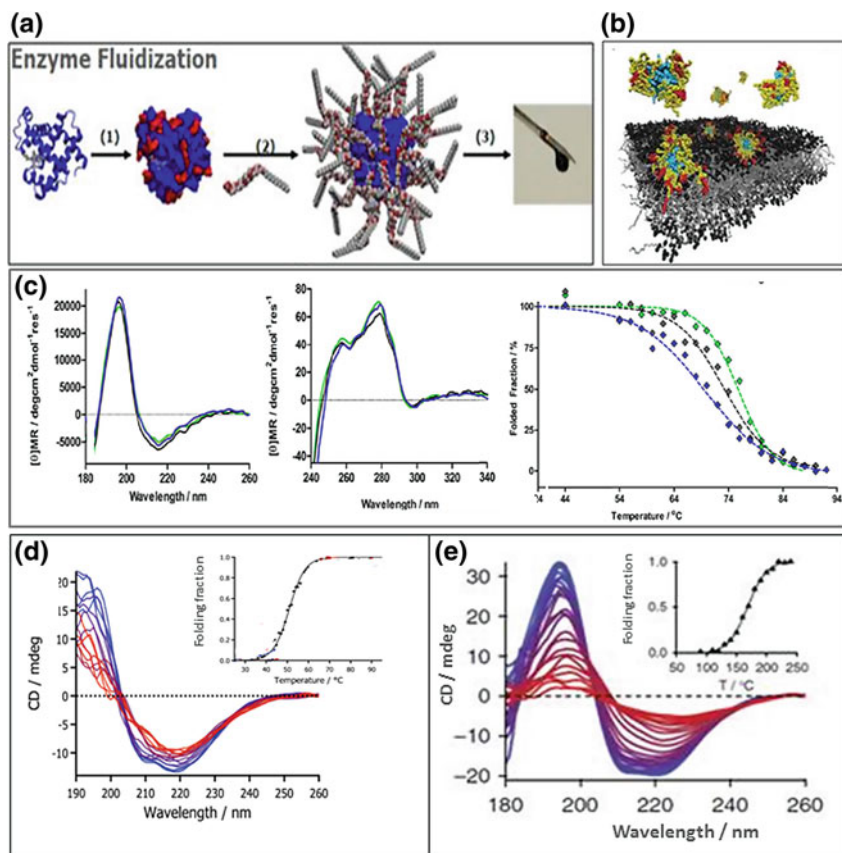


Fig. 5.8 **a** Scheme of enzyme fluidization of solvent-free enzyme that became viscous liquids. **b** Cartoon of the “lipidated proteins” anchored to the surface of muscle cells. **c** Variable temperature study up to 95 °C demonstrating that the various protein solvent-free though showing almost identical folding at room temperature had significant different thermal stability that correlated with increased stimulated oxygenation of stem cells. Figures (a), (b) and (c) redrawn from Brogan et al. (2014). **d** Thermal stability of aqueous solution of enzyme with T_m of 50 °C. **e** Thermal stability solvent-free lipidated lenzyme showing T_m of 175 °C. Figures (d) and (e) redrawn from Armstrong et al. (2015)

module B end station. This configuration enables the conformational studies of samples both in cryogenic solutions and in solid state thin films that are located directly on the temperature controlled stage. It is important to note that the Linkam stage, in order to heat and cool the sample efficiently has a central hole of 2 mm in diameter for the light to pass through (Fig. 5.7a–d). Unlike for bench-top CD instruments, such a pinhole does not obstruct the highly collimated microbeam of B23 for the measurements of SRCD spectra. The application of this system to biological samples, such as peptides and proteins that are commonly stored in cryogenic conditions, has been

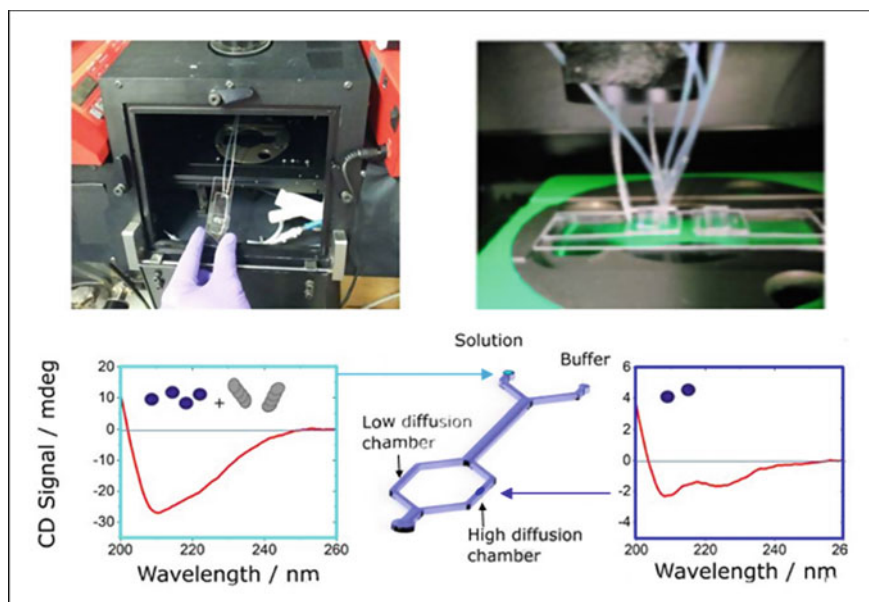


Fig. 5.9 Microfluidic chip inserted into the larger motorised XY stage. The injection chamber, the low and high diffusion chambers of sub-millimeter diameter become the cuvette cells of known pathlength that can be interrogated alternating the measurements that are controlled via a script program. The pathlength can vary according to the solution concentration. Dilute solutions will require long pathlength whilst concentrated solutions short pathlengths or an array of chambers of different pathlengths (redrawn from Bortolini et al. 2019)

recently achieved to assess whether conformational changes were indeed induced at cryogenic conditions.

Conformational studies carried out on antimicrobial peptides in cryogenic solvents (ethanediol-water (2:1)) showed a substantial increased positive SRCD signal at about 215 nm characteristic of left-handed extended helix of polyproline type II (PPII) structure (collagen type) upon cooling to $-100\text{ }^{\circ}\text{C}$ (Fig. 5.7e). The peptide which showed antimicrobial activity against MRSA bacteria is thought to form a raft on the surface of the bacterial membrane (Hussain et al. 2006). This conformational behaviour is revealed when the peptide is perturbed, in this case by cryogenic temperatures. This folding propensity cannot be identified solely on “static” measurements at room temperature. Conversely, another peptide, inhibitor of protein kinase C substrate, was not affected under similar cryogenic conditions (Fig. 5.7f) retaining the dominating α -helical structure observed at room temperature. Of course the latter peptide has a different function activity than the former one. Further scientific highlight published using this feature is described below.

The B23 Linkam vertical chamber (Fig. 5.7a–d) was also used to conduct high temperature studies on functionalised proteins (Armstrong et al. 2015; Brogan et al. 2014). Enzyme proteins were colonized and then lipidated to obtain proteins that

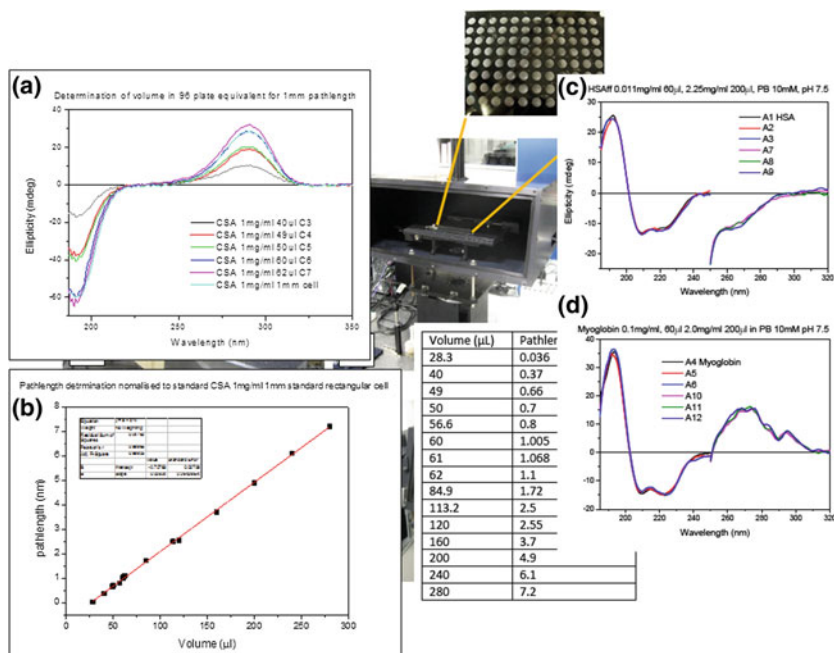


Fig. 5.10 First proof-of-concept of B23 HTCD measurement using the vertical sample chamber for multiplates (photo on the background with inserted also the photo of the black 96-well multiplate with transparent quartz cover of 1.25 mm thickness). **a** SRCD spectra of (R)-10-Camphorsulfonic acid (CSA) in water (1 mg/ml) measured at different well volume capacity. **b** Linear correlation between well volume and CD intensity at 290 nm used to calculate the equivalent pathlength for each well listed in the central table. SRCD spectra in the far-UV and near-UV regions of HSA (**c**) and myoglobin (**d**) proteins (redrawn from Hussain and Siligardi 2016; Hussain et al. 2016)

when purified as solvent-free became viscous liquid rather than lyophilised powder. One of the application of this type of functionalised proteins was to improve the production of engineered biotissues (Armstrong et al. 2015). The “lipidated proteins” added to carbohydrate matrices seeded with stem cells increased the survival of the stem cells because of better oxygenation. A better bio-engineered cartilages of type II collagen were obtained with the use of “lipidated proteins” behaving like supplementary oxygen tanks. The choice of “lipidated” protein among the products of enzyme fluidification process with good cell survival activity was achieved by selecting the “lipidated enzyme” with the highest thermal stability (Fig. 5.8a–c). The nature of the material being a very viscous liquid required the protein to be squeezed between to fused silica windows and held horizontal as otherwise in a vertical position the high temperatures, in this case up to 250 °C fluidified the “lipidated protein” to leak out by gravity. Another example is the catalytic activity of “lipidated enzymes” that were substantially increased when operating at 150 °C (Fig. 5.8e) but not with the native enzyme (Fig. 5.8d) (Brogan et al. 2014). These thermal stability experiments

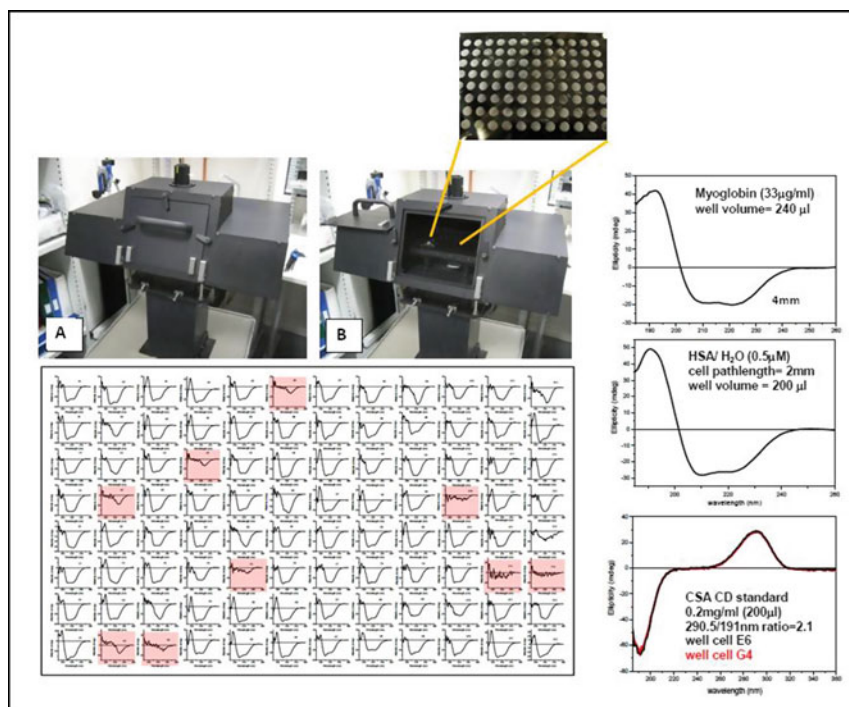


Fig. 5.11 B23 vertical chamber with large motorised XY stage for HTCD using 96 and 384 multiplates. Open (A) and closed (B) door with enlarged photo of the 96-well plate. (Left) The CDApps suite of programs (Appendix 2) enables the highlighting of the 96 SRCD spectra selected in terms of similarity or dissimilarity. In this case the least similar, consistent with protein precipitations were highlighted in red. (Right) Examples of SRCD spectra of proteins and the CD standard (+) Camphor Sulfonic Acid (CSA) (redrawn from Hussain and Siligardi 2016; Hussain et al. 2016)

for the “lipidated” proteins were only possible using the horizontally held Linkam temperature controlled stage in the B23 vertical chamber.

5.3.5 Microfluidic Lab-on-a-Chip

For a protein in a heterogeneous mixture of soluble associated/aggregated species of different molecular sizes at equilibrium, typically only average spectroscopic features can be resolved. In the recent article of Bortolini et al. (2019) the authors overcame this limitation by using for the first time free-flow microfluidic size separation in-line with the highly collimated microbeam of B23 beamline in order to resolve the secondary structure of each component of a model protein mixture containing monomers and fibrils (Fig. 5.9), which is unattainable with bench-top CD instruments. To enable this objective, the authors integrated far-UV (180–250 nm) compatible measure-

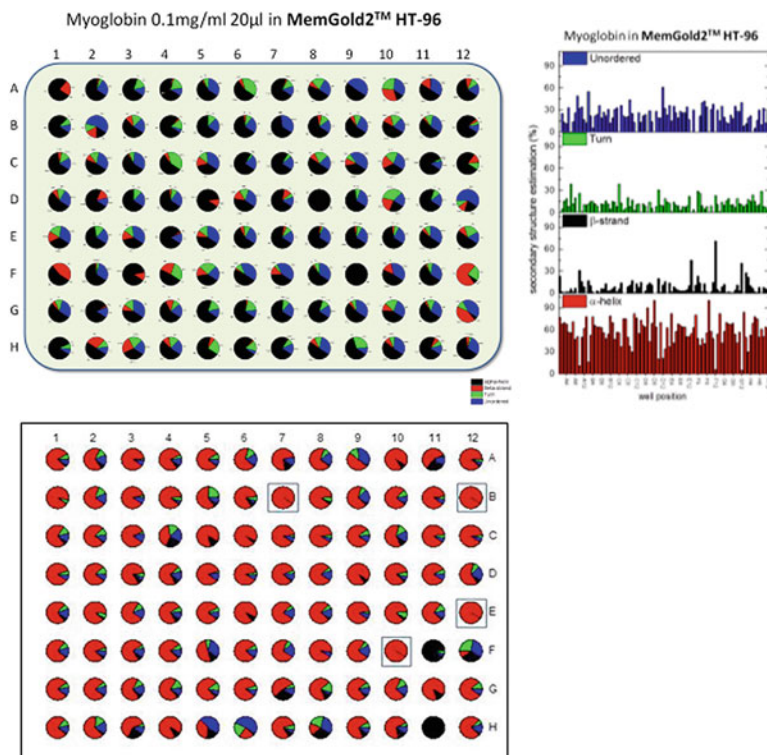


Fig. 5.12 (Top) Myoglobin secondary structure estimation from HT-SRCD spectra using ContinLL algorithm displayed in pie (left) and bar (right) charts from CDApps (redrawn from Hussain and Siligardi 2016; Hussain et al. 2016). (Bottom) Pie chart of SSE of Membrane protein in MemGold2 using ContinLL. Only 4 formulations inscribed in square boxes (B7, B12, E12 and F10) did induce 100% of α -helical conformation (red: α -Helix; black: β -Strand; green: Turn; blue: Unordered)

ment chambers into conventional polydimethylsiloxane (PDMS)-based microfluidic devices (Fig. 5.9). Two architectures were proposed so as to accommodate for a wide range of protein concentrations. This novel approach, which can be used in combination with other bulk measurement techniques, paves the way to the study of complex mixtures such as the ones associated with protein misfolding and aggregation diseases including Alzheimer's and Parkinson's diseases.

5.3.6 High-Throughput Circular Dichroism (HTCD)

As the understanding of protein behaviour has led to a dramatically increased rate of discovery of novel functions, there is an urgent need to characterise speedily these systems. The development of the vertical chamber equipped with a large motorised

XY stage has enabled the measurements of CD using 96- and 384-well multiplates at Diamond B23 beamline. The data acquisition for the HTCD multiplates was achieved by implementing the appropriate script carrying the instruction to scan the spectrum of the first well, move to the next well/cell and scan the second spectrum and so on until the 96th or 384th cycle was completed.

The impact of this development to the screening of protein for assessing their conformational behaviour as a function of buffer/formulation or ligand binding interactions is substantial. For example, the average time to measure one SRCD spectrum for a protein sample is about 30 min that includes 6 min of actual measurements and the rest dedicated for the thorough cleaning of the cuvette cell and the parameter setting to start the scan measurement. Therefore, for a large number of measurements, say about 100 or more, the bottleneck is the time required to clean the cuvette cell that cannot be decreased. In terms of actual measurement time, 100 spectra scanned using a single cell will require about 3000 min or beamtime 6.25 shifts even though the actual beamtime measurement is 600 min or 1.25 shifts of beamtime.

The use of many cells of the same pathlength could be done but because each cuvette has its own birefringent signature that has to be subtracted from that of the sample, this approach is risky and has been abandoned because errors of mixing different cells cannot be completely eliminated. For these reasons, the use of the 96-well multiplate increases by 10 folds the beamtime productivity. For the user point of view the improvement will be even greater because, once the multiplate is loaded it is considered as a single cell measurement rather than 100.

Figure 5.10 illustrates the first HT-SRCD measurement successfully carried out at B23 showing reproducible SRCD spectra of (+) camphor sulfonic acid (CSA), measured for various well volumes from 20 to 280 μl . The linear correlation between the pathlength and the solution volume has been validated with the spectra of the same solution measured in cylindrical cuvette cells of known pathlength. The results indicated that the wells could be used to generate a large pathlength range simply by varying the solution volume filled in each well following the pathlength-volume plot of Fig. 5.16. Human serum albumin and myoglobin, two common proteins were also used as reference standards. Near and far UV region were also investigated using HT-SRCD showing that both the local environment of aromatic side-chains and dihedral angle of disulphide bonds and secondary protein structure associated to the architecture of the amide bond chromophores of the amino acid residues could be monitored in one measurement by varying accordingly the solution volume in the wells.

Further optimisations of the HTCD sample environment were carried out and recent results showed that the 384-well multiplate could also be used in a reproducible manner even with lower sample volumes of 20 μl for different crystallisation buffer conditions. In Fig. 5.11, myoglobin dissolved in MEMGold2 (see Appendix 3) crystallisation buffer kit (Molecular Dimensions, <https://www.moleculardimensions.com/products/4234-MemGold2/>) showed a variability of the myoglobin folding with 9 conditions highlighted in red, in which the protein did precipitate.

It is known that the protein folding can be affected by the solvent environment. The secondary structure content estimated from HTCD data of myoglobin

and another membrane protein both in MemGold2 buffers were consistent with this view (Fig. 5.12). In structural biology and drug screening this is an important observation that should not be neglected. The identification of conformational changes could be used for the optimisation of the screening of crystallisation conditions as well as binding-interaction assays.

The impact of the use of multiplates and CDApps (see Appendix 2) to B23 beamline is to enable also the screening of molecular crowding effects of proteins for crystallisation purposes, the qualitative screening of ligand binding interactions and batch control in terms of folding reproducibility of biopolymers such as proteins and nucleic acids under a broad variety of environment.

5.4 Summary

The unique broad wavelength range available at B23 (vacuum UV, far-UV, near-UV and visible, from 125 to 650 nm) enables the CD spectroscopic investigations to be carried out for an unprecedented variety of states from liquid, gels, colloid and solid state under a large range of conditions such as temperature, pH, solvent, and high salt concentration otherwise unattainable with bench top CD instruments and to the other SRCD beamlines worldwide.

The implication of protein conformational behaviour induced under different environmental conditions, witnessed in neurodegenerative diseases due to protein misfolding, is that it can significantly affect the protein function by perturbing its drug binding affinity hence reducing the potential therapeutic efficacy. It is therefore important to conduct HTCD screenings in parallel with the determination of 3D crystallographic structures at high atomic resolution like those used in fragment-based drug design from which new potential lead compounds can be designed. This is because the structure of the designed drug is biased by the fact that the protein 3D structure obtained on a limited number of crystallization conditions, even smaller for membrane proteins, may not represent completely the whole active protein folding behaviour.

Acknowledgements We like to thank Diamond Light Source for access to B23 beamline (SM8714, SM9786, SM11563, SM18011, CM2023, CM2074, CM5718, CM5950, CM4980, CM12182, C14484, CM16778, CM19680 and MX8681-52 beamtimes).

Appendix 1: Layout of B23 Beamline from SRCD

B23 provides a light source of higher photon flux and brilliance in the vacuum-UV (VUV: 125–170 nm) and far-UV (170–250 nm) region (Table 5.1) extending the wavelength range to the VUV region below 180 nm that is unattainable with bench top CD instruments using Xu arc lamp sources.

Table 5.1 Summary of the key parameters for B23

Beamline parameters	Module A	Module B
Wavelength range	125–500 nm	160–650 nm
Image size at the sample position (20 cm from exit slit) (slit width: 0.5 mm) ^a	0.7 × 0.8 mm	0.7 × 0.8 mm
Beam divergence	1% horizontal × 0.5° vertical, (equivalent to 20 mRad (H) × 10 mRad (V))	1% horizontal × 0.5° vertical, (equivalent to 20 mRad (H) × 10 mRad (V))
Photon flux (measured at the sample position (ph/s/0.1%bw) at 6.2 eV (200 nm) normalised for 300 mA ring current)	0.9 × 10 ^{12b}	3.2 × 10 ¹²

^aWith lens before the Rochon prism

^bThe measured photon flux of module A is about a third of that of module B due to the lower efficiency of its two silicon gratings compared to those of MgF₂ coated Aluminium gratings of module B. The latter cannot be used for module A as the grooves will be destroyed very quickly

To maximise the photon-flux and brilliance B23 has been designed with a 1:1 magnification of the light source point (SP) (Fig. 5.1b) (Hussain et al. 2011). At 10.06 m from the SP an uncoated plane silicon mirror M1 at 15° grazing angle of the incident light reflects vertically the VUV/UV/Visible radiation to a second – 15° grazing angle uncoated toroidal silicon mirror M2 at 11.39 m from SP. In this manner the 20 mrad (horizontally) × 8 mrad (vertically) cone of light emitted from the synchrotron bending magnet (BM) is focused by M2 to the entrance slitwidth of 0.5 mm of the module A double grating subtracting monochromator at 23 m from the bending magnet light source (Fig. 5.1c). The whole BM light passes through the double grating subtracting monochromator that is unique in the SRCD beamline world giving rise to the minimum stray light like that experienced with benchtop CD instruments. Currently all existing SRCD beamlines are based on one single grating monochromator that can be used only from vacuum UV to 320 nm wavelength range due to the spectral overlapping of high order diffracted light. In the experimental end-station cabin at 21.5 m, a third plane silicon mirror M3 is used to switch a variable portion, from 0 to 100% of the beam from Module A that is tuned to operate in the 125–500 nm spectral region to Module B in the 165–650 nm region (Fig. 5.1d). With the current Diamond synchrotron operating at 300 mA, the beamline can operate efficiently either with Module A or Module B. The beam can be switched from module A to module B within a minute enabling two different sample chamber configurations to be used without delays.

Table 5.2 Beamline features/measurements capabilities

Module A (vertical sample chamber)	Module B (horizontal sample chamber)
Horizontal temperature stage (Linkam system –150 to 300 °C) for cryogenic and very high temperature measurements	Peltier temperature system (–5 to 90 °C) for standard variable temperature solution studies
Horizontal XY stage for homogeneity film measurements and location of differential domains and particles	6-cell turret for automated temperature and UV protein denaturation assay studies
Standard far UV and near UV measurement for solution measurement	Motorised XY stage for low volume small aperture long pathlength cells for membrane protein in near UV and nanoparticle low concentration (nM) measurements
Demountable cell sample holder for high concentration studies	Ligand interaction studies in far and near UV region
Stopped-flow (>4 ms mixing time)	Stopped-flow (>4 ms mixing time)
	Rotating cell sample environment to eliminate UV protein denaturation
	Demountable cell of 5, 10, 50, and 100 micron pathlength to study highly concentrated samples in high ionic strength solutions

The high ultra vacuum monochromator of Module A enables SRCD measurements to be conducted in the 125–500 nm wavelength range that is useful to study the conformation of dry films of biological materials and the chirality of thin metal layers (up to 30 nm in thickness) coated on VUV and far-UV transparent substrates. The monochromator of module B purged with nitrogen gas operating in the 165–650 nm region is primarily used to characterise samples in solution. However, as the components of the beamline are modular, they can be easily swapped between the two stations allowing an even large degree of flexibility that is, to our knowledge, unattainable with other SRCD beamlines worldwide and bench top CD instruments.

A summary of B23 features and capabilities are listed in Table 5.2.

Appendix 2: CDApps—Data Processing and Data Analysis

Good practice for any research project using spectroscopic techniques relies on an optimised designed experiments, planning, data processing and analysis. To maximise beamtime, the tendency is to collect as much data as possible. This is understandable considering the time constraint to which users are subjected to (average beamtime awarded for B23 is 12 shifts of 8 h per shift) and, for this reason, efforts have been made to improve the performance of the beamline by simplifying the measurement procedures for ligand binding titration and protein UV denaturation assay experiments and increasing productivity using 6-cell turret, and 96- or 384-

The image shows a composite screenshot of the CD Apps software interface with three callout boxes labeled A, B, and C. Box A points to the 'B23 CD Apps' splash screen, which includes a diagram of HSA (Pdb: 1bmo) and Diazepam binding to it, and a 'Terms and Conditions of Use' section. Box B points to the 'B23 Visit Information' table, which lists visits with columns for VISITNAME, TITLE, FULLNAME, VISITSTART, VISITEND, and ABSTRACT. Box C points to the 'CD Titration' window, which displays a table of titration data and various experimental parameters.

Table 1: B23 Visit Information

VISITNAME	TITLE	FULLNAME	VISITSTART	VISITEND	ABSTRACT
0000033-4	Feasibility study for CD imaging using the home...	Dr. Fuharsh Hussain	26/07/2013	26/07/2013	Summary Th...
0000033-2	Characterisation of amphoteric activity of thera...	Dr. Fuharsh Hussain	26/07/2013	26/07/2013	The projec...
0000033-3	Feasibility study for CD imaging using the home...	Dr. Fuharsh Hussain	11/07/2013	11/07/2013	Summary Th...

Table 2: CD Titration Data

Titration Point (A:B)	Stock Number	Volume of Stock Solution to Add (µl)	Total Cell Volume (µl)	Oxidation Factor (This must be kept below a max. of 10% of the total)	Total Volume of Stock Solution B to Add (Titration) (µl)
0:100	1	0.0	2000.0	1.000	0.0
1:99	1	0.0	2019.8	1.01	19.8
2:98	1	19.8	2000.0	1.016	0.0
3:97	2	11	2045	1.022	45
4:96	2	11	2060	1.03	60
5:95	2	30	2090	1.045	90
6:94	3	20	2150	1.055	110
7:93	3	30	2160	1.07	140
8:92	3	30	2200	1.11	200

Fig. 5.13 CDApps software version 4.0 can be open on B23 website (<http://www.diamond.ac.uk/Beamlines/Soft-Condensed-Matter/B23/manual/Beamline-software.html>). Instruction on how to open the CD Titration program following three simple steps from A to C

well multiplates. For large amount of data collected, data processing is always the limiting factor.

Since operation, the B23 team has proactively supported the users in their data processing on-site during beamtime, as well as offering offline post-beamtime visits for data processing. This process is, however, very labour intensive for the limited B23 man power resources.

To address this critical issue of processing data on the fly, providing inexperienced users with user friendly application to process data and assistance in the preparation of experimental reports as part of the requirement of using the Diamond Light Source facilities, in-house software called CDApps was developed for this purpose. CDApps was the result of the expansion of the in-house CD Titration software created by the B23 team in 2011, which was popular but unstable and not easily supportable as it had been developed organically to assist the users in the design and planning of their experiments. In 2012, the software was re-programmed and a stable version was released to the B23 Users community. As an increased number of applications and novel protocols became available at B23 with enhanced functionality to address the wider needs of different disciplines of the users' community, CD Titration software was renamed CDApps. To date, CDApps includes many types of measurements carried out at B23 such as: (i) ligand binding titration for K_d determination, (ii)

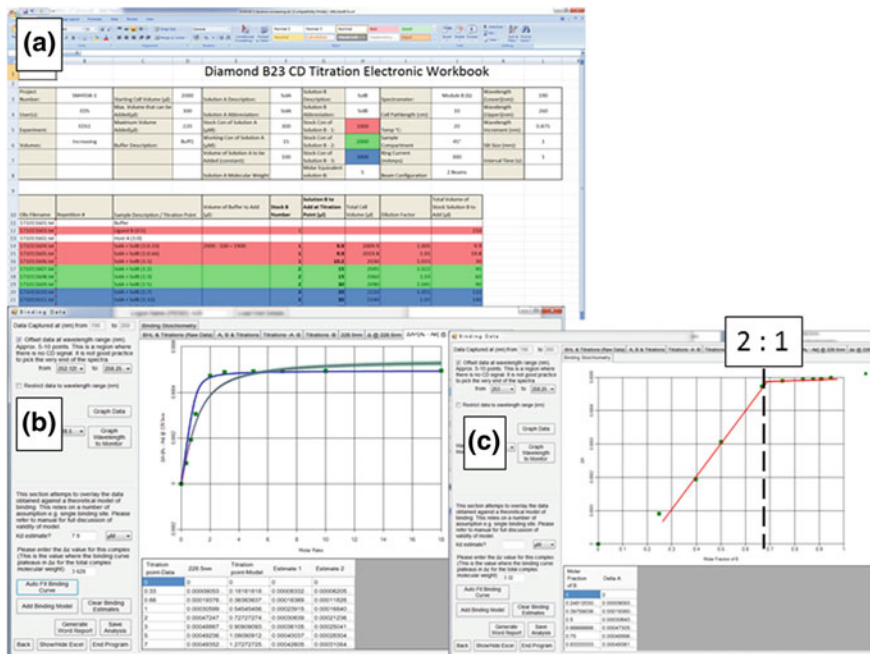


Fig. 5.14 Cascade of CDApps screens of CD Titration command: **a** Titration plan made using the CD Titration Electronic Workbook opened from CDApps as illustrated in Fig. 5.13. **b** Fitting of experimental ΔA data at single wavelength versus ligand concentration to determine dissociation constant K_d (Siligardi et al. 2002, 2014). **c** Plot of experimental ΔA data at single wavelength versus molar fraction of $\{[Ligand]/([ligand] + [host])\}$ to determine the stoichiometry of the ligand-host binding interaction. In this example a stoichiometry of ligand to host suggested is 2:1

consecutive repeated (1 to n) scans, (iii) protein UV denaturation assay pioneered at B23 and (iv) thermal denaturation (Hussain et al. 2015). The CDApps template is based on the Windows operating system with the requirement for availability of Excel files for all desktop/laptops.

In summary the functionalities in CDApps are:

For CD Titrations:

- CDApps enables the experimental design and planning of CD titration experiments off-site and saving the file for retrieval on-site for the implementation of the experiments during beamtime.
- Direct data input into CDApps (Hussain et al. 2015) for data processing.
- Auto-fitting of binding curves for K_d determination using the non-linear regression analysis for one binding site (Siligardi et al. 2002, 2014).

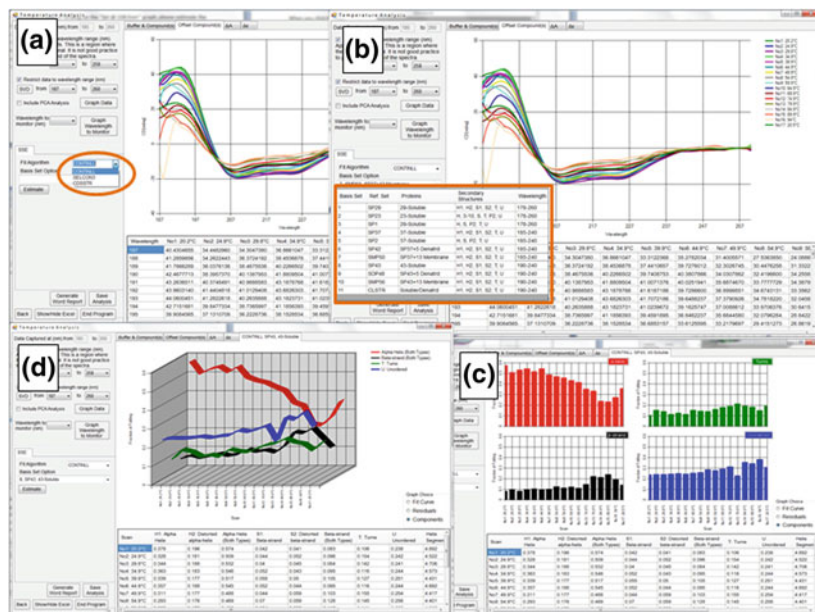


Fig. 5.15 Cascade of CDApps screens of CD Titration command: **a** Secondary Structure Estimation (SSE) for each of the CD spectra of the experimental data selected from CDApps as from the procedure illustrated in figure (a) screen (b). Circled in orange is the blue highlighted chosen algorithm, in this example CONTINLL for the SSE calculations (Sreerama and Woody 2004; Provencher and Glockner 1981). **b** Highlighted in orange are the datasets spectral libraries available from which to select the more appropriate for the SSE calculations. The consensus is to use the average SSE calculated from many dataset and more than one algorithm if a large variation in SSE is observed. **c** Bar chart representation of SSE for all CD spectra of screen (a). **d** 3D plot representation of the SSE calculations

For standard CD Measurements:

- Consecutive repeated (1 to n) scans, allowing the conversion to ΔA and $\Delta \epsilon$ and plotting of spectra automatically.
- UV denaturation assay, allowing the single wavelength plot to see the rate of change of the UV denaturation assay experiment on the screen as well as generating overlapping spectral plots in millidegrees, ΔA and $\Delta \epsilon$ automatically.
- Thermal denaturation measurements, allowing the creation of temperature script for input into the data acquisition operating system. Data analysed can be auto-fitted for T_m determination using the single Boltzmann equation algorithm at single wavelength and displayed overlaid spectra.
- 6-cell turret for up to 6 sample thermal measurements conducted in one experiment. Data splitting into six sample files for data processing of individual samples.

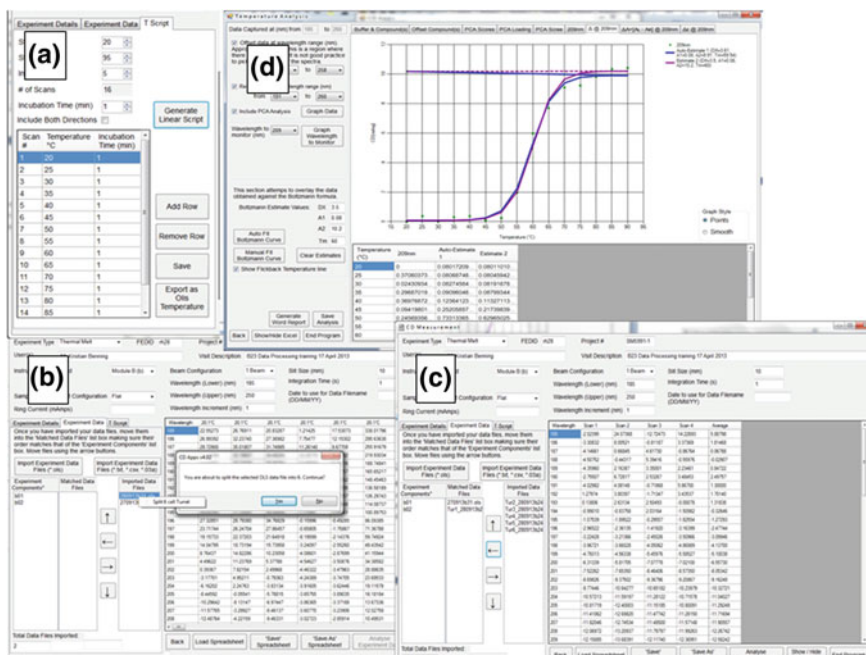


Fig. 5.16 Cascade of CDApps screens for SRCD temperature study of 6 samples conducted in one experiment using the 6-cell turret operated via script. **a** CDApps temperature script planning using the 6-cell turret. **b** Splitting of data from 6-cell turret into individual sample datafiles. **c** Selected data of one of the individual cells of the turret for data analysis. **d** Melting temperature (T_m) determination using the Boltzmann equation

- Protein secondary structure estimation content with choice of algorithms between CONTINL, CDSSTR, SELCON3 and various dataset libraries of reference spectra.
- Automated creation of the experimental report template, which includes the Users project number, title and abstract of the beamtime proposal, figures prepared from the processed data, list of experimental parameters, discussion and conclusions. This important feature is enabling the users to generate the experimental report rapidly and easily as part of the Diamond beamtime requirement process.

The outcome of the display using CDApps illustrated below (Figs. 5.13, 5.14, 5.15, 5.16 and 5.17) is for various scenarios: from accessing the software, viewing the visit details of the beamtime project, planning the experimental parameters for ligand-host titrations, access the excel workbook, calculate K_d and binding stoichiometry from CD titration data, estimation, not prediction, of secondary structure content from

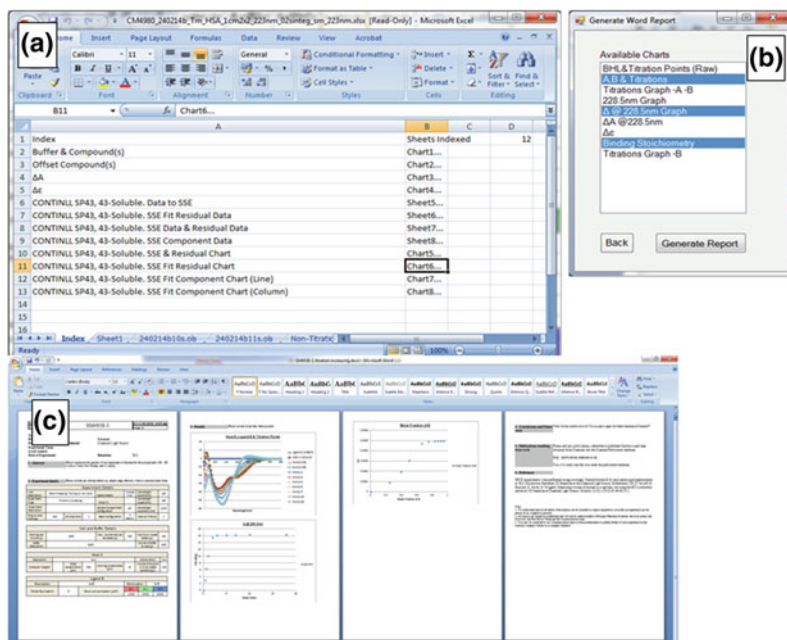


Fig. 5.17 Cascade of CDApps screens. **a** Indexing sheet in excel for chart location and report generation in word document. **b** List of figures of the SRCD beamtime data generated with CDApps. **c** Experimental report template created with CDApps for the users' beamtime visits that is compatible with Diamond's User Administration System (UAS) [<http://uas.diamond.ac.uk/uas/>] hence ready to be submitted online to Diamond User Office

SRCD data, access and editing temperature scripts for data acquisition, editing script for temperature study and analysis with determination of melting temperature T_m , 6-cell turret data splitting and generation of the experimental report.

The CDApps v4.0 can be found at Diamond B23 website (<http://www.diamond.ac.uk/Beamlines/Soft-Condensed-Matter/B23/manual/Beamline-software.html>). Documentation can be accessed on-site through CDApps itself or confluence page or at Diamond B23 website (<http://confluence.diamond.ac.uk/display/B23Tech/CD+Apps+documentation>). A summary of the CDApps feature is summarised in Table 5.3.

Table 5.3 Summary of the CDApps features

Features available	Notes
Identifying project number	Associated with beamtime visit
ΔA and $\Delta \epsilon$ auto-conversion	Base on molecular weight and concentration input
Overlay of 1 to n spectra	Comparative viewing and assessment
Kd auto and manual fitting	Non-linear regression single binding equation
Stoichiometric determination	Indication of single or more binding complex
Tm auto and manual fitting	Single Boltzmann algorithm
Secondary structure estimation for protein and peptide auto-fit from various reference dataset libraries and 3 main algorithms	CONTINLL algorithm
	CDSSTR algorithm
	SELCON3 algorithm
Single wavelength job plot	Monitoring change with temperature or UV denaturation
Splitting of data from 6-cell turret to individual 6 samples labelled with turret position	Specific turret positioned sample can be individually data processed
Copy of excel file compiled	Raw and processed data in one excel file
Report generation in word document	Include, project number, name of users, abstract from peer-reviewed proposal, experimental details, selected figures, discussion, conclusion and future work input by users, and references. Compatible with Diamond Experimental Report template in UAS system

We have also released a video tutorial available for viewing from B23 website with step by step live tutorial on how to process the variable temperature measurement as an example (<http://www.diamond.ac.uk/Beamlines/Soft-Condensed-Matter/B23/manual/Beamline-software/video-tutorials.html>).

Appendix 3: MemGold2 Crystallization Buffer Conditions

See Fig. 5.18.

A1 0.2M Magnesium chloride heptahydrate 0.1M Tris 7.5 1% w/v PEG 5000ME 0.005M Cadmium chloride hemipentahydrate	A2 0.1M Potassium acetate 0.02M Tris 7.0 44% w/v PEG 3000 0.07M Potassium chloride	A3 0.02M Magnesium sulfate heptahydrate 0.02M HEPES 6.0 0.02M Sodium chloride	A4 0.04M Magnesium sulfate heptahydrate 0.02M HEPES 5.5 0.1% w/v PEG 400 0.02M Sodium chloride	A5 0.05M Sodium sulfate 0.05M Tris 5.5 32% w/v PEG 400 0.05M L-methionine chloride	A6 0.1M Sodium phosphate monobasic monohydrate 0.1M Bis-Tris propane 7.5 0.1% w/v PEG 3300 0.1M Potassium phosphate dibasic	A7 0.1M Sodium chloride 0.1M ADA 5.5 11% w/v PEG 4000 0.1M L-methionine sulfate	A8 0.1M Lithium chloride 0.1M Sodium acetate 4.52% w/v PEG 400 0.1M Calcium chloride hemipentahydrate	A9 0.2M Ammonium sulfate 0.1M Sodium citrate 0.201% w/v PEG 2000 0.1M Sodium chloride	A10 0.2M Lithium sulfate 0.1M PEG 7.0 33% w/v PEG 400 0.1M Sodium chloride	A11 0.2M Ammonium phosphate monobasic 0.1M Sodium citrate 4.5 0.1M Ammonium sulfate	A12 0.05M Sodium citrate dibasic 0.2M Tris 5.5 1% w/v PEG 400 0.1M Potassium chloride
B1 0.1M Sodium chloride 0.1M HEPES 5.5 1% w/v PEG 1000 0.5M Ammonium sulfate	B2 0.01M NaCl sulfate heptahydrate 0.1M Sodium citrate 0.5 93% w/v PEG 2000	B3 0.02M Magnesium sulfate heptahydrate 0.02M HEPES 6.0 0.02M Sodium chloride	B4 0.02M Magnesium chloride heptahydrate 0.05M HEPES 5.5 1% w/v PEG 350ME	B5 0.02M Magnesium chloride heptahydrate 0.02M HEPES 7.0 33% w/v PEG 400	B6 0.03M Magnesium chloride heptahydrate 0.1M Tris 7.5 33% w/v PEG 400	B7 0.04M Sodium chloride 0.04M Tris 8.0 25% w/v PEG 350ME	B8 0.04M Magnesium sulfate heptahydrate 0.1M HEPES 6.0 36% w/v PEG 400	B9 0.05M NaCl acetate 0.05M ADA 6.3 11% w/v PEG 8000	B10 0.05M Magnesium acetate tetrahydrate 0.1M HEPES 6.0 26% w/v PEG 400	B11 0.05M Magnesium acetate tetrahydrate 0.1M Quin 3.5 31% w/v PEG 400	B12 0.06M Sodium chloride 0.2M Tris 7.5 3% w/v PEG 400
C1 0.07M Magnesium chloride heptahydrate 0.1M Sodium cacodylate 6.5 30% w/v PEG 2000 MPE	C2 0.08M Magnesium acetate tetrahydrate 0.1M Sodium citrate 0.5 1% w/v PEG 5000 MPE	C3 0.01M ZnO acetate 0.01M HEPES 6.0 15M Sodium chloride	C4 0.08M Ammonium sulfate 0.01M Tris 7.0 22% w/v PEG 250ME	C5 0.1M Magnesium chloride heptahydrate 0.1M Tris 7.5 13% w/v PEG 8000 MPE	C6 0.1M Magnesium formate dihydrate 0.1M HEPES 7.0 17% w/v PEG 3300	C7 0.1M Potassium chloride 0.1M Bis-Tris 6.0 18% w/v PEG 400	C8 0.1M Potassium chloride 0.1M Potassium phosphate 7.5 18% w/v PEG 400	C9 0.1M Potassium acetate tetrahydrate 0.1M HEPES 6.0 22% w/v PEG 400	C10 0.1M Calcium acetate hydrate 0.1M HEPES 6.0 22% w/v PEG 8000	C11 0.1M Ammonium sulfate 0.1M HEPES 6.5 23% w/v PEG 3300	C12 0.1M Potassium chloride 0.1M HEPES 6.0 32% w/v PEG 400
D1 0.1M Sodium chloride 0.1M HEPES 5.5 36% w/v PEG 300	D2 0.1M Sodium chloride 0.1M HEPES 6.0 45% w/v PEG 300	D3 0.15M Calcium chloride dihydrate 0.1M Quin 3.0 35% w/v PEG 400	D4 0.2M Ammonium sulfate 0.05M ADA 6.5 13% w/v PEG 400	D5 0.2M ZnO chloride 0.1M Tris 7.5 1% w/v PEG 2000 MPE	D6 0.2M Sodium chloride 0.05M HEPES 7.0 13% w/v PEG 1000	D7 0.05M Sodium chloride 0.05M HEPES 7.0 13% w/v PEG 1000	D8 0.2M Magnesium formate dihydrate 0.05M Tris 6.0 13% w/v PEG 3300	D9 0.2M Calcium chloride dihydrate 0.1M HEPES 6.0 20% w/v PEG 350ME	D10 0.2M Ammonium citrate 0.05M HEPES 7.0 20% w/v PEG 250	D11 0.02M Lithium chloride 0.02M Quin 6.0 33% w/v PEG 1000 0.05M Sodium cacodylate 5.5 22% w/v PEG 3000	D12 0.2M Calcium acetate hydrate 0.1M HEPES 7.0 24% w/v PEG 400
E1 0.2M Sodium acetate dihydrate 0.1M HEPES 6.5 28% w/v PEG 400	E2 0.2M Sodium chloride 0.2M Calcium acetate 5.0 29% w/v PEG 400	E3 0.2M Sodium chloride 0.1M Quin 3.0 29% w/v PEG 400	E4 0.2M Ammonium formate 0.1M Tris 7.0 31% w/v PEG 400	E5 0.2M Ammonium sulfate 0.1M Tris 8.5 35% w/v PEG 250	E6 0.2M Calcium acetate hydrate 0.1M Sodium acetate 5.0 38% w/v PEG 400	E7 0.2M Sodium chloride 0.05M HEPES 7.0 13% w/v PEG 400	E8 2.0M Ammonium sulfate 0.05M Tris 6.5 0.05M Sodium cacodylate 6.5 0.2M Sodium chloride	E9 0.25M Potassium chloride 0.1M HEPES 6.0 20% w/v PEG 400	E10 0.25M Sodium chloride 0.05M HEPES 7.0 4.5 33% w/v PEG 400	E11 0.25M Magnesium formate dihydrate 0.1M Sodium cacodylate 5.5 22% w/v PEG 3000	E12 0.25M Magnesium chloride heptahydrate 0.1M Tris 8.5 40% w/v PEG 1000
F1 0.3M Lithium sulfate 0.1M HEPES 5.5 25% w/v PEG 400	F2 0.3M Ammonium formate 0.05M Tris 3.0 33% w/v PEG 350ME	F3 0.3M Bis-tris chloride dihydrate 0.1M HEPES 6.0 34% w/v PEG 400	F4 0.3M Lithium chloride dihydrate 0.1M Sodium citrate 5.5 1% w/v PEG 400	F5 0.3M Ammonium sulfate 0.1M Sodium citrate 5.5 12% w/v PEG 400	F6 0.35M Lithium sulfate hydrate 0.1M Sodium acetate 4.0 11% w/v PEG 400	F7 0.37M Potassium citrate 0.1M HEPES 6.5 22% w/v PEG 400	F8 0.4M Ammonium sulfate 0.1M HEPES 6.5 10% w/v PEG 250	F9 0.4M Ammonium chloride heptahydrate 0.1M HEPES 7.5 12% w/v PEG 400	F10 0.4M Potassium citrate 0.05M HEPES 7.5 12% w/v PEG 400	F11 0.4M Ammonium thiocyanate 0.1M Sodium acetate 4.0 9% w/v PEG 400	F12 0.4M Sodium thiocyanate 0.1M Tris 8.5 1% w/v PEG 400
G1 0.5M Potassium chloride 0.05M HEPES 6.5 20% w/v PEG 400	G2 0.5M Magnesium chloride heptahydrate 0.05M Tris 7.5 21% w/v PEG 350ME	G3 0.1M Potassium formate 0.1M HEPES 7.0 31% w/v PEG 400	G4 0.1M HEPES 7.0 31% w/v PEG 8000	G5 0.1M HEPES 6.0 11% w/v PEG 20,000	G6 0.1M HEPES 6.5 14% w/v PEG 400	G7 0.1M ADA 5.5 14% w/v PEG 6000	G8 0.06M Tris 7.5 4.5 22% w/v PEG 300	G9 0.07M Sodium citrate 4.5 22% w/v PEG 300	G10 0.05M ADA 6.5 24% w/v PEG 400	G11 0.1M Sodium cacodylate 6.5 2% w/v PEG 1500	G12 0.1M HEPES 7.5 28% w/v PEG 400
H1 0.05M Tris 5.5 28% w/v PEG 400	H2 0.1M HEPES 3.0 31% w/v PEG 600	H3 0.1M ADA 7.0 31% w/v PEG 600	H4 0.1M Tris 8.5 32% w/v PEG 500ME	H5 0.1M HEPES 7.5 33% w/v PEG 400	H6 0.1M Sodium citrate 4.0 34% w/v PEG 3300	H7 0.1M Tris 8.5 44% w/v PEG 200	H8 0.1M Tris 8.5 65% w/v PEG 400	H9 2.75M Ammonium chloride 0.025M Bis-Tris 7.0	H10 2.8M Ammonium sulfate 0.1M HEPES 7.5	H11 3.0M Ammonium sulfate 0.1M HEPES 7.5	H12 3.25M 16-Picramide

Fig. 5.18 List of crystallization buffers displayed as 8 rows of 12 cells in the shape of the 96-well multiplate frame prepared from Molecular Dimensions, MemGold2™ MD1–63 datasheet (Molecular Dimensions, <https://www.moleculardimensions.com/products/4234-MemGold2/>)

References

- Armstrong JPK, Shakur R, Horne JP, Dickinson SC, Armstrong CT, Lau K, Kadiwala J, Lowe R, Seddon A, Mann S, Anderson JLR, Perriman AW, Hollander AP (2015) Artificial membrane-binding proteins stimulate oxygenation of stem cells during engineering of large cartilage tissue. *Nat Commun* 6:7405
- Berova N, Nakanishi K, Woody RW (2000) Circular dichroism principles and applications, 2nd edn. Wiley-VCH, New York
- Bortolini C, Kartanas T, Copic D, Morales IC, Zhang Y, Challa PK, Peter Q, Jávorfí T, Hussain R, Dong M, Siligardi G, Knowles TPJ, Charmet J (2019) Resolving protein mixtures using microfluidic diffusional sizing combined with synchrotron radiation circular dichroism. *Lab Chip* 19:50–58
- Brogan APS, Sharma KP, Perriman AW, Mann S (2014) Enzyme activity in liquid lipase melts as a step towards solvent-free biology at 150 C. *Nat Commun* 5:5058
- Fasman GD (ed) (1996) Circular dichroism and the conformational analysis of biomolecules. Springer
- Hussain R, Benning K, Myatt D, Jávorfí T, Longo E et al (2015) CDApps: integrated software for experimental planning and data processing at beamline B23 Diamond Light Source. *J Syn Rad* 22:465–468
- Hussain R, Jávorfí T, Siligardi G (2011) Circular dichroism beamline B23 at the Diamond Light Source. *J Synchrotron Radiat* 19:32–135
- Hussain R, Jávorfí T, Siligardi G (2012) Spectroscopic analysis: synchrotron radiation circular dichroism. *Compr Chirality* 8:438–448

- Hussain R, Siligardi G (2016) Characterisation of conformational and ligand binding properties of membrane proteins using synchrotron radiation circular dichroism. The next generation in membrane protein structure determination. *Adv Exp Med Biol* 922:43–59
- Hussain R, Javorfi T, Rudd TR, Siligardi G (2016) High-throughput SRCD using multiwall plates and its applications. *Sci Rep* 6:38028–38033
- Hussain R, Joannou C, Siligardi G (2006) Identification and characterization of novel lipophilic antimicrobial peptides derived from naturally occurring proteins. *Int J Pep Res Ther* 12:269–273
- Laera S, Ceccone G, Rossi F, Gilliland D, Hussain R, Siligardi G, Calzolari L (2011) Measuring protein structure and stability of protein nanoparticle systems with synchrotron radiation circular dichroism. *Nano Lett* 11:4480–4484
- Molecular dimensions. <https://www.moleculardimensions.com/products/4234-MemGold2/>
- Pazderková M, Profant V, Seidlerová B, Dlouhá H, Hodačová J, Javorfi T, Siligardi G, Baumruk V, Bednářová L, Maloň P (2014) Electronic circular dichroism of the chiral rigid tricyclic dilactam with nonplanar tertiary amide groups. *J Phys Chem B* 118:11100–11108
- Provencher SW, Glockner J (1981) Estimation of globular protein secondary structure from circular dichroism. *Biochemistry* 20:33–37
- Siligardi G, Hussain R (1998) Biomolecules interactions and competitions by non-immobilised ligand interaction assay by circular dichroism. *Enantiomer* 3:77–87
- Siligardi G, Hussain R (2010) Applications of circular dichroism. In: Lindon J, Tranter G, Koppenaal D (eds) *Encyclopedia of spectroscopy and spectrometry*, vol 1, 2nd edn. Elsevier, Oxford, pp 9–14
- Siligardi G, Hussain R (2015) CD spectroscopy: an essential tool for quality control of protein folding. In: Raymond JO (ed) *Structural proteomics: high throughput methods, methods in molecular biology*, vol 1261. Springer, New York, pp 255–276
- Siligardi G, Panaretou B, Meyer P, Singh S, Woolfson DN, Piper PW, Pearl LH, Prodromou C (2002) Regulation of Hsp90 ATPase activity by the co-chaperone Cdc37p/p50cdc37. *J Biol Chem* 277:20151–20159
- Siligardi G, Hussain R, Patching SG, Phillips-Jones MK (2014) Ligand- and drug-binding studies of membrane proteins revealed through circular dichroism spectroscopy. *Biochim Biophys Acta* 1838:34–42
- Sreerama N, Woody RW (2004) On the analysis of membrane protein circular dichroism spectra. *Protein Sci* 13:100–112

Chapter 6

Dynamic Light Scattering (DLS)



Principles, Perspectives, Applications to Biological Samples

Sven Falke and Christian Betzel

Abbreviations and Acronyms

ACF	Auto-Correlation Function
BSA	Bovine Serum Albumin
DDLS	Depolarized Dynamic Light Scattering
MALS	Multi-Angle Light Scattering
MES	2-(<i>N</i> -morpholino)ethanesulfonic acid
ML-I	Mistletoe Lectin I
PDI	Polydispersity Index
PDMS	Polydimethylsiloxane
SANS	Small-Angle Neutron Scattering
SARS	Severe Acute Respiratory Syndrome
SAXS	Small-Angle X-ray Scattering
SLS	Static Light Scattering
Tris	Tris(hydroxymethyl)aminomethane
XFEL	X-ray Free Electron Lasers

Focus a laser on dissolved particles and analyze the scattered light to reveal their size. This well established principle is used in dynamic light scattering (DLS), or also called photon-correlation spectroscopy, which is a widely popular and highly adaptable analytical method applied in different fields of life and material sciences, as well as in industrial quality control processes. Fluctuations of elastic laser light scattering due to the particle's individual *Brownian motion* in a solvent can be

S. Falke · C. Betzel (✉)

Laboratory for Structural Biology of Infection and Inflammation, Department of Chemistry, University of Hamburg, c/o DESY, 22607 Hamburg, Germany
e-mail: Christian.Betzel@uni-hamburg.de

S. Falke

e-mail: Falke@chemie.uni-hamburg.de

© Springer Nature Switzerland AG 2019

A. S. Pereira et al. (eds.), *Radiation in Bioanalysis*, Bioanalysis 8,
https://doi.org/10.1007/978-3-030-28247-9_6

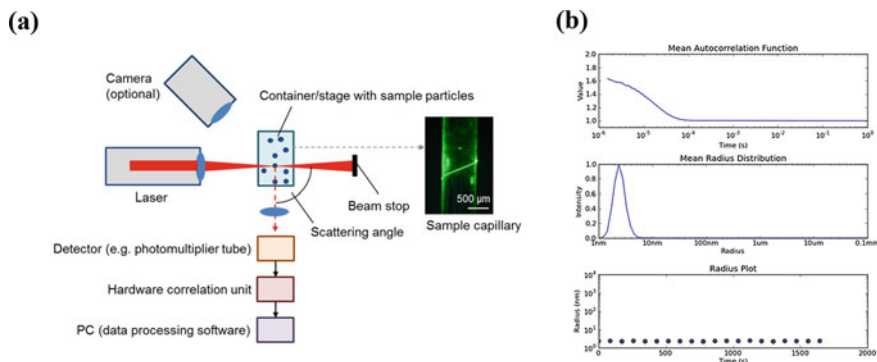


Fig. 6.1 **a** Scheme of a light scattering setup. Light scattered by the particles over time at a scattering angle θ is focused onto a detector or detector-connected fiber cable for further downstream data processing. **b** Exemplary DLS data of an L-form DNAzyme (5'-GAAGTTAGCAACATCGATCGGAGGCGG-3') in solution containing MES buffer as evaluated by the accompanying software. *Autocorrelation function*, *half-logarithmic mean particle radius distribution* and *particle radius plot* of the molecules are indicating a homogeneous monodisperse solution and a hydrodynamic radius of 2.4 ± 0.1 nm. Details about data processing are described in the following sections

utilized to determine particle size distributions in real-time. DLS usually uses non-invasive visible laser light that is focused on a sample solution, suspension, emulsion or aerosol inside a sample container, commonly a cuvette or a capillary. Besides, a few more general components are required for a typical DLS device, as shown in Fig. 6.1.

The method DLS and underlying principles are known for several decades already (Mueller and Givens 1961; Cummins et al. 1964; Chu 1970; Fujime 1972), whereas the development of single-mode fiber cables, improvement of detection optics, variation of sample containers and introduction of affordable diode-pumped solid-state lasers as light source advanced the applications of DLS tremendously later on and particularly during the last years (Brown 1987; Dhadwal and Chu 1989; Brown and Smart 1997; Minton 2016). In terms of data processing, digital autocorrelators (Foord et al. 1970), the monomodal cumulant analysis (Koppel 1972) and the CONTIN algorithm (Provencher 1982) are a few of the milestones.

After briefly explaining the physical principles and requirements of light scattering techniques, different biological samples, recently established setups for in situ DLS experiments and selected applications will be introduced. An additional section will provide practical guidelines and hints for sample preparation. Further a short section is summarizing selected complementary analytical methods. The chapter overall focuses on exemplary biochemical sample solutions and the respective applications, even though all principles are well applicable to other fields of natural sciences targeting nano particles. Areas of applications and especially much further physical detail of light scattering and data processing were covered for example by Berne and Pecora (2000) and within the series of *Light Scattering Reviews* books edited by

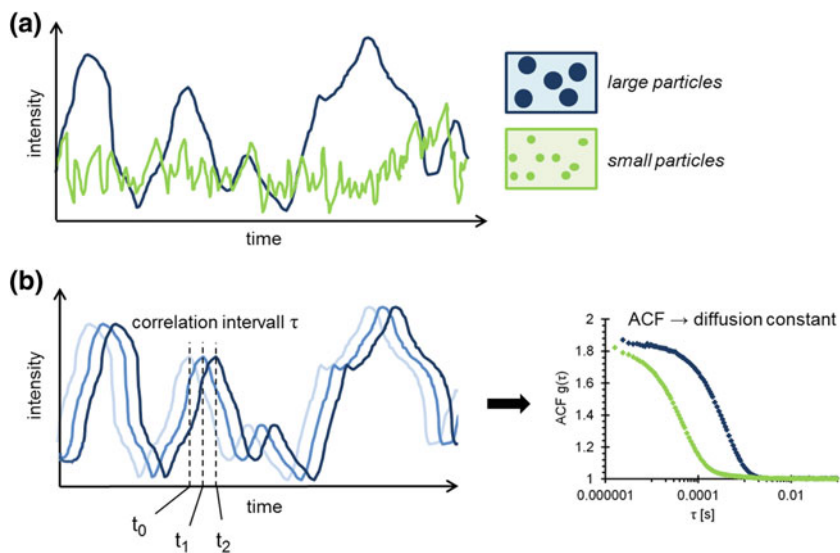


Fig. 6.2 DLS determines particle sizes based on the velocity of Brownian motion: **a** Generalized illustration of the time-dependent intensity of light scattered by particles, which is fluctuating due to Brownian motion. Mixtures of small and large particles would result in a weighted average of the two displayed scattering intensity pattern. **b** Schematic illustration of the auto-correlation. Depending on the particle size, the diffusion speed and hence the time scale of the correlation coefficient decay is varying. Accordingly two auto-correlation functions ($g(\tau)$) for a small (green) and a larger (blue) particle species are shown on the right side

Kokhanovsky (2006). Exemplary biological applications were discussed in addition more recently (Minton 2016).

In general, all kinds of particles scatter electromagnetic waves in all directions, depending on their size isotropically or anisotropically. The laser light that is scattered by the particles inside a small focal volume of a DLS sample is continuously recorded and quantified by a photon-counting detector positioned at a specific angle; if not hindered by other geometrical restraints, an angle of 90° might be suitable for the experimental setup. The number of photons hitting the detector, which can be a photomultiplier tube, is fluctuating over time. This is explained by Brownian motion of particles in and around the sample volume that is in focus of the laser (Fig. 6.2), which results in characteristic *size-dependent* fluctuation intervals of the electric field component of the scattered light. Scattering intensity patterns are correlated with themselves (*auto-correlation*) after short delay intervals of time (τ) to monitor the continuous decay of correlation. Depending on how fast particles are diffusing, the correlation decay time constants, which are derived from the exponential **auto-correlation function (ACF)** are individually different. Decay time constants of small particles are shorter in agreement with the dependency of diffusion speed on particle mass (Fig. 6.2). The ACF can be evaluated by the **CONTIN** algorithm according to Provencher (1982), which allows to fit even a complex decay of correlation in

polydisperse solutions to calculate the respective diffusion constants (D) and process the data. As for most measurements the temperature T is kept constant and the viscosity η of the sample solution is known, or can be determined rather easily, this translational diffusion constant D can be used to determine the **hydrodynamic radius** r_h of a corresponding spherical particle, according to the **Stokes-Einstein equation** (Eq. 6.1). This relationship between diffusion and size was established in 1906 and is also useful for complementary methods like Taylor-Dispersion analysis or nano particle tracking analysis (k_B is the *Boltzmann constant* $1.380648 \times 10^{-23} \text{ J K}^{-1}$):

$$D = \frac{k_B T}{6\pi \eta r_h} \quad (6.1)$$

Depending on the implemented auto-correlation unit (and a few other parameters of the setup), particles in a wide range of hydrodynamic radii, typically from below 1 nm up to a few μm , which corresponds to a molecular weight range from approx. 10 kDa to several MDa for compact globular macromolecules, can be investigated. Further, all changes of D over time for given particles, typically due to particle size changes, can also be followed in real time. DLS is very often used in preparation and systematic optimization of sample solutions (pH-value, ionic strength, solvent etc.) to meet strict requirements of particle homogeneity and long-term stability in further structural investigation of macromolecules, see e.g. Borgstahl (2006) in terms of X-ray crystallography or exemplified for RNA-protein complexes (Stetefeld et al. 2016). In this context DLS is frequently used in combination with other scattering techniques or mass spectrometry. For example small-angle X-ray scattering (SAXS), NMR spectroscopy and crystallization experiments usually require a high degree of particle size homogeneity, i.e. a monodisperse solution (Jeffries et al. 2016). Today, individual light scattering techniques and setups allow to manipulate the solution composition during the experiment (Meyer et al. 2012), investigate sample solutions in flow, to investigate a sample suspension at different neighboring positions in parallel (Falke et al. 2018), determine the net surface charge of molecules (Ware 1974) or even allow to obtain limited shape and structure information in situ (Cantor and Schimmel 1980; Minton 2007; Haghighi et al. 2013; Schubert et al. 2015) as outlined in following sections of this chapter. Especially for in situ DLS instruments with freely adjustable laser probe the alignment of the optics, i.e. the superposition of the focal points of the laser and the focal point of the lens that focusses the scattered light on a receiver fiber should be verified via a set of screws with μm precision to obtain optimal performance.

6.1 Principles of Light Scattering

In contrast to methods like Raman spectroscopy, DLS is based on *elastic* electromagnetic scattering of the dispersing particles. The electric field component of laser light waves is interacting with sample molecules by inducing oscillating (point source)

electric dipoles within the molecule at the same frequency, resulting in the emission of light. Light is scattered spherically in all directions, while maintaining nearly constant energy of the photons. Most samples of interest for a biochemist, like proteins in solution, are much smaller than the wavelength of the applied DLS laser ($<0.1\lambda$) allowing light penetration and isotropic scattering according to the laws of **Rayleigh scattering** (Barnett 1942) named after the British physicist Lord Rayleigh. The scattered light is typically not coherent and the spherical waves interfere with each other. The intensity of scattered light I depends on other setup parameters such as the wavelength λ , the scattering angle θ , the distance from the scattering particle s , the refractive index n of the medium and the particle radius r :

$$I = I_0 \frac{16\pi^4}{\lambda^4} \frac{1 + \cos^2\theta}{2s^2} \left(\frac{n^2 - 1}{n^2 + 2} \right)^2 r^6 \quad (6.2)$$

The average value of I over all scattering angles is commonly called **scattering cross section**. The scattering intensity is notably inverse proportional to the forth power of the laser wavelength, which makes a shorter wavelength very attractive for the detection of otherwise weakly scattering molecules. However, an increased intensity of “background” reflections of laser light can obviously reduce the sensitivity of the instrument again. Further, the focal lengths of lenses should be shortened as possible, according to $I \sim s^{-2}$. Also probe position and fiber cables should be optimized accordingly. For additional optimization, glass surfaces may be coated with a thin layer of MgF_2 or a similar solid material with low refractive index, to minimize reflection of laser light. Further, the light scattering intensity depends on the sixth power of the particle diameter. Consequently, larger particles contribute to the total scattering intensity exponentially more with increasing size, making DLS particularly sensitive for clustering (very large oligomers or unspecific large aggregates) compared to smaller molecules. When the diameter of the particles increases to the size regime of the laser wavelength, the particles create shape dependent anisotropic **Mie scattering** (referring to the German physicist Gustav Adolf Mie) distorted in forward direction (Mie 1908). One example is sun light scattered by spherical lipid droplets in diluted milk. For particles significantly larger than the wavelength, surface reflection becomes predominant and the scattering cross section, which determines how much light is scattered by the particle, only weakly depends on the light frequency.

Accordingly, it is important to consider a suitable scattering angle for an experimental DLS setup. DLS measurements of inhomogeneous and therefore polydisperse solutions with large particles should ideally be expanded to measurements at different scattering angles exploiting multi-angle light scattering (MALS) (Fernández and Minton 2009). MALS is beneficially combined with size-exclusion chromatography, which can optionally be equipped with a UV absorbance and refractive index detector for a most accurate approximation of the molecular weight M (Graewert et al. 2015; Minton 2016) of unknown biological macromolecules using scattering intensity I and refractive index RI :

$$I = \left(\frac{dn}{dc} \right)^2 cM \quad (6.3)$$

$$\text{and } RI = \frac{dn}{dc} c \quad (6.4)$$

6.2 Scattering Data Processing

As illustrated by Fig. 6.2, an ACF of scattered light at time point t , depending on the correlation time delay τ , is generated during a DLS experiment. A second order ACF is generally given by:

$$g(\tau) = \frac{\langle I(t)I(t+\tau) \rangle}{\langle I(t)^2 \rangle} \quad (6.5)$$

The additional brackets indicate averaging over time of the respective intensity value products in a single measurement. For experiments that use different scattering angles and therefore different values for the scattering vector q , g depends on τ and q , as summarized by Provencher and Štěpánek (1996). In good approximation a DLS ACF can also be expressed and fitted as the following exponential function (or multiple exponential functions), where b_∞ is the ACF baseline value at infinite values of time delay, b_0 is the maximum ACF value at a time delay of nearly zero and Γ is a measure for the decay rate (Chu 1991):

$$g(\tau) = b_\infty + b_0 \exp(-2\Gamma\tau) \quad (6.6)$$

In principle this exponential ACF function can be evaluated using an algorithm in order to obtain values for D and a mean radius distribution with multiple particle species, e.g. in a sample suspension: Γ is proportional to the diffusion constant D for a given DLS setup (Eq. 6.7), n_0 is the solvent's refractive index, θ the scattering angle and λ the wavelength in vacuum.

$$\Gamma = Dq^2 = D \left(\frac{4\pi n_0 \sin \frac{\theta}{2}}{\lambda} \right)^2 \quad (6.7)$$

The scattering vector q is used to determine D , which allows to calculate r_h based on the Stokes-Einstein equation (Eq. 6.1). D and subsequently r_h values with standard deviations can be directly obtained from the CONTIN algorithm (Provencher 1982), which is solving the inverse Laplace transform of the ACF for the size distribution analysis. As an alternative, a **cumulant analysis** of the ACF (Friskén 2001) can be applied, which provides polydispersity index (PDI) and the intensity weighted Z-average size value. PDI can express the homogeneity of the radii: For a Gaussian

size distribution of a single particle species the width or standard deviation (σ) of an individual r_h peak is squared and divided by the square of the mean size to yield the PDI. The distribution of r_h values can commonly be weighted by molecular mass, volume, particle number or scattering intensity.

Assuming that the investigated particle is *spherical*, the molecular weight (M) of dissolved macromolecules might be approximated as following, which is explained in more detail elsewhere (Cantor and Schimmel 1980). V_S is the specific particle density, the hydration is represented by h (mass of water per mass of protein) and N_A is the Avogadro constant:

$$r_{h,theor} = \left(\frac{3M(V_S + h)}{4\pi N_A} \right)^{\frac{1}{3}} \quad (6.8)$$

For *non-globular* particles the mass equivalent spherical radius is usually smaller than the determined r_h . The Perrin factor F , which is the ratio of the frictional coefficients of the mass equivalent solid sphere (f_s) and the sphere corresponding to the measured r_h (f_h), provides a first estimate about the degree of elongation of an ellipsoid particle. The frictional coefficients are derived from Stokes law as specified by Eq. 6.9, with the inclusion of Eq. 6.8, with l being the thickness of a single solvent layer:

$$F = \frac{f_s}{f_h} = \frac{6\pi\eta(r_h - l)}{6\pi\eta r_{h,theor}} = (r_h - l) \left(\frac{4\pi N_A}{3M(V_S + h)} \right)^{\frac{1}{3}} \quad (6.9)$$

6.3 Sample Preparation and Selected Results

The capability of DLS to determine particle size distributions in a wide size range and to roughly compare the quantity of particles in different samples via the scattering intensity opens applications for a variety of different samples. Further, indirectly it is also possible to determine the solution viscosity applying a sample with known hydrodynamic radius r_h , which is shifting to a higher or lower r_h value proportional to the viscosity difference according to the Stokes-Einstein equation.

In preparation of samples even minor amounts of artificial large environmental particles need to be removed due to their disturbing scattering properties, i.e. a “shielding” effect of the weaker scattering of smaller particles (Eq. 6.2) and the limited size-resolution in a typical DLS experiment (Ruf 1993; Karow et al. 2015). Next to other optical parameters those environmental particles also hinder the characterization of particles larger than approx. 1 μm . Most commonly sample solutions are simply filtered or centrifuged at the time of the experiment or fractionated according to their size by chromatographic methods. Also extensive optimization of solution additives or ultra-centrifugation typically helps to minimize polydispersity

and undesired peak broadening. High-throughput additive screens for optimization of the solution dispersity are supported by experiments in multi-well plates, which are ideally covered by transparent oil rather than by foils to hinder evaporation of aqueous solutions. Cleanness of optical and quartz glass components can be maintained by removing dust particles by pressured air and other remaining material by diluted nitric acid.

Hydrodynamic radii of some exemplary proteins and other biological samples investigated by DLS are listed in Table 6.1. To also ensure that r_h is not concentration dependent, typically in an artificial manner, the diffusion constant D can be determined at different concentrations. Those diffusion constants should be evaluated by a Debye plot. A linear dependency of D on the concentration allows to extrapolate D to a value at infinite dilution (unbiased by attractive or repulsive interactions), similar to the extrapolation of size parameters in X-ray scattering data processing. A high correlation value of the ACF at correlation time values of nearly zero (y-axis intercept), which is considered as an essential “signal-to-noise ratio” parameter, will obviously improve the accuracy of the ACF evaluation. However, if the sample concentration is too high or the solution becomes nearly non-transparent, the ACF and the applicability of DLS will suffer from multiple photon scattering. The calculation of an ACF can generally be completed in around 2 s. Nonetheless, static DLS experiments are typically running for 10–30 s and are repeated several times for averaging and verification. Scattering intensity data of weakly scattering molecules can to some extent be statistically improved by prolonging the measurement time. Required minimum concentrations heavily depend on several parameters of the instrumentation, most obviously laser intensity and detector sensitivity. Commonly, a monomeric protein of 30–40 kDa has a sufficient scattering intensity at concentrations of around 1–2 g l⁻¹ (or around 50 μM) in a typical cuvette DLS instrument. For larger proteins the concentration can be reduced according to $I \sim r^6$.

Based on the considerations before, DLS is most suitable to study macromolecule degradation, disassembly, homo- and hetero-oligomerization, polymerization (also enzyme-catalyzed), clustering and amplification in real-time. Examples are the pH-dependent dissociation and hydrolysis of Apoferritin (Jaenicke 1987), human prion protein (PrP) aggregation upon specific proteolytic cleavage or UV irradiation (Georgieva et al. 2004; Redecke et al. 2009) stages of protein crystallization (Dierks et al. 2008; Meyer et al. 2012; Oberthuer et al. 2012; Schubert et al. 2017), monitoring density of cell culture (Loske et al. 2014), assembly of lipid nano discs (Petrache et al. 2016) and pharmaceutical kinetics (Fávero-Retto et al. 2013). For some of these experiments the option to adjust the temperature is essential and also allows to investigate and optimize the thermal stability or assembly of a native biological macromolecule. Figures 6.3 and 6.6 further display DLS data of crystallization processes exemplified by the protein mistletoe lectin I (ML-I) from *Viscum album* and ferritin. After addition of the precipitant solution larger clusters and nanocrystals are forming while the smaller protein oligomers observed in the beginning are still highly abundant. Typically 2–4 major fractions of particles sizes are observed in parallel towards later stages of crystal growth, recognized for different proteins with different solution composition.

Table 6.1 Hydrodynamic radii of selected exemplary biological particles with different shape in a broad molecular weight range

Sample particle	MW ^a (kDa)	Structure/composition	r _h (nm)	Sample container	Experiment reference
n-dodecyl-β-D-maltopyranoside	–	Globular micelles forming in aqueous solutions	3.3 ± 0.5	Quartz cuvette	Meyer et al. (2015)
Influenza virus particles	–	Enveloped virus particles, Influenza A (H5N1)	59 ± 4	Quartz cuvette	Vajda et al. (2016)
Aprotinin	6.5	58 amino acids, Kunitz-type serine protease inhibitor, 3 disulfide bonds	1.8 ± 0.1	Quartz cuvette	Stetefeld et al. (2016)
Prion (hPrP ^{Sc} ; amino acids 121–231)	13	Soluble partially unfolded monomeric domain of recombinant human prion protein in acetate buffer	1.9 ± 0.1	Quartz cuvette	–
RNase A	14	154 amino acids, typically monomeric, nearly globular ribonuclease	2.0 ± 0.2	Capillary	Falke et al. (2018)
OvEC-SOD	40	Dimeric extracellular <i>Onchocerca volvulus</i> super oxide dismutase (Monomer: 20 kDa)	2.2 ± 0.1	Quartz cuvette	Falke et al. (2018)
West Nile virus RNA 5'-translated region	48	Elongated RNA; the non-globular shape is indicated by nearly identical values for r _h and radius of gyration (r _g)	3.5 ± 0.1	Quartz cuvette	–
BSA	66	383 amino acids, predominantly monomeric, acidic pI; dissolved in phosphate buffered saline	5.1 ± 0.1	Quartz cuvette	Deo et al. (2014)
SARS Coronavirus main protease	69	Dimeric protease cleaving pre-processed polyproteins	3.5 ± 0.4	Quartz cuvette	Falke et al. (2018)
SARS Coronavirus main protease R298A	34	Predominantly monomeric and reduced in catalytic activity due to the point mutation	4.2 ± 0.1	Multi-well plate	–
			3.5 ± 0.1	Multi-well plate	–

(continued)

Table 6.1 (continued)

Sample particle	MW ^a (kDa)	Structure/composition	r _h (nm)	Sample container	Experiment reference
S-layer protein slp-B53	116	Elongated surface layer protein from <i>Lysinibacillus sphaericus</i> ; monomeric state	4.9 ± 1.1	Multi-well plate	Liu et al. (2017)
Nidogen-1	139	Protein of the extra-cellular matrix	6.8 ± 0.1	Quartz cuvette	Patel et al. (2014)
Aldolase	158	Heterotetrameric glycolytic enzyme; 50 mM Tris, 150 mM NaCl, pH8.0	5.0 ± 0.1	Quartz cuvette	Stetefeld et al. (2016)
Apo ferritin	440	24-meric globular complex, one function is iron storage	7.8 ± 0.3	Capillary	Falke et al. (2018)
Human thyroglobulin	670	Dimeric globular protein of the follicular cells; 50 mM Tris, 150 mM NaCl, pH8.0	8.7 ± 0.2	Quartz cuvette	Stetefeld et al. (2016)

^aTotal molecular weight expected for the oligomeric state in solution and the respective solution composition

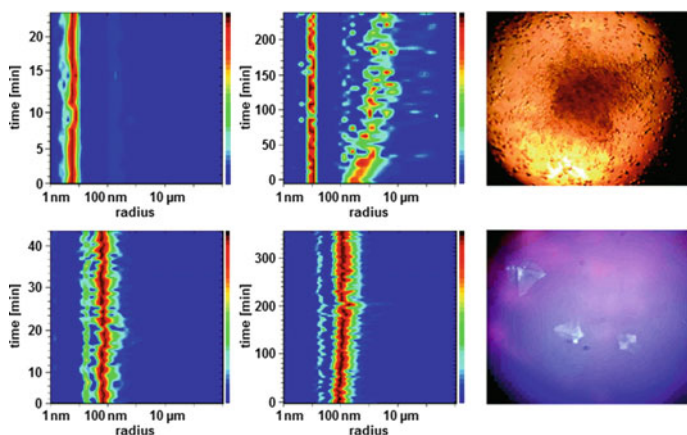


Fig. 6.3 The half-logarithmic size distribution plots on the left were recorded applying ML-I (top left) and ferritin (bottom left) in solution respectively. The plots in the middle display the respective size-distribution over time after mixing with an appropriate crystallization solution. The abundance of radii is color-coded from blue (low) to red (high). The pictures obtained from a microscope show crystals grown upon long-term incubation. The displayed ferritin crystals (bottom right), which are $>100 \mu\text{m}$ in all dimensions in size, are exposed to UV-light as well to confirm the intrinsic fluorescence of the protein. Reproduced from Dierks et al. (2008), *Crystal Growth and Design* with permission of the American Chemical Society, copyright 2008

6.4 *In Flow* DLS

As DLS is determining particle sizes based on Brownian motion, it is not self-evident that sample solutions can be analyzed while they are flowing. However, it is well established that below a critical velocity the ACF of scattering particles for a nearly laminar flow is dominated by Brownian motion and the resulting hydrodynamic radii are consequently not significantly different compared to static samples. The application of DLS under shear flow conditions and in a microfluidic channel, both mathematically and via an initial experimental approach with regard to flow channel dimensions, shear rate, velocity profile of the Poiseuille flow and Doppler shift interferences has been verified (Destremaut et al. 2009). The obtained theoretical approximation of an ACF with some geometrical restrains underlined the applicability of DLS in flow mode. The DLS experiments in this study were performed in a widened channel segment of a microfluidic PDMS chip with dimensions of 500 by 700 μm . Further stopped-flow DLS experiments have already been performed to study stages of protein folding (Gast et al. 1997) and characterize spherical latex particles in flow utilizing a specific fiber optic laser probe (Leung et al. 2006). This experimental setup is potentially indicating a huge variety of further applications to count and determine the size of macromolecules in place and in flow.

To properly design innovative DLS instrumentation for characterization of samples in flow, orientation of the scattering vector as well as velocity profile of the sample need to be taken into account. Moreover, the focal volume of the laser should

be minimized in order to minimize the time required for the particles to pass the scattering volume at a certain flow rate (Taylor and Sorensen 1986). The applicability of sample solutions in shear flow to DLS is also interesting due to the altered oligomerization, fiber formation or aggregation of protein molecules recognized under shear flow stress, which is still lacking some understanding (Bekard et al. 2011; Dobson et al. 2017).

6.5 Latest Methods and Experimental DLS Setups

As discussed, DLS is a highly adaptable technique, which can be applied in situ to characterize samples in various sample containers in different phase states and under different physico-chemical environments, as well as in flow. Besides, DLS setups were expanded and varied even further.

6.5.1 Cross-Correlation and Multi-channel DLS

Light scattering samples with a very high particle concentration or otherwise not perfectly transparent samples are more prone to multiple light scattering (Fernández and Minton 2009). The respective data sets can be analyzed by utilizing a particular **3D cross correlation** DLS setup (Medebach et al. 2007; Block and Scheffold 2010). It contains a split laser beam, which essentially hits the sample particles typically at two different angles with the same scattering vector. A potential contribution of multiple scattering is expected to vary for the two scattering pattern recorded in parallel, whereas the contribution of single scattering remains constant. Thereby, a cross-correlation of two intensity pattern can identify and suppress multiple scattering. Alternatively, for highly dense colloidal suspensions, gels or biological media, which scatter even stronger, *diffusing-wave spectroscopy* is most suitable (Zakharov et al. 2006).

In contrast to cross-correlation DLS, the term multi-channel DLS was recently used for a setup that allows to record multiple DLS data sets in parallel (Falke et al. 2018). The setup uses one laser and records the scattering data in different neighboring and statistically independent positions of a sample solution close to the focal point of the laser. Each data set is processed by an individual detector. This is most time efficient and also allows to see local differences at different positions of a solution or suspension.

6.5.2 Electrophoretic Light Scattering

In combination with a homogeneous electric field, DLS can be utilized to determine the electrophoretic mobility and thus the Debye-Hückel-Henry charge of unknown particles, which is called *electrophoretic light scattering* (Ware 1974; Minton 2016). The underlying principle is the quantification of the Doppler effect of the light scattered by particles migrating in the electric field: The light scattered by particles in the direction of migration, i.e. towards the oppositely charged electrode, is upshifted in its frequency, while the frequency in the opposite direction is downshifted. At equal intensity of incident light, the difference of these frequencies is proportional to the electrophoretic mobility.

6.5.3 Depolarized Dynamic Light Scattering (DDLS)

Some DLS setups investigate intrinsic birefringence or form birefringence (Allen 1996), i.e. anisotropy of the individual molecule, or a crystal lattice, in order to obtain valuable additional information on structure and shape of dissolved particles. The DDLS method quantifies depolarization of the scattered light using additional optical components, e.g. as essentially described before (Schubert et al. 2015; Rifaie-Graham et al. 2018) as well as illustrated by Fig. 6.4. This is particularly challenging due to rather low intensities of depolarized light and multiple scattering of

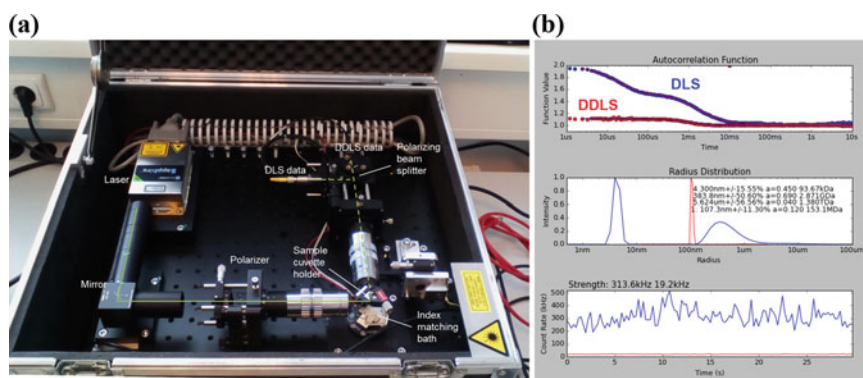


Fig. 6.4 **a** Portable DDLS cabinet. The path of the laser beam is indicated by green lines; light scattered by particles inside the cuvette is represented by dashed lines. A CPU is attached for data processing and display. **b** A single exemplary 20 s measurement to monitor the oligomerization process of the bacterial β -lactamase CTX-M14 (30 kDa) in an early stage of crystallization. The DLS autocorrelation function (blue spheres and lines) indicates a polydisperse sample solution containing a mixture of small oligomers with a radius of approximately 4 nm and larger particles with a radius of a few hundred nm. The intensity of scattered light that is depolarized is quantified by a separate detector (red spheres and lines)

light which perhaps kept the method from being more common till now. In addition to the translational diffusion constant (Eq. 6.1) the *rotational diffusion constant* D_{rot} is calculated to evaluate the ACF of the depolarized light scattering according to the similar Stokes–Einstein–Debye equation:

$$D_{rot} = \frac{k_B T}{8\pi \eta r^3} \quad (6.10)$$

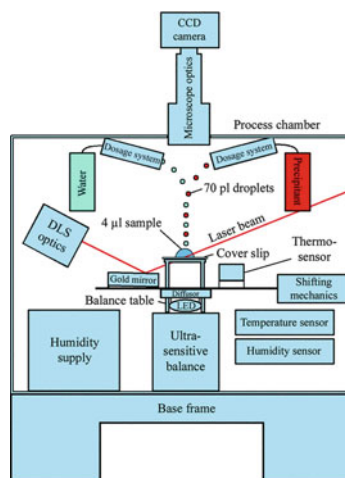
A combination of both diffusion constants allows to calculate the dimensions of both half axes of elongated particles, e.g. fibers, virus particles or synthetic nano particles or tubes, considered as rotational ellipsoids (Glidden and Muschol 2012). Based on the birefringence of crystals, DDLs was also utilized to distinguish between protein nano and micro crystals and amorphous precipitation, e.g. for glucose isomerase (Schubert et al. 2015). Rod-shaped gold particles are frequently used for calibration. Besides, oxygen-binding *Limulus polyphemus* hemocyanin, which is forming large hexa-, dodeca- and 24-mers were applied as well as the oblate membrane-bound photosystem I for which dimensions of 10 by 26 nm were determined in good agreement with X-ray diffraction data (Chayen et al. 2004; Beltramini et al. 2005). The method was discussed to be ideally suitable for scoring of protein crystal suspensions used at X-ray free-electron laser (XFEL) sources also in combination with second order harmonic generation (SHG) microscopy.

6.5.4 “Combinatory” Devices for Online Sample Scoring

As discussed DLS is most suitable to verify sample homogeneity to match a high standard of sample quality in nano particle sample preparation towards imaging and manufacturing techniques. Consequently, a few setups and devices have been developed to continuously monitor and score the sample quality in situ and in parallel to other experimental procedures, including growth of macromolecular crystals (Meyer et al. 2012), SAXS (Schwamberger et al. 2015; Falke et al. 2018), asymmetrical field flow fractionation (Sitar et al. 2017) and to score nanocrystal suspensions to be measured at XFEL radiation sources in the future as well as in context of other experimental procedures in biochemistry, genetics, material science, sorting and chemical synthesis.

In order to induce, optimize and study the crystal nucleation of the protein ML-I in detail and analyze complex liquid-liquid phase separation and phase transition mechanisms in general, the DLS setup shown in Fig. 6.5 was utilized. The time-resolved development of nuclei in this experiment is summarized as an example in Fig. 6.6, starting with a single drop of protein solution positioned on a glass cover slip in a humidity-controlled environment.

Fig. 6.5 Schematic representation of a setup to monitor individual solution drops and the micromanipulation towards optimized macromolecule crystallization using in situ DLS and a highly sensitive balance. Reproduced from Meyer et al. (2012), *Acta Crystallographica* with permission of the International Union of Crystallography, <https://journals.iucr.org/>, copyright 2012



6.6 Complementary Techniques and Conclusion

A technique that is closely related to DLS and is not in focus of this chapter is static light scattering (SLS), which allows to record the scattering intensity as an average over time. Data recorded for a serial dilution and at different detector angles can be visualized by Zimm plots (Hashim et al. 2014) and are combined in order to determine the shape-dependent radius of gyration (r_g), *the second virial coefficient* B_2 and also molecular weight as well as to verify ideal diffusion. The ratio of r_g and r_h also called *shape factor* can reveal shape information as well. The expected shape factor for globular particles is the square root of 0.6, which means $r_g/r_h \approx 0.775$. The second virial coefficient is highly useful in analyzing intermolecular interactions, e.g. in crystallography—a negative B_2 value is indicating repulsion, as explained and summarized in more detail elsewhere, e.g. Yadav et al. (2011).

Further, *X-ray photon correlation spectroscopy*, which is using an X-ray beam, i.e. a much shorter wavelength, and is otherwise highly similar to DLS, should be mentioned (Sutton et al. 1991). Moreover, a variety of distinct techniques to complement data based on light scattering is available, including but not limited to Taylor dispersion analysis, microscopic nano particle tracking, SAXS or small-angle neutron scattering (SANS), native mass spectrometry, native gel electrophoresis, analytical ultracentrifugation or analytical size exclusion chromatography to obtain certain size information of (biological) particles (see for example Boivin et al. 2016). SAXS and SANS as well as electron microscopy techniques or even native ion-mobility mass spectrometry are superior in analyzing the shape of molecules at moderately low resolution in solution, Taylor dispersion analysis is capable of determining the size of small compounds, also <1 kDa, and native mass spectrometry is known for high mass accuracy. However, DLS (and SLS) has huge advantages in terms of sample preparation/consumption, experimental effort, particle size range or instru-

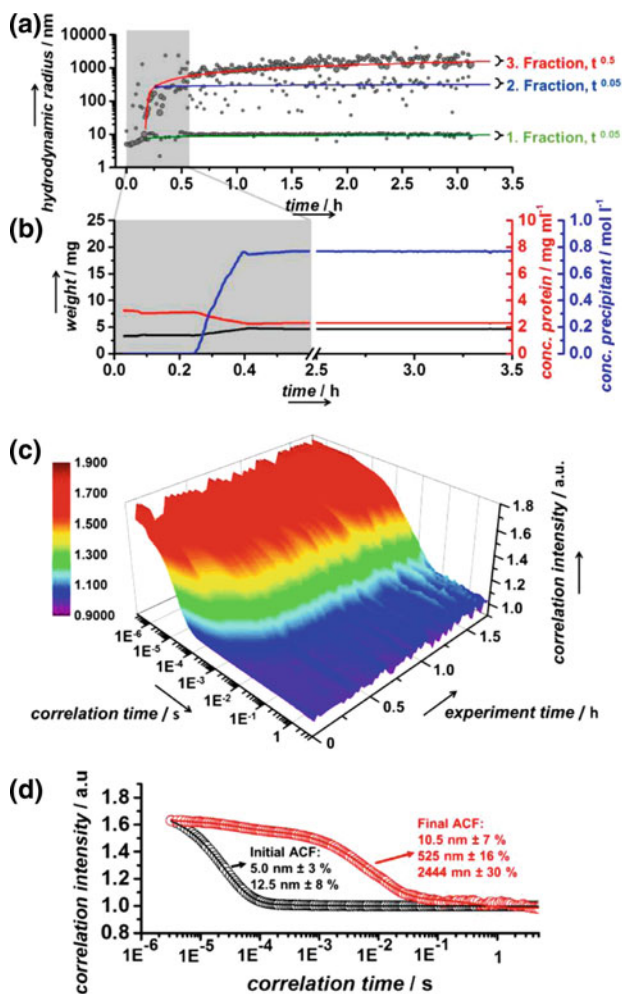


Fig. 6.6 Induction and characterization of ML-I nucleation utilizing in situ DLS according to Fig. 6.5. **a** Radius plot of the experiment showing the time course of the hydrodynamic radii. After adding the precipitant solution to supersaturate the protein solution and induce crystal nucleation three distinct radius fractions are detected indicated by the green, blue and red line respectively. **b** The solution composition and precipitant addition is actively regulated by piezo pumps and monitored over the experiment as displayed. **c** 3D plot of ACFs indicating increasing polydispersity due to multimodal correlation decay in later stages of the experiment. **d** Comparison of initial (black) and final (red) ACF visualizing also the particle species composition during a later stage of ML-I crystal growth. Reproduced from Schubert et al. (2017), *Crystal Growth and Design* with permission of the American Chemical Society, copyright 2017

mental adaptability respectively, especially for long-term time-resolved experiments and in an authentic solution environment for biomolecules. Some of the described in situ DLS instruments can monitor sample volumes around or even below 2 μl . A strongly curved drop surface for very small solution volumes might hinder the laser alignment in those cases. The option to apply DLS to solutions and suspensions in nearly laminar flow—with some restraints as mentioned—is another mayor benefit in combination with chromatographic purification, automated analytical pipelines and high-throughput or iterative sample analysis.

In this context, applications of DLS further include preparation of ceramic nano particles (Sōmiya 2013), size determination in SiO_2 particle suspensions (Wojciechowski et al. 2018), conjugation of gold nano particles and proteins (Jans et al. 2009), liposomes used in cosmetics and medical research (Hupfeld et al. 2006), monitoring of the gelation of milk related to food quality control (Dagleish and Hallett 1995) or gelation of organic-inorganic hybrid polymers (Norisuye et al. 1999). Moreover, the applicability of DLS and scattering intensity measurements to hydrogel environments was evaluated (Rochas and Geissler 2014). Dynamic light scattering can also be applied to verify oligomerization and crystallization of Macromolecules in preparation for experiments under microgravity conditions. Studying macromolecular interactions and symmetry under microgravity conditions has always been attractive, e.g. to obtain crystals of superior size, lattice homogeneity and maximized diffraction capability (Drebes et al. 2016). Gels or microfluidic chips, which are “down to earth” tools to partially mimic microgravity conditions, can be combined with in situ DLS as mentioned before to follow the crystal growth. Further, time-resolved experiments in outer space like at the International Space Station could be monitored by DLS in this context. A National Aeronautics and Space Administration research institute applied a DLS technique to detect clinical eye cataract in an early stage (Ansari et al. 2000).

Those individual examples and applications in structural biology as discussed before underline the expectation that the applications of light scattering techniques will even expand in the near future using further improved instrumentation modules.

Acknowledgements The corresponding research and complex instrument development activities have been supported by the Cluster of Excellence ‘Advanced Imaging of Matter’ of the Deutsche Forschungsgemeinschaft (DFG) - EXC 2056 - project ID 390715994 and DFG project BE 1443/29-1, by the German Aerospace Center (DLR) via project 50WB1423 and BMBF via project 05K16GUA. Further, the authors acknowledge helpful and critical discussion with all colleagues and cooperation partners in all aspects of DLS.

References

- Allen G (1996) Comprehensive polymer science and supplements. In: Chapter 33: Optical microscopy. Elsevier, New York
- Ansari RR, Datiles III MB, King (2000) New clinical instrument for the early detection of cataract using dynamic light scattering and corneal topography. In: Rol PO, Joos KM, Manns F (eds). San Jose, CA pp. 38–49
- Barnett CE (1942) Some applications of wave-length turbidimetry in the infrared. *J Phys Chem* 46:69–75
- Bekard IB, Asimakis P, Bertolini J, Dunstan DE (2011) The effects of shear flow on protein structure and function. *Biopolym* 95:733–745
- Beltramini M, Colangelo N, Giomi F, Bubacco L, Di Muro P, Hellmann N, Jaenicke E, Decker H (2005) Quaternary structure and functional properties of *Penaeus monodon* hemocyanin: P. monodon hemocyanin structure and function. *FEBS J* 272:2060–2075
- Berne BJ, Pecora R (2000) Dynamic light scattering: with applications to chemistry, biology, and physics. Dover Publications, Mineola, NY
- Block ID, Scheffold F (2010) Modulated 3D cross-correlation light scattering: Improving turbid sample characterization. *Rev Sci Instrum* 81:123107
- Boivin S, Kozak S, Rasmussen G, Nemtanu IM, Vieira V, Meijers R (2016) An integrated pipeline for sample preparation and characterization at the EMBL@PETRA3 synchrotron facilities. *Methods* 95:70–77
- Borgstahl GEO (2006) How to use dynamic light scattering to improve the likelihood of growing macromolecular crystals. In: *Macromolecular crystallography protocols*, vol 1. Humana Press, New Jersey, pp 109–130
- Brown RG (1987) Dynamic light scattering using monomode optical fibers. *Appl Opt* 26:4846–4851
- Brown RG, Smart AE (1997) Practical considerations in photon correlation experiments. *Appl Opt* 36:7480–7492
- Cantor CR, Schimmel PR (1980) The behavior of biological macromolecules. W. H. Freeman, San Francisco
- Chayen N, Dieckmann M, Dierks K, Fromme P (2004) Size and shape determination of proteins in solution by a noninvasive depolarized dynamic light scattering instrument. *Ann N Y Acad Sci* 1027:20–27
- Chu B (1970) Laser Light Scattering. *Annu Rev Phys Chem* 21:145–174
- Chu B (1991) Laser light scattering 2e: basic principles and practice. Elsevier Science, Oxford
- Cummins HZ, Knable N, Yeh Y (1964) Observation of diffusion broadening of Rayleigh scattered light. *Phys Rev Lett* 12:150–153
- Dalgleish DG, Hallett FR (1995) Dynamic light scattering: applications to food systems. *Food Res Int* 28:181–193
- Deo S, Patel TR, Dzananovic E, Booy EP, Zeid K, McEleney K, Harding SE, McKenna SA (2014) Activation of 2' 5'-oligoadenylate synthetase by stem loops at the 5'-end of the West Nile virus genome. *PLoS ONE* 9:e92545
- Destremaut F, Salmon JB, Qi L, Chapel JP (2009) Microfluidics with on-line dynamic light scattering for size measurements. *Lab Chip* 9:3289
- Dhadwal HS, Chu B (1989) A fiber-optic light-scattering spectrometer. *Rev Sci Instrum* 60:845–853
- Dierks K, Meyer A, Einspahr H, Betzel C (2008) Dynamic light scattering in protein crystallization droplets: adaptations for analysis and optimization of crystallization processes. *Cryst Growth Des* 8:1628–1634
- Dobson J, Kumar A, Willis LF, Tuma R, Higazi DR, Turner R, Lowe DC, Ashcroft AE, Radford SE, Kapur N, Brockwell DJ (2017) Inducing protein aggregation by extensional flow. *Proc Natl Acad Sci* 114:4673–4678
- Drebes J, Künz M, Windshügel B, Kikhney AG, Müller IB, Eberle RJ, Oberthür D, Cang H, Svergun DI, Perbandt M, Betzel C, Wrenger C (2016) Structure of ThiM from Vitamin B1 biosynthetic

- pathway of *Staphylococcus aureus*—insights into a novel pro-drug approach addressing MRSA infections. *Sci Rep* 6:22871
- Falke S, Dierks K, Blanchet C, Graewert M, Cipriani F, Meijers R, Svergun D, Betzel C (2018) Multi-channel in situ dynamic light scattering instrumentation enhancing biological small-angle X-ray scattering experiments at the PETRA III beamline P12. *J Synchrotron Rad* 25:361–372
- Fávero-Retto MP, Palmieri LC, Souza TACB, Almeida FCL, Lima LMTR (2013) Structural meta-analysis of regular human insulin in pharmaceutical formulations. *Eur J Pharm Biopharm* 85:1112–1121
- Fernández C, Minton AP (2009) Static light scattering from concentrated protein solutions II: Experimental test of theory for protein mixtures and weakly self-associating proteins. *Biophys J* 96:1992–1998
- Foord R, Jakeman E, Oliver CJ, Pike ER, Blagrove RJ, Wood E, Peacocke AR (1970) Determination of diffusion coefficients of haemocyanin at low concentration by intensity fluctuation spectroscopy of scattered laser light. *Nature* 227:242–245
- Friskken BJ (2001) Revisiting the method of cumulants for the analysis of dynamic light-scattering data. *Appl Opt* 40:4087–4091
- Fujime S (1972) Quasi-elastic scattering of laser light. A new tool for the dynamic study of biological macromolecules. *Adv Biophys* 3:1–43
- Gast K, Nöppert A, Müller-Frohne M, Zirwer D, Damaschun G (1997) Stopped-flow dynamic light scattering as a method to monitor compaction during protein folding. *Eur Biophys J* 25:211–219
- Georgieva D, Koker M, Redecke L, Perbandt M, Clos J, Bredehorst R, Genov N, Betzel C (2004) Oligomerization of the proteolytic products is an intrinsic property of prion proteins. *Biochem Biophys Res Commun* 323:1278–1286
- Glidden M, Muschol M (2012) Characterizing gold nanorods in solution using depolarized dynamic light scattering. *J Phys Chem C* 116:8128–8137
- Graewert MA, Franke D, Jeffries CM, Blanchet CE, Ruskule D, Kuhle K, Flieger A, Schäfer B, Tartsch B, Meijers R, Svergun D (2015) Automated pipeline for purification, biophysical and X-ray analysis of biomacromolecular solutions. *Sci Rep* 5:10734
- Haghighi M, Plum MA, Gantzounis G, Butt H-J, Steffen W, Fytas G (2013) Plasmon-enhanced dynamic depolarized light scattering. *J Phys Chem C* 117:8411–8419
- Hashim H, El-Mekawey F, El-Kashef H, Ghazy R (2014) Determination of scattering parameters of polyvinyl alcohol by static laser scattering. *Beni-Suef Univ J Basic Appl Sci* 3:203–208
- Hupfeld S, Holsæter AM, Skar M, Frantzen CB, Brandl M (2006) Liposome size analysis by dynamic/static light scattering upon size exclusion-/field flow-fractionation. *J Nanosci Nanotechnol* 6:3025–3031
- Jaenicke R (1987) Folding and association of proteins. *Prog Biophys Mol Biol* 49:117–237
- Jans H, Liu X, Austin L, Maes G, Huo Q (2009) Dynamic light scattering as a powerful tool for gold nanoparticle bioconjugation and biomolecular binding studies. *Anal Chem* 81:9425–9432
- Jeffries CM, Graewert MA, Blanchet CE, Langley DB, Whitten AE, Svergun DI (2016) Preparing monodisperse macromolecular samples for successful biological small-angle X-ray and neutron-scattering experiments. *Nat Protoc* 11:2122–2153
- Karow AR, Götzl J, Garidel P (2015) Resolving power of dynamic light scattering for protein and polystyrene nanoparticles. *Pharm Dev Technol* 20:84–89
- Kokhanovsky AA (eds) (2006) Light scattering reviews 4. Springer Praxis Books. Springer, Berlin, Heidelberg
- Koppel DE (1972) Analysis of macromolecular polydispersity in intensity correlation spectroscopy: the method of cumulants. *J Chem Phys* 57:4814–4820
- Liu J, Falke S, Drobot B, Oberthuer D, Kikhney A, Guenther T, Fahmy K, Svergun D, Betzel C, Raff J (2017) Analysis of self-assembly of S-layer protein slp-B53 from *Lysinibacillus sphaericus*. *Eur Biophys J* 46:77–89
- Loske AM, Tello EM, Vargas S, Rodriguez R (2014) *Escherichia coli* viability determination using dynamic light scattering: a comparison with standard methods. *Arch Microbiol* 196:557–563

- Medebach M, Moitzi C, Freiberger N, Glatter O (2007) Dynamic light scattering in turbid colloidal dispersions: a comparison between the modified flat-cell light-scattering instrument and 3D dynamic light-scattering instrument. *J Colloid Interface Sci* 305:88–93
- Meyer A, Dierks K, Hilterhaus D, Klupsch T, Mühlig P, Kleesiek J, Schöpflin R, Einspahr H, Hilgenfeld R, Betzel C (2012) Single-drop optimization of protein crystallization. *Acta Crystallogr Sect F: Struct Biol Cryst Commun* 68:994–998
- Meyer A, Dierks K, Hussein R, Brilllet K, Brognaro H, Betzel C (2015) Systematic analysis of protein–detergent complexes applying dynamic light scattering to optimize solutions for crystallization trials. *Acta Crystallogr F Struct Biol Commun* 71:75–81
- Mie G (1908) Beiträge zur Optik trüber Medien, speziell kolloidaler Metallösungen. *Ann Phys* 330:377–445
- Minton AP (2007) Static light scattering from concentrated protein solutions, I: General theory for protein mixtures and application to self-associating proteins. *Biophys J* 93:1321–1328
- Minton AP (2016) Recent applications of light scattering measurement in the biological and biopharmaceutical sciences. *Anal Biochem* 501:4–22
- Mueller PK, Givens RG (1961) Dynamic calibration and data interpretation of a light-scattering instrument. *J Air Pollut Control Assoc* 11:576–580
- Norisuye T, Shibayama M, Tamaki R, Chujo Y (1999) Time-resolved dynamic light scattering studies on gelation process of organic–inorganic polymer hybrids. *Macromolecules* 32:1528–1533
- Oberthuer D, Melero-García E, Dierks K, Meyer A, Betzel C, Garcia-Caballero A, Gavira JA (2012) Monitoring and scoring counter-diffusion protein crystallization experiments in capillaries by in situ dynamic light scattering. *PLoS ONE* 7:e33545
- Patel TR, Bernards C, Meier M, McEleney K, Winzor DJ, Koch M, Stetefeld J (2014) Structural elucidation of full-length nidogen and the laminin–nidogen complex in solution. *Matrix Biol* 33:60–67
- Petrache AI, Machin DC, Williamson DJ, Webb ME, Beales PA (2016) Sortase-mediated labelling of lipid nanodiscs for cellular tracing. *Mol BioSyst* 12:1760–1763
- Provencher SW (1982) CONTIN: a general purpose constrained regularization program for inverting noisy linear algebraic and integral equations. *Comput Phys Commun* 27:229–242
- Provencher SW, Štěpánek P (1996) Global analysis of dynamic light scattering autocorrelation functions. *Part Part Syst Charact* 13:291–294
- Redecke L, Binder S, Elmallah MIY, Broadbent R, Tilkorn C, Schulz B, May P, Goos A, Eich A, Rübhausen M, Betzel C (2009) UV-light-induced conversion and aggregation of prion proteins. *Free Radic Biol Med* 46:1353–1361
- Rifaie-Graham O, Hua X, Bruns N, Balog S (2018) The kinetics of β -hematin crystallization measured by depolarized light scattering. *Small* e1802295
- Rochas C, Geissler E (2014) Measurement of dynamic light scattering intensity in gels. *Macromolecules* 47:8012–8017
- Ruf H (1993) Data accuracy and resolution in particle sizing by dynamic light scattering. *Adv Coll Interface Sci* 46:333–342
- Schubert R, Meyer A, Dierks K, Kapis S, Reimer R, Einspahr H, Perbandt M, Betzel C (2015) Reliably distinguishing protein nanocrystals from amorphous precipitate by means of depolarized dynamic light scattering. *J Appl Crystallogr* 48:1476–1484
- Schubert R, Meyer A, Baitan D, Dierks K, Perbandt M, Betzel C (2017) Real-time observation of protein dense liquid cluster evolution during nucleation in protein crystallization. *Cryst Growth Des* 17:954–958
- Schwamberger A, De Roo B, Jacob D, Dillemans L, Bruegemann L, Seo JW, Locquet JP (2015) Combining SAXS and DLS for simultaneous measurements and time-resolved monitoring of nanoparticle synthesis. *Nucl Instrum Methods Phys Res Sect B* 343:116–122
- Sitar S, Vežočník V, Maček P, Kogej K, Pahovnik D, Žagar E (2017) Pitfalls in size characterization of soft particles by dynamic light scattering online coupled to asymmetrical flow field-flow fractionation. *Anal Chem* 89:11744–11752

- Sōmiya S (ed) (2013) Handbook of advanced ceramics: materials, applications, processing, and properties, 2nd edn. Academic Press, imprint of Elsevier, Amsterdam; Boston
- Stetefeld J, McKenna SA, Patel TR (2016) Dynamic light scattering: a practical guide and applications in biomedical sciences. *Biophys Rev* 8:409–427
- Sutton M, Mochrie SGJ, Greytak T, Nagler SE, Berman LE, Held GA, Stephenson GB (1991) Observation of speckle by diffraction with coherent X-rays. *Nature* 352:608–610
- Taylor TW, Sorensen CM (1986) Gaussian beam effects on the photon correlation spectrum from a flowing Brownian motion system. *Appl Opt*, AO 25:2421–2426
- Vajda J, Weber D, Brekel D, Hundt B, Müller E (2016) Size distribution analysis of influenza virus particles using size exclusion chromatography. *J Chromatogr A* 1465:117–125
- Ware BR (1974) Electrophoretic light scattering. *Adv Coll Interface Sci* 4:1–44
- Wojciechowski T, Shopa YI, Derkachov G, Jakubczyk D, Kolwas K, Woźniak M (2018) Application of dynamic light scattering for studying the evolution of micro- and nano-droplets. In: Angelsky OV (ed). SPIE, p 84
- Yadav S, Scherer TM, Shire SJ, Kalonia DS (2011) Use of dynamic light scattering to determine second virial coefficient in a semidilute concentration regime. *Anal Biochem* 411:292–296
- Zakharov P, Cardinaux F, Scheffold F (2006) Multispeckle diffusing-wave spectroscopy with a single-mode detection scheme. *Phys Rev E* 73:011413

Chapter 7

Pulsed Electron-Electron Double Resonance (PELDOR) and Electron Spin Echo Envelope Modulation (ESEEM) Spectroscopy in Bioanalysis



B. E. Bode and D. G. Norman

7.1 Background and History

Electron Paramagnetic Resonance (EPR) has a long history with the first spectrum being reported in 1945 (Zavoisky 1945) and is adopted widely, in its original continuous wave (CW) form, as a tool for the analysis of both biological systems and materials bearing unpaired electrons. The related technique of “Nuclear Magnetic Resonance” (NMR) developed rapidly thanks to the technological advances that enabled the use of pulsed radiofrequency and Fourier Transformation (FT). In EPR, the challenges posed by needing to generate short and very powerful microwave pulses and the fast relaxation times, of the electron spin, led to a much slower adaptation of pulsed excitation schemes. Nevertheless, early experiments using an NMR spectrometer with a greatly reduced magnetic field had shown the feasibility of pulse EPR (Blume 1958). It was not until the availability of commercial systems in the 1980s that this technique began to be applied more widely outside laboratories focused on the development of instrumentation. Over the last decades the application of pulse EPR has seen a very wide variety of systems studied from biological systems to those of materials science. This development was paralleled by a constant innovation in EPR instrumentation and methodology. Recent success in using arbitrary waveform generators (AWGs) and the commercial implementation and user uptake indicates that EPR is just entering a new era with tremendous opportunities offered by bespoke excitation schemes.

B. E. Bode

Biomedical Sciences Research Complex, Centre of Magnetic Resonance and EaStCHEM School of Chemistry, University of St Andrews, St Andrews KY16 9ST, UK
e-mail: beb2@st-andrews.ac.uk

D. G. Norman (✉)

School of Life Sciences, University of Dundee, Dow St., Dundee DD1 5EH, UK
e-mail: d.g.norman@dundee.ac.uk

© Springer Nature Switzerland AG 2019

A. S. Pereira et al. (eds.), *Radiation in Bioanalysis*, Bioanalysis 8,
https://doi.org/10.1007/978-3-030-28247-9_7

7.2 EPR Resonance and Frequency Bands

The EPR resonance phenomenon relies on the non-degeneracy of the two possible spin states of an unpaired electron in a half-occupied molecular orbital in the presence of a magnetic field. In close analogy to NMR the two energy levels are split by the interaction with the external magnetic field (the Zeeman interaction). The size of the splitting is linearly dependent on the magnetic field strength. Thus, the resonance frequency will be proportional to the magnetic field strength.

Several effects can influence the EPR resonance and result in further features of the signal. Most common are interaction with magnetic nuclei (e.g., ^{14}N nuclei in common nitroxide spin labels) and anisotropies resulting from different orientations of the molecule having different resonance frequencies. The latter becomes important in powered and frozen solution samples when the orientations do not average quickly as commonly observed in solution (e.g., in high-resolution NMR).

In comparison to high-resolution NMR, where increasing the strength of the magnetic fields used leads to greater sensitivity and chemical shift dispersion, EPR field strengths can have a more complex effect (similar to solid-state NMR). The microwave frequencies corresponding to EPR field strengths used are generally classified into bands (originating from military designation of frequencies with minimal atmospheric absorption when used for radar) and the most noticeable effect of moving to a different band is that the shape of the EPR spectrum can change significantly. A common example is stable nitroxide spin probes: the competing effects of the field-independent coupling to the nitrogen nucleus (hyperfine interaction—in analogy to a J-coupling in NMR the magnitude does not change with the magnetic field) and the field-dependent anisotropic interaction of the electron spin with the magnetic field (Zeeman interaction—in analogy to chemical shifts in NMR the dispersion of signals increases with the magnetic field strength) affects the shape and appearance of the EPR spectrum.

Most advanced EPR applications use immobilised samples (crystals, powders or frozen solutions) which often leads to enhanced relaxation times but also to more complex spectra due to different resonance frequencies and interactions for different anisotropies. (Note: The averaging of these anisotropies that has revolutionised solid-state NMR by magic-angle spinning is not practical for EPR as spinning speeds needed would lead to supersonic surface velocities not achievable in these setups.) X-band was the first band to be significantly exploited for pulse EPR (~9.5 GHz and 0.3 T) (Fig. 7.1a). Generation, manipulation and detection of microwaves was extensively developed for radar applications in World War 2 and components were readily available for this frequency. At this field the spectrum of a nitroxide spin label is dominated by splitting intrinsic to the chemical environment of the unpaired electron (dominated by the nuclear spin of the nitrogen ^{14}N , $I = 1$, 99.6% abundance). Although already present at X-band the dispersion due to the different strengths of interaction with the external magnetic field for the different orientations is small. However, as the field is increased this interaction becomes more dominant.

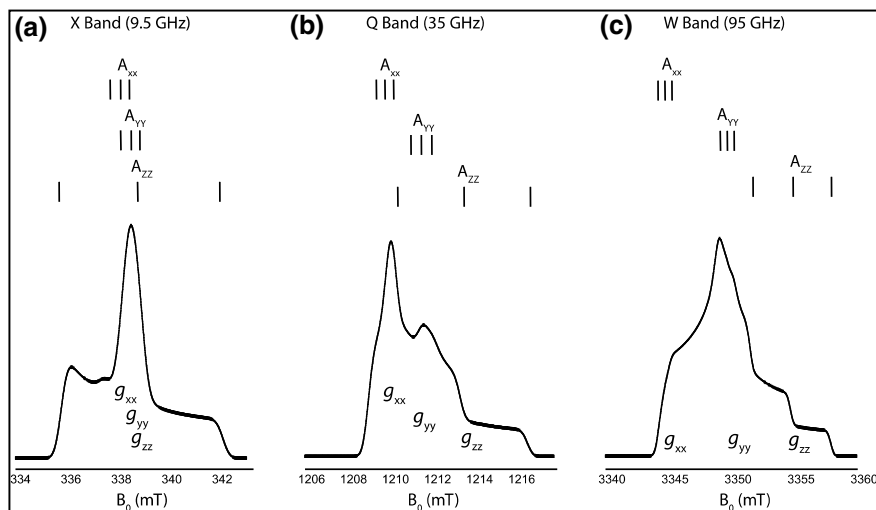


Fig. 7.1 The absorption spectra of nitroxides at X (a), Q (b), and W (c) band (9.5, 35 and 95 GHz, respectively). Increasing the microwave frequency resolves the g anisotropy of the sample, broadening the spectra from X to W band. The A and g anisotropy of a nitroxide are aligned, so as the g anisotropy of the spectra is resolved, the different A tensor components occupy different areas of the spectra

Later evolution in microwave technology has allowed for the development and commercial availability of Q (35 GHz), W (95 GHz), and J (260 GHz) band EPR spectrometers, and especially the provision of increased microwave power has greatly enhanced sensitivity. Until recently, commercial EPR spectrometers would only use rectangular pulses, essentially generated by turning the power on and then off. These pulses have the effect of exciting the spectra in a rather complex form giving uneven and not well constrained excitation of the electron spins, described by a sinc function. The incorporation of complex wave forming capability has opened the opportunity for intricate excitation schemes mirroring the successes of NMR in selective excitation and manipulation (Spindler et al. 2013; Doll and Jeschke 2014).

7.3 Pulse Excitation

The simplest acquisition scheme in magnetic resonance is detection of a free induction decay (FID). Here, the equilibrium magnetisation of the sample is turned into transverse magnetisation under the influence of a microwave pulse. Monitoring the time evolution of this magnetisation, records the FID and its FT gives the spectrum. This is widely applicable in solution NMR. Unfortunately, EPR brings additional challenges such as very broad spectra and fast relaxation times. The FID of a broad spectrum will decay very fast. The use of powerful microwave pulses mandates

some dead-time in which the power can dissipate before the weak signal is allowed to reach the sensitive detector (earlier detection would overload and possibly destroy the detector by residual microwave power from the pulse). In combination with the fast decay of the FID, this will often leave very little signal to be detected after the dead-time. To overcome this problem, the signal is recovered by refocusing it as an echo (see section on the spin echo in the following) and the FT of the second half of the echo will give the spectrum. However, this assumes the full spectrum has been excited by the microwave pulse and this is not always the case. If only part of the spectrum is excited the FT will only give the spectrum of the spins excited. The broader the spectrum the shorter and more powerful the excitation needs to be (only very short pulses will excite a broad energy spectrum). In addition, to turn the magnetisation into transverse the overall rotation of the spins must be a quarter circle (90° or $\pi/2$) and the rotation angle is given by pulse length multiplied by its magnetic field strength acting on the spins. The magnetic field strength increases with the square root of the microwave power put into the pulse; therefore, a pulse that halves the length (and doubles the width of excitation) needs fourfold higher microwave power. The absolute scaling of the magnetic field strength per microwave wattage depends on the resonator used; for the purpose here, it suffices to say that larger active volumes require more power but allow more sample (and thus more spins) to contribute, boosting sensitivity. Typically pulses in the tens of nanoseconds are used with high power microwave amplification (1 kW at X-band, 150–300 W at Q-band (Polyhach et al. 2012), up to 1 kW at W-band (Cruickshank et al. 2009)) allowing excitation of about half of the nitroxide spectrum. Usually using shorter and more powerful pulses does increase sensitivity because more spins participate in the experiment and development has led towards the adaptation of ever more powerful spectrometers.

7.4 Relaxation

The relaxation of an excited electron spin is a subject that lies at the heart of EPR spectroscopy with important effects on the EPR spectrum and experiments used to extract information from spin systems. There are essentially two types of relaxation, that are described as T_1 and T_2 . T_1 is also known as spin-lattice relaxation and originates from the interaction of the unpaired electron with surrounding atoms (the lattice). One can imagine T_1 relaxation as the rate that excited (high energy) spin states relax back to the low energy state. It should be remembered that, under the influence of a magnetic field the population of high and low energy spins are almost equal. The difference in population is described by the Boltzmann equation which is dependent on the energy difference between the two spin states (determined by the magnetic field strength) and the temperature. T_2 is also called spin-spin or cross-relaxation and is caused by the interaction between the excited electron and other electrons or magnetic nuclei. T_2 is essentially a dephasing of coherent electron spins

and does not involve energy dissipation to the lattice. The processes of T_1 and T_2 relaxation can be visualised in diagrams such as Fig. 7.2.

One of the consequences of spin relaxation is changes to the spectral linewidth. The linewidth is the inverse of the sum of the relaxation rates. Because relaxation in EPR is very fast compared to NMR, the linewidths of EPR signals are much greater. In solids the linewidths are often dominated by differences in microscopic environment (the inhomogeneous linewidth) and this can also influence the effective T_2 (in EPR the phase memory time, T_m , is often given rather than T_2 to also cover other processes with similar effect but of different nature as T_2). T_1 is the fundamental

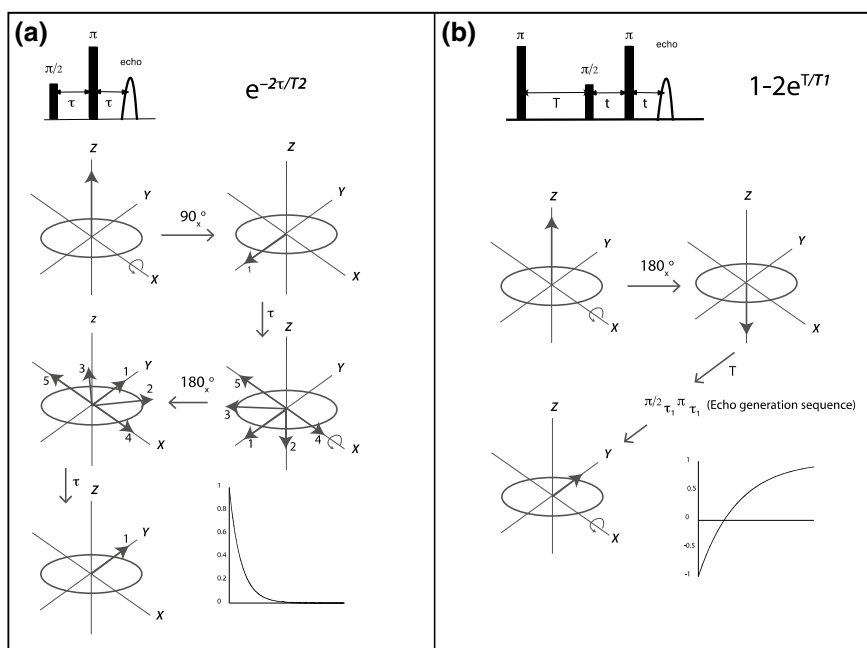


Fig. 7.2 Diagram illustrating the T_2 (a) and T_1 (b) modes of relaxation and their measurement. **a** The pulse sequence shows the first $\pi/2$ pulse which rotates the electron spin into the transverse orientation in the xy plane. After a time (τ) the spins have dephased according to their local environment (and corresponding resonance frequency). The application of a π pulse then rotates the spin vectors by 180° around the x -axis. The spins again lie in the xy plane but since the direction and speed of dephasing of individual spins remain the same, after a further delay of time τ , the spins re-phase along the y axis giving rise to an echo. The graph illustrates the decay of phase over time when increasing τ and the decay is described by the exponential factor shown (which includes the time-constant T_2). **b** Diagram illustrating the spin inversion and the decay of longitudinal magnetisation. Initially the magnetisation is inverted by a π pulse and is now opposite to the thermal equilibrium. Applying the echo sequence leads to an echo pointing into the opposite direction. Incrementing the delay T between the inversion and the echo sequence provides increasing time for the spins to return to thermal equilibrium. The exponential recovery of the magnetisation after inversion (called inversion recovery) is recorded as a function of T and shows the characteristic time constant T_1

restriction on how fast an experiment can be repeated in pulse EPR often making a short time constant beneficial. T_2 is a fundamental restriction on the persistence of the spin-echo (see section on spin-echo) that restricts the resolution of frequencies and by that also the magnitude of distances that can be measured by pulse EPR often making longer time constants highly beneficial (see section on PELDOR). Manipulation of relaxation using temperature is one of the fundamental techniques used in the RIDME experiment (see section of RIDME).

7.5 Relaxation and the Spin-Echo

To get around the dead-time problem discussed above, most pulsed EPR experiments make use of the spin echo. A carefully chosen pair of microwave pulses spaced with a timing delay τ will allow the FID generated by the first pulse but hidden in the deadtime to refocus at delay τ after the last pulse. If τ can be chosen long enough the deadtime can be circumvented. This is a technique that has found use in NMR spectroscopy but is almost ubiquitous in pulse EPR.

7.6 The Measurement of Dipolar Coupling

One of the most frequently used techniques in EPR, as applied to bioanalysis in recent years, has been the measurement of the dipolar coupling between spin centres and the determination of distances that can be derived from those measurements. Although the pulsed experiment, “pulsed electron-electron double resonance” (PELDOR), also known widely as the “double electron-electron resonance” (DEER) experiment, is the most widespread technique tested and applied, there are other experiments and extensions to PELDOR that are becoming popular. Dipolar coupling between electron spins is a through-space interaction. The frequency of the dipolar coupling is directly related to the distance between the two centres and the frequency is proportional to the inverse of the distance cubed. Alternative approaches have been developed to extract dipolar couplings and to enable distance measurements from systems with two or more unpaired electrons (spins), these include relaxation induced dipolar modulation enhancement (RIDME) (Kulik et al. 2001; Milikisyants et al. 2009), single frequency technique for refocusing (SIFTER) (Jeschke et al. 2000) and double quantum coherence filtered (DQF) (Borbat and Freed 1999) EPR. Each experiment has its place in the toolbox of techniques that can be applied in specific circumstances and are being developed further, especially as hardware capabilities develop.

In a disordered powder sample (this includes frozen solutions) the dipolar coupling between two spins will be determined by the spin-spin distance r and the angle between the distance vector and the external magnetic field θ (Eq. 7.1):

$$\omega_{\text{dd}} = \frac{\mu_0 \mu_B^2}{4\pi \hbar} \frac{g_A g_B}{r^3} (1 - 3 \cos^2 \theta) \quad (7.1)$$

where g_A and g_B are the g -values of the two coupled spins and assumed to be isotropic, μ_0 is the vacuum permeability, μ_B is the Bohr magneton, \hbar is the reduced Planck constant.

7.7 Pulsed Electron-Electron Double Resonance (PELDOR) Experiment

In its basic form the PELDOR experiment is a two-frequency experiment that takes advantage of the broad EPR spectra to excite separate populations of spins. Figure 7.3 shows the sequence of microwave pulses used in 4-pulse PELDOR.

The top line of Fig. 7.3 shows the pulses, at what is called the observer or detection frequency (ω_1), and first develops a spin echo using the 2-pulse sequence that was previously described. Shown on the lower line is the second frequency (ω_2) pulse, known as the pump pulse, which is set to excite a separate population of spins at a variable time t after the echo from the top line forms. The pump pulse is moved along by small time increments as the experiment develops. This pulse switches the orientation of the second set of spins and sets the spin-spin interaction, *via* dipolar

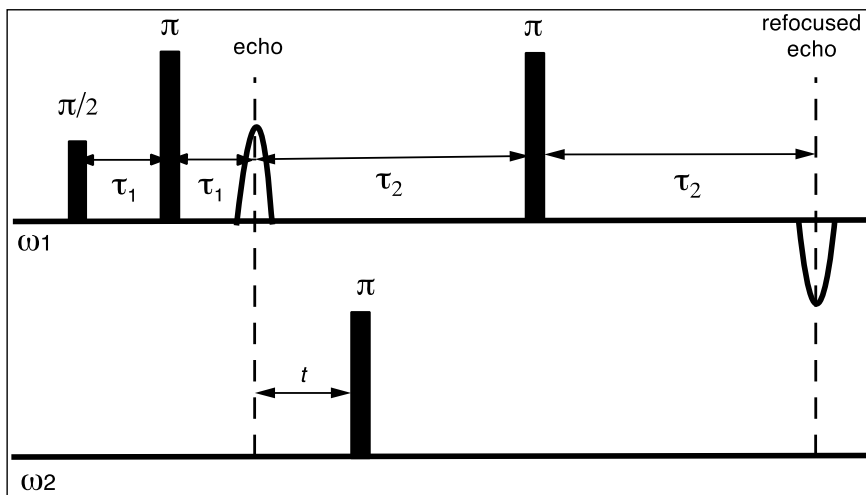


Fig. 7.3 The pulse sequence for the 4-pulse PELDOR experiment. The microwave pulses are represented by solid rectangles on the two, time axes representing the two frequencies ω_1 and ω_2 . Frequency ω_1 is showing the echo-forming pulse sequence and subsequent refocusing by a further pulse. The pulse with frequency ω_2 is inverting the second set of spins at a defined delay with respect to the primary echo. This delay is incremented and the intensity of the refocused echo with respect to this delay is recorded

coupling. The interaction between the spins changes the resonance frequency of the first set of spins according to the interaction frequency. The time t of the pump pulse determines the net time the coupling is switched. A further pulse is used at the observer frequency to again refocus the signal and so develop a spin echo (called refocused echo) shown at the end of the diagram. The final echo is detected and its intensity is recorded for each increment of the pump pulse. The signal recorded from this experiment, is echo intensity against time and if pairs of spins are situated at a fixed distance from each other, in the molecule under study, then a damped oscillation will be observed (Fig. 7.4a). The background signal derived from the interaction between spins on different molecules can be fitted to a simple model based on a random (homogeneous) 3D distribution of molecules in the sample, and that contribution removed (Fig. 7.4b). As sketched above, the frequency of this echo oscillation reports on the dipolar coupling and consequently the distance (Eq. 7.1). A short distance would give high frequency, short period, amplitude modulations. If the distance between the spins was longer, then the frequency of the amplitude

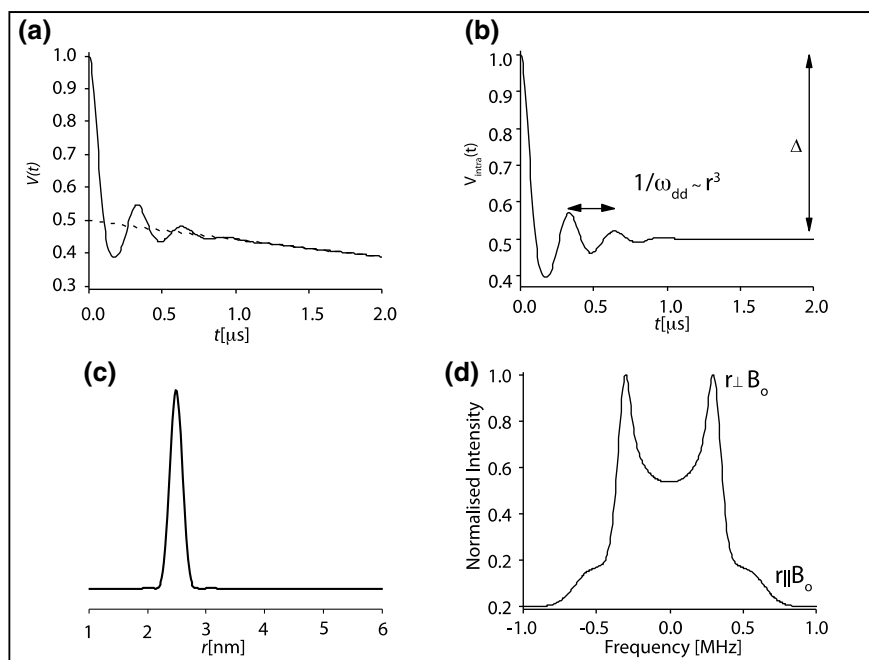


Fig. 7.4 Data derived from the PELDOR experiment and its treatment to extract distance data. **a** Raw data from measurement of the echo amplitude modulation, the dashed line indicates a fitted background signal. **b** The background-corrected data from the PELDOR experiment with indication of a single oscillation whose frequency is proportional to the cube of the distance. **c** The background corrected PELDOR data can be transformed to reveal the distance and the distance distribution between spins. **d** The Fourier transform of the background-corrected PELDOR data (a so-called Pake pattern) reveals the frequency distribution of the dipolar spin-spin interaction

modulation would be smaller and the wavelength longer. The more similar two distances are, the more similar their frequencies become. This means to recover long distances or small differences, then long times of t must be recorded (Ackermann and Bode 2018).

The recorded echo amplitude modulation can be read off directly and converted into a distance (this can be done from the FT of the oscillation, see Fig. 7.4c), although more powerful techniques use mathematical fitting algorithms to extract not only a distance measurement but also a measure of the distance distribution (Jeschke et al. 2006) that exists between the two spins (Fig. 7.4d). It should be noted that the depth of the oscillation (Δ in Fig. 7.4b) depends on the average excitation of partner spins. This in turn depends on the probability of exciting a spin under the second frequency pulse and the number of partner spins in the molecule or complex. Carefully performed these experiments can be used to count the number of interacting spins and determine oligomerisation equilibria (Bode et al. 2007; Ackermann et al. 2015).

The typical PELDOR experiment, using 100 μM spin concentration and 100 μL sample, for not too challenging distances (up to 60 \AA), will take several hours at X-band and mere minutes at Q and W-band (this assumes high power setups). The range of distances between spins, that can be measured is from around 15 \AA up to about 160 \AA depending on the relaxation rate (T_2) of the spin echo which is a consequence of the chemical environment present in both the molecule under study and the solvent used in the sample. The factor dictating how far a measurement can go is largely the persistence of the refocused echo. The PELDOR experiment, in its normally used form, is a constant time experiment and the time axis, on which the decaying signal is gathered, is set by the delays (τ_2 on Fig. 7.3). As one increases the length of the delay τ_2 , then one pushes the refocused echo farther out and allows one to gather data over a longer period of time. The echo decreases as the time period τ_2 is increased due to relaxation that cannot be refocused and so there is a limit to the delay τ_2 and the time axis of the recorded data. To measure a frequency or a distance from the decaying signal one must record enough data to capture sufficient oscillations in the signal. As the distance between the spins increases so the wavelength of the echo oscillation increases (Eq. 7.1) and one needs to record more time. At some point the echo becomes too small to be recorded and this fixes the limitation to the measurable distance.

7.8 Single Frequency Experiments

The double frequency experiments such as the PELDOR experiment have some limitations that arise from the limited spectral width that is accessible on most present-day spectrometers. Because the two frequencies must both lie within the resonant cavity, one is generally forced into a compromised sensitivity. If one can use a single frequency then it can be placed at the most resonant position within the cavity (with a high-quality factor), maximising sensitivity. The width of EPR spectra often makes these experiments practically inferior to PELDOR (judging from uptake by EPR

practitioners). The limited excitation bandwidth of the pulses leads to incomplete refocusing and thus, all intricate multi-pulse schemes will suffer from a mixture of signals arising from different coherence transfer pathways where one or more pulses have not been equally effective. Nevertheless, for narrow EPR spectra as e.g. triarylmethyl (TAM) radicals, SIFTER has been successfully applied (Meyer et al. 2018).

In an early adaptation of NMR methodology Freed and co-workers have shown that DQF methods allow extraction of dipolar interactions at superior sensitivity (Yang et al. 2012). However, the methodology is instrumentally demanding (requiring very short microwave pulses and accurate phase cycles) and the robustness of PELDOR methods has led to most applications relying on the double frequency method.

7.9 Relaxation Induced Dipolar Modulation Enhancement (RIDME)

In PELDOR we have seen that two frequencies are used to excite two separate groups of spins that then interact to give an oscillating intensity to the spin echo. RIDME is an experiment that, rather than using a second frequency, uses the naturally fast relaxation, of at least one component (spin) to set the coupling interaction. In RIDME the second frequency of PELDOR is essentially substituted by a time delay in which the second spin is allowed to flip by spontaneous relaxation and substitutes for the active spin flip caused by the pump pulse on the second frequency. This relaxation delay in RIDME is moved across the first echo and then the echo oscillation is either detected or, in a more advanced form, the echo is reformed, removing it from the dead-time (Fig. 7.5). Setting up a RIDME experiment requires knowledge of the T_1 relaxation rate and the tailoring of that rate by suitable choice of temperature (T_1 is generally strongly affected by temperature). RIDME data can be analysed very similarly to PELDOR to extract distance distributions (Abdullin et al. 2015) and numbers of interacting spins (Giannoulis et al. 2017). The RIDME experiment has been shown to have great utility and potential for measurements involving at least one suitable paramagnetic metal ion and another spin. In particular, RIDME has been used successfully in systems containing Cu^{2+} and Gd^{3+} ions as well as Mn^{2+} and Fe^{3+} (Meyer and Schiemann 2016; Meyer et al. 2016; Abdullin et al. 2015; Akhmetzyanov et al. 2016; Kaur et al. 2018).

As well as offering an alternative to PELDOR, at some frequencies RIDME can be used for combinations of spins that, with extremely wide spectral widths and separations, would not be suitable for PELDOR due to the spectra being so far separated that they cannot simultaneously be excited by the pulses. In fact, RIDME can use a deliberately reduced resonator bandwidth thereby boosting sensitivity even further. One of the severe problems to overcome in RIDME has been the production of echo oscillations containing ESEEM derived signal (see ESEEM section), from

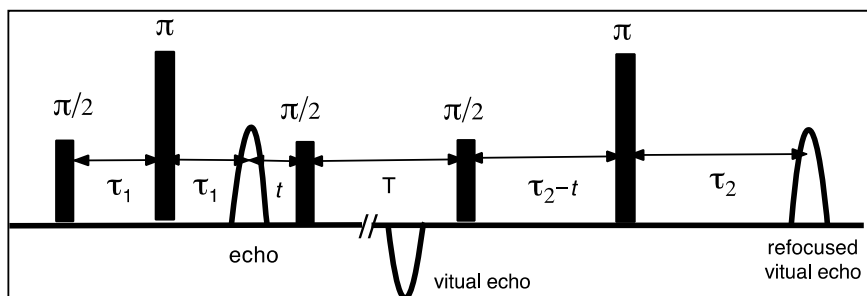


Fig. 7.5 The pulse sequence for the 5-pulse RIDME experiment. The microwave pulses are represented by solid rectangles on the time axes. The time delay (t) is incremented and the intensity of the refocused echo with respect to this delay is recorded. This sequence is easiest rationalised by replacing the second frequency π pulse of the PELDOR sequence with a $\pi/2 - T - \pi/2$ sequence that is called “mixing block”. During this time the dipolar coupling is set by the B spins flipping an odd number of times (for an even number of flips there is no net effect)

either proton or deuterons in the vicinity. These can currently be addressed by either averaging different pulse delay timings (Keller et al. 2016) (effectively averaging the oscillations) or deconvoluting them from experiments that only show unwanted ESEEM and those showing both ESEEM and RIDME effects (Abdullin et al. 2015).

7.10 The Use of Shaped Pulses

The advent of arbitrary waveform generators (AWG) that allow generation of arbitrary amplitude, phase and frequency of microwaves on sub-nanosecond timescales has brought many concepts from NMR into reach. While the limited excitation bandwidth and excitation sidebands of rectangular microwave pulses have been severely limiting in the use of multi-pulse excitation, the use of shaped and chirped (frequency swept) pulses allows one to boost sensitivity and execute bespoke control of spin population excitation. Quite excitingly it might bring the NMR paradigm to EPR. As explained when introducing pulse excitation, the EPR echo is the refocused FID of the part of the EPR spectrum that has been excited. Thus, the echo is mostly recorded as a function of magnetic field to obtain a spectrum despite the limited excitation. In practice, that means that using FID detection (in NMR) or echoes that represent the excitation of the full spectrum (in solid-state NMR) the spectrum dimension can be obtained from a single experiment and subsequent FT. In common echo detected EPR each point on the axis of the spectrum is a separate experiment. With AWGs now allowing the excitation of the full spectrum, the latter can be retrieved from either the FID (dead-time permitting) or the second half of the echo (i.e., refocused FID).

This gives the EPR spectrum from FT (similarly to the direct dimension in NMR) and allows, for instance, measuring relaxation times by only sampling the relaxation

delays and still obtaining information for all parts of the spectrum. Currently, if one wants to know relaxation times as a function of the spectral position in EPR, both the field and the relaxation delays must be sampled individually in two-dimensional experiment which can easily be prohibitively expensive in terms of measurement time and cryogen consumption. One striking example how AWGs enable this concept is the 2D SIFTER experiment (Doll and Jeschke 2016; Bowen et al. 2018).

7.11 Experimental Conditions (Sample Size, Concentration, Cryoprotectant and Solvent Deuteration)

The small energies involved in the spin-transitions underpinning magnetic resonance experiments make the method non-destructive and highly reproducible but also less sensitive than, for example optical spectroscopy. Magnetic resonance often compensates by using repeated signal acquisition and averaging. The signal will increase linearly with increasing repetition but unfortunately the measured noise also increases, with the square root of the number of experiments. In consequence, the signal-to-noise ratio (SNR) that determines what can be resolved from the data will improve only with the square root of the number of experiments. This means that one has to increase the acquisition time by a factor of four in order to merely double the signal quality. This shows why the optimisation of the signal is paramount as compensation of a poor signal by longer measurement is severely limited. Sample sizes are normally chosen to fill the active volume of the probe head used and larger volume samples (~3 mm tubes) have brought significant advances at Q- and W-band (Polyhach et al. 2012; Cruickshank et al. 2009). However, probe heads with smaller active volumes generally provide better SNR per volume and so it is usually best to take the smallest active volume probe head that will still accommodate the sample available. If the sample amount is limiting a probe head with a small active volume will have higher SNR than a probe head with larger active volume used with the same sample (better absolute sensitivity). On the other hand, if sample concentration is limiting, it is advisable to fill a large volume probe rather than a small volume probe head as more spins will be contributing to the experiment (better concentration sensitivity). Distance measurements by EPR are performed in immobilised samples for a number of reasons, one being that rapid tumbling in solution would average the dipolar interaction to zero. Frozen aqueous buffers tend to crystallise and this causes high local concentration or aggregation of the solute biomolecules. Extreme local concentration leads to a drastic shortening of the echo decay (or relaxation) times and considerably limits the measurable distances. It is standard practice to use cryoprotectants such as ethylene glycol or glycerol to inhibit ice crystal formation and allow the formation of a frozen glassy solution. The effect on biological function and biomolecular stability has to be carefully considered and concentrations between 20 and 60% have been found to be useful without impairing function in most cases.

Even if aggregation can be avoided, the length of traces that can be recorded will be limited by the echo lifetime and this will be limited by the sample concentration and by the type of magnetic nuclei surrounding the electron spins. The relaxing effects of nearby protons can be decreased by deuteration. Replacing the protons of the buffer and cryoprotectant by deuterons is done routinely and can significantly increase the distances measurable. The longest distances measured have been achieved in systems where all the protons in the protein are replaced by deuterons as well, although this requires special procedures for the production of the samples. The sample concentration increases relaxation and the PELDOR background decay (Fig. 7.4 part a) (Jeschke and Polyhach 2007). This limits the measurable distances and leads to lower concentrations required when long distances are to be measured.

7.12 Some Examples of PELDOR Studies

One striking example of PELDOR application is the measurement of distances up to 16 nm in the tetradecameric membrane protein GroEL (Schmidt et al. 2016b). This experiment requires to minimise dephasing due to T_2 and avoidance interference effects by multiple spin labels (Giannoulis et al. 2013; von Hagens et al. 2013) (in a homo-tetradecamer all 14 subunits are identical and the complex yields 14 labels when each monomer is labelled). This achievement was a combination of protein deuteration (Bowman et al. 2014; Ward et al. 2010; El Mkami and Norman 2015), reducing the excitation strength of the pump pulse and reducing spin labelling. The effects of the latter two have been shown systematically on the homo-heptameric mechanosensitive channel of small conductance (MscS). Biological mechanosensing is a very active field of research with implications for health and disease. In the search for a structural basis of the gating of the channel PELDOR was employed to unravel the MscS gating state in frozen solution (Pliotas et al. 2012; Ward et al. 2014). During these investigations, high quality-distance distributions could be obtained when the simultaneous pumping of multiple spins was deliberately suppressed by weakening the second frequency pulse in PELDOR (Valera et al. 2016). When reducing the number of spins per protein monomer by a procedure blocking some cysteine residues with a non-magnetic analogue, the data quality was improved even further (Ackermann et al. 2017). Ultimately PELDOR has informed structural biology about the solution state of MscS and contributed to the overall understanding of the role of lipids in mechanosensation (Pliotas et al. 2015).

While PELDOR and other dipolar techniques are widely explored for the measurement of distances opportunities for scrutinising multimerisation equilibria are emerging. Recent examples include concentration dependent dimerisation of influenza proteins (Georgieva et al. 2015; Kerry et al. 2014) as well as dimerisation of fibril modelling peptides (Kotler et al. 2019) that can be rationalised by multimerisation studies (Schmidt et al. 2016a).

7.13 ESEEM

While EPR spectroscopy is based on observing changing populations of energy levels of the electron spin, there are also transitions of nuclear spins. At low magnetic field, where the anisotropy of the electron nuclear (hyperfine) interaction is not small compared to the Zeeman interaction, electron and nuclear spins can both flip simultaneously under a microwave pulse. The probability of this depends on pulse timings and interaction strengths and as a consequence, when the delay times between pulses are changed, an oscillatory signal occurs. In the simplest case of changing τ in a Hahn echo sequence one can observe the echo decay (caused by T_2 relaxation) being superimposed with a modulation with nuclear Larmor frequencies. This Electron Spin Echo Envelope Modulation (ESEEM) (Van Doorslaer 2017) is a powerful technique that has been shown to provide a wealth of information on the interaction of the electron spin with nuclei which are in close vicinity. The fact that we can detect ESEEM type interactions means we can interrogate the chemical nature of the material that surrounds an unpaired electron. Conversely, as ESEEM originates from changing pulse delays leading to oscillatory signals, it becomes likely to occur as a side product of other pulse experiments.

There are a large number of experimental variants used to study the ESEEM effect, also extending to multiple dimensions, and tailored to specific situations allowing the study of paramagnetic centres including metal ions and stable radicals. These are covered in several excellent reviews (Van Doorslaer 2017; McCracken 2011; Deligiannakis et al. 2000; Prisner et al. 2001). In the context of long-range structural constraints there are two important aspects. Firstly, ESEEM can be used to study interactions with solvent nuclei. This is exploited to determine topologies upon deuterium exchange of buffers and/or membranes or even protein deuteration. Comparing deuterium ESEEM modulation depths at different levels of deuteration of the sample (protein or buffer/detergent/membrane) allows a semiquantitative assessment of solvent accessibility or membrane exposure. Secondly, unwanted ESEEM modulations can appear in any pulse EPR experiment where electron spins experience pulses with incremented delays. In PELDOR this is circumvented by diminishing the spectral overlap between the two frequencies used in the experiment, albeit the excitation sidebands can overlap causing some residual ESEEM. As moving frequencies further apart is not always feasible, schemes averaging the ESEEM modulation are often used. This is possible as the ESEEM artefacts are often caused by solvent nuclei and couplings are commonly small leading to modulation with nuclear Larmor frequency. Setting pulse delays to a multiple of the inverse Larmor frequency and averaging them over one modulation period has largely abolished this problem for PELDOR. In RIDME all pulses are at single frequency making ESEEM often much more severe. There are different approaches to tackle this problem, including averaging (Keller et al. 2016), deconvolution of reference experiments (Abdullin et al. 2015) and reducing excitation strengths (Giannoulis et al. 2018). This remains a very active field of research. However, the use of high fields will be particularly beneficial (Kaur et al. 2018).

One landmark study exploiting ESEEM to infer changing solvent accessibility during protein folding was performed on plant light harvesting complexes and allowed understanding water accessibility (Volkov et al. 2009) as well as monitoring refolding of the integral membrane (Dockter et al. 2009) protein. Similarly, water accessibility and interactions with phospholipids could be traced by ESEEM on spin-labelled potassium channel KcsA (Cieslak et al. 2010). This information can be used to model the phosphate interaction surface of the integral membrane protein on a crystallographic structure. Both studies demonstrate the value of ESEEM for spin-labelled proteins and add to the value hyperfine methods are known to have for intrinsic paramagnetic centres.

References

- Abdullin D, Duthie F, Meyer A, Muller ES, Hagelueken G, Schiemann O (2015) Comparison of PELDOR and RIDME for distance measurements between nitroxides and low-spin Fe(III) ions. *J Phys Chem B* 119(43):13534–13542. <https://doi.org/10.1021/acs.jpcc.5b02118>
- Ackermann K, Bode BE (2018) Pulse EPR distance measurements to study multimers and multimerisation. *Mol Phys* 116(12):1513–1521. <https://doi.org/10.1080/00268976.2017.1421324>
- Ackermann K, Giannoulis A, Cordes DB, Slawin AMZ, Bode BE (2015) Assessing dimerisation degree and cooperativity in a biomimetic small-molecule model by pulsed EPR. *Chem Commun* 51(84):15472. <https://doi.org/10.1039/c5cc90439k>
- Ackermann K, Pliotas C, Valera S, Naismith JH, Bode BE (2017) Sparse labeling PELDOR spectroscopy on multimeric mechanosensitive membrane channels. *Biophys J* 113(9):1968–1978. <https://doi.org/10.1016/j.bpj.2017.09.005>
- Akhmetzyanov D, Ching HYY, Denysenkov V, Demay-Drouhard P, Bertrand HC, Tabares LC, Policar C, Prisner TF, Un S (2016) RIDME spectroscopy on high-spin Mn²⁺ centers. *Phys Chem Chem Phys* 18(44):30857–30866. <https://doi.org/10.1039/c6cp05239h>
- Blume RJ (1958) Electron spin relaxation times in sodium-ammonia solutions. *Phys Rev* 109(6):1867–1873. <https://doi.org/10.1103/PhysRev.109.1867>
- Bode BE, Margraf D, Plackmeyer J, Durner G, Prisner TF, Schiemann O (2007) Counting the monomers in nanometer-sized oligomers by pulsed electron—electron double resonance. *J Am Chem Soc* 129(21):6736–6745. <https://doi.org/10.1021/ja065787t>
- Borbat PP, Freed JH (1999) Multiple-quantum ESR and distance measurements. *Chem Phys Lett* 313(1–2):145–154. [https://doi.org/10.1016/S0009-2614\(99\)00972-0](https://doi.org/10.1016/S0009-2614(99)00972-0)
- Bowen AM, Erlenbach N, van Os P, Stelzl LS, Sigurdsson ST, Prisner TF (2018) Orientation selective 2D-SIFTER experiments at X-Band frequencies. *Appl Magn Reson* 49(12):1355–1368. <https://doi.org/10.1007/s00723-018-1057-3>
- Bowman A, Hammond CM, Stirling A, Ward R, Shang WF, El-Mkami H, Robinson DA, Svergun DI, Norman DG, Owen-Hughes T (2014) The histone chaperones Vps75 and Nap1 form ring-like, tetrameric structures in solution. *Nucleic Acids Res* 42(9):6038–6051. <https://doi.org/10.1093/nar/gku232>
- Cieslak JA, Focia PJ, Gross A (2010) Electron spin-echo envelope modulation (ESEEM) reveals water and phosphate interactions with the KcsA potassium channel. *Biochem-US* 49(7):1486–1494. <https://doi.org/10.1021/bi9016523>
- Cruikshank PAS, Bolton DR, Robertson DA, Hunter RI, Wylde RJ, Smith GM (2009) A kilowatt pulsed 94 GHz electron paramagnetic resonance spectrometer with high concentration sensitivity, high instantaneous bandwidth, and low dead time. *Rev Sci Instrum* 80(10):103102. <https://doi.org/10.1063/1.3239402>

- Deligiannakis Y, Louloudi M, Hadjiliadis N (2000) Electron spin echo envelope modulation (ESEEM) spectroscopy as a tool to investigate the coordination environment of metal centers. *Coord Chem Rev* 204:1–112. [https://doi.org/10.1016/S0010-8545\(99\)00218-0](https://doi.org/10.1016/S0010-8545(99)00218-0)
- Dockter C, Volkov A, Bauer C, Polyhach Y, Joly-Lopez Z, Jeschke G, Paulsen H (2009) Refolding of the integral membrane protein light-harvesting complex II monitored by pulse EPR. *Proc Natl Acad Sci USA* 106(44):18485–18490. <https://doi.org/10.1073/pnas.0906462106>
- Doll A, Jeschke G (2014) Fourier-transform electron spin resonance with bandwidth-compensated chirp pulses. *J Magn Reson* 246:18–26. <https://doi.org/10.1016/j.jmr.2014.06.016>
- Doll A, Jeschke G (2016) EPR-correlated dipolar spectroscopy by Q-band chirp SIFTER. *Phys Chem Chem Phys* 18(33):23111–23120. <https://doi.org/10.1039/c6cp03067j>
- El Mkami H, Norman DG (2015) EPR distance measurements in deuterated proteins. *Method Enzym* 564:125–152. <https://doi.org/10.1016/bs.mie.2015.05.027>
- Georgieva ER, Borbat PP, Norman HD, Freed JH (2015) Mechanism of influenza A M2 transmembrane domain assembly in lipid membranes. *Sci Rep-UK* 5:11757. <https://doi.org/10.1038/srep11757>
- Giannoulis A, Ward R, Branigan E, Naismith JH, Bode BE (2013) PELDOR in rotationally symmetric homo-oligomers. *Mol Phys* 111(18–19):2845–2854. <https://doi.org/10.1080/00268976.2013.798697>
- Giannoulis A, Oranges M, Bode BE (2017) Monitoring complex formation by relaxation-induced electron paramagnetic resonance distance measurements. *ChemPhysChem* 18(17):2318–2321. <https://doi.org/10.1002/cphc.201700666>
- Giannoulis A, Motion CL, Oranges M, Buhl M, Smith GM, Bode BE (2018) Orientation selection in high-field RIDME and PELDOR experiments involving low-spin Co-II ions. *Phys Chem Chem Phys* 20(4):2151–2154. <https://doi.org/10.1039/c7cp07248a>
- Jeschke G, Polyhach Y (2007) Distance measurements on spin-labelled biomacromolecules by pulsed electron paramagnetic resonance. *Phys Chem Chem Phys* 9(16):1895–1910. <https://doi.org/10.1039/b614920k>
- Jeschke G, Pannier M, Godt A, Spiess HW (2000) Dipolar spectroscopy and spin alignment in electron paramagnetic resonance. *Chem Phys Lett* 331(2–4):243–252. [https://doi.org/10.1016/S0009-2614\(00\)01171-4](https://doi.org/10.1016/S0009-2614(00)01171-4)
- Jeschke G, Chechik V, Ionita P, Godt A, Zimmermann H, Banham J, Timmel CR, Hilger D, Jung H (2006) DeerAnalysis2006—a comprehensive software package for analyzing pulsed ELDOR data. *Appl Magn Reson* 30(3–4):473–498. <https://doi.org/10.1007/Bf03166213>
- Kaur H, Abreu B, Akhmetzhanov D, Lakatos-Karoly A, Soares CM, Prisner T, Glaubitz C (2018) Unexplored nucleotide binding modes for the ABC exporter MsbA. *J Am Chem Soc* 140(43):14112–14125. <https://doi.org/10.1021/jacs.8b06739>
- Keller K, Doll A, Qi MA, Godt A, Jeschke G, Yulikov M (2016) Averaging of nuclear modulation artefacts in RIDME experiments. *J Magn Reson* 272:108–113. <https://doi.org/10.1016/j.jmr.2016.09.016>
- Kerry PS, Turkington HL, Ackermann K, Jameison SA, Bode BE (2014) Analysis of influenza A virus NS1 dimer interfaces in solution by pulse EPR distance measurements. *J Phys Chem B* 118(37):10882–10888. <https://doi.org/10.1021/jp508386r>
- Kotler SA, Tugarinov V, Schmidt T, Ceccon A, Libich DS, Ghirlando R, Schwieters CD, Clore GM (2019) Probing initial transient oligomerization events facilitating Huntingtin fibril nucleation at atomic resolution by relaxation-based NMR. *Proc Natl Acad Sci USA* 116(9):3562–3571. <https://doi.org/10.1073/pnas.1821216116>
- Kulik LV, Dzuba SA, Grigoryev IA, Tsvetkov YD (2001) Electron dipole-dipole interaction in ESEEM of nitroxide biradicals. *Chem Phys Lett* 343(3–4):315–324. [https://doi.org/10.1016/S0009-2614\(01\)00721-7](https://doi.org/10.1016/S0009-2614(01)00721-7)
- McCracken J (2011) Electron spin echo envelope modulation (ESEEM) spectroscopy. In: *Encyclopedia of inorganic and bioinorganic chemistry*. Wiley. <https://doi.org/10.1002/9781119951438.eibc0311>

- Meyer A, Schiemann O (2016) PELDOR and RIDME measurements on a high-spin manganese(II) bisnitroxide model complex. *J Phys Chem A* 120(20):3463–3472. <https://doi.org/10.1021/acs.jpca.6b00716>
- Meyer A, Abdullin D, Schnakenburg G, Schiemann O (2016) Single and double nitroxide labeled bis(terpyridine)-copper(II): influence of orientation selectivity and multispin effects on PELDOR and RIDME. *Phys Chem Chem Phys* 18(13):9262–9271. <https://doi.org/10.1039/c5cp07621h>
- Meyer A, Jassoy JJ, Spicher S, Berndhauser A, Schiemann O (2018) Performance of PELDOR, RIDME, SIFTER, and DQC in measuring distances in trityl based bi- and triradicals: exchange coupling, pseudosecular coupling and multi-spin effects. *Phys Chem Chem Phys* 20(20):13858–13869. <https://doi.org/10.1039/c8cp01276h>
- Milikisyants S, Scarpelli F, Finiguerra MG, Ubbink M, Huber M (2009) A pulsed EPR method to determine distances between paramagnetic centers with strong spectral anisotropy and radicals: The dead-time free RIDME sequence. *J Magn Reson* 201(1):48–56. <https://doi.org/10.1016/j.jmr.2009.08.008>
- Pliotas C, Ward R, Branigan E, Rasmussen A, Hagelueken G, Huang HX, Black SS, Booth IR, Schiemann O, Naismith JH (2012) Conformational state of the MscS mechanosensitive channel in solution revealed by pulsed electron-electron double resonance (PELDOR) spectroscopy. *Proc Natl Acad Sci USA* 109(40):E2675–E2682. <https://doi.org/10.1073/pnas.1202286109>
- Pliotas C, Dahl ACE, Rasmussen T, Mahendran KR, Smith TK, Marius P, Gault J, Banda T, Rasmussen A, Miller S, Robinson CV, Bayley H, Sansom MSP, Booth IR, Naismith JH (2015) The role of lipids in mechanosensation. *Nat Struct Mol Biol* 22(12):991–998. <https://doi.org/10.1038/nsmb.3120>
- Polyhach Y, Bordignon E, Tschaggelar R, Gandra S, Godt A, Jeschke G (2012) High sensitivity and versatility of the DEER experiment on nitroxide radical pairs at Q-band frequencies. *Phys Chem Chem Phys* 14(30):10762–10773. <https://doi.org/10.1039/c2cp41520h>
- Prisner T, Rohrer M, MacMillan F (2001) Pulsed EPR spectroscopy: biological applications. *Annu Rev Phys Chem* 52:279–313. <https://doi.org/10.1146/annurev.physchem.52.1.279>
- Schmidt T, Ghirlando R, Baber J, Clore GM (2016a) Quantitative resolution of monomer-dimer populations by inversion modulated deer epr spectroscopy. *ChemPhysChem* 17(19):2987–2991. <https://doi.org/10.1002/cphc.201600726>
- Schmidt T, Walti MA, Baber JL, Hustedt EJ, Clore GM (2016b) Long distance measurements up to 160 angstrom in the GroEL tetradecamer using Q-Band DEER EPR spectroscopy. *Angew Chem Int Edit* 55(51):15905–15909. <https://doi.org/10.1002/anie.201609617>
- Spindler PE, Glaser SJ, Skinner TE, Prisner TF (2013) Broadband inversion PELDOR spectroscopy with partially adiabatic shaped pulses. *Angew Chem Int Edit* 52(12):3425–3429. <https://doi.org/10.1002/anie.201207777>
- Valera S, Ackermann K, Pliotas C, Huang HX, Naismith JH, Bode BE (2016) Accurate extraction of nanometer distances in multimers by pulse EPR. *Chem-Eur J* 22(14):4700–4703. <https://doi.org/10.1002/chem.201505143>
- Van Doorslaer S (2017) Hyperfine spectroscopy: ESEEM. *Emagres* 6(1):51–69. <https://doi.org/10.1002/9780470034590.emrstm1517>
- Volkov A, Dockter C, Bund T, Paulsen H, Jeschke G (2009) Pulsed EPR determination of water accessibility to spin-labeled amino acid residues in LHCIIB. *Biophys J* 96(3):1124–1141. <https://doi.org/10.1016/j.bpj.2008.09.047>
- von Hagens T, Polyhach Y, Sajid M, Godt A, Jeschke G (2013) Suppression of ghost distances in multiple-spin double electron-electron resonance. *Phys Chem Chem Phys* 15(16):5854–5866. <https://doi.org/10.1039/c3cp44462g>
- Ward R, Bowman A, Sozudogru E, El-Mkami H, Owen-Hughes T, Norman DG (2010) EPR distance measurements in deuterated proteins. *J Magn Reson* 207(1):164–167. <https://doi.org/10.1016/j.jmr.2010.08.002>

- Ward R, Pliotas C, Branigan E, Hacker C, Rasmussen A, Hagelueken G, Booth IR, Miller S, Lucocq J, Naismith JH, Schiemann O (2014) Probing the structure of the mechanosensitive channel of small conductance in lipid bilayers with pulsed electron-electron double resonance. *Biophys J* 106(4):834–842. <https://doi.org/10.1016/j.bpj.2014.01.008>
- Yang ZY, Liu YP, Borbat P, Zweier JL, Freed JH, Hubbell WL (2012) Pulsed ESR dipolar spectroscopy for distance measurements in immobilized spin labeled proteins in liquid solution. *J Am Chem Soc* 134(24):9950–9952. <https://doi.org/10.1021/ja303791p>
- Zavoisky E (1945) Spin-magnetic resonance in paramagnetics. *J Phys USSR* 9:211–245

Chapter 8

Mössbauer Spectroscopy



João Carlos Waerenborgh, Pedro Tavares and Alice S. Pereira

8.1 Introduction

Mössbauer spectroscopy is based on nuclear resonance involving the emission and absorption of γ radiation.

The nuclei of the atoms of the same chemical element have the same number of protons, the atomic number. Nuclei of Fe atoms, for example, have 26 protons. However, the number of neutrons in the nuclei of the same element may vary. A nuclear species, or nuclide, is defined by both numbers. It is represented by the chemical symbol of the element, which defines the number of protons, preceded by the total number of nucleons, the atomic mass number. For example, ^{57}Fe refers to the Fe nuclide with mass number 57, i.e., 26 protons + 31 neutrons = 57 nucleons. The most common nuclide of Fe is ^{56}Fe with 26 protons + 30 neutrons. Atoms of ^{56}Fe and ^{57}Fe have the same chemical behavior but the nuclides have quite different properties.

Like the electron cloud in atoms, nuclei are quantum systems and can only have discrete values of energy characteristic of each nuclide. When an atom decays from an excited to the ground electronic state it emits radiation that can be absorbed by an identical atom in the ground state which in turn decays re-emitting radiation with the same energy. This phenomenon of resonance was evidenced by Wood in 1904

J. C. Waerenborgh (✉)

Departamento de Engenharia e Ciências

Nucleares, Centro de Ciências e Tecnologias Nucleares, Instituto Superior Técnico, Universidade de Lisboa, Estrada Nacional 10 (km 139,7), 2695-066 Bobadela LRS, Portugal

e-mail: jcarlos@ctn.tecnico.ulisboa.pt

P. Tavares · A. S. Pereira

Molecular Biophysics Laboratory, UCIBIO/Requimte, Department of Chemistry, Faculdade de Ciências e Tecnologia, Universidade NOVA de Lisboa, 2829-516 Caparica, Portugal

e-mail: pabt@fct.unl.pt

A. S. Pereira

e-mail: masp@fct.unl.pt

© Springer Nature Switzerland AG 2019

A. S. Pereira et al. (eds.), *Radiation in Bioanalysis*, Bioanalysis 8,
https://doi.org/10.1007/978-3-030-28247-9_8

with the yellow spectral emission line of Na. In the same way, a nucleus decays from an excited to the ground state releasing energy, either emitting electromagnetic radiation, γ radiation, which can be absorbed by an identical nucleus, or by ejecting an electron from the corresponding atom, the internal conversion electron.

In contrast to electron resonance, nuclear resonance or γ resonance between identical nuclides was observed experimentally long after it was suggested and even then only under very special conditions. Why did the nuclei refuse to cooperate?

If the energy of the photons emitted by a large number of motionless identical nuclei or atoms in the same excited state is recorded, a curve analogous to that of Fig. 8.1, a Lorentzian curve, described by the Breit-Wigner's expression, is observed

$$W(\varepsilon) = \frac{\Gamma_n^2/4}{(\varepsilon - \varepsilon_o)^2 + \Gamma_n^2/4} \quad (8.1)$$

The most probable energy of the emitted photons is equal to the energy difference between the excited and ground levels, $\varepsilon_o = E_{ex} - E_g$. Γ_n is the width at half-height of the curve, the energy uncertainty, typical of quantum systems. The observation of Γ_n is explained by Heisenberg's uncertainty principle. Since the excited state does not have an infinite lifetime, the energy cannot be determined with as high a precision as we wish. The minimum error with which it is possible to determine ε_o is given by Γ_n , according to

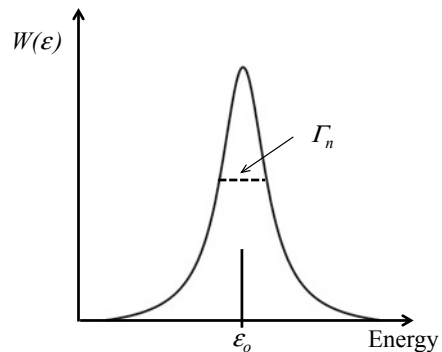
$$\Gamma_n \cdot \tau_n = h/(2 \cdot \pi) \quad (8.2)$$

where h is the Planck constant and τ_n is the half-life of the excited state.

The probability of γ photons absorption with energy ε_o by nuclei in the ground state identical to those used in the previous experiment, is given by a curve similar to that of Fig. 8.1 and also centered in ε_o .

Radiation emission and absorption curves for motionless systems are therefore similar and overlap in an energy diagram. The behaviour of real systems is, however, more complex.

Fig. 8.1 The emission spectrum of an excited nucleus has the shape of a Lorentzian curve. The non-zero halfwidth of this curve, Γ_n , is due to the energy uncertainty of the excited state



A photon of energy ϵ_o has a linear momentum $p = \epsilon_o/c$ where c is the speed of light in vacuum. When an atom or nucleus initially at rest emits a photon, in order to conserve the linear momentum of the system, the atom must recoil in the opposite direction to the emission, with a linear momentum p equal to that of the photon. The most suggestive macroscopic image of this phenomenon is the recoil of a firing weapon. If the atom recoils, its kinetic energy varies

$$\epsilon_R = \frac{p^2}{2M} = \frac{\epsilon_o^2}{2c^2M} \tag{8.3}$$

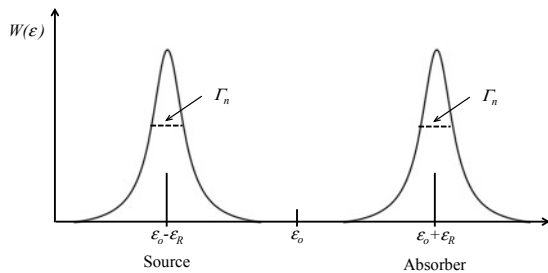
ϵ_R is the recoil energy and M the mass of the nucleus, practically equal to that of the corresponding atom. Energy conservation now comes into play. What is the source of the energy needed for this recoil? The electronic or nuclear transition. This means that actually the photon will only be emitted with the energy

$$\epsilon_{em} = \epsilon_o - \epsilon_R = \epsilon_o - \frac{\epsilon_o^2}{2c^2M}$$

A similar analysis for the absorbing nucleus leads to the conclusion that the photon, in order to be absorbed, should have the transition energy plus the recoil energy of the absorbing nucleus, i.e., $\epsilon_{abs} = \epsilon_o + \epsilon_R = \epsilon_o + \frac{\epsilon_o^2}{2c^2M}$.

The energies corresponding to the maxima of the emission and absorption curves thus differ by $\frac{\epsilon_o^2}{c^2M}$ and this explains why the observation of nuclear resonance is so difficult. While the emission of a visible photon with an energy ϵ_o of the order of a few eV corresponds to a recoil energy $\epsilon_R \approx 10^{-10}$ eV, the emission of a γ photon with an energy $\epsilon_o \approx 10$ keV is related to a recoil energy $\epsilon_R \approx 10^{-3}$ eV. The half-lives of the excited electronic and nuclear states are of the same order of magnitude (1–100 ns) corresponding, according to Eq. 8.2, to an energy uncertainty $\Gamma_n \approx 10^{-9}$ to 10^{-8} eV. The recoil energy associated with the emission of a γ photon is much higher than Γ_n whereas, in the case of the emission of a visible photon, it is lower than Γ_n . This means that while for optical resonance the emission and absorption curves practically overlap, for nuclear resonance they are far apart (Fig. 8.2). The overlapping integral of $W_{em}(\epsilon)$ and $W_{abs}(\epsilon)$, η , which is proportional to the probability of nuclear resonance,

Fig. 8.2 Emission and absorption curves considering the recoil effect when $\epsilon_R \gg \Gamma_n$



is very low, typically $\eta \sim 10^{-11}$, thus explaining why this phenomenon is very difficult to detect.

Another phenomenon also has a significant impact in resonance experiments. In a real system, due to thermal motion, even before the emission or absorption of a photon the atoms are already moving relative to each other. The well-known Doppler effect increases the frequency of a sound when the emitting source approaches us and decreases its frequency when the source moves away. Likewise, when an emitting nucleus is moving relative to the absorbing nucleus, the photon emitted with a frequency ν_o and therefore an energy $\varepsilon_o = h \cdot \nu_o$ will have, from the point of view of the absorber, a higher energy, given by

$$\varepsilon = \varepsilon_o + \frac{\varepsilon_o V_x}{c} \quad (8.4)$$

where V_x is the velocity of the source relative to the absorber. V_x is positive if the nuclei are moving closer and negative if they are moving away. In a gas, as the motions of the atoms are random, V_x shows a nearly continuous range of positive and negative values which may be described by a Maxwell distribution. The resulting distribution of $\frac{\varepsilon_o V_x}{c}$ values (Fig. 8.3) will thus lead to broadening of the emission and absorption curves and consequently to a reduction of their maximum intensity, as the area below the curves remains constant, equal to the total number of nuclei in the system. As the temperature of the system increases, so does the probability of particles reaching higher velocities and, therefore, the thermal broadening of the emission and absorption curves also increases. In optical resonance, where the curves are practically overlapping, the effect of the thermal motion is only a slight reduction of the overlap integral η due to the reduction of the curves intensities close to ε_{em} and ε_{abs} . In the case of nuclear resonance, however, where the maxima of the curves are far apart, their broadening leads first to an increase in the range of energies in which there is a significant overlap of the curves (Fig. 8.3) favoring the increase of η . However, this increase only occurs up to a certain temperature value, T_{opt} , above which the effect of reducing the intensity of the curves around ε_{em} and ε_{abs} becomes predominant.

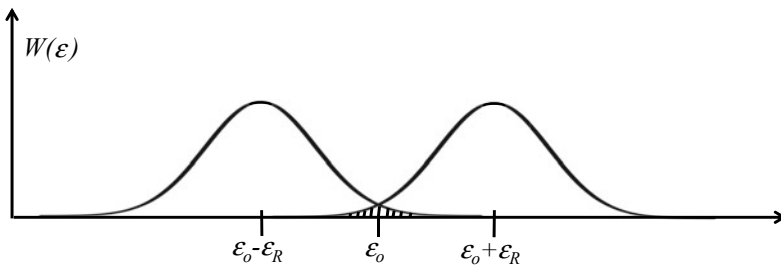


Fig. 8.3 Emission and absorption curves considering recoil and broadening by the thermal Doppler effect

This analysis has not only explained the failure of the first attempts to observe nuclear resonance but also suggested possibilities to get around the difficulties. In fact, nuclear resonance was eventually observed in three kinds of tests: (i) the source was moved towards the absorber with a velocity high enough to compensate the recoil energy by the Doppler effect; (ii) the source and the absorber were heated or cooled to temperatures near T_{opt} ; (iii) the occurrence of a preceding nuclear decay or particle reaction conveyed a velocity to the nucleus that compensated the recoil energy by the Doppler effect. These experiments, however, are difficult to perform. In the first case the velocity of the source must be very high, e.g. of the order of 10^5 cm/s for ^{191}Ir ; in the last two cases the resonance probability was very low, e.g. for $^{119\text{m}}\text{Sn}$ at $T_{opt} = 28$ K this probability is only $\eta \sim 10^{-6}$.

8.2 Mössbauer Effect

In 1957 in Heidelberg, Rudolf Mössbauer was studying for his *PhD* thesis the resonance of the $\varepsilon_o = 129$ keV transition of ^{191}Ir in metallic Ir, for which $T_{opt} = 550$ K. Contrary to expectations, the resonance increased when the temperature dropped from 300 to 78 K. On the other hand if the source was moving relative to the absorber no resonance was observed (Frauenfelder 1962).

How to explain this effect? This discovery, thanks to which Mössbauer was awarded the Nobel Prize for Physics in 1961, was by no means unexpected. Lamb in 1938 had developed the theory of resonance absorption of slow neutrons in crystals, demonstrating that it is possible to observe absorption lines with the natural width. X-ray diffraction technique had also shown that while the intensity of the diffraction lines decreased with increasing temperature their width did not. All the theoretical formalism was available but before Mössbauer no one thought to apply it to γ resonance. At the time, in Nuclear Physics there was a general tendency to ignore the chemical bonds of the atoms whose nuclei were investigated. This was understandable considering that the energies involved in nuclear reactions are several orders of magnitude higher than the energies of chemical bonding. Before the Mössbauer experiment whenever nuclear phenomena were studied, only free atoms were considered.

The cornerstone of the discovery of the Mössbauer effect, the explanation of the unexpected and startling observation with ^{191}Ir , lies on a change of perspective that led to the realization that some nuclear phenomena do not necessarily happen on a different scale from those of atomic phenomena, their energy being comparable to the energies of chemical bonding or the atomic vibrations in solids (Wertheim 1964).

Thus, in the case of emission or absorption of γ photons, the recoil energy transmitted to a free nucleus is usually sufficient to destroy the resonance conditions, unless the atom is incorporated in the lattice of a crystalline or amorphous solid. The energies of the chemical bonds in a solid are of the order of 1–10 eV, considerably higher than the recoil energy $\varepsilon_R \approx 10^{-4}$ to 10^{-1} eV of a free atom that emits a γ photon with energy lower than 200 keV, the case of transitions for which the Möss-

bauer effect is observed. This means that the chemical bonds will not be broken, the emitting nucleus cannot recede freely, and the momentum associated with the emission of the photon will be transmitted to the entire lattice. Instead of the mass M of an isolated nucleus the mass M_C of the whole atom domain must be considered. These domains are typically comprised of more than 10^{15} atoms and therefore their recoil energy will be about 10^{15} times lower than that of an isolated nucleus (Eq. 8.3), i.e., even smaller than the natural line width Γ_n .

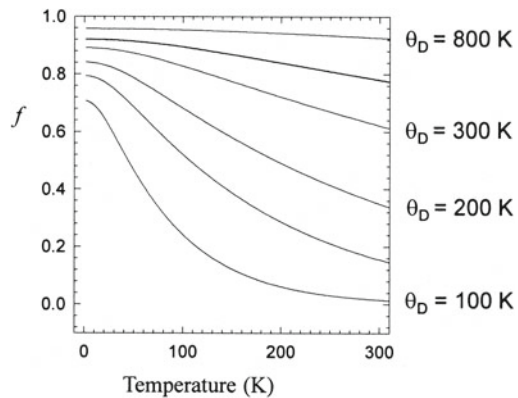
Although chemical bonds may not be broken, excitation of phonons occur since ε_R is of the same order of magnitude of the atomic vibration energies, i.e., ε_R may be dissipated by heating the lattice. When there is emission/absorption of γ rays there is a finite probability for zero-phonon events, which is called the recoil-free or recoilless emission/absorption. In these cases resonance is observed. The probability of recoilless events, the recoilless factor f , decreases with increasing ε_R , i.e. with increasing γ photon energy. When ε_R is high enough all the emission/absorption of γ photons takes place with phonon excitation and no resonance is observed. Using the simple Debye model for the thermal vibrations the following dependence of the recoilless factor on temperature, on recoil and on phonon energies, is deduced (Fig. 8.4)

$$f = \exp\left[-\frac{\varepsilon_R}{k_B\theta_D}\left(\frac{3}{2} + \frac{\pi^2 T^2}{\theta_D^2}\right)\right] \quad T < \theta_D$$

$$f = \exp\left(-\frac{6\varepsilon_R T}{k_B\theta_D^2}\right) \quad T > \theta_D \quad (8.5)$$

where θ_D is the Debye temperature of the solid (Greenwood and Gibb 1971). θ_D is higher for solids with stronger chemical bonds and higher phonon energies. The probability of recoilless events increases therefore with θ_D . f decreases with increasing ε_R and with increasing temperature thus explaining the temperature dependence observed by Mössbauer in his experiment with ^{191}Ir .

Fig. 8.4 Temperature dependence of the recoilless factor f for different Debye temperatures θ_D



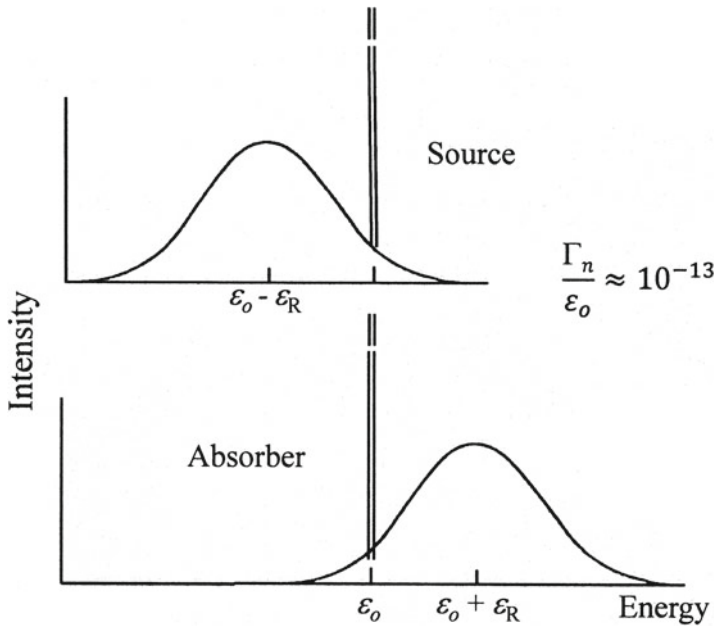


Fig. 8.5 γ ray emission and absorption spectra in a solid lattice. The energy of the recoilless emission and absorption lines is measured with a precision up to $1:10^{13}$

When resonance is observed the only energy loss during emission is the recoil of the lattice which is negligible compared to Γ_n . Therefore, the zero-phonon component of the γ emission spectrum has exactly the energy of the nuclear transition with an uncertainty or linewidth determined alone by the widths of the nuclear levels involved in the transition $\sim 2 \Gamma_n$ (Fig. 8.5). This line overlaps a band due to thermally excited events with an effective width of the order of the phonon energies. The fraction of the area of the emission spectrum corresponding to the line with $2 \cdot \Gamma_n$ half width is equal to the recoilless fraction f of the source. A similar result is obtained for the absorption spectrum.

8.3 Mössbauer Spectroscopy

The Mössbauer effect consists on the observation of recoilless nuclear resonance with lines with natural linewidth.

The important applications of the Mössbauer effect, which earned R. Mössbauer the Nobel Prize, result from the aforementioned possibility of measuring energies ϵ_0 with a resolution of $\Gamma_n/\epsilon_0 \sim 10^{-11}$ to 10^{-13} . Such a degree of precision allows the observation of relativistic effects in laboratory scale experiments (Greenwood and Gibb 1971). For example, an experiment placing a radiation source and absorber at

different heights, a few tens of meters apart, allows the measurement of the gravitational red shift. The experimental values confirm within 99.7% accuracy those predicted by the theory.

However, the most important application of the Mössbauer effect arises from the possibility of measuring hyperfine interactions, i.e., the electrostatic and magnetic interactions between a nucleus and the electron cloud. These interactions cause small shifts and splittings of the nuclear energy levels which for many nuclides are larger than the natural width Γ_n .

If the emitting and absorbing nuclei are located in atoms with different chemical environments the hyperfine interactions in the source and absorber are different. If this difference is larger than Γ_n the nuclear resonance will not be observed when the source and absorber are stationary. However, differences in hyperfine interactions may be compensated by a Doppler effect resulting from a mechanical motion of the source relative to the absorber with precisely controlled velocity.

The basic configuration of a transmission spectrometer consists of a source containing the studied nuclide in the first excited state. The source is mounted at the end of the movable shaft of a vibrator, the velocity transducer. The absorber is placed as shown in Fig. 8.6, between the source and a γ radiation detector. The source is moved back and forth following a variable periodic velocity while the absorber is kept stationary. If chemically identical, single line, source and absorber are used, the counting rate measured by the detector as a function of the velocity of the source varies according to the curve shown in Fig. 8.6. A maximum absorption is measured when the relative velocity V between source and absorber is zero. As V increases the absorption decreases and when $|V| > (2 \Gamma_n c)/\epsilon_0$, the Doppler effect (Eq. 8.4) modifies the frequency of the γ radiation by twice the natural line width and resonance condi-

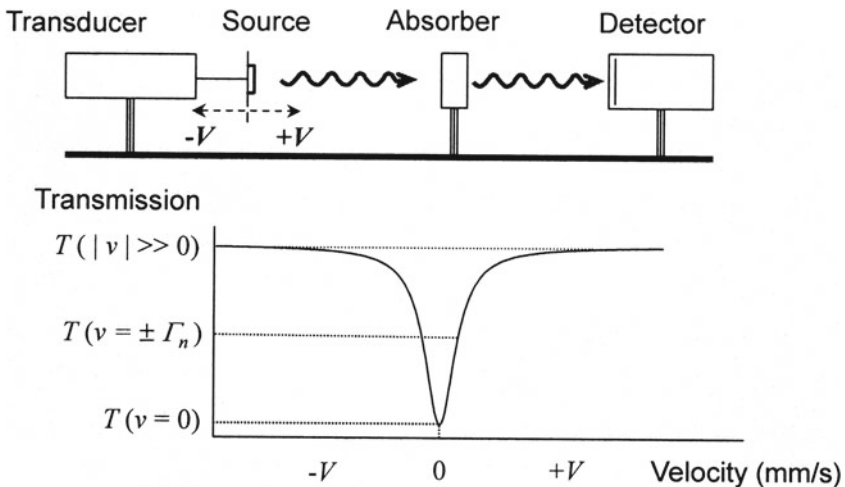


Fig. 8.6 Basic setup of a Mössbauer spectrometer (top) and spectrum (bottom) obtained with a single line source and absorber which are chemically identical

tions are no longer met. In the case of ^{57}Fe , $\varepsilon_o = 14.4 \text{ keV}$, $\Gamma_n = 9.1 \times 10^{-9} \text{ eV}$ the Doppler velocity corresponding to Γ_n is 0.095 mm/s. For $V > 0.2 \text{ mm/s}$ resonance is no longer observed. Under ideal conditions the curve is Lorentzian (Fig. 8.1) with twice the width of the emission or absorption curves.

If the absorber is chemically different from the source the maximum absorption, i.e., resonance, will be observed for $V \neq 0$, a velocity value related to a Doppler effect which compensates the difference in hyperfine interactions. In the case of the 14.4 keV transition of ^{57}Fe , velocities within the $\pm 15 \text{ mm/s}$ range are suitable for measuring hyperfine interactions in almost all known Fe-containing materials.

Using a reference material as a single line source the velocity values where resonance is observed give us a wealth of information concerning the oxidation and electronic states of the atoms containing the probed nucleus, the chemical bonds and coordination, and often the atomic magnetic moments and magnetic sublattices of a sample, as shown below. On the other hand, in many instances it is also possible to identify Fe-containing phases based on their typical spectra which may be particularly relevant whenever their identification by other techniques such as X-ray diffraction is not possible.

8.3.1 Isomer Shift

The first hyperfine interaction is the electric monopole interaction. The energies of the nuclei ground and excited states depend on the electron density at the nuclei. Since the ^{57}Fe nucleus is larger in the ground state than in the first excited state, the electrostatic interaction is stronger for the former state as shown in Fig. 8.7.

Let us consider a source where Fe is in the metallic state and an absorber where Fe is in the formal 3+ oxidation state. The electron configurations may be described to a first approximation as $[\text{Ar}]4s^2 3d^6$ for metallic Fe and $[\text{Ar}]3d^5$ for Fe^{3+} . The s and relativistic $p_{1/2}$ electrons are the only ones with non-zero electron charge density at the nuclei. This means that the nucleus/electron cloud interaction in Fe^{3+} with no $4s$ electrons, is lower than in metallic Fe. Considering the relative sizes of ^{57}Fe nuclei in the ground and first excited states the energy of the nuclear transition in metallic Fe is lower than in Fe^{3+} (Fig. 8.7). Since this energy difference ΔE_δ is higher than Γ_n no resonance would be observed if the source and absorber were standing still. If the source moves towards the absorber with the velocity V , such that the Doppler effect compensates the energy difference

$$\Delta E_\delta = \frac{\varepsilon_o \cdot V}{c}$$

resonance is established and an absorption peak is observed. This velocity V is called the isomer shift, IS , of Fe^{3+} in the absorber relative to the source we are using. If in the absorber there was Fe^{2+} , electronic configuration $[\text{Ar}]3d^6$, the number of s electrons would be the same as in Fe^{3+} . There is however one additional d electron in Fe^{2+} . d

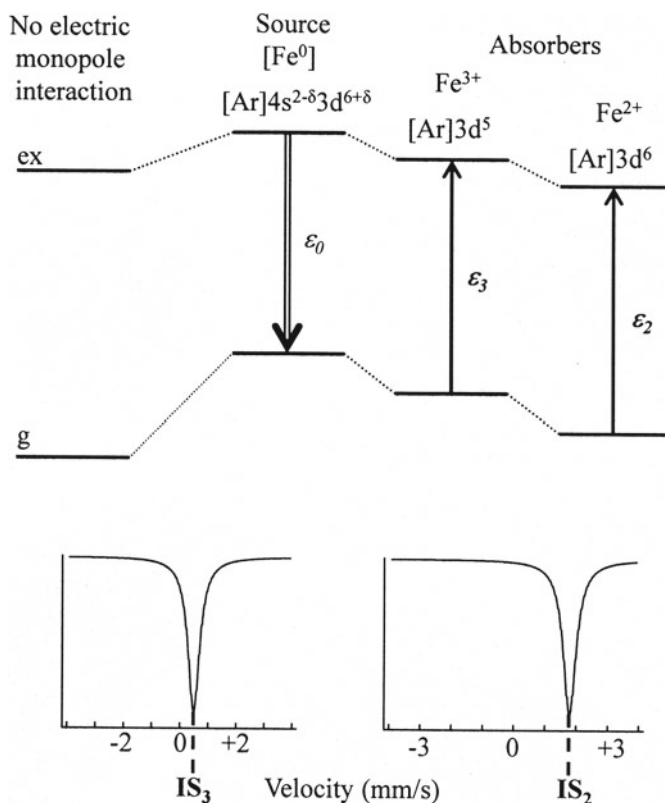


Fig. 8.7 Nuclear levels considering no electric monopole interaction and considering this interaction for different electronic states of the Fe atoms (top). Isomer shift values IS_3 and IS_2 for high-spin Fe^{3+} and Fe^{2+} , respectively (bottom, see text)

electrons have zero probability at the nucleus but they have a shielding effect on the s electrons. A fraction of s electron density, particularly $3s$ electron density is further away from the nucleus than $3d$ electrons. The electrostatic repulsion that s electrons experience there depends on the screening effect of inner electrons. When the d electron density increases the shielding effect also increases causing an expansion of the s electrons and a decrease of the s electron density at the nucleus. As shown in Fig. 8.7 this implies that the energy of the nuclear transition is higher in Fe^{2+} than in Fe^{3+} . The IS of Fe^{2+} is therefore higher than the IS of Fe^{3+} .

The IS value also depends on the electronegativity of the ligands and the coordination of the Fe atoms. Normally for both oxidation states IS decreases with decreasing coordination number and decreasing electronegativity of the ligands, which can be understood as resulting from a higher degree of covalence of the bonds. Nevertheless the ranges of IS values for the Fe^{2+} and Fe^{3+} in the so-called high-spin state, where the electron configurations for Fe^{2+} and Fe^{3+} are closer to the formal $[Ar]3d^6$ and $[Ar]3d^5$, are clearly distinct (Gütlich et al. 2011). These high-spin states are observed

in compounds with predominant ionic bonds such as Fe oxides, hydroxides, silicates, phosphates, sulphates, etc. where the ligand field is weak, weaker than the spin coupling energy. In these compounds Fe^{2+} and Fe^{3+} are thus readily distinguished on the basis of their IS values.

In compounds where the chemical bond has a significant covalent character Fe^{2+} and Fe^{3+} are in the so-called low-spin state, the electron sharing between the Fe cations and the ligands becomes significant, the $4s$ electron orbitals occupancy is no longer zero which causes a significant decrease of IS . In addition to the s orbital population the relative importance of p and d orbitals in the bonding as well as the extent to which the electrons are delocalized play a role in determining the IS value. As a result, the range of IS values for low-spin Fe^{2+} and Fe^{3+} are very similar and overlap the lower IS values of high-spin Fe^{3+} (Gütlich et al. 2011).

IS values are generally given as velocities, units mm/s, according to Baggio-Saitovitch et al. (2002) and are commonly given relative to the metallic αFe standard, the same standard used for velocity calibration as referred below.

8.3.2 Quadrupole Splitting

The second hyperfine interaction is the electric quadrupole interaction. As for electrons in an atom where the quantum number J specifies the total angular momentum (orbital + spin), for nuclei the quantum number I defines the nuclear spin. The distribution of nuclear charges may have a non-spherical symmetry. This is the case for the ^{57}Fe nucleus in the 14.4 keV state, with $I = 3/2$, whose nuclear charge distribution is observed as a prolate ellipsoid (Fig. 8.8) thus presenting a positive electric quadrupole moment Q . If the electric charge distribution around the nucleus has neither spherical nor cubic symmetry, i.e., if it gives rise to an electric field gradient $\nabla \cdot \mathbf{E}$ at the nucleus position, the nucleus/electron cloud interaction energy depends on the direction of the nucleus spin relative to the electronic and lattice charge distributions.

Let us assume an electric charge distribution with axial symmetry in which there is a larger concentration of negative charge along the axis of symmetry, the z axis (Fig. 8.8). In a classical system any orientation of the nucleus relative to that axis would be possible. Since we are dealing with a quantum system, the nucleus can only adopt a discrete number of orientations, determined by the value of the spin quantum number which for the 14.4 keV state is $I = 3/2$. Each of those orientations is, in turn, defined by the m_I values ($-3/2$, $-1/2$, $1/2$ and $3/2$). Note that for $m_I = 3/2$ the nuclear charge distribution is on the average closer to the z axis of the system than when $m_I = 1/2$. Since the density of negative charges along this axis is the highest, the configuration $m_I = 3/2$ corresponds to a lower energy of the system (energy diagram in Fig. 8.8), as it increases the attractive interaction between the negative electronic charges and the positive nuclear charge. $m_I = -1/2$ corresponds to an inversion in the direction of the magnetic moment of the nucleus relative to $m_I = 1/2$, which, from the point of view of the average distribution of the nuclear charges has no effect on the interaction energy with the electric field gradient. The

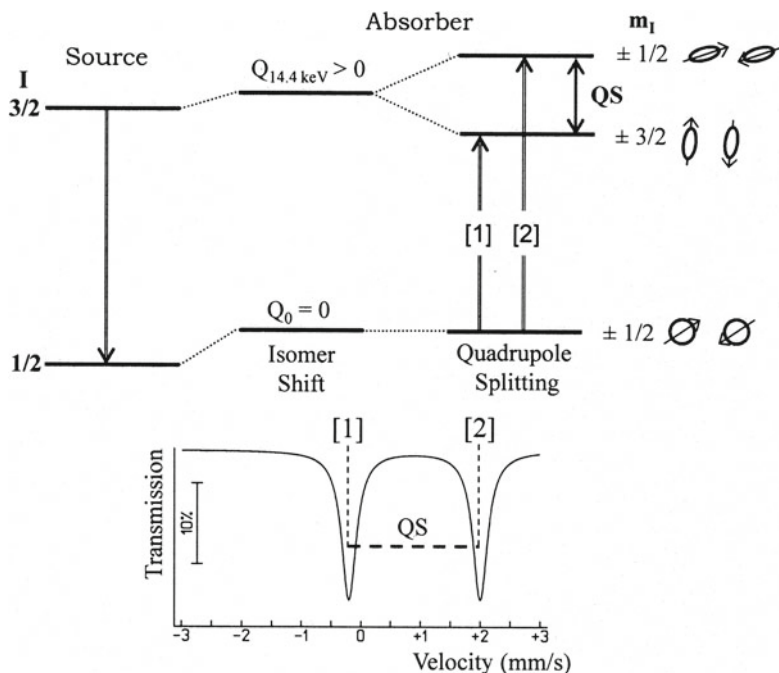


Fig. 8.8 Electric quadrupole interaction in the case of an $\nabla.E$ with higher negative charge density along the z axis than on the perpendicular plane (top, see text). Quadrupole doublet observed in the Mössbauer spectrum (bottom) for this $\nabla.E$ in the case of randomly oriented powder samples with no anisotropic f factors

energy of the system is therefore equal for both $m_I = \pm 1/2$ substates. The same is true for $m_I = \pm 3/2$.

Therefore, when the position occupied by Fe in the solid lattice has point symmetry lower than cubic, the degeneracy of the first excited state of the ^{57}Fe nucleus is partially raised and two sublevels with different energies are observed (Fig. 8.8). Since in the ground state the nucleus has spin $I = 1/2$, no interaction with an $\nabla.E$ is observed. This is easy to understand since m_I may only have two symmetric values $\pm 1/2$. The nucleus behaves as if its quadrupole moment is zero and the nuclear charge distribution is spherical.

This means that in the Mössbauer spectra of a sample where Fe is in a position with symmetry lower than cubic two lines, one doublet, is observed (as long as no magnetic interactions are observed, see below). The energy difference between both lines of a doublet is called the quadrupole splitting, QS , measured in mm/s as the isomer shift. When the coordination polyhedron of the Fe cation is a distorted octahedron or tetrahedron, or even when it is a regular polyhedron but the ligands of Fe are not all the same, a non-zero QS is observed. For example, in the spectra of $[\text{Fe}(\text{CN})_6]^{4-}$ or $[\text{Fe}(\text{CN})_6]^{3-}$, where the octahedral configuration of the 6 CN^- ligands has cubic symmetry, only one line is observed. The substitution of one of the CN^- ligands by

NO^+ in $[\text{Fe}(\text{CN})_5(\text{NO})]^{2-}$ creates a charge distribution asymmetry even if the six ligands are at the corners of a regular octahedron, and in the corresponding spectrum a doublet is observed.

The value of QS depends on the degree of asymmetry and the electronic state of Fe. Each of the five $3d$ orbitals of high-spin Fe^{3+} has one electron. The half-filled $3d$ subshell, such as fully filled electronic subshells, creates a spherically symmetric charge distribution, whatever the $\nabla \cdot \mathbf{E}$ due to the ligand field or any other lattice electric charge distribution. In this case if QS is different from zero there is only the component due to the lattice $\nabla \cdot \mathbf{E}_{latt}$ as $\nabla \cdot \mathbf{E}_{elect}$ due to the electron cloud is always zero.

In the case of high spin Fe^{2+} there is a sixth electron $3d$. If the lattice field has spherical symmetry the six $3d$ orbitals have the same energy, their occupancy by the sixth $3d$ electron is the same and no quadrupole splitting is observed. If the symmetry is cubic as in a regular octahedral field the three t_{2g} orbitals (d_{xy} , d_{xz} , d_{yz}) will have lower energy than the remaining $3d$ orbitals, the e_g ($d_{x^2-y^2}$, d_{z^2}). The occupancy of the three t_{2g} orbitals by the sixth d electron is the same and since this set of $3d$ orbitals has cubic symmetry no $\nabla \cdot \mathbf{E}$ is observed either. A similar analysis of a cubic tetrahedral field, where the e_g orbitals have lower energy leads to the same conclusion. It is not surprising that if the Fe cation is on a lattice position with cubic symmetry there is neither a lattice $\nabla \cdot \mathbf{E}_{latt}$ nor an electronic $\nabla \cdot \mathbf{E}_{elect}$. A quadrupole splitting will only be observed if the crystal field is lower than cubic, for instance if there is a tetragonal or trigonal distortion of an octahedral crystal field. If the field is a distorted octahedron the degeneracy of the three t_{2g} orbitals is lifted. Since each one or any set of two t_{2g} orbitals has symmetry lower than cubic the electronic charge distribution also creates a $\nabla \cdot \mathbf{E}_{elect}$. d electrons are, on average, much closer to the nucleus than the lattice charges around the respective atom. The $\nabla \cdot \mathbf{E}_{elect}$ created by the d electron is therefore much higher than the lattice one. Hence, under similar conditions for high-spin Fe cations, QS of Fe^{2+} is significantly higher than Fe^{3+} . Moreover, when spectra are carried out at different temperatures within a range where the energy difference between the e_g or between the t_{2g} orbitals due to the non-cubic ligand field is of the order of magnitude of the thermal energy $k_b \cdot T$, the QS of Fe^{2+} decreases with increasing temperature whereas QS of Fe^{3+} remains practically constant. The temperature dependence of the Fe^{2+} QS is a result of the temperature dependence of the thermal population of the low-lying first excited electronic state. On the other hand, as long as there is no phase transition QS of high-spin Fe^{3+} will only slightly change due to the thermal expansion of the lattice.

In compounds where the chemical bond has a significant covalent character a different behaviour is observed. In the case of Fe^{2+} in strong octahedral crystal fields the six $3d$ electrons may fully occupy the lowest energy t_{2g} orbitals. The electronic contribution for $\nabla \cdot \mathbf{E}$ is then zero even on a lattice site with non-cubic symmetry. On the other hand, in the case of Fe^{3+} the five $3d$ electrons will not fully occupy the t_{2g} orbitals and an electronic contribution for $\nabla \cdot \mathbf{E}$ is expected. Therefore, in the low-spin case, in a distorted octahedral environment QS of Fe^{2+} is normally lower than the temperature dependent QS of Fe^{3+} .

On the basis of the IS and QS values high-spin Fe^{2+} may be unambiguously identified. For the remaining electronic states however, namely low-spin Fe^{2+} and Fe^{3+} and high-spin Fe^{3+} the measurement of magnetic hyperfine interactions is necessary.

8.3.3 Magnetic Hyperfine Splitting

This hyperfine interaction is the magnetic dipole interaction. When there is a magnetic field at the nucleus, the hyperfine magnetic field \mathbf{B}_{hf} , a nuclear Zeeman effect is observed. \mathbf{B}_{hf} interacts with the magnetic dipole moment of the nucleus by fully raising the degeneracy of nuclear levels. Each m_I will correspond to a different energy, depending on the angle between the nuclear magnetic moment μ_{nuc} and \mathbf{B}_{hf} , as shown in Fig. 8.9. For the ground state of ^{57}Fe $I = 1/2$ ($m_I = -1/2$ and $1/2$) there are two sub-levels and for the excited state $I = 3/2$ four ($m_I = -3/2, -1/2, 1/2$ and $3/2$). Only six transitions are allowed between the ground and excited sublevels by the selection rules; those corresponding to $\Delta m_I > 1$ are not allowed since the total angular momentum of the γ photon is only 1. These six transitions are observed in a Mössbauer spectrum as a six-line pattern, the sextet, or the magnetic splitting. The relative intensities of these six lines are determined by the transition probabilities between the different sub-levels of the excited and ground states. In a sample consisting of randomly oriented powder the relative intensities are 3:2:1:1:2:3 (Fig. 8.9). The splitting of the six lines is proportional to the value of the modulus of \mathbf{B}_{hf} .

\mathbf{B}_{hf} results from the magnetic moment of the atom. Atoms with full electronic subshells, where all the electron spins are coupled, have zero magnetic moment. This is the case of low-spin Fe^{2+} with electron spin quantum number $S = 0$. A non-zero magnetic moment arises from unpaired electrons on the outer layers which are not fully filled. In addition to their contribution to \mathbf{B}_{hf} these electrons polarize the inner shells. The polarization of s electrons whose density at the nuclei is non-zero gives rise to the so-called Fermi contact term, the most important contribution to \mathbf{B}_{hf} .

Except for low-spin Fe^{2+} , the outer electron shells of Fe atoms or Fe^{2+} and Fe^{3+} cations contain unpaired electron spins. This implies that they have a non-zero magnetic moment μ_{Fe} . However, in compounds in the paramagnetic state, which do not exhibit a spontaneous global magnetization, μ_{Fe} of each atom has, in the absence of an external magnetic field, a random orientation which, with a few exceptions, varies too rapidly from the Mössbauer effect point of view. This means that the frequency of the μ_{Fe} and resulting \mathbf{B}_{hf} changing directions, is higher than 10^8 Hz, the order of magnitude of the nuclear moment precession frequency around \mathbf{B}_{hf} . In other words the nuclear magnetic moment μ_{nuc} , during its precession movement does not have time to complete a single rotation around \mathbf{B}_{hf} before this hyperfine field changes direction several times. In classical physics we might say that the average of the \mathbf{B}_{hf} is zero during the time that the nucleus is ‘observing’ it. Thus, in the Mössbauer spectrum rather than a sextet, one singlet, or if the quadrupole electric interaction is non-zero, a doublet, is observed.

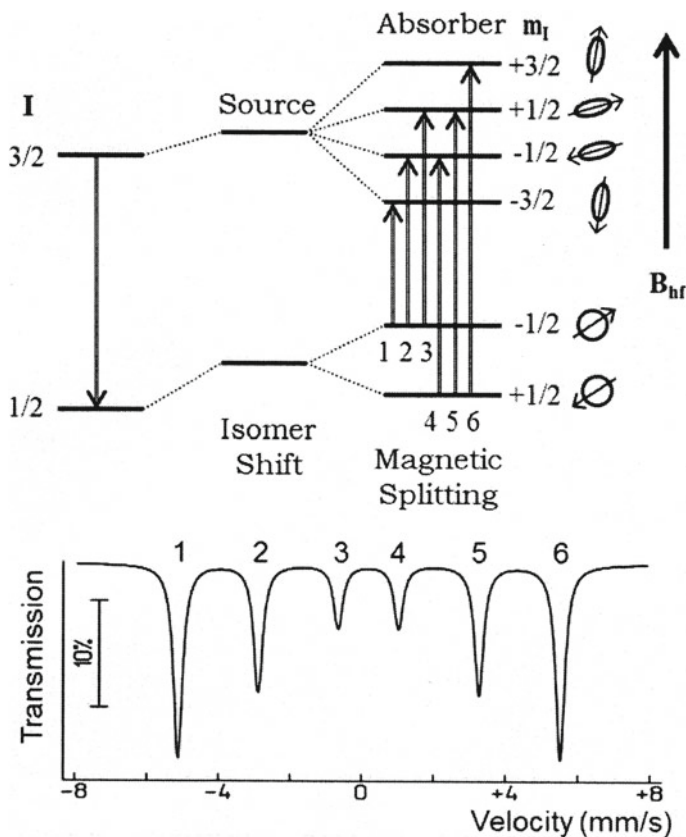


Fig. 8.9 Magnetic hyperfine interaction (top, see text). Magnetic splitting observed in the Mössbauer spectrum (bottom) in the case of randomly oriented powder samples with no anisotropic f factors

When strong, long-range magnetic correlations are established among the Fe atoms the μ_{Fe} are “frozen” from the Mössbauer effect point of view. The frequency with which their directions change, determined by the magnons frequency, is much lower than 10^8 Hz. This is the case for magnetically ordered materials and for spin glasses. The best known example of a magnetically ordered material at room temperature is magnetite, which attracts iron or non-austenitic steel objects. Many materials only become magnetically ordered at low temperatures.

In a paramagnetic compound an external magnetic field may also slow down the μ_{Fe} long enough to allow the observation of a magnetic splitting.

While in the case of rare-earths $|B_{hf}|$ is directly proportional to the atom magnetic moment, in the case of Fe the hyperfine magnetic coupling, the constant of proportionality relating $|B_{hf}|$ with $|\mu_{Fe}|$, depends on the electron densities at the bonding orbitals, particularly the $4s$ ones, and therefore on the chemical composition of the material. This dependence however is not high enough to prevent the estimation of

the number of unpaired electrons and therefore the oxidation degree of the Fe cations. Furthermore, within the same compound or in compounds with similar composition and structure, $|B_{hf}|$ increases with increasing $|\mu_{Fe}|$.

α Fe is a standard sample whose B_{hf} is known, 33.0 T at room temperature. Calibration of Mössbauer spectra is performed on the basis of the well known velocities of the six lines of the sextet observed for this standard at room temperature.

Usually both electric quadrupole and magnetic dipole interactions are observed. When the $\nabla.E$ is axially symmetric and the quadrupole interaction is significantly lower than the magnetic one it may be treated as a perturbation of the magnetic hyperfine interaction. In this case a sextet is still observed in the spectrum but the centre of gravity of the four inner lines is shifted relative to the centre of gravity of both outer lines. When the quadrupole and magnetic interactions are similar, or when $\nabla.E$ is not axially symmetric and the magnetic axis does not lie along one of the main $\nabla.E$ axes, the position and relative intensities of the absorption lines have to be calculated by solving the complete Hamiltonian for the hyperfine interactions in both the excited and ground nuclear states of the ^{57}Fe nuclei.

8.4 Mössbauer Spectrometer

The basic components of a Mössbauer spectrometer are the source, the γ ray detection system (detector, high voltage source, amplifiers, single channel analyser) the Mössbauer system itself (velocity transducer, drive unit, function generator) and the acquisition system where the spectra are recorded.

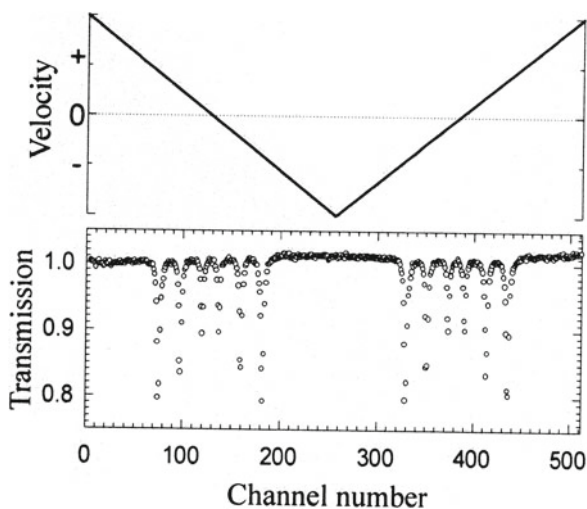
The source is a radioactive nuclide which has a long enough half-life and which decays to an excited state of the studied nuclide. At least a fraction of the decays to the ground state of this nuclide takes place through an excited state that allows the observation of the Mössbauer effect. In the case of iron the ^{57}Fe nuclide has two Mössbauer transitions, 136 and 14.4 keV. The former one has no practical application since its energy is high and consequently the recoilless factor very low. Mössbauer spectroscopy is therefore exclusively performed with the 14.4 keV transition. The radioactive nuclide in the source is ^{57}Co with a half-life of 271 days. This source is commercially available. ^{57}Co is produced in a nuclear facility and deposited on a metallic matrix foil chemically inert and with high electric and thermal conductivity in order to minimize the aftereffects of the nuclear decay preceding the Mössbauer γ ray emission. Furthermore, the matrix and the concentration of ^{57}Co should be such that no strong magnetic correlations are established and the source emits a single narrow line. The most common matrixes are Pd or Rh. ^{57}Co (Rh) sources have better recoilless factors and only slightly worse line widths than the Pd ones. Usually sources with an activity of 925 or 1.85 MBq are used. In addition to the 14.4 keV these sources also emit 122 and 136 keV γ -rays as well as Fe and Pd or Rh X-rays. Operation with these sources requires therefore special care. Particularly while mounted in the spectrometer lead shields with appropriate thickness should be used to reduce external radiation exposure to values comparable to the natural

background. While assembling or removing the source from the velocity transducer every reasonable effort to maintain exposures to the ionizing radiation as far below the dose limits as practical should be made.

The most appropriate radiation detector for ^{57}Fe Mössbauer spectroscopy is a proportional counter with krypton or xenon fill gas and a small amount of a so-called quench gas, usually methane. Argon is also suitable as fill gas but requires larger detectors due to its lower absorption cross section for the 14.4 keV radiation. A high voltage supply, a stable low-capacitance preamplifier and amplifier are needed. The height of the voltage pulses output by the detector, amplified by the amplifier units, is proportional to the energy dissipated in the proportional counter by the radiation. The voltage pulses from the amplifier may be collected directly or through a single channel analyzer by an acquisition board associated with a computer where the spectra are displayed. Either this acquisition board or the single channel analyzer selects the voltage pulses within a voltage range corresponding to the photoelectric absorption of the 14.4 keV γ -rays of ^{57}Fe . Only these pulses are accumulated in the acquisition board within a memory composed of different channels (usually 512 or 1024). In the so-called fast multiscaling mode the acquisition boards accumulate these pulses in only one channel at a time. Each channel corresponds to a specific velocity as explained below.

The Mössbauer system itself comprises a velocity transducer, an electromechanical device that imparts the Doppler velocity to the source. When operated in constant acceleration mode this transducer is driven by a symmetric triangular waveform, in such a way that the source is periodically moved in opposite directions, with a velocity that varies linearly with time between a maximum positive and a minimum negative value (Fig. 8.10) relative to a stationary absorber, usually the studied sample, as described above (Fig. 8.6). Positive velocities correspond to movement of the source toward the absorber and negative velocities away from the absorber. A

Fig. 8.10 Constant acceleration mode where velocity of the transducer varies linearly with time following a triangular wave form (top). Mirror image spectra are obtained (bottom)



drive unit and a function generator sometimes coupled in the same module control the transducer. Feedback circuitry in these units gets the transducer to follow the waveform precisely. Simultaneously the function generator sends the digital pulses that synchronize the sweeping of the acquisition board memory channels with the source movement, in such a way that each channel always corresponds to the same narrow velocity range. For example, a spectrum collected in a 512 channels memory for velocities between +12 and -12 mm/s. The velocity changes between +12 and -12 mm/s, i.e., 24 mm/s, within each memory half, 256 channels. The velocity gradient per channel is therefore $\frac{24}{256}$ mm/s. Assuming that the detector pulse counts corresponding to linearly decreasing velocity from +12 mm/s down to -12 mm/s accumulate in the first memory half (as shown in Fig. 8.10),

channel 1 corresponds to velocity range between 12 and $12 - \frac{24}{256}$ mm/s

channel 2 corresponds to velocity range between $12 - \frac{24}{256}$ and $12 - 2 \times \frac{24}{256}$ mm/s

... ..

channel 256 corresponds to velocity range between $12 - 255 \times \frac{24}{256}$ and $12 - 256 \times \frac{24}{256} = -12$ mm/s.

On the 2nd half of the memory a mirror image spectrum is obtained corresponding to linearly increasing velocity from -12 mm/s down to +12 mm/s, when a full period of the to and fro movement is achieved (Fig. 8.10). After reaching +12 mm/s a new memory sweep is restarted from channel 1 and the velocity increases again.

In order to obtain spectra with the absorber at low temperature cryostats are used. For temperatures in the range 1.5–300 K liquid helium bath cryostats are very reliable. The sample is kept in liquid He at 4 K and below or in He exchange gas above 4 K. For measurements above 77 K only liquid nitrogen may be used and the sample is kept in nitrogen exchange gas. Bath cryostats have liquid helium and liquid nitrogen reservoirs within a vacuum chamber. Thermal shields at liquid nitrogen temperature minimize heat transfer by radiation to the helium reservoir. A tube with narrow cross section leads liquid helium from the reservoir to a thermally isolated sample chamber. The liquid He flow is controlled by a needle valve. In order to stabilize a temperature value above 4 K a temperature controller connected to a temperature sensor and a heating coil located in the sample chamber is used. Between 1.5 and 4 K the desired temperature is achieved by keeping a constant value of the He pressure below 1 atm in the sample chamber. Closed cycle or cryogen-free cryo-cooler systems are increasingly popular since their operation is cheaper as no liquid helium is needed and a considerable progress in isolating the sample chamber from the cooler unit vibrations has been achieved.

8.5 Absorber Preparation

Long et al. (1983) have demonstrated that the ideal sample absorber thickness, t_{ideal} , that allows us to obtain the desired results in the shortest time and with the best signal to noise ratio, lies between the reverse of the mass absorption coefficient of

the sample and twice this value. The value of t_{ideal} for samples with high electronic absorption when compared with the resonant Mössbauer absorption should be close to the former value.

In addition to t_{ideal} one should also be careful to avoid saturation effects i.e., spectral distortions due to the thickness effect, such as peak broadening, and to prevent overestimating the absorption areas of the Fe species with lower concentrations in the specimen. Due to its simplicity a rule of thumb considering $t_{thick} \sim 1\text{--}5 \text{ mg/cm}^2$ of total Fe has been widely used, t_{thick} increasing with the number of spectral lines (Gütlich et al. 2011). In fact, it is still often used when peaks with ideal linewidths and very accurate measurements of the fraction of different Fe species based on the estimated relative areas of the corresponding peaks are not required. When very accurate quantitative results are at stake, in addition to careful calculation of the sample thickness, different recoilless factors for the distinct Fe species and fitting of the spectra with the full transmission integral should be considered (Rancourt et al. 1993).

Very often for biological or medical applications the amount of Fe in the samples is too low to obtain reasonable spectra. In these cases one should bear in mind that natural Fe has four stable isotopes, ^{54}Fe , ^{56}Fe , ^{57}Fe and ^{58}Fe and that their isotopic abundances are, respectively, 5.8%, 91.4%, 2.2% and 0.3%. This means that in natural samples or in compounds synthesized with natural Fe only 2.2% of the total Fe is Mössbauer “active”. If the specimens are prepared using Fe enriched in the ^{57}Fe isotope instead of natural Fe t_{ideal} or t_{thick} may be lowered down to ~ 50 times.

8.6 Mössbauer Spectroscopy of Other Elements

In order to perform Mössbauer spectroscopy the chemical element should have at least one isotope where the Mössbauer effect is observed. The probability of recoilless emission and absorption is only non-negligible for low energy nuclear transitions, typically lower than 200 keV. This is the reason why it is not observed for light nuclides which have no low energy first excited states.

In practice for transitions above 50–60 keV the source or the absorber should be kept at low temperatures, typically liquid helium temperature, as the recoilless factor f increases with decreasing temperature.

The higher the energy of chemical bonds, the higher θ_D , i.e., the higher the energy required to excite thermal vibrations, and therefore the higher f (Eq. 8.5). In the case of ^{57}Fe , for instance, oxide or silicate spectra are easily obtained at room temperature, whereas for many organometallic or protein materials samples are measured at low temperatures in order to obtain in a reasonable time statistically good spectra.

Even when an element has an isotope where the Mössbauer effect is observed it may not be suitable for Mössbauer spectroscopy. This is the case for long-lived excited states with half lives $\tau_N > 10^{-6} \text{ s}$ where line widths $\Gamma_n < 0.019 \text{ mm/s}$ are so narrow, that a very high precision of the velocity measurement is required or ultimately Γ_n is lower than the recoil energy of the entire lattice and the absorption

and emission lines do not overlap sufficiently. On the other hand, for short-lived excited states $\tau_N < 10^{-11}$ s hyperfine interactions are not observed because their energy is lower than the line widths.

Another issue is the availability of suitable sources for Mössbauer spectroscopy. The source must consist of radioactive nuclei that decay to an excited state of the probed nucleus. This nucleus further decays to the ground state through a cascade of transitions including the Mössbauer transition. In order to allow the collection of spectra the half-life of the parent radioactive nuclide should be long enough. That is the main reason why the only commercially available Mössbauer sources are ^{57}Co , $^{119\text{m}}\text{Sn}$ and ^{151}Sm whose half-lives are 271 days, 250 days and 87 years, respectively. For other parent nuclides whose half-lives are shorter or similar to the time necessary to obtain a spectrum a neutron source or a particle accelerator must be available at the same facility as the spectrometer.

Radioactive sources are not necessary if synchrotron radiation is used for Mössbauer spectroscopy. Experiments with synchrotron radiation are discussed in Gütlich et al. (2011).

Finally, the Mössbauer effect can only be observed in solids, crystalline or amorphous, rarely in liquids of high viscosity. The study of samples in solution can only be performed with the sample at a temperature lower than the melting point.

8.7 Mössbauer Spectroscopy of Biological Systems

Mössbauer spectroscopy has been successfully applied to the study of iron containing biological systems, proving to be a powerful tool to investigate the electronic structure of such compounds. As described above, information about magnetism, electronic relaxation, chemical bonding and redox properties can easily be obtained. Historically, Mössbauer spectroscopy was first used to provide a detailed description of oxidation and spin state of heme-containing proteins, which were available in proper quantities to be studied (Lang and Marshall 1966). Iron cofactors oxidation and spin state and character of bonds, electronegativity of ligands and molecular symmetry can be probed by *IS* and *QS*, as seen above. Magnetic hyperfine splitting can add additional information about coupled systems, nuclearity and can be related to results obtained by other spectroscopic techniques.

One of the initial challenges to use Mössbauer spectroscopy to characterize iron-containing proteins was the fact that the natural abundance of the ^{57}Fe isotope is only 2.2% and that Mössbauer spectra need samples with ca. 1 mM iron concentration. A simple calculation points to the fact that a natural abundance sample of a simple mononuclear iron protein needs to be close to 45 mM. In the case of proteins purified from microorganism, and to circumvent this problem, growth media can be supplemented with an ^{57}Fe solution which will enrich the iron cofactors in this isotope. This can be a costly process when applied to large scale growths. Fortunately, over-expression methods are routine laboratory tools to obtain more protein of interest in lab scale batch growths. Thus, over the past decades Mössbauer spectroscopy has

been used to discover new iron cofactors, determining the nuclearity and electronic properties of multi-iron containing centers, unveiling the organization of iron atoms in case of proteins containing multiple iron centers, showing number of attainable redox states and their correspondent redox potential, identifying substrate/inhibitor binding sites, and discovering and characterizing new kinetic intermediate species.

In the next subsections we will cover the known types of iron species studied by Mössbauer spectroscopy, using IS and QS as a roadmap to the spin and redox state of iron ions and centers (see also Fig. 8.11). It is relevant to note that, for each system, important information can be derived from the magnetic hyperfine splitting interaction and parallel EPR sample data.

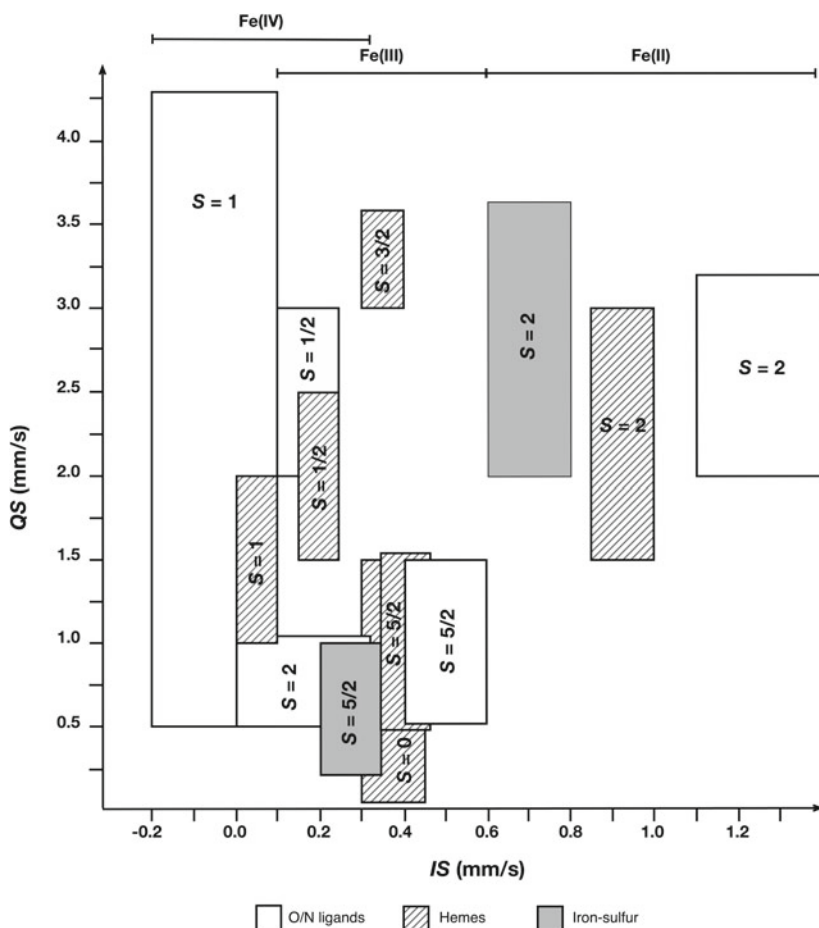


Fig. 8.11 Typical values of IS and QS for iron centers/types present in biological molecules (heme iron, iron-sulfur centers, iron with N/O ligands). Parameters of valence-delocalized iron-sulfur iron pairs are not included. Additional details can be found in Sect. 8.7. Values are given relative to the centroid of the room-temperature spectrum of a metallic iron foil

Appropriate references are included to direct the reader for further information about each system. Please note that, unless otherwise specified, Mössbauer parameters quoted in the next sections are obtained from data acquired at 4.2 K.

8.7.1 Iron-Sulfur Centers

Iron-sulfur centers (or iron-sulfur clusters) are widespread in nature, being part of several proteins and enzymes (Pandelia et al. 2015). Their role in biology can go from simple electron transfer cofactors to participate in important metabolic pathways such as the citric acid cycle or nitrogen fixation. In many cases the identification of the iron-sulfur center was associated to Mössbauer studies that were capable of distinguish nuclearity and redox states not accessible by other techniques. Simple iron-sulfur centers are characterized by the number of iron and sulfur atoms present in their structure.

The simplest iron-sulfur center, the rubredoxin-type site FeCys_4 , is constituted by a single iron coordinated by four cysteinyl residues in a tetrahedral coordination. This center can be either in a ferrous or ferric state. In the high-spin ferric state ($S = 5/2$) it has an IS ranging from 0.25 to 0.32 mm/s and a QS between 0.5 and 0.75 mm/s. Upon one electron reduction, this center becomes high-spin ferrous ($S = 2$) and its IS changes to a value of 0.7 mm/s with QS ranging from 3.25 to 3.55 mm/s. These values set a reference to all other iron-sulfur centers.

Binuclear iron-sulfur centers, $[2\text{Fe}-2\text{S}]$, can undergo one-electron reduction. The fully oxidized center is in the $2+$ state since it has two high-spin ferric ions. For iron-sulfur centers with more than one iron, total oxidation state is determined based on the formal charge of iron and sulfur atoms, so in this case we have $2 \times (3+) + 2 \times (2-) = 2+$. The two ferric ions are antiferromagnetically coupled to yield a diamagnetic ground state ($S_{total} = 0$). The Mössbauer spectrum shows two almost equal quadrupole doublets with IS and QS approximately equal to 0.27 mm/s and 0.60 mm/s, respectively. The one-electron reduction ($1+$ state) gives rise to a paramagnetic $S_{total} = 1/2$ spin system. In the Mössbauer spectrum two components of equal intensity are now observable. One of these components can be attributed to sulfur coordinated high-spin ferric ion (IS and QS of 0.35 mm/s and 0.65 mm/s) while the other dramatically changes with IS and QS approximately equal to 0.60 mm/s and 2.70 mm/s, respectively. These values are closer to the ones obtained for the reduced rubredoxin-type site and support the existence of valence-trapped sites in this type of binuclear center. The $S_{total} = 1/2$ ground state can thus be explained by antiferromagnetically coupled high-spin ferric and ferrous ions. In certain cases, an additional one-electron reduction is possible, producing the fully reduced center with two high-spin ferrous ions antiferromagnetically coupled, resulting in a diamagnetic ground state with IS ranging from 0.70 to 0.81 mm/s and a QS ranging from 2.32 to 2.76 mm/s. One example of how Mossbauer can distinguish between different coordination types for otherwise similar centers is the so-called Rieske cluster. This type of center is almost identical to the $[2\text{Fe}-2\text{S}]$, but in one of the irons the cys-

teiny coordination is replaced by two histidine residues. In this case two resolved quadrupole doublets are observed, displaying higher QS and IS values.

One other well-known iron-sulfur center in nature is the $[4\text{Fe}-4\text{S}]$. This center is best described as a cubane-type structure with four iron ions at alternate vertices bound to four labile sulfur atoms and protein bound to four cysteinyl groups. Each iron retains an all sulfur coordination in an almost tetrahedral geometry. Four oxidation states are known for this center (3+ to 0) but each cluster will almost only cycle between two oxidation states. Centers cycling between the 2+/1+ oxidation states are the most common $[4\text{Fe}-4\text{S}]$ centers and are both used in intra- and intermolecular electron transfer chains as well as enzyme active sites. In the 2+ state, with a diamagnetic ground state, the four iron ions are almost indistinguishable with IS around 0.45 mm/s and a QS ranging from 1.0 to 1.3 mm/s. These spectra can be explained by the presence of two valence-delocalized iron ion pairs ($S = 9/2$). The formal oxidation state of the iron ions in the pair is 2.5+. The two valence-delocalized pairs are antiferromagnetically coupled to produce the diamagnetic ground state. The one electron reduction produces a full ferrous pair ($S = 4$) with IS of approximately 0.60 mm/s, which remains antiferromagnetically coupled to the remaining valence-delocalized pair resulting in a $S_{total} = 1/2$ paramagnetic state. The oxidation state 0 ($S_{total} = 4$) is only known in a few examples, with all iron ions in the ferrous state displaying parameters typical of high-spin ferrous ions with sulfur coordination. Centers cycling between the 3+/2+ oxidation states are known as HIPIP centers (for High Potential Iron-sulfur Proteins). The 3+ state is explained by the presence of a full ferric pair with parameters typical of sulfur-coordinated high-spin ferric ions antiferromagnetically coupled to the remaining valence-delocalized pair resulting in a $S_{total} = 1/2$ paramagnetic state.

The $[3\text{Fe}-4\text{S}]$ shares a similar cubane structure, but one of the vertices is now empty. It cycles between a 1+ state ($S_{total} = 1/2$) with all high-spin ferric ions having IS and QS of around 0.28 and 0.53 mm/s, respectively. The one electron reduction produces a valence-delocalized pair ($S = 9/2$), with the extra iron ion remaining in the high-spin ferric state ($S = 5/2$) resulting in a system with a $S_{total} = 2$ ground state.

Iron-sulfur centers of higher nuclearity and mixed coordination state also exist. These more complex systems such as the P-cluster, MoFe-cofactor or novel tetranuclear hybrid cluster (Ravi et al. 1994; Bjornsson et al. 2017; Tavares et al. 1998) share some of the characteristics described above for the simpler systems.

Mössbauer spectroscopy can also help in identifying binding sites in the iron-sulfur cluster. This is of particular importance for enzyme active sites. The first substrate-bound observation was made for the enzyme aconitase, that contains a $[4\text{Fe}-4\text{S}]$ center at the active site (Emptage et al. 1983). In this case the authors were able to determine a specific iron site that was able to bind citrate. Substrate binding resulted in a change to IS of 0.84–0.89 mm/s an QS of 1.26–1.83 mm/s, which are distinct from the previous typical $[4\text{Fe}-4\text{S}]$ center parameters.

8.7.2 Heme Proteins

Heme proteins and enzymes are among the best studied systems in biology and among some of the first used in biological Mössbauer studies (Münck and Champion 1975). These proteins contain at least one heme prosthetic group that can be covalently attached to the protein polypeptide chain and are involved in electron transfer processes, molecular oxygen storage and transport, detoxification, etc. Different heme groups can be found in nature, although the most common are heme *b*, *a* and *c*. The heme basic structure is an iron ion tetracoordinated by a porphyrin. Heme cofactors differ on the tetrapyrrole rings substituents and the number and type of axial coordination, that can be an amino acid side chain (e.g. histidine, cysteine, methionine or tyrosine residues), or small molecules (e.g. molecular oxygen, nitric oxide, nitrite, water, hydroxide). Mössbauer spectroscopy has played an important role in the characterization of heme structure and catalytic activity, either helping to identify the nature of axial ligands or by enabling the study of oxidation states difficult to probe by other techniques, such as the ferrous and ferryl heme states.

In the high-spin ferric state heme proteins display quite complex spectra and several measurements at variable temperature and field need to be performed to properly characterize such a system. Fortunately, in this redox state heme cofactors are EPR active and correlation with EPR results greatly simplifies Mössbauer data analysis. Typically, *IS* and *QS* ranging from 0.35 to 0.45 mm/s and 0.5 to 1.5 mm/s, respectively, are observed. Heme cofactors can also be found in the low-spin ferric heme state. Sometimes this state is promoted by the binding of divalent ions or by temperature changes. In this case it is helpful to use the method proposed by Griffith for the binding of azide to hemoglobin (Griffith 1957). This state has distinctive *IS* and *QS*, ranging from 0.15 to 0.25 mm/s and 1.5 to 2.5 mm/s.

Heme cofactors can undergo one-electron reduction in which case they become either high-spin ferrous ($S = 2$) or low-spin ferrous ($S = 0$). Both states can be properly analyzed by Mössbauer spectroscopy with particular emphasis on the high-spin ferrous state, for which a detailed description of the electronic structure is possible. Characteristic values of *IS* and *QS* are observed, with high-spin ferrous heme cofactors having *IS* and *QS* ranging from 0.85 to 1.0 mm/s and 1.5 to 3.0 mm/s, while for the low-spin case *IS* varies between 0.30 and 0.45 mm/s with *QS* being less than 1.5 mm/s.

Under catalytic conditions it is possible to obtain a more oxidized ferryl (Fe^{4+}) state. The characterized reaction intermediates show a small *IS* value, between 0.0 and 0.1 mm/s, and *QS* of 1.0–2.0 mm/s.

8.7.3 Non-heme Iron Centers

Enzymes containing non-heme iron perform important biological reactions, in most cases involving molecular oxygen or reactive oxygen species. For all purposes the

iron cofactors that are not iron-sulfur centers or heme cofactors are considered to be non-heme iron centers and are usually referred to as iron cofactors with nitrogen and/or oxygen containing ligands. However, in some known cases, a cysteine residue will contribute to the coordination sphere. Essentially, two types of centers exist. Monomeric centers such as the ones present in dioxygenases and superoxide reductases (Zimmermann et al. 1978; Tavares et al. 1994; Pereira et al. 2007) or μ -oxo, μ -hydroxo or peroxo diiron centers like the ones found in ribonucleotide reductase, methane monooxygenase or ferritin (Bollinger et al. 1991; Fox et al. 1993; Pereira et al. 1997).

Monomeric iron sites will have three attainable redox states. In the ferric state the center is a high-spin system ($S = 5/2$) with IS of 0.40–0.6 mm/s and $QS = 0.5$ –1.5 mm/s. Mössbauer is sensitive to small changes in the coordination sphere and it is expected that the lower IS values in that range be from 5-coordinated and/or from additional single cysteine residue coordination. In one known case, the enzyme nitrile hydratase, the monomeric ferric center is present in the low-spin state ($S = 1/2$). This is mainly due to the fact that the coordination sphere is constituted by three cysteinyl residues (two of them are post-translationally modified to cysteine sulfinic and cysteine sulfenic acid forms) and two deprotonated backbone amides from a serine and a cysteine residue (Mascharak 2013). This quite unique coordination sphere will result in a smaller than expected $IS = 0.25$ mm/s consistent with a low-spin ferric configuration (Popescu et al. 2001). Monomeric centers can be reduced to the ferrous state. In the high-spin ferrous configuration the site parameters are very similar to other high-spin ferrous complexes, with $IS = 1.1$ –1.3 mm/s and $QS = 2.0$ –3.2 mm/s. Under catalytic conditions that require molecular oxygen activation, a high-spin oxoferryl ($S = 2$) state was detected for the enzyme taurine/ α -ketoglutarate dioxygenase (Price et al. 2003). In this case the authors report an $IS = 0.31$ mm/s and $QS = 0.88$ mm/s. Also, in a superoxide reductase enzyme system, upon reaction with hydrogen peroxide, another intermediate species with IS of 0.54 mm/s and QS of 0.80 mm/s was found (Horner et al. 2004). This was proposed to be a high-spin side-on ferric peroxo species.

Dinuclear non-heme iron centers are quite important in nature and have been reported in several cases either as a cofactor or as an intermediate species of iron-processing reactions. This type of centers consists of two iron atoms each with nitrogen and/or oxygen containing ligands (usually carboxylate and imidazole groups) and at least one bridging carboxylate group. The type and number of non-bridging ligands, as well as the availability of an open coordination site will determine if molecular oxygen will bind reversibly. Depending on the reactivity of the center, an additional bridging carboxylate, oxo/hydroxo or peroxo group can be found. Such structural plasticity makes this type of centers well suited for a number of different functions from simple oxygen transport (hemerythrin) (Clark and Webb 1981; Stenkamp 1994), to having key roles in DNA biosynthesis (ribonucleotide reductase) (Atkin et al. 1973; Stubbe et al. 2003), hydrocarbon oxidation (methane monooxygenase, toluene/*o*-xylene monooxygenase or phenol hydroxylase) (Fox et al. 1993; Sazinsky and Lippard 2006; Cadieux et al. 2002; Murray et al. 2006), iron biomineralization (ferritins) (Liu and Theil 2005; Pereira et al. 1997, 2012), regulation of cell

proliferation (deoxyhypusine hydroxylase) (Vu et al. 2009) or fatty acid desaturation (Δ^9 stearoyl-acyl carrier protein desaturase) (Shanklin et al. 1997, 2009).

Dinuclear non-heme iron centers are known to have five oxidation states where iron ions formal oxidation state range from 2+ to 4+. The all ferrous state Mössbauer spectra shows two very similar quadrupole doublets with high-spin ferrous characteristic parameters (QS varying from 2.7 to 3.1 mm/s and IS of approximately 1.3 mm/s). When both iron ions are in the ferrous state the center binds molecular oxygen and, in most cases, intermediate species of higher oxidation states are generated. The type and number of reaction intermediates depends on the type of catalysis, but an almost ubiquitous first intermediate is a peroxodiiron species. In this case two ferric irons are antiferromagnetically couple producing a diamagnetic ground state ($S_{total} = 0$). In all but one cases, the peroxodiiron intermediate shows a visible band with λ_{max} between 620 and 720 nm (ϵ of 1000–1500 $M^{-1} cm^{-1}$) as well as IS between 0.55 and 0.68 mm/s and QS higher than 0.9 mm/s. The known exception is an intermediate found in the Toluene/*o*-Xylene Monooxygenase Hydroxylase component which has distinctive IS and QS Mössbauer parameters (0.67 and 0.54 mm/s, respectively), also lacking an observable UV-visible absorption band. Quite interestingly, a crystal structure of a peroxodiferric intermediate was possible to obtain in a Deoxyhypusine Hydroxylase, only possible due to the extreme unusual longevity of such peroxo intermediate (Han et al. 2015).

Under catalytic conditions, and after O–O bond cleavage, two other states of dinuclear non-heme iron centers were observed. These are high-valent iron species formed in soluble methane monooxygenase hydroxylase component (MMOH) and ribonucleotide reductase subunit R2 (RNR-R2) proteins. In the case of MMOH an all ferryl intermediate was detected. The so-called intermediate Q has IS of 0.14–0.21 mm/s and QS of 0.53–0.68 mm/s and exhibits a bis- μ -oxo diamond core structure (Lee et al. 1993; Liu et al. 1994; Banerjee et al. 2015). The low IS value is indicative of a formal oxidation state of 4+. Akin of what was reported to the peroxodiferric intermediate, high-field spectra show this intermediate to be diamagnetic. For the case of RNR-R2, Mössbauer spectroscopy was successfully used to characterize another high-valent iron species. In this case the so-called intermediate X was characterized as being “a spin-coupled Fe^{3+}/Fe^{4+} center without a radical, but with significant spin delocalization onto the oxygen ligands”. In this case the two iron sites show IS of 0.56 and 0.26 mm/s, which can be assigned to a high-spin ferric ($S = 5/2$) and a high-spin ferryl ($S = 4$), antiferromagnetically coupled to produce a paramagnetic ground state ($S_{total} = 1/2$) (Sturgeon et al. 1996).

Interestingly, it was possible to use Mössbauer spectroscopy to probe the similarity between Q and X intermediates. Since Q is formally in a one-electron more oxidized state than X, reduction of Q could produce X if intermediate structures are similar. The Mössbauer spectra of a sample obtained by cryoreduction of intermediate Q clearly show the appearance of a mixed-valent Fe^{3+}/Fe^{4+} center with parameters similar to intermediate X, which reinforces the assignment done in the intermediate Q spectroscopic analysis (Valentine et al. 1998).

The above cited kinetic intermediates will eventually decay into an all ferric dinuclear iron center, which shows a diamagnetic ground state ($S_{total} = 0$) and can be

explained by two similar quadrupole doublets with Mössbauer parameters typical of high-spin ferric ions (QS varying from 1.0 to 1.9 mm/s and IS of 0.45 to 0.55 mm/s).

Dinuclear non-heme iron centers can also occur in a mixed-valence oxidation state, also known as semimet form reminiscent of a nomenclature first used for hemerythrin proteins. Generated by one electron reduction of the diferric form, a system with spin-coupled Fe^{3+}/Fe^{2+} center is obtained. The Mössbauer spectrum shows two quadrupole doublets with parameters typical of high-spin ferric and ferrous ions supporting a localized mixed-valence state.

8.7.4 Iron Cores

Iron is an essential element that, as seen so far, mainly contributes as a cofactor of many different proteins and enzymes. The bioavailability of iron at physiological conditions is poor, due to its low solubility in aqueous solutions. The ferric form is extremely insoluble, whereas the ferrous form is relatively soluble, although very toxic in the presence of molecular oxygen, potentiating the non-enzymatic production of reactive oxygen species (ROS) that cause oxidative damage of cellular components, contributing to the development of cancer, neurodegenerative and cardiac diseases, and many other pathophysiological conditions. As such, organisms have developed mechanisms to acquire and concentrate iron and thus resist to ROS toxic effects, keeping an effective iron homeostasis. In all organisms, iron is stored by proteins from the ferritin-family: In eukaryotes by canonical ferritins, (Ft) and in prokaryotes by bacterial ferritins (Ftn), heme-containing bacterioferritins (Bfr) or by Dps (DNA-binding protein from starved cells). With exception of Dps that are 12-oligomers, all other ferritins are composed of 24 subunits (24-mer) organized into a hollow spherical protein shell. Most ferritin molecules from higher eukaryotic organisms are heteropolymers, containing two types of subunits that differ on their molecular masses, the L (ca. 19 kDa) and H subunit (ca. 21 kDa). The H subunits catalyze the initial step of rapid oxidation of ferrous ions (ferroxidation) due to the presence of a catalytic center (ferroxidase center) and direct the oxidized ferric species into the inner cavity, while the L subunits promote the formation of the mineral core (mineralization). Prokaryotic ferritins are homopolymers composed of subunits more homologous to H. The protein inner cavity size, of approximately 8 nm, that can store up to 4,500 iron atoms in the form of a ferrihydrite mineral. Dps inner cavities are smaller (ca. 5 nm) forming iron mineral cores of as much as 500 iron. However, for both cases, iron particles can be smaller with as little as 48 iron ions showing core related properties (Yang et al. 1987; Pereira et al. 1997; Penas et al. 2018). At low temperature, the characteristic Mössbauer spectra of iron cores is composed of a magnetic sextet. Raising the acquisition temperature leads to a conversion of the magnetic sextet into central quadrupole doublets. The temperature at which the doublet and sextet components have equal intensity is defined as the blocking temperature, T_B (Mørup and Topsøe 1976; Coey et al. 1984; St Pierre et al. 1986). T_B is linearly proportional to particle volume (V) and to the magnetic anisotropy

constant (K) which are a function of material characteristics such as particle size and mass density. Because iron cores are ferrihydrite particles with poor crystallinity, a distribution of hyperfine parameters is needed to fully explain the magnetic spectrum (Rancourt and Ping 1991). At higher temperatures the spectrum can be explained by two or more quadrupole doublets with IS ranging from 0.47 to 0.54 and QS of 0.57 to 1.2 mm/s. It was also shown that iron cores can oxidize and incorporate additional ferrous ions (Penas et al. 2018). In this case the incorporation is accompanied by the appearance of a new iron species with IS of 0.7 mm/s and QS of 2.10 mm/s, which was explained as mixed-valence iron species due to fast electron hopping between iron pairs in the core mineral.

8.7.5 Whole Cell Mössbauer Spectroscopy

Mössbauer spectroscopy has been also successfully applied to whole cells, contributing to explain differences in distribution of cellular iron content. Some of these studies benefit from either ^{57}Fe enrichment or the use of overexpression systems. Careful analysis makes possible to sort different groups of Fe-containing species such as high-spin ferric ions (ferritin, non-heme centers with N and O ligands), low-spin heme ferric ions, iron-sulfur centers and high-spin ferrous ions. The use of Mössbauer spectroscopy enabled the study of in vivo behavior of (overexpressed) FNR protein (regulator of fumarate and nitrate reduction) and pyruvate formate-lyase activating enzyme showing the molecular oxygen dependent iron-sulfur center interconversion (Popescu et al. 1998; Yang et al. 2009). Whole cell Mössbauer spectroscopy was also used to demonstrate that iron sulfur centers present in purified recombinant biotin synthase were present in vivo, not being an artifact of the protein purification procedure, establishing that under aerobic growth this protein is expressed in an inactive form (Cosper et al. 2002). Studies were also done in *Escherichia coli* cells (wild-type and cell variants with deletion of ferric uptake regulatory protein—Fur, and different ferritins—Ftn, Bfr, and Dps) grown with different iron concentrations, carbon sources, aerobic or anaerobic conditions, and harvested in different growth phases (Wofford 2019). These studies point to a respiratory shield that protects a low-molecular-mass ferrous iron pool from molecular oxygen dependent oxidation, showing that the iron content of *Escherichia coli* cells is very similar to what was found for mitochondria. Mössbauer spectroscopy has also been applied to unambiguously detect and quantify all hemoglobin forms present in blood samples (Khvastunov et al. 2013).

Acknowledgements The Portuguese National Funding Agency FCT-MCTES through Research Grants POCTI/QUI/37413/2001, POCTI/QUI/47273/2002, POCI/QUI/57475/2004, PTDC/QUI/64248/2006, PTDC/QUI/67142/2006, PTDC/SAU-SAP/111482/2009, PTDC/BIA-PRO/111485/2009, and PTDC/OCE-ETA/32567/2017. This work was also supported by Radiation Biology and Biophysics Doctoral Training Programme (RaBBiT, PD/00193/2010); UID/Multi/04378/2019 (UCIBIO); UID/FIS/00068/2013 (CEFITEC). UID/Multi/04349/2013 (C2TN).

References

- Atkin CL, Thelander L, Reichard P, Lang G (1973) Iron and free radical in ribonucleotide reductase. Exchange of iron and Mössbauer spectroscopy of the protein B2 subunit of the *Escherichia coli* enzyme. *J Biol Chem* 248(21):7464–7472
- Baggio-Saitovitch E, Berry FJ, De Waard H, Greneche JM, Gütlich P, Stevens J (2002) New recommendations for nomenclature and the reporting of Mössbauer data. IBAME (International Board on the Applications of the Mössbauer Effect). <https://app.box.com/s/9pun6671zzdhyh16myb6f7dypz4mtgud>
- Banerjee R, Proshlyakov Y, Lipscomb JD, Proshlyakov DA (2015) Structure of the key species in the enzymatic oxidation of methane to methanol. *Nature* 518(7539):431–434. <https://doi.org/10.1038/nature14160>
- Bjornsson R, Neese F, DeBeer S (2017) Revisiting the Mössbauer isomer shifts of the FeMoco cluster of nitrogenase and the cofactor charge. *Inorg Chem* 56(3):1470–1477. <https://doi.org/10.1021/acs.inorgchem.6b02540>
- Bollinger JM Jr, Edmondson DE, Huynh BH, Filley J, Stubbe J (1991) Mechanism of assembly of the tyrosyl radical-dinuclear iron cluster cofactor of ribonucleotide reductase. *Science* 253(5017):292–298. <https://doi.org/10.1126/science.1650033>
- Cadieux E, Vrajmasu V, Achim C, Powlowski J, Münck E (2002) Biochemical, Mössbauer, and EPR studies of the diiron cluster of phenol hydroxylase from pseudomonasp. Strain CF 600. *Biochemistry* 41(34):10680–10691. <http://doi.org/10.1021/bi025901u>
- Clark PE, Webb J (1981) Mössbauer spectroscopic studies of hemerythrin from *Phascolosoma lurco* (syn. *Phascolosoma arcuatum*). *Biochemistry* 20(16):4628–4632. <http://doi.org/10.1021/bi00519a017>
- Coe JMD, Meagher A, Kelly JM, Vos JG (1984) A Mössbauer study of polymers prepared from polyvinylpyridine and ferric chloride or ferric nitrate. *J Polym Sci Part A: Polym Chem* 22(2):303–318. <http://doi.org/10.1002/pol.1984.170220203>
- Cosper MM, Jameson GNL, Eidsness MK, Huynh BH, Johnson MK (2002) Recombinant *Escherichia coli* biotin synthase is a [2Fe-2S](2+) protein in whole cells. *FEBS Lett* 529(2–3):332–336. [https://doi.org/10.1016/S0014-5793\(02\)03390-2](https://doi.org/10.1016/S0014-5793(02)03390-2)
- Emptage MH, Kent TA, Kennedy MC, Beinert H, Münck E (1983) Mössbauer and EPR studies of activated aconitase: development of a localized valence state at a subsite of the [4Fe-4S] cluster on binding of citrate. *Proc Natl Acad Sci USA* 80(15):4674–4678. <https://doi.org/10.1073/pnas.80.15.4674>
- Fox BG, Hendrich MP, Surerus KK, Andersson KK, Froland WA, Lipscomb JD, Münck E (1993) Moessbauer, EPR, and ENDOR studies of the hydroxylase and reductase components of methane monooxygenase from *Methylosinus trichosporium* OB3b. *J Am Chem Soc* 115(9):3688–3701. <http://doi.org/10.1021/ja00062a039>
- Frauenfelder H (1962) The Mössbauer effect. W. A. Benjamin Inc., New York
- Greenwood NN, Gibb TC (1971) Mössbauer spectroscopy. Chapman and Hall, Ltd., London
- Griffith JS (1957) Binding in hæmoglobin azide as determined by electron resonance: theory of electron resonance in ferrihæmoglobin azide. *Nature* 180(4575):30–31. <https://doi.org/10.1038/180030a0>
- Gütlich P, Bill E, Trautwein AX (2011) Mössbauer spectroscopy and transition metal chemistry, 1st edn. Springer, Berlin, Heidelberg
- Han Z, Sakai N, Böttger LH, Klinke S, Hauber J, Trautwein AX, Hilgenfeld R (2015) Crystal structure of the peroxo-diiron(III) intermediate of deoxyhypusine hydroxylase, an oxygenase involved in hypusination. *Structure* 23(5):882–892. <https://doi.org/10.1016/j.str.2015.03.002>
- Horner O, Mouesca J-M, Oddou J-L, Jeandey C, Nivière V, Mattioli TA et al (2004) Mössbauer characterization of an unusual high-spin side-on peroxo–Fe³⁺ species in the active site of superoxide reductase from *Desulfoarculus baarsii*. Density functional calculations on related models. *Biochemistry* 43(27):8815–8825. <http://doi.org/10.1021/bi0498151>

- Khvastunov SM, Novakova AA, Kiseleva TY (2013) Applying Mössbauer spectroscopy to studies of red blood cells in donated blood. *Bull Russ Acad Sci: Phys* 77(6):726–729. <http://doi.org/10.3103/S1062873813060178>
- Lang G, Marshall W (1966) Mössbauer effect in some haemoglobin compounds. *Proc Phys Soc Lond* 87:3–34. [https://doi.org/10.1016/S0022-2836\(66\)80032-3](https://doi.org/10.1016/S0022-2836(66)80032-3)
- Lee SK, Fox BG, Froland WA, Lipscomb JD, Münck E (1993) A transient intermediate of the methane monooxygenase catalytic cycle containing an Fe^{IV}Fe^{IV} cluster. *J Am Chem Soc* 115(14):6450–6451. <https://doi.org/10.1021/ja00067a086>
- Liu X, Theil EC (2005) Ferritins: dynamic management of biological iron and oxygen chemistry. *Acc Chem Res* 38(3):167–175. <https://doi.org/10.1021/ar0302336>
- Liu KE, Wang D, Huynh BH, Edmondson DE, Salifoglou A, Lippard SJ (1994) Spectroscopic detection of intermediates in the reaction of dioxygen with the reduced methane monooxygenase/hydroxylase from *Methylococcus capsulatus* (bath). *J Am Chem Soc* 116(16):7465–7466. <https://doi.org/10.1021/ja00095a083>
- Long GJ, Cranshaw TE, Longworth G (1983) The ideal Mössbauer effect absorber thicknesses. *Mossb Effect Ref Data J* 6(2):42–49. [https://doi.org/10.1016/0029-554X\(80\)90872-1](https://doi.org/10.1016/0029-554X(80)90872-1)
- Mascharak PK (2013) The active site of nitrile hydratase: an assembly of unusual coordination features by nature. In: *Molecular design in inorganic biochemistry*, vol 160. Springer Berlin Heidelberg, Berlin, Heidelberg, pp 89–113. http://doi.org/10.1007/430_2012_85
- Mørup S, Topsøe H (1976) Mössbauer studies of thermal excitations in magnetically ordered microcrystals. *Appl Phys* 11(1):63–66. <https://doi.org/10.1007/BF00895017>
- Münck E, Champion PM (1975) Heme proteins and model compounds: Mössbauer absorption and emission spectroscopy. *Ann N Y Acad Sci* 244(1):142–162. <https://doi.org/10.1111/j.1749-6632.1975.tb41528.x>
- Murray LJ, García-Serres R, Naik S, Huynh BH, Lippard SJ (2006) Dioxygen activation at non-heme diiron centers: characterization of intermediates in a mutant form of toluene/o-xylene monooxygenase hydroxylase. *J Am Chem Soc* 128(23):7458–7459. <https://doi.org/10.1021/ja0627621>
- Pandelia M-E, Lanz ND, Booker SJ, Krebs C (2015) Mössbauer spectroscopy of Fe/S proteins. *Biochim Biophys Acta Mol Cell Res* 1853(6):1395–1405. <http://doi.org/10.1016/j.bbamcr.2014.12.005>
- Penas D, Pereira AS, Tavares P (2018) Direct evidence for ferrous ion oxidation and incorporation in the absence of oxidants by Dps from *Marinobacter hydrocarbonoclasticus*. *Angew Chem Int Ed* 58(4):1013–1018. <http://doi.org/10.1002/anie.201809584>
- Pereira AS, Tavares P, Lloyd SG, Danger D, Edmondson DE, Theil EC, Huynh BH (1997) Rapid and parallel formation of Fe³⁺ multimers, including a trimer, during H-type subunit ferritin mineralization. *Biochemistry* 36(25):7917–7927. <https://doi.org/10.1021/bi970348f>
- Pereira AS, Tavares P, Folgosa F, Almeida RM, Moura I, Moura JGG (2007) Superoxide reductases. *Eur J Inorg Chem* 2007(18):2569–2581. <https://doi.org/10.1002/ejic.200700008>
- Pereira AS, Timoteo CG, Guilherme M, Folgosa F, Naik SG, Duarte AG et al (2012) Spectroscopic evidence for and characterization of a trinuclear ferroxidase center in bacterial ferritin from *Desulfovibrio vulgaris* Hildenborough. *J Am Chem Soc* 134(26):10822–10832. <https://doi.org/10.1021/ja211368u>
- Popescu CV, Bates DM, Beinert H, Münck E, Kiley PJ (1998) Mössbauer spectroscopy as a tool for the study of activation/inactivation of the transcription regulator FNR in whole cells of *Escherichia coli*. *Proc Natl Acad Sci USA* 95(23):13431–13435. <https://doi.org/10.1073/pnas.95.23.13431>
- Popescu V-C, Münck E, Fox BG, Sanakis Y, Cummings JG, Turner IM, Nelson MJ (2001) Mössbauer and EPR studies of the photoactivation of nitrile hydratase. *Biochemistry* 40(27):7984–7991. <https://doi.org/10.1021/bi010198f>
- Price JC, Barr EW, Tirupati B, Bollinger JM, Krebs C (2003) The first direct characterization of a high-valent iron intermediate in the reaction of an α -ketoglutarate-dependent dioxygenase: a high-spin Fe(IV) complex in taurine/ α -ketoglutarate dioxygenase (TauD) from *Escherichia coli*. *Biochemistry* 42(24):7497–7508. <https://doi.org/10.1021/bi030011f>

- Rancourt DG, Ping JY (1991) Voigt-based methods for arbitrary-shape static hyperfine parameter distributions in Mössbauer spectroscopy. *Nucl Instrum Methods Phys Res B* 58(1):85–97. [http://doi.org/10.1016/0168-583X\(91\)95681-3](http://doi.org/10.1016/0168-583X(91)95681-3)
- Rancourt DG, McDonald AM, Lalonde AE, Ping JY (1993) Mössbauer absorber thicknesses for accurate site populations in Fe-bearing minerals. *Amer Miner* 78:17
- Ravi N, Moore V, Lloyd SG, Hales BJ, Huynh BH (1994) Mössbauer characterization of the metal clusters in *Azotobacter vinelandii* nitrogenase VFe protein. *J Biol Chem* 269(33):20920–20924
- Sazinsky MH, Lippard SJ (2006) Correlating structure with function in bacterial multicomponent monooxygenases and related diiron proteins. *Acc Chem Res* 39(8):558–566. <https://doi.org/10.1021/ar030204v>
- Shanklin J, Achim C, Schmidt H, Fox BG, Münck E (1997) Mössbauer studies of alkane omega-hydroxylase: evidence for a diiron cluster in an integral-membrane enzyme. *Proc Natl Acad Sci USA* 94(7):2981–2986. <https://doi.org/10.1073/pnas.94.7.2981>
- Shanklin J, Guy JE, Mishra G, Lindqvist Y (2009) Desaturases: emerging models for understanding functional diversification of diiron-containing enzymes. *J Biol Chem* 284(28):18559–18563. <https://doi.org/10.1074/jbc.R900009200>
- St Pierre TG, Bell SH, Dickson DP, Mann S, Webb J, Moore GR, Williams RJ (1986) Mössbauer spectroscopic studies of the cores of human, limpet and bacterial ferritins. *Biochim Biophys Acta* 870(1):127–134. [https://doi.org/10.1016/0167-4838\(86\)90015-4](https://doi.org/10.1016/0167-4838(86)90015-4)
- Stenkamp RE (1994) Dioxygen and hemerythrin. *Chem Rev* 94(3):715–726. <https://doi.org/10.1021/cr00027a008>
- Stubbe J, Nocera DG, Yee CS, Chang MCY (2003) Radical initiation in the class I ribonucleotide reductase: long-range proton-coupled electron transfer? *Chem Rev* 103(6):2167–2202. <https://doi.org/10.1021/cr020421u>
- Sturgeon BE, Burdi D, Chen S, Huynh BH, Edmondson DE, Stubbe J, Hoffman BM (1996) Reconsideration of X, the diiron intermediate formed during cofactor assembly in *E. coli* ribonucleotide reductase. *J Am Chem Soc* 118(32):7551–7557. <http://doi.org/10.1021/ja960399k>
- Tavares P, Ravi N, Moura JJ, LeGall J, Huang YH, Crouse BR et al (1994) Spectroscopic properties of desulfoferrodoxin from *Desulfovibrio desulfuricans* (ATCC 27774). *J Biol Chem* 269(14):10504–10510
- Tavares P, Pereira AS, Krebs C, Ravi N, Moura JJ, Moura I, Huynh BH (1998) Spectroscopic characterization of a novel tetranuclear Fe cluster in an iron-sulfur protein isolated from *Desulfovibrio desulfuricans*. *Biochemistry* 37(9):2830–2842. <https://doi.org/10.1021/bi9723008>
- Valentine AM, Tavares P, Pereira AS, Davydov R, Krebs C, Hoffman BM et al (1998) Generation of a mixed-valent Fe^(III)Fe^(IV) form of intermediate Q in the reaction cycle of soluble methane monooxygenase, an analog of intermediate X in ribonucleotide reductase R2 assembly. *J Am Chem Soc* 120(9):2190–2191. <https://doi.org/10.1021/ja974169x>
- Vu VV, Emerson JP, Martinho M, Kim YS, Münck E, Park MH, Que L (2009) Human deoxyhypusine hydroxylase, an enzyme involved in regulating cell growth, activates O₂ with a non-heme diiron center. *Proc Natl Acad Sci USA* 106(35):14814–14819. <https://doi.org/10.1073/pnas.0904553106>
- Wertheim GK (1964) Mössbauer effect: principles and applications. Academic Press Inc., London
- Wofford JD, Bolaji N, Dziuba N, Outten FW, Lindahl PA (2019) Evidence that a respiratory shield in *Escherichia coli* protects a low-molecular-mass FeII pool from O₂-dependent oxidation. *J Biol Chem* 294(1):50–62. <http://doi.org/10.1074/jbc.RA118.005233>
- Yang CY, Meagher A, Huynh BH, Sayers DE, Theil EC (1987) Iron(III) clusters bound to horse spleen apoferritin: an X-ray absorption and Mössbauer spectroscopy study that shows that iron nuclei can form on the protein. *Biochemistry* 26(2):497–503. <https://doi.org/10.1021/bi00376a023>

- Yang J, Naik SG, Ortillo DO, García-Serres R, Li M, Broderick WE et al (2009) The iron–sulfur cluster of pyruvate formate-lyase activating enzyme in whole cells: cluster interconversion and a valence-localized $[4\text{Fe-4S}]^{2+}$ state. *Biochemistry* 48(39):9234–9241. <https://doi.org/10.1021/bi9010286>
- Zimmermann R, Huynh BH, Münck E, Lipscomb JD (1978) High-field Mössbauer studies of reduced protocatechuate 3,4-dioxygenase. *J Chem Phys* 69(12):5463–5467. <https://doi.org/10.1063/1.436538>

Chapter 9

Principles of Nuclear Magnetic Resonance and Selected Biological Applications



Carlos A. Salgueiro, Joana M. Dantas and Leonor Morgado

9.1 Nuclear Magnetic Resonance Spectroscopy

9.1.1 What Is Measured?

Nuclear Magnetic Resonance (NMR) spectroscopy is a widely explored technique to study a variety of molecules. It measures the interaction of specific molecular components with the radiofrequency electromagnetic radiation, which occurs at the lowest-energy end of the electromagnetic spectrum (Fig. 9.1).

The molecular components under scrutiny are the atomic nuclei. Atoms consist of positively charged nucleus surrounded at a relatively large distance by electrons. Regardless of the concept of spin, which can only be precisely addressed by the quantum mechanics, a nucleus can be considered as a positive spherical spinning particle with a magnetic dipole moment (μ) along the axis of rotation in an over-simplified model (Fig. 9.2a). As electrons, neutrons and protons have spin numbers of $\frac{1}{2}$. The atomic nuclei have a characteristic nuclear spin quantum number (I) and only those with values different from zero ($I \neq 0$) can be detected by NMR (Table 9.1). Nuclei with $I \neq 0$ are designated as NMR-active, whereas those with $I = 0$ are NMR-inactive.

C. A. Salgueiro (✉) · J. M. Dantas · L. Morgado
UCIBIO, REQUIMTE, Departamento de Química, Faculdade de Ciências e Tecnologia,
Universidade NOVA de Lisboa, Campus Caparica, 2829-516 Caparica, Portugal
e-mail: csalgueiro@fct.unl.pt

© Springer Nature Switzerland AG 2019
A. S. Pereira et al. (eds.), *Radiation in Bioanalysis*, Bioanalysis 8,
https://doi.org/10.1007/978-3-030-28247-9_9

245

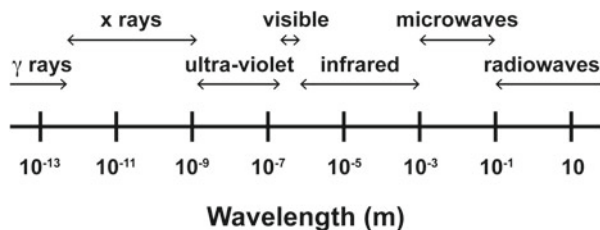
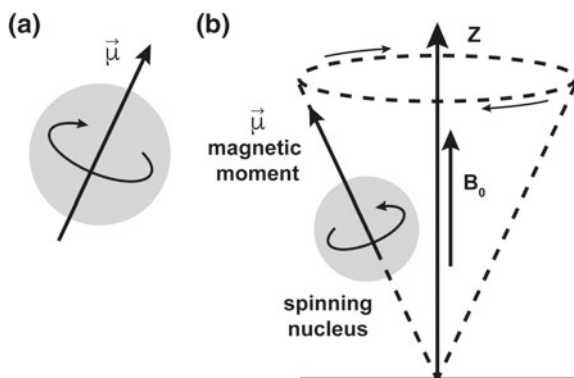


Fig. 9.1 Electromagnetic spectrum. The distribution of electromagnetic radiation is indicated from the highest-energy/shortest wavelength (at the left) to lowest-energy/longest wavelength (at the right)

Fig. 9.2 **a** Schematic representation of the magnetic dipole moment ($\vec{\mu}$) of a nucleus. **b** Precessional motion of the magnetic dipole moment of a nucleus in the direction of the applied magnetic field (\mathbf{B}_0)



9.1.2 Energy Levels

In the absence of a magnetic field, the orientation of the magnetic dipole moments is randomized, and the possible energy levels are degenerated. On the other hand, the classic interaction between a body with a magnetic dipole moment ($\vec{\mu}$) and a magnetic field (\mathbf{B}_0) is described by an associated torque T (Eq. 9.1) and by an orientation-dependent potential energy (Eq. 9.2).

$$\mathbf{T} = \vec{\mu} \times \mathbf{B}_0 \quad (9.1)$$

$$E = -\vec{\mu} \cdot \mathbf{B}_0 \quad (9.2)$$

In addition, the rotation of an electrically charged particle is related to the angular momentum (\mathbf{L}) and to its particular gyromagnetic ratio, γ (Eq. 9.3).

$$\vec{\mu} = \gamma \cdot \mathbf{L} \quad (9.3)$$

Thus, in presence of a magnetic field, the magnetic moment of the nuclei will precess about the direction of the field (Fig. 9.2b). The frequency of this motion is designated by Larmor frequency, which is proportional to the intensity of the applied magnetic field and to the gyromagnetic ratio of the nucleus.

Considering the component of the spin angular momentum in the direction of the applied field (Eq. 9.4), the z component of the nuclear magnetic moment can be rewritten as described in Eq. 9.5. In Eqs. 9.4 and 9.5, h is Planck's constant.

$$L = \left(\frac{h}{2\pi} \right) I \quad (9.4)$$

$$\mu = \left(\frac{h}{2\pi} \right) \gamma I \quad (9.5)$$

As the magnetic moment depends on the nuclear spin quantum number (Eq. 9.5), NMR-active nuclei adopt precise orientations along the z -axis in the presence of an applied magnetic field, therefore creating distinct energy levels. The number of energy levels associated with one nuclear spin is determined by the spin quantum number I and is given by $2nI + 1$, whereas n is the number of spins in the molecule. The energy levels are characterized by the quantum number m and are restricted to the values $-I$ to $+I$ in integer steps. This description can be better interpreted by considering one nucleus with $I = 1/2$ (e.g. ^1H). In this case, in the presence of a magnetic field, two energy levels are defined, corresponding to $m_I = +1/2$ and $m_I = -1/2$ values. In the NMR terminology, the energy levels $m_I = +1/2$ and $m_I = -1/2$ are denoted as state α (lowest energy) and β (higher energy), respectively (Fig. 9.3a).

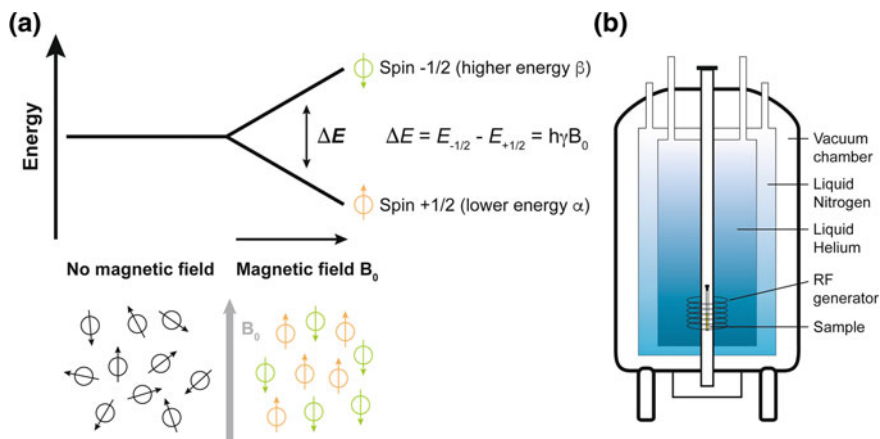


Fig. 9.3 Energy levels of a spin $1/2$ nucleus. **a** The orientation of the magnetic dipole moments is randomized in the absence of magnetic field. Nuclei align with (orange, $+1/2$) or against (green, $-1/2$) the external magnetic field (B_0). **b** Schematic representation of an NMR spectrometer. A pulse of radiofrequency (RF) radiation with energy that matches the ΔE value causes flipping of nuclei from $+1/2$ and $-1/2$ levels (see also Figs. 9.4 and 9.5)

Table 9.1 Properties of some NMR-active nuclei

Nuclei	I	$\gamma \times 10^7$ (T ⁻¹ s ⁻¹)	Natural abundance (%)
¹ H	1/2	26.75	99.98
² H(D)	1	4.11	0.0156
¹³ C	1/2	6.73	1.108
¹⁹ F	1/2	25.18	100.0
¹⁴ N	1	1.93	99.63
¹⁵ N	1/2	-2.75	0.37
¹⁷ O	5/2	-3.63	0.037
³¹ P	1/2	10.84	100

According to the quantum mechanical treatment of nuclear spins in a magnetic field of strength \mathbf{B}_0 the energy of each level can be determined by Eq. 9.6 (see also Eq. 9.2):

$$E = -\left(\frac{h}{2\pi}\right)B_0\gamma m_I \quad (9.6)$$

Values of the nuclear spin quantum number, gyromagnetic ratio and natural abundance for some nuclei of biological interest are presented in Table 9.1. For a revision on NMR active nuclei for biological applications see reference (Hammes 2005). It should be noted that despite the more sensitivity shown by nuclei with higher gyromagnetic ratios, their natural abundance is also important. Thus, the relative receptivity of a nucleus, given by the product of its relative sensitivity and isotopic natural abundance, compared to that of the proton nucleus is a more useful guide to the nuclear response in natural abundance NMR experiments. For example, the relative receptivity of ¹³C nuclei compared to ¹H is 1.8×10^{-4} .

9.1.3 The Basic NMR Experiment

An outline of a basic NMR experiment for a nucleus with $\mathbf{I} = 1/2$ is depicted in Fig. 9.4. According to Eq. 9.6, the energy difference between the two quantized levels (E_β and E_α) increases with the applied magnetic field \mathbf{B}_0 (Eq. 9.7):

$$\Delta E = \left(\frac{h}{2\pi}\right)B_0\gamma \quad (9.7)$$

Therefore, the energy necessary to cause transition between the two levels is proportional to both the NMR spectrometer magnetic field and the nucleus gyromagnetic ratio. Regardless the value of the applied magnetic field of modern spectrometers, as well as the nuclei gyromagnetic ratios, the energy difference is considerably small as

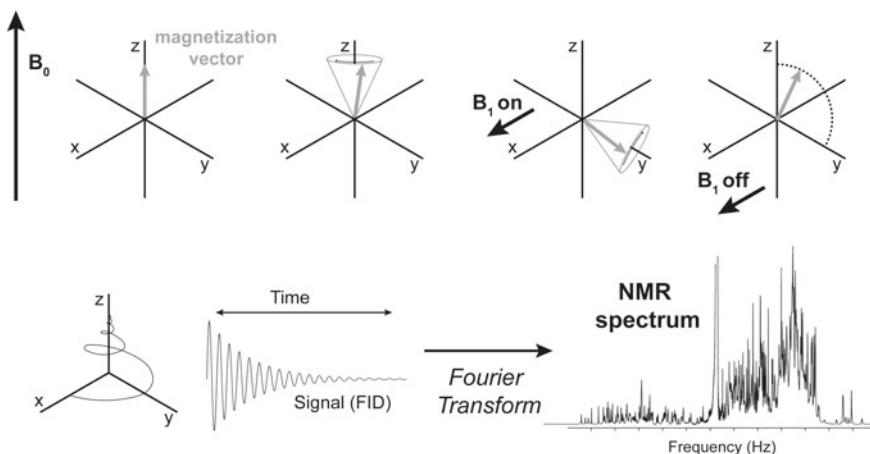


Fig. 9.4 Basic NMR experiment. In presence of the applied field (B_0) the bulk magnetization precesses at Larmor frequency around the z-axis; a short burst of RF radiation (B_1) rotates the bulk magnetization from its equilibrium position toward xy-plan; after switching-off the RF pulse, the magnetization returns to its equilibrium position while generating an oscillating magnetic field that induces a current in the receiver coil; the induced current is measured as a function of time and is referred as Free Induction Decay (FID); the subsequent Fourier transformation of the FID originates the normal NMR spectrum

it is the population ratio between the highest and lowest energy levels at equilibrium. The ratio of population is given by the Boltzmann's distribution law (Eq. 9.8):

$$\frac{N_\beta}{N_\alpha} = \exp\left(-\frac{\Delta E}{kT}\right) \quad (9.8)$$

In this equation, N_β and N_α are the populations of β and α energy levels, k the Boltzmann's constant and T the temperature. The ratio of populations is 0.999936 and 0.999871, considering a ^1H nucleus for magnetic fields values of 9.4 and 18.8 T at 25 °C, respectively. The small population ratio makes the NMR technique considerably insensitive. For this reason, it is common to increase the signal-to-noise ratio of the overall spectrum by signal averaging. This is one of the reasons why NMR spectroscopy is highly sample demanding. On the other hand, the small energy difference between the ground and excited states brings several advantages to the technique. In fact, the high life time of the excited state (on the order of milliseconds to seconds) produces narrow spectral lines, enhances sensitivity to measure molecular motions and allows the design of multi-dimensional experiments (see below).

As a result of the slightly excess of spins in the low energy level, there is a net magnetization along the direction of the applied magnetic field at equilibrium. This is the so-called bulk magnetization of the sample, which can be represented by a vector pointing along the z-direction (see Fig. 9.2b). This formalism, known as *vector model*, can be used in very limited situations. However, the model is adequate to describe

how a simple NMR spectrum is obtained. As mentioned above, the motion of the nuclear moments along the z -axis, in the presence of \mathbf{B}_0 , is designated by the Larmor frequency.

The units of the angular frequency, ω , are radians per second (rad s^{-1}) and is related with the frequency ν (measured in Hz or s^{-1}) by Eq. 9.9:

$$\omega = 2\pi\nu \quad (9.9)$$

By rewriting the energy difference (Eq. 9.7) in terms of the resonant frequency (Eq. 9.10) the well-known Larmor equation is obtained (Eq. 9.11)

$$h\nu = \left(\frac{h}{2\pi}\right)B_0\gamma \quad (9.10)$$

$$\omega = \gamma B_0 \quad (9.11)$$

The Larmor equation refers to the resonance frequency of a nucleus, which is proportional to the strength of the magnetic field and its gyromagnetic ratio. In an NMR experiment the precession of the magnetization vector is what is actually detected.

To obtain information on the system under study it is necessary to promote transitions between the ground and the excited state(s), as in any other spectroscopic technique. As described, in the presence of an applied magnetic field, two energy levels are permitted and a bulk magnetization along the z -axis is produced for a nucleus with $\mathbf{I} = \frac{1}{2}$. This magnetization precesses around this direction at a Larmor frequency ω . To rotate the bulk magnetization from its equilibrium position, i.e. to promote transitions between the two energy levels, an oscillating magnetic field at, or near to, the Larmor frequency is applied along the x -axis. This is accomplished by a short burst of radiofrequency (RF) radiation, often designated as 90° pulse, to the small coil of wire around the sample. The 90° pulse-width is the length of a pulse, usually in microseconds, which will produce the maximum response from a given NMR-active nuclei. The resultant excited states produce an oscillating magnetic field that induces a current in the receiver coil along the x -direction. Following the switching-off of the RF pulse, the bulk magnetization will return to its equilibrium position and the induced current in the receiver coil is measured as function of time. This is designated Free Induction Decay (FID). A Fourier transform of the FID yields the familiar NMR spectrum with absorption peaks at different frequencies (Fig. 9.4). Each line in the spectrum is associated with a transition (energy difference) between the ground and excited levels of a particular nucleus.

The mentioned procedure summarizes the one-pulse experiment, which can be also described into two discrete time periods: *preparation* and *detection* (Fig. 9.5). In the *preparation* period, before the switch-on of the 90° excitation pulse, the spins are at thermal equilibrium yielding a bulk magnetization along the z -axis, which is then rotated to the xy -plane by the application of the oscillatory excitation field along x -axis (\mathbf{B}_1). The *detection* period, starts after the switch-off of the 90° pulse

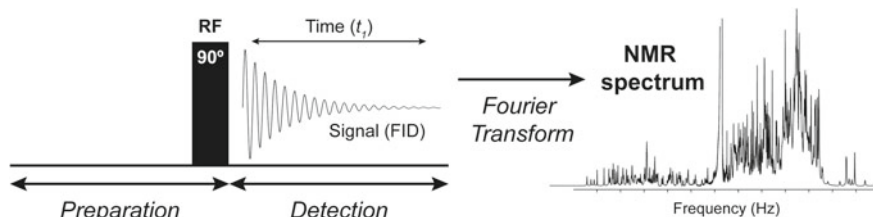


Fig. 9.5 Illustration of the simplest 1D NMR experiment. After thermal equilibration of the spins, the experiment starts with the sample irradiation with a 90° pulse of radiofrequency (RF) radiation (*preparation* period). The signal (FID) is measured during the time length t_1 (*detection* period). A Fourier transform of the FID gives the familiar NMR spectrum (signal absorption *versus* frequency). See also Fig. 9.4 for details

and measures the return of the excited spins to the thermal equilibrium under the static \mathbf{B}_0 field with the concomitant generation of the FID.

9.1.4 Relaxation Times

The return to the equilibrium of the excited spins can be described by two different relaxation mechanisms. One is responsible for the re-alignment of the bulk magnetization along the \mathbf{B}_0 direction and restores the Boltzmann population differences. This relaxation mechanism follows first-order rate kinetics, and the reciprocal of this rate constant (\mathbf{R}_1) is called the longitudinal (or spin-lattice) relaxation time, T_1 . The mechanism depends upon the interactions of the nuclear spins with the environment, including the solvent, which will also ultimately depend upon the fluctuating fields experienced as the molecules tumble and, hence upon the molecular rotational correlation time (τ_c). On the other hand, an additional relaxation mechanism describes the loss of the magnetization in the xy -plane. Known as transversal (or spin-spin) relaxation mechanism, it also follows a first-order kinetics and measures alterations in the precession frequency during nuclear spin relaxation. The reciprocal of this rate constant (\mathbf{R}_2) is called the transversal relaxation time, T_2 . The changes in the precession frequency are not similar for all nuclear spins in the sample, i.e. the rates of precession vary with respect to each other. However, it is worth to note that this process does not affect the net population of excited states and, therefore the system is not returned to thermal equilibrium by this mechanism. Inhomogeneous magnetic fields that cause the spins to differ from location to location within the sample, dipolar coupling between magnetic dipoles and anisotropic electron density surrounding the nucleus are all contributing processes to transversal relaxation. The dominant factor determining T_2 is the molecular rotational correlation time. This parameter is generally much shorter than T_1 in liquids and, therefore, the signal linewidths are determined by T_2 . Larger molecules have larger (τ_c) values originating broader NMR signals.

9.1.5 Chemical Shifts

To this point, nuclei have been presented as isolated identities. In fact, if all nuclear spins of the same isotope in one molecule could be unaffected by their neighborhood, they would have the same frequency. However, the typical dispersion of the nuclei NMR signals is indeed caused by their different chemical environment. One of the well-known factors triggering the differences in nuclei frequencies is the electronic shielding caused by surrounding electrons. Consequently, the effective magnetic field at a particular nucleus (\mathbf{B}_{eff}) might differ from \mathbf{B}_0 , according to Eq. 9.12.

$$B_{\text{eff}} = B_0(1 - \sigma) \quad (9.12)$$

In this equation, σ is the shielding constant, which can be either positive or negative, depending on whether the local magnetic field caused by the electrons decreases or reinforces the applied magnetic field. Thus, taking into account Eq. 9.10, the frequency of a nucleus is given by:

$$\nu = \frac{\gamma B_0(1 - \sigma)}{2\pi} \quad (9.13)$$

The shielding effect can be expressed as a relative change in frequency with respect to a standard, thereby rendering it independent of the strength of \mathbf{B}_0 . The frequency shifts caused by the shielding effects are very small compared to the NMR spectrometer operating frequencies, on a scale of Hz, as compared to MHz. For this reason, the chemical shift (δ) is expressed in parts per million (ppm), as described in Eq. 9.14.

$$\delta = \frac{(\nu - \nu_{\text{ref}})}{\nu_{\text{spectrometer}}} \times 10^6 \quad (9.14)$$

In this equation, ν is the frequency of a particular nucleus, ν_{ref} is the reference frequency of a standard and $\nu_{\text{spectrometer}}$ corresponds to the NMR operating frequency. All frequency values in Eq. 9.14 are in Hz.

There are two compounds that are typically used for ^1H NMR referencing: tetramethylsilane (TMS) and 2,2-dimethyl-2-silapentane-5-sulfonic acid (DSS). It is always preferable not to add the reference compounds directly into the sample to prevent specific interactions between the reference compound and the molecules under study. This is particularly crucial in the study of biomolecules. Nowadays, calibration of ^1H signals can be obtained by measuring the chemical shift of the water signal according to Eq. 9.15, which describes the temperature dependence of the water signal as referenced to DSS:

$$\delta_{\text{H}_2\text{O}} (\text{ppm}) = 4.76 - (T(^{\circ}\text{C}) - 25) \times 0.01 \quad (9.15)$$

In addition, spectra calibration through indirect referencing is currently a very convenient method to calibrate the chemical shifts of other nuclei (e.g. ^{13}C or ^{15}N). The heteronuclear dimensions can be simple obtained by using the ratio of the gyromagnetic ratios of the heteronucleus and that of ^1H , together with the ^1H frequency of the reference compound (Wishart et al. 1995).

As described, the electron density is crucial in determining the chemical shift, but it is not the unique factor. Nevertheless, high electronic density around a nucleus X creates a large shielding so that, the effective magnetic field is smaller compared to a bare nucleus. In order to get resonance for nucleus X at the same value of the bare nucleus, the applied field must be increased. Because of this, nucleus X is said to be up-field shifted (smaller frequency and chemical shift values). As consequence of the shielding effects, there are typical chemical shift ranges for different nuclei. However, as these nuclei are part of a larger molecule, such as a protein, their chemical shifts are differently affected by secondary elements or cofactors, i.e. by the different structural environment. For this reason, the available tables of chemical shifts should be envisaged merely as guides for signal assignment. A striking example is observed for cytochromes. The interaction between the delocalized electrons of the heme aromatic rings with the external magnetic field are responsible for the unusual chemical shifts observed for their own substituents, as well as for those of amino acids placed in their vicinity (Hammes 2005; Rule and Hitchens 2006; Teng 2005). Nuclei above or below the ring plane usually are more shielded and have smaller chemical shifts (up-field shifts). The opposite is observed to nuclei placed near the edges of the ring (Fig. 9.6).

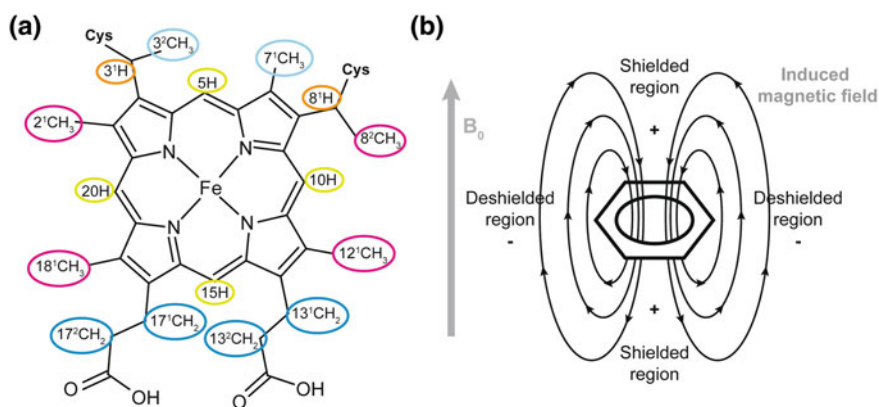


Fig. 9.6 **a** Diagram of a heme *c* numbered according to the IUPAC-IUB nomenclature (Moss 1988). **b** Ring-current effects caused by the circulation of π electrons in the porphyrin ring. The circulating electrons produce an additional magnetic field whose direction is opposite to the external applied magnetic field (B_0) in the center and axial regions of the heme and along B_0 at the outside edges of the heme. In the first case, nuclei are more shielded (up-field shifts), whereas in the second are less (down-field shifts). Panel **a** was partially reproduced with permission from Elsevier, reference (Morgado et al. 2010)



Fig. 9.7 1D ^1H NMR spectra obtained for the reduced (a) and oxidized (b) states of triheme cytochrome PpcA from *G. sulfurreducens* (pH 5.5, 298 K, Bruker Avance 800 spectrometer). The typical regions of the heme substituents are indicated in both spectra using the color code of the heme *c* represented in Fig. 9.6a. This figure was partially reproduced with permission from Elsevier, reference (Morgado et al. 2010)

These effects, called ring-current shifts, can cause large variations on the typical chemical shift values and provide extremely important structural information. In addition to this, when the cytochromes have unpaired electrons in the heme iron, the effect is usually even more dramatic. In fact, in addition to ring-current shifts, the paramagnetic contribution of the unpaired electrons in the heme molecular orbitals contributes strongly to the final observed chemical shift due to the higher electron magnetic moment (Bertini et al. 2001). The paramagnetic effect encompasses a through-bond contribution, given by an additional magnetic field generated at the nucleus by the electron magnetic moment located at the nucleus itself, and a spatial effect caused by the spatial interaction between the two moments. The first contribu-

tion is designated scalar or Fermi contact shift and the second dipolar pseudo contact shift. Additionally, the unpaired electrons also contribute to the broadening of the signals, which is higher for the nuclei closer to the heme iron(s) so that the side chain signals of the heme axial ligands are hardly or not detected (for a review see reference Bertini et al. 2001).

The ring-current and paramagnetic effects are illustrated in the 1D NMR spectra of the triheme cytochrome PpcA from the bacterium *Geobacter sulfurreducens*. This protein is diamagnetic when reduced (Fe(II), $S = 0$ – Fig. 9.7a) and paramagnetic when oxidized (Fe(III), $S = \frac{1}{2}$ – Fig. 9.7b). In the diamagnetic reduced form, the proton chemical shifts of the heme substituents are essentially affected by the heme ring-current effects. Therefore, for the fully reduced cytochrome, typical regions for the signals of the heme substituents can be easily identified in the NMR spectra: 8–10 ppm meso protons (5H, 10H, 15H and 20H); 6–8 ppm thioether methines (3^1H and 8^1H); 2.5–5 ppm methyl groups (2^1CH_3 , 7^1CH_3 , 12^1CH_3 and 18^1CH_3); and – 1 to 3 ppm thioether methyls (3^2CH_3 and 8^2CH_3). On the contrary, in the oxidized form of PpcA, the paramagnetic effect of each heme iron causes significant shifts on the heme substituents signals.

9.1.6 Spin-Spin Coupling

In addition to the chemical shift, the splitting or multiplicity of the NMR signals also gives important information about the nuclei chemical environment. As described, the chemical shift is caused by interactions between the nucleus and nearby electrons. On the other hand, spin-spin coupling (also designated J , indirect or scalar coupling) arises from nuclei interactions across bonding electrons. It is typically observed between nuclei that are up to three bonds away and depends on the dihedral angle between vicinal protons, accordingly to the Karplus relationship (see references Bertini et al. 2001; Hammes 2005; Rule and Hitchens 2006; Teng 2005 for details). Therefore, J coupling provides important geometric and structural information. In simple terms, spin-spin coupling is the effect on a nuclear spin caused by the local magnetic field of its neighbor spin and the magnitude decreases significantly with the number of bonds. This effect splits the spectral lines of the coupled spins by the coupling constant amount. The nomenclature for the J constant is ${}^nJ_{\text{AB}}$, where n refers to the number of intervening chemical bonds between the two coupled spins (A and B). For example, ${}^3J_{\text{HH}}$ represents the coupling constant for protons that are separated by three bonds. The total number of frequencies for equivalent nuclei that have n equivalent protons on the adjacent carbon will split into $n + 1$ peaks with a coupling constant J . The intensity of these peaks is given by the Pascal's triangle rule. More complex coupling is observed in the case of non-equivalent nuclei. Non-equivalent nuclei will split a common nucleus independently, yielding even more complex spectra.

9.1.7 Multi-dimensional NMR Experiments

Due to severe overlapping and/or signal broadening that decreases the spectral resolution, the signals of biomolecules cannot be fully assigned in one-dimensional NMR spectra. Thus, the development of multi-dimensional experiments was extremely important to extend the biological applications of NMR spectroscopy. A detailed presentation of multi-dimensional experiments, particularly the physical chemistry formalism is beyond the scope of this text. Books that address this topic in detail are provided in the references section for further reading (Bertini et al. 2001; Hammes 2005; Rule and Hitchens 2006; Teng 2005). Instead, a qualitative and practical application of multi-dimensional NMR will be described, particularly the more relevant experiments to the selected biological applications.

NMR spectral resolution limitation is inherent to biomolecules due to their high molecular weight. Larger molecules also have high number of signals whose scalar coupling will make the spectra uninterpretable. In fact, the scalar coupling and the concomitant line splitting reduce the spectral signal-to-noise ratio and disperse the signal intensity over all of the peaks of the multiplets. Regardless the important information associated with scalar coupling, this effect can be cancelled by experimental decoupling schemes, which restore the loss in the signal-to-noise by collapsing the multiplets to single lines (Rule and Hitchens 2006). Therefore, the mono- and multi-dimensional experiments acquired for biomolecules are typically obtained in a decoupling mode. Even though, the number of signals is still extremely high to allow a complete and unambiguous assignment in 1D NMR spectra. This can be overcome by adding a second frequency dimension that disperses the signals, the so-called two-dimensional (2D) NMR spectroscopy.

As described, in a 1D NMR experiment the FID is recorded as a function of one time variable and then Fourier transformed to give a spectrum as a function of one variable frequency (Fig. 9.5). In a 2D spectrum, the signal is recorded as a function of two-time variables, t_1 and t_2 , and the resulting data Fourier transformed twice to yield a spectrum that is now a function of two variable frequencies. The general scheme is summarized in Fig. 9.8. Compared to the simplest 1D pulse sequence (Fig. 9.5), one additional time period (*evolution*) is placed after the *preparation* time in 2D NMR sequences. During the *evolution* time, the resulting magnetization is allowed to evolve by the variable time delay t_1 . Then, depending upon the specific

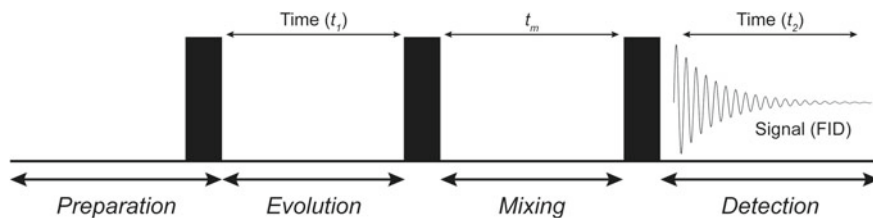


Fig. 9.8 Illustration of a typical 2D NMR experiment. The filled rectangles represent 90° pulses

2D experiment, the evolution is followed by a *mixing* period that might include further pulse(s). After this period the signal is recorded as a function of the second time variable, t_2 , during the *detection* period. Thus, 2D NMR spectra can be viewed as the assembly of several 1D spectra acquired with different t_1 values. In fact, the signal is only recorded at the end of the pulse sequence, during the time t_2 (Fig. 9.8).

The 2D signals are recorded in the following way. In a first spectrum of the sequence, the t_1 is set to zero, the pulse sequence is executed and the resulting FID recorded. Then, the nuclear spins are allowed to return to equilibrium. In the second spectra, t_1 is then set to the sampling interval Δx and the pulse sequence repeated, the FID recorded and stored separately from the first. The whole process is then repeated for the desired number of experiments (n), each differing by Δx increment. Following the Fourier transform of the two data sets (t_1 and t_2), the final output contains two frequency axes (ν_1 and ν_2), plus a third one containing the intensities of the signals (Fig. 9.9a). Typically, a 2D NMR spectrum is displayed as contour plots (Fig. 9.9b).

2D NMR homonuclear experiments (e.g. $^1\text{H}, ^1\text{H}$) originate squared spectra with diagonal peaks. In contrast, heteronuclear experiments (e.g. $^1\text{H}, ^{15}\text{N}$) originate asymmetric spectra. The diagonal peaks represent the 1D spectrum, whereas the off-diagonal signals correlate nuclei with different frequencies. The nature of the correlation is “designed” during the *mixing* period in which through bond (scalar) or through space (dipolar) couplings are allowed to evolve. In the absence of a mixing time, the frequencies that evolve during t_1 and t_2 would be the same and only diagonal-peaks would appear in the spectrum. On the other hand, if one signal evolved at ν_X during t_1 and during the mixing period part of its magnetization is transferred into another signal that evolves at ν_Y at t_2 , thus the unaffected part of the first signal continues to evolve at ν_X during t_2 (originating a diagonal peak) that correlates with an off-diagonal signal at ν_Y .

2D ^1H COrrrelation Spectroscopy (COSY) explores scalar coupling (through bond nuclear interaction) to correlate nuclei up to three covalent bonds within a spin system. Similarly, 2D ^1H Total Correlation Spectroscopy (TOCSY) also explores scalar coupling, but correlates nuclei within the entire spin system, i.e. not limited

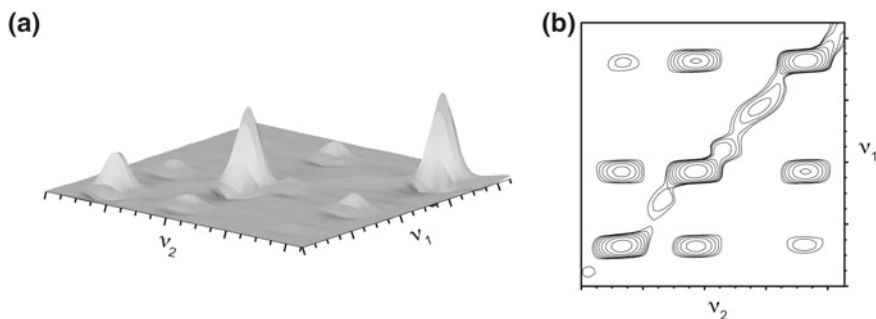


Fig. 9.9 Stacked (a) and contour (b) plot of a 2D spectral region

to three covalent bonds. The pulse sequences of the 2D ^1H COSY and TOCSY experiments are illustrated in Fig. 9.10.

A typical application of 2D ^1H COSY and ^1H TOCSY is the specific assignment of amino acid side chain signals. This is illustrated in Fig. 9.11 for the heme axial methionine in the monoheme cytochrome OmcF from *G. sulfurreducens*. This example also illustrates the ring-current effects of the heme group in the axial methionine.

Another important 2D NMR experiment is the Nuclear Overhauser Effect Spectroscopy (NOESY). In NOESY experiments, the magnetization transfer during the *mixing* period explores the through-space spin dipolar interactions (Fig. 9.10). Therefore, the spectral correlations depend exclusively on the distance between the nuclei

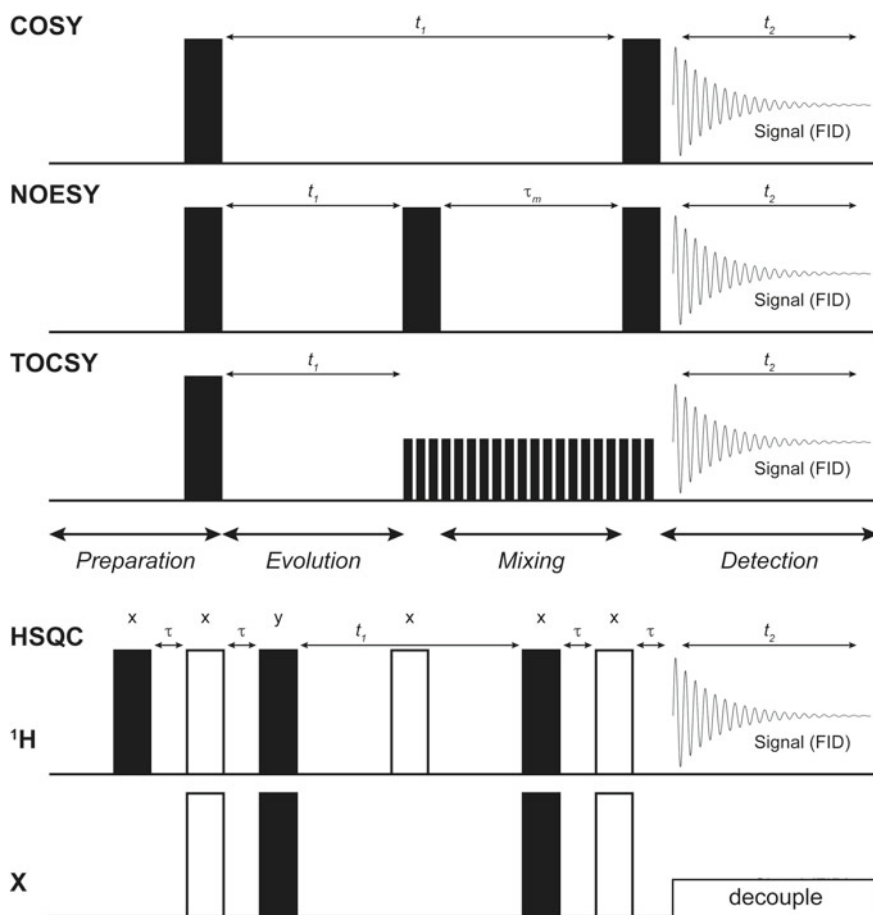


Fig. 9.10 Illustration of some 2D NMR pulse sequences. From top to bottom: COSY, NOESY, TOCSY, HSQC. The filled and open rectangles represent 90° and 180° pulses, respectively. The delay τ is set to $1/(2J_{\text{HX}})$. All pulses have phase x , except in the HSQC sequence. In this sequence, the phases of the pulses are indicated on the top of each pulse

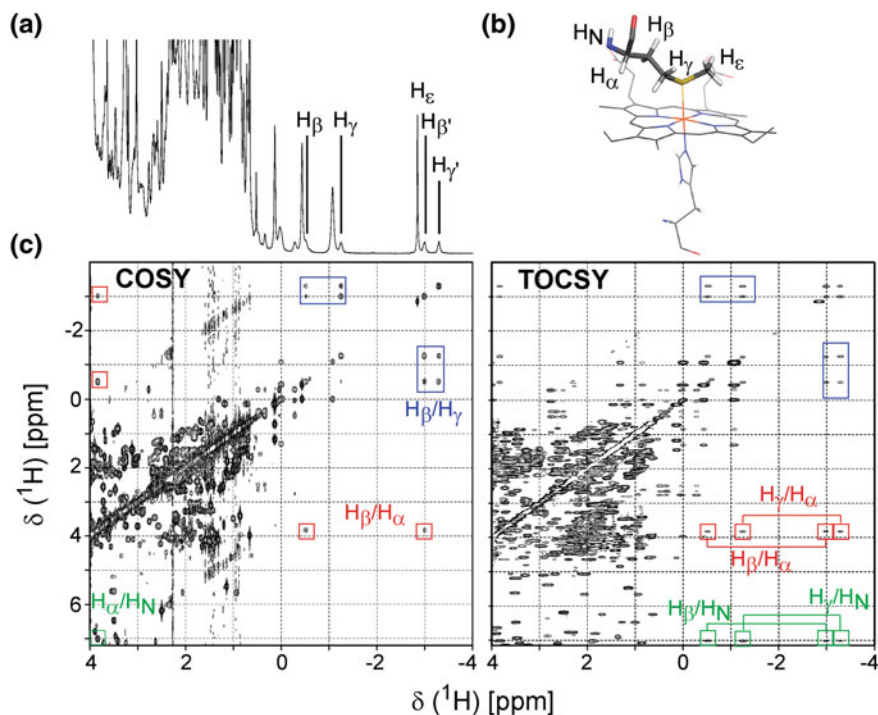


Fig. 9.11 Assignment of the ^1H signals of axial methionine (Met^{79}) of cytochrome OmcF from *G. sulfurreducens* in the reduced state (pH 7, 298 K, Bruker Avance III 600 spectrometer). **a** Expansion of the high-field region of the 1D ^1H NMR spectrum. **b** Heme group and respective axial ligands using the heteroatom color-coding (PDB code 5MCS (Dantas et al. 2017b)). **c** Expansions of 2D ^1H COSY and TOCSY spectra. Signals correspondent to the side chain protons of Met^{79} are labeled in all panels. The H_α and H_N signals are also labeled. Scalar coupling in the COSY spectrum correlates nuclei up to three covalent bonds ($\text{H}_\alpha/\text{H}_\beta$, $\text{H}_\beta/\text{H}_\gamma$ and $\text{H}_\alpha/\text{H}_\text{N}$) and allow distinguishing all type of protons. The full set of correlations is then observed in the TOCSY spectrum. Due to the heme ring-current effects, the ^1H chemical shifts of Met^{79} are considerably up-field shifted

(up to approximately 5 Å) and their intensity/volume is proportional to their inter-nuclear distance (r) by a factor of $1/r^6$. Although NOESY can complement COSY and TOCSY experiments in the specific assignment of resonances, the technique is mostly used to obtain structural restraints for molecular solution structural determination (Sect. 9.2).

2D ^1H Exchange Spectroscopy (EXSY) shares the same pulse sequence with NOESY. However, in this case the magnetic transfer during the *mixing* period takes place through chemical exchange. Mixing-time values used for 2D ^1H EXSY experiments are typically shorter, since exchange is usually faster than NOE build up. Examples of 2D ^1H EXSY experiments are provided in Sect. 9.4.

Heteronuclear experiments (e.g. ^1H , ^{15}N or ^1H , ^{13}C) are extremely useful in modern NMR. The most used is the Heteronuclear Single Quantum Correlation (HSQC)

pulse sequence (Fig. 9.10), which is also included in more complex sequences used in 2D and 3D experiments for ^{13}C and/or ^{15}N isotopic labeled proteins (see Sect. 9.2.1). The $^1\text{H},^{15}\text{N}$ or $^1\text{H},^{13}\text{C}$ HSQC spectra detect only pairs of directly covalently attached nuclei. In these asymmetric spectra, each peak represents the proton resonance frequency with that of the attached nitrogen or carbon nucleus. The $^1\text{H},^{15}\text{N}$ HSQC is known as the fingerprint of a protein because, with exception of proline residues, all the backbone residues have amide groups whose signals are represented in the spectrum. Examples of $^1\text{H},^{15}\text{N}$ and $^1\text{H},^{13}\text{C}$ HSQC spectra are provided in the following sections either as isolated experiments or as part of 3D pulse sequences.

Modern biomolecular NMR also utilizes different types of 3D experiments. In general, 3D experiments include a combination of the same elements as 2D experiments (e.g. NOESY-HSQC, TOCSY-HSQC, etc.). In a typical 3D pulse sequence there are three evolution periods. The first two correspond to the two indirectly-detected dimensions (t_1 and t_2) and the third to the directly detected dimension (t_3).

9.2 Structural Studies of Proteins

Polypeptide chains fold to form defined tri-dimensional structures in proteins. This specific fold is encoded in the amino acid sequence, which constitutes the protein primary structure. The amino acids can then be organized in segments with defined dihedral angles in the backbone, forming regular conformations designated secondary structure elements, as α -helices and β -sheets. The packing of the several secondary structure elements defines the protein's tertiary structure. A quaternary structure exists when independent polypeptide chains interact with each other forming domains in the proteins. NMR provides insights at the different levels of protein structural organization. While NOEs give information on the distance between two atoms, chemical shifts contain information on the residues dihedral angles to describe the secondary structural elements.

9.2.1 Protein Isotopic Labeling

NMR studies of proteins usually require the incorporation of NMR-active isotopes as nitrogen ^{15}N and carbon ^{13}C , and sometimes deuterium ^2H , to improve the spectral quality and facilitate the interpretation of the spectra. To produce isotopic labeled samples, a variety of expressing systems can be used, from bacterial, yeast or insect cells, to cell-free expression (Dutta et al. 2012; Franke et al. 2018; Klopp et al. 2018; Rosenblum and Cooperman 2014). The size and complexity of the target protein determines the labeling scheme to be used (Ohki and Kainosho 2008; Zhang and van Ingen 2016). When proteins have up to 20–25 kDa, conventional uniform [$^{13}\text{C},^{15}\text{N}$] labeling is usually the strategy of choice (McIntosh and Dahlquist 1990). For proteins of about 10 kDa size, ^{15}N labelling only can be used. M9 minimal

medium supplemented with ^{13}C labeled glucose, as carbon source, and ^{15}N labeled ammonium chloride, as nitrogen source, is used for protein expression. When proteins are larger than 20–25 kDa, [^{13}C , ^{15}N] labeling is combined with deuteration by using $^2\text{H}_2\text{O}$ in the expression medium instead of H_2O , or additionally with ^2H , ^{13}C -glucose for full deuteration (Gardner and Kay 1998). Deuteration reduces the relaxation rates of the remaining protons and leads to higher signal-to-noise and smaller linewidths with the concomitant improvement of the spectral quality (Sattler and Fesik 1996). Nevertheless, the number of signals and complexity of the spectra increases with protein size and, therefore these approaches are valid for proteins up to 50 kDa. For higher molecular weight systems, more complex labeling schemes have been developed along the years, namely amino acid specific labeling, methyl labeling, segmental labeling, LEGO subunit labeling or stereo-array isotope labeling (SAIL).

Amino acid specific labeling was one of the first selective labeling approaches developed (McIntosh and Dahlquist 1990). It can be used to reduce spectral overlap, helping in the assignment of large proteins, as well as a tool to study certain amino acids without interference from signals from other residues. However, expression of the proteins in *Escherichia coli* can lead to scrambling, since the bacteria's metabolism causes the interconversion between amino acids. Scrambling can be avoided by the use of auxotrophic strains (Lin et al. 2011) or cell-free expression. Reverse labeling or unlabeled is a different approach for amino acid specific labeling (Krishnarjuna et al. 2011). In this case, unlabeled amino acids are added to the minimal media in a ^{13}C and/or ^{15}N labeled background.

Methyl groups are usually abundant in the hydrophobic cores of proteins and give rise to intense and well-resolved NMR signals. The specific labeling of methyl groups consists on the usage of amino acid precursors ^1H , ^{13}C labeled on the methyl group of interest in a deuterated background (Tugarinov et al. 2006; Tugarinov and Kay 2004). This strategy was first developed for the labeling of isoleucine- δ_1 , valine and leucine methyl groups (Goto et al. 1999). It was then further extended to isoleucine- γ_2 , methionine, alanine and threonine residues (Ayala et al. 2009; Fischer et al. 2007; Ruschak et al. 2010; Velyvis et al. 2012). One of the drawbacks of deuteration is the loss of H-H information obtainable from NOESY spectra. This labeling scheme is of particular importance in structural studies of high-molecular weight systems where the measurement of distances is necessary, since it allows the acquisition of methyl-methyl and methyl-NH distance restraints.

In segmental labeling, unlabeled and labeled protein segments are produced separately and after fused together using either inteins or the transpeptidase sortase A. Intein approaches are based on protein splicing and take advantage of internal protein domains that have the ability to excise themselves in a traceless way (Muir et al. 1998; Muralidharan and Muir 2006). In the case of the usage of sortase, this enzyme recognizes a motif on the N-terminal segment (LPXTG) and catalyzes the ligation to a glycine residue on N-terminal of the C-terminal segment (Freiburger et al. 2015; Mao et al. 2004). These approaches can be useful in the study of large proteins by labeling only part of it, or in the study of multidomain proteins since it considerably reduces peak overlap.

The LEGO-NMR labeling methodology (“Label, Express, and Generate Oligomers”) was introduced to surpass aggregation problems in the assembly of protein complexes *in vitro* (Mund et al. 2013). Two plasmids with different inducible promoters are used for sequential protein expression in *E. coli* in two different expression media, allowing different labeling in different subunits.

SAIL labeling relies on synthetically prepared amino acids with features that reduce the number of NOE cross-peaks in the spectra, while keeping essential information to define side-chain conformations (Kainosho and Guntert 2009; Kainosho et al. 2006). In these amino acids one ^1H atom in each methylene group is stereoselectively replaced by a ^2H atom, two ^1H atoms in each methyl group are replaced by ^2H atoms, the prochiral methyl groups of leucine and valine residues are stereoselectively labeled and six-membered aromatic rings have alternating $^{12}\text{C}^2\text{H}$ and $^{13}\text{C}^1\text{H}$ labeling. For this labeling approach, cell-free protein synthesis is required.

9.2.2 Sequential Assignment

Resonance assignment is an essential step for the usage of NMR to study proteins. The 2D ^1H , ^{15}N HSQC spectrum, besides providing information on proper protein folding, is the starting point for backbone assignment. With the exception of prolines and the N-terminal residue, all the other residues show a H-N correlation arising from the backbone amide. The side chains of tryptophan ($\text{N}_\epsilon\text{-H}_\epsilon$), asparagine ($\text{N}_{\delta 2}\text{-H}_{\delta 2}$) and glutamine ($\text{N}_{\epsilon 2}\text{-H}_{\epsilon 2}$) residues are also identifiable. The assignment of the resonances on the 2D ^1H , ^{15}N HSQC spectrum relies on the acquisition and analysis of a combination of different tridimensional spectra.

If only ^{15}N labeling is used, a 3D ^1H , ^{15}N TOCSY-HSQC and a 3D ^1H , ^{15}N NOESY-HSQC spectrum are necessary for backbone assignment (Fig. 9.12a) (Marion et al. 1989). In the first, for each H-N resonance and as for the 2D ^1H TOCSY already described, H-H connectivities are observed along the side chain of the corresponding residue, allowing identifying residue types. For example, glycine, alanine and valine residues are unambiguously identified since these residues show unique resonance patterns (Fig. 9.12b).

The NOESY spectra will provide information on the residues that are spatially close to the selected amide proton. The signals between neighboring HN groups are strong, as well as between the HN and the H_α of the preceding residue ($i - 1$), and are used to perform the sequential assignment. As mentioned, ^{15}N labeling is usually only used for proteins up to about 10 kDa, as resonance overlap and the number of NOESY connectivities increase with increasing protein size. Also, if the protein structure is not known and since the sequential assignment relies on NOE cross peaks, special attention has to be taken because this method can lead to incorrect assignments.

When the protein is ^{15}N and ^{13}C labeled, the following 3D experiments can be used for sequential assignment of the backbone resonances: HNCACB, HN(CO)CACB,

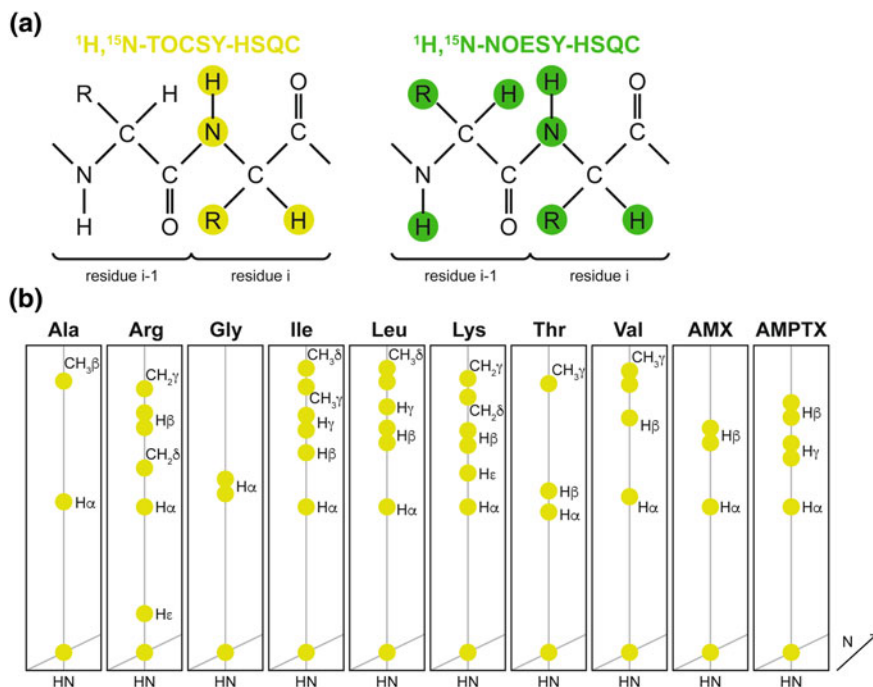


Fig. 9.12 Assignment in ^{15}N -labeled proteins: **a** Correlations observed in 3D $^1\text{H}, ^{15}\text{N}$ TOCSY-HSQC and 3D $^1\text{H}, ^{15}\text{N}$ NOESY-HSQC spectra. **b** TOCSY patterns in 3D $^1\text{H}, ^{15}\text{N}$ TOCSY-HSQC strips for each amino acid type. AMX spin systems are Asn, Asp, Cys, His, Phe, Ser, Trp or Tyr residues and AMPTX are Gln, Glu or Met residues

HNCA, HN(CO)CA, HNCO and HN(CA)CO (Fig. 9.13) (Kay et al. 1990; Sattler et al. 1999).

The 3D HNCACB correlates the H-N from one residue with its own carbon alpha (C_α) and carbon beta (C_β), and the C_α and C_β from the preceding residue ($C_{\alpha(i-1)}$, $C_{\beta(i-1)}$) (Grzesiek and Bax 1992b; Wittekind and Mueller 1993). In combination with the HN(CO)CACB (Grzesiek and Bax 1992a; Yamazaki et al. 1994), that correlates the H-N from one residue with the $C_{\alpha(i-1)}$ and $C_{\beta(i-1)}$, it is possible to determine the sequential backbone assignment. The chemical shifts of the C_α and C_β are characteristic of each amino acid (Fig. 9.14), thus provide information on the amino acid type and help to locate stretches of residues within the protein sequence (Grzesiek and Bax 1993). The C_α and C_β chemical shifts also provide information on the protein secondary structure when analyzed in the software TALOS-N (Shen and Bax 2013) or CSI (Hafsa et al. 2015). However, for proteins with more than 15 kDa these experiments become less sensitive. In these cases, the more sensitive HNCA and HN(CO)CA (Bax and Ikura 1991; Grzesiek and Bax 1992c; Kay et al. 1990) are used to complete the sequential assignment. The HNCA correlates the H-N from one residue with its C_α and the $C_{\alpha(i-1)}$, while the HN(CO)CA correlates with the $C_{\alpha(i-1)}$

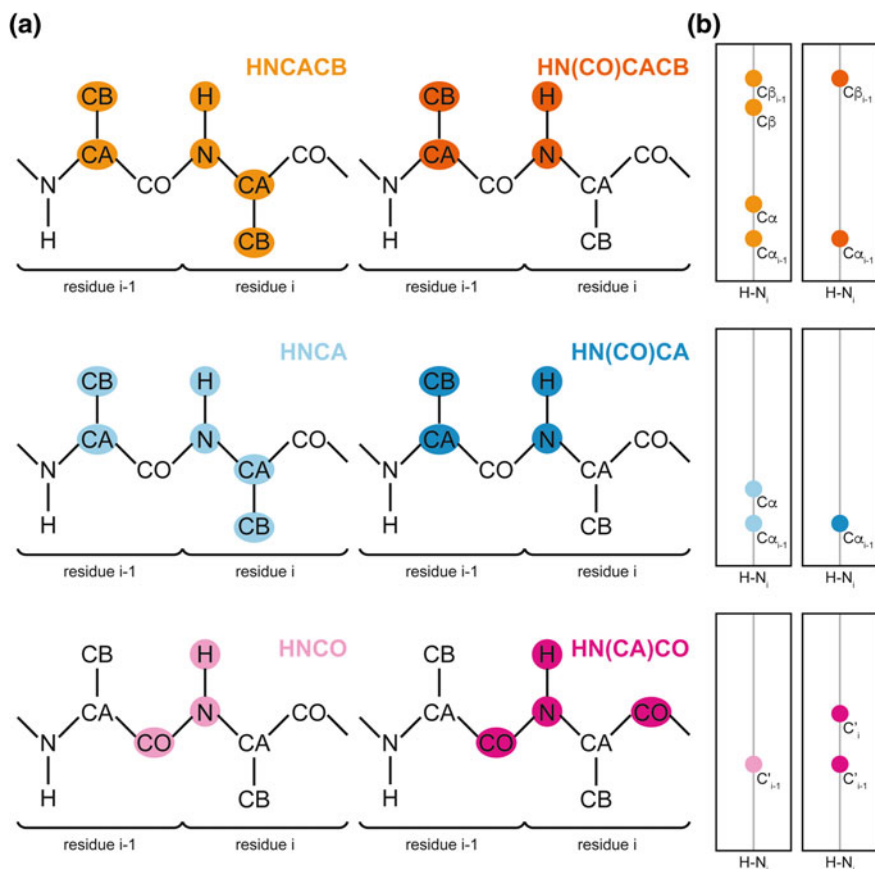


Fig. 9.13 Backbone assignment in $^{13}\text{C}/^{15}\text{N}$ labeled proteins. **a** Correlations observed in 3D experiments HNCACB, HN(CO)CACB, HNCA, HN(CO)CA, HNCO and HN(CA)CO. **b** Schematic representation of the peaks observed in each pair of spectra

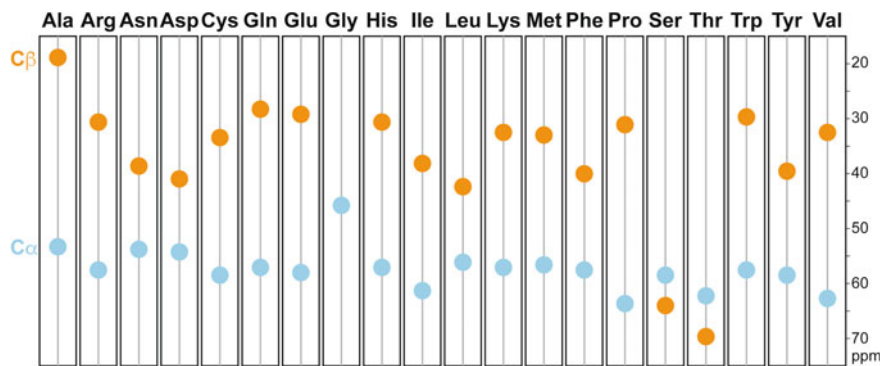


Fig. 9.14 Typical C_α and C_β chemical shifts for the twenty amino acids

only (Fig. 9.13). If there are still some ambiguities, the HNCO and the HN(CA)CO can also be used. The HNCO is the most sensitive experiment and correlates the H-N resonance from one residue with the carbonyl C' from the preceding residue (C'_{i-1}) allowing to solve overlaps in the HSQC spectra (Grzesiek and Bax 1992c; Kay et al. 1990). The HN(CA)CO correlates the H-N resonance with both the intra-residue carbonyl C' and the inter-residue C'_(i-1) (Clubb et al. 1992).

For larger proteins, TROSY versions of these pulse sequences are available (Pervushin et al. 1997). To solve the problem of resonance overlap and spectral crowding in larger proteins, higher dimensionality experiments as 4D HNCOCA have been developed (Frueh 2014; Yang and Kay 1999).

9.2.3 Side Chain Assignment

After the sequential assignment, the amino acid side chain resonances can be assigned. The assignment of these proton signals is essential for the analysis of NOE interactions that can be further used to get distance restraints for structure calculations, and also for the determination of binding surfaces in protein complexes. For side chain assignment, the 3D spectra (H)CCH-TOCSY and HC(C)H-TOCSY are used (Bax et al. 1990). In these spectra the carbon and proton side chain resonances are observed for each CH, respectively, and the C_α and C_β resonances obtained in the sequential assignment are used as starting points for the assignment (Fig. 9.15).

However, these experiments are not used for the assignment of the aromatic side chains, since the difference in carbon chemical shift between aliphatic (70–15 ppm) and aromatic (110–175 ppm) protons is very large. The latter can be assigned using 2D ¹H TOCSY and linked to the residue by inspection of the NOE connectivities.

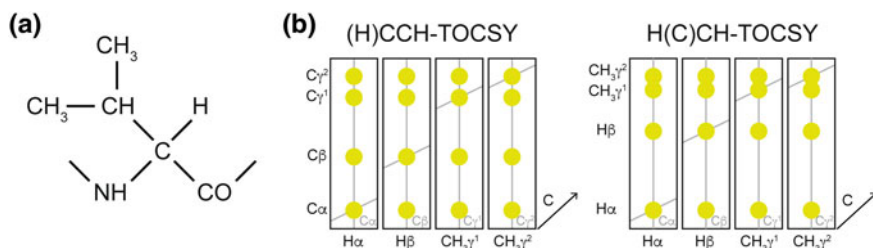


Fig. 9.15 **a** Valine chemical structure. **b** Schematic representation of the peaks observed for a Valine residue in 3D (H)CCH TOCSY and in H(C)CH TOCSY spectra

9.2.4 Assignment of the Heme Signals

In the particular case of cytochromes, the heme signals also provide important information for solution structure determination or molecular interaction studies. As illustrated in Fig. 9.7, in the fully reduced form, typical regions for the heme substituent signals are easily identified. Thus, in the reduced state, the first step of the assignment encompasses the analysis of 2D ^1H TOCSY spectra, in which the connectivities between thioether methines (3^1H or 8^1H) and thioether methyl groups (3^2CH_3 and 8^2CH_3) are identified (see Fig. 9.6a). Meso protons have short-range intraheme connectivities and, thus present a characteristic pattern in the 2D ^1H NOESY spectra. Protons 15H are not connected to either methyl groups or thioether substituents. Protons 20H are connected to two heme methyls (2^1CH_3 and 18^1CH_3) and can be easily assigned. Finally, the most ambiguous assignment arises with the 5H and 10H protons, since they both present connectivities with a thioether methine (3^1H or 8^1H , respectively), a thioether methyl (3^2CH_3 and 8^2CH_3 , respectively) and one heme methyl group (7^1CH_3 or 12^1CH_3 , respectively). This ambiguity is solved by observing the connectivities between the heme methyls near the 20H protons (2^1CH_3) with the closest thioether groups (3^1H or 3^2CH_3), which were previously assigned in the 2D ^1H TOCSY spectrum. This allows the connection between the 20H and 5H edges of each heme. The heme methyls 7^1CH_3 are part of the 5H edges of the heme and also show connectivities with thioether groups (8^1H and 8^2CH_3). After the identification of these three heme edges, 15H protons can be identified by observing the connectivities between cross-peaks that connect 15H and 12^1CH_3 or 18^1CH_3 protons in 2D ^1H NOESY acquired with long mixing-times (e.g. 300 ms). This strategy of assignment was initially described by Keller and Wüthrich (1978) for the horse heart ferrocycytochrome *c* and later applied to multiheme ferrocycytochromes by Turner and co-workers (1992). On the other hand, as also illustrated in Fig. 9.7, the dispersion of the heme substituent signals in the oxidized form, renders their assignment more complex. A strategy that simplifies the assignment of these signals was developed by Morgado and co-workers (2010) and consists in the analysis of ^1H , ^{13}C HSQC NMR spectra obtained for a natural abundance sample and for a sample ^{13}C -labeled exclusively in its polypeptide chain. The simple comparison of these spectra allows a straightforward discrimination between the heme and the polypeptide chain signals and is illustrated for the triheme cytochrome PpcA in Fig. 9.16.

9.2.5 Determination of Protein Solution Structures

Protein structures determined by NMR consist of an ensemble of conformers that satisfy the restraints obtained experimentally. The structure determination is an iterative process where experimental data is interpreted, resonances assigned and the assigned interactions converted into structural restraints (Fig. 9.17). These restraints are then used to calculate a bundle of structures in programs as CYANA (Herrmann et al.

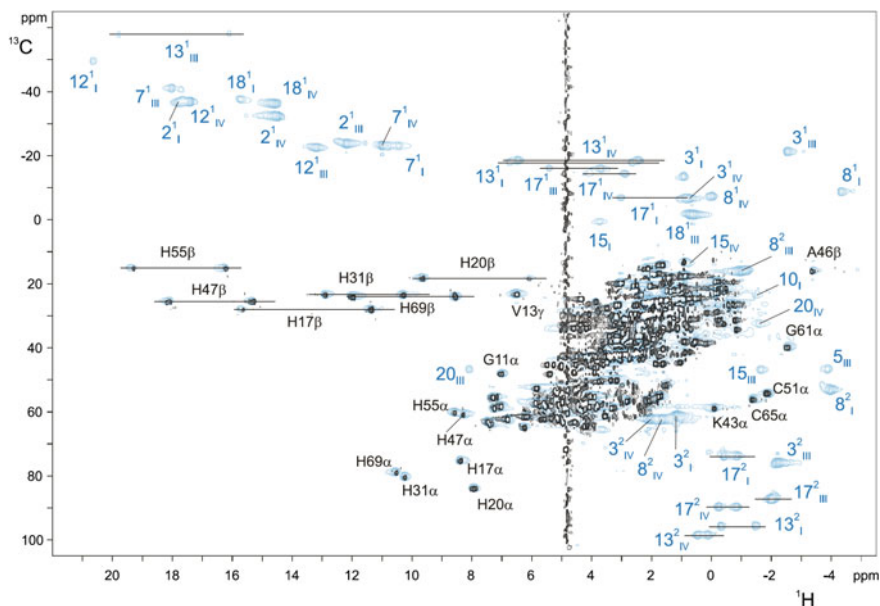


Fig. 9.16 2D ^1H , ^{13}C HSQC NMR spectra of oxidized PpcA (pH 5.5 and 298 K). The spectra correspond to PpcA samples: labeled ($^{13}\text{C}/^{15}\text{N}$) exclusively in its polypeptide chain (black contours) and unlabeled sample (blue contours). The blue contours that are not overlapped with black contours correspond to the heme signals. This figure was reproduced with permission from Elsevier, reference (Morgado et al. 2010)

2002), XPLOR-NIH (Schwieters et al. 2003) or PARADYANA (Turner et al. 1998) in the particular case of cytochromes. This bundle is analyzed in terms of restraint violations and incorrect assignments, and the experimental data is re-interpreted for a next round of calculations, until a consistent number of restraints has been collected. The accuracy of the ensemble is quantitatively measured by the root mean square deviation (RMSD) of the structure atomic coordinates. Regions of the structure with low RMSD are expected to be rigid, while regions with higher RMSD may be associated with local flexible regions, or an insufficient and/or inconsistent number of restraints. The final set of conformers also goes through a step of validation and quality check in programs as PROCHECK-NMR (Laskowski et al. 1996), that analyses the protein dihedral angles (ϕ and ψ) and prepares Ramachandran plots for all the residues in the protein.

The majority of structural restraints are obtained from NOESY spectra, which can be 2D, 3D or 4D spectra. As referred above, the volume of the NOESY cross-peaks is proportional to the inter-nuclear distance between the nuclei and can be converted into distances. In larger proteins, structural models can also be obtained from NOEs between amide-amide/amide-methyl/methyl-methyl groups in methyl labeled samples in a deuterated background. Besides NOEs, other types of restraints are used in large proteins. These include bond orientations from residual dipolar couplings

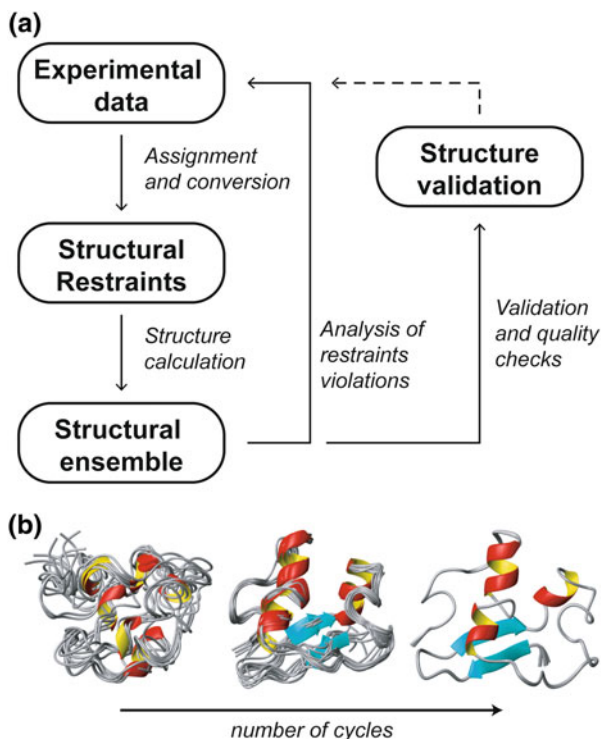
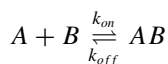


Fig. 9.17 **a** Flowchart of the steps of the iterative process of NMR structure calculation. **b** Example of the improvement of the quality of the structure with the increase number of cycles represented in **(a)**

(Tolman et al. 1995), paramagnetic relaxation enhancement measurements between a spin label and other atoms (Battiste and Wagner 2000) or solvent accessibility determined by hydrogen/deuterium exchange experiments (Ippel et al. 2002).

9.3 Biomolecular Interactions

A simple binding reaction between molecules A and B can be described as:



where k_{on} and k_{off} are the rate constants for complex formation and dissociation, respectively. In this reaction it is also assumed that: (i) the reaction is reversible, (ii) the biological response is proportional to the number of binding sites and (iii) the molecules do not degrade or participate in further reactions, i.e. only exist in the

unbound (A or B) or in the complex (AB) forms. In this case, the binding equilibrium can be described by Eq. 9.16.

$$K_d = \frac{1}{K_a} = \frac{k_{off}}{k_{on}} = \frac{[A][B]}{[AB]} \quad (9.16)$$

In this equation, K_d and K_a are the equilibrium dissociation and association constants, respectively. $[A]$, $[B]$ and $[AB]$ are the molar concentrations of the intervenient molecules. Typically, K_d and K_a have dimensions of M and M^{-1} , respectively. K_d measures the tendency of the complex to dissociate and can be directly compared with the concentrations of the interacting species. For this reason, rather than the equilibrium association constant, K_d is the most used parameter to describe biomolecular interactions.

In general, a reversible complex is formed by non-covalent interactions and its rate of formation is usually diffusion controlled, which means that every two-molecule collision is binding-effective. The environment is a crucial factor to the complex formation. For example, the pH, ionic strength, temperature and the polarity of the solvent can significantly affect the dynamics of the interactions. Regarding the functional framework of the interacting molecules, the magnitude of the interactions results in different ranges for the dissociation/association (K_d , K_a) and rate (k_{on} , k_{off}) constants. The interactions can be divided in permanent and transient. Permanent interactions are stronger and irreversible, typically characterized by K_d values in the nM range (1×10^{-9} M) or lower. This is the case of enzyme-inhibitor, antigen-antibody and large enzyme complex structures that are required to bind tightly and permanently. In contrast, a transient complex is characterized by K_d values in the μ M range (1×10^{-6} M) or higher. Examples of transient interactions include electron transfer complexes or signal-transduction cascades (La et al. 2013; Perkins et al. 2010). To maintain a high turn-over in electron transfer reactions, the rate constants k_{off} are usually high ($k_{off} \geq 10^3 \text{ s}^{-1}$) together with the high rate constants k_{on} between 10^7 and $10^9 \text{ M}^{-1} \text{ s}^{-1}$ (Crowley and Ubbink 2003; Liu et al. 2016; Perkins et al. 2010). The large k_{off} rates convert into the K_d values in mM– μ M range, considering this kind of interactions transient.

9.3.1 *Methods to Study Protein-Protein and Protein-Ligand Interactions*

In addition to protein solution structure determination, NMR can also be used to study biomolecular transient interactions, providing information at atomic level about whether a small molecule or a macromolecule (e.g. nucleic acids, proteins) bind to a target protein. This is possible because the concentrations of the samples are in the range of μ M–mM and, therefore the molecular interactions can be observed without artifacts. Particularly, this technique can be used to verify whether two molecules interact, to map their interaction surfaces, to determine the equilibrium dissociation

tion/association constants, to determine the structure of the complex and to identify indirect effects or conformational changes upon binding.

As described, the chemical shifts are highly sensitive to the chemical environment and, therefore, modifications in the nuclei surroundings can be detected. Macromolecules have slower rotational correlation time (τ_c) compared to small molecules, which can rotate faster in solution. Therefore, the relaxation parameters (T_1 and T_2) and NOE-based effects can also be explored to study biomolecular interactions. Based on these properties several methods can be used, such as saturation transfer difference (STD) and transfer NOE (tr-NOE).

Transfer NOE experiments take advantage of the difference in relaxations times between small and large molecules. Small molecules ($\tau_c < 0.3$ ns, MW < 500 Da) have large relaxation times and, consequently, 2D ^1H NOESY experiments are acquired with long mixing-times (typically in the range 0.5–2 s). In this case, the intramolecular NOE connectivities have different sign relative to the diagonal signals in the 2D ^1H NOESY spectrum (positive NOEs). On the other hand, larger molecules ($\tau_c > 1.5$ ns, MW > 1500 Da) have smaller relaxation times. Thus, short mixing-times are used (<0.2 s) and NOE connectivities have the same sign of cross signals relative to the diagonal signals (negative NOEs). Consequently, during the residence time on the protein, and due to chemical exchange upon binding, small molecules adopt relaxation properties of the target molecule: they will have larger τ_c values and negative NOEs. Additionally, the connectivities between the small molecule and the protein can be observed in the 2D ^1H NOESY spectra, if the magnetization is transferred from the protein to the ligand. These signals should be in phase with the diagonal of the spectrum. All information present in the spectrum can be further used to determine the solution structure of the protein-ligand complex. WaterLOGSY or tr-NOE are ligand-based methods widely used as screening techniques for drug discovery (for review see references Dalvit 2009; Lepre et al. 2004; Pellicchia et al. 2008, 2002).

9.3.2 Mapping of Binding Interfaces

The identification of the binding surface of a protein or ligand in a complex is crucial to understand the functional role of a molecule in a given biological process. In some cases, this can be successfully achieved by measuring the perturbations on the NMR signals in the absence and in the presence of increasing amounts of the possible interacting partner. At least, the assignment of the chemical shifts of one molecule should be determined, to easily associate the chemical shift perturbation of a signal to the interacting interface of the protein or ligand. Usually, the most used experiment to monitor chemical shift perturbations is the 2D ^1H , ^{15}N HSQC. As described, the 2D ^1H , ^{15}N HSQC spectrum is the fingerprint of a protein, therefore are extremely useful to identify interacting regions between partners.

9.3.3 Determination of Affinity Binding Constants

If the k_{off} is significantly slower than the difference between the chemical shifts of free and bound protein (in Hz), in the presence of the ligand, the signal correspondent to the free form gradually disappears being replaced by the signal correspondent to the bound form. The volumes of the two signals reflect the concentrations of free and bound forms. When the exchange rate is similar to the chemical shift difference, then the signals broaden and shift at the same time. However, if the exchange is fast (k_{off} is much larger than the chemical shift difference), the signals will move smoothly from their position correspondent to the free form to those of the bound form, with the frequency of the signal at any titration point being weighted averaged by the free and bound populations. Moreover, the shape of the titration curve (chemical shift *versus* concentration of ligand) can often be fitted straightforwardly to obtain a value for the equilibrium dissociation constant. Usually, increasing amounts of unlabeled protein or ligand are titrated into the sample of the labeled protein and 2D HSQC spectra collected after each addition until the chemical shifts are no longer perturbed. In this spectrum, the chemical shift changes in ^{15}N or ^{13}C and ^1H dimensions are used to determine a weighted average chemical shift ($\Delta\delta_{comb}$) that compensates for the scaling differences in accordance to Eq. 9.17.

$$\Delta\delta_{comb} = \sqrt{(\Delta\delta_H)^2 + (w_i\Delta\delta_i)^2} \quad (9.17)$$

$\Delta\delta_i$ is the chemical shift change in ppm in ^{15}N or ^{13}C dimension and the term $w_i = |\gamma^{15}\text{N}|/|\gamma^1\text{H}|$ or $w_i = |\gamma^{13}\text{C}|/|\gamma^1\text{H}|$ compensates for the scaling differences between ^{15}N and ^{13}C , and ^1H ($\Delta\delta_H$) chemical shifts (Schumann et al. 2007). $\gamma^1\text{H}$, $\gamma^{15}\text{N}$ and $\gamma^{13}\text{C}$ are the gyromagnetic ratio of nucleus ^1H , ^{15}N and ^{13}C , respectively (see Table 9.1). The weighting factors (w_i) for ^1H , ^{15}N and ^{13}C nuclei are 1.000, 0.102 and 0.251, respectively (Schumann et al. 2007). To select the signals with the most significant variations to be used in the calculation of the K_d values, a statistical analysis should be carried out. Typically, chemical shift changes larger than three times the standard deviation (σ) are considered significant (Schumann et al. 2007). Thus, a cut-off value is determined iteratively with the standard deviation to zero value, σ_0^{corr} (Eq. 9.18).

$$\sigma_0^{corr} = \sqrt{\frac{1}{N} \sum (\Delta\delta_{comb} - 0)^2} \quad (9.18)$$

In this equation, N corresponds to the number of $\Delta\delta_{comb}$ values determined. In an initial step, a value of σ_0 is determined from all $\Delta\delta_{comb}$ values. The $\Delta\delta_{comb}$ exceeding three times the determined σ_0 are removed and a first corrected standard deviation σ_0^{corr} is obtained for the remaining $\Delta\delta_{comb}$ values. If there are $\Delta\delta_{comb}$ values larger than three times the new σ_0^{corr} value, they will be excluded and a new σ_0^{corr} will be determined. This process is repeated until no $\Delta\delta_{comb}$ value larger than three times that of the actual σ_0^{corr} remained, which is then taken as the cut-off criterion.

The binding curves for the interaction between molecules A and B can be obtained by plotting the magnitude of the chemical shift change ($\Delta\delta_{comb}$) as function of concentration of B. The data is then fitted with $\Delta\delta_{comb}$ and ligand concentration as dependent and independent variables, respectively and, K_d and $\Delta\delta_{A-B}$, in accordance with the equilibrium described above (Eq. 9.19).

$$\Delta\delta_{comb} = (\Delta\delta_{A-B}) \frac{([A] + [B] + K_d) - \sqrt{([A] + [B] + K_d)^2 - 4[A][B]}}{2[A]} \quad (9.19)$$

In this equation, $\Delta\delta_{A-B}$ is the maximum chemical shift change, when $[B] \gg K_d$ and the binding site is saturated; $[A]$ and $[B]$ are the total concentration of the species A and B, respectively.

9.3.4 Selected Biological Applications

In this section, selected examples for electron transfer proteins and complexes are presented. Electron transfer within biological respiratory chains relies on a precise network of interacting events between pairs of proteins or between proteins and small molecules, including terminal acceptors or freely-diffusing quinones within the phospholipid layer. As mentioned, these are generally short lifetime events to ensure rapid and efficient electron transfer within the transient complexes. In the case of *G. sulfurreducens* bacterium, the production and presence of *c*-type cytochromes is crucial for its metabolism. During growth of *G. sulfurreducens* cells with acetate and fumarate as electron donor and acceptor, respectively, it was identified the presence of cytochromes both in the periplasm and associated to membranes. No cytochrome was detected in the cytoplasm. The concentrations of periplasmic and membrane-associated cytochromes are in the range of 0.05–0.1 μM (Seeliger et al. 1998).

The first selected example summarizes the results obtained in a study performed to investigate the interaction between the triheme cytochrome PpcA (10 kDa) from *G. sulfurreducens* and anthraquinone-2,6-disulphonate (AQDS), that can be used either as electron donor or acceptor (Dantas et al. 2014; Lovley et al. 1996, 1999). The chemical shift perturbations of the backbone NH signals of a ^{15}N -labelled PpcA sample with increasing amounts of AQDS were monitored by a series of 2D ^1H , ^{15}N HSQC NMR spectra. The more perturbed PpcA signals are indicated in Fig. 9.18. For small cytochromes the interaction regions can be further confirmed by the chemical shift perturbation on the heme substituents signals. In this case, it is not necessary to selectively labeled the protein because the ^1H signals of the most down-field shifted heme substituents in the oxidized form are, in generally, easily monitored. This is the case of PpcA whose heme groups are covered by a small polypeptide chain with 71 residues (approximately 1 heme per 24 amino acids). Each heme has four methyl substituents and their ^1H NMR signals are found in less crowded regions of the 1D ^1H NMR spectrum (Fig. 9.6a, b). For this reason, they constitute excellent probes for

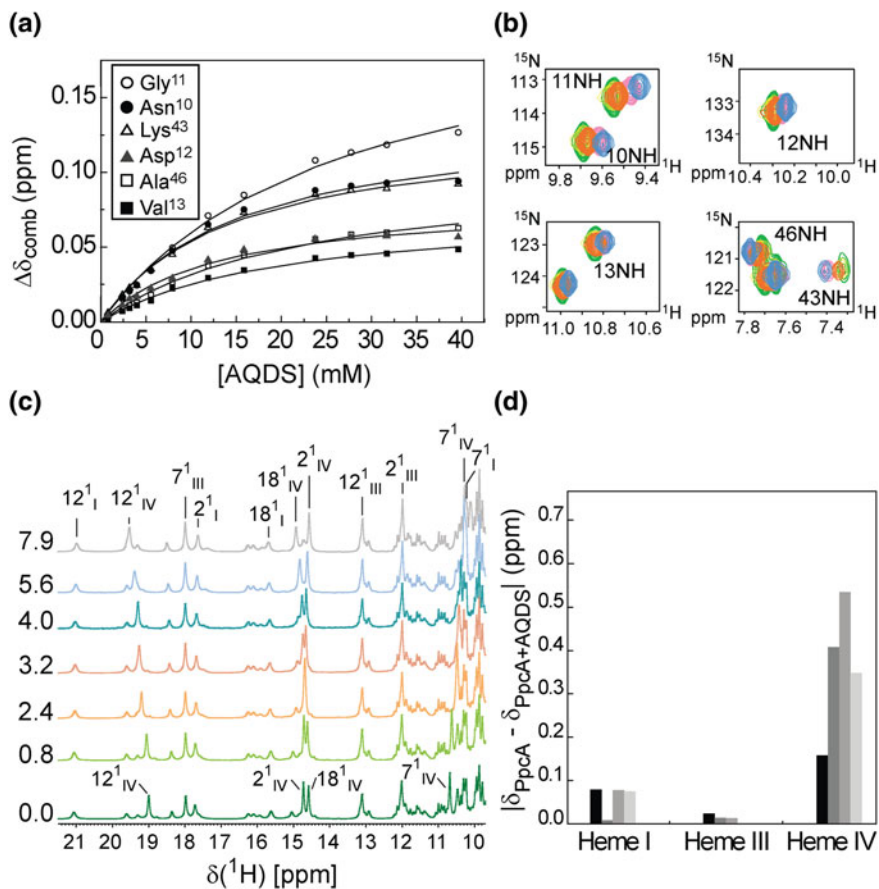


Fig. 9.18 a Binding isotherms for PpcA-AQDS interaction. Labels indicate representative NH signals that were monitored in the chemical shift perturbation experiments. Each data set was fit to a 1:1 binding model considering fast exchange conditions (solid lines). An average K_d value was calculated as 18 ± 5 mM from the titration curves. b Selected regions from overlaid 2D ^1H , ^{15}N HSQC NMR spectra. The amount of AQDS increases from green to blue contours. c Expansions of the low-field region of 1D ^1H NMR spectra obtained for PpcA in presence of increasing amounts of AQDS. The heme methyl signals are labeled, except heme methyl $18^1\text{CH}_3^{\text{III}}$ whose signal appears at a chemical shift of approximately 1 ppm. The value of AQDS concentration (mM) used in each experiment is indicated on the left of each spectrum. d Variation of the heme methyl group chemical shifts $|\delta_{\text{PpcA}} - \delta_{\text{PpcA+AQDS}}|$. The bars represent the ^1H chemical shift variations of methyl groups in the following order from left to right: 2^1CH_3 , 7^1CH_3 , 12^1CH_3 and 18^1CH_3 (see Fig. 9.6a). This figure was reproduced with permission from Elsevier, reference (Dantas et al. 2014)

monitoring the chemical shift perturbations caused by the binding of an exogenous molecule to the cytochrome. In triheme cytochromes c_7 , the hemes are numbered I, III and IV, a designation that derives from the superimposition with those of the structurally homologous tetraheme cytochromes c_3 (Turner et al. 1997).

The low-field region of the 1D ^1H NMR spectra, acquired during the titration of PpcA with increasing amounts of AQDS, is indicated in Fig. 9.18c. The analysis of the chemical shift perturbation clearly shows that signals of heme IV methyls are the most affected (Fig. 9.18d). This data further confirms the interaction of AQDS with PpcA and is in accordance with the data obtained with 2D ^1H , ^{15}N HSQC NMR spectra (Fig. 9.18a, b). The interface region of PpcA in the redox complex with AQDS is mapped in the cytochrome structure (Fig. 9.19).

In addition to the low-field region of 1D ^1H NMR spectra of cytochromes, the typical and highly dispersed region covered by the signals of the heme substituents of low spin cytochromes in a 2D ^1H , ^{13}C HSQC spectrum can also be explored to map interacting regions involving these proteins. This strategy was used to monitor the interaction between the inner membrane associated diheme cytochrome MacA and PpcA from *G. sulfurreducens* (Dantas et al. 2017a). 2D ^1H , ^{13}C HSQC NMR obtained for PpcA in presence of MacA allowed to monitor the most affected PpcA heme substituents and axial ligands (Fig. 9.20a). This information was complemented by titrations followed by 2D ^1H , ^{15}N HSQC experiments, as described in the previous example. MacA is a 35 kDa diheme cytochrome with peroxidase activity. One of the hemes, designated as low-potential heme (LP), is involved in the degradation of

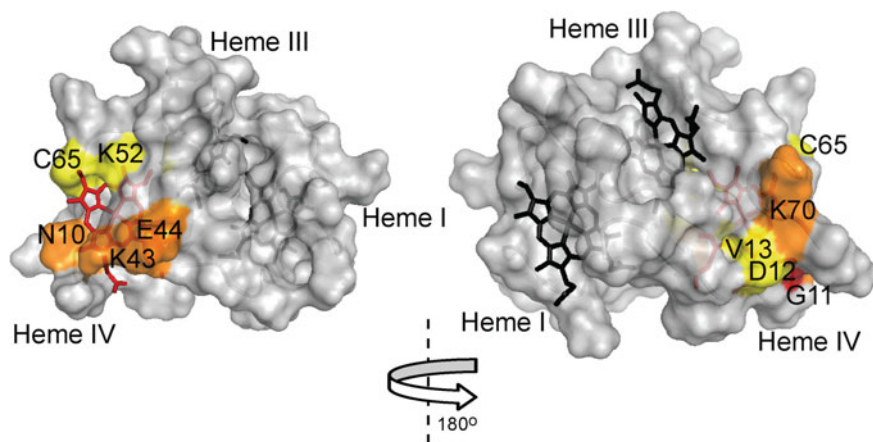


Fig. 9.19 Surface map of the most significantly perturbed residues in PpcA upon AQDS binding. The molecular surface was generated in PyMOL (DeLano 2002) by using the PpcA structure (PDB code, 2LDO (Morgado et al. 2012)). Residues for which the amide resonances experienced small ($0.04 < \Delta\delta_{comb} < 0.07$ ppm), medium ($0.07 < \Delta\delta_{comb} < 0.10$ ppm) or large ($\Delta\delta_{comb} > 0.10$ ppm) perturbations are colored yellow, orange and red, respectively. Heme IV is shown in red and hemes I and III are shown in black. The left and right panels are related by a 180° rotation. This figure was reproduced with permission from Elsevier, reference (Dantas et al. 2014)

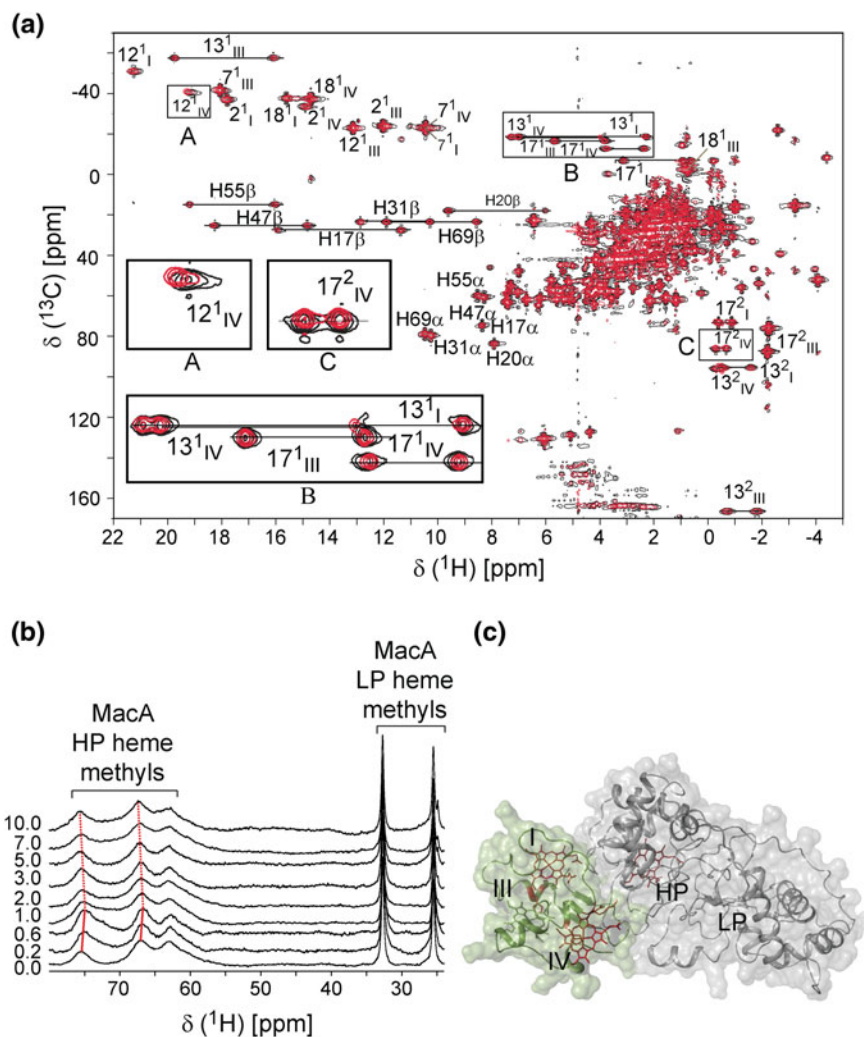


Fig. 9.20 **a** Overlay of the 2D ^1H , ^{13}C HSQC NMR spectra of cytochrome PpcA obtained in the absence and in the presence of MacA (pH 7, 298 K). The signal contours in the reference spectrum and in the presence of MacA are shown in black and red, respectively. The assignment of the heme methyl signals, heme propionates and $\text{H}\alpha/\text{H}\beta$ protons from the heme axial histidines are indicated. The signals of the protons connected to the same carbon atom (CH_2 groups) are linked by a straight line. For clarity, the regions of the spectra boxed (A–C) were expanded to show the most affected PpcA signals in the presence of MacA. **b** Chemical shift perturbation on MacA (180 μM) heme methyl signals in the presence of increasing amounts of a 6.5 mM PpcA sample. The [PpcA]/[MacA] ratios are indicated on the left side of each 1D NMR spectrum. The red lines highlight the HP heme methyl signals that showed chemical shift variation during the titration. **c** PpcA-MacA docked complex calculated using the HADDOCK2.2 webserver (van Zundert et al. 2016). The low-energy binding conformation for PpcA (green) and MacA (gray) complex is illustrated as a ribbon diagram with the heme groups shown in green and gray sticks, respectively. The hemes that experience more chemical shift variations are shown in red. This figure was reproduced with permission from John Wiley and Sons, reference (Dantas et al. 2017a)

hydrogen peroxide, whereas the other supplies electrons to the redox center and is designated high-potential heme (HP). Due to the molecular weight of MacA the same strategy could not be used to map the interacting regions of MacA in the complex. Instead, the low-field shifted MacA heme signals were used, revealing that the HP heme is involved in the interaction interface with PpcA.

NMR spectroscopy can be useful even without chemical shift assignment of the interacting species, shedding light if the interaction occurs. Indeed, if the ligand or protein does not bind, there will be no chemical shift perturbation (Dantas et al. 2013), which is a widely used strategy in drug discovery (Dalvit 2009; Lepre et al. 2004; Pellecchia et al. 2002, 2008).

9.4 Functional Characterization of Multiheme Cytochromes

The final selected NMR-based application illustrates the functional characterization of multiheme cytochromes. Contrarily to monoheme cytochromes, where only the fully reduced and oxidized states co-exist in solution, in the case of multiheme cytochromes more than two microstates can co-exist in solution. For example, in a triheme cytochrome containing a protonable center (denominated redox-Bohr center) sixteen microstates can be grouped, according to the number of oxidized hemes in four macroscopic oxidation stages linked by successive one-electron reductions (Fig. 9.21).

In order to fully characterize the redox properties of a triheme cytochrome over the full range of pH and solution potential, taking as reference the fully reduced and protonated protein it is necessary to determine ten parameters: the three energies of oxidation of the hemes (reduction potentials), the pK_a of the redox-Bohr center, three heme-heme redox interactions and, finally three redox-Bohr interactions (for a review see reference Turner et al. 1996). This full set of parameters cannot be obtained by a simple redox titration followed by visible spectroscopy, as in case of monoheme cytochromes. In fact, due to the co-existence of only the fully reduced and fully oxidized microstates, the reduction potential of a monoheme cytochrome can be obtained directly from the Nernst equation. If the same methodology is applied for multiheme cytochromes, particularly in case of identical axial ligands, only the whole-protein macroscopic redox behavior is attainable and the reduction potentials of the individual redox centers are not discriminated.

NMR spectroscopy is the best technique to discriminate the individual redox behavior of the heme groups in multiheme cytochromes. 2D ^1H EXSY NMR experiments are very useful to study chemical exchange events (Jeener et al. 1979). These experiments can be explored to study molecular motions and molecular exchanges that occur within a timescale of $1-10^{-3}$ s. The exchange between two environments (A and B) is considered slow, if the exchange rate constant is smaller than the resonance frequencies of the signal in the environments ($k \ll |\nu_A - \nu_B|$), intermediate if k

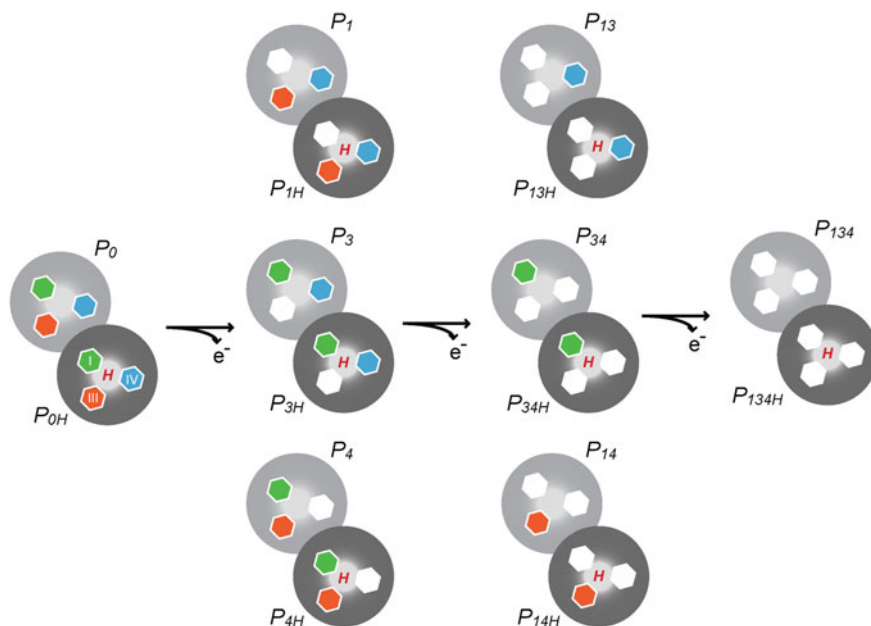


Fig. 9.21 Electronic distribution scheme for a triheme cytochrome with a proton-linked equilibrium, showing the 16 possible microstates. The light and dark gray circles correspond to the deprotonated and protonated microstates, respectively. The protonated microstates are also identified with a red “H”, which mimics the redox-Bohr center. Inner hexagons represent heme groups. The reduced hemes I, III and IV are colored green, orange and blue, respectively. The oxidized hemes are colored white. The microstates are grouped, according to the number of oxidized hemes, in four oxidation stages connected by three one-electron redox-steps. P_{0H} and P_0 represent the reduced protonated and deprotonated microstates, respectively. P_{ijkH} and P_{ijk} indicate, respectively, the protonated and deprotonated microstates, where i, j and k represent the heme(s) that are oxidized in that particular microstate. This figure was reproduced with permission from Portland Press, reference (Fernandes et al. 2018)

$\approx |v_A - v_B|$ and fast if $k \gg |v_A - v_B|$. Since chemical shift differences are magnetic field dependent, a system that is in the fast exchange regime on a low field instrument, may enter the slow exchange regime when studied at a higher field. Sample concentration, temperature or ionic strength are also variables that can be explored to modify the exchange regime (Dantas et al. 2015). In slow exchange regime, two separate signals are observed. Contrarily, in fast exchange regime, only a single chemical shift is observed at the population-weighted average position (Fig. 9.22a). In case of slow exchange, during the mixing-time, nuclei that have not undergone exchange will resonate at the same characteristic frequency during t_1 and t_2 , and thus lie along the diagonal of the 2D spectrum. On the other hand, nuclei that have undergone exchange will show off-diagonal signals (Fig. 9.22b).

The first application of 2D ^1H EXSY NMR experiments to study multiheme cytochromes was reported by Santos and co-workers (Santos et al. 1984). Since then,

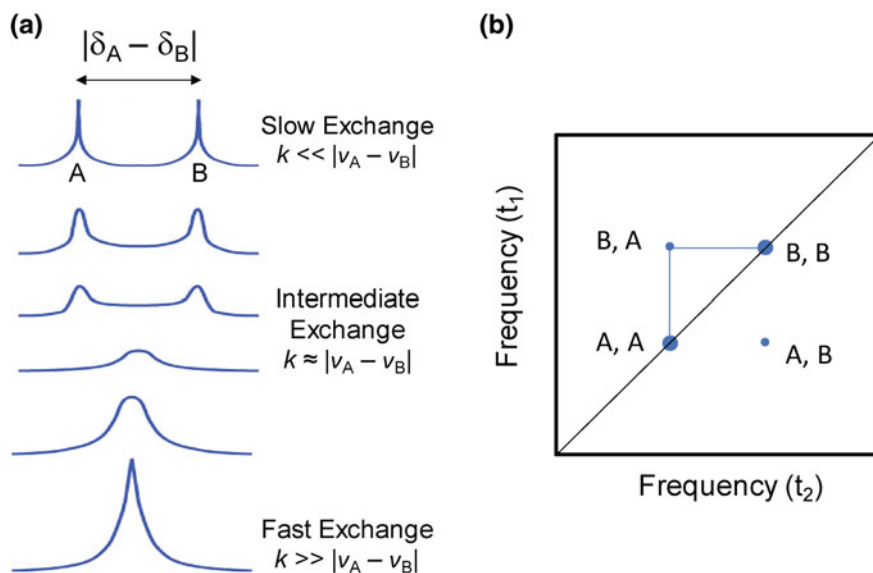


Fig. 9.22 a Variation of the NMR spectra for two molecular environments (A and B) as a function of the reaction exchange constant (slow, intermediate and fast exchange) and resonance frequencies. b Schematic 2D ^1H EXSY NMR spectrum in the slow exchange regime. The off-diagonal peaks correspond to peaks that undergo exchange during the experiment

the functional properties of several multiheme cytochromes have been addressed (for a review see references Salgueiro and Dantas 2016; Turner et al. 1996).

Considering the electronic distribution scheme for a triheme cytochrome with a proton-linked equilibrium illustrated in Fig. 9.21, to proper study the redox behavior of each heme it is necessary to monitor their oxidation profiles during the redox cycle of the protein. NMR explores the highly distinct features of the diamagnetic and paramagnetic forms. As illustrated in Fig. 9.7b, the heme methyl signals are typically shifted to low-field regions as the oxidation of the proteins progresses and, therefore, are ideal candidates to monitor the stepwise oxidation of the individual hemes throughout the different oxidation stages (see Fig. 9.21). The heme methyl chemical shift variations are proportional to the oxidized fraction of a particular heme, thus containing information about the redox properties of each heme. However, in order to probe the stepwise oxidation of the hemes, it is necessary to meet conditions of fast intramolecular electron exchange (between the different microstates within the same oxidation stage) and slow intermolecular electron exchange (between different oxidation stages) on the NMR timescale. In the case of a triheme cytochrome, 12 heme methyls can be potentially used to monitor the individual heme oxidation profiles. However, it was shown that a single heme methyl per heme is sufficient (Turner et al. 1996). However, from the available candidates, only heme methyl with negligible extrinsic contribution to their observed paramagnetic shift must be chosen to warrant that the observed variations reflect its own heme level of oxidation. The

proper selection of the heme methyls can be achieved by inspection of the structure and/or by the evaluation of the sums of their oxidation fractions at each oxidation stage. In the first case the best heme methyls are those pointing away from neighboring hemes. In the absence of the protein structure, the selection of the heme methyls can be also validated by the inspection of the sums of the oxidation fractions at each oxidation stage, which should be close to integers.

This is illustrated for the triheme cytochrome PpcA from *Geobacter metallireducens* in Fig. 9.23 and Table 9.2. In this case, the chemical shifts of the selected heme methyls ($2^1\text{CH}_3^{\text{I}}$, $12^1\text{CH}_3^{\text{III}}$ and $2^1\text{CH}_3^{\text{IV}}$) in the fully reduced and fully oxidized protein were used to monitor the heme oxidation profiles.

The analysis of Table 9.2 confirms that the extrinsic shifts for the selected heme methyls are not significant, since the sums of the oxidation fractions at each oxidation stage are close to integers and, therefore, each methyl reflects the oxidation state of its own heme. The heme that dominates the first oxidation step is heme IV (68%), followed by hemes I (63%) and III (84%) in the second and third oxidation step, respectively. However, this information only gives the sequential order of oxidation of the hemes and not their redox potentials and interactions. In order to obtain the entire set of thermodynamic parameters for a multiheme cytochrome, it is firstly necessary to obtain the pH dependence of the heme methyl chemical shifts in the different oxidation stages, as well as data from visible redox titrations (for a review see reference Turner et al. 1996).

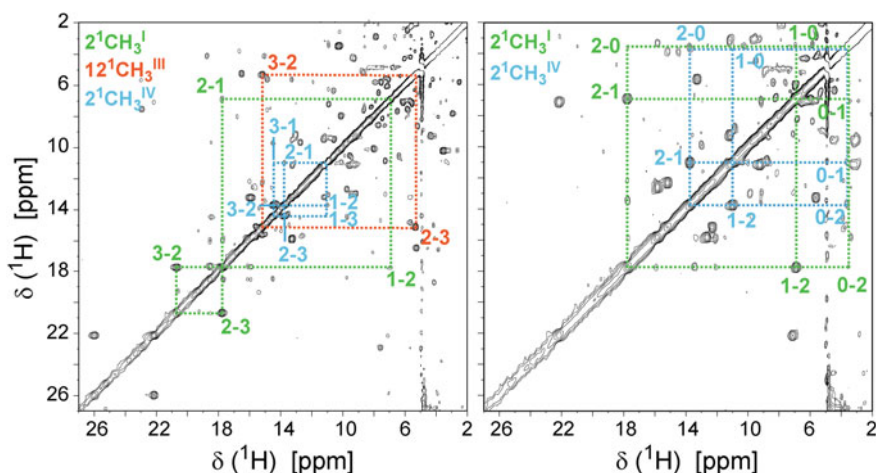


Fig. 9.23 Heme oxidation profiles for PpcA from *G. metallireducens* (pH 5.8, 288 K) monitor by 2D ^1H EXSY NMR spectra. In the expansions of the spectra the cross-peaks resulting from intermolecular electron transfer between the different oxidation stages (0–3) are indicated by dashed lines for heme methyls $2^1\text{CH}_3^{\text{I}}$ (green), $12^1\text{CH}_3^{\text{III}}$ (orange) and $2^1\text{CH}_3^{\text{IV}}$ (blue). This figure was reproduced with permission from Portland Press, reference (Fernandes et al. 2018)

Table 9.2 Redox-dependence of the heme methyl proton chemical shifts and heme oxidation fractions of PpcA from *G. metallireducens* (pH 5.8 and 288 K). The heme oxidation fractions, x_i , in each stage of oxidation, were calculated according to the equation $x_i = (\delta_i - \delta_0)/(\delta_3 - \delta_0)$, where δ_i , δ_0 , and δ_3 are the observed chemical shifts of the heme methyl in stage i , 0 (fully reduced) and 3 (fully oxidized), respectively. The heme methyl signal not detected is indicated by “n.d.”. This Table was reproduced with permission from Portland Press, reference (Fernandes et al. 2018)

Oxidation stage	Chemical shift (ppm)			x_i			Σx_i
	$2^1\text{CH}_3^{\text{I}}$	$12^1\text{CH}_3^{\text{III}}$	$2^1\text{CH}_3^{\text{IV}}$	I	III	IV	
0	3.55	3.51	3.65	0	0	0	0
1	6.93	n.d.	11.03	0.20	0.12 ^a	0.68	1.00
2	17.78	5.33	13.76	0.83	0.16	0.94	1.93
3	20.71	15.18	14.43	1	1	1	3

^aEstimated from the values obtained for the other hemes

In the case of PpcA from *G. metallireducens* the pH dependence of the selected heme methyls was measured in the pH range 6–9 together with data from visible redox titrations obtained at pH 7 and 8 (Fig. 9.24).

The thermodynamic parameters obtained from the fittings shown in Fig. 9.24 are indicated in Table 9.3.

From the thermodynamic parameters it is possible to describe the heme oxidation profiles at any pH, as well as to evaluate the relevant microstates to obtain functional mechanistic insights on the electron transfer pathways of the protein (Fig. 9.25).

The data obtained for the cytochrome showed that the solution pH modulates the affinity of the hemes for electrons (Fig. 9.25a). The analysis of Fig. 9.25b shows that the relevant microstates are quite distinct at different pH values. At values outside the physiological pH range, the dominant microstates are all protonated (pH 5) or deprotonated (pH 9). However, at pH 7, stage 0 is dominated by the protonated form P_{0H} and stage 1 is dominated by the oxidation of heme IV (P_{4H}), while keeping the redox-Bohr protonated. Stage 2 is then dominated by the oxidation of heme I and deprotonation of the acid-base center (P_{14}), which remains deprotonated in stage 3 (P_{134}). Therefore, at pH 7, the following route is defined for the electrons: $P_{0H} \rightarrow P_{4H} \rightarrow P_{14} \rightarrow P_{134}$ (see Fig. 9.25b). This clearly indicates that at physiological pH, a concerted e^-/H^+ transfer occurs between oxidation stages 1 and 2.

The high number of co-existent microstates in solution makes the characterization of multiheme cytochromes extremely complex. The described example, using the triheme cytochrome from PpcA from *G. metallireducens* as model, provided a clear illustration of powerfulness of NMR in the elucidation of functional mechanisms in this group of proteins. Besides contributing to the elucidation of respiratory pathways the mechanistic information can be further explored to design improved forms of the cytochromes for a wide range of practical applications.

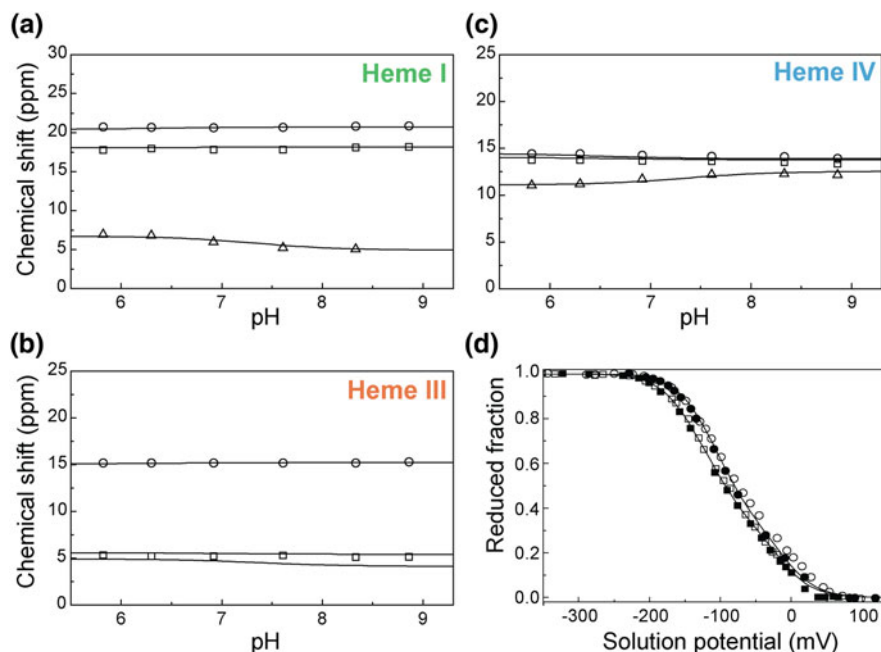


Fig. 9.24 Fitting of the thermodynamic model (see reference Turner et al. 1996) to the experimental data for PpcA from *G. metallireducens*. The solid lines are the result of the simultaneous fitting of the NMR and visible data. Panels a–c show the pH dependence of heme methyl chemical shifts at oxidation stages 1 (Δ), 2 (\square), and 3 (\circ). The chemical shift of the heme methyls in the fully reduced stage (stage 0) are not plotted since they are unaffected by the pH. Panel d represents the reduced fractions of the cytochrome determined by visible spectroscopy at pH 7 (\circ) and pH 8 (\square). The open and filled symbols represent the data points in the reductive and oxidative titrations, respectively. This figure was reproduced with permission from Portland Press, reference (Fernandes et al. 2018)

Table 9.3 Thermodynamic parameters for PpcA from *G. metallireducens* in the fully reduced and protonated form. Diagonal values (in bold) correspond to the oxidation energies of the hemes and deprotonating energy of the redox-Bohr center. Off-diagonal values are the redox (heme-heme) and redox-Bohr (heme-proton) interactions energies. All energies are reported in meV, with standard errors given in parenthesis. This Table was reproduced with permission from Portland Press, reference (Fernandes et al. 2018)

Protein	Energy (meV)			
	Heme I	Heme III	Heme IV	Redox-Bohr center
Heme I	−80 (6)	35 (4)	3 (5)	−22 (6)
Heme III		−70 (7)	37 (7)	−23 (7)
Heme IV			−113 (6)	−49 (6)
Redox-Bohr center				463 (13)

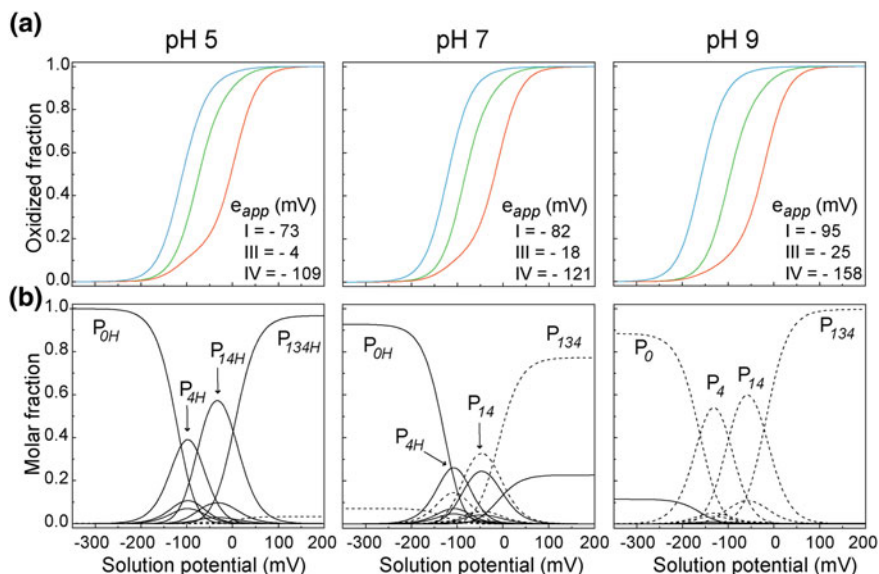


Fig. 9.25 **a** Redox dependence of the heme oxidation fractions of PpcA from *G. metallireducens* at different pH values. The midpoint reduction potentials of the hemes (e_{app}) are also indicated. **b** Redox dependence of the molar fractions of the 16 microstates of the cytochrome, at different pH values. Solid and dashed lines indicate the protonated and deprotonated microstates, respectively (see Fig. 9.21). For clarity, only the dominant microstates are labelled. The curves in panels **a** and **b** were calculated as a function of the solution reduction potential (relative to NHE) using the parameters listed in Table 9.3. This figure was reproduced with permission from Portland Press, reference (Fernandes et al. 2018)

Acknowledgements We would like to thank the current and former members of the Biochemistry and Bioenergetics of Heme Proteins Research Group. Special thanks are due to Dr. Marianne Schiffer, Dr. Raj Pokkuluri and Dr. Yuri Londer (National Argonne Laboratory—University of Chicago, USA), Prof. Marta Bruix (Instituto Química Física Rocasolano, CSIC, Madrid, Spain) and Prof. David L. Turner (Instituto Tecnologia Química e Biológica António Xavier, Oeiras, Portugal) for the very stimulating collaborations. Research in the authors' group is currently supported by Fundação para a Ciência e Tecnologia (Portugal) grants PTDC/BBB-BQB/3554/2014 (to CAS), PTDC/BIA-BQM/31981/2017 (to CAS) and SFRH/BPD/114848/2016 (to LM), and by the Applied Molecular Biosciences Unit—UCIBIO (UID/Multi/04378/2019).

References

- Ayala I, Sounier R, Use N et al (2009) An efficient protocol for the complete incorporation of methyl-protonated alanine in perdeuterated protein. *J Biomol NMR* 43:111–119
- Battiste JL, Wagner G (2000) Utilization of site-directed spin labeling and high-resolution heteronuclear nuclear magnetic resonance for global fold determination of large proteins with limited nuclear overhauser effect data. *Biochemistry* 39:5355–5365

- Bax A, Ikura M (1991) An efficient 3D NMR technique for correlating the proton and ^{15}N backbone amide resonances with the alpha-carbon of the preceding residue in uniformly $^{15}\text{N}/^{13}\text{C}$ enriched proteins. *J Biomol NMR* 1:99–104
- Bax A, Clore GM, Gronenborn AM (1990) ^1H - ^1H correlation via isotropic mixing of ^{13}C magnetization, a new three-dimensional approach for assigning ^1H and ^{13}C spectra of ^{13}C -enriched proteins. *J Magn Reson* 88:425–431
- Bertini I, Luchinat C, Parigi G (2001) Solution NMR of paramagnetic molecules: applications to metalloproteins and models. Current methods in inorganic chemistry, 1st edn. Springer, Netherlands
- Clubb RT, Thanabal V, Wagner G (1992) A constant-time three-dimensional triple-resonance pulse scheme to correlate intraresidue ^1HN , ^{15}N , and $^{13}\text{C}'$ chemical shifts in ^{15}N - ^{13}C -labelled proteins. *J Magn Reson* 97:213–217
- Crowley PB, Ubbink M (2003) Close encounters of the transient kind: protein interactions in the photosynthetic redox chain investigated by NMR spectroscopy. *Acc Chem Res* 36:723–730
- Dalvit C (2009) NMR methods in fragment screening: theory and a comparison with other biophysical techniques. *Drug Discov Today* 14:1051–1057
- Dantas JM, Tomaz DM, Morgado L et al (2013) Functional characterization of PccH, a key cytochrome for electron transfer from electrodes to the bacterium *Geobacter sulfurreducens*. *FEBS Lett* 587:2662–2668
- Dantas JM, Morgado L, Catarino T et al (2014) Evidence for interaction between the triheme cytochrome PpcA from *Geobacter sulfurreducens* and anthrahydroquinone-2,6-disulfonate, an analog of the redox active components of humic substances. *Biochim Biophys Acta* 1837:750–760
- Dantas JM, Morgado L, Aklujkar M et al (2015) Rational engineering of *Geobacter sulfurreducens* electron transfer components: a foundation for building improved *Geobacter*-based bioelectrochemical technologies. *Front Microbiol* 6:752
- Dantas JM, Brausemann A, Einsle O et al (2017a) NMR studies of the interaction between inner membrane-associated and periplasmic cytochromes from *Geobacter sulfurreducens*. *FEBS Lett* 591:1657–1666
- Dantas JM, Silva MA, Pantoja-Uceda D et al (2017b) Solution structure and dynamics of the outer membrane cytochrome OmcF from *Geobacter sulfurreducens*. *Biochim Biophys Acta* 1858:733–741
- DeLano WL (2002) The PyMOL molecular graphics system. <http://www.pymol.org>
- Dutta A, Saxena K, Schwalbe H et al (2012) Isotope labeling in mammalian cells. *Methods Mol Biol* 831:55–69
- Fernandes TM, Morgado L, Salgueiro CA (2018) Thermodynamic and functional characterization of the periplasmic triheme cytochrome PpcA from *Geobacter metallireducens*. *Biochem J* 475:2861–2875
- Fischer M, Kloiber K, Hausler J et al (2007) Synthesis of a ^{13}C -methyl-group-labeled methionine precursor as a useful tool for simplifying protein structural analysis by NMR spectroscopy. *ChemBioChem* 8:610–612
- Franke B, Opitz C, Isogai S et al (2018) Production of isotope-labeled proteins in insect cells for NMR. *J Biomol NMR* 71:173–184
- Freiburger L, Sonntag M, Hennig J et al (2015) Efficient segmental isotope labeling of multi-domain proteins using Sortase A. *J Biomol NMR* 63:1–8
- Frueh DP (2014) Practical aspects of NMR signal assignment in larger and challenging proteins. *Prog Nucl Magn Reson Spectrosc* 78:47–75
- Gardner KH, Kay LE (1998) The use of ^2H , ^{13}C , ^{15}N multidimensional NMR to study the structure and dynamics of proteins. *Annu Rev Biophys Biomol Struct* 27:357–406
- Goto NK, Gardner KH, Mueller GA et al (1999) A robust and cost-effective method for the production of Val, Leu, Ile (δ 1) methyl-protonated ^{15}N -, ^{13}C -, ^2H -labeled proteins. *J Biomol NMR* 13:369–374
- Grzesiek S, Bax A (1992a) Correlating backbone amide and side chain resonances in larger proteins by multiple relayed triple resonance NMR. *J Am Chem Soc* 114:6291–6293

- Grzesiek S, Bax A (1992b) An efficient experiment for sequential backbone assignment of medium-sized isotopically enriched proteins. *J Magn Reson* 99:201–207
- Grzesiek S, Bax A (1992c) Improved 3D triple-resonance NMR techniques applied to a 31 kDa protein. *J Magn Reson* 96:432–440
- Grzesiek S, Bax A (1993) Amino acid type determination in the sequential assignment procedure of uniformly $^{13}\text{C}/^{15}\text{N}$ -enriched proteins. *J Biomol NMR* 3:185–204
- Hafsa NE, Arndt D, Wishart DS (2015) CSI 3.0: a web server for identifying secondary and super-secondary structure in proteins using NMR chemical shifts. *Nucl Acids Res* 43:W370–377
- Hammes GG (2005) Spectroscopy for the biological sciences. Wiley, Hoboken, New Jersey
- Herrmann T, Guntert P, Wuthrich K (2002) Protein NMR structure determination with automated NOE assignment using the new software CANDID and the torsion angle dynamics algorithm DYANA. *J Mol Biol* 319:209–227
- Ippel JH, Olofsson A, Schleucher J et al (2002) Probing solvent accessibility of amyloid fibrils by solution NMR spectroscopy. *Proc Natl Acad Sci USA* 99:8648–8653
- Jeener J, Meier BH, Bachmann P et al (1979) Investigation of exchange processes by two-dimensional NMR spectroscopy. *J Chem Phys* 71:4546–4553
- Kainosho M, Guntert P (2009) SAIL—stereo-array isotope labeling. *Q Rev Biophys* 42:247–300
- Kainosho M, Torizawa T, Iwashita Y et al (2006) Optimal isotope labelling for NMR protein structure determinations. *Nature* 440:52–57
- Kay LE, Ikura M, Tschudin R et al (1990) Three-dimensional triple-resonance NMR spectroscopy of isotopically enriched proteins. *J Magn Reson* 89:496–514
- Keller RM, Wuthrich K (1978) Assignment of the heme *c* resonances in the 360 MHz ^1H NMR spectra of cytochrome *c*. *Biochim Biophys Acta* 533:195–208
- Klopp J, Winterhalter A, Gebleux R et al (2018) Cost-effective large-scale expression of proteins for NMR studies. *J Biomol NMR* 71:247–262
- Krishnarajuna B, Jaipuria G, Thakur A et al (2011) Amino acid selective unlabeled for sequence specific resonance assignments in proteins. *J Biomol NMR* 49:39–51
- Laskowski RA, Rullmann JA, MacArthur MW et al (1996) AQUA and PROCHECK-NMR: programs for checking the quality of protein structures solved by NMR. *J Biomol NMR* 8:477–486
- La D, Kong M, Hoffman W et al (2013) Predicting permanent and transient protein-protein interfaces. *Proteins: Structure. Funct Bioinform* 81:805–818
- Lepre CA, Moore JM, Peng JW (2004) Theory and applications of NMR-based screening in pharmaceutical research. *Chem Rev* 104:3641–3676
- Lin MT, Sperling LJ, Schmidt HLF et al (2011) A rapid and robust method for selective isotope labeling of proteins. *Methods* 55:370–378
- Liu Z, Gong Z, Dong X et al (2016) Transient protein-protein interactions visualized by solution NMR. *Biochim Biophys Acta* 1864:115–122
- Lovley DR, Coates JD, Blunt-Harris EL et al (1996) Humic substances as electron acceptors for microbial respiration. *Nature* 382:445–448
- Lovley DR, Fraga JL, Coates JD et al (1999) Humics as an electron donor for anaerobic respiration. *Environ Microbiol* 1:89–98
- Mao H, Hart SA, Schink A et al (2004) Sortase-mediated protein ligation: a new method for protein engineering. *J Am Chem Soc* 126:2670–2671
- Marion D, Driscoll PC, Kay LE et al (1989) Overcoming the overlap problem in the assignment of ^1H NMR spectra of larger proteins by use of three-dimensional heteronuclear ^1H - ^{15}N Hartmann-Hahn-multiple quantum coherence and nuclear Overhauser-multiple quantum coherence spectroscopy: application to interleukin 1 beta. *Biochemistry* 28:6150–6156
- McIntosh LP, Dahlquist FW (1990) Biosynthetic incorporation of ^{15}N and ^{13}C for assignment and interpretation of nuclear magnetic resonance spectra of proteins. *Q Rev Biophys* 23:1–38
- Morgado L, Fernandes AP, Londer YY et al (2010) One simple step in the identification of the cofactors signals, one giant leap for the solution structure determination of multiheme proteins. *Biochem Biophys Res Commun* 393:466–470

- Morgado L, Paixão VB, Schiffer M et al (2012) Revealing the structural origin of the redox-Bohr effect: the first solution structure of a cytochrome from *Geobacter sulfurreducens*. *Biochem J* 441:179–187
- Moss GP (1988) Nomenclature of tetrapyrroles. Recommendations 1986 IUPAC-IUB Joint Commission on Biochemical Nomenclature (JCBN). *Eur J Biochem* 178:277–328
- Muir TW, Sondhi D, Cole PA (1998) Expressed protein ligation: a general method for protein engineering. *Proc Natl Acad Sci* 95:6705–6710
- Mund M, Overbeck JH, Ullmann J et al (2013) LEGO-NMR spectroscopy: a method to visualize individual subunits in large heteromeric complexes. *Angew Chem Int Ed Engl* 52:11401–11405
- Muralidharan V, Muir TW (2006) Protein ligation: an enabling technology for the biophysical analysis of proteins. *Nat Methods* 3:429–438
- Ohki SY, Kainosho M (2008) Stable isotope labeling methods for protein NMR spectroscopy. *Prog Nucl Magn Reson Spectrosc* 53:208–226
- Pellecchia M, Sem DS, Wuthrich K (2002) NMR in drug discovery. *Nat Rev Drug Discov* 1:211–219
- Pellecchia M, Bertini I, Cowburn D et al (2008) Perspectives on NMR in drug discovery: a technique comes of age. *Nat Rev Drug Discov* 7:738–745
- Perkins JR, Diboun I, Dessailly BH et al (2010) Transient protein-protein interactions: structural, functional, and network properties. *Structure* 18:1233–1243
- Pervushin K, Riek R, Wider G et al (1997) Attenuated T_2 relaxation by mutual cancellation of dipole-dipole coupling and chemical shift anisotropy indicates an avenue to NMR structures of very large biological macromolecules in solution. *Proc Natl Acad Sci USA* 94:12366–12371
- Rosenblum G, Cooperman BS (2014) Engine out of the chassis: cell-free protein synthesis and its uses. *FEBS Lett* 588:261–268
- Rule GS, Hitchens TK (2006) Fundamentals of protein NMR spectroscopy. In: Kaptein R (ed) Focus on structural biology, 1st edn. Springer, Netherlands
- Ruschak AM, Velyvis A, Kay LE (2010) A simple strategy for ^{13}C , ^1H labeling at the Ile- $\gamma 2$ methyl position in highly deuterated proteins. *J Biomol NMR* 48:129–135
- Salgueiro CA, Dantas JM (2016) Multiheme cytochromes. In: Gomes CM (ed) Protein folding and structure, 1st edn. Springer, Berlin, Heidelberg
- Santos H, Turner DL, Xavier AV et al (1984) Two-dimensional NMR studies of electron transfer in cytochrome c_3 . *J Magn Reson* 59:177–180
- Sattler M, Fesik SW (1996) Use of deuterium labeling in NMR: overcoming a sizeable problem. *Structure* 4:1245–1249
- Sattler M, Schleucher J, Griesinger C (1999) Heteronuclear multidimensional NMR experiments for the structure determination of proteins in solution employing pulsed field gradients. *Prog NMR Spectrosc* 34:93–158
- Schumann FH, Riepl H, Maurer T et al (2007) Combined chemical shift changes and amino acid specific chemical shift mapping of protein-protein interactions. *J Biomol NMR* 39:275–289
- Schwieters CD, Kuszewski JJ, Tjandra N et al (2003) The Xplor-NIH NMR molecular structure determination package. *J Magn Reson* 160:65–73
- Seeliger S, Cord-Ruwisch R, Schink B (1998) A periplasmic and extracellular c -type cytochrome of *Geobacter sulfurreducens* acts as a ferric iron reductase and as an electron carrier to other acceptors or to partner bacteria. *J Bacteriol* 180:3686–3691
- Shen Y, Bax A (2013) Protein backbone and sidechain torsion angles predicted from NMR chemical shifts using artificial neural networks. *J Biomol NMR* 56:227–241
- Teng Q (2005) Structural biology: practical NMR applications. Springer, USA
- Tolman JR, Flanagan JM, Kennedy MA et al (1995) Nuclear magnetic dipole interactions in field-oriented proteins: information for structure determination in solution. *Proc Natl Acad Sci U S A* 92:9279–9283
- Tugarinov V, Kay LE (2004) An isotope labeling strategy for methyl TROSY spectroscopy. *J Biomol NMR* 28:165–172
- Tugarinov V, Kanelis V, Kay LE (2006) Isotope labeling strategies for the study of high-molecular-weight proteins by solution NMR spectroscopy. *Nat Protoc* 1:749–754

- Turner DL, Salgueiro CA, LeGall J et al (1992) Structural studies of *Desulfovibrio vulgaris* ferrocytochrome c_3 by two-dimensional NMR. *Eur J Biochem* 210:931–936
- Turner DL, Salgueiro CA, Catarino T et al (1996) NMR studies of cooperativity in the tetrahaem cytochrome c_3 from *Desulfovibrio vulgaris*. *Eur J Biochem* 241:723–731
- Turner DL, Costa HS, Coutinho IB et al (1997) Assignment of the ligand geometry and redox potentials of the trihaem ferricytochrome c_3 from *Desulfuromonas acetoxidans*. *Eur J Biochem* 243:474–481
- Turner DL, Brennan L, Chamberlin SG et al (1998) Determination of solution structures of paramagnetic proteins by NMR. *Eur Biophys J* 27:367–375
- van Zundert GC, Rodrigues JP, Trellet M et al (2016) The HADDOCK2.2 Web server: user-friendly integrative modeling of biomolecular complexes. *J Mol Biol* 428:720–725
- Velyvis A, Ruschak AM, Kay LE (2012) An economical method for production of ^2H , $^{13}\text{CH}_3$ -threonine for solution NMR studies of large protein complexes: application to the 670 kDa proteasome. *PLoS ONE* 7:e43725
- Wishart DS, Bigam CG, Yao J et al (1995) ^1H , ^{13}C and ^{15}N chemical shift referencing in biomolecular NMR. *J Biomol NMR* 6:135–140
- Wittekind M, Mueller L (1993) HNCACB, a High-sensitivity 3D NMR experiment to correlate amide-proton and nitrogen resonances with the alpha- and beta-carbon resonances in proteins. *J Magn Reson B* 101:201–205
- Yamazaki T, Lee W, Arrowsmith CH et al (1994) A suite of triple resonance NMR experiments for the backbone assignment of ^{15}N , ^{13}C , ^2H labeled proteins with high sensitivity. *J Am Chem Soc* 116:11655–11666
- Yang D, Kay LE (1999) TROSY triple-resonance four-dimensional NMR spectroscopy of a 46 ns tumbling protein. *J Am Chem Soc* 121:2571–2575
- Zhang H, van Ingen H (2016) Isotope-labeling strategies for solution NMR studies of macromolecular assemblies. *Curr Opin Struct Biol* 38:75–82

Chapter 10

Near Edge X-ray Absorption Fine Structure (NEXAFS) Spectroscopy of Molecules of Biological Interest: From Chemically Pure to Complex Samples



G. Gerson B. de Souza and Joselaine C. Gonzalez

10.1 Introduction

In Near Edge X-ray Absorption Fine Structure (NEXAFS) spectroscopy, molecular inner-shell (core) electrons are excited to partially filled and empty states. Excitation of core electrons leads to a complex manifold of decay processes involving both radiative (fluorescence emission) and non-radiative (Auger electron emission, ionic dissociation) processes (Nenner and Morin 1996). Due to the localized nature of core orbitals, features observed in NEXAFS have a definite atomic or element-specific character, in similarity with the X-ray photoelectron spectroscopy (XPS) technique. An important difference between the two techniques consists nevertheless in the fact that while in XPS the collected data (photoelectrons) are related to the ionization of core electrons, in NEXAFS the observed bands are related to the excitation of inner-shell electrons to unfulfilled electronic states, energetically located below and above the ionization edge. While in XPS the principal information consists of the binding energies (ionization potentials, IPs) of the core electrons, in NEXAFS information is obtained concerning the intensity and energy of electronic excitations to excited molecular states and the corresponding de-excitation processes. X-ray absorption spectra provides information related both to the ground electronic state and to the nature of unoccupied states. As such, NEXAFS probes the chemical environment around a given atom in a molecule, providing information on the chemical binding and valence (oxidation) state of the atom. From the experimental point of view, a most significant difference consists in the fact that while XPS measurements are

G. G. B. de Souza (✉) · J. C. Gonzalez

Department of Physical-Chemistry, Institute of Chemistry, Universidade Federal do Rio de Janeiro, Avenida Athos da Silveira Ramos, 149 Bloco A, 4° andar, Rio de Janeiro, RJ 21941-909, Brazil
e-mail: gerson@iq.ufrj.br

J. C. Gonzalez
e-mail: jcaceres@fing.edu.uy

often based on the use of a fixed-energy photon beam, in NEXAFS the capacity to continuously tune the incident photon energy is essential. The use of a synchrotron radiation source is consequently essential to the realization of NEXAFS experiments.

The theoretical and experimental fundamentals of NEXAFS have been thoroughly discussed on the “classical” book by Stöhr (1992). The fundamentals of the technique have also been reviewed by several authors. See for instance, Gaur et al. (2013), Sedlmair (2011), Rehr and Albers (2000) and references therein. Excellent reviews on the application of NEXAFS to more specific subjects such as polymers (Ade and Urquhart 2002; Urquhart et al. 1999), minerals (Henderson et al. 2014), soils and plant sciences (Leinweber et al. 2014; Lombi and Susini 2009; Solomon et al. 2009) are available. Recent developments in X-ray absorption, based on the use of third generation synchrotron radiation sources and X-ray lasers are discussed in Evans (2006) and in Pascarelli and Mathona (2010). A special issue of *Physical Chemistry Chemical Physics* has been dedicated to the theme, “Recent developments in X-ray absorption spectroscopy” (Themed collection: Recent developments in X-ray absorption spectroscopy 2010). It should also be pointed out that although X-ray absorption spectroscopy (XAS) has become a very powerful technique for the study of inner-shell electron excitation processes in gas-phase and solid state materials, mainly due to the spectacular progress observed in the development of intense and tunable synchrotron radiation sources in the last 20 years, the present understanding of the processes associated with the excitation of core shell electrons owes much to a different technique, namely, electron energy-loss spectroscopy. As reviewed by Hitchcock (2000) a long list of low-Z molecules has been studied using inner-shell electron energy-loss spectroscopy, ISEELS, prior to the availability of synchrotron radiation beamlines dedicated to NEXAFS measurements. For instance, and as also pointed out in Stöhr’s book, the first observation of the vibrational fine structure in the K-shell excitation of molecules was made through ISEELS (Tronc et al. 1976; Hitchcock and Brion 1977). The fundamentals of the inelastic electron scattering technique, particularly in the high incident energy regime have been described in an excellent review by Inokuti (1971). Despite attractive characteristics of electron energy-loss spectroscopy (possibility of exciting both dipole allowed and dipole forbidden transitions, low cost machine when compared to the cost of setting up a first rate beamline, let alone building a synchrotron radiation light source), it should be strongly emphasized that the field of inner shell electron excitation and related techniques nowadays is almost entirely based on the use of synchrotron radiation.

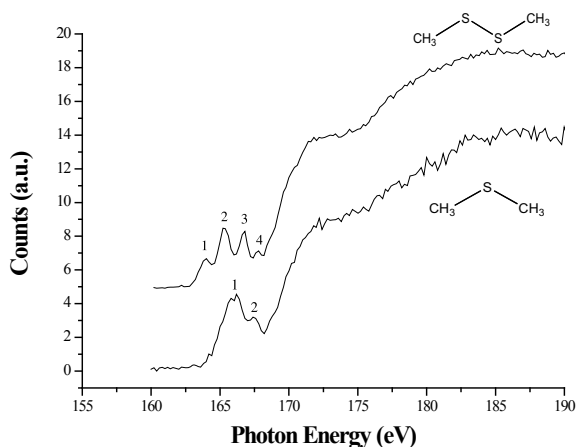
The inner-shell photoabsorption spectra of molecules in the soft X-ray energy range show pronounced resonances which correspond to electronic transition of K or L-shell electrons to unfulfilled states with excitation energies near (below and above) the corresponding ionization potential, IP. Below the IP, the observed sharp resonances are usually associated with transitions to antibonding molecular states. In gas-phase, peaks associated with transitions to Rydberg states are also observed, converging to the IP, albeit with lower intensities. Above the IP, features associated with multi-electron excitations are observed, along with very broad structures, usually assigned as shape resonances or as the result of multiple scattering processes. The nature and stability of the inner shell resonances has been the focus of many

publications, and excellent discussions on this subject can be found for instance in the book by Stöhr (1992) and in reviews by Nenner and Morin (1996) and Miron and Morin (2011).

10.2 Gas Phase Inner Shell Excitation of Molecules of Biological Interest

The inner shell excitation of molecules usually gives rise to unstable uncharged and charged species. These highly excited molecules decay mainly by photon emission (X-ray fluorescence) and electronic emission (Auger and Resonant Auger processes). While X-ray fluorescence predominates in molecules containing high Z elements (roughly, $Z = 20$ and higher). In molecules composed mainly by low Z -elements (C, N, O), electronic decay predominates, with the formation of singly (or multiply) charged species. NEXAFS spectra of these molecules may therefore be obtained from the measurement of the ionic yield as a function of the photon energy. We illustrate this by examining the S 2p and S 1s NEXAFS spectra obtained for a sulfur-containing molecule, dimethyl disulfide, ($\text{CH}_3\text{-S-S-CH}_3$), DMDS. The DMDS molecule can be seen as an ideal prototype molecule towards the study of the disulfide (-S-S-) chemical bond. Disulfide chemical bonds play an important role in the stability and functioning of several peptides and proteins, such as glutathione and insulin. The S 2p spectrum of DMDS, obtained by Bernini et al. (2012) is compared to the S 2p spectrum of another volatile sulfur-containing molecule, dimethyl sulfide, ($\text{CH}_3\text{-S-CH}_3$), DMS, in Fig. 10.1. Both spectra have been obtained in the Total Ion Yield (TIY) mode, using a time-of-flight mass spectrometer. The DMS molecule, in which the sulfur atom is bonded to two carbon atoms, plays a very important role in the sulfur ocean-atmosphere cycle.

Fig. 10.1 NEXAFS spectra for the DMS (below) and DMDS (above) molecules measured around the S 2p edge. Reproduced from Bernini et al. (2012), with the permission of AIP Publishing



In the DMDS NEXAFS spectrum, features associated with the spin-orbit components of the $S\ 2p \rightarrow \sigma^*$ (S–S) and $S\ 2p \rightarrow \sigma^*$ (C–S) electronic transitions (resonances) are observed. In order to illustrate the ionic dissociation decay mechanism of the core-excited molecule, on and off the resonant features, the time-of-flight mass spectra of DMDS has been measured at selected photon energies below the resonances (160.0 eV), on resonances (163.8, 166.5 and 167.6 eV) and above the S 2p ionization edge (180.0 eV). The results are presented in Fig. 10.2.

At 160.0 eV the observed ions are due to “direct” ionization, that is to single and multiple ionization of valence-shell electrons. On the resonances (163.8, 166.5, and 167.6 eV), resonant Auger processes are expected to play a role in the formation of the ionic species, while above the ionization edge (180.0 eV) the “normal” Auger process will efficiently give rise to doubly- and triply-charged ionic species. In resonant Auger processes, the core electron is excited to an unoccupied state, and the subsequent electronic decay gives rise to a singly charged molecular cation. The excited electron may participate or not on the electronic decay, which will be accordingly classified either as “participator” or “spectator” Auger decay. Resonant Auger processes have been thoroughly reviewed by Piancastelli (2000). In all DMDS mass spectra, a large contribution is observed from the CHS^+ cation ($m/z = 45$), which can be associated with the breakage of the disulfide chemical bond. On the other hand, ionic fragments in which the disulfide bond remains intact, such as S_2^+ ($m/z = 64$), CH_3S_2^+ ($m/z = 79$) and the molecular ion ($m/z = 94$) also contribute to the mass spectra. The “coexistence” of these ions in the mass spectra points out to a complex decaying mechanism following excitation and ionization of the S 2p electron. At 180.0 eV, above the ionization edge, it is observed that the peaks in the mass spectrum become significantly broader. This is particularly noticeable in the peak related to the CHS^+

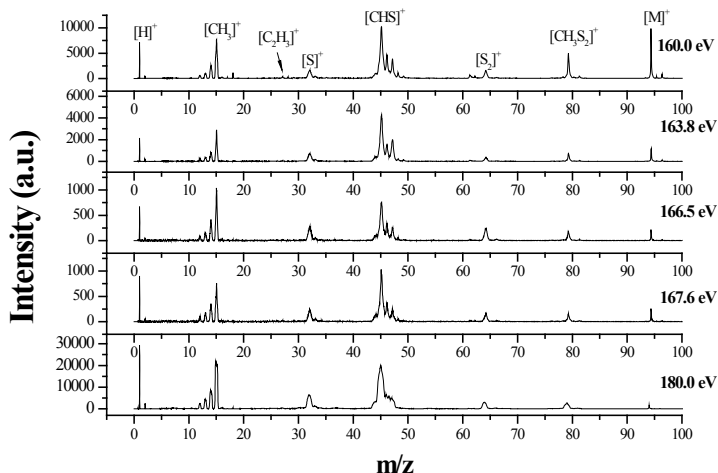


Fig. 10.2 Mass spectra of DMDS measured around the S 2p edge. Reproduced from Bernini et al. (2012), with the permission of AIP Publishing

ion. In TOF-MS, this broad character is usually interpreted as a manifestation that the ion has been formed with a high kinetic energy, such as it would be expected in a Coulomb “explosion”. In other words, following Auger electron emission, the unstable doubly- (or triply-) charged ions “explode” due to charge repulsion.

The branching ratios (BR) have been determined for the ions, using Eq. 10.1:

$$BR(\%) = \frac{A_{peak}}{\sum_{i=1}^N A_i} \times 100 \quad (10.1)$$

where A_{peak} corresponds to the area of a given peak and the denominator corresponds to the sum of the areas of all peaks observed in the spectra. The photon energy dependence for the branching ratios for some of the DMDS fragments are presented in Fig. 10.3.

It is observed from Fig. 10.3 that, around the S 2p edge, disulfide bond-breaking events giving rise to the formation of the CHS^+ ionic fragment are maximized at the first resonance (feature 1 in Fig. 10.1). The intensities of fragments associated with the preservation of the disulfide bond (S_2^+ , CH_3S_2^+ and M^+), on the other hand, go through a minimum at the first resonance and then through a less accentuated maximum at a different resonant feature. This behavior corroborates the antibonding character, σ^* (S–S), of the first resonance.

We next compare the excitation and de-excitation processes observed in the DMDS molecule excited around the S 2p edge with processes induced by higher energy photons. The NEXAFS spectrum of DMDS has been measured around the S 1s edge (2460–2490 eV) (Varas et al. 2017) and the result is shown in Fig. 10.4.

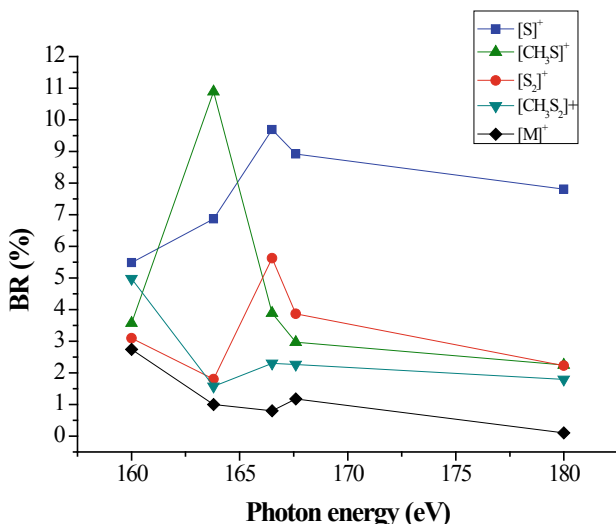


Fig. 10.3 Photon energy dependence for the branching ratios (BR) of selected DMDS fragments around the S 2p edge. Reproduced from Bernini et al. (2012), with the permission of AIP Publishing

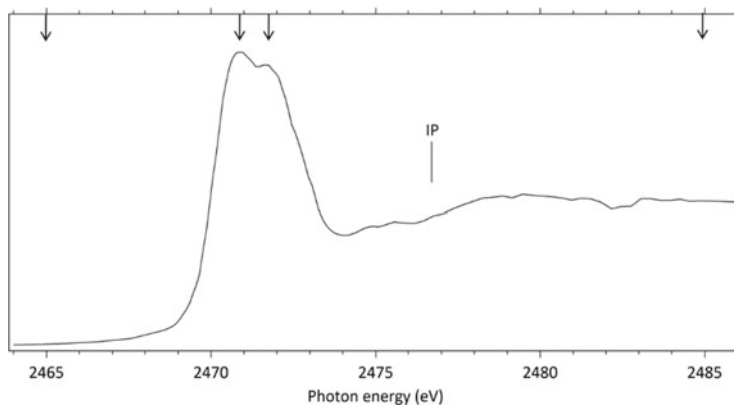


Fig. 10.4 NEXAFS spectrum of the DMDS molecule measured around the S 1s edge. The ionization potential (IP) position is included. The arrows indicate the energy positions in which TOF-MS spectra were recorded. Reproduced from Varas et al. (2017)

The first structure in the spectrum is composed by two main σ resonances, while a broad shape resonance is observed around 2480 eV. Theoretical results confirm that the first resonance (2470.9 eV) can be attributed to a transition to a σ^* (S–S) orbital while the second resonance (2471.8 eV) corresponds to a transition to a σ^* (S–CH₃) orbital. The ionic dissociation pathways of DMDS following K-edge excitation have also been studied using time-of-flight mass spectrometry. Mass spectra have been obtained at 2465.0 eV (below resonances), 2470.9 eV (first resonance), 2471.8 eV (second resonance) and at 2485.0 eV (above the ionization edge) and the results are shown in Fig. 10.5.

As expected, around the S 1s edge the photon-induced fragmentation of the molecule increases significantly, with multiple Auger and cascade Auger processes now playing important roles in the decaying mechanisms of the highly excited species. The overall fragmentation pattern around the S 1s edge is similar, both below (2465.0 eV), on the first and second resonances (2470.9 and 2471.8 eV) and above the ionization edge (2485.0 eV). Some aspects are worth emphasizing. Compared to the excitation around the S 2p edge, the much higher degree of fragmentation of the molecule is evidenced by the fact that the most intense fragment in all high photon energy mass spectra is S⁺ ($m/z = 32$). This suggests that complete atomization of the molecule may also occur. Previously unobserved doubly and triply charged species such as S²⁺ ($m/z = 16$) and S³⁺ ($m/z = 10.7$) as well as rearrangement ions such as C₂H₄⁺ ($m/z = 28$) and C₂H₆⁺ ($m/z = 30$) are clearly observed. Taking into consideration that S 1s excited states have lifetimes of the order of a femtosecond (Marchenko et al. 2015) these ions may be the result of very fast (femtosecond or attosecond regime) chemical reactions. Finally, observation of the molecular ion even at photon energies as high as 2465 eV points out to the high stability of the DMDS molecule.

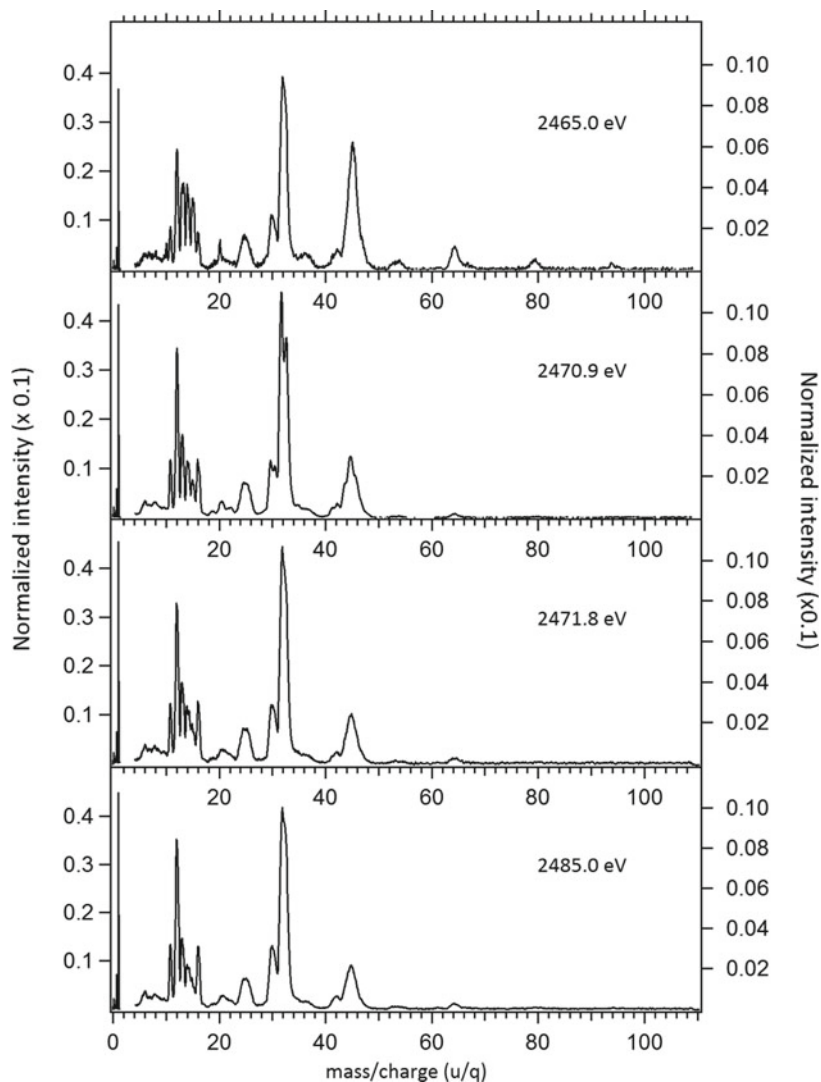


Fig. 10.5 Mass spectra of the DMDS molecule obtained below resonances (2465.0 eV), on the first resonance (2470.9 eV), second resonance (2471.8 eV) and above the S 1s ionization edge (2485.0 eV). The left axis applies only to the intensity of the H^+ ion, while the right axis applies to the intensities of the remaining fragments. Reproduced from Varas et al. (2017)

The NEXAFS S 1s investigation of disulfide solutions, including DMDS, has been recently discussed by Pickering and collaborators (2016).

10.3 Inner Shell Excitation of Amino Acids

Amino acids are considered as the building blocks of proteins and as such essential components of living organisms. They are also believed to play a role in the origin and development of life (Brack et al. 1998) and have been found in the interstellar medium and meteoritic materials (Engel and Nagy 1982; Snyder 1997). In solid state as well as in unbuffered aqueous solution, amino acids are found as a zwitterion ($\text{H}_3\text{N}^+\text{-CHR-COO}^-$, where R is the amino acid residue). In solution there is an equilibrium between the zwitterionic and ground uncharged state forms. This state of equilibrium is dependent on the solution pH.

A comprehensive study of the C 1s NEXAFS spectra of 20 amino acids commonly occurring in nature has been published in 2002 by Kaznacheyev et al. (2002). They employed dried films obtained from a solution using trifluoroacetic acid as solvent in the NEXAFS measurements. Features associated with the carboxylic acid group and the amino group attached to a saturated carbon atom were identified in each spectrum. Although each amino acid presents a unique spectrum, the authors concluded that only five of them have sufficiently distinct features which can be used for chemical identification: arginine and the four aromatic amino acids (phenyl-alanine, tyrosine, tryptophan and histidine). In 2005, the C 1s, N 1s and O 1s NEXAFS spectra of the 20 essential amino acids plus cystine and hydroxyproline were determined in zwitterionic form from powder-free films by Zubavichus and collaborators (2005). The majority of the C 1s spectra showed three dominant features: a narrow resonance at around 288.6 eV (C 1s $\rightarrow \pi^*(\text{COO})$ transition) and broader σ^* resonances at ca. 293.0 and 300.0 eV. The N 1s spectra are dominated by relatively broad σ^* (N-C) peak at 406.2–406.6 eV. The O 1s spectra of the amino acids, quite similar to each other, exhibited a dominant π^* peak associated with the carboxylate group at 532.3–532.5 eV and the respective σ^* component at ca. 543.5 eV. As part of a systematic study of the NEXAFS spectra of soil and environment samples, the N 1s spectra of thirteen amino acids (arginine, aspartic acid, lysine, methionine, alanine, glutamic acid, threonine, valine, leucine, glutamine, serine, histidine, and proline) were determined in total fluorescence mode by Leinweber and collaborators (2014). The majority of the amino acid spectra were dominated by a relatively broad σ^* resonance peaked at around 406 eV. Except for aspartic acid, methionine, proline and histidine, all spectra showed a more or less pronounced peak at around 399 eV, followed by peaks or shoulders at around 401 eV.

Observation of the inner shell resonances of amino acids in gas phase and consequently free of solvent effects can be exemplified by the N 1s and O 1s NEXAFS spectra of L-alanine (Marinho et al. 2006). The spectra are presented in Figs. 10.6 and 10.7, respectively. The N 1s spectrum of the N_2 molecule has been also included

Fig. 10.6 NEXAFS spectrum of the amino acid L-Alanine measured around the N 1s edge. The N 1s spectrum of N₂ (in red) has been included for comparison

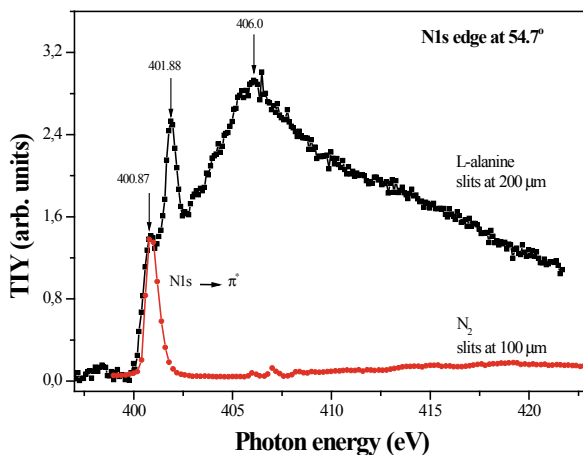
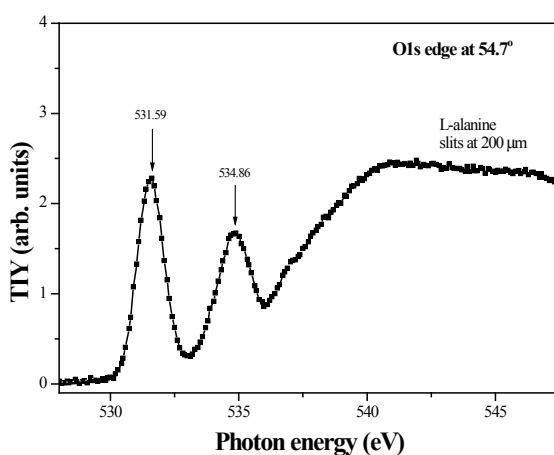


Fig. 10.7 NEXAFS spectrum of the amino acid L-Alanine measured around the O 1s edge



in Fig. 10.6 and helps to emphasize the sensitivity of the technique to the chemical ambience.

In the N 1s spectrum, the sharp peaks observed at 400.8 and 401.8 eV are attributed to Rydberg transitions, while the broad feature centered at 406.0 eV has been assigned to a N 1s \rightarrow σ^* (C–N) transition. In the O 1s spectrum, Fig. 10.7, the first (531.59 eV) and second (534.86 eV) resonances correspond, respectively, to transitions originating from the carbonyl (C=O) and from the hydroxyl (OH) oxygen atoms.

In order to unveil the ionic decay mechanisms following core electron excitation in this amino acid, mass spectra of L-alanine have been recorded at different photon energies around the N 1s and O 1s edge and the results are shown in Fig. 10.8.

It is observed that the fragmentation pattern of L-alanine does not change significantly with photon energy in the N 1s and O 1s energy ranges. Basically, four different fragment groups can be identified from the mass spectra. The first group

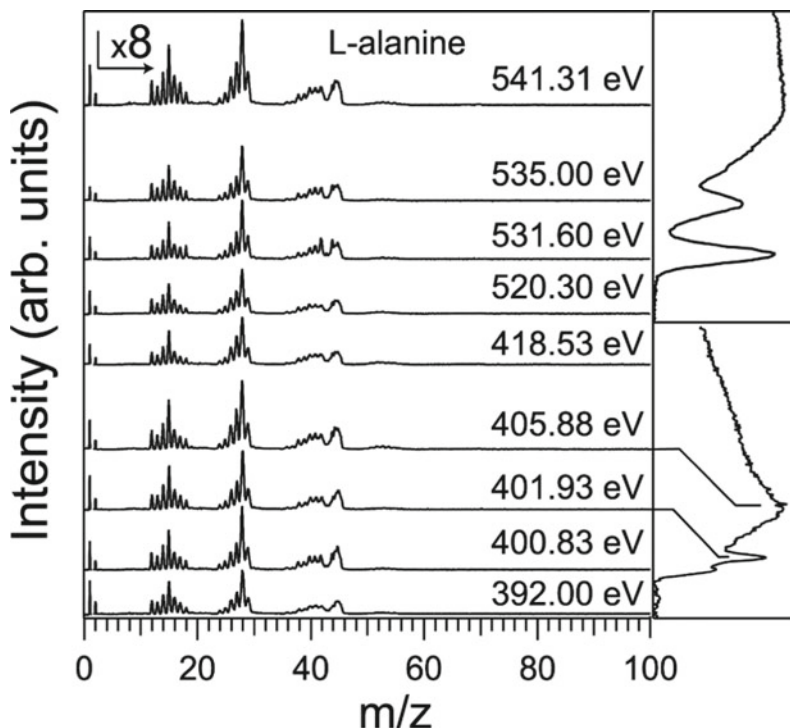


Fig. 10.8 Mass spectra for L-Alanine measured around the N 1s and O 1s edges

corresponds to the H^+ and H_2^+ fragments. The second can be assigned to the ions CH_x^+ ($x = 0-3$). The third group corresponds to the $C_2H_x^+$ family of ions. The intense peak observed at $m/z = 28$ is mainly assigned to CO^+ . Peaks observed at $m/z = 38-42$ are assigned to $C_2NH_x^+$ ($x = 0-4$). Finally, peaks at $m/x = 44$ and 45 correspond mainly to $COO^+/COOH^+$.

If we consider biomolecules containing elements with higher Z and consequently with higher energy K-edges, such as sulfur, calcium, iron and many others, measurement of NEXAFS spectra of these compounds will in general imply working in different beamlines, capable of providing soft and hard X-ray photons in the desired photon energy range. Taking as an example sulfur-containing biomolecules, only two protein constituent amino acids contain a sulfur atom in their molecular structure: cysteine ($C_3H_7NO_2S$) and methionine ($C_5H_{11}NO_2S$). While in methionine the sulfur atom is bonded to two carbon atoms ($-C-S-C-$), in cysteine a thiol group ($-SH$) is present. Thiol groups are very reactive; as a result, presence of more than one cysteine molecule in an adequate chemical ambience may result in the formation of a disulfide ($-S-S-$) chemical bond. In a simple case, two cysteine molecules may react to form a dimer, cystine, from two cysteine molecules (Fig. 10.9).

In proteins like insulin (Fig. 10.10), immunoglobulin G, and albumin, which contain cysteine amino acids in their primary structure, formation of disulfide bonds

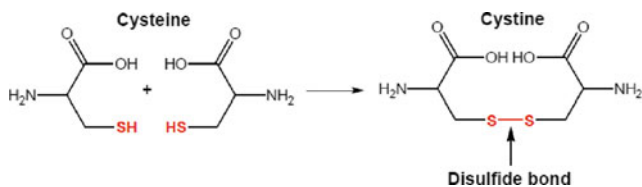


Fig. 10.9 Chemical structures of cysteine and cystine molecules and formation of the disulfide chemical bond. Reproduced from Simões et al. (2014), with the permission of Elsevier

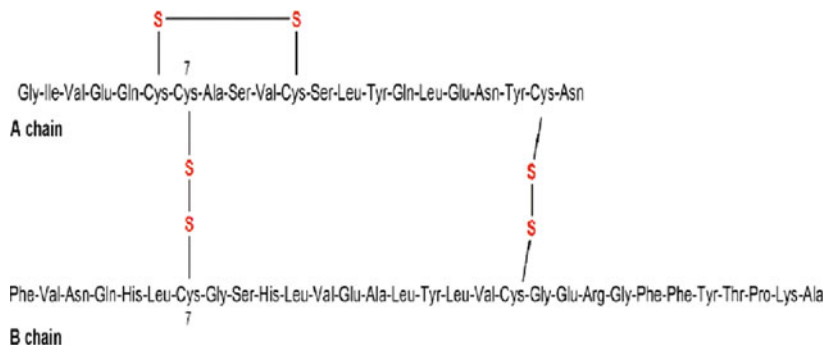


Fig. 10.10 Bovine insulin structure. This two-chain protein has one intra- and two inter-chain disulfide chemical bonds. Reproduced from Simões et al. (2014), with the permission of Elsevier

(“disulfide bridges”) will have definite consequences on their secondary and tertiary structures.

Measurement and interpretation of the NEXAFS spectra of sulfur-containing amino acids are consequently important steps towards understanding the stability or the dissociation processes of sulfur-containing peptides and proteins subjected to chemical reactions or submitted to harsh conditions (ionizing radiation, excessive heating...) (Almkvist et al. 2010; Jalilehvand 2006).

The S 1s NEXAFS spectra of cysteine and methionine powders, measured in the TEY mode, are presented in Figs. 10.11 and 10.12. Both spectra present sharp peaks centered at ca. 2471 eV followed by a broad shape resonance. Very useful discussions on the S 1s spectra of sulfur-containing biomolecules such as cysteine, methionine, cystine, glutathione and other compounds may be found for instance in Vairavamurthy (1998), Rompel et al. (1998) Pickering et al. (1998) and Jalilehvand (2006).

NEXAFS has also been used in the study of the inner shell excitation of important biomolecules such as DNA and nucleobases. For example, in a investigation of the radiation damage in DNA and 2-deoxyribose caused by soft X rays, the resonant X-ray absorption around the O 1s edge was measured for both biomolecules by Akamatsu and Yokoya (2001). 2-deoxy-D-ribose was subsequently irradiated with 538 eV photons, corresponding to the intense O 1s \rightarrow σ^* (C–O) transition and the

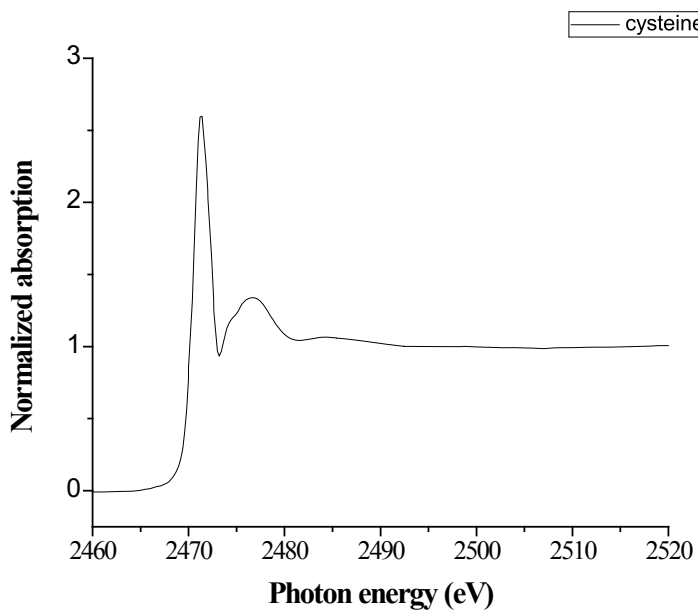


Fig. 10.11 S 1s NEXAFS spectrum of cysteine

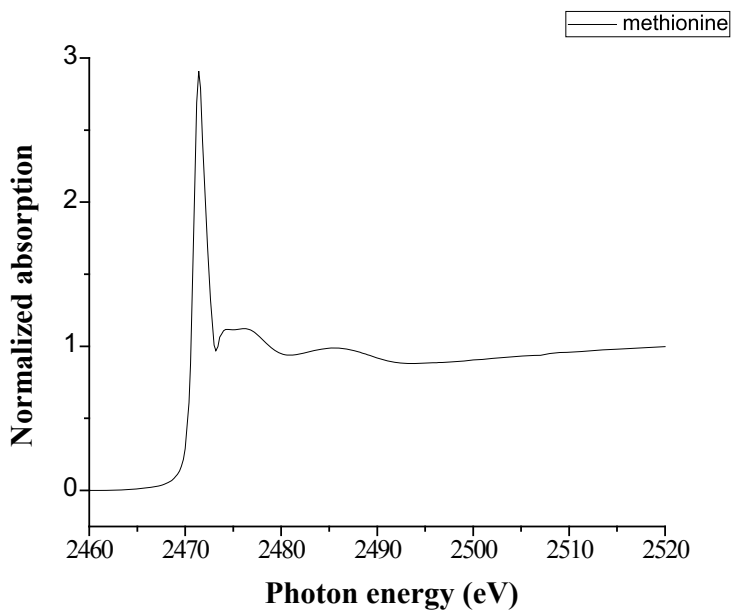


Fig. 10.12 S 1s NEXAFS spectrum of methionine

NEXAFS spectrum was measured in the 525–565 eV as a function of the irradiated dose. As a result of the irradiation, significant changes were observed in the NEXAFS spectra, with the $1s \rightarrow \pi^*$ transition (ca. 531.5 eV) splitting into two peaks (531.4 and 532.0 eV). It was also observed that the efficiency of production of strand breaks in DNA using X-rays with an energy range less than 1 keV was 6–8 times larger than the corresponding yields from 2 keV photons.

The NEXAFS spectra of the nucleobases thymine and adenine have been measured, in gas phase, around the C 1s, N 1s and O 1s edges by Plekan et al. (2008). The photon absorption spectra were acquired in a total ion yield mode. The spectra were interpreted by means of ab initio calculations.

Use of synchrotron radiation-based techniques (NEXAFS, XPS, XRF) to the study of biomolecules naturally raises a question concerning the possibility of radiation damage. Of course, and depending on the dose, all kinds of ionizing radiation will induce structure modifications or even inactivate biomolecules. With no intention of presenting a comprehensive review of this important subject, we refer the readers to a few excellent papers and references therein (Weik et al. 2000; Howells et al. 2009; Wang et al. 2009; Meents et al. 2010).

The damage caused by 0.8 keV electrons in sulfur-containing biomolecules, was investigated by Simões et al. (2014) using the NEXAFS technique. They observed that while the irradiated and non-irradiated S 1s spectra of cysteine (Fig. 10.13) remained practically unchanged, a definite modification was observed in the insulin spectra (Fig. 10.14). The relative stability of cysteine towards irradiation evidences some similarity with respect to our K-edge study of the DMDS molecule, in the sense

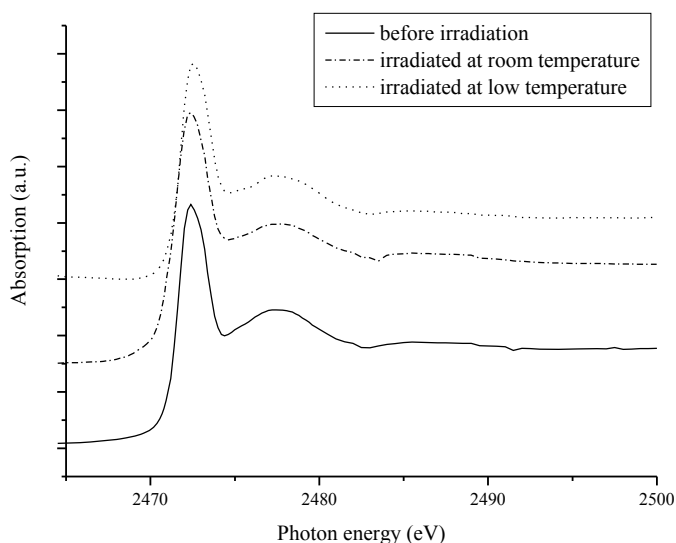


Fig. 10.13 S 1s NEXAFS spectrum of pristine and irradiated cysteine. Irradiation at room and low (77 K) temperatures. Reproduced Simões et al. (2014), with the permission of Elsevier

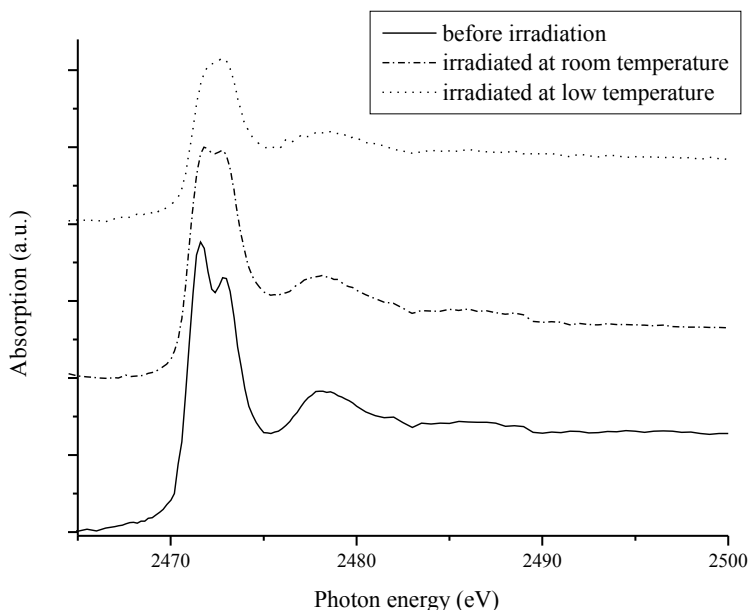


Fig. 10.14 S 1s NEXAFS spectrum of pristine and irradiated insulin. Irradiation at room and low (77 K) temperatures. Reproduced from Simões et al. (2014), with the permission of Elsevier

that the mass spectra pattern of DMDS, obtained at photon energies around the K-edge, did not change significantly, with the molecular ion remaining observable even at photon energies above 2460 eV. The observed modification in the insulin spectra, on the other hand, displays the capability of the NEXAFS technique to evidence molecular structure modifications induced by ionizing radiation.

10.4 NEXAFS Studies of Complex Samples: Chemical Speciation

In NEXAFS spectra, the observed resonances are not only element specific but can also be taken as a fingerprint of the chemical ambience surrounding each atom. When dealing with complex compounds or mixtures, NEXAFS spectroscopy can also be used to investigate the relative proportion of chemical species for each element and, depending on the case and complexity, to identify the oxidation states and functional groups present in the samples. In other words, NEXAFS allows for the chemical speciation of elements in complex materials.

According to the International Union of Pure and Applied Chemistry (IUPAC), chemical speciation should reflect the diversity of differentiation between various species, from isotopic composition to oxidation states, functional groups or com-

plete molecular definition (IUPAC 2000). IUPAC recommends the use of the term “speciation analysis” when it comes to the identification and measurement of the species present in complex compounds or mixtures. It is important to keep in mind how far in determining chemical speciation we can go with NEXAFS. Since this technique reflects transitions to unoccupied bound states, it will allow for the identification of the oxidation states of the elements and the functional groups to which they belong. The possibility that NEXAFS provides to differentiate the various chemical forms of a given element is explained by the fact that the edge position is strongly correlated to the oxidation state, and it is shifted to higher energies as the oxidation state increases. Besides, the intensity of the absorption also increases as the oxidation state increases. It is important to point out that in the NEXAFS approach, oxidation states reflect the relative electronic charge density around the absorbing atoms. A change in oxidation state is reflected by a shift of the absorption edge. This might not be the formal idea of oxidation number as defined to ionic compounds (Vairavamurthy 1998).

One of the principal advantages of using NEXAFS spectra to perform chemical speciation is that no digestion or extraction procedures are needed in principle. Although some samples might require special care to avoid radiation damage, other samples are robust and do not undergo damage during measurements. Chemical extraction, digestion, and other procedures for sample preparation may produce modification in the distribution of species and alter the speciation of the sample, or the relative proportion of species present in the sample (Scheinost et al. 2002). In NEXAFS spectroscopy, if due care is taken to a correct sample preparation and to avoid radiation damage, the spectra may provide a fingerprint of the species present in the samples.

The basic procedures involved in NEXAFS chemical speciation will be exemplified with the speciation of sulfur in samples obtained from plants. A somewhat detailed description of the speciation procedures will be provided, hoping that this description may be useful to researchers new in the field and particularly to graduate students. Chemical speciation using NEXAFS spectra can be performed either by Spectral Deconvolution (Gauss curve fitting—GCF) using Gaussians functions to fit resonances and arctangent functions to model transitions to the continuum; or by Linear Combination Fitting (LCF) using real spectra to model each functional group. Other approaches were used in the 80s and 90s, in the first attempts to discriminate between different species and to quantify them. For instance, George and Gobarty used the third derivative of the spectra to discriminate mixtures of sulfides and thiophenes and used the height of the third derivative of spectra features to estimate the amount of each component in the mixture (George and Gorbaty 1989). Huffman et al. used the GCF approach to speciate sulfur in coals and desulfurized coals, but instead of using one arctangent function to model each species transition to the continuum, they used one arctangent function to characterize all reduced compounds and another arctangent function to characterize the oxidized ones (Huffman et al. 1991, 1995). The power of LCF to perform sulfur chemical speciation was also early recognized, with several applications related to the analysis of petroleum samples (Waldo et al. 1991, 1992); sediments and humic substances (Vairavamurthy et al. 1997), biological

samples (Pickering et al. 1998; Prange et al. 2002), and, more recently, to study the covalent bond breakage of proteins subjected to irradiation (Simões et al. 2014). In this section we will explain some practical aspects and use a basic theory of Linear Combination Fitting. A comparison between GCF and LCF shows that both are suited to work with complex mixtures, but LCF may lead to better results (Prietz et al. 2011).

10.4.1 Data Acquisition and Processing

In order to perform a reliable chemical speciation through LCF, several practical aspects must be taken into consideration before data collection and data processing. Those aspects are so relevant that they might be the difference between useful and useless data.

Once samples have been adequately prepared and beamline instrumentation is available, the beamline energy calibration must be checked. Beamlines usually have defined calibration procedures which might be performed previously to any data acquisition, or in a concomitant way with data acquisition. This information must be recorded since it will be useful in order to compare data taken in different beamlines or even in the same beamline but in different periods of time. If a standard is not concomitantly measured with the sample, it might be a good practice, after performing energy calibration, to measure a well-known and stable standard repeatedly in between time intervals in order to check the energy calibration stability. If any energy shift occurs during data acquisition, this procedure will allow its identification and correction. For concomitant standards measurements, this information is used to calibrate each spectrum relative to the standard measurement. Even small energy shifts, if not taken into consideration, might introduce errors in spectra interpretation. Chemical speciation with NEXAFS makes use of the energy shift related to the oxidation state so that maintenance of a consistent energy scale is of paramount importance.

Once we have a good energy calibration, we must decide which energy interval the spectra acquisition should cover, and we will see that this is very important to perform quantitative analysis. Once acquired, the spectra will be subjected to a procedure called “step height normalization”. This procedure is crucial to perform quantitative analysis, such as chemical speciation based in Linear Combination Fitting, which must be performed using normalized spectra. In order to have a good step height normalization, spectra acquisition must be done in such a way as to make sure that we have enough data point both in the pre-edge and in the post edge regions (Ravel 2014). While spectrum acquisition in the resonances zone is usually done using small energy steps (0.1–0.2 eV), pre-edge and post-edge data are usually acquired using larger energy steps (0.5, 1, or 2 eV). If the sample to be measured presents a high concentration in the element whose edge is being scanned, it is recommended to dilute it in order to avoid self-absorption. Samples that are thick and concentrated

might present self-absorption problems, which causes main resonances to dampen and compromise the quantitative results (Pickering et al. 1998).

Usually, each sample spectrum is measured several times in order to improve spectra statistics. These repetitions are usually merged together, resulting in one sample spectrum with better statistics. Before merging, it is important to normalize each spectrum with respect to the intensity of the beam during acquisition (I_0); this procedure is called I_0 normalization. From this procedure results experimental data independent of the beam intensity. In this way, two spectra of the same sample taken in different times and at the same experimental conditions should have the same feature intensity.

Following this procedure, a good data set is obtained, properly calibrated in energy, with good statistics, and normalized to the intensity of the beam. Next, step height normalization can be applied.

Step height normalization is a routine procedure available in specialized software for NEXAFS data treatment. It basically consists of fitting the pre-edge portion of the spectrum with a linear function and the post edge portion with a linear or quadratic function, depending on the data. These functions are extrapolated to the edge position (E_0) and the difference between the value of both functions at E_0 is called the edge step (Schnohr and Ridgway 2015). Normalization therefore consists on subtracting the pre-edge function from the whole data and dividing the result of the subtraction by the edge step. In this way, the pre-edge portion of the spectra will become equal to zero and the post-edge spectrum intensity value will oscillate around one. Some softwares (like ATHENA (Ravel and Newville 2005)) allows for the compensation between differences in the slopes of the pre-edge and post-edge functions, the so called “flatten normalized data”.

Step height normalization has been performed at the sulfur K-edge NEXAFS spectrum of L-methionine sulfone, using ATHENA (Ravel and Newville 2005) and the result is shown in Fig. 10.15. In Fig. 10.15a the raw data (I_0 normalized) is plotted along with the pre-edge and post-edge functions. The circles show the intervals considered in the adjustment of the pre-edge and post-edge functions. The circle in the main resonance shows the E_0 position as determined by the position of the zero of the second derivative. In Fig. 10.15b the normalized data is shown with a pre-edge equal to zero and a step height equal to one. I_0 normalization takes away the effect of beam intensity, and step height normalization eliminates the effect of dilution, detection mode, detector response, sample thickness, etc. allowing a quantitative comparison between different spectra (Kelly et al. 2008).

10.4.2 Linear Combination Fitting and Complementary Techniques

Linear combination fitting allows to perform chemical speciation of a sample using spectra of model compounds. It is based on the fact that the total absorption coefficient

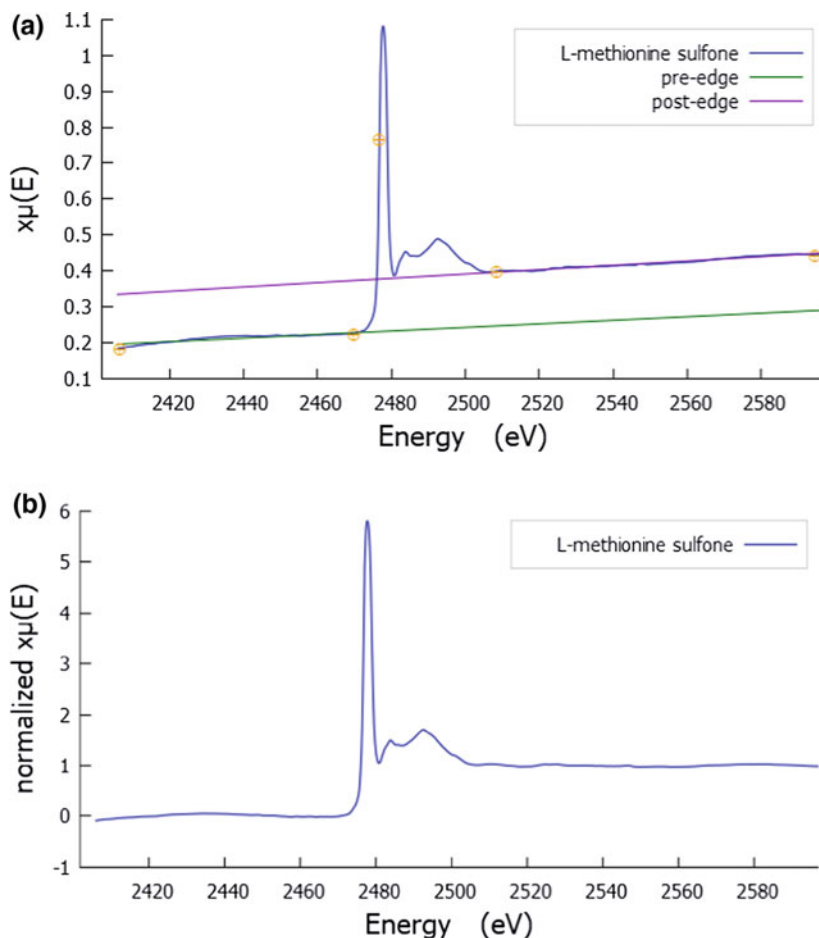


Fig. 10.15 Example of “step height” normalization of the sulfur K-edge spectrum of L-methionine sulfone. **a** Absorption spectrum showing the pre-edge and post-edge curves. **b** L-methionine sulfone normalized spectrum

is the sum of the contributions from all species present in a sample, either from the point of view of the elements or of the constituent compounds. Spectra of a set of model compounds (standards) representative of the species present on the sample (measured and normalized under the same conditions) is used to perform a linear combination in which the difference between the experimental spectrum and the proposed LCF combination is minimized. The characteristic features of the model compounds and the chemical shifts related to definite oxidation states allow for the use of the LCF procedure and subsequent interpretation of the results. As said before, chemical shifts should be directly related to oxidation states. This is one of

the important reasons why so much care must be taken in order to obtain a consistent energy calibration.

Based on the set of normalized spectra from model compounds, LCF determines a set of coefficients f_i which represents the fraction of the model spectrum that composes the sample spectrum:

$$\sum f_i \times Model_i = LCF \quad (10.2)$$

In theory, the sum of all f_i must be equal to one:

$$\sum f_i = 1 \quad (10.3)$$

If the sum is not equal to one, the normalization procedure must be inspected and redone in order to look for inconsistencies. Besides inconsistent normalization and missed species, spectra broadening may also cause the sum of f_i to be different from one (Schnohr and Ridgway 2015).

A basic question remains: how to start an LCF analysis in a sample from which little is known? How many model compounds and which ones should be used? Determining the number and nature of the standards which should be used in LCF is not a simple task. Fortunately, there are complementary tools from spectra analysis that can help with this task, depending on how the experiments were designed, and the data set to be considered. If a set of related samples are available (for example, NEXAFS spectra taken at different stages of a chemical reaction that might be showing the transformation of one specie into another; a set of soils samples or biological samples with different proportions of the same species; etc.) a procedure called Principal Components Analysis (PCA) can help to identify the **number** of species present. PCA allows to identify how many species are responsible for the source of structural variability in a set of samples, provided that the samples are linearly independent (i.e. they are not linear combination of the other samples in the set), but PCA does not allow to identify **which** standards may compose the samples. A related procedure called Target Transformation (TT) can help with this task. PCA and TT analysis are in some cases far from simple, requiring attention and careful interpretation of the associated results. A complete explanation of the theory and application of these methods can be found in Scheinost et al. (2002), Wasserman et al. (1999), Beauchemin et al. (2002).

We are now in condition to start the spectra analysis of complex matrices. So far, relevant aspects of data acquisition, pre-processing and normalization have been discussed. Complementary methods have also been introduced (PCA, TT) in order to shed light in the determination of the number and identity of standards to be considered in a LCF. We exemplify the application of these procedures with the chemical speciation of sulfur in a plant material. Sulfur is an element that presents a real challenge for chemical speciation, and it was once considered spectroscopically “silent” (Pickering et al. 1998; Jalilehvand 2006). Determination of sulfur species based on chemical and extraction procedures might be complex and prone to experi-

mental errors, alteration of the distribution of oxidation states, time consuming, etc. Application of nuclear magnetic resonance (NMR) spectroscopy to this element is difficult because the predominant sulfur isotope ^{32}S (94.99%), lacks nuclear spin, while the ^{33}S isotope (0.75%) provides weak and broad signals. In environmental and biological samples, sulfur is present in several oxidation states and functional groups, performing a variety of crucial roles to ecosystems and to life, as part of sulfur cycles. Sulfur can be present in complex samples with oxidation states ranging from -2 to $+6$. The S 1s absorption spectrum presents sharp linewidths and large chemical shifts (Frank et al. 1999). Sulfur chemical speciation using NEXAFS spectroscopy becomes consequently a very attractive option.

In our laboratory and in collaboration with the Amazonian research institution INPA, a systematic study of the inorganic composition of Amazonian plants and their chemical speciation is currently under development. In order to obtain the sulfur chemical speciation in these plants, the NEXAFS spectra of dried plant samples and from several standards of relevant biological significance were obtained and then submitted to a LCF procedure. Plants obtain sulfur predominantly in sulfate form from the soil and it is transported to different tissues where it is either transformed into metabolites of biological relevance or stored. Sulfur-containing amino acids such as cysteine, cystine and methionine are expected to be present in plants samples and were accordingly used as part of the model (standard) compounds. Other standard compounds included reduced and oxidized glutathione (reduced glutathione is considered to be one of the most abundant thiols present in plant cells) as well as dimethyl sulfoxide, L-methionine sulfone, cysteic acid and sulfate, covering a wide range of functional groups and oxidation states.

As an example of the results obtained applying LCF, the sulfur K-edge NEXAFS spectra of samples of the Amazonian plant, *Andira surinamensis*, are shown in Fig. 10.16. Results of the chemical speciation are presented in Table 10.1 (Gonzalez et al. 2019).

The sulfur K-edge spectra of plant samples usually contain three main features. The first feature, around 2471 eV, accounts for metabolized sulfur (organic sulfur). The second feature, observed around 2474 eV, is usually associated with intermediate oxidized species such as sulfoxide groups. The last feature, observed around 2480 eV, is generally associated with highly oxidized species such as sulfone, sulfonate and sulfate groups.

From Fig. 10.16 it can be seen that up to six components have been necessary in order to perform a best fit analysis of the samples spectra. This evidences how complex biological and environmental samples can be. In this example, it was not possible to distinguish between thiol and thioether in a single sample, due to the similarity between their spectra. The main resonances observed in the cysteine and methionine spectra have similar intensities and lie approximately 0.2 eV from each other. Although the post edge features are different, a distinction between the two chemical species is jeopardized by the presence of a sulfoxide main resonance which appears energetically in the same position. Finally, it is important to mention that the set of model compounds used must be as similar as possible to those presumed to be in the sample under study. Vairavamurthy and coworkers concluded that identical

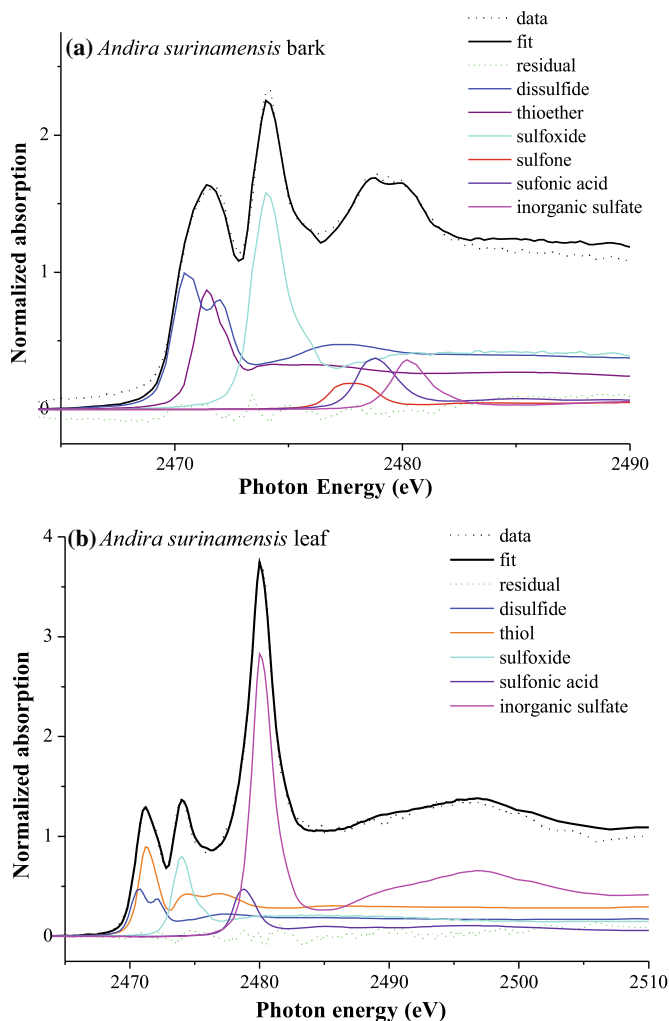


Fig. 10.16 LCF analysis of spectra from samples of parts of the Amazonian plant, *Andira surinamensis* **a** bark; **b** leaf. Reproduced from Gonzalez et al. (2019), with the permission of J. Braz. Chem. Soc.

sulfur functional groups have fine structure that are characteristic of the functional group and almost not dependent on the side chains (Vairavamurthy 1998). This makes possible the use of a standard as a model for a given functional group even though it is not identical to the species present in the sample. This assumption must nevertheless be treated with care. Since NEXAFS probes the transition to unoccupied molecular orbitals and scattering from neighboring atoms, it reflects differences in atomic neighborhood with respect to the atom being probed (first and second shell of coordination, bond substituents, etc.). In a sequence of papers, Pickering and

Table 10.1 Speciation of *Andira surinamensis* samples (LCF results). Reproduced from Gonzalez et al. (2019), with the permission of J. Braz. Chem. Soc.

Compound	Functional group	Oxidation state (Waldo et al. 1991; Xia et al. 1998; Vairavamurthy 1998)	Bark %	Leaf %
Oxidized glutathione	Disulfide	0.2	34.8 ± 1.3	16.4 ± 1.5
Reduced glutathione	Thiol	0.4	–	27.8 ± 1.5
Methionine	Thioether	0.5	21.8 ± 1.1	–
DMSO	Sulfoxide	2	31.4 ± 0.5	15.9 ± 0.4
L-methionine sulfone	Sulfone	4	3.1 ± 0.5	–
Cysteic acid	Sulfonic acid	5	4.5 ± 0.5	5.8 ± 0.3
Inorganic sulfate	Inorganic sulfate	6	4.3 ± 0.3	34.1 ± 0.3

coworkers have clearly shown that identical functional groups may show differences in spectral features (George et al. 2014; Pickering et al. 2016; Cotelesage et al. 2017). It is also well known that spectra of standard compounds may change on going from solid state to solution. In the latter case, the pH can also strongly influence NEXAFS spectra (Pickering et al. 1998; Jalilehvand 2006; Sarangi et al. 2008; Risberg et al. 2009). All in all, these differences, if not appropriately considered, may lead to an enhancement in the uncertainty in quantification of functional groups and even to misinterpretation.

10.5 Final Remarks

The material presented in this chapter reflects a personal perspective from both co-authors. It was not our intention to present a comprehensive review of NEXAFS, a very large and important subject. For more details concerning experimental and theoretical aspects of the technique the reader is kindly directed to the representative references which have been provided. We apologize in advance to researchers who may consider their contributions under represented in our discussion.

Acknowledgements G.G.B.S. and J.C.G. gratefully acknowledge the contribution of the colleagues who co-authored our articles included in this chapter. We are very much thankful to F.C. Stedile for critical reading.

References

- Ade HW, Urquhart SG (2002) NEXAFS spectroscopy and microscopy of natural and synthetic polymers. In: Sham T-K (ed) Chemical application of synchrotron radiation, Part I: Dynamics and VUV spectroscopy. World Scientific
- Akamatsu K, Yokoya A (2001) X-ray absorption near edge structures of DNA or its components around the oxygen K-shell edge. *Radiat Res* 155:449–452. [https://doi.org/10.1667/0033-7587\(2001\)155%5b0449:xranes%5d2.0.co;2](https://doi.org/10.1667/0033-7587(2001)155%5b0449:xranes%5d2.0.co;2)
- Almkvist G, Boyeb K, Persson I (2010) K-edge XANES analysis of sulfur compounds: an investigation of the relative intensities using internal calibration. *J Synchrotron Radiat* 17:683–688. <https://doi.org/10.1107/S0909049510022946>
- Beauchemin S, Hesterberg D, Beauchemin M (2002) Principal component analysis approach for modeling sulfur K-XANES spectra of humic acids. *Soils Sci Soc Am J* 66:83–91. <https://doi.org/10.2136/sssaj2002.0083>
- Bernini RB, da Silva LBG, Rodrigues FN, Coutinho LH, Rocha AB, de Souza GGB (2012) Core level (S 2p) excitation and fragmentation of dimethyl sulfide and dimethyldisulfide molecules. *J Chem Phys* 136(14):144307. <https://doi.org/10.1063/1.3701567>
- Brack A, Owen TC, Kasting JF, Brown LL, Miller SL, Holm NG, Anderson EM, Delsemme AH, Cronin JR, Maurette M, Deamer DW, Wächtershauser G, Duve Cd, Schwartz AW, Ferris JP, James KD, Ellington AW, Burmeister J, Kiedrowski Gv, Stetter KO, Schopf JW, Raulin F, McKay CP (1998) The molecular origins of life: assembling pieces of the puzzle. In: Brack A (ed). Cambridge University Press. <https://doi.org/10.1017/cbo9780511626180>
- Gonzalez JC, Simões G, Bernini RB, Coutinho LH, Stedile FC, Nunez CV, Vicentin FC, de Souza GGB (2019) Elemental concentration and sulfur chemical speciation in the Amazonian plant *Andira surinamensis* using synchrotron radiation techniques (SR-XRF, XANES), RBS and WD-XRF. *J Braz Chem Soc* (in press). <https://doi.org/10.21577/0103-5053.20190098>
- Cotelesage JJH, Barney M, Vogt L, Pickering IJ, George GN (2017) X-ray absorption spectroscopy of aliphatic organic sulfides. *J Phys Chem A* 121:6256–6261. <https://doi.org/10.1021/acs.jpca.7b04395>
- Engel MH, Nagy B (1982) Distribution and enantiomeric composition of amino acids in the Murchison meteorite. *Nature* 296(5860):837–840. <https://doi.org/10.1038/296837a0>
- Evans J (2006) Brilliant opportunities across the spectrum. *Phys Chem Chem Phys* 8:3045–3058. <https://doi.org/10.1039/B604369K>
- Frank P, Hedman B, Hodgson KO (1999) Sulfur allocation and vanadium-sulfate interactions in whole blood cells from the tunicate *Ascidia ceratodes*, investigated using X-ray absorption spectroscopy. *Inorg Chem* 38(2):260–270. <https://doi.org/10.1021/ic980792m>
- Gaur A, Shrivastava BD, Nigam HL (2013) X-ray absorption fine structure (XAFS) spectroscopy—a review. *Proc Indian Natl Sci Acad Spec Iss Part B* 79(4):921–966
- George GN, Gorbaty ML (1989) Sulfur K-edge X-ray absorption spectroscopy of petroleum asphaltenes and model compounds. *J Am Chem Soc* 111(9):3182–3186. <https://doi.org/10.1021/ja00191a012>
- George GN, Hackett MJ, Sansone M, Gorbaty ML, Kelemen SR, Prince RC, Harris HH, Pickering IJ (2014) Long-range chemical sensitivity in the sulfur K-edge X-ray absorption spectra of substituted thiophenes. *J Phys Chem A* 118:7796–7802. <https://doi.org/10.1021/jp505766f>
- Henderson GS, De Groot FMF, Moulton BJA (2014) X-ray absorption near-edge structure (XANES) spectroscopy. *Rev Miner Geochem* 78:75–138. <https://doi.org/10.2138/rmg.2014.78.3>
- Hitchcock AP (2000) Inner shell excitation spectroscopy of molecules using inelastic electron scattering. *J Electron Spectrosc Relat Phenom* 112:9–29. [https://doi.org/10.1016/S0368-2048\(00\)00200-0](https://doi.org/10.1016/S0368-2048(00)00200-0)
- Hitchcock AP, Brion CE (1977) Carbon K-shell excitation of C₂H₂, C₂H₄, C₂H₆ and C₆H₆ by 2.5 keV electron impact. *J Electron Spectrosc Relat Phenom* 10(3):317–330. [https://doi.org/10.1016/0368-2048\(77\)85029-9](https://doi.org/10.1016/0368-2048(77)85029-9)

- Howells MR, Hitchcock AP, Jacobsen CJ (2009) Introduction: special issue on radiation damage. *J Electron Spectrosc Relat Phenom* 170(1–3):1–3. <https://doi.org/10.1016/j.elspec.2009.01.004>
- Huffman GP, Mitra S, Huggins FE, Shah N, Vaidya S, Lu F (1991) Quantitative analysis of all major forms of sulfur in coal by X-ray absorption fine structure spectroscopy. *Energy Fuels* 5:574–581. <https://doi.org/10.1021/ef00028a008>
- Huffman GP, Shah N, Huggins FE, Stock LM, Chatterjee K, Kilbane JJ, Chou M-IM, Buchanan DH (1995) Sulfur speciation of desulfurized coals by XANES spectroscopy. *Fuel* 74(4):549–555. [https://doi.org/10.1016/0016-2361\(95\)98358-L](https://doi.org/10.1016/0016-2361(95)98358-L)
- Inokuti M (1971) Inelastic collisions of fast charged particles with atoms and molecules—the Bethe theory revisited. *Rev Mod Phys* 43(3):297–347. <https://doi.org/10.1103/RevModPhys.43.297>
- IUPAC (2000) Guidelines for terms related to chemical speciation and fractionation of elements. Definitions, structural aspects, and methodological approaches. *Pure Appl Chem* 72(8):1453–1470. <https://doi.org/10.1351/pac200072081453>
- Jalilehvand F (2006) Sulfur: not a “silent” element any more. *Chem Soc Rev* 35:1256–1268. <https://doi.org/10.1039/b417595f>
- Kaznatcheyev K, Osanna A, Jacobsen C, Plashkevych O, Vahtras O, Agren H, Carravetta V, Hitchcock AH (2002) Inner-shell absorption spectroscopy of amino acids. *J Phys Chem A* 106:3153–3168. <https://doi.org/10.1021/jp013385w>
- Kelly SD, Hesterberg D, Ravel B (2008) Analysis of soils and minerals using X-ray absorption spectroscopy. In: *Methods of soil analysis—Part 5: Mineralogical methods*, vol. ser. 5.5. SSSA. SSSA Book, Madison
- Leinweber P, Kruse J, Walley FL, Gillespie A, Eckhardt K-U, Blyth RI, Regier T (2014) Nitrogen K-edge XANES—an overview of reference compounds used to identify unknown organic nitrogen in environmental samples. *J Synchrotron Rad* 14(6):500–511. <https://doi.org/10.1107/S0909049507042513>
- Lombi E, Susini J (2009) Synchrotron-based techniques for plant and soil science: opportunities, challenges and future perspectives. *Plant Soil* 320:1–35. <https://doi.org/10.1007/s11104-008-9876-x>
- Marchenko T, Carniato S, Journal L, Guillemin R, Kawerk E, Žitnik M, Kavčič M, Bučar K, Bohinc R, Petric M, Vaz da Cruz V, Gel'mukhanov F, Simon M (2015) Electron dynamics in the core-excited CS₂ molecule revealed through resonant inelastic X-ray scattering spectroscopy. *Phys Rev X* 5(3):031021. <https://doi.org/10.1103/PhysRevX.5.031021>
- Marinho RRT, Lago AF, Homem MGP, Coutinho LH, de Souza GGB, Naves de Brito A (2006) Gas phase photoabsorption and mass spectra of L-alanine and L-proline in the soft X-ray region. *Chem Phys* 324:420–424. <https://doi.org/10.1016/j.chemphys.2005.10.038>
- Meents A, Gutmann S, Wagner A, Schulze-Briese C (2010) Origin and temperature dependence of radiation damage in biological samples at cryogenic temperatures. *Proc Natl Acad Sci* 107(3):1094–1099. <https://doi.org/10.1073/pnas.0905481107>
- Miron C, Morin P (2011) High-resolution inner-shell photoionization, photoelectron and coincidence spectroscopy. In: Quack M, Merkt F (eds) *Handbook of high-resolution spectroscopy*. Wiley. <https://doi.org/10.1002/9780470749593.hrs066>
- Neuner I, Morin P (1996) Electronic and nuclear relaxation of core-excited molecules. In: Becker U, Shirley DA (eds) *VUV and soft X-ray photoionization*. Plenum Press, New York
- Pascarelli S, Mathona O (2010) Advances in high brilliance energy dispersive X-ray absorption spectroscopy. *Phys Chem Chem Phys* 12:5535–5546. <https://doi.org/10.1039/B926509K>
- Piancastelli MN (2000) Auger resonant Raman studies of atoms and molecules. *J Electron Spectrosc Relat Phenom* 107:1–26. [https://doi.org/10.1016/S0368-2048\(99\)00099-7](https://doi.org/10.1016/S0368-2048(99)00099-7)
- Pickering IJ, Barney MM, Cotelesage JJJ, Vogt L, Pushie MJ, Nissan A, Prince RC, George GN (2016) Chemical sensitivity of the sulfur K-edge X-ray absorption spectra of organic disulfides. *J Phys Chem A* 37(120):7279–7286. <https://doi.org/10.1021/acs.jpca.6b06790>
- Pickering IJ, Prince RC, Divers T, George GN (1998) Sulfur K-edge X-ray absorption spectroscopy for determining the chemical speciation of sulfur in biological systems. *FEBS Lett* 441:11–14. [https://doi.org/10.1016/S0014-5793\(98\)01402-1](https://doi.org/10.1016/S0014-5793(98)01402-1)

- Plekan O, Feyer V, Richter R, Coreno M, de Simone M, Prince KC, Trofimov AB, Gromov EV, Zaytseva IL, Schirmer J (2008) A theoretical and experimental study of the near edge X-ray absorption fine structure (NEXAFS) and X-ray photoelectron spectra (XPS) of nucleobases: thymine and adenine. *Chem Phys* 347:360–375. <https://doi.org/10.1016/j.chemphys.2007.09.021>
- Prange A, Chauvistré R, Modrow H, Hormes J, Truper HG, Dahl C (2002) Quantitative speciation of sulfur in bacterial sulfur globules: X-ray absorption spectroscopy reveals at least three different species of sulfur. *Microbiology* 148:267–276. <https://doi.org/10.1099/00221287-148-1-267>
- Prietzl J, Botzaki A, Tyufekchieva N, Brettholle M, Thieme J, Klysubun W (2011) Sulfur speciation in soil by S K-edge XANES spectroscopy: comparison of spectral deconvolution and linear combination fitting. *Environ Sci Technol* 45:2878–2886. <https://doi.org/10.1021/es102180a>
- Ravel B (2014) ATHENA user's guide
- Ravel B, Newville M (2005) ATHENA, ARTEMIS, HEPHAESTUS: data analysis for X-ray absorption spectroscopy using IFFFIT. *J Synchrotron Radiat* 12(12):537–541. <https://doi.org/10.1107/S0909049505012719>
- Rehr JJ, Albers RC (2000) Theoretical approaches to X-ray absorption fine structure. *Rev Mod Phys* 72:621–654. <https://doi.org/10.1103/RevModPhys.72.621>
- Risberg ED, Jalilvand F, Leung BO, Pettersson LGM, Sandstrom M (2009) Theoretical and experimental sulfur K-edge X-ray absorption spectroscopic study of cysteine, cystine, homocysteine, penicillamine, methionine and methionine sulfoxide. *R Soc Chem-Dalton Transl* 3542–3558. <https://doi.org/10.1039/b819257j>
- Rompel A, Cinco RM, Latimer MJ, Mcdermott AE, Guiles RD, Quintanilha A, Krauss RM, Sauer K, Yachandra VK, Klein MP (1998) Sulfur K-edge X-ray absorption spectroscopy: a spectroscopic tool to examine the redox state of S-containing metabolites in vivo. *Proc Natl Acad Sci* 95. <https://doi.org/10.1073/pnas.95.11.6122>
- Sarangi R, Frank P, Hodgson KO, Hedman B (2008) When identical functional groups are not identical DFT study of the effects of molecular environment on sulfur K-edge X-ray. *Inorg Chim Acta* 361:956–964. <https://doi.org/10.1016/j.ica.2007.05.047>
- Scheinost AC, Kretzschmar R, Pfister S (2002) Combining selective sequential extractions, X-ray absorption spectroscopy, and principal component analysis for quantitative zinc speciation in soil. *Environ Sci Technol* 36(23):5021–5028. <https://doi.org/10.1021/es025669f>
- Schnorr CS, Ridgway MC (eds) (2015) X-ray absorption spectroscopy of semiconductors. Springer series in optical sciences. Springer, Berlin, Heidelberg
- Sedlmair J (2011) Soft X-ray spectromicroscopy of environmental and biological samples, vol 7. Göttingen series in X-ray physics. Universitätsverlag Göttingen
- Simões G, Rodrigues FN, Bernini RB, Castro CSCd, Souza GGBd (2014) A NEXAFS and mass spectrometry study of cysteine, cystine and insulin irradiated with intermediate energy (0,8 keV) electrons. *J Electron Spectrom Relat Phenom* 193:21–26. <https://doi.org/10.1016/j.elspec.2014.02.002>
- Snyder LE (1997) The search for interstellar glycine. *Orig Life Evol Biosph* 27:115–133. <https://doi.org/10.1023/A:1006522230405>
- Solomon D, Lehmann J, Kinyangi J, Liang BQ, Heymann K, Dathe L, Hanley K, Wirick S, Jacobsen C (2009) Carbon (1s) NEXAFS spectroscopy of biogeochemically relevant reference organic compounds. *Soil Sci Soc Am J* 73:1817–1830. <https://doi.org/10.2136/sssaj2008.0228>
- Stöhr J (1992) NEXAFS spectroscopy. Springer, San Jose, CA
- Themed collection: Recent developments in X-ray absorption spectroscopy (2010) *Phys Chem Chem Phys* 12(21):5489–5724
- Tronc M, King GC, Bradford RC, Read FH (1976) K-shell excitation of carbon in CO and CH₄ using electron impact. *J Phys B* 9(17):L555–L558. <https://doi.org/10.1088/0022-3700/9/17/011>
- Urquhart SG, Hitchcock AP, Smith AP, Ade HW, Lidy W, Rightor EG, Mitchell GE (1999) NEXAFS spectromicroscopy of polymers: overview and quantitative analysis of polyurethane polymers. *J Electron Spectrosc Relat Phenom* 100(1–3):119–135. [https://doi.org/10.1016/S0368-2048\(99\)00043-2](https://doi.org/10.1016/S0368-2048(99)00043-2)

- Vairavamurthy MA (1998) Using X-ray absorption to probe sulfur oxidation states in complex molecules. *Spectrochim Acta Part A* 54:2009–2017. [https://doi.org/10.1016/S1386-1425\(98\)00153-X](https://doi.org/10.1016/S1386-1425(98)00153-X)
- Vairavamurthy MA, Maletic D, Wang S, Manowitz B, Eglinton T, Lyons T (1997) Characterization of sulfur-containing functional groups in sedimentary humic substances by X-ray absorption near-edge structure spectroscopy. *Energy Fuels* 11(3):546–553. <https://doi.org/10.1021/ef960212a>
- Varas LR, Coutinho LH, Bernini RB, Betancourt AM, Moura CEVd, Rocha AB, Souza GGBd (2017) Breaking the disulfide chemical bond using high energy photons: the dimethyl disulfide and methyl propyl disulfide molecules. *RSC Adv* 7:36525–36532. <https://doi.org/10.1039/c7ra05001a>
- Waldo GS, Carlson RMK, Moldowan JM, Peters KE, Penner-Hahn JE (1991) Sulfur speciation in heavy petroleum: information from X-ray absorption near-edge structure. *Geochim Cosmochim Acta* 55:801–814. [https://doi.org/10.1016/0016-7037\(91\)90343-4](https://doi.org/10.1016/0016-7037(91)90343-4)
- Waldo GS, Mullins OC, Penner-Hahn JE, Cramer SP (1992) Determination of the chemical environment of sulphur in petroleum asphaltene by X-ray absorption spectroscopy. *Fuel* 71:53–57. [https://doi.org/10.1016/0016-2361\(92\)90192-Q](https://doi.org/10.1016/0016-2361(92)90192-Q)
- Wang J, Morin C, Li L, Hitchcock AP, Scholl A, Doran A (2009) Radiation damage in soft X-ray microscopy. *J Electron Spectrosc Relat Phenom* 170(1–3):25–36. <https://doi.org/10.1016/j.elspec.2008.01.002>
- Wasserman SR, Allen PG, Shuh DK, Bucher JJ, Edelstein NM (1999) EXAFS and principal component analysis: a new shell game. *J Synchrotron Radiat* 6:284–286. <https://doi.org/10.1107/S0909049599000965>
- Weik M, Ravelli RBG, Kryger G, McSweeney S, Raves ML, Harel M, Gros P, Silman I, Kroon J, Sussman JL (2000) Specific chemical and structural damage to proteins produced by synchrotron radiation. *PNAS* 97:623–628. <https://doi.org/10.1073/pnas.97.2.623>
- Xia K, Weesner F, Blam WF, Bloom PR, Skyllberg UL, Helmke PA (1998) XANES studies of oxidation states of sulfur in aquatic and soil humic substances. *Soil Sci Soc Am J* 62:1240–1246. <https://doi.org/10.2136/sssaj1998.03615995006200050014x>
- Zubavichus Y, Shaporenko A, Grunze M, Zharnikov M (2005) Innershell absorption spectroscopy of amino acids at all relevant absorption edges. *J Phys Chem A* 109(32):6998–7000. <https://doi.org/10.1021/jp0535846>

Chapter 11

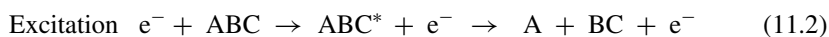
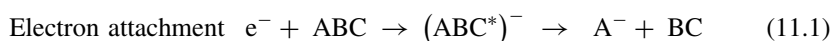
Electron Impact Spectroscopy



Alexander Dorn

11.1 Introduction

Collisions of electrons with molecules are relevant in a wide range of scientific and technical applications, including plasma physics, planetary atmospheres and radiation-interactions with living tissue. In the biosciences their importance is manifold. One example is the analytical technique of mass spectrometry (MS). Here the purpose of electron beams is to electrically charge the molecules within a sample under investigation such that they can be mass separated with electric and magnetic fields (Gross 2011). Furthermore, electron collisions play a central role if biological tissue is irradiated by X-rays or swift charged particles like ions and electrons. These stem on one hand from the abundant natural radioactivity inevitably acting on living organisms on earth and on the other hand from medical imaging or the treatment of cancer tumors by radiotherapy. The latter is done by irradiation with X-rays or ions resulting, e.g., in DNA lesions and subsequent cell death. A large part of the actual damage is caused by secondary electrons which are abundantly produced by the primary radiation exciting or ionizing many molecules along their track. The understanding of the physical and chemical processes underlying the harmful effects of these projectiles on living cells and organisms is still very incomplete. Nevertheless, the elementary processes initiated by free electrons colliding with molecules are well known from spectroscopic studies in the gas phase. If we consider a three-atomic sample molecule ABC these are:



A. Dorn (✉)

Max Planck Institute for Nuclear Physics, 69117 Heidelberg, Germany

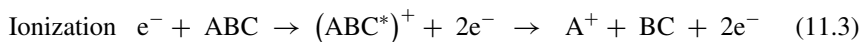
e-mail: A.Dorn@mpi-k.de

© Springer Nature Switzerland AG 2019

A. S. Pereira et al. (eds.), *Radiation in Bioanalysis*, Bioanalysis 8,

https://doi.org/10.1007/978-3-030-28247-9_11

313



In electron attachment (11.1) an electron is captured by the molecule resulting in a potentially excited negative ion. For excitation (11.2) the projectile electron transfers energy into internal molecular degrees of freedom populating vibrational and electronically excited states. In ionization (11.3) the energy transfer is sufficiently large such that an initially bound electron is ejected (ionized) and a positively charged molecular ion is produced. In all cases the excited molecular state undergoes some structural rearrangement. Regularly its internal energy is sufficient to overcome reaction barriers to dissociation into two or more fragments as it is indicated in the last step of the Eqs. (11.1–11.3).

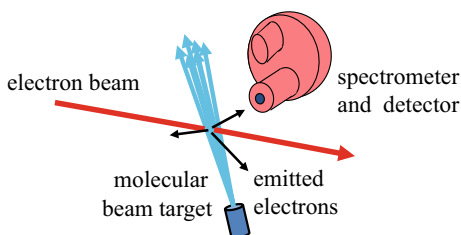
The different reactions can be identified and characterized with various experimental techniques. Also their absolute rates can be determined from which cross section data can be derived. Diverse theoretical methods have been developed to describe electron molecule scattering processes. There are on one hand empirical formulas which provide cross sections which are sufficiently accurate for many purposes. On the other hand there are ab initio models which describe the process based on the well-known interactions between the particles involved and which aim at understanding the details of the reaction mechanisms and dynamics. Experimental data can test theoretical results and, therefore, guide the development of improved models and theories. Accurate cross sections for the different processes are also required in applications for modeling the density and kind of damage in materials.

In the following we describe some selected experimental techniques used to analyze the products of reactions (11.1–11.3) where we concentrate primarily on the electrons and ions in the final state. Subsequently we present exemplary experimental results for excitation and ionization of tetrahydrofuran (THF) monomers and clusters. THF is a reasonable surrogate for the pentose sugar in DNA and RNA.

11.2 Experimental Aspects

Experiments where projectile electrons undergo single collisions with target molecules with a well-defined initial state must take place in a vacuum environment such that the mean free path of all particles is larger than the dimensions of the spectrometer. Under these conditions mono-energetic and collimated electron beams can be produced and directed to a target molecular beam. In the overlap region reactive scattering processes take place. The reaction products namely electrons and ions can travel towards mass and energy analyzers and are subsequently registered by detectors. Such a crossed beam experiment is sketched in Fig. 11.1. Since the projectile beam is coming in along a particular direction all charged particles emerging from the gas target and going to other directions are collision products. These can be analyzed in their mass, charge state, kinetic energy and emission angle by means of electron and ion spectrometers.

Fig. 11.1 Schematics of an electron scattering apparatus in form of a crossed beam arrangement



From the different types of existing spectrometers we will briefly introduce two, the electrostatic spectrometer and the time of flight spectrometer. The working principle of the electrostatic energy analyzer is demonstrated in Fig. 11.2a. Here a deflecting electron analyzer in form of a parallel plate capacitor is shown. It is based on two parallel conducting plates from which one is electrically grounded and the other is on negative voltage U_{sp} such that a homogenous electric field is produced in between. The electrons start from a source point O and enter the field region where they are deflected. They leave the spectrometer through an aperture and for a particular kinetic energy reach a detector at point D. In this way the electron kinetic energy is reflected in the distance z . The signal intensity can be maximized if the spectrometer has focusing properties. As is shown in Fig. 11.2b for the polar angle ϑ in the vicinity of 45° the distance z in first order is independent of variations of ϑ such that a certain angular range is focused, e.g. onto a detector slit. The signal intensity can be further increased if focusing is also achieved in azimuthal φ direction. Therefore, instead of planar plates cylindrical plates are used which have their common cylinder axis on the connecting line from the electron origin to the spectrometer focusing point. This kind of spectrometer was named cylindrical mirror analyzer (CMA). Finally, we briefly mention a type of electrostatic analyzer where two concentric hemispherical plates form the electric deflection field and which, therefore, is named hemispherical analyzer. Principally, these energy analyzers can be used also as monochromators in order to produce rather mono-energetic incoming projectile beams. The disadvan-

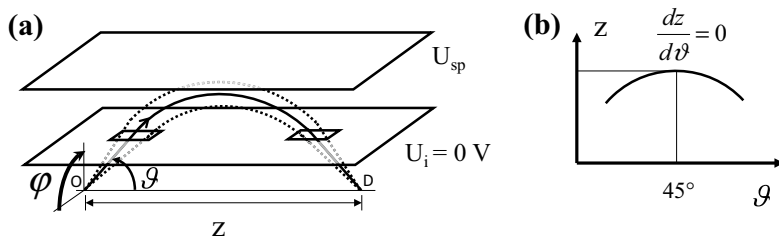


Fig. 11.2 **a** Scheme of a deflecting electrostatic electron energy analyzer in form of a parallel plate capacitor. The bottom plate is grounded, the upper plate is on negative potential U_{sp} . **b** Flight distance z as function of ϑ . For incoming electron angle $\vartheta = 45^\circ$ the distance z is in first order independent of ϑ

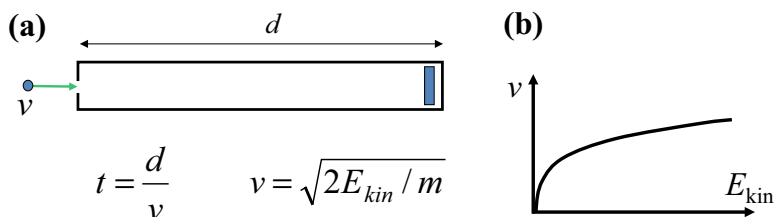


Fig. 11.3 Working principle of a time-of-flight spectrometer, **a** spectrometer scheme and basic relations between the traveling distance to the detector d , the particle velocity v and time-of-flight t , **b** the velocity v of a particle as function of its kinetic energy E_{kin}

tage of this kind of analyzers is their low detection efficiency due to a small solid angle coverage which is in the order of a few percent of the full solid angle or below.

In contrast to these deflecting field analyzers a second kind of spectrometer uses the time-of-flight (TOF) technique as illustrated in Fig. 11.3. It relies simply on the time of flight measurement of electrons or ions which have to travel a defined distance d from their origin to the detector. The TOF t is inversely proportional to the velocity v which in turn is proportional to the square root of the kinetic energy E_{kin} . As result for a given TOF resolution this spectrometer has a particularly good energy resolution at low electron energies while electrostatic spectrometers are superior at higher energy above few electron volts (eV). The TOF measurement can only be performed if the starting time of the collision product is known. Therefore, e.g. the projectile beam has to have a pulsed time structure or a simultaneous measurement of the scattered projectile is required.

In order to obtain the maximum information on a reaction it would be desirable to obtain the full kinematical information of a collision. Therefore, the momentum vectors (which is equivalent to the kinetic energies and directions) of all final state particles have to be determined. This can be done in coincidence experiments where two or more spectrometers are combined. Then, the time-correlated detection of several particles can indicate that they stem from the same collision event. For single ionization there are two electrons and one ion in the final state (Eq. 11.3). From momentum conservation and for known projectile momentum the detection of the two electron momenta in the final state is sufficient to fix the residual ion momentum and to perform a kinematically complete, so-called (e, 2e) experiment. While this technique has been used for many years to study the details of electron impact ionization it is essentially limited to the coincident detection of two particles. This is because the combined detection efficiency of several spectrometers which is the product of the individual efficiencies is very low. Therefore, for multi-particle coincidences which are required to study double ionization or if the ion has to be detected to identify molecular fragmentation more efficient spectrometer techniques have to be applied. In the following we present a highly efficient multi-particle imaging technique which was named reaction microscope since it allows very detailed views into atomic and molecular multi-particle fragmentation processes (Ullrich et al. 2003).

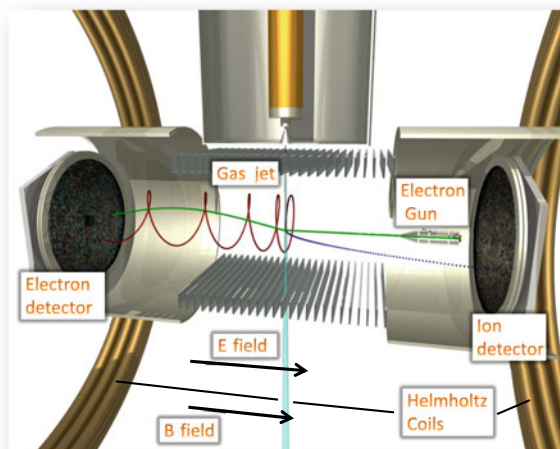


Fig. 11.4 Schematics of a reaction-microscope (Ullrich et al. 2003). An electron gun produces a pulsed electron beam (horizontal, green) crossing a target gas jet (vertical, cyan). Secondary particles are registered by an electron detector (left) and an ion detector (right)

Figure 11.4 shows a scheme of the reaction-microscope which is an extension of the above mentioned TOF technique. As in the conventional techniques in the center a pulsed and mono-energetic electron beam crosses a collimated target gas beam at right angle. The overlap region constitutes the reaction zone where the ionizing collisions take place. As a new ingredient an electric field which is produced by electrodes above and below the collision zone accelerates the electrons and ions to opposite directions and guides them to detectors. The micro-channel plate detectors with 8 cm active diameter can register the TOF and the hit positions of the particles. From these quantities it is possible to reconstruct the initial start directions and velocities (the linear momentum vectors) and, therefore, the full kinematics of the collision. It is mandatory that the experimental conditions are chosen such that the probability to cause more than one ionizing collision per projectile pulse is small. Then, all detected particles can be assigned to a single ionization process. Again due to the requirement that electrons and ions travel unhindered over macroscopic distances this technique requires high-vacuum conditions and furthermore gaseous target species. So far smaller molecules which can be brought to the gas phase by heating were studied. In future sources for larger biomolecules will be employed as, e.g., the commonly used electrospray technique (ESI) or matrix assisted laser desorption (MALDI) (Gross 2011). On the other hand the presently employed supersonic gas jet technique provides molecules with internal temperatures in the 10 K range far below room temperature. As result some internal degrees of freedom of the molecules can be frozen and the molecule can be provided in more specific initial conformations. In addition, as will be discussed below clusters can be produced, i.e., aggregates or droplets of few to many molecules which allow to study how electron

induced reactions change in going from monomers to the condensed phase and how they depend on the environment. An example is the comparison of ionization of monomers and hydrated molecules briefly discussed below which can show how an aqueous environment enhances or quenches reactions.

11.3 Electron Impact Excitation

Excitation normally does not produce ionic fragments which can be detected and therefore a preferred way to obtain insight is the analysis of the scattered projectiles concerning energy loss and scattering angle. Molecules can be excited electronically but also rotationally and vibrationally (rovibrationally). An exemplary spectrum obtained with electron energy loss spectroscopy (EELS) is shown in Fig. 11.5 for excitation of rovibrational modes of gaseous THF (THF, C_4H_8O). The measurement was performed by M. Allan at Fribourg University/Switzerland (Allan 2007) for 6 eV impact energy and covers the low energy loss region up to about 1 eV. An excellent total energy resolution of 20 meV was achieved due to the usage of an electrostatic hemispherical monochromator and a respective energy analyzer. For the considered low energy loss only rovibrational modes are excited while the excitation of molecular electrons to higher states requires more energy. A number of rather well resolved lines are found with energies which are characteristic for the vibrational modes of THF. A ring bending mode with low frequency and, therefore, low vibrational energy is found as well as stretch vibrations between the heavier carbon atoms and higher energy modes involving hydrogen atoms. Similar experiments could also be per-

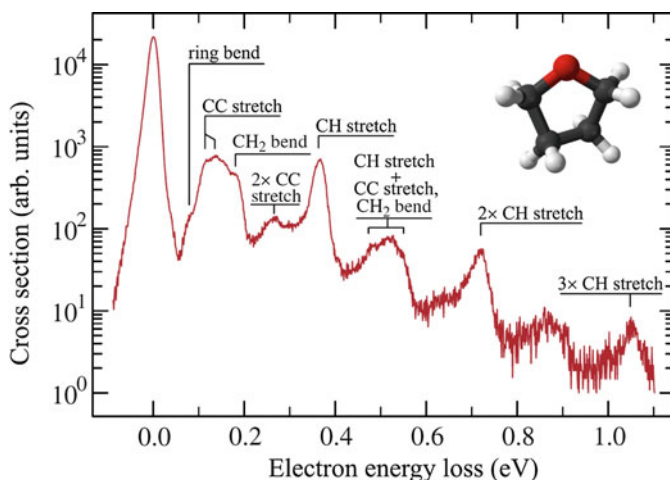


Fig. 11.5 Electron energy loss spectrum for tetrahydrofuran. The incident energy is 6 eV, the electron scattering angle is 135° (Allan 2007)

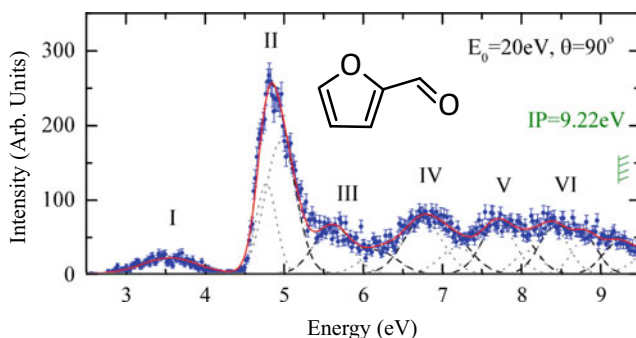


Fig. 11.6 Electron energy loss spectrum for furfural for $E_0 = 20$ eV impact energy and $\theta = 90^\circ$ projectile scattering angle. From the shape of the spectrum six different bands can be identified and assigned to various orbital excitation processes (Ferreira da Silva et al. 2015). IP: ionization energy

formed in the condensed phase by deposition of a monolayer of THF molecules on a surface within a vacuum environment. Again a mono-energetic electron beam was directed to the surface and the backscattered electrons were analyzed with an electron spectrometer (Lemelin et al. 2016).

For higher energies transferred to the molecule also bound molecular electrons can be excited to energetically higher lying states. Figure 11.6 shows an energy loss spectrum for furfural (2-furaldehyde, $C_5H_4O_2$) (Ferreira da Silva et al. 2015). The interpretation of such spectra can be rather challenging since the lines for different excited states strongly overlap due to their large number and their large energy widths as can be seen from the dashed and dotted Gaussian lines which are fitted to the experimental data. In the spectrum shown line II corresponds to the excitation of the highest occupied molecular orbital (HOMO) to the lowest unoccupied orbital (LUMO) while the lines III–VI involve also excitation of stronger bound electrons and higher lying excited states.

An interesting aspect of electron scattering is the so called exchange effect. Here during the collision both, projectile and a target electron can exchange their role such that the projectile becomes bound and the target electron is ejected. This process becomes particularly strong if the incoming or outgoing projectile is slow, i.e. at energies up to a few eV and below. As result of the exchange process also the spin of the bound electrons can change which results in so-called triplet states where the spins of two bound unpaired electrons are parallel. Line I in Fig. 11.6 is assigned to the excitation of such a triplet state in furfural and this is confirmed by the observation that its intensity relative to the other lines goes down strongly for faster projectiles where the exchange effect is suppressed. Also in photo-absorption where triplet states are not excited this feature is not observed.

Another phenomenon of low energy electron scattering are resonances found in the cross sections or intensities of the various excitation processes which manifest if they are measured as function of the impact energy. At the resonance energies the projectile can be temporarily trapped and the molecule forms a transient negative ion.

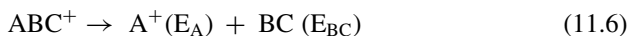
The trapping can be due to the shape of the molecular ground state potential (shape resonance) which might be accompanied by exciting a valence or core electron (core-excited shape resonance, Feshbach resonance). At these resonances the molecule can show enhanced dissociation into a negative ion and neutrals. This process is called dissociative electron attachment (DEA).

11.4 Electron Impact Ionization

In electron impact ionization a projectile electron scatters off a molecule and transfers sufficient kinetic energy to one or more bound electrons that they can escape from the molecular potential and become unbound with some excess kinetic energy E_2 (Eq. 11.3). Thus, the projectile with energy E_0 in the initial state has a reduced energy E_1 in the final state. The projectile energy loss ($E_0 - E_1$) corresponds to the ionization or binding energy E_b energy plus the kinetic energy of the ejected electron E_2 . Therefore, the binding energy E_b of the ionized orbital can be determined by

$$E_b = E_0 - E_1 - E_2. \quad (11.5)$$

The residual ion due to its high mass compared to electrons obtains only little kinetic energy in the collision which is neglected here. Its momentum on the other side can be comparable to the ionized electron. The ionizing collision takes place on a timescale much shorter than any molecular dynamics such that the possible fragmentation of the molecular ion can be considered as a subsequent process



Here the kinetic energies E_A and E_{BC} can be considerable and in the few eV range. The initial and final state of the complete reaction is illustrated in Fig. 11.7 for ionization and break-up of THF in two fragments.

In order to measure all relevant quantities of this reaction the above described multi-particle imaging technique can be utilized. A reaction microscope can measure the vector momenta of both final state electrons and therefore, also their kinetic energies are known. As consequence the binding energy E_b of the initially bound electron is obtained according to Eq. 11.5 and the ionized molecular orbital can be identified. In addition the knowledge of the electron emission angles can give insight into the collision dynamics and the interactions of the projectile and ejected electron with the numerous other molecular constituents. These interactions play no role if the incoming and outgoing projectile and the ionized electron have high energies. In this case the collision can be described as a pure binary knockout of the bound electron with momentum transfer known from the projectile scattering angle. Then, from the measured momenta of the electrons and taking into account momentum conservation the momentum of the ionized electron in its initial bound orbital can be determined. As a consequence the quantum mechanical wave function of the electron

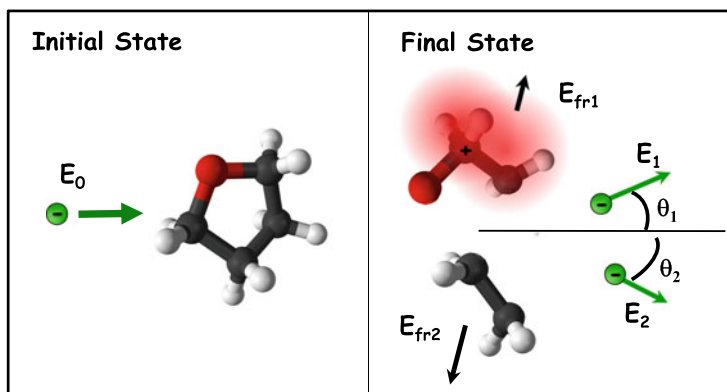


Fig. 11.7 Initial and exemplary final state of electron impact ionization of a molecule (here tetrahydrofuran, C_4H_8O)

orbital can be obtained. This technique is called electron momentum spectroscopy (EMS) (McCarthy and Weigold 1976) and has been applied to atoms, molecules and also to solids.

In addition to the electrons the reaction microscope can detect the residual ion and its mass over charge ratio as well as its momentum and kinetic energy. Therefore, the different molecular ion fragmentation channels are identified. Figure 11.8 presents exemplary spectroscopic data obtained for ionization of THF at $E_0 = 27$ eV impact energy (Ren et al. 2014). The top panel (a) shows the mass spectrum of the fragment ions. In addition to the parent ion which causes a peak at mass 72 amu there is a hydrogen loss reaction producing a peak with similar intensity at mass 71 amu. Furthermore, there are various ring cleavage channels which result in two line groups of ions which differ in the number of heavy atoms (O and C). The lines within each group differ by the number of hydrogen atoms. One line group with two carbon atoms or one carbon and one oxygen atoms is found in the mass range from 27 to 31 amu and a second group with three heavy atoms is found in the range 39–44 amu. The fragmentation of larger molecular ions like THF^+ mostly follows from the transfer of electronic excitation energy (which is present if an inner-valence orbital is ionized) into vibrational modes of the ion. The subsequent fragmentation can be well described by the so-called statistical unimolecular decay. Here the rate to overcome a particular reaction (dissociation) barrier is obtained by considering how likely it is that the energy distributed among all vibrational modes gathers in the mode leading to dissociation. Therefore, the binding energy of the ionized orbital determines the subsequent fragmentation channel.

In in panel (b) of Fig. 11.8 for each THF ion fragment the associated binding energy distribution obtained with Eq. 11.5 is shown. It is obvious that the stable parent ion correlates with rather low binding energy slightly below 10 eV while fragmentation and in particular ring breaking reactions require the ionization of orbitals with higher binding energies. A typical example for the unimolecular statistical fragmentation is

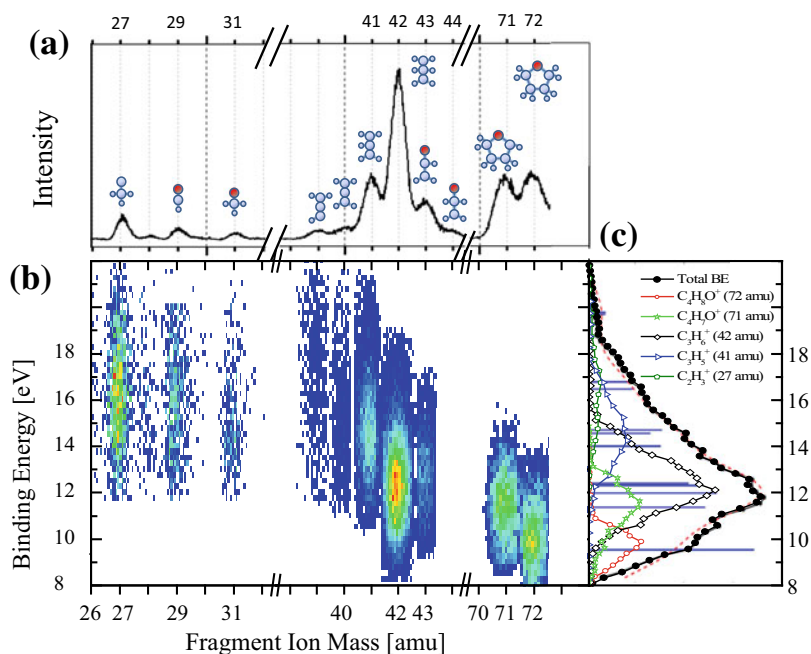


Fig. 11.8 Spectroscopic data for electron impact ionization of tetrahydrofuran. **a** Fragment ion mass spectrum. The fragment structures of the ions with particular mass are shown. **b** For each ionic fragment mass the ionized orbital binding energy spectrum is shown. **c** Summed and individual binding energy spectra for particular ionic fragments. Blue bars are theoretical state energies and respective ionization cross sections (Ren et al. 2014)

the sequence of peaks assigned to $C_3H_6^+$, $C_3H_5^+$, $C_3H_4^+$, $C_3H_3^+$ with masses $m = 42$ – 39 amu. For this sequence the measured binding energies increase monotonically. This illustrates that the more internal energy is available the more hydrogen atoms can be abstracted in the final state. Also the kinetic energy distributions of the ions (not shown here) extend to higher energies for the lighter fragments due to the increasing recoil from the larger number of hydrogen emission processes (Ren et al. 2014). In the right panel (c) of Fig. 11.8 the experimental individual binding energy spectra are shown together with theoretically calculated ionization energies which are shown as blue lines. The lengths of the lines indicate the theoretical relative cross sections for ionization of the orbitals (Irikura 2017). Apparently the ionization cross section decreases for increasing binding energy of the orbitals which is a general phenomenon for electron impact ionization. Additionally the cross section decreases if the binding energy approaches the projectile energy due to threshold effects which we do not discuss here. From the binding energy spectrum of the orbitals it becomes clear that the high intensity of the $C_3H_6^+$ channel is due to the large number of states with binding energies around 12 eV which provide the required internal energy for this particular fragmentation channel.

These results illustrate that electron impact spectroscopy with the coincident detection of several fragments can provide very detailed information on molecular ionization and the subsequent fragmentation reactions. Nevertheless, it remains a question how the reactions which are observed in the gas phase are modified if the same molecule is in the condensed phase or in solution like in an aqueous environment.

11.5 From Single Molecules to Clusters

In order to better understand the molecular reaction dynamics in biological systems it would be desirable to study electron impact ionization not in the gas phase but in a condensed target. One approach which allows applying the experimental toolset introduced above is to use gas targets containing clusters which are aggregates of several up to large numbers of molecules. As mentioned above these can be produced in supersonic gas jets where a gas at high stagnation pressure of several atmospheres expands through a small nozzle into the vacuum. The adiabatic expansion results in a strong temperature decrease of the gas and a radial motion away from the nozzle. Depending on the gas jet parameters the formation of clusters with different sizes up to small droplets can be achieved. To illustrate that the molecular fragmentation dynamics can be different for monomers and in the condensed phase here we compare results for different supersonic jet target beams. In one experiment pure THF vapor is used and in the other experiment a mixture of THF and water vapor is used. In both cases small clusters are formed since THF molecules bind to each other or to water by forming hydrogen bonds between the negatively charged oxygen in the THF ring and the positive excess charge at hydrogen atoms of the neighbor. The fraction of clusters was a few percent and consisting mainly from dimers. Typical fragment ion mass spectra are shown in Fig. 11.9 for the pure THF beam (black line) and for a mixed THF and water jet (red line). For the pure THF target several peaks corresponding to masses above the parent THF ion at 72 amu are found. There is the protonated parent ion $(\text{THF} + \text{H})^+$ at mass 73 amu, as well as the protonated dimer $(\text{THF}_2 + \text{H})^+$ at mass 145 amu. Protonated species are regularly found for hydrogen bonded clusters due to the rather low reaction barriers for proton transfer across the hydrogen bonds. The mass spectrum also shows the product $(\text{THF} + \text{C}_2\text{H}_4\text{O})^+$ at 116 amu corresponding to a ring-break reaction. Interestingly, no stable dimer ion THF_2^+ is found. As described above the internal energy required for the different channels can be obtained from the binding energy spectra (not shown here). It turns out that the ring-break product $(\text{THF} + \text{C}_2\text{H}_4\text{O})^+$ requires only $E_B = 9.7$ eV which corresponds to the binding energy of the outermost (HOMO) orbital of the THF monomer. Therefore, we see a new fragmentation behavior since as seen in Fig. 11.8 HOMO ionization for the THF monomer results in stable THF^+ ions and a ring-break reaction providing $\text{C}_2\text{H}_4\text{O}^+$ requires about 12.5 eV, i.e. more than 2.5 eV higher energy than for the dimer.

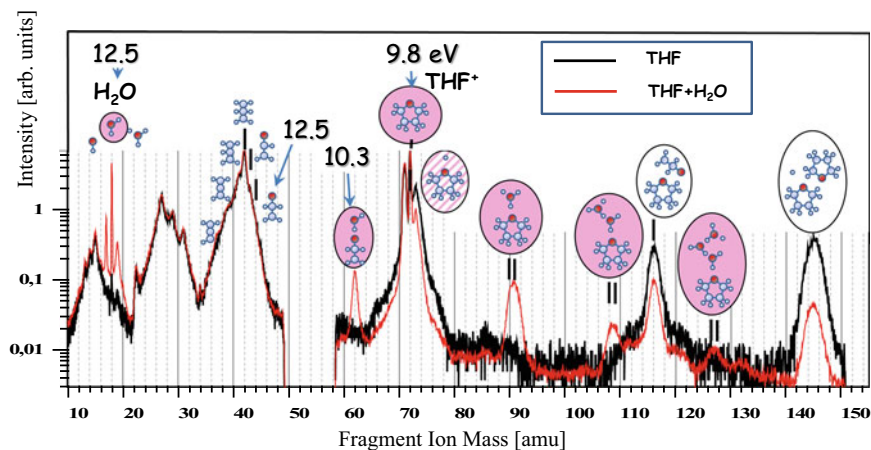


Fig. 11.9 Ion mass spectrum for electron impact ionization of a THF gas target produced in a supersonic gas jet (black line). The red line shows the mass spectrum if water vapor is admixed to the THF gas. Compared to the spectrum in Fig. 11.8 the mass range shown is extended to 150 amu. For selected fragment ions the binding energy of the ionized electron orbital is given (see text)

The mass spectrum obtained for the mixed THF-water clusters shows a number of peaks with one or several water molecules bound to the intact THF ring. All are protonated which again shows that proton transfer is an important reaction channel after ionization of hydrogen bonded systems. As for the THF-cluster spectrum a ring-break product ($\text{H}_2\text{O} + \text{C}_2\text{H}_4\text{O}$)⁺ is found and this channel requires 10.3 eV energy transfer which is again a considerably reduced reaction barrier compared to the non-hydrated THF molecule. Quantum chemical calculations confirm that the reaction barrier for ring-opening of THF is significantly reduced in the dimer systems since if the THF ring opens the hydrogen bond lengths are reduced and, therefore, strengthened.

Finally, it should be mentioned that in going from single molecules to molecular aggregates more reaction pathways become available which involve close-by molecules. One prominent example is the intermolecular Coulombic decay (ICD) where one molecule is ionized in an inner valence orbital. If this vacancy is filled by an electron from an outer valence orbital the released energy can be transferred to a neighboring molecule ionizing it as well. This reaction was observed in diverse aggregates and also in the THF·H₂O dimers (Ren et al. 2018). Here it can be identified by the appearance of two ions, THF⁺ and H₂O⁺ which are emitted back-to-back due to their mutual repulsion in a so-called Coulomb explosion.

11.6 Summary

In this article we have introduced possible elementary reactions caused by electrons colliding with molecules. The understanding of these reactions and the knowledge of their abundance is of paramount importance for fundamental science, for various applications and also for life sciences. Using electron impact spectroscopy the collisions take place under well-defined and preselected conditions and the reaction products are analyzed in mass, direction and energy with different spectroscopic methods. Some basic techniques have been briefly introduced as the different types of electrostatic electron energy spectrometers, the time-of-flight spectrometer and the reaction-microscope which is suitable to detect two or more charged fragments emerging from one collision. Exemplary experimental results of the various possible impact-induced reactions have been presented. It is clear that while gas-phase experiments provide valuable information they are limited in not accounting for condensed phase effects and in the size of molecules which can be studied. The first limitation can be partly overcome by using target beam preparation techniques which provide clusters or small droplets. Another approach would be to deposit the molecules of interest on a substrate surface and irradiate this surface by an electron beam. This method also allows for investigation of larger molecules which cannot easily be brought to the gas phase and was successfully applied to study single and double strand breaks in DNA induced by low energy electron impact (Boudaïffa et al. 2000). Therefore, electron impact spectroscopy can give very detailed insight in the collision processes and the initiated molecular dynamics and also can be very a valuable bioanalytical tool.

References

- Allan M (2007) Absolute angle-differential elastic and vibrational excitation cross sections for electron collisions with tetrahydrofuran. *J Phys B* 40:3531–3544
- Boudaïffa B, Cloutier P, Hunting D et al (2000) Resonant formation of DNA strand breaks by low-energy (3–20 eV) electrons. *Science* 287:1658–1660
- Ferreira da Silva F, Lange E, Limão-Vieira P et al (2015) Electronic excitation of furfural as probed by high-resolution vacuum ultraviolet spectroscopy, electron energy loss spectroscopy, and ab initio calculations. *J Chem Phys* 143:144308
- Gross JH (2011) *Mass spectrometry*. Springer, Berlin, Heidelberg
- Irikura KK (2017) Ab initio computation of energy deposition during electron ionization of molecules. *J Phys Chem A* 121:7751–7760
- Lemelin V, Bass AD, Cloutier P et al (2016) Absolute vibrational cross sections for 1–19 eV electron scattering from condensed tetrahydrofuran (THF). *J Chem Phys* 144:074701
- McCarthy IE, Weigold E (1976) (e, 2e) spectroscopy. *Phys Rep* 27:275–371
- Ren X, Pflüger Th, Weyland M et al (2014) An (e, 2e + ion) study of low-energy electron-impact ionization and fragmentation of tetrahydrofuran with high mass and energy resolutions. *J Chem Phys* 141:134314

- Ren X, Wang E, Skitnevskaya AD et al (2018) Experimental evidence for ultrafast intermolecular relaxation processes in hydrated biomolecules. *Nat Phys* 14:1062–1066
- Ullrich J, Moshhammer R, Dorn A et al (2003) Recoil-ion and electron momentum spectroscopy: reaction-microscopes. *Rep Prog Phys* 66:1463–1545

Part II
Reaction Kinetics and Modelling

Chapter 12

Charge Transfer Processes in Key Biological Systems



Filipe Ferreira da Silva, Mónica Mendes, Gustavo García
and Paulo Limão-Vieira

12.1 Introduction

The interaction of high-energy ionising radiation (e.g. X-rays, γ -rays, ions, protons and electrons) with biological systems generates a large amount of secondary species along the radiation track. Briefly, the primary high-energy ionising radiation interaction with living organisms occurs on a time scale triggers within the early stages of irradiation ($\sim 10^{-16}$ to 10^{-15} s), multiple sequences of physical and chemical reactions, resulting mainly in electronic excitation and ionisation of the molecular constituents, with subsequent bond breaks creating large amounts of secondary electrons and radicals. The damage in DNA macromolecule created by these secondary species are characterized by single strand breaks (SSB), double strand breaks (DSB), clustered damage, base damage and loss of the supercoiled helix integrity. The consequences of these injuries in a long-term time scale can lead to severe consequences, namely mutations, chromosome aberrations, cell inactivation and other effects that compromise the genome integrity which may even result in cancer (Goodhead et al. 1993; Goodhead 1994; Nikjoo et al. 1997; Little 2000). Given this complexity, a complete understanding of these processes represents a challenging task.

F. Ferreira da Silva · M. Mendes · P. Limão-Vieira (✉)

Atomic and Molecular Collisions Laboratory, CEFITEC, Department of Physics, Faculdade de Ciências e Tecnologia, Universidade NOVA de Lisboa, 2829-516 Caparica, Portugal
e-mail: plimaovieira@fct.unl.pt

F. Ferreira da Silva

e-mail: f.ferreiradasilva@fct.unl.pt

M. Mendes

e-mail: mf.mendes@fct.unl.pt

M. Mendes · G. García

Instituto de Física Fundamental, Consejo Superior de Investigaciones Científicas (CSIC), Serrano 113-bis, 28006 Madrid, Spain
e-mail: g.garcia@csic.es

© Springer Nature Switzerland AG 2019

A. S. Pereira et al. (eds.), *Radiation in Bioanalysis*, Bioanalysis 8,
https://doi.org/10.1007/978-3-030-28247-9_12

329

It is now well-established that low-energy electrons (LEE) can act as primary damage agent in biological medium or induce indirect reactions through the interaction with other molecules, e.g. water or oxygen molecules, producing large quantities of highly reactive species (radicals, cations and anions). Typically, 5×10^4 secondary electrons (<20 eV) are produced per MeV of primary radiation (Cobut et al. 1998; Uehara et al. 1999; Swiderek 2006; Alizadeh et al. 2015). Along the track and due to successive inelastic interactions with the medium, these secondary electrons transfer their kinetic energy until they reach a near-zero energy (thermalisation) prior to undergoing solvation (Alizadeh and Sanche 2012; Neustetter et al. 2015). At this energy range, different electron induced processes can occur yielding different levels of molecular alterations, either producing ionisations (energies typically above 7 eV), bond rupture or resonant attachment, among several others.

In order to understand the mechanisms induced by radiation in biosystems it is necessary to describe the atomic and molecular processes involved in such interactions, through the knowledge of number of dissociative events, type of interactions, neutral and ionic species created, energy deposition, angular distribution functions and cross-section values. This comprehensive information is highly relevant to the use of radiation in medicine, namely for the development of new radiation treatments and production of new molecular compounds (Limão-Vieira et al. 2012). A pioneering study, performed by Boudaïffa et al. (2000) (updated by Huels et al. 2003), has demonstrated that electrons with energies up to 20 eV are capable to induce SSB and DSB in plasmid DNA. This study has also established that DNA damage is highly dependent on the initial kinetic energy of the incident electron, particularly below 15 eV, and even that SSB and DSB yields in the region of 7–10 eV incident electrons are one to two orders of magnitude larger than those for 10–25 eV photons. Since the quantum yields for DSBs and SSBs show a resonant-like behaviour with electron energy, electron attachment to DNA subunits was proposed to be the initial degradation step (Martin et al. 2004). Another relevant aspect of the recent experimental DEA studies to DNA pyrimidine bases (Ptaśńska et al. 2005b) is that the process is both bond (C–H vs. C–N) and site selective (N1–H vs. N3–H) as to the abstraction of an hydrogen atom. Thus, a new mechanism for DNA damage has been established where dissociative electron attachment is the prevalent mechanism in the electronic interaction with biomolecules after irradiation.

Electron attachment is set as a direct electron capture by a target molecule leading to formation of a transient negative ion (TNI) with a lifetime of $\sim 10^{-16}$ s (Denifl et al. 2012). The process is considered as a resonant scattering, which means that the energy of the incident electron must be exactly the energy necessary to reach a *quasibound* state of the molecular target (resonance) (Illenberger and Mominy 1992). The formation of a TNI represents a transition in the Franck-Condon region from the electronic ground state of the neutral molecule (ABC) to the potential energy surface of the molecular anion (ABC⁻). The TNI has a very short lifetime which depends on the size of the molecule as well as the width of the resonance according to the Heisenberg's uncertainty principle. As the TNI is unstable it can decay through three different channels: radiative stabilization, auto-detachment and dissociation (Eq. 12.1). DEA occurs when the TNI decay results in bond-breaking

yielding anions and one (or more) neutral species, such process typically occurring on a timescale of 10^{-14} to 10^{-12} s (Illenberger and Momigny 1992). In other words, the TNI dissociates through the instability created by the extra electron, adding an excess of internal energy to the neutral molecule, which is initially captured into an unoccupied molecular orbital (anti-bonding) and has the capability to change the intramolecular potential and. It is a competitive process with auto-detachment.



where, ABC stems for the polyatomic target molecule and $(ABC)^{-\#}$ for the TNI with an excess of internal energy.

However, many elementary collisional processes are not direct electron impact but rather depend upon electron transfer, the latter certainly more prevalent under biological conditions. In this context, the studies on molecular damage by free electron attachment processes must be complemented with studies on electronic capture of “bound” electrons (as in atom-molecule collisions).

Studies on electron transfer experiments using several complex molecular targets were previously performed showing the influence of a third body (cationic projectile post-collision) as stabiliser agent leading to different reaction channels as in contrast to DEA. Such observations were verified by Antunes et al. (2010) in a former study on nitromethane as a molecular target, where formation of a parent anion ($\text{CH}_3\text{NO}_2^{-}$) was detected in contrast to DEA studies. Other relevant studies dealt with tuning the collision energy of the hyperthermal neutral potassium beam in collisions with methylated and deuterated pyrimidine molecules. In these studies, Almeida et al. (2013a) have shown that H^{-} loss proceeds not only through the breaking of the (C–H) against (N–H) bonds but also through N1 against N3 sites. These results have shown that electron transfer to pyrimidines is also site and bond-selective (Almeida et al. 2013a). Furthermore, these authors have also studied D-Ribose (Almeida et al. 2013b) and THF (Almeida et al. 2014) where major enhancements in the formation of OH^{-} and O^{-} were observed compared to DEA experiments. Investigation on gas-phase thymine and uracil molecules by Almeida et al. (2011) also provide information about the dissociation channels and the fragmentation pattern by electron transfer as well as CNO^{-} formation as the major ring breaking anionic product for both molecules. These findings lead to novel methods in controlling chemical reactions with respect to the atomic and molecular mechanisms involved in biological damage caused by secondary electrons (Almeida et al. 2013a).

As previously mentioned, LEE are capable of inducing chemical and physical alterations in the main molecular components of cells. Within these set of molecular constituents, we find the proteins. Proteins are important structural and functional biomolecules that are a major part of every cell consisting of long chains of building block molecules termed amino acids. The amino acids can combine with each other forming chains assembled in a specific way producing a three-dimensional protein with a specific cellular function. The amino acids and subsequently proteins are close related with DNA and RNA molecular structures in a protein synthesis (Frauenfelder

2010) process. Thus, it appears essential to investigate the role of LEE interactions on proteins and their constituents to fully understand the direct and indirect mechanism of radiation induced damage processes in proteins and, consequently, in DNA.

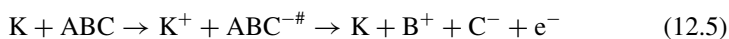
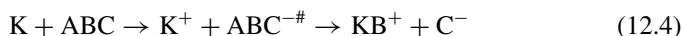
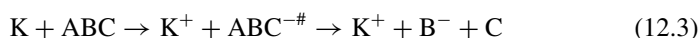
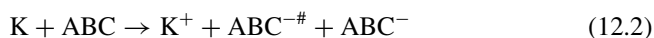
The alterations induced by LEE (<40 eV) in aliphatic amino acids (glycine, alanine and cysteine) adsorbed on a Pt substrate were investigated through mass spectrometry experiments (Abdoul-Carime and Sanche 2004). For energies below 15 eV the anions produced were due to DEA processes while above 15 eV, the anion desorption was mainly assigned to non-resonant dipolar dissociation. Negative anions formation from thin condensed films of aromatic amino acids, such as tryptophan, histidine and proline, were also studied by electron impact (Abdoul-Carime and Sanche 2003), showing the dominance of DEA processes at low energy. These studies have revealed that the fragmentation yield of amino acids was found to be as intense as that of the nucleic acid bases. Studies in gas-phase amino acids were also performed by different research groups, where decomposition of tryptophan by LEE attachment (<10 eV) was investigated by means of a crossed electron/molecular beam experiment demonstrating that the most predominant dissociation processes occur at sub-excitation energies (Abdoul-Carime et al. 2005). Many other gas-phase amino acids were also investigated by dissociative electron attachment (Gohlke et al. 2002; Ptasíńska et al. 2003, 2005a; Papp et al. 2006; Mauracher et al. 2007; Scheer et al. 2007; Ferreira da Silva et al. 2010; Muftakhov and Shchukin 2010) and electron impact ionisation (Papp et al. 2012). Electron transmission spectroscopy measurements were carried out on several amino acids in order to investigate the vertical attachment energies for the formation of low-lying temporary anion states, where attachment to the empty π^* orbital of the $-\text{COOH}$ group was assigned in all the molecular targets probed (Aflatooni et al. 2001). Other studies include electron impact ionisation of gas-phase and hydrated valine (Denifl et al. 2009), theoretical calculations were also performed to calculate the cross-section for elastic scattering by glycine (dos Santos et al. 2012) and alanine (Loupas and Gorfinkiel 2019) as well as a comprehensive analysis of the decarboxylation mechanism of amino acids with and without water (Li and Brill 2003).

Concerning electron transfer processes in gas-phase amino acids, studies were performed in atom-molecule collisions showing several differences as to the fragmentation pattern compared with free electron attachment measurements (Ferreira da Silva et al. 2010, 2014, 2016). Such experimental studies will be comprehensively discussed in this chapter.

In the next section we will discuss the main aspects about electron transfer processes in atom-molecule collisions. Further, we will briefly introduce and describe the experimental setup used in collisions with neutral potassium atoms and several molecular targets. Finally, we provide measurements of potassium collisions on different amino acids (e.g. tryptophan, tyrosine, glycine, alanine and uridine) as well as on acetic acid. We will finish with concluding remarks.

12.2 Fundamental Aspects of Electron Transfer Processes

In atom-molecule collisions the electron is not free but weakly bounded to a neutral atom, which acts as an electron donor. In such collisions, the electron is transferred from the neutral atom (e.g. alkali) to a neutral molecular target, and a negative ion is formed as part of an intermediate step or as a final product. Alkali atoms have very low ionisation energies and are therefore excellent electron donors. The alkali atom in the present case is a potassium atom (K), which has a low ionisation energy ($IE(K) = 4.34$ eV). After the electron transfer process in the interaction of the alkali atom with the molecule, several reaction channels can be accessed, such as non-dissociative ionisation (Eq. 12.2), dissociative ionisation (Eq. 12.3), associative chemionisation (Eq. 12.4) and polar dissociation (Eq. 12.5).



The electron transfer process may also be described in two separate stages. First, it is necessary for the alkali atom to undergo ionisation in the vicinity of the target molecule. The ejected electron must then be captured by the molecular target leading to formation of a transient negative ion. The electron transfer processes happens when, at small atom-molecule distances the stationary non-perturbed states, the covalent and ionic diabatic states have the same potential energy surface value (termed crossing point). In first approximation the rotational and vibrational periods are considered *zero*, which means that the molecular target is “frozen” (the molecule is rigid during the collision). This assumption is valid if the atom-molecule potential is isotropic and the electronic properties of the molecule, especially its electron affinity, are independent of its internal degrees of freedom. This is true in the case that the vibrational time is much larger than the collision time. When the collision time is approximately identical to the vibrational time, the second crossing radius is different from the first and the probability of a diabatic transition at the second crossing increases as well as ion-pair formation (Kleyn et al. 1982). For large atom-molecule distances the ionic potential energy lies above the covalent potential and the endoergicity (ΔE) of the system is given by:

$$\Delta E = IE(K) - EA(ABC) \quad (12.6)$$

where $IE(K)$ is the potassium ionisation energy and $EA(ABC)$ is the electron affinity of the target molecule. The crossing radius (R_c) in Å can be determined through the following equation:

$$R_c = \frac{e^2}{\Delta E} = \frac{14.42}{\Delta E} \quad (12.7)$$

Consequently, in a reaction where a cation and an anion (ion-pair formation) are formed, only the lowest ionic state will be involved. On the other hand, it should be noted that in these processes the electron transfer is only possible between configurations of the same symmetry and multiplicity (Hubers et al. 1976; Kleyn and Moutinho 2001; Limão-Vieira et al. 2012). Indeed, the presence of a third body (cationic projectile post-collision) in the collisional mechanism acts as a “stabiliser” in the vicinity of the system (TNI) which leads to differences in the reactions pathways that are accessible when compared with free electron attachment processes.

12.3 Experimental Section

The negative ion time-of-flight (TOF) mass spectra were obtained in collisions of potassium atoms with glycine molecules in a crossed beam set-up configuration described elsewhere (Antunes et al. 2010). Briefly, an effusive molecular beam crosses a primary beam of fast neutral potassium (K) atoms. K^+ ions produced in a potassium ion source are accelerated to 20–100 eV in the lab frame. The K^+ beam passes through an oven where it resonantly charge exchanges with neutral potassium to produce a beam of fast (hyperthermal, K°) atoms. Residual ions from the primary beam are removed by electrostatic deflecting plates outside the oven. The intensity of the neutral potassium beam is monitored using a Langmuir-Taylor ionisation detector, before and after the collection of each TOF mass spectra. The glycine effusive beam was introduced into the collision chamber through a 1 mm diameter aperture, where it was crossed with the neutral hyperthermal potassium beam between two parallel plates at 1.2 cm mutual separation. The anions produced were extracted by a 250 V cm^{-1} pulsed electrostatic field. The typical base pressure in the collision chamber was $4 \times 10^{-5} \text{ Pa}$ and the working pressure was $2 \times 10^{-4} \text{ Pa}$ upon heating the powder sample. Mass spectra (resolution $m/\Delta m \approx 125$) were obtained by subtracting the background signal (without the heated sample) from the sample measurements. Mass calibration was carried out on the basis of the well-known anionic species formed after potassium collisions with the nitromethane molecule (Antunes et al. 2010).

Glycine samples used were purchased from Sigma-Aldrich with a minimum purity of 99% and used as delivered. The samples were heated to 428 K and the temperature was controlled using a PID unit. In order to test for thermal decomposition products in the target beam, mass spectra were recorded at different temperatures. No differences were observed in the relative peak intensities as a function of temperature. The extraction region and the TOF system were heated to approximately 393 K throughout measurements in order to prevent any sample condensation and thence charge accumulation on the electrodes.

12.4 Results

Here we describe a set of experimental results on electron transfer upon potassium collisions to gas phase biomolecules. Proteins, that are polymeric structures of amino acids, are present in every biological processes. The sequence of the amino acids in the protein determines their shape. The protein function is determined by the three-dimensional structure or conformation. To understand the function mechanism of proteins, it is essential to explore the structure and chemical properties of isolated amino acids and related molecules such as simple carboxylic acids.

The proteins of all organisms use the same 20 amino acids, as building blocks. Although the limited number of amino acids, its constitution confers different properties, and the order in which those are connected confers a limitless variety of proteins. The common 20 amino acids are α -amino acids since they have an amino and carboxylic group attached to the α -carbon. In Fig. 12.1 a representation of a general structure of an amino acid, where R is the side chain, is shown. Within the 20 amino acids present in the proteins, 19 are chiral molecules. Chiral molecules are asymmetric molecules, since they have four different groups bound to the α -carbon. The simplest amino acid, glycine, is the only among the 20 amino acids that exhibits two identical groups bounded to the α -carbon (glycine has two hydrogen atoms bounded to the α -carbon). The different R groups or side chains confer different properties to the amino acids. The 20 amino acids are organized according to their side chain group yielding therefore different properties. The side chains fall into the chemical classes of aliphatic, aromatic, sulphur containing, alcohols, basis, acids and amines (Horton et al. 1996). The mammals have a limited capability for amino acids' biosynthesis. They can produce only about half of the amino acids that they require; the others must be obtained from the in-take diet. As so, the essential amino acids are those that must be obtained from the diet and no-essential amino acids are those that mammals can synthesize in sufficient quantity for their survival.

Electron transfer studies upon potassium collisions with biological relevant molecules, have been performed comprehensively investigated over the last decade (Almeida et al. 2011, 2013b; Ferreira da Silva et al. 2013). In this chapter we describe the fragmentation patterns upon potassium collisions with acetic acid, aliphatic amino acids, such as glycine, alanine and valine, aromatic amino acid such as tyrosine

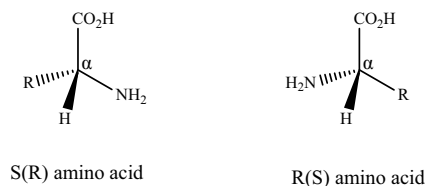


Fig. 12.1 General structure of an amino acid where R represents the side chain; depending on the type of side chain, the chiral form is represented by R or S; in brackets is the chiral form when R is heavier than acid group

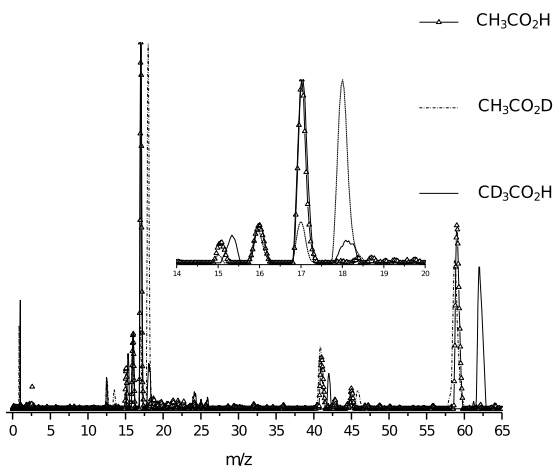
and tryptophan. Acetic acid, although is an intermediate product in the synthesis of acetyl-CoA, in its ionic form yields acetate, which is also a product in the amino acid cysteine biosynthesis from serine that occurs in bacteria and plants.

12.5 Acetic Acid

Acetic acid, ($\text{CH}_3\text{CO}_2\text{H}$, HAc) is one of the simplest molecules that can act as biological prototype and a possible building block of biomolecules, namely amino acids and proteins. Within organic molecules, such as formic acid, it is considered to be an important trace species in the Earth's atmosphere (Khare et al. 1999) and has been found in the interstellar medium (Wootten et al. 1992). Simple organic molecules play an important role in atmospheric pollution (Gallego et al. 2014; Welz et al. 2014), food (Theron and Lues 2007) and solvent chemical industry (Krupadam et al. 2011). Low-energy electron (LEE) interactions with simple molecules have been widely studied in recent decades (Flosadóttir et al. 2007; Tanzer et al. 2014). LEE can efficiently induce remarkably selective reactions followed by distinctive fragmentation not only via dissociative electron attachment (DEA) (Ptasińska et al. 2005c) but by electron transfer (ET) (Almeida et al. 2013a). HAc can also be used as a prototype system for comprehensive studies on the role of the carboxylic group in the fragmentation mechanisms of biological compounds, and its interactions with LEE provide an ideal system to study the fragmentation of more complex molecules, such as amino acids. Several experimental DEA studies of simple molecules as HCOOH and HAc (Sailer et al. 2003; Prabhudesai et al. 2005; Janečková et al. 2013), as well as several ET studies of simple amino acids, have been performed in order to explore how LEE can induce fragmentation (Ferreira da Silva et al. 2012, 2014). In these studies, the role of the incoming electron yielding molecular fragmentation has been thoroughly discussed, with particular attention to the dehydrogenated formic acid anion formation and neutral hydrogen atoms. Rescigno et al. (2006) theoretical studies have shown that DEA to formic acid proceeds through a π^* resonance on the C=O bond leading to excision of the OH bond. Such mechanism was proposed to involve a σ^* (OH) orbital coupling with a π^* (C=O) in the transient negative ion with considerable geometry change from the neutral. However, Gallup et al. (2009) calculations on the DEA cross-sections for formic acid and glycine, have shown that the mechanism of H loss involves electron capture into a σ^* (OH) orbital with no need of a π^*/σ^* coupling. Recently, Allan and co-workers (Janečková et al. 2013) DEA experimental data lent support to the mechanism proposed by Gallup et al. (2009). As far as other fragmentation patterns in HCOOC and/or HAc yielding anion formation are concerned, we note the experimental studies of Sailer et al. (2003) and Prabhudesai et al. (2008). Both sets of experimental data describe OH^- formation with no explanation for the underlying molecular mechanism yielding such anion.

Time-of-flight (TOF) mass spectra upon potassium collisions with the three different acetic acid analogues were recorded at 100 eV and a combined data is shown in Fig. 12.2 with an inset of OH/OD formation mass range, i.e. 16–18 m/z.

Fig. 12.2 Time-of-flight mass spectra of acetic acid upon potassium collisions at 100 eV lab-frame



Electron transfer in collisions of neutral K atoms with HAc molecules, leads to formation of a temporary negative ion with an excess of internal energy resulting in dissociation of anionic and neutral species. From this comprehensive study as a function of the collision energy, we focus our attention on the OH anion yield only, in order to explore the underlying mechanism that result in either direct cleavage of the OH bond from the carboxylic group or any other competitive (and even concerted) process.

Meneses et al. (2017) have explored three fragmentation pathways after electron transfer to acetic acid leading to OH anion formation and have proposed: (a) H transfer from CH₃ to form the diol structure followed by OH⁻ cleavage; (b) H release from COOH and subsequent intramolecular H transfer from CH₃ yielding OH⁻; (c) direct OH radical fragmentation. Although theoretical calculations support pathway (b) as the most favourable decay mechanism, experimental results suggest a competition between pathways (a) and (b). The presence of OH⁻ formation upon electron transfer in the case of CD₃COOH (Fig. 12.2) is supported by pathway (b), namely H release from COOH and subsequent rearrangement to eliminate OH⁻, while in CH₃COOD it is formed according to pathway (a). In both cases, the diol structure is a transient species. Although, the most evident pathway for OH⁻ formation would result from direct cleavage of the C–OH bond pathway (c), however this pathway leads to OH radical formation.

12.6 Aliphatic Amino Acids

12.6.1 Glycine, Alanine and Valine

Amino acids in general have caught the attention of many scientists of different research fields across the globe. Special attention has been devoted to gas phase experimental studies on dissociative electron attachment to isolated aliphatic amino acids molecules (Abdoul-Carime and Sanche 2004; Ptasińska et al. 2005a; Papp et al. 2006; Denifl et al. 2009; Shchukin et al. 2010) electron impact ionisation (Denifl et al. 2009; Papp et al. 2012) and electron transmission spectroscopy (Aflatooni et al. 2001) as well as to amino acids clusters embedded in helium nanodroplets (Ferreira da Silva et al. 2010). Theoretical studies have been performed using density functional theory (DFT) calculations (Ban et al. 2000; Li and Brill 2003), the binary-encounter-Bethe (BEB) model procedure (Scheer et al. 2007) and the Schwinger multichannel method (dos Santos et al. 2012). Glycine, alanine and valine are aliphatic amino acids, differing on the aliphatic side chain. In this section the fragmentation pattern of the three simplest aliphatic amino acids, glycine ($C_2H_5NO_2$), alanine ($C_3H_7NO_2$) and valine ($C_5H_{11}NO_2$) (Fig. 12.3) is discussed.

Table 12.1 summarises the fragment anions formed at 100 eV collision energy and for the three amino acids, we can identify several common fragments as is the case of the dehydrogenated parent anion. In the case of glycine and alanine, for lower collision energies (i.e. 20 eV and 15 eV, respectively), the dehydrogenated parent anion yield is well pronounced, in contrast with valine, that for lower and higher energies the evidence is residual. In the case of formic acid, Rescigno et al. (2006) have proposed that hydrogen abstraction is due to the σ^*/π^* coupling with further O–H excision, leading to H^- formation.

Indeed, increasing the collision energy results in fewer heavier fragments produced in favour to lighter anion species. This can be rationalised in terms of the number of degrees of freedom in these molecular targets and the consequent energy distribution. Valine has an isobutyl side chain in contrast with alanine and glycine which have a methyl and hydrogen atom, respectively. The energy distribution in the case of valine will be likely redistributed leading to more prominent fragmentation for lighter masses.

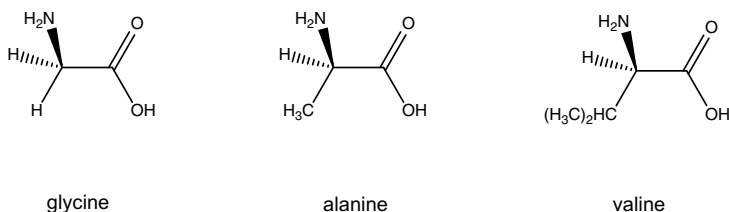


Fig. 12.3 Aliphatic amino acids molecular structure, from left to the right: glycine, alanine and valine

Table 12.1 Fragment anions assigned at 100 eV potassium collisions with glycine (G), alanine (A) and valine (V) amino acids

m/z	Assignment	Glycine	Alanine	Valine
1	H ⁻	✓	✓	✓
12	C ⁻	✓	✓	✓
13	CH ⁻	✓	✓	✓
15	CH ₃ ⁻ /NH ⁻	✓	×	×
16	O ⁻ /NH ₂ ⁻	✓	✓	✓
17	OH ⁻	✓	✓	✓
24	C ₂ ⁻	✓	✓	✓
25	C ₂ H ⁻	✓	✓	✓
26	CN ⁻ /C ₂ H ₂ ⁻	✓	✓	✓
41	CHCO ⁻	✓	✓	✓
45	HCO ₂ ⁻	×	✓	×
71	C ₃ H ₃ O ₂ ⁻ /C ₄ H ₉ N ⁻	×	×	✓
74	G-H ⁻	✓	×	×
88	A-H ⁻	×	✓	×
116	V-H ⁻	×	×	✓

The fragment anion 71 m/z is only barely visible in the case of valine at 100 eV collision energy, while in alanine, at low collision energy, the fragment anion can be assigned to C₃H₃O₂⁻ due to its (neutral) high electron affinity (3.57 ± 0.18 eV (Graul et al. 1990)) and results from the loss of 18 m/z from the parent anion. However, in the case of valine such fragment anion is only observed at 100 eV and its most plausible assignment is C₄H₉N⁻ together with a neutral formic acid from the decomposition of the TNI.

HCOO/COOH anion formation occurs only in alanine at 100 eV collision energy. This negative ion was also reported in DEA studies to alanine (Ptasińska et al. 2005a) and glycine (Gohlke et al. 2002; Ptasińska et al. 2003; Muftakhov and Shchukin 2010; Shchukin et al. 2010), and formed upon electron capture into the carboxylic π* orbital.

Another interesting aspect of negative ion formation in small amino acids is formation of isobaric species which, however are difficult to assign due to the low-mass resolution of the linear TOF setup used in these measurements. The fragments NH₂⁻/O⁻ (16 m/z) and CN⁻/C₂H₂⁻ (26 m/z) are present for the three amino acids in contrast with CH₃⁻/NH⁻ (15 m/z) that is only visible in the case of glycine. High-mass resolution DEA to glycine (Mauracher et al. 2007) reported two structures due to resonant electron capture, for each isobaric species, one in the low energy region, the other at higher energies. The fragment anion 15 m/z in glycine is formed through two distinct resonances in the electron capture process. The electron energy profile shows resonance structures peaking at 6 and 11.5 eV. The CH₃ anion formation was attributed to the lower energy resonance while the NH anion to the higher energy res-

onance. Fragment anion 16 m/z, yields NH_2^- formed via a resonance placed between 4 and 8 eV whereas O^- via a high energy resonance located between 7 and 15 eV. The 26 m/z fragment anion shows a similar behaviour, the low energy resonance, located between 4 and 8.5 eV and peaking at 6.5 eV, leads to CN^- formation while a high energy resonance, placed between 8.5 and 14 eV and peaking at 11 eV leads to C_2H_2^- formation. Electron transfer processes in potassium-amino acids collisions, yield anions formed through low-energy resonances at low-energy collisions, i.e., 20 eV in the lab-frame, i.e. 7.8, 8.2 and 9.2 eV in the centre-of-mass frame for glycine, alanine and valine, respectively. However, increasing the collision energy to 100 eV, 56.5, 58.2 and 63.2 eV in the centre-of-mass frame for glycine, alanine and valine, respectively, formation of both isobaric molecular anions is possible.

The high dipole moment for the most stable conformer for these amino acids, 5.6 D, 5.49 D for glycine and alanine respectively, can promote a strong coupling between DBS and valence state providing a doorway for the decay of valence anions via vibrationally excited dipole bound states. Similar process has been put forward for thymine and uracil (Burrow et al. 2006) and we believe that this process may also hold for the probed amino acids.

In summary, the high impact potassium energy is inducing a rich fragmentation pattern leading to lighter fragments in contrast with lower impact potassium energy, which leads to heavier fragment anions. The dehydrogenated parent anion is observed in all three amino acids, which yield decreases with increasing the number of atoms of the side chain, due to the increase of degrees of freedom. The loss of a hydrogen radical can be explained by initial electron capture into a π^* orbital that couples with an σ^* orbital leading to O–H dissociation. Three distinct fragment anions have been attributed to six isobaric fragments, i.e. 15, 16 and 26 m/z and their formation discussed on the light of the main resonances involved.

12.7 Aromatic Amino Acids

12.7.1 Tyrosine and Tryptophan

Aromatic amino acids are characterized by the aromatic side chain. There are four aromatic amino acids within the twenty existing from bacteria to humans, histidine, phenylalanine, tyrosine and tryptophan. Tyrosine ($\text{C}_9\text{H}_{11}\text{NO}_3/\text{Tyr}$) and tryptophan ($\text{C}_{11}\text{H}_{12}\text{N}_2\text{O}_2/\text{Trp}$) (Fig. 12.4), are two amino acids that will be discussed within this section. Tyrosine has a phenol moiety as side chain whereas tryptophan an indole side chain. In both cases, the side chain moiety is aromatic ring characterised by a delocalized π system.

In Table 12.2 we list the fragment anions formed upon potassium interactions with tyrosine and tryptophan for the energy range between 20 and 75 eV in the lab frame.

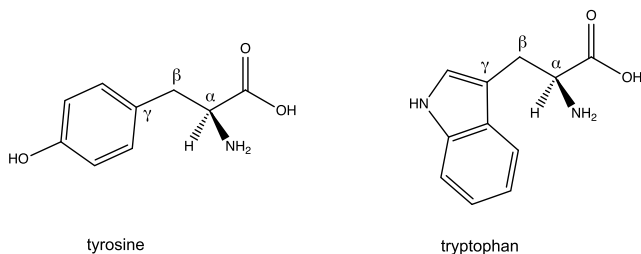


Fig. 12.4 Aromatic amino acids molecular structure, left tyrosine and right tryptophan

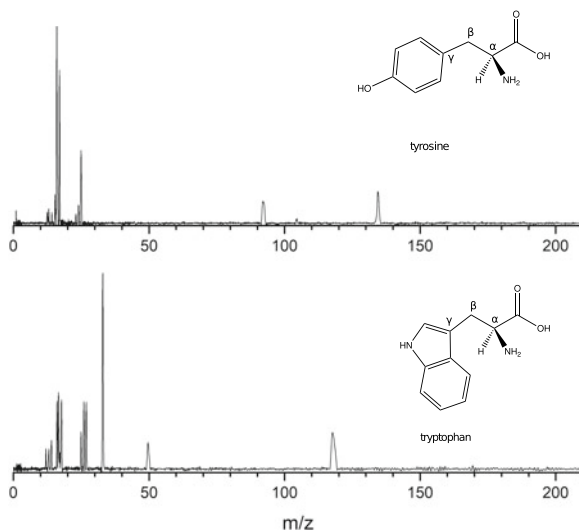
Table 12.2 Fragment anions in potassium collisions with tyrosine and tryptophan, for energy range 20–75 eV in the lab frame

m/z	Assignment	Tyrosine	Tryptophan
16	O^-/NH_2^-	✓	✓
17	OH^-	✓	✓
24	C_2^-	✓	✓
25	C_2H^-	✓	✓
26	$CN^-/C_2H_2^-$	✓	✓
33	OOH^-	✗	✓
92	$C_6H_4O^-$	✓	✗
105	$C_7H_5O^-$	✓	✗
118	$C_8H_7NH^-$	✗	✓
133	$C_8H_7NO^-$	✓	✗
180	$Tyr-H^-$	✓	✗
203	$Trp-H^-$	✗	✗

Figure 12.5 shows the negative ion mass spectra of tyrosine (upper panel) and tryptophan (lower panel) at 75 eV collision energy, respectively.

Formation of the dehydrogenated parent anion is only visible in the case of tyrosine, which yield decreases with increasing collision energy; at 75 eV collision energy, such anion becomes almost indistinguishable from the background noise level. The hydrogen loss proceeds either from the carboxylic group or from the phenolic hydroxyl group. The dehydrogenation site must depend on the pK_a of each site, although in gas-phase these values are also related to the preceding negative ion state. The most prominent dissociation channel at low-energy collision, 35 eV, is 92 m/z negative ion assigned to $C_6H_4O^-$. The branching ratio trending of this anion is similar to the dehydrogenated parent anion (Ferreira da Silva et al. 2016). The pathway leading to this fragment involves a cleavage of β -C and phenol ring *para*-C. DEA experimental results do not exhibit this anionic fragment (Vasil'ev et al. 2006). In order to fragmentation proceed yielding such anion, a coupling between low-lying π^* states with σ^* states should occur. In such π^*/σ^* coupling the nuclear wave packet needs to survive long enough allowing for diabatic crossing of both states. Furthermore, this process may also compete with autodetachment and disso-

Fig. 12.5 Time-of-flight mass spectra of tyrosine (upper panel) and tryptophan (lower panel) at 75 eV collision energy



ciation will be suppressed. In the present case, the presence of K^+ in the collision complex system may delay autodetachment long enough allowing for an intramolecular electron transfer along the π^*/σ^* states. The cleavage of α -C- β -C bond leads to C_7H_5O , 105 m/z anion formation with loss of two additional hydrogen atoms that may presumably stem from one hydroxyl side-chain group and another from the β -C. Additionally, the remaining hydrogen atom at β -C position may be transferred to the α -C remaining counterpart with neutral glycine formation. The formation of this fragment shows an independent energy collision behaviour. The branching ratio is approximately 5% over all energy range investigated. The loss of a carboxylic group and two additional hydrogen atoms leads to formation of 133 m/z $C_8H_7NO^-$ ion, which was not observed in DEA studies. Furthermore, the energy dependency shows similar behaviour as in the case of 105 m/z anion (see Fig. 12.3 in Ref. Ferreira da Silva et al. 2016). The branching ratio of low m/z increases with the increasing collision energy, following the opposite dehydrogenated trend that decreases with increasing collision energy. This trend can be explained in terms of the available energy in the system that will be channelled to further fragmentation pathways. On the other hand, if the dehydrogenated anion is formed with excess of internal energy, as in the case of the high collision energy regime, fragmentation may be the favourable channel the accommodate the excess energy. As it was observed for the aliphatic amino acids (Ferreira da Silva et al. 2012, 2014), apart from OH^- , formation of isobaric fragments NH_2^-/O^- and $CN^-/C_2H_2^-$ is also possible. In the case of OH^- , such anion formation should proceed from direct cleavage of OH in the carboxylic group, or as in acetic acid (Meneses et al. 2017), through internal rearrangement via diol formation.

Figure 12.5 lower panel shows the negative ion mass spectrum from collisions of potassium atoms with tryptophan, and in Table 12.2 we list the negative ions

together with their assignments. Apart from lighter anions (<26 m/z), the reaction leading to the side chain moiety fragmentation is the dominant channel. Neither the parent anion nor the dehydrogenated parent anion are detected. The heavier fragment detected at 188 m/z was assigned to the dehydrogenated indoline (C_8H_9N), and as far as the authors are aware this was not reported in previously gas-phase studies. The mechanism leading to dehydrogenated indoline is a complex process evolving several intramolecular rearrangements. The indole moiety is linked to the backbone chain between γ -C3 and β -C, as schematically depicted in Fig. 12.4. In the dissociation process this bond must be broken, where the electron may remain in the aromatic moiety, and the transfer of two hydrogen atoms from the amino acid backbone chain to the indole ring should take place. The intensity of this fragment anion diminishes rapidly with increasing collision energy, with no signal above 75 eV collision energy. Figure 12.6 shows the branching ratios as a function of the collision energy for indoline, HO_2^-/NH_2OH^- , OH^- , O^-/NH_2^- and CN^- .

Formation of indoline anion is favoured for low collision energies while OH^- and O^-/NH_2^- are favoured for higher energies. This fact can be rationalised in terms of available collision time: formation of indoline requires transfer of two hydrogen atoms from the amino acid backbone to the indole moiety while OH^- and O^-/NH_2^- may be formed via a direct process (simple bond breaking) since no new bonds are required to yield such fragment anions. The branching ratios for these anions are energy dependent, since they increase with increasing collision energy, meaning that they are more pronounced in shorter collision times. The branching ratio for HO_2^-/NH_2OH^- formation describes a maximum in the energy range 30–75 eV

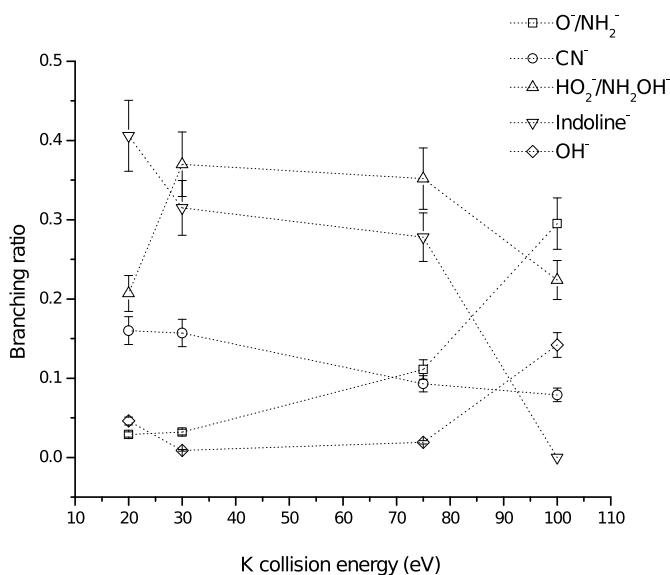


Fig. 12.6 The collision energy dependency of the branching ratios for the fragments formed upon potassium-tryptophan collisions at 20, 30, 75 and 100 eV lab-frame

(30–19 fs), while CN^- slightly decreases with increasing collision energy, showing a similar trend to that observed for the dehydrogenated indoline anion.

12.8 Conclusions

Electron transfer mechanisms in biological relevant molecules have been proven to play an important role at molecular level. Such modifications were not only fundamental processes such as electron transport in the cellular membrane, but indirect processes triggered when high energy radiation interact with biological tissue are relevant to the nature of the chemical environment where they occur. The relevance of gas-phase electron transfer processes in potassium-molecule collisions is to better understand the fragmentation processes of biologic and biological related molecules, after electron attachment. As the outermost electron in potassium is weakly bound, the proposed experiments may provide an analogy for electron transfer from electronically excited secondary neutrals in the biological environmental.

Electron transfer mechanism yielding ion-pair formation in gas-phase acetic acid, aliphatic amino acids, such as glycine, alanine and valine, and aromatic amino acids, such as tyrosine and tryptophan through collisions with a hyperthermal neutral potassium beam, have been investigated using a crossed molecular-beam technique. The negative ions formed upon electron transfer in potassium-molecule collision were TOF mass analysed. The fragmentation pathway can be strongly influenced by the presence of the potassium cation in the vicinity of the TNI.

In the case of acetic acid, special attention has been dedicated to OH^- formation, showing the competition between two possible fragmentation pathways, with intermediate diol formation. Regarding the investigation on aliphatic amino acids, we have observed a decrease of the dehydrogenated parent anion yield with increasing the complexity of the side chain. This fact can be attributed to the increase of degrees of freedom favouring energy redistribution and consequently formation of lighter fragment anions. Additionally, electron transfer to aromatic amino acids shows the influence of delocalized π system leading to prominent formation of anionic fragments from the aromatic side chain. It has been shown in the case of tryptophan that keeping the extra electron in the aromatic side chain, yields proton transfer leading to the dehydrogenated indoline formation and in the case of tyrosine to fragment anions at 133, 105 and 92 m/z assigned to derivatives from the benzophenolic side chain. For the studied amino acids, isobaric fragments are formed and have been assigned to O^-/NH_2^- and $\text{CN}^-/\text{C}_2\text{H}_2^-$. The increase of energy transferred at higher collision energies favours direct fragmentation channels, increasing the branching ratios of those fragments, as well as and OH^- formation.

Acknowledgements MM acknowledges the Portuguese National Funding Agency FCT-MCTES through PD/BD/106038/2015 and together with FFS and PLV the Research Grants UID/FIS/00068/2019 (CEFITEC, Centre of Physics and Technological Research), PTDC/FIS-AQM/31215/2017 and PTDC/FIS-AQM/31281/2017. This work was also supported by Radi-

ation Biology and Biophysics Doctoral Training Programme (RaBBiT, PD/00193/2010); UID/Multi/04378/2013 (UCIBIO). GG acknowledges partial financial support from the Spanish Ministerio de Economía, Industria y Competitividad, Project No. FIS2016-80440.

References

- Abdoul-Carime H, Sanche L (2003) Alteration of protein constituents induced by low-energy (<35 eV) electrons: II. Dissociative electron attachment to amino acids containing cyclic groups. *Radiat Res* 160:86–94. <https://doi.org/10.1667/RR3025>
- Abdoul-Carime H, Sanche L (2004) Alteration of protein constituents induced by low-energy (<40 eV) electrons. III. The aliphatic amino acids. *J Phys Chem B* 108:457–464. <https://doi.org/10.1021/jp030413x>
- Abdoul-Carime H, Gohlke S, Illenberger E (2005) Fragmentation of tryptophan by low-energy electrons. *Chem Phys Lett* 402:497–502. <https://doi.org/10.1016/j.cplett.2004.12.073>
- Aflatooni K, Hitt B, Gallup GA, Burrow PD (2001) Temporary anion states of selected amino acids. *J Chem Phys* 115:6489–6494. <https://doi.org/10.1063/1.1404147>
- Alizadeh E, Sanche L (2012) Precursors of solvated electrons in radiobiological physics and chemistry. *Chem Rev* 112:5578–5602. <https://doi.org/10.1021/cr3000063r>
- Alizadeh E, Orlando TM, Sanche L (2015) Biomolecular damage induced by ionizing radiation: the direct and indirect effects of low-energy electrons on DNA. *Annu Rev Phys Chem* 66:379–398. <https://doi.org/10.1146/annurev-physchem-040513-103605>
- Almeida D, Antunes R, Martins G et al (2011) Electron transfer-induced fragmentation of thymine and uracil in atom-molecule collisions. *Phys Chem Chem Phys* 13:15657–15665. <https://doi.org/10.1039/c1cp21340g>
- Almeida D, Ferreira Da Silva F, García G, Limão-Vieira P (2013a) Selective bond cleavage in potassium collisions with pyrimidine bases of DNA. *Phys Rev Lett* 110:1–5. <https://doi.org/10.1103/PhysRevLett.110.023201>
- Almeida D, da Silva FF, García G, Limão-Vieira P (2013b) Dynamic of negative ions in potassium-D-ribose collisions. *J Chem Phys* 139:114304. <https://doi.org/10.1063/1.4820949>
- Almeida D, Ferreira Da Silva F, Eden S et al (2014) New fragmentation pathways in K-THF collisions as studied by electron-transfer experiments: negative ion formation. *J Phys Chem A* 118:690–696. <https://doi.org/10.1021/jp407997w>
- Antunes R, Almeida D, Martins G et al (2010) Negative ion formation in potassium-nitromethane collisions. *Phys Chem Chem Phys* 12:12513–12519. <https://doi.org/10.1039/c004467a>
- Ban F, Gauld JW, Boyd RJ (2000) Theoretical studies of the radiation products of hydroxyproline. *J Phys Chem A* 104:8583–8592. <https://doi.org/10.1021/jp001692g>
- Boudaiffa B, Cloutier P, Hunting D et al (2000) Resonant formation of DNA strand breaks by low-energy (3–20 eV) electrons. *Science* 287:1658–1660. <https://doi.org/10.1126/science.287.5458.1658>
- Burrow PD, Gallup GA, Scheer AM et al (2006) Vibrational Feshbach resonances in uracil and thymine. *J Chem Phys* 124. <https://doi.org/10.1063/1.2181570>
- Cobut V, Frongillo Y, Patau JP et al (1998) Monte Carlo simulation of fast electron and proton tracks in liquid water—I. Physical and physicochemical aspects. *Radiat Phys Chem* 51:229–243. [https://doi.org/10.1016/S0969-806X\(97\)00096-0](https://doi.org/10.1016/S0969-806X(97)00096-0)
- Denifl S, Mähr I, Ferreira Da Silva F et al (2009) Electron impact ionization studies with the amino acid valine in the gas phase and (hydrated) in helium droplets. *Eur Phys J D* 51:73–79. <https://doi.org/10.1140/epjd/e2008-00092-4>
- Denifl S, Mark TD, Scheier P (2012) The role of secondary electrons in radiation damage. In: García Gómez-Tejedor G, Fuss MC (eds) *Radiation damage in biomolecular systems. Biological and medical physics, biomedical engineering*, 1st edn. Springer, Dordrecht, pp 45–58

- dos Santos JS, da Costa RF, Varella MTDN (2012) Low-energy electron collisions with glycine. *J Chem Phys* 136:084307. <https://doi.org/10.1063/1.3687345>
- Ferreira da Silva F, Denifl S, Märk TD et al (2010) Electron attachment to amino acid clusters in helium nanodroplets: glycine, alanine, and serine. *J Chem Phys* 132. <https://doi.org/10.1063/1.3429743>
- Ferreira da Silva F, Lança M, Almeida D et al (2012) Anionic fragmentation of glycine upon potassium-molecule collisions. *Eur Phys J D* 66:78. <https://doi.org/10.1140/epjd/e2012-20751-y>
- Ferreira da Silva F, Matias C, Almeida D et al (2013) NCO⁻, a key fragment upon dissociative electron attachment and electron transfer to pyrimidine bases: site selectivity for a slow decay process. *J Am Soc Mass Spectrom* 24:1787–1797. <https://doi.org/10.1007/s13361-013-0715-9>
- Ferreira da Silva F, Rafael J, Cunha T et al (2014) Electron transfer to aliphatic amino acids in neutral potassium collisions. *Int J Mass Spectrom* 365–366:238–242. <https://doi.org/10.1016/j.ijms.2014.01.003>
- Ferreira da Silva F, Meneses G, Ingólfsson O, Limão-Vieira P (2016) Side chain effects in reactions of the potassium-tyrosine charge transfer complex. *Chem Phys Lett* 662:19–24. <https://doi.org/10.1016/j.cplett.2016.08.004>
- Flosadóttir HD, Denifl S, Zappa F et al (2007) Combined experimental and theoretical study on the nature and the metastable decay pathways of the amino acid ion fragment [M-H]⁻. *Angew Chem Int Ed Engl* 46:8057–8059. <https://doi.org/10.1002/anie.200703327>
- Frauenfelder H (2010) *The physics of proteins: an introduction to biological physics and molecular biophysics*. Springer, New York
- Gallego E, Perales JF, Roca FJ, Guardino X (2014) Surface emission determination of volatile organic compounds (VOC) from a closed industrial waste landfill using a self-designed static flux chamber. *Sci Total Environ* 470–471:587–599. <https://doi.org/10.1016/j.scitotenv.2013.09.105>
- Gallup G, Burrow P, Fabrikant I (2009) Electron-induced bond breaking at low energies in HCOOH and glycine: the role of very short-lived σ^* anion states. *Phys Rev A* 79:046702. <https://doi.org/10.1103/PhysRevA.79.042701>
- Gohlke S, Rosa A, Illenberger E et al (2002) Formation of anion fragments from gas-phase glycine by low energy (0–15 eV) electron impact. *J Chem Phys* 116:10164–10169. <https://doi.org/10.1063/1.1479348>
- Goodhead DT (1994) Initial events in the cellular effects of ionizing radiations: clustered damage in DNA. *Int J Radiat Biol* 65:7–17
- Goodhead DT, Thacker J, Cox R (1993) Effects of radiations of different qualities on cells: molecular mechanisms of damage and repair. *Int J Radiat Biol* 63:543–556. <https://doi.org/10.1080/09553009314450721>
- Graul ST, Schnute ME, Squires RR (1990) Gas-phase acidities of carboxylic acids and alcohols from collision-induced dissociation of dimer cluster ions. *Int J Mass Spectrom* 96:181–198. <https://doi.org/10.1097/WNR.0b013e32819f8f3f>
- Horton HR, Moran LA, Ochs RS et al (1996) Amino acids and the primary structures of proteins. *Principles of biochemistry*, 2nd edn. Prentice Hall, Upper Saddle River, NJ, pp 61–78
- Hubers MM, Kleyn AW, Los J (1976) Ion pair formation in alkali-halogen collisions at high velocities. *Chem Phys* 17:303–325. <https://doi.org/10.1017/CBO9781107415324.004>
- Huels MA, Boudaïffa B, Cloutier P et al (2003) Single, double, and multiple double strand breaks induced in DNA by 3–100 eV electrons. *J Am Chem Soc* 125:4467–4477. <https://doi.org/10.1021/ja029527x>
- Illenberger E, Mominy J (1992) *Gaseous molecular ions: an introduction to elementary processes induced by ionization*, 1st edn. Steinkopff-Verlag, Heidelberg, Darmstadt, New York
- Janečková R, Kubala D, May O et al (2013) Experimental evidence on the mechanism of dissociative electron attachment to formic acid. *Phys Rev Lett* 111:213201. <https://doi.org/10.1103/PhysRevLett.111.213201>
- Khare P, Kumar N, Kumari KM (1999) Atmospheric formic and acetic acids: an overview. *Rev Geophys* 32:227–248

- Kleyn AW, Moutinho AMC (2001) Negative ion formation in alkali-atom—molecule collisions. *J Phys B: At Mol Opt Phys* 34:R1–R44. <https://doi.org/10.1088/0953-4075/34/14/201>
- Kleyn AW, Los J, Gislason EA (1982) Vibronic coupling at intersections of covalent and ionic states. *Phys Rep (Rev Sect Phys Lett)* 90:1–71. [https://doi.org/10.1016/0370-1573\(82\)90092-8](https://doi.org/10.1016/0370-1573(82)90092-8)
- Krupadam RJ, Sridevi P, Sakunthala S (2011) Removal of endocrine disrupting chemicals from contaminated industrial groundwater using chitin as a biosorbent. *J Chem Technol Biotechnol* 86:367–374. <https://doi.org/10.1002/jctb.2525>
- Li J, Brill TB (2003) Decarboxylation mechanism of amino acids by density functional theory. *J Phys Chem A* 107:5993–5997. <https://doi.org/10.1021/jp022477y>
- Limão-Vieira P, Ferreira da Silva F, Gómez-Tejedor G (2012) Electron transfer-induced fragmentation in (bio)molecules by atom-molecule collisions. In: García Gómez-Tejedor G, Fuss MC (eds) *Radiation damage in biomolecular systems*, 1st edn. Springer, Dordrecht, pp 59–70
- Little JB (2000) Ionizing Radiation. In: Bast RC, Kufe DW, Pollock RE et al (eds) *Holland Free cancer medicine*, 5th edn. B. C. Decker Inc., Hamilton, London, pp 207–218
- Loupas A, Gorfinkiel JD (2019) Shape and core-excited resonances in electron scattering from alanine. *J Chem Phys* 150:064307. <https://doi.org/10.1063/1.5081813>
- Martin F, Burrow PD, Cai Z et al (2004) DNA strand breaks induced by 0–4 eV electrons: the role of shape resonances. *Phys Rev Lett* 93:068101. <https://doi.org/10.1103/PhysRevLett.93.068101>
- Mauracher A, Denifl S, Aleem A et al (2007) Dissociative electron attachment to gas phase glycine: exploring the decomposition pathways by mass separation of isobaric fragment anions. *Phys Chem Chem Phys* 9:5680–5685. <https://doi.org/10.1039/b709140k>
- Meneses G, Widmann C, Cunha T et al (2017) Unravelling the dissociation pathways of acetic acid upon electron transfer in potassium collisions: experimental and theoretical studies. *Phys Chem Chem Phys* 19:1083–1088. <https://doi.org/10.1039/c6cp06375f>
- Muftakhov MV, Shchukin PV (2010) Resonant dissociative electron capture by the simplest amino acids and dipeptides. *Russ Chem Bull* 59:896–911. <https://doi.org/10.1007/s11172-010-0183-3>
- Neustetter M, Aysina J, Da Silva FF, Denifl S (2015) The effect of solvation on electron attachment to pure and hydrated pyrimidine clusters. *Angew Chemie Int Ed* 54:9124–9126. <https://doi.org/10.1002/anie.201503733>
- Nikjoo H, O'Neill P, Goodhead DT, Terrissol M (1997) Computational modelling of low-energy electron-induced DNA damage by early physical and chemical events. *Int J Radiat Biol* 71:467–483
- Papp P, Urban J, Matejčík Š et al (2006) Dissociative electron attachment to gas phase valine: a combined experimental and theoretical study. *J Chem Phys* 125. <https://doi.org/10.1063/1.2400236>
- Papp P, Shchukin P, Kočíšek J, Matejčík Š (2012) Electron ionization and dissociation of aliphatic amino acids. *J Chem Phys* 137. <https://doi.org/10.1063/1.4749244>
- Prabhudesai VS, Kelkar AH, Nandi D, Krishnakumar E (2005) Functional group dependent site specific fragmentation of molecules by low energy electrons. *Phys Rev Lett* 95:1–4. <https://doi.org/10.1103/PhysRevLett.95.143202>
- Prabhudesai VS, Nandi D, Kelkar AH, Krishnakumar E (2008) Functional group dependent dissociative electron attachment to simple organic molecules. *J Chem Phys* 128:154309. <https://doi.org/10.1063/1.2899330>
- Ptasińska S, Denifl S, Abedi A et al (2003) Dissociative electron attachment to gas-phase glycine. *Anal Bioanal Chem* 377:1115–1119. <https://doi.org/10.1007/s00216-003-2254-x>
- Ptasińska S, Denifl S, Candori P et al (2005a) Dissociative electron attachment to gas phase alanine. *Chem Phys Lett* 403:107–112. <https://doi.org/10.1016/j.cplett.2004.12.115>
- Ptasińska S, Denifl S, Grill V et al (2005b) Bond- and site-selective loss of H- from pyrimidine bases. *Phys Rev Lett* 95:1–4. <https://doi.org/10.1103/PhysRevLett.95.093201>
- Ptasińska S, Denifl S, Scheier P et al (2005c) Bond- and site-selective loss of H atoms from nucleobases by very-low-energy electrons (<3 eV). *Angew Chem Int Ed Engl* 44:6941–6943. <https://doi.org/10.1002/anie.200502040>

- Rescigno T, Trevisan C, Orel A (2006) Dynamics of low-energy electron attachment to formic acid. *Phys Rev Lett* 96:213201. <https://doi.org/10.1103/PhysRevLett.96.213201>
- Sailer W, Pelc A, Probst M et al (2003) Dissociative electron attachment to acetic acid (CH₃COOH). *Chem Phys Lett* 378:250–256. [https://doi.org/10.1016/S0009-2614\(03\)01285-5](https://doi.org/10.1016/S0009-2614(03)01285-5)
- Scheer AM, Mozejko P, Gallup GA, Burrow PD (2007) Total dissociative electron attachment cross sections of selected amino acids. *J Chem Phys* 126:0–7. <https://doi.org/10.1063/1.2727460>
- Shchukin PV, Muftakhov MV, Morf J et al (2010) High resolution mass analysis of N- and C-terminal negative ions resulting from resonance electron capture by aliphatic amino acids. *J Chem Phys* 132:1–11. <https://doi.org/10.1063/1.3436719>
- Swiderek P (2006) Fundamental processes in radiation damage of DNA. *Angew Chem Int Ed* 45:4056–4059. <https://doi.org/10.1002/anie.200600614>
- Tanzer K, Feketeová L, Puschnigg B et al (2014) Reactions in nitroimidazole triggered by low-energy (0–2 eV) electrons: methylation at N1-H completely blocks reactivity. *Angew Chem Int Ed Engl* 53:12240–12243. <https://doi.org/10.1002/anie.201407452>
- Theron MM, Lues JFR (2007) Organic acids and meat preservation: a review. *Food Rev Int* 23:141–158. <https://doi.org/10.1080/87559120701224964>
- Uehara S, Nikjoo H, Goodhead D (1999) Comparison and assessment of electron cross sections for Monte Carlo track structure codes. *Radiat Res* 152:202–213. <https://doi.org/10.2307/3580095>
- Vasil'ev YV, Figard BJ, Voinov VG et al (2006) Resonant electron capture by some amino acids and their methyl esters. *J Am Chem Soc* 128:5506–5515. <https://doi.org/10.1021/ja058464q>
- Welz O, Eskola AJ, Sheps L et al (2014) Rate coefficients of C(1) and C(2) Criegee intermediate reactions with formic and acetic acid near the collision limit: direct kinetics measurements and atmospheric implications. *Angew Chem Int Ed Engl* 53:4547–4550. <https://doi.org/10.1002/anie.201400964>
- Wooten A, Wlodarczak G, Mangum JG et al (1992) Search for acetic acid in interstellar clouds. *Astron Astrophys* 257:740–744

Chapter 13

Fast Kinetics—Stopped-Flow and Rapid Freeze-Quench



Pedro Tavares and Alice S. Pereira

13.1 Introduction

Previous chapters explain the fundamentals of different spectroscopic techniques that can be used to characterize solution structure of macromolecules and/or cofactors, oxidation and spin states of redox active centers, and molecular interactions. In most cases these are complementary techniques that can bring together a picture of how a macromolecule behaves in solution in respect to substrates, inhibitors, partners in metabolic pathways, etc. This picture is usually representative of a particular equilibrium state such as an enzyme ready state or a cofactor bound to a substrate analogue or inhibitor. However, the description of molecular mechanisms strongly benefits from an additional dimension: time.

To be able to acquire spectroscopic data over a time interval is of great importance to study reaction mechanisms at the molecular level. Data obtained for different reaction times can enable the characterization of reaction intermediates allowing a proper step-by-step description of what is occurring at a molecular level.

Most biological reactions of interest are too fast for conventional spectroscopic measurements. For example, enzyme catalyzed reactions have turnover rates between 1 and 10^7 s^{-1} (above which the reaction becomes diffusion-controlled), with most enzymes having turnover rates below 10^3 s^{-1} . In this chapter, we will cover fast kinetic techniques specifically designed to circumvent this problem and make possible data collection on reaction times in the milliseconds timescale.

When studying rapid reactions one of the issues that has impact on the time resolution is the method used to start the reaction. For cases where small dead

P. Tavares · A. S. Pereira (✉)

Molecular Biophysics Laboratory, UCIBIO/Requimte, Department of Chemistry, Faculdade de Ciências e Tecnologia, Universidade NOVA de Lisboa, 2829-516 Caparica, Portugal
e-mail: masp@fct.unl.pt

P. Tavares
e-mail: pabt@fct.unl.pt

times are needed one can resort to methods using premixed solutions containing all reagents/reagent precursors and that will respond to a specific perturbation such as a light pulse. Flash photolysis has successfully been used in the study of light induced processes measuring dissociation and recombination processes that occur on the femto to picosecond time scale. Other methods, such as temperature, pressure or electric field jumps, can be applied to reversible reactions. The rapid change in one of these parameters perturbs the equilibrium and kinetic parameters can be derived from the rate at which the equilibrium is re-established (relaxation). Using relaxation methods dead times of a microsecond or less can be reached. While these methods are able to monitor very fast reactions, they are rather limited to reactions where one of the reagents possesses chemical bonds that can be cleaved by a light pulse and/or processes that do not involve one or more irreversible steps.

An alternative, and quite obvious, method of starting a reaction is to have reagents in separate vessels that can be mixed in a controlled manner. In this case the dead time of our technique will be dependent on how reagent mixing is achieved. With rapid mixing techniques, reactions can be started by mixing two, or more, reagent solutions in less than a millisecond to a few milliseconds (depending on the instrumentation used). Such technique is appropriate for reactions with turnover numbers lower than 10^3 s^{-1} , which makes rapid mixing useful in the study of most biological processes of interest. Thus, for the purpose of this book we will limit our discussion to rapid mixing techniques since these are also adequate to couple to some of the spectroscopies discussed in previous chapters.

After a reaction is started there is the need for tools that can identify and characterize reaction intermediates. This is a task particularly suited for spectroscopic techniques such as UV/visible, Resonance Raman, CD, EPR, EXAFS and Mössbauer spectroscopies, among others. However, the spectroscopic tool used has to be capable of fast data acquisition in order to have a time resolution big enough to describe the kinetic process under study. For example, a spectroscopic tool that requires 1 min to acquire a single spectrum is not useful if the entire molecular mechanism requires hundreds of milliseconds to reach completion. Also, for some spectroscopic tools there is the need to acquire data at low temperature (frozen samples). To address this issue, one has to be able of produce frozen samples for different reaction times. Therefore, detection methods/sampling techniques are also particular important.

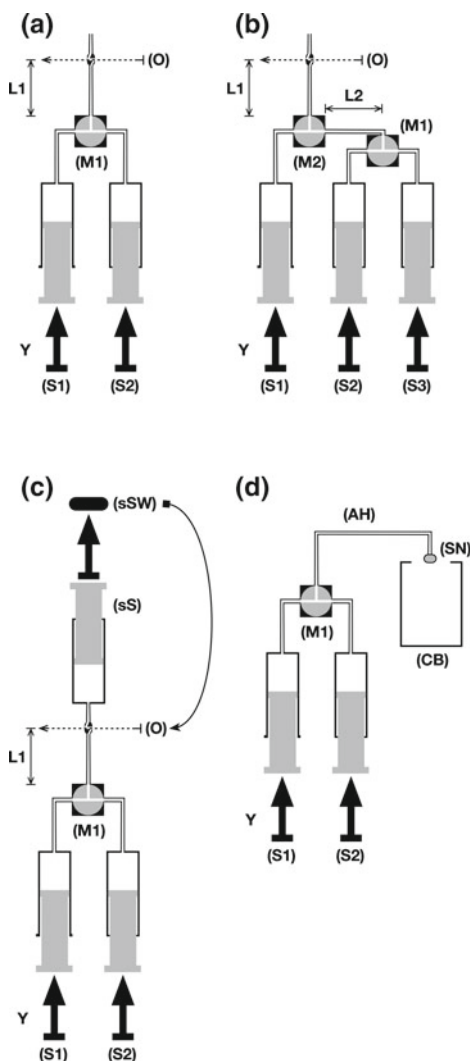
13.2 Rapid Mixing Techniques

All rapid mixing techniques share the same basic setup: (i) a propulsion mechanism; (ii) two, or more, syringes where reagents are stored; and (iii) a mixer. The propulsion mechanism will drive the syringes pushing forward, at a constant flow, small volumes of reagents into the mixer. Usually the propulsion mechanism is either a pneumatic or stepper motor-based system. The latter is usually preferred since it can be fitted with one stepper motor per syringe, thus making the delivered volume controlled independently. This is especially relevant in systems with more than two syringes

and sequential mixing (also denominated by double mixing or multi-mixing) for which concentration dependence experiments become faster and more efficient (see Fig. 13.1b). More complex experiments can also be devised with sequential mixing where reagents are sequentially added at different reaction times. Reagents will flow through a high efficiency mixer to initiate the reaction, thus defining the initial time of reaction (t_0). What happens next regarding detection defines which type of fast kinetic method is used.

Fig. 13.1 Different configurations for rapid mixing methods.

a Continuous-flow setup with two syringes (S1 and S2) and one mixer (M1). The length of line from M1 to the detection point (O) and the flow velocity Y will define the experimental dead time ($L1/Y$). **b** Setup with three syringes (S1, S2 and S3) and two mixers (M1 and M2). A delay line connects M1 to M2. Reagents in S2 and S3 will react during the time $L2/Y$ before being mixed with reagent in S1. From that point on the total mixture will react during the time $L1/Y$. **c** Stopped-flow setup. An extra syringe (sS) is used to stop the flow and trigger the detection by hitting a switch (sSW). **d** Rapid freeze-quench setup. After mixing, the reagents in S1 and S2 are allowed to react during the time defined by the length of the aging hose (AH) plus the flying time (time it takes the droplets leaving the spray nozzle, SN, to reach the cold bath, CB).



13.2.1 *Continuous-Flow Method*

In the *continuous-flow* method reagents are constantly mixed together during the experiment. Let's assume that detection occurs at a point x , at a distance L from the mixer. For a linear flow velocity of Y after mixing, when reaching the detection point the reaction time is equal to L/Y (see Fig. 13.1a). Thus, to vary the reaction time one has to change either the flow velocity or the distance between mixer and detection point. The setup dead time is the smallest detection time possible to achieve and depends on the highest flow velocity and smallest distance usable. In continuous flow there is also a maximum reaction time limit, since there will be a physical limit to how long can the distance between mixer and detection point be. More importantly, usually the flow velocity should be sufficiently high to avoid laminar flow problems. For example, using tubing with a diameter of 1 mm and for flow velocities lower than 2 ms^{-1} the liquid will flow faster at the center of the tube in regard to the tubing walls giving unacceptable reaction time errors.

13.2.2 *Stopped-Flow Method*

There is however a different approach to monitor reactions where longer times do not present problems and lesser amount of reagent is used. The improved method is known as *stopped-flow* and in this case the same mixing method is applied but instead of continuously mixing together the reagents, the syringes are mechanically stopped (see Fig. 13.1c). Initially, as in the *continuous-flow* method, the reagents reach the detection point with a reaction time equal to L/Y . When the flow is stopped, the solution at the detection point will not be replaced and reaction times longer than L/Y will be monitored, with no upper time limit. Depending on the experimental setup used, each experiment (single time course) will require volumes between 10 and $400 \mu\text{L}$ for dead times of 1 ms or lower. The reaction can easily be monitored for several minutes. Currently, this is the technique of choice and has become the standard tool to monitor fast reactions. However, less desirable aspects have to be taken into account. The way the flow is stopped can generate experimental difficulties. The flow can be stopped either by introducing a third syringe placed after the detection system that once full will trigger a plunger to hit a block, causing the flow to be stopped almost instantaneously or, in systems with stepper motors, the synchronized stop of motors and closing of an exit valve. In any case, stopping the flow will take microseconds which can give rise to convection problems. This will also be dependent on experimental conditions such as temperature, solution viscosity, among others, and can impact on dead time values. Also, when compared to *continuous flow* methods, one has to be aware that detection equipment (e.g. spectrophotometers, spectrofluorimeters, CD spectrometers) requirements are more stringent obliging fast detection and recording systems. While in the *continuous-flow* method the detection system can have slow acquisition times, since at the detection point reaction time

is constant, time resolution in the *stopped-flow* method is dependent on how fast detectors can record a single measurement. For example, if the monitored reaction involves one single intermediate which maximum concentration is obtained at 30 ms, then a monitoring system that records a data point every each 10 ms will have a maximum of 3 data points describing the formation of such intermediate. Because of this, in stopped-flow apparatus, detection system will have detectors capable of recording a data point in microseconds, either at a single wavelength or, using diode array detectors, for a range of predefined wavelengths.

13.2.3 Rapid Freeze-Quench

So far, we assumed that detection systems will measure absorption or emission in the liquid state. But for some spectroscopies described in previous chapters such in not an option (e.g. EPR and Mössbauer spectroscopies). Data has to be acquired at temperatures lower than solutions freezing point, usually ranging from 2 to 200 K. For this reason, the methods described above are not suitable and a different sample preparation method is needed. For these cases, the method of choice is based on quenching techniques. In this type of techniques, a physical or chemical agent will prevent the reaction to proceed further, stopping the reaction at a predetermined time. Dropping the temperature is indeed the most useful way, since it will effectively freeze the reaction producing at the same time a sample that can be analyzed by the above cited spectroscopies. The method relies on an experimental setup, very similar to the one described for the *continuous-flow* method (see Fig. 13.1d) and is called *rapid freeze-quench*. At least two solutions of reagents are mixed together and will react while passing through a tube (with specific dimensions). As before, the tube (also called ageing hose) length and flow velocity will determine the reaction time until the end of the tube is reached. At that point the tube is fitted with a spray nozzle which will cause the solution to disperse over a cooling bath, usually isopentane kept at 130–135 K with liquid nitrogen. Upon reaching the liquid isopentane the droplets instantaneously freeze, giving rise to snow-like flakes, stopping the reaction. The flakes can then be packed into cells of any size or shape suitable for the spectroscopic tool to be used. The volume used per sample is also dependent on the chosen spectroscopic method. Typically, volumes of 150–250 μL of each reagent at twice the optimal concentration are needed per reaction time point. This makes the method quite reagent consuming to establish a single time course. For long reaction times, one can let the reagents stay inside the aging hose for as long as needed, before spraying into the cold bath. Alternatively, for reaction times of several minutes, the reagents can be mixed into the cell which, when the desired reaction time is reached, is then frozen with liquid nitrogen. The freezing process takes longer, but for these long reaction times, will not introduce significant error. For quantitative measurements one should be aware that packed flakes will have gaps and residual cryogenic solvent and are not the equivalent of a frozen solution. Thus, it is important to do some test experiments and calibrate the packing factor which is setup/packer dependent and

can be as low as 0.7. The instrument dead time will depend on the smallest reaction ageing hose and faster flow velocity used, which will give the shorter L/Y possible. The flying time, the time taken by the droplets to reach the cold bath, as well as the freezing time, will contribute to the dead time. To minimize the flying time the spray nozzle is kept as close as possible to the cryosolvent level in the cooling bath.

In our experience, reproducible results can be obtained for experimental dead times of 8–10 ms. Nevertheless, modified setups with ultrafast freeze-quenching techniques for which dead times of 100 μs can be achieved (Cherepanov and de Vries 2004; Belevich et al. 2009). In these cases, the authors refer to the technique by *ultra-fast freeze-quench*.

13.2.4 Calibration of Dead Time

In all the above cases, the instrument dead time is an important parameter since it is the time for which no signal detection is possible. Calibration with appropriate standard reactions is strongly advised. For example, the reduction reaction of 2,6-dichlorophenolindophenol (DCPIP) by ascorbic acid has been successfully used. The high molar absorptivity of oxidized DCPIP at 524 nm (reduced, protonated DCPIPH₂ is colorless) makes it suitable to monitor the reduction reaction by visible spectroscopy. The second order reduction rate strongly depends on pH, varying more than two orders of magnitude between pH 2 and 8. For (*ultra-*)*rapid freeze-quench* instruments, calibration can be made using the binding reaction of azide to horse heart metmyoglobin. Binding of azide will change heme spin state, from the high-spin to low-spin ferric state, and can be easily monitored by EPR spectroscopy. For azide concentrations lower than 1 mM, the binding reaction has a rate constant of 19,500 M⁻¹ s⁻¹¹.

13.3 Data Analysis

Analysis of the experimental data collected by the above cited methods has two important requirements:

- Interpretation of the spectroscopic data for the full time course, by spectral deconvolution of different kinetic species and corresponding quantitation;
- Use of a kinetic model that can explain the total number and kinetic behavior of identified species.

While the first requirement has been covered in the chapters dedicated to each spectroscopic method, the second will be discussed next.

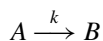
Rapid kinetic methods are used to study a single, first, turnover of the reaction. When we focus on enzyme-catalyzed reactions, it is usual to perform kinetic measurements in steady-state conditions, i.e. when the enzyme-substrate (ES) complex

concentration remains constant. While great amounts of information can be obtained in this type of analysis, there is an initial short time window, the so-called pre-steady-state (or transient) region, for which the ES complex changes in concentration (from zero to the steady-state concentration) and a first turnover can be observed. During this time short-lived reaction intermediates form and decay in a specific order, in accordance with a multi-step mechanism. Reaction intermediates are transient species that “can be defined only in relation to a time scale fixed by the experimental conditions and the limitations of the technique employed in the detection” (IUPAC 1997). They really define the transformations that occur in the ES complex during the catalytic reaction. Thus, the events associated with these changes occur on the enzyme active site, and one necessary experimental condition is that the enzyme is used in concentrations comparable to the substrate. It is important to note that the rates of formation and decay of any reaction intermediate must be consistent with the global reaction rate, i.e. none of the reaction intermediates can have a formation or decay rate slower than the global reaction rate. If an intermediate species is detected that does not conform to the global kinetic mechanism, then that species is not kinetically competent and probably is due to some artifact or non-homogeneous protein sample.

The use of a kinetic model is essential to try to explain the step-by-step molecular mechanism. While complex models require the use of numeric tools designed for modeling and analysis of dynamical systems, simpler kinetic mechanisms can be solved to find analytic expressions for species concentration as function of reaction time. In the next paragraphs we describe different kinetic models. In all cases, individual steps are considered to be irreversible and for most cases first order kinetics is used.

13.3.1 *Single First Order Irreversible Reaction*

The simplest kinetic model is the one that describes a single first order irreversible reaction, where a reagent A reacts to form product B. No intermediate species can be detected. This is the situation most commonly depicted in transition state diagrams with a single transition state (see Fig. 13.2). For this case:



$$-\frac{d[A]}{dt} = k[A]$$

and

$$\begin{aligned} [A] &= [A]_0 \times e^{-kt} \\ [B] &= [A]_0 \times (1 - e^{-kt}) \end{aligned}$$

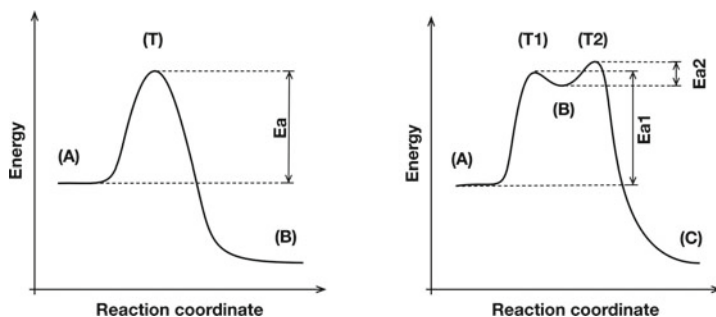
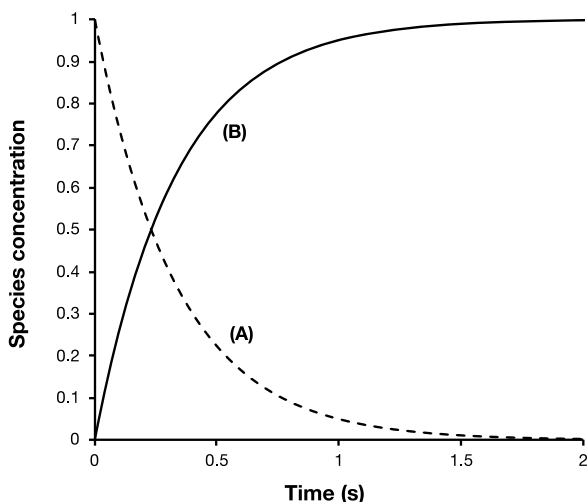


Fig. 13.2 Reaction energy profiles for one-step (left panel) and two-step (right panel) step reactions showing successive transition states and intermediates. In the first case product B forms from reagent A, with the decay rate of A being equal to the formation rate of B. In the second case two consecutive reactions exist with an intermediate B being formed from reagent A and decaying into product C. Decay and formation rates depend on energies E_{a1} and E_{a2}

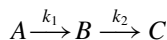
Fig. 13.3 Plot of the concentration of species A and B for a single first order irreversible reaction for $k = 3 \text{ s}^{-1}$



Since reagent A is directly transformed into the final product B, the rate of disappearance of A is always equal to the rate of appearance of B (see Fig. 13.3).

13.3.2 Two Consecutive First Order Reaction

A possible interpretation for the case where a single intermediate species is detected is the use of two consecutive, irreversible, first order reactions. In this case, the transition state diagrams will show two transition states (see Fig. 13.2), according with:



$$-\frac{d[A]}{dt} = k_1[A]$$

$$\frac{d[B]}{dt} = k_1[A] - k_2[B]$$

$$\frac{d[C]}{dt} = k_2[B]$$

and

$$[A] = [A]_0 \times e^{-k_1 t}$$

$$[B] = \frac{k_1[A]_0}{k_2 - k_1} \times (e^{-k_1 t} - e^{-k_2 t})$$

$$[C] = [A]_0 \left(1 - \frac{1}{k_2 - k_1} \times (k_2 e^{-k_1 t} - k_1 e^{-k_2 t}) \right)$$

It should be noticed that the rate of appearance of the final product C is independent of the rate of disappearance of the reagent A (see Fig. 13.4). Also, the accumulation of the intermediate species B is strongly dependent on the relative values of kinetic constants k_1 and k_2 . Thus, reaction intermediates are easier to detect when their formation rate is an order of magnitude different from their decay rate. This can be particularly important for situations where more than one reaction intermediate is detected.

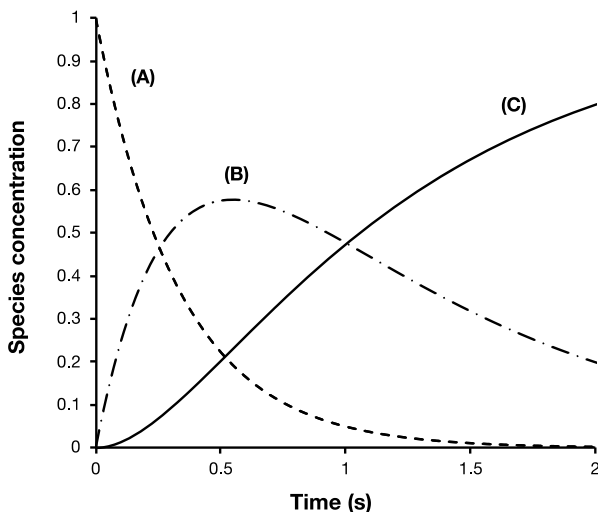
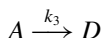
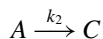
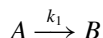


Fig. 13.4 Plot of the concentration of species A, B and C for two consecutive reactions with $k_1 = 3 \text{ s}^{-1}$ and $k_2 = 1 \text{ s}^{-1}$

13.3.3 Three Parallel First Order Reactions

One particular case of interest is that of parallel reactions, usually due to a reagent that can be involved in two or more simultaneous reactions. Assuming three parallel reactions we have:



$$-\frac{d[A]}{dt} = k_1[A] + k_2[A] + k_3[A]$$

$$\frac{d[B]}{dt} = k_1[A]$$

$$\frac{d[C]}{dt} = k_2[A]$$

$$\frac{d[D]}{dt} = k_3[A]$$

and

$$[A] = [A]_0 \times e^{-(k_1+k_2+k_3)t}$$

$$[B] = \frac{k_1[A]_0}{k_1 + k_2 + k_3} \times \left(1 - e^{-(k_1+k_2+k_3)t}\right)$$

$$[C] = \frac{k_2[A]_0}{k_1 + k_2 + k_3} \times \left(1 - e^{-(k_1+k_2+k_3)t}\right)$$

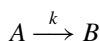
$$[D] = \frac{k_3[A]_0}{k_1 + k_2 + k_3} \times \left(1 - e^{-(k_1+k_2+k_3)t}\right)$$

As can be expected, the decay rate of reagent A is equal to the sum of formation rates of products B, C and D. Each individual formation rate, and final relative concentrations, of products is proportional to the ratio of individual rate constants (see Fig. 13.5).

13.3.4 Other Models

Several different models are listed below. For each the analytic solution of species concentration as a function of time is given. An Excel spreadsheet with custom functions that use these equations can be obtained upon request.

Single reaction, nth order



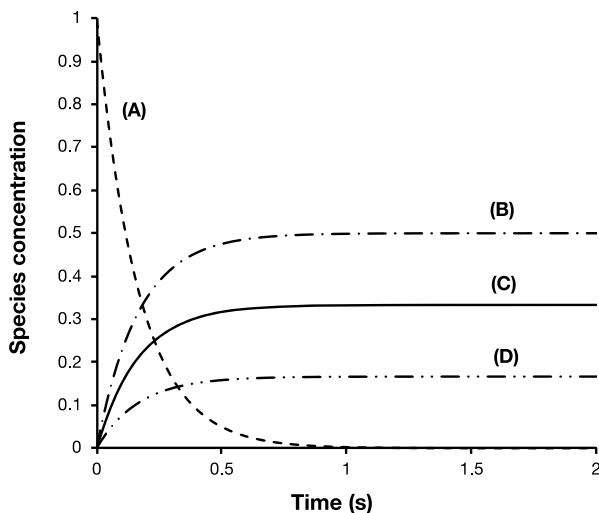


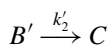
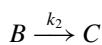
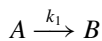
Fig. 13.5 Plot of the concentration of species A, B, C and D for three parallel reactions with $k_1 = 3 \text{ s}^{-1}$, $k_2 = 2 \text{ s}^{-1}$ and $k_3 = 1 \text{ s}^{-1}$

$$-\frac{d[A]}{dt} = k[A]^n$$

and

$$[A] = \left[\frac{1}{\frac{1}{[A]_0^{n-1}} + (n+1) \times kt} \right]^{\frac{1}{n-1}} \quad [B] = [A]_0 - [A]$$

Two consecutive reactions with two reaction intermediates



$$-\frac{d[A]}{dt} = (k_1 + k'_1)[A]$$

$$\frac{d[B]}{dt} = k_1[A] - k_2[B]$$

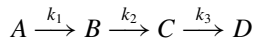
$$\frac{d[B']}{dt} = k'_1[A] - k'_2[B']$$

$$\frac{d[C]}{dt} = k_2[B] + k_2'[B']$$

and

$$\begin{aligned} [A] &= [A]_0 \times e^{-(k_1+k_1')t} \\ [B] &= \frac{k_1[A]_0}{k_2 - (k_1 + k_1')} \times \left(e^{-(k_1+k_1')t} - e^{-k_2t} \right) \\ [B'] &= \frac{k_1'[A]_0}{k_2 - (k_1 + k_1')} \times \left(e^{-(k_1+k_1')t} - e^{-k_2't} \right) \\ [C] &= [A]_0 \left(1 - e^{-(k_1+k_1')t} - \frac{k_1}{k_2 - (k_1 + k_1')} \times \left(e^{-(k_1+k_1')t} - e^{-k_2t} \right) \right. \\ &\quad \left. - \frac{k_1'}{k_2 - (k_1 + k_1')} \times \left(e^{-(k_1+k_1')t} - e^{-k_2't} \right) \right) \end{aligned}$$

Three consecutive first order reactions



$$\begin{aligned} -\frac{d[A]}{dt} &= k_1[A] \\ \frac{d[B]}{dt} &= k_1[A] - k_2[B] \\ \frac{d[C]}{dt} &= k_2[B] - k_3[C] \\ \frac{d[D]}{dt} &= k_3[C] \end{aligned}$$

and

$$\begin{aligned} [A] &= [A]_0 \times e^{-k_1t} \\ [B] &= \frac{k_1[A]_0}{k_2 - k_1} \times \left(e^{-k_1t} - e^{-k_2t} \right) \\ [C] &= k_1 k_2 [A]_0 \left(\frac{e^{-k_2t}}{(k_2 - k_1)(k_3 - k_1)} - \frac{e^{-k_2t}}{(k_2 - k_1)(k_3 - k_2)} + \frac{e^{-k_3t}}{(k_3 - k_1)(k_3 - k_2)} \right) \\ [D] &= [A]_0 \left(1 - \frac{k_2 k_3 e^{-k_2t}}{(k_2 - k_1)(k_3 - k_1)} - \frac{k_1 k_3 e^{-k_2t}}{(k_2 - k_1)(k_3 - k_2)} + \frac{k_1 k_2 e^{-k_3t}}{(k_3 - k_1)(k_3 - k_2)} \right) \end{aligned}$$

13.4 The Ferroxidation Reaction—Case Study

The combination of rapid kinetic methods with different spectroscopies has been successfully applied for the detection and characterization of reaction intermediates of many different reactions. From the experimental point of view the biggest challenge will be the number of samples needed for a complete kinetic description of the system. Particularly for biological macromolecules, such as proteins/enzymes, this can be a drawback, sometimes only solved by using overexpression systems capable of overcoming the need for milligrams of pure enzyme. Also, a single dataset or the use of a single spectroscopy is sometimes not enough to fully understand the molecular mechanism. The following system is one of these examples. Over several years fast kinetic methods coupled to four different spectroscopies were used to prove the involvement of a specific intermediate in the catalytic cycle.

Iron is an essential nutrient for almost all forms of life, but its insolubility and reactivity lead to problems of poor availability and toxicity. To provide sufficient quantities of iron and maintaining it in a nontoxic state, cells use a mechanism that involves iron storage proteins, generically known as ferritins. Ferritin is the only protein known to direct a reversible phase transition from a metal ion in solution to a metal ion in a solid matrix. Bone and tooth formation and resorption processes are formally analogous to the mineralization of ferritin, but a large number of cells and extracellular macromolecules are required in contrast to the case of ferritin. The major role of ferritin in the cells is to concentrate and store iron, since the metal is used in amounts that are effectively one hundred billion times the solubility of free iron. During oxidative stress or with iron excess, ferritin appears to protect against radical damage by managing iron-dioxygen interactions. Ferritins have been found in all three domains of life, animals, plants and microorganisms, playing an important role as housekeeping cellular iron homeostasis. Despite the differences in their amino acid sequences, all ferritins are structurally and functionally similar. Ferritins are comprised of 24 subunits organized into a hollow spherical protein shell with a total molecular weight of ~480 kDa. The protein shell has an outer diameter of approximately 120 Å. The central spherical cavity has a diameter of approximately 80 Å and can store up to ~4,500 iron atoms in the form of a ferrihydrite ($\text{Fe}_2\text{O}_3 \cdot n\text{H}_2\text{O}$)-phosphate mineral core.

The frog M-ferritin (see Fig. 13.6) was used to study the mechanism of ferroxidation and core formation. Ferritin substrates are ferrous ions and molecular oxygen. During catalysis, ferritin molecules bind ferrous ions in solution at specific ferroxidation sites located on the protein shell, and use molecular oxygen to promote an oxidation reaction that results in the appearance of a first reaction intermediate. Subsequent intermediates are formed until nucleation sites located in the inner cavity promote mineral growth.

The nature of this first intermediate was evaluated using fast kinetic methods and several spectroscopies such as UV/visible, Mössbauer, XAS and Resonance Raman. In a paper published in 1998 (Pereira et al. 1998), rapid freeze-quench Mössbauer and stopped-flow absorption spectroscopy were used to monitor the ferroxidase reaction.

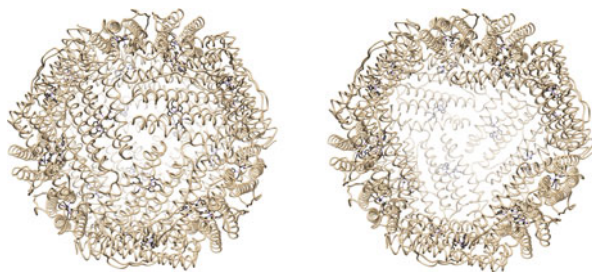


Fig. 13.6 Representation of M-ferritin structure. Left: Ribbon diagram of the 24-meric quaternary structure of bullfrog M-ferritin (PDB ID: 1MFR, figure prepared with UCSF Chimera, <http://www.cgl.ucsf.edu/chimera/>). Right: Same representation with three polypeptide chains hidden revealing the interior nanocavity

M-ferritin in the apo form (devoid of iron atoms) in a buffered molecular oxygen saturated solution was mixed with a ferrous ions solution to a final ratio of 36 Fe^{2+} /ferritin molecule. Mössbauer experimental data allowed determine the fast oxidation rate of ferrous ions (85% of the ferrous iron in samples was oxidized with a rate constant of 80 s^{-1}) with the concomitant appearance of a single transient species. This iron intermediate is characterized by a diamagnetic ground state with parameters $\Delta E_Q = 1.08 \pm 0.03 \text{ mm/s}$ and $\delta = 0.62 \pm 0.02 \text{ mm/s}$ which are indicative of an antiferromagnetically coupled diiron species. In particular, the parameters are typical of peroxodiferric complexes. The decay rate of this first intermediate species was estimated to be approximately 4 s^{-1} . In accordance with the observed formation and decay rates, accumulation of this intermediate was maximum at about 25 ms (ca. 70% of the total iron in the sample). In stopped-flow absorption spectroscopy measurements a transient blue species ($\lambda_{\text{max}} = 650 \text{ nm}$, $\epsilon_{650} \approx 10^3 \text{ M}^{-1} \text{ cm}^{-1}$) was detected with the same formation and decay rates. The observed optical properties agree with the ones obtained for peroxodiferric compounds and can be attributed to peroxodiferric-to-Fe charge-transfer transitions.

In 1999 a second publication presented a study where resonance Raman was used to further characterize the first reaction intermediate (Moënné-Loccoz et al. 1999). Since the time course was already known, rapid freeze-quench samples were prepared for a reaction time equal to 25 ms. This would ensure that the intermediate was the major iron species in the sample. Since vibrational energy will depend on the isotope used, samples were prepared using $^{16}\text{O}_2$, $^{16}\text{O}^{18}\text{O}$ or $^{18}\text{O}_2$. Samples prepared with $^{16}\text{O}_2$, showed discrete vibrational modes which, as observed in the Mössbauer spectra, and supported the presence of a single chromophore in a homogeneous state. The frequency at 851 cm^{-1} was assigned to a $\nu(\text{O}-\text{O})$ of the iron bound peroxide with an additional pair of frequencies at 485 and 499 cm^{-1} assigned to ν_s and ν_{as} of the $\text{Fe}-\text{O}_2-\text{Fe}$ moiety. When pure $^{18}\text{O}_2$ was used, the frequency at 851 cm^{-1} shifted to 800 cm^{-1} in accordance with a predicted value for the shift of -49 cm^{-1} . For the case where a mixed-isotope gas containing ca. 50% $^{16}\text{O}^{18}\text{O}$ was used a broad

peak with maximum lying between the 851 and 800 cm^{-1} could be observed. The resonance Raman data supported previous Mössbauer observations.

One year later, seeking to further characterize the reaction intermediate species, X-ray absorption spectroscopic techniques was used to probe rapid freeze-quench samples trapped at 25 ms and 1 s (Hwang et al. 2000). According with the very first rapid freeze-quench experiments, in these samples the peroxodiferric intermediate decreased from 70% to less than 5%, respectively. Particular care was taken and Mössbauer spectra collected in all samples before and after X-ray irradiation, to properly quantify all iron species and ensure sample integrity. XAS spectrum showed incomplete oxidation for the 25 ms quenched sample, in agreement with Mössbauer quantification. Importantly, EXAFS data for the 25 ms quenched sample showed a rather unique peak modelled as an Fe–Fe shell at ~ 2.53 Å. Smaller than expected for a peroxodiferric intermediate, this data suggested the presence of a small Fe–O–O angle of $\sim 106^\circ$ – 107° , that would favor the decay of the peroxodiferric intermediate into a μ -oxo or μ -hydroxo diferric mineral precursor, with concomitant release of hydrogen peroxide. These experiments also found Fe–Fe distances compatible with μ -oxo or μ -hydroxo diferric complexes in the 1 s sample.

In 2002 an attempt was made to identify the products of the decay of the peroxodiferric intermediate (Jameson et al. 2002; Krebs et al. 2002). The reported experiment used the rapid-freeze quench technique to quantify one possible product of the reaction. By doing so, the mixing conditions used for all previous experiments were maintained and reaction time was precisely controlled at the millisecond scale. The experiments done close resembled the rapid freeze-quench sample preparation, but instead of spraying the reaction mixture in a cold bath, the sample was sprayed into a cell containing horseradish peroxidase, 4-aminoantipyrine and vanillin acid in buffer solution. As a result, any hydrogen peroxide produced would be used as substrate by the peroxidase enzyme to oxidize 4-aminoantipyrine. The product of this oxidation condenses with vanillin acid to form a red quinone mine dye with well characterize absorption band at 490 nm, making possible its quantitation. Using this assay, it was possible to demonstrate that the decay reaction of the peroxodiferric intermediate produced hydrogen peroxide. More, monitoring this decay by rapid-freeze quench Mössbauer it was also possible to show that the peroxodiferric intermediate was converted into μ -oxo and/or μ -hydroxo ferric dimers and small polynuclear ferric clusters, since this species are formed at rate constants identical to the decay of the peroxodiferric intermediate.

Figure 13.7 summarizes the findings described here. It must be said that this is only one of the many examples found in the literature where rapid mixing methods were used in conjunction with spectroscopic tools to unravel biological reaction mechanisms. Such results demonstrate without doubt, that such experimental approach is a powerful way of making “stop-motion films” of enzyme’s reactions and have become a powerful way to understand reaction mechanisms at the molecular level.

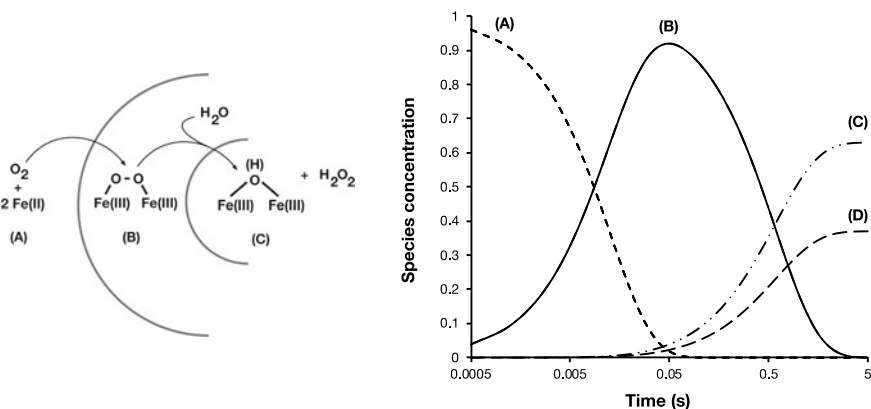


Fig. 13.7 Left: Schematic representation of the molecular mechanism proposed for the fast ferrooxidation process in M-ferritin. Right: Plot of the concentration of species involved in the ferrooxidation. A—ferrous substrate; B—peroxodiferric intermediate, C— μ -hydroxo ferric dimers, and D—small polynuclear ferric clusters

13.5 Further Reading

This chapter is just a short primer to understand the use of rapid mixing methods. More examples and detailed coverage on some of the aspects addressed in this chapter can be found in the following bibliographic list.

13.5.1 Rapid Kinetic Methods

Kaufmann, R., Yadid, I., & Goldfarb, D. (2013). A novel microfluidic rapid freeze-quench device for trapping reactions intermediates for high field EPR analysis. *J. Magn. Reson.*, 230(C), 220–226. <http://doi.org/10.1016/j.jmr.2013.01.016>

Krebs, C., Price, J. C., Baldwin, J., Saleh, L., Green, M. T., & Bollinger, J. M. (2005). Rapid Freeze-Quench ^{57}Fe Mössbauer Spectroscopy: Monitoring Changes of an Iron-Containing Active Site during a Biochemical Reaction. *Inorg. Chem.*, 44(4), 742–757. <http://doi.org/10.1021/ic0485231>

Kim, S. H., Perera, R., Hager, L. P., Dawson, J. H., & Hoffman, B. M. (2006). Rapid Freeze-Quench ENDOR Study of Chloroperoxidase Compound I: The Site of the Radical. *J. Am. Chem. Soc.*, 128(17), 5598–5599. <http://doi.org/10.1021/ja060776l>

Srouf, B., Strampraad, M. J. F., Hagen, W. R., & Hagedoorn, P.-L. (2018). Refolding kinetics of cytochrome c studied with microsecond timescale continuous-flow UV–vis spectroscopy and rapid freeze-quench EPR. *J. Inorg. Biochem.*, 184, 42–49. <http://doi.org/10.1016/j.jinorgbio.2018.04.011>

Matsumura, H., & Moëne-Loccoz, P. (2014). Characterizing Millisecond Intermediates in Hemoproteins Using Rapid-Freeze-Quench Resonance Raman Spec-

troscopy. In B. P. Leblanc & S. Rodrigue (Eds.), *DNA-Protein Interactions* (Vol. 1122, pp. 107–123). Totowa, NJ: Humana Press. http://doi.org/10.1007/978-1-62703-794-5_8

Mitić, N., Saleh, L., Schenk, G., Bollinger, J. M., & Solomon, E. I. (2003). Rapid-Freeze-Quench Magnetic Circular Dichroism of Intermediate X in Ribonucleotide Reductase: New Structural Insight. *J. Am. Chem. Soc.*, 125(37), 11200–11201. <http://doi.org/10.1021/ja036556e>

Nami, F., Gast, P., & Groenen, E. J. J. (2016). Rapid Freeze-Quench EPR Spectroscopy: Improved Collection of Frozen Particles. *Appl. Magn. Reson.*, 47(6), 643–653. <http://doi.org/10.1007/s00723-016-0783-7>

Pievo, R., Angerstein, B., Fielding, A. J., Koch, C., Feussner, I., & Bennati, M. (2013). A Rapid Freeze-Quench Setup for Multi-Frequency EPR Spectroscopy of Enzymatic Reactions. *ChemPhysChem*, 14(18), 4094–4101. <http://doi.org/10.1002/cphc.201300714>

de Vries, S., 2011. Encyclopedia of Inorganic and Bioinorganic. Freeze-Quench Kinetics. *Wiley Online Library*. <http://doi.org/10.1002/9781119951438.eibc0314>

13.5.2 General Kinetic Theory

Cornish-Bowden, A. “Fundamentals of Enzyme Kinetics” 4th Edition (2012), Wiley-Blackwell, ISBN 978-3-527-33074-4

Johnson, K. A. (2013). A century of enzyme kinetic analysis, 1913 to 2013. *FEBS Lett.*, 587(17), 2753–2766. <http://doi.org/10.1016/j.febslet.2013.07.012>

Nagar, S., Argikar, U. A., & Tweedie, D. J. (Eds.). (2014). Enzyme Kinetics in Drug Metabolism. *Methods in Molecular Biology*. <http://doi.org/10.1007/978-1-62703-758-7>

Purich, D. “Enzyme Kinetics: Catalysis and Control” 1st Edition (2010), Elsevier, ISBN 9780123809247

Sassa, A., Beard, W. A., Shock, D. D., & Wilson, S. H. (2013). Steady-state, Pre-steady-state, and Single-turnover Kinetic Measurement for DNA Glycosylase Activity. *J. Visualized Exp.: JoVE*, (78), 1–8. <http://doi.org/10.3791/50695>

Acknowledgements The Portuguese National Funding Agency FCT-MCTES through Research Grants POCTI/QUI/37413/2001, POCTI/QUI/47273/2002, POCI/QUI/57475/2004, PTDC/QUI/64248/2006, PTDC/QUI/67142/2006, PTDC/SAU-SAP/111482/2009, PTDC/BIA-PRO/111485/2009, and PTDC/OCE-ETA/32567/2017. This work was also supported by Radiation Biology and Biophysics Doctoral Training Programme (RaBBiT, PD/00193/2010); UID/Multi/04378/2019 (UCIBIO); UID/FIS/00068/2013 (CEFITEC).

References

- Belevich NP, Verkhovskaya ML, Verkhovsky MI (2009) Chapter 4 Electron transfer in respiratory complexes resolved by an ultra-fast freeze-quench approach. *Methods Enzymol* 456:75–93. [http://doi.org/10.1016/S0076-6879\(08\)04404-2](http://doi.org/10.1016/S0076-6879(08)04404-2)
- Cherepanov AV, de Vries S (2004) Microsecond freeze-hyperquenching: development of a new ultrafast micro-mixing and sampling technology and application to enzyme catalysis. *Biochim Biophys Acta Bioenerg* 1656(1):1–31. <http://doi.org/10.1016/j.bbabi.2004.02.006>
- Hwang J, Krebs C, Huynh BH, Edmondson DE, Theil EC, Penner-Hahn JE (2000) A short Fe-Fe distance in peroxodiferric ferritin: control of Fe substrate versus cofactor decay? *Science* 287(5450):122–125. <https://doi.org/10.1126/science.287.5450.122>
- IUPAC. Compendium of chemical terminology, 2nd ed (the “Gold Book”). Compiled by McNaught AD, Wilkinson A. Blackwell Scientific Publications, Oxford (1997). XML on-line corrected version: <http://goldbook.iupac.org> (2006–) created by Nic M, Jirat J, Kosata B; updates compiled by Jenkins A. ISBN 0-9678550-9-8. <https://doi.org/10.1351/goldbook>
- Jameson GNL, Jin W, Krebs C, Pereira AS, Tavares P, Liu X et al (2002) Stoichiometric production of hydrogen peroxide and parallel formation of ferric multimers through decay of the diferric-peroxo complex, the first detectable intermediate in ferritin mineralization. *Biochemistry* 41(45):13435–13443. <https://doi.org/10.1021/bi026478s>
- Krebs C, Edmondson DE, Huynh, BH (2002) Demonstration of peroxodiferric intermediate in M-ferritin ferroxidase reaction using rapid freeze-quench Mössbauer, Resonance Raman, and XAS spectroscopies. *Methods Enzymol* 436–454. [http://doi.org/10.1016/s0076-6879\(02\)54034-9](http://doi.org/10.1016/s0076-6879(02)54034-9)
- Moëgne-Loccoz P, Krebs C, Herlihy K, Edmondson DE, Theil EC, Huynh BH, Loehr TM (1999) The ferroxidase reaction of ferritin reveals a diferric μ -1,2 bridging peroxide intermediate in common with other O₂-activating non-heme diiron proteins †. *Biochemistry* 38(17):5290–5295. <https://doi.org/10.1021/bi990095l>
- Pereira AS, Small W, Krebs C, Tavares P, Edmondson DE, Theil EC, Huynh BH (1998) Direct spectroscopic and kinetic evidence for the involvement of a peroxodiferric intermediate during the ferroxidase reaction in fast ferritin mineralization. *Biochemistry* 37(28):9871–9876. <https://doi.org/10.1021/bi980847w>

Chapter 14

Radiobiological Effects Induced by X-ray (LINAC) Irradiation: Experiments and Modelling



A. Traoré-Dubuis, L. Ellis-Gibblings, K. Krupa, A. I. Lozano, R. Colmenares, A. Muñoz, J. C. Oller, F. Blanco, A. García Grande, M. J. Coronado, S. Rosado, E. Ramil, L. Núñez, Paulo Limão-Vieira and G. García Gómez-Tejedor

A. Traoré-Dubuis · L. Ellis-Gibblings · K. Krupa · A. I. Lozano · G. García Gómez-Tejedor (✉)
Instituto de Física Fundamental, Consejo Superior de Investigaciones Científicas (CSIC), Serrano
113-bis, 28006 Madrid, Spain
e-mail: g.garcia@csic.es

L. Ellis-Gibblings
Department of Chemistry, Faculty of Maths & Physical Sciences, University College London,
Gower St., London WC1E 6BT, UK

K. Krupa · P. Limão-Vieira
Atomic and Molecular Collisions Laboratory, CEFITEC, Department of Physics, Faculdade de
Ciências e Tecnologia, Universidade NOVA de Lisboa, 2829-516 Caparica, Portugal

R. Colmenares
Servicio de Radiofísica, Hospital Universitario Ramón y Cajal, Ctra Colmenar Viejo km 9.1,
28034 Madrid, Spain

A. Muñoz · J. C. Oller
Departamento de Tecnología, Centro de Investigaciones Energéticas, Medioambientales y
Tecnológicas (CIEMAT), Avenida Complutense 22, 28040 Madrid, Spain

F. Blanco
Departamento de Física Atómica, Departamento de Estructura de la Materia Física Térmica y
Electrónica, Universidad Complutense de Madrid, Plaza de Ciencias 1, 28040 Madrid, Spain

A. García Grande · M. J. Coronado · S. Rosado · E. Ramil
Instituto de Investigación Sanitaria Puerta de Hierro-Segovia de Arana (IDIPHIM), Joaquín
Rodrigo 2, Majadahonda, 28222 Madrid, Spain

L. Núñez
Servicio de Radiofísica y Protección Radiológica, Hospital Universitario Puerta de Hierro –
Majadahonda, Manuel de Falla 1, 28222 Madrid, Majadahonda, Spain

© Springer Nature Switzerland AG 2019

A. S. Pereira et al. (eds.), *Radiation in Bioanalysis*, Bioanalysis 8,
https://doi.org/10.1007/978-3-030-28247-9_14

14.1 Introduction

Photon radiotherapy has long been established as a useful tool for cancer treatment. The first powerful irradiation units were based on Co-60 radioactive sources (Johns et al. 1951) emitting gamma rays of 1.17 and 1.33 MeV photon energies. A few years later linear electron accelerators (LINAC) were adapted to be suitable for radiotherapy applications. To produce ionising radiation, LINACs use either high energy electron beams or the corresponding X-ray photon beams generated by stopping the electron beam with an appropriate tungsten target (Bremsstrahlung). These LINAC units have been used extensively in radiotherapy treatments, now reaching accelerator voltages up to 12–25 MeV (see Thwaites and Tuohy 2006 for historical details). A large representative percentage of these treatments were carried out at accelerating voltages around 6 MeV. The average energy of the corresponding continuous X-ray energy distribution from a 6 MeV LINAC is around 1 MeV and is therefore similar to the average gamma-ray energy of the former Co-60 units. This allowed a translation of radiation dose concepts between the two techniques. The reference unit for all these treatments is the absorbed dose (ICRU 2010), i.e. the total energy absorbed per unit mass of the medium in Gray [Joule/Kilogram = Gray] (ICRU 2011). As a direct measurement of the absorbed dose (D) is not feasible the standard procedure to evaluate D consists of measuring, with an ionisation chamber, the number of ions (N_i) produced by the radiation. Assuming a constant energy (w) required to generate an ion-electron pair we can write $D = wN_i$. Similarly, the radiobiological effect of the radiation is determined by its Relative Biological Effectiveness (RBE) which is assumed to be proportional of the absorbed dose $RBE = kD = kwN_i$, k being a constant which depends on the type of radiation and the type of irradiated tissue (ICRP 2003).

After pioneering experiments to analyse the capability of non-ionizing radiation to produce biological damage, Boudaïffa et al. (2000) demonstrated in 2000 that low energy electrons were able to efficiently induce single (SSD) and double (DSB) strand breaks to DNA (Boudaïffa et al. 2000) through a resonant electron attachment process. Additional proof of these processes were found in the anion yield spectra observed by Abdoul-Carime et al. (2004) and Ptasinska et al. (2005), and these DNA bond breaks have been positively identified as generated by dissociative electron attachment (DEA). In DEA, incident electrons with energies much lower than the ionisation energy can resonantly attach to a molecule, thus forming a temporary negative ion which decays by dissociating the molecule. These low energy dissociation processes in some cases include electronic and vibrational excitation. Despite their relevance, these low-energy dissociations are not accounted for in traditional dosimetric methods focusing solely on the absorbed dose. As DEA can occur with electrons with energies close to zero (thermal energies), inducing molecular dissociation with almost no energy deposition, they can therefore provide a null contribution

G. García Gómez-Tejedor
Centre for Medical Radiation Physics (CMRP), University of Wollongong, Wollongong, NSW,
Australia

to the absorbed dose while still damaging the target. This damage, in the form of molecular dissociations, constitutes the beginning of possible biological damage if DNA repair mechanisms fail (Santivasi and Xia 2014). Molecular dissociations can therefore be seen as the radiation induced damage at the molecular level (RDML) and should be the basis for a new molecular level dosimetry termed “nanodosimetry”. A review on the main mechanisms to generate radiation damage at the molecular level can be found in García Gómez-Tejedor and Fuss (2012). One method to model nanodosimetry to the required level of detail is a Monte Carlo simulation procedure (The Beginning 1987), if the user incorporated all the required molecular level interaction data (interaction cross sections, angular and energy loss distribution functions). These would be included as input parameters in order to provide a detailed 3-dimensional map containing information on the energy deposition and type and number of interactions taking place in any defined volume of interest.

Since 2000, research groups world-wide have been devoted to measuring and calculating these input parameters, in order to establish complete databases for modelling radiation damage at the molecular level. These include electron scattering cross sections with biologically relevant molecules and energy loss distribution functions, both in the gas and the condensed phase. Some of these results can be found in García Gómez-Tejedor and Fuss (2012) and references therein together with a summary of the most representative modelling procedures. Some simulation programs (Geant4-DNA (Incerti et al. 2010), PENELOPE (Salvat et al. 2003), LEPTS (Muñoz et al. 2005), PARTRAC (Friedland et al. 2010), EPOTRAN (Champion et al. 2012)) as well as others not mentioned in García Gómez-Tejedor and Fuss (2012) (Fluka (Battistoni et al. 2011), TRAX (Krämer and Kraft 1994)) have been specially designed to provide detailed information on single particle tracks and energy deposition in biological media, paying special attention to induced molecular damage to DNA components.

Of the simulations developed to model nanodosimetry, the Low Energy Particle Track Simulation (LEPTS) code was developed by our group in 2004 (Muñoz et al. 2005; Roldán et al. 2004) as a way to describe radiation damage at the molecular level. LEPTS focuses on low-energy electron generation and induced target dissociations as descriptors of radiation damage. In this study we apply the LEPTS simulation procedure to a 1 m³ water phantom irradiated with a LINAC accelerator operating at 6 MV acceleration voltage. We also observe experimentally the biological damage to Jurkat cell line cultures under the same irradiation conditions. The result of the simulation, in terms of energy deposition and type and number of processes taking place in selected points in the water phantom, is compared with the observed biological damage at those same points. The correlation between energy deposition and the number of induced molecular dissociations with the observed early apoptosis and nuclear DNA fragmentation provides relevant information on the radiobiological effect of the radiation and could be used to assign RBE values based on molecular damage considerations.

The remaining sections of this chapter are organised as follows: the main features of the present modelling procedures are summarised in Sect. 14.2, including a review of the required input data with special attention to the recently incorporated

processes. The radiobiological experiment performed by irradiating Jurkat cell lines (immortalised human T lymphocytes associated with leukaemia disease (Schneider et al. 1977)) within a liquid water phantom is described in Sect. 14.3. Experimental and simulated results are presented, analysed and compared in Sect. 14.4 and finally, some conclusions of the present study together with new perspectives and future directions are summarised in Sect. 14.5.

14.2 Modelling Photon and Electron Interactions in Water

The simulation procedures used in this study are Monte Carlo based methods. A general review of the most representative algorithms used for this type of simulation can be found in Muñoz et al. (2012). Within the present modelling procedure, all processes connected with photons are simulated with Geant4 (Agostinelli et al. 2003) using its standard electromagnetic physics package through the Geant4-based Architecture for Medicine-Oriented Simulations (GAMOS). Some details on this procedure will be given in Sect. 14.2.1. Every time a secondary electron via either Compton scattering, photoelectric effect or pair creation is generated along the simulation procedure, their coordinates, kinetic energy and initial momentum vectors are stored in a text file which will be used to generate the subsequent electron track simulation procedure. This has been carried out with our Low Energy Particle Track Simulation (LEPTS) procedure (Muñoz et al. 2005), an event by event Monte Carlo code especially designed to be fully compatible with Geant4 and particularly with the GAMOS interface. The LEPTS code has been detailed in previous publications (Muñoz et al. 2005, 2007a, 2008; Roldán et al. 2004; Blanco et al. 2013) and therefore only features relevant to the present study will be described in Sect. 14.2.2.

14.2.1 *Simulation of X-ray Photon Interactions in Water Using GAMOS*

The primary photon beam used for this experimental and modelling study is constituted by the Bremsstrahlung X-ray radiation beam generated in a Varian LINAC electron accelerator (CLINAC iX System) operating at 6 MV. A schematic diagram of the arrangement is shown in Fig. 14.1.

Due to the high flux conditions required by such an accelerator in order to maintain a stable energy distribution of the emitted photons, experimental spectra are not available. A Monte Carlo simulation of the electron beam production, X-ray generation on the tungsten anode and further collimation has been carried out by Lagares (2017). The energy and angular distributions simulated with this procedure are shown in Fig. 14.2.

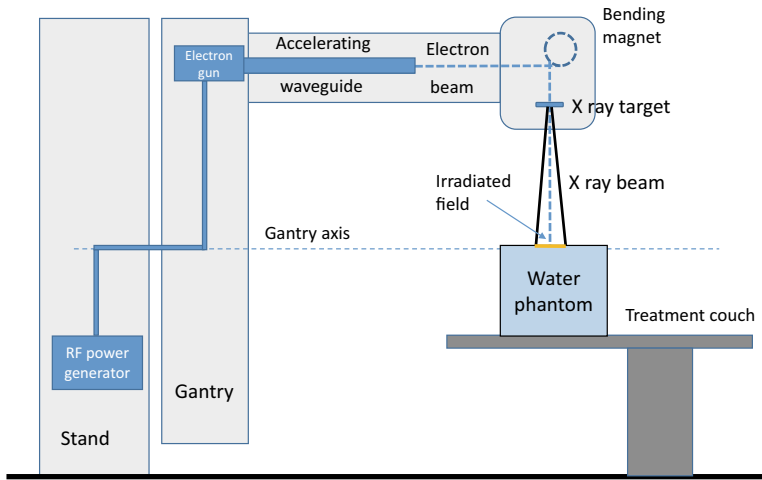


Fig. 14.1 Schematic diagram of the irradiating arrangement

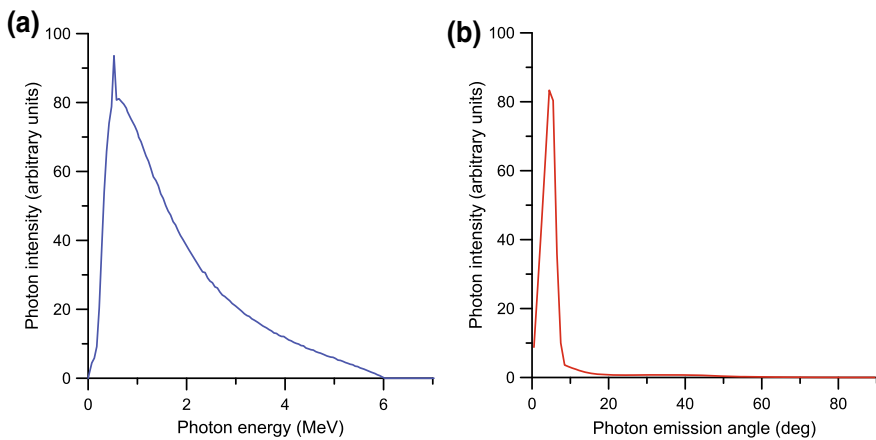


Fig. 14.2 X-ray energy (a) and angular (b) distributions for 6 MV electron acceleration voltage

The photon beam is directed onto the top surface of a 1 m^3 water phantom. The irradiated area on the phantom surface has $10 \times 10\text{ cm}^2$ and it is placed at a vertical distance of 0.45 m from the X ray output collimators.

As mentioned, photon interactions with liquid water have been simulated with the electromagnetic standard physics package of the Geant4 simulation toolkit. This Geant4 physics package is based on the Evaluated Photon Data Library “EPDL97” (Cullen et al. 1997) which considers photoelectric, Compton, Rayleigh, pair production and Bremsstrahlung processes. In order to illustrate the relevance of these

processes in the incident energy range the corresponding integral cross sections are plotted in Fig. 14.3.

Figure 14.4 shows the simulated interaction map of 5×10^4 photons by assuming the initial energy distribution shown in Fig. 14.2, a 10 cm^2 irradiated area and a vertical penetration of the photon beam into the 1 m^3 water phantom. The total initial energy transported by the primary photon beam is about $3.5 \times 10^{10} \text{ eV}$ which, according to the energy distribution shown in Fig. 14.2, gives an average energy of the beam of $1.76 \times 10^6 \text{ eV}$. Some details of the photon interactions close to the border of the irradiated volume are shown in Fig. 14.4b, indicating with different coloured and sized spheres the different photon interaction processes we are considering in this simulation (Compton scattering, photoelectric interaction, Rayleigh scattering and pair creation).

Secondary electrons produced by these photon interactions are generated by the simulation programme according to the Geant4-Livermore physics. As already mentioned, their positions and initial momentum vectors are stored in a file which will be incorporated to the subsequent electron track simulation.

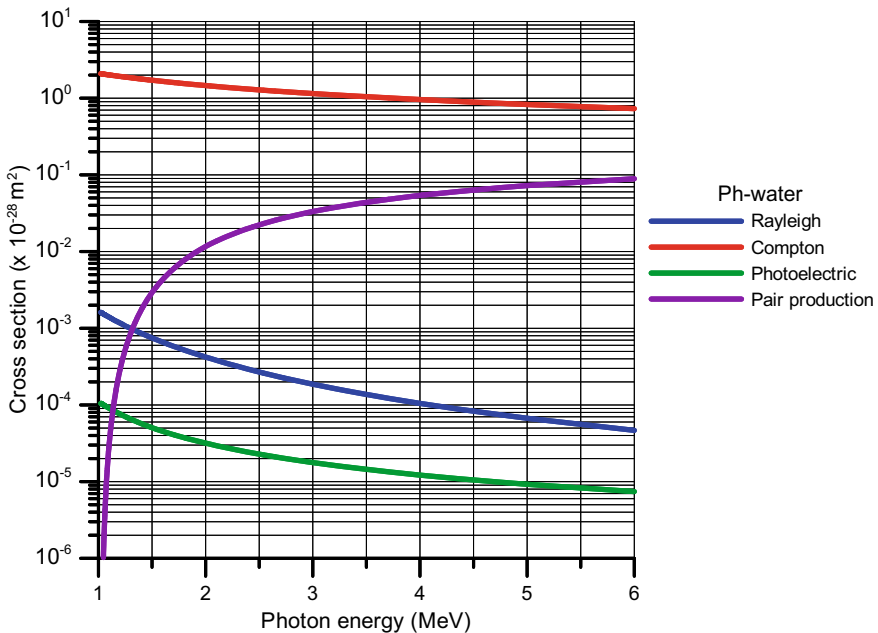


Fig. 14.3 Integral cross sections for photon interaction with water derived from the EPDL97 data library

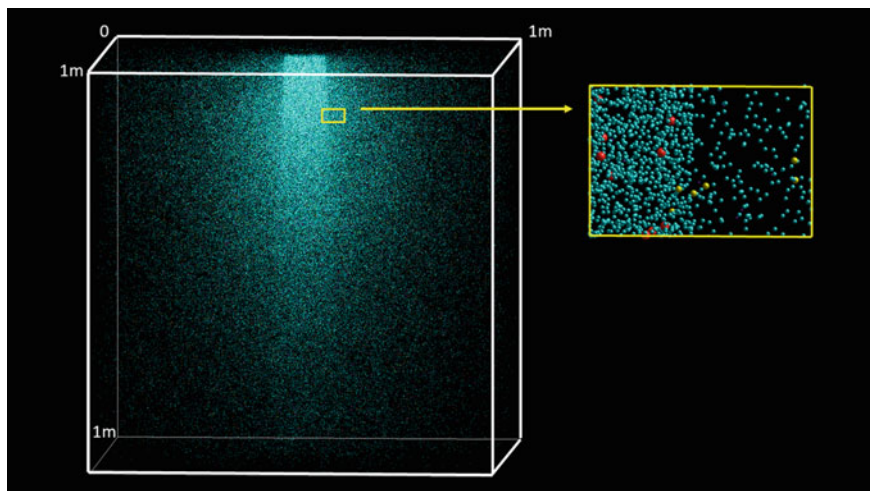


Fig. 14.4 Simulated map of interactions caused by X-ray photons generated by the LINAC accelerator (6 MV operation voltage) in the 1 m^3 liquid water phantom. Insert: detail of the selected area showing a colour code to indicate different events: ● scattering Compton; ● pair creation; ● photoelectric effect

14.2.2 *Modelling Electron Interactions with the Low Energy Particle Track Simulation (LEPTS) Code*

The LEPTS procedure has been described with detail in previous publications (Muñoz et al. 2005, 2007a, 2008, 2012; Roldán et al. 2004; Blanco et al. 2013). Briefly, it is an event by event Monte Carlo simulation programme based on the GAMOS architecture (GAMOS). As mentioned above, the input electron source (position and momentum vector of each electron generated by any of the considered photon interactions) is determined by the Geant4-GAMOS simulation described in the previous section. The energy distribution of these electrons is broad, varying from the low energy of those generated by small angle Compton scattering and low-energy-photon photoelectric processes, the intermediate energies from pair creation events, to the high energy (close to the energy of the primary photons) of those generated by primary photoelectric interactions and backscattered photons. Figure 14.5 shows the energy distributions of the electrons generated by the considered photon interaction processes as given by the Geant4 simulation, using standard electromagnetic physics. In order to simplify the data requirements, the electron energy range has been divided into two impact energy regions from 0 to 10 keV and above 10 keV. For the higher energies, from 10 keV to 6 MeV, the electron energy distributions are represented in Fig. 14.5 for each of the considered photon interaction processes. For these we have assumed that the incident energy is high enough to validate the Born approximation (Inokuti 1971; Inokuti and McDowell 1974). This assumption is based on previous electron scattering cross section experiments that we published

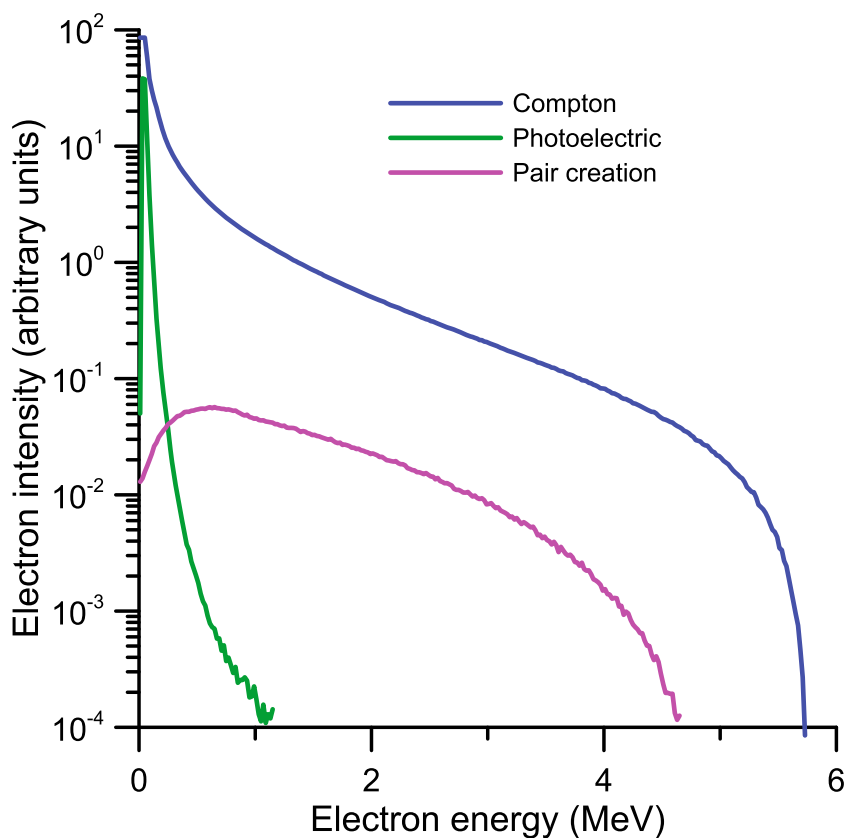


Fig. 14.5 Energy distribution of the secondary electrons generated by the considered photon interaction processes

some years ago for different molecules (García and Manero 1998; García and Blanco 2000), including water (Muñoz et al. 2007b). In this context, using the Born based data from the LLNL Evaluated Electron Data Library (Perkins et al. 1991) for the O and H atoms and considering the momentum transfer relation with the incident energy derived from this approximation, all the required data in terms of interaction probabilities, angular distribution of scattered electrons and energy deposition are straightforwardly derived.

For energies below 10 keV different theoretical and experimental techniques, depending on the scattering process and the incident energy, are used to obtain the required input information for water. These inputs are namely the interaction probabilities (derived from the integral cross sections-ICS), the angular distribution functions (derived from the differential cross sections-DCS) and the energy loss distribution functions (derived from the experimental energy loss spectra-ELS). Details on the experimental and theoretical procedures used to derive these data are given

in Blanco et al. (2013) and therefore we only give a brief summary here focused on the three main categories of the required input information.

14.2.2.1 Interaction Probabilities

These data are directly derived from the integral elastic (IECS) and integral inelastic (IICS) cross sections. IECS values used in this simulation come 100% from calculations. In fact, it is not possible to directly measure IECSs but they are commonly derived from the integration of differential cross section (DCS) measurements which requires some additional theoretical approaches (Hishiyama et al. 2017). To produce the IECS we used our Independent Atom Model (IAM) calculation complemented with the Screening Corrected Additivity Rule (SCAR) and considering interference effects (IAM-SCAR+I), see Blanco et al. (2016) and references therein for details. This procedure has been demonstrated to be reliable within 10% for impact electron energies ranging from 10 eV to 10 keV for a great variety of molecular targets (Sanz et al. 2013, 2014; Loupas et al. 2018). We should note here that we consider as elastic processes only those in which no energy is transferred to excite any internal degree of freedom of the target molecule, i.e. when the total kinetic energy of the projectile-target molecule system remains constant under the collision. Below 10 eV more sophisticated approaches considering molecular orbitals and using “ab initio” methods to account for electron correlations have been considered. In particular we included the R-matrix (Tennyson 2010) calculation for water (Faure et al. 2004), which showed a remarkable consistency with the IAM-SCAR+I calculations for different molecular targets (Sanz et al. 2013, 2014; Loupas et al. 2018). The IECS values in this simulation are shown in Fig. 14.6 together with those corresponding to the inelastic processes that will be described in the next paragraph. As shown in this figure, elastic collisions are important at any incident energy. Being dominant for the lower energies they still represent about 50% of all the collision processes at the higher energies. As detailed previously (Blanco et al. 2013), our SCAR procedure has also been used to account for the overlapping of the molecular integral cross sections when considering a liquid environment. Liquid water is then modelled here as 10^3 kg/m^3 density material constituted by single water molecules whose electron collision cross sections are reduced by the energy dependent condensation factor calculated with the SCAR method (see Blanco et al. 2013 for details).

IICS is formed by the sum of the contributions of all the inelastic channels that are open (energetically accessible) at a given incident energy. For increasing excitation energies, the first inelastic open channel corresponds to rotational excitation processes (0.012 eV average excitation energy at 300 K (Polyansky et al. 2013)). Vibrational excitation, electronic excitation and ionisation of water molecules have their threshold energies at 0.2 eV (Nishimura and Gianturco 2004), 4.5 eV (Trajmar et al. 1973) and 12.8 eV (Müller and Cederbaum 2006), respectively. Condensation effects tend to lower the ionisation energy (Müller and Cederbaum 2006; Barth et al. 2009) hence we assumed an extrapolated ionisation energy of 10.79 eV for the liquid water. In these conditions, our IAM-SCAR+I calculation provided the reference

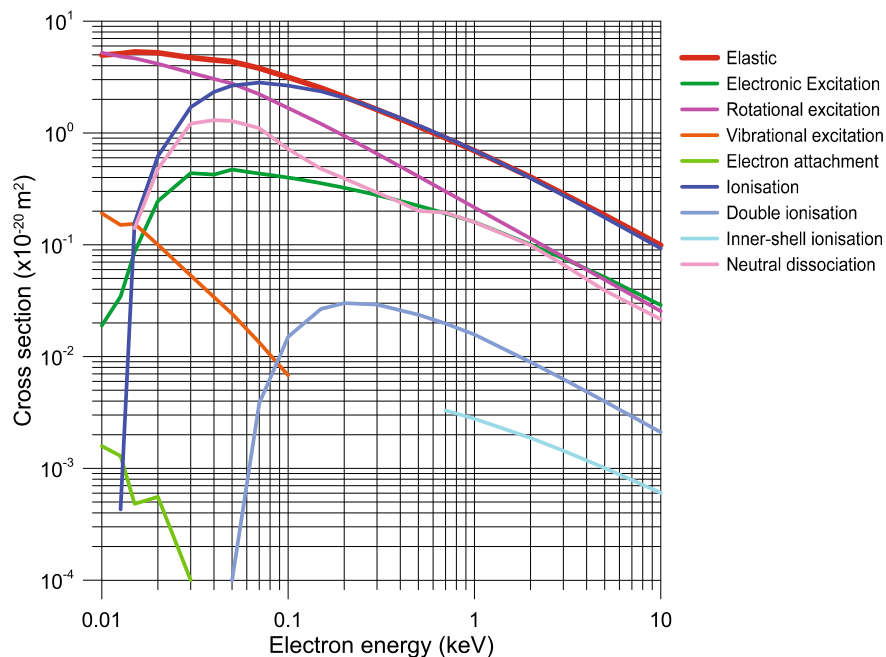


Fig. 14.6 Electron scattering cross sections used for the LEPTS simulation for incident electron energies below 10 keV (see text for details)

data from which are derived most of the IICS values, although in some cases they needed to be complemented with available theoretical or experimental data. The selected input cross section sources for the 0–10 keV impact energy range can be summarised for each considered inelastic channel as follows:

Rotational excitation cross-sections are calculated by assuming that the molecule behaves as a free rotor and making use of the first Born approximation (Muñoz et al. 2007b, Sanz et al. 2012).

Vibrational excitation cross-section data come from a detailed compilation from the experimental data available in the literature as described in Muñoz et al. (2008), Blanco et al. (2013). The overall experimental uncertainties assigned to these data are within 20–25%.

Ionisation cross sections were measured by us by combining a transmission- beam apparatus with a time of flight mass spectrometer (Fuss et al. 2009). Typical uncertainties assigned to these experimental data are within 7–10% (Muñoz et al. 2007b, 2008).

Electronic excitation cross-sections are taken from the literature (Muñoz et al. 2008). Having theoretical or experimental data on all electronic excited state available at each incident energy is almost impossible, even in the case of such an intensively studied molecule like water. As explained in Muñoz et al. (2008) we compiled individual electronic excited state cross sections from previous experimental studies

which were validated by comparison with recommended data from review articles such as that by Itikawa and Mason (2005).

Neutral dissociation cross sections. As explained in Muñoz et al. (2008) the difference between our calculated total inelastic cross section and the sum of the cross sections corresponding to the ionisation, vibrational and electronic excitations, i.e. the “remaining” inelastic channels, are considered to be neutral dissociation processes. Direct measurements of neutral dissociation cross sections are very complicated and thus scarce but in a previous study we showed that this assumption is compatible with the few measurements available in the literature (Kedzierski et al. 1998; Harb et al. 2001).

Inner-shell excitation and ionisation. The probability of exciting and ionising the k-shell of the oxygen atom forming the water molecule has been estimated from the energy loss spectra by correlating the total electron intensity corresponding to these processes with that corresponding to the molecular excitation and ionisation processes. Although the cross section for inner-shell excitation and ionisation is about two orders of magnitude less than that corresponding to the valence shell, its average energy loss (around 535 eV (Hitchcock and Brion 1980)) is more than one order of magnitude higher than the average energy of the outermost electron shell (around 35 eV (Muñoz et al. 2007b)) and therefore they must be considered in the simulation procedure.

Multiple ionisation cross sections. This is an inelastic channel recently incorporated to our modelling procedure. In our previous simulations using LEPTS we assumed that double ionisation of the water molecules was irrelevant due to the low cross section we may expect for this process. However, a recent calculation from Oubaziz et al. (2015) revealed that the energy transferred in this type of process is several orders of magnitude higher than that for single ionisation and increases with the incident energy, being therefore important in terms of energy deposition. In fact, some discrepancies we showed between our simulated electron stopping power in water (Muñoz et al. 2007b) and that given on the NIST webpage for energies above 1 keV disappear when this process is included in the simulation.

Electron attachment cross section. This is a resonant process whose cross sections have been accurately measured in several experiments which were compiled by Itikawa and Mason (2005). We have taken the recommended cross section values from Itikawa and Mason (2005).

Thermalisation. Electrons with energy below 25 meV are considered as thermalised electrons in equilibrium with the medium.

The scattering cross sections used to include all the above scattering processes in the present simulation are plotted in Fig. 14.6.

14.2.3 Angular Distribution Function

An important feature of an event-by-event Monte Carlo simulation procedure is sampling the angular distribution of scattered electrons for each single collision. We will distinguish here between elastic and inelastic collision processes.

For elastic scattering the calculated differential cross sections are normalised to constitute the angular distribution probabilities for each incident energy. For inelastic scattering processes the sampling procedure is more complicated since this angular distribution depends on the energy transferred to the target. In addition, for ionising collisions the energy and angular distribution of the ejected electron are also needed. In theory we could derive this information from the double (DDCS) and triple (TDCS) differential cross sections. In practice this information is not available for all the required energies and the full integration of the available DDCS data is not always consistent with the measured total integral inelastic cross sections. For this reason, we proposed a relatively simple empirical formula (Blanco et al. 2013) to derive the angular distribution of the inelastically scattered electrons as a function of the angular distribution corresponding to the elastic scattering and the transferred energy. This formula is the result of systematic energy loss spectrum measurements for different scattering angles and can be written as:

$$\frac{d^2\sigma(E)}{d\Omega\Delta E} \propto \left(\frac{d\sigma(E)}{d\Omega}\right)_{el}^{1-\Delta E/E}, \quad (14.1)$$

where $\left(\frac{d\sigma(E)}{d\Omega}\right)_{el}$ is the angular distribution of elastically scattered electrons for the same incident energy and ΔE is the energy loss during the collision. For ionising collisions, the energy of the ejected electron is given by $\Delta E - IP$, where IP is the ionisation potential, and its angular distribution is derived according to the energy and momentum conservation laws.

14.2.3.1 Energy Distribution Functions

The kinetic energy transferred in elastic processes is simply derived from the projectile to target molecule mass ratio and the scattering angle. For inelastic processes we followed different procedures depending on the inelastic channel considered. For rotational excitation we assumed a constant energy loss which is the averaged rotational excitation energy at a temperature of 300 K, i.e. 0.015 eV. For vibrational excitation, electronic excitation and ionisation (valence and inner-shell) processes the energy loss distribution functions have been derived from the experimental energy loss spectra. For double ionisation processes we adopted the energy loss energies calculated by Oubaziz et al. (2015). The energy loss distribution functions used in this simulation are plotted in Fig. 14.7 for the most representative inelastic channels.

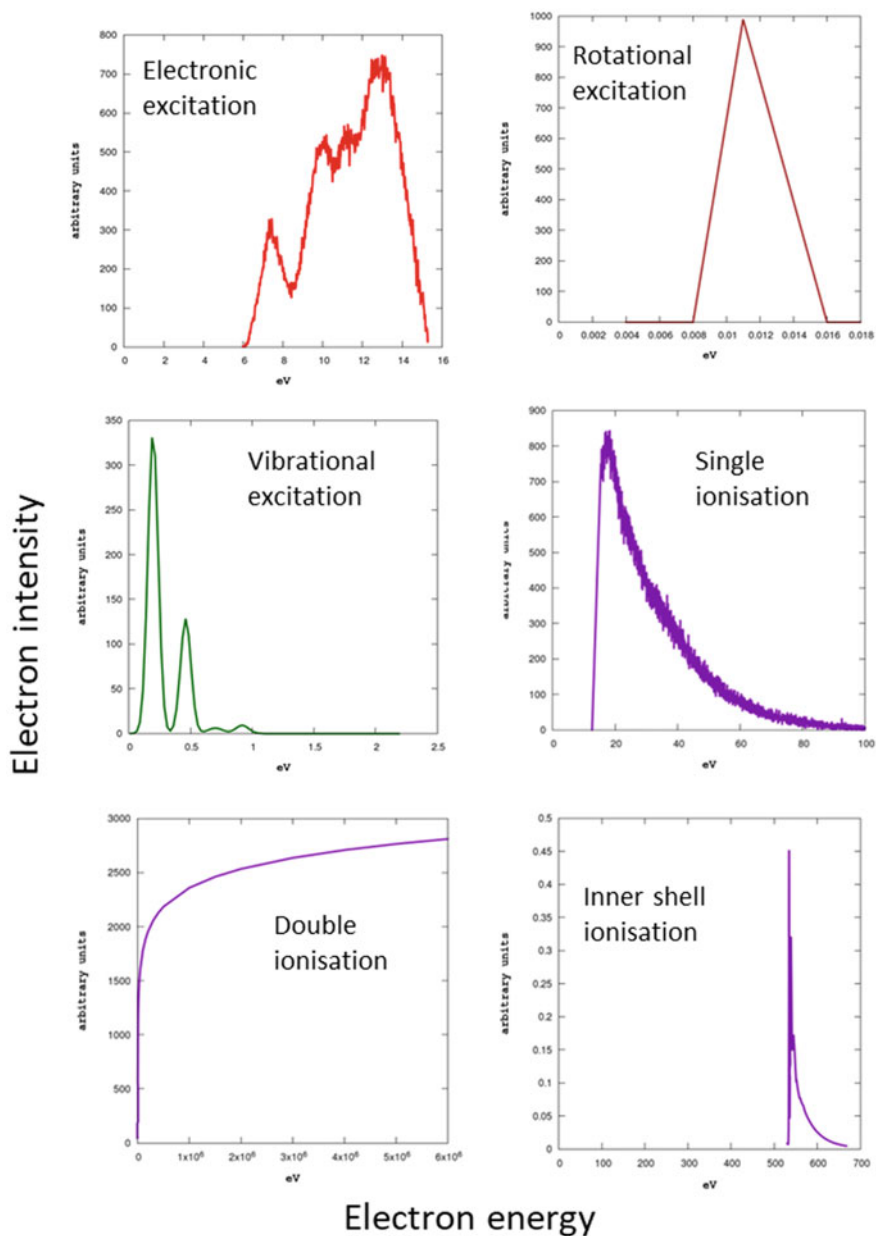


Fig. 14.7 Energy loss distribution functions for different electron scattering processes

As already mentioned, the simulation programme generates a file of the positions and momenta (phase space) of all the electrons generated by the photon interactions. This is used as an electron source generator for the LEPTS code, hence constituting the primary particles for the event-by-event single track simulation procedure described above. To illustrate the electron track simulation procedure, Fig. 14.8 shows three representative stages: (a) A top view of the photon interaction simulation shown in Fig. 14.4. Each dot represents a single photon collision event, most of them occurring within the irradiated $10 \times 10 \text{ cm}^2$ field, but events also take place outside of this region, defining a penumbra region. (b) Detail of electron tracks generated on the border of the irradiated field (penumbra). Note that the most energetic photoelectrons penetrate up to 13 mm into the liquid water. (c) A selected nanovolume at the end of one of the electron tracks showing the type of collision events (see the legend of Fig. 14.8). (d) Numerical data, type and number of events taking place in the nanovolume.

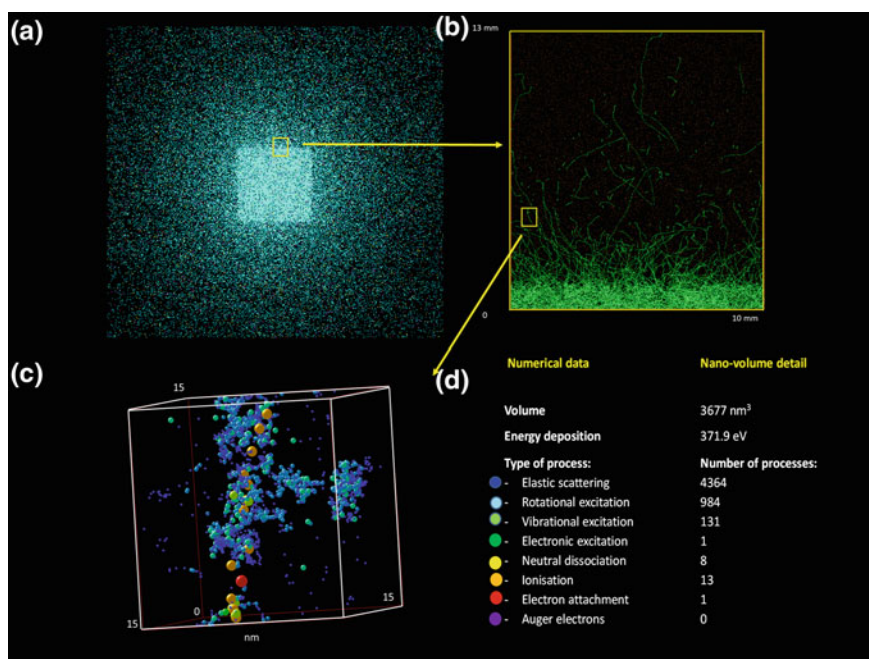


Fig. 14.8 **a** Top view of the irradiated area by the 6 MV primary photons; **b** detail of secondary electron tracks close to the border of the irradiated area; **c** detail (nanovolume) of the end of an electron track; **d** information about the number and type of collision events taking place in the nanovolume (note the colour code)

14.3 Radiobiological Effects on Jurkat Cell Cultures

The X-ray beam generated by the Varian LINAC accelerator characterised in the previous sections, operating at 6 MV acceleration voltage, has been used to investigate the effect of radiation on Jurkat T lymphocyte cultures. Studies on Jurkat T cell signalling mechanisms have been summarised by Abrahan and Weiss (2004). The experimental part of the present analysis includes a preliminary study to evaluate the radiation dose and time analysis required to distinguish alterations of the cell cycle and apoptotic processes. Various experimental techniques were used to characterise the induced biological damage. Cell apoptosis was determined by analysing induced membrane damage using an Annexin V staining technique (Kenis et al. 2004), and DNA fragmentation measurements were accomplished with a TUNEL assay method (Darzynkiewicz et al. 2008). This is then compared with the full Monte Carlo simulation of the irradiation experiment, carried out using the LEPTS procedure described above, in order to correlate the energy deposition and the number of induced molecular dissociations with the observed cell alterations. Details on these experiments and modelling procedures will be given in the remainder of this section.

14.3.1 *Materials and Experimental Methods*

For this study, Jurkat cell (immortalised line of human T lymphocytes) cultures were grown in a RPMI medium supplemented with 2 mM of L-glutamine, 10% of fetal bovine serum and 1% of antibiotics (penicillin/streptomycin) at 37 °C in a 5% CO₂, 100% humidity environment to reach the logarithmic phase. Cells were counted and introduced into the growth medium with a concentration of 130,000–170,000 cell/ml and then distributed into a 96-well polystyrene cell culture cluster in order to be used the following day. As mentioned, the preliminary experiment consisted of different doses (0.5, 1 and 2 Gy) of radiation and different time (6, 24, 48 and 72 h) analysis in order to determine the appropriate conditions for the cell cycle, membrane integrity and DNA damage measurements.

14.3.1.1 **The Effect of Radiation Dose on the Cell-Division Cycle as a Function of Time**

In order to determine the percentage of cells in different cell cycle phases (G_0/G_1 , S, and G_2/M) a staining DNA method has been used. Cells were first treated with ethanol to make the membranes firm and permeable and then quantitatively stained with a fluorescent dye, propidium iodide. This dye locates within the DNA double helix, as such the amount of DNA is proportional to the amount of collocated dye, and also proportional to the fluorescence intensity. In these conditions the percentage

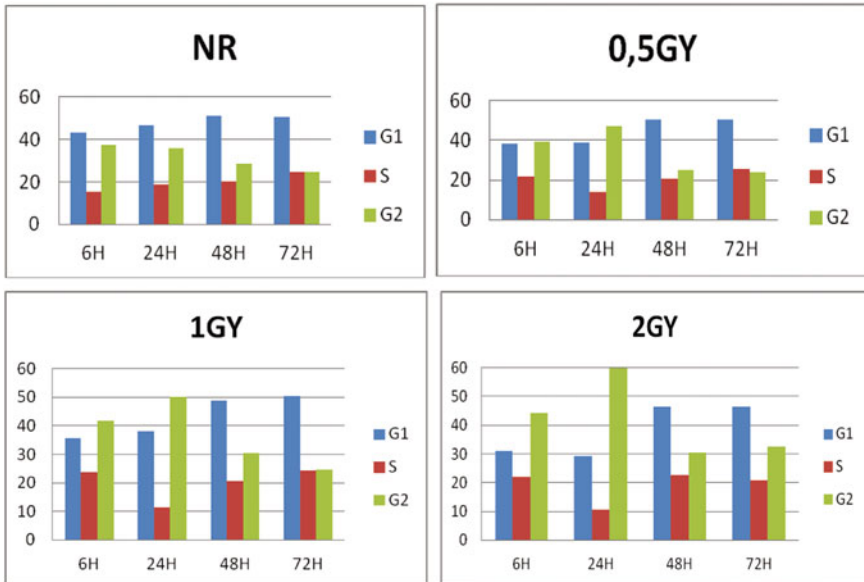


Fig. 14.9 Time evolution (6, 24, 48 and 72 h) of the cell cycle phase distribution for 96-well samples containing Jurkat cell cultures (see text for details) for different radiation doses (0.5, 1 and 2 Gy)

of emitted fluorescence is correlated with the percentage of cells in each cycle phase. This study employed flow cytometry by acquiring 20,000 events for each sample.

Figure 14.9 shows the results of the cell cycle evolution, from 6 to 72 h, for different radiation doses, including those for the control non irradiated (NR) target. As shown, the effect of the radiation on the cell cycle is noticeable 6 h after the irradiation for delivered doses higher than 0.5 Gy. However, the maximum effect (decreasing G_1 and increasing G_2) occurs at 24 h, particularly for the 2 Gy radiation dose.

14.3.1.2 Integrity of Cell Membrane Evaluation Using an Annexin-V Assay

The integrity of the cell membrane has been evaluated by means of an Annexin-V marking procedure. Phosphatidylserine (PS) is a phospholipidic component of the membrane which is held facing the inner side of the cytoplasmic membrane of normal cells. However, for apoptotic cells PS moves from the inner to the outer side, exposing the PS to the extracellular environment. This event occurs very early within the programmed cell death process and can be quantified by flow cytometry by adding the Annexin-V protein linked to a fluorescein isothiocyanate (FITC). Annexin-V positive cells are then identified as those with the integrity of the plasmatic

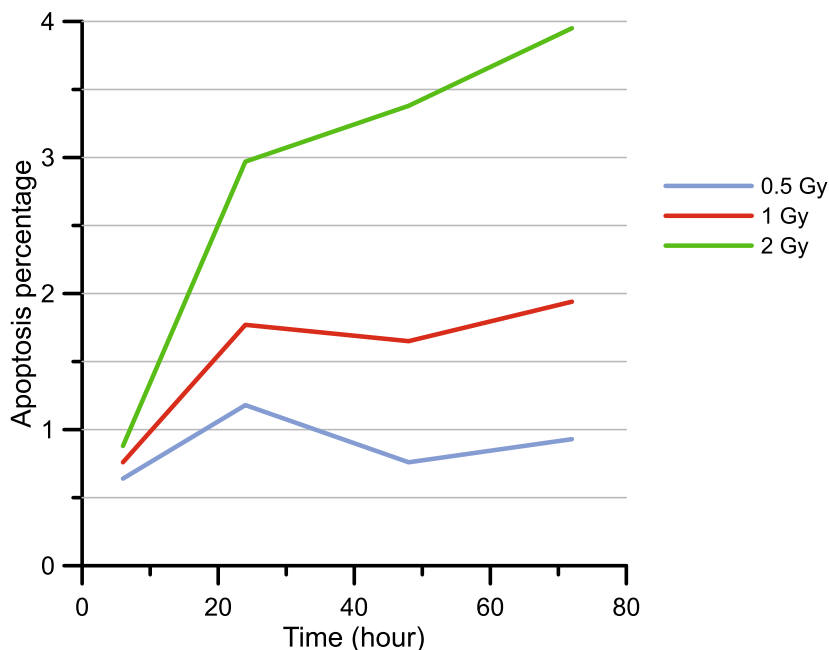


Fig. 14.10 Percentage of Annexin-V positive cells, normalised to the control (NR) sample, for different radiation doses

membrane damaged. In order to quantify this phase of the apoptotic process (early apoptosis) 20,000 cells/sample were acquired by the cytometer to accurately obtain the percentage of Annexin-V positive cells. The corresponding results for different radiation doses (0.5, 1, 2 Gy) are shown in Fig. 14.10.

As shown in Fig. 14.10 early apoptosis processes are present from 24 h and they increase with both time and radiation dose. For 0.5 Gy this effect is almost inappreciable, less than 1%, showing a proportional dependence on radiation dose and reaching a maximum value of 4% 72 h after the 2 Gy irradiation.

14.3.1.3 Apoptosis Analysis Based on a TUNEL Assay Technique

Terminal deoxynucleotidyl transferase (TdT) dUTP Nick-End Labelling (TUNEL) assay is a well-established technique (Kyrylkova et al. 2012) to label DNA damage produced by apoptosis and other possible agents. It is based on measuring the fragmentations of nuclear DNA, the biochemical hallmark of apoptosis, thus providing a simple and accurate detection of apoptotic cells even at the single cell level. In this experiment we used a DeadEnd™ Fluorometric TUNEL System in combination with a confocal microscope to directly visualise the induced nuclear DNA fragmentations. This system catalytically incorporates fluorescein-12-dUTP to the 3'-OH DNA ends

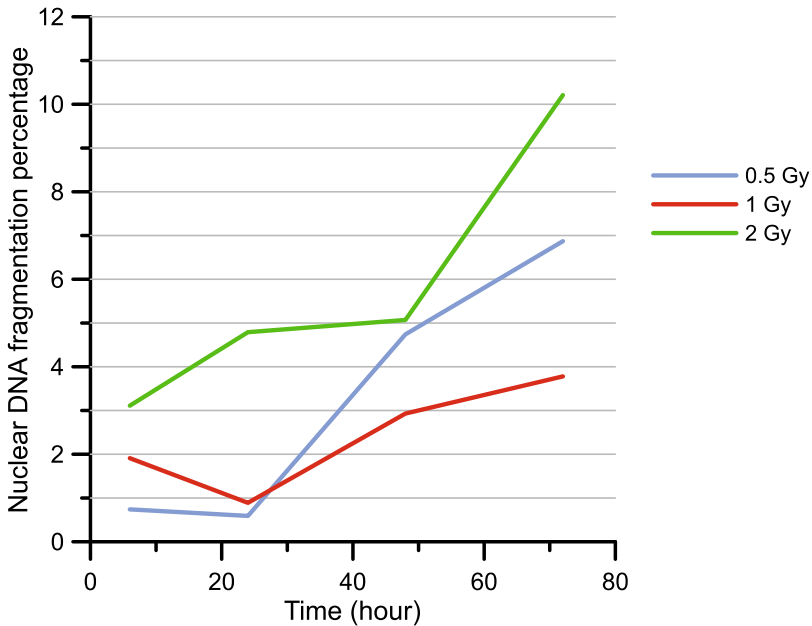


Fig. 14.11 Percentage of DNA fragmentation observed with the TUNEL assay for different times of analysis

by using Terminal Deoxynucleotidyl Transferase (TdT) to attach the polymer tail. The DNA labelled with fluorescein-12-dUTP can be visualised with a fluorescence microscope and were counted within 5 visualised fields. The results are presented in terms of percentage of TUNEL positive cells with respect to the total number of cells.

The results corresponding to the TUNEL assay are shown in Fig. 14.11. As expected, the maximum percentage of TUNEL positive cells is found for 2 Gy and 72 h after the irradiation. Note that the increase from 48 to 72 h is even more remarkable than in the case of the Annexin-V assay.

14.4 Radiobiological Experiment Versus Monte Carlo Simulation

Once the suitability of the 6 MV X-ray beam delivering 2 Gy doses was confirmed to produce biological damage within the sensitivity range of our experimental techniques, a radiobiological experiment was designed to compare to the prediction of our Monte Carlo modelling procedure. The irradiation took place in the $1 \times 1 \times 1 \text{ m}^3$ water phantom shown in Fig. 14.12a, according to the schematic shown in Fig. 14.11. Two 96-well plates, Plate 1 and Plate 2, were prepared to contain the same number

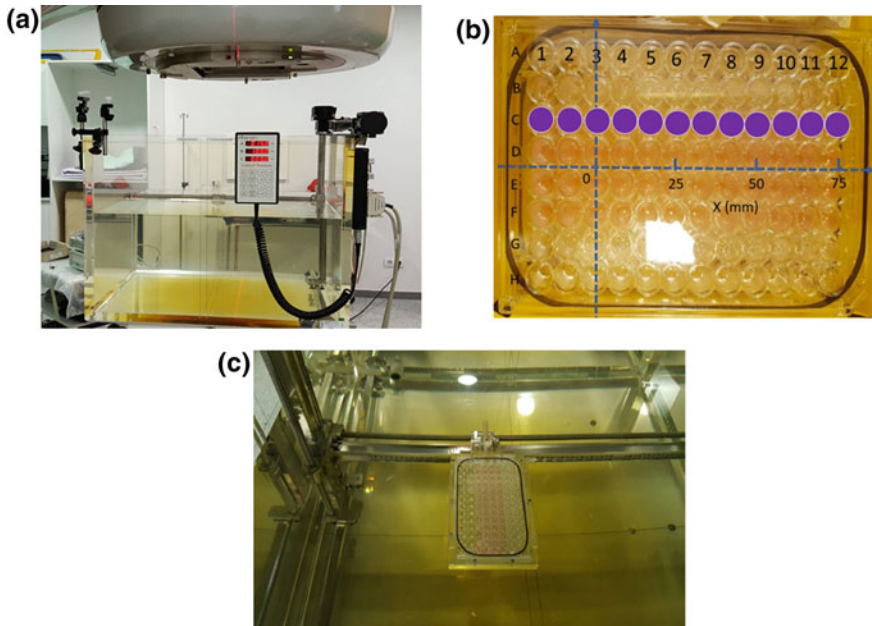


Fig. 14.12 **a** Water phantom used for the radiobiological experiment; **b** 96-well cell culture cluster configuration; **c** cell culture cluster on the sample holder to be introduced into the water phantom

of cells in each well. Each target plate was alternatively attached to the motorised X-Y-Z coordinate axis device installed in the water phantom (see Fig. 14.12a) which is remotely operated. As indicated in Fig. 14.12b, the 96-wells constitute a 12 column (1–12) and 8 row (A–H) matrix for which the relevant position coordinates of each target are given by the distance between the well in question and column 3. The centre of the irradiated area is then placed between the D3 and E3 wells, while the C1 to C12 wells contain the target cells. Plate 1 was placed exactly in the zero position, i.e. with $X = 0$ between D3 and E3, and Plate 2 was placed further along the positive X axis by 4 column widths, so that column 3 was now coincident with the location of column 7 of the previous plate. Note that under these conditions, columns from 3 to 9 of Plate 1 were within the irradiated area while for Plate 2 columns from 7 to 12 are out of the irradiated area. With this configuration we cover the three regions of interest (irradiated, penumbra and low dose regions) including an overlap area to check the consistency between both results and estimate statistical uncertainties. We also prepared a third plate (NR plate) following the same treatment as that for the other two, which was not irradiated, as the control reference. The 12 wells of interest for the present experiment, represented as W1 to W12, are then defined by their respective X coordinate which ranges from $X = 0$ to $X = 94.6$ mm and they represent a combination of the utilised wells from Plate 1 and Plate 2. Plates were introduced into the water phantom by means of an appropriate sample holder designed by us for this purpose (Fig. 14.12c).

Taking into consideration the results of the previous experiment for different radiation doses the study followed the cell cycle at 24 and 48 h after the 2 Gy irradiation and the induced apoptosis (Annexin-V and TUNEL assays) at 48, 72 and 96 h after the 2 Gy irradiation.

For the Monte Carlo simulation, we assumed the configuration represented in Fig. 14.13. The simulated phase space of the primary radiation (see Sect. 14.2.1) covers a $100 \times 100 \text{ mm}^2$ area centred on the surface of the water phantom. The sample was located parallel but 100 mm below this surface (see Fig. 14.13) so the radiation was initially transported through this 100 mm depth of water before reaching the target wells which for the simulation were assumed to contain just water.

In order to determine the statistical uncertainty of the simulation, the reference value used was the energy deposited in each well. The criterion was to reproduce the energy deposited in the farthest well (W12) within 1%. In order to reach this limit, we generated 10^{10} initial photons whose energy and momentum distributions were given by the previous phase space simulation (see Sect. 14.2.1). As mentioned above, the LEPTS simulation procedure will provide information about the energy deposition and the number of processes taking place into each well both for incident photons (photoelectric, Compton scattering, Rayleigh scattering and pair creation processes) and secondary electrons (elastic scattering, single and multiple ionisation, inner shell ionisation, electronic excitation, neutral dissociation, vibrational and rotational excitation and electron attachment processes).

We will now present the results and comparison of the radiobiological experiment and the simulation.

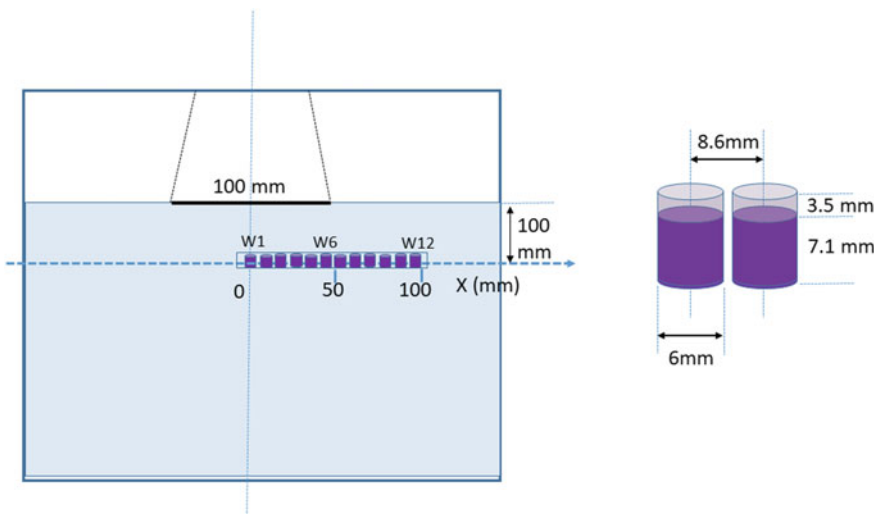


Fig. 14.13 Schematic configuration of the cell irradiation experiment used for the Monte Carlo simulation

14.4.1 Cell Cycle Results

The observed effect of the radiation on the cell cycle is the variation in the percentage of cells in each cycle phase. In a normal cycle the percentage of cells in the G1 phase (no proliferation phase) is higher than the percentage of cells in the G2 phase (preparing cell division). The results of the experiment for the selected wells W1–W12 are shown in Figs. 14.14 and 14.15 for 24 and 48 h post irradiation, respectively. 24 h post irradiation, between the positions W1–W6, there is an increase in the number of cells in the G2 phase with respect to the control (NR). This is interpreted as a halt

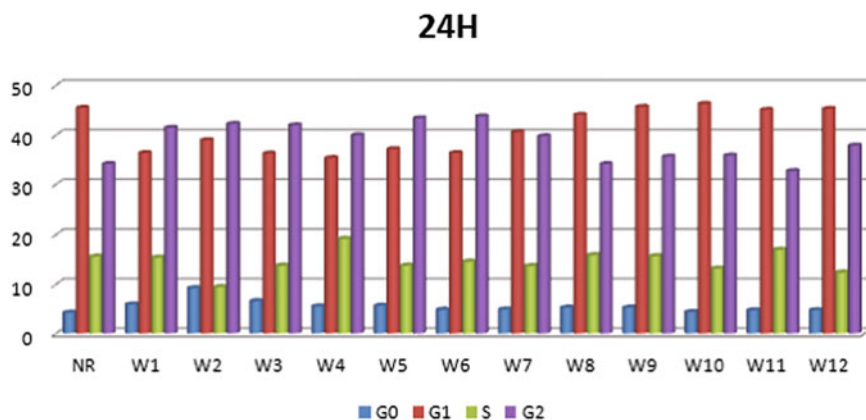


Fig. 14.14 Percentage of cells in each phase (G0, G1, S, G2) as measured 24 h after the 2 Gy irradiation

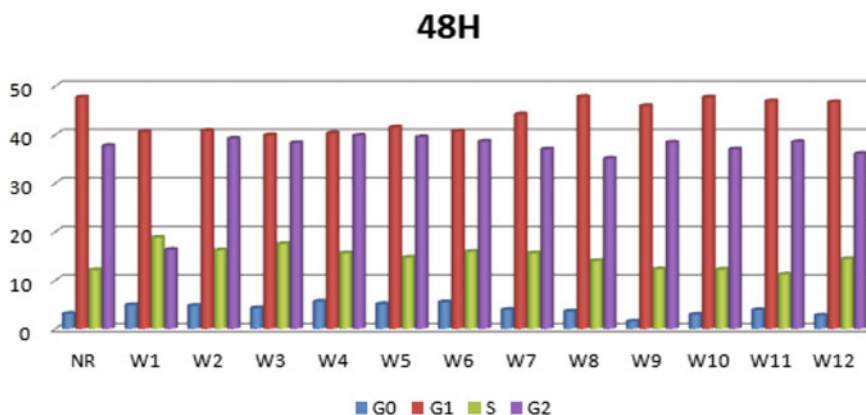


Fig. 14.15 Percentage of cells in each phase (G0, G1, S, G2) as measured 48 h after the 2 Gy irradiation

in the normal cell cycle. Note that these positions are located in the irradiated area (see Fig. 14.13) where the radiation level is higher, and its effect is stronger.

At 48 h post irradiation, the attenuation of the radiation effect is appreciable (see Fig. 14.15), with some recovery of the culture observed. This can be explained in terms of repair mechanisms.

14.4.2 Results on the Apoptotic Process

As shown in Fig. 14.16, 48 h post irradiation early apoptosis (Annexin-V positive) is dominant versus nuclear DNA fragmentation (TUNEL positive). They do however follow a similar pattern. Both present a local broad maximum around the positions W5–W6 which are close to the penumbra area. Beyond this point both decrease, and then tend to increase again for the last wells, W10–W12.

For the analysis carried out 72 h after the irradiation we found an inversion of the process observed in the previous analysis (see Fig. 14.17). DNA fragmentation notably increases from W2 to W9 indicating that the apoptotic process is progressing.

Finally, 96 h after the irradiation results show large variation with little to no correlation between the observed cell death and the radiation regions (see Fig. 14.18). At this stage other cellular mechanisms related to cell regeneration (proliferation and survival by damage repair) and the aging of the culture are present.

Fig. 14.16 Early apoptosis and DNA fragmentation 48 h after the irradiation

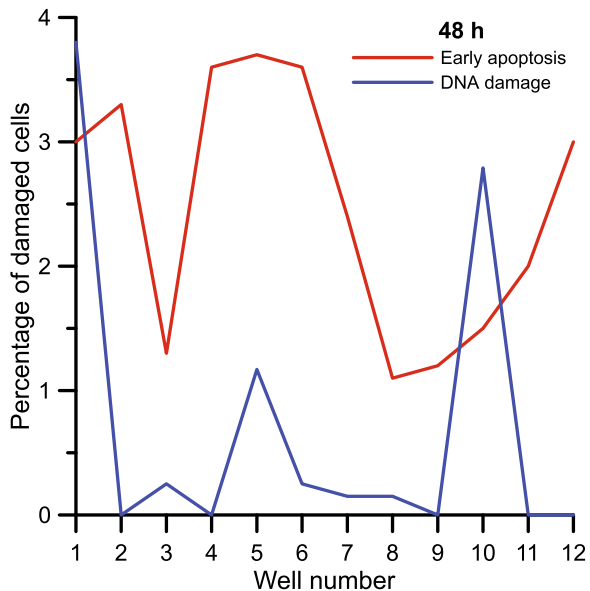


Fig. 14.17 Early apoptosis and DNA fragmentation 72 h after the irradiation

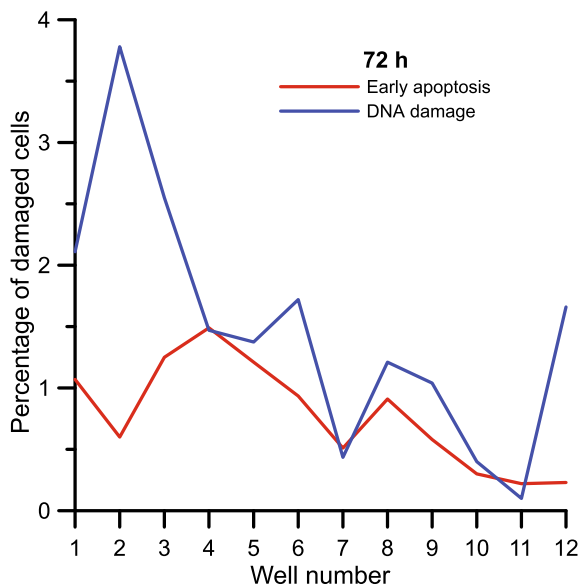
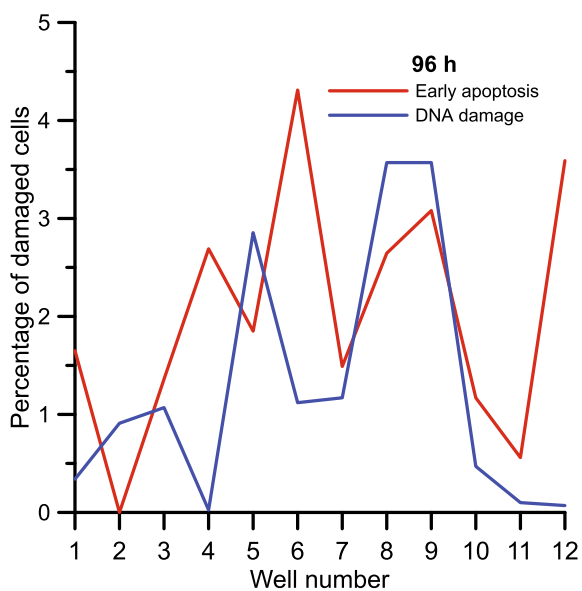


Fig. 14.18 Early apoptosis and DNA fragmentation 96 h after the irradiation



14.4.3 Results of the Monte Carlo Simulation

As mentioned above, the combined GAMOS-LEPTS simulation provided information about the energy deposition and the type and number of collision events taking place in each target well, both for photons and electrons.

These results are numerically presented in Table 14.1 for each considered well. The energy deposition in the wells is given in eV and the number of events taking place are given by primary photon, i.e. the number of collision events for each considered process within the corresponding cell.

In order to illustrate the relationship between the energy deposition and the number of events, in Fig. 14.19 we have plotted the energy deposited in each well together with the number of ionisations and electron attachment processes taking place in the well. As can be seen from this figure, the number of events is higher than the energy deposition for the wells far from the penumbra area, from W9 to W12. This is easily understood when considering that the average energy of both photons and electrons out of the irradiated area tends to be lower, and therefore the interaction cross section tend to be higher. Note that the electron impact ionisation cross section is maximum at 70 eV incident energy, and that for electron attachment maxima values correspond to impact energies below 10 eV. Only a slight difference is expected (note that Fig. 14.19 is plotted on a logarithmic scale), mainly due to the quantised way in which photons interact with matter, while charged particles have a cascade of ‘slowing’ processes. This non-proportionality is also seen in the case of positrons, where we recently showed (Roldán et al. 2016) that there is a region at the very end of the positron tracks where the number of dissociative collision events is not proportional to the energy deposition, i.e. to the absorbed dose.

14.4.4 Correlation Between the Observed Cell Damage and the Simulated Energy Deposition

In Fig. 14.20 we have plotted the energy deposition and the observed cell damage (early apoptosis and DNA fragmentation) for each target well as a function of its distance from the centre of the irradiated area, measured 48 h after the 2 Gy irradiation. Statistical uncertainties of the measured cell damage can be established within 15–30%. These are derived from the deviations of the results corresponding to the overlapping wells during the two sets of measurements (Plate 1 and Plate 2, see the experimental arrangement described in the introduction of Sect. 14.4). Within this uncertainty at 48 h most of the biological damage is produced in the irradiated area. Beyond the irradiated limit ($X > 50$ mm) this damage persists, and tends to increase, for distances between 65 and 85 mm from the centre. This increase confirms and justifies the relevance of low doses in producing biological alterations, as well as the importance of the penumbra region in dose control (Fowler 1990; Rupnow et al. 1998).

Table 14.1 Simulated number of events, per incident photon, taking place in each target well by type of collision process for photons and electrons

# Well	Edep (eV)	Photons				Electrons									
		Photo ^a ($\times 10^6$)	Ray ^b ($\times 10^6$)	Com ^c ($\times 10^6$)	Pair ^d ($\times 10^6$)	EI ^e	Rot ^f	Att ^g	eExc ^h	vExc ⁱ	nD ^j	s-I ^k	d-I ^l	i-I ^m	Ther ⁿ
1	50.0	1.96	1.99	114	0.54	168	302	0.069	0.399	0.392	2.67	1.00	0.014	0.006	0.79
2	49.6	1.67	1.71	113	0.54	167	301	0.069	0.397	0.390	2.66	1.00	0.014	0.006	0.79
3	49.7	1.59	1.80	114	0.54	167	301	0.069	0.397	0.391	2.66	1.00	0.014	0.006	0.79
4	48.5	1.85	1.90	110	0.47	163	293	0.067	0.387	0.380	2.60	0.98	0.014	0.006	0.77
5	48.9	1.82	1.72	110	0.61	164	295	0.067	0.390	0.383	2.61	0.98	0.014	0.006	0.77
6	47.7	1.63	1.62	104	0.50	160	289	0.066	0.381	0.375	2.55	0.96	0.014	0.006	0.76
7	42.8	1.48	1.46	97	0.44	144	259	0.059	0.341	0.335	2.29	0.86	0.012	0.005	0.68
8	6.79	1.55	1.40	46	0.02	25	44	0.010	0.059	0.057	0.39	0.15	0.002	0.001	0.12
9	4.31	1.44	1.28	40	0.01	16	29	0.007	0.039	0.037	0.26	0.09	0.001	0.001	0.08
10	2.49	1.32	1.15	30	0.01	10	17	0.004	0.023	0.022	0.15	0.06	0.001		0.05

(continued)

Table 14.1 (continued)

# Well	Edep (eV)	Photons					Electrons								
		Pho ^a (× 10 ⁶)	Ray ^b (× 10 ⁶)	Com ^c (× 10 ⁶)	Pair ^d (× 10 ⁶)	El ^e	Rot ^f	Att ^g	eExc ^h	vExc ⁱ	nD ^j	s-I ^k	d-I ^l	i-I ^m	Ther ⁿ
11	1.99	1.22	1.07	26		8	14	0.003	0.018	0.018	0.12	0.05	0.001		0.04
12	1.59	1.19	1.00	23		6	11	0.003	0.015	0.014	0.10	0.04	0.001		0.03

^aPhotoelectric interaction

^bRayleigh scattering

^cCompton scattering

^dPair creation

^eElastic scattering

^fRotational excitation

^gElectron attachment

^hElectronic excitation

ⁱVibrational excitation

^jNeutral dissociation

^kSingle ionisation

^lDouble ionisation

^mInner shell ionisation

ⁿThermalisation

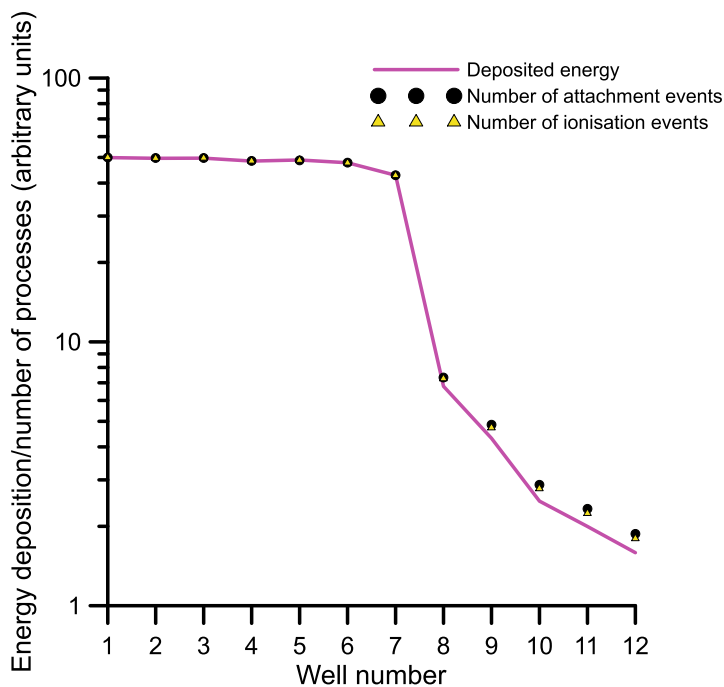


Fig. 14.19 Results of the Monte Carlo simulation for the energy deposition, number of ionising and electron attachment events in each target well

As expected, 72 h after the irradiation the situation changes. As shown in Fig. 14.21, early apoptosis clearly decays in the irradiated area, probably due to repair mechanisms. However early apoptosis still occurs outside of the irradiated region, reaching maximum values at 60 mm from the centre. Note that this is the penumbra area where, as shown in Fig. 14.7b it was exposed to a high density of secondary electrons coming out of the central area. The DNA fragmentation shows a different trend, increasing within the irradiated area, indicating an evolution of the apoptotic process. DNA fragmentation also increases in the penumbra area.

As previously mentioned, 96 h after the irradiation no correlation between the observed cell damage and the irradiation was found, indicating that at that time other cellular processes are dominating the evolution of the culture.

14.5 Conclusions

We have presented a modelling procedure that combines the standard electromagnetic physics of Geant4 for photons with the LEPTS event by event Monte Carlo simulation programme for secondary electrons. This provides detailed information

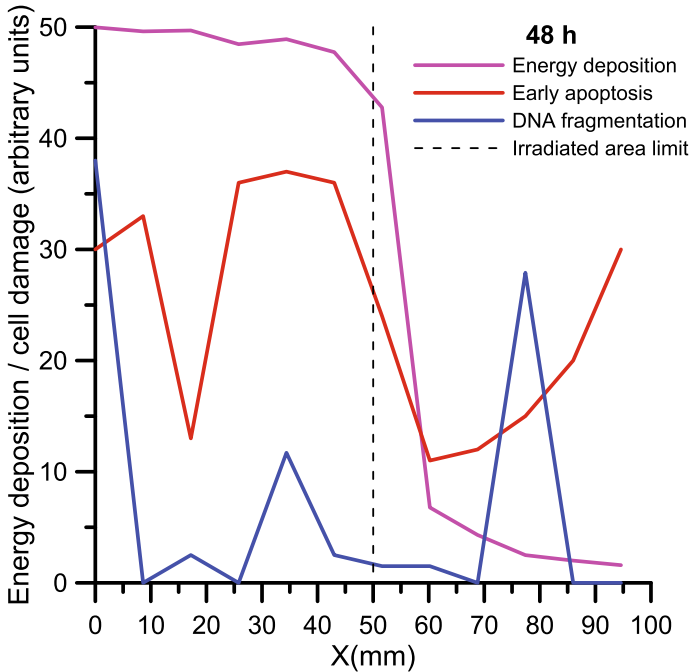


Fig. 14.20 Correlation between the energy deposition and the observed biological damage as a function of the distance to centre of the irradiated area, after 48 h of the 2 Gy irradiation

on the energy deposition and the type and number of collision events taking place in a 1 m^3 liquid water phantom when irradiated with 6 MV photons generated by a LINAC accelerator. Input data sources on interaction probabilities (cross sections) and energy and angular distribution functions have been critically discussed to obtain a complete set over the whole electron and photon energy range considered (0–6 MeV). This model has been used to simulate a radiobiological experiment to correlate these outputs with the biological effects (cell cycle alteration, early apoptosis, DNA fragmentation) induced in a Jurkat T lymphocyte culture by the described radiation. In these conditions early apoptosis and DNA fragmentation have been analysed 48, 72 and 96 h after the irradiation. Notable cell cycle alterations were found between 24 and 48 h after the irradiation when the dose delivered was 2 Gy. As expected, the irradiated area showed apoptotic processes up to 48 h after the irradiation. However, substantial apoptotic cells have also been identified outside of this area, in the penumbra, and even in the low dose area, where a clear maximum percentage of DNA fragmentation is shown. We attribute this effect to the fact that despite the average energy of primary and secondary particles in these areas being lower than in the irradiated area, their interaction cross sections are much higher, increasing the probability of producing damage. This effect is reduced when using photons as the primary particle, but we would expect a remarkable effect when the primary beam

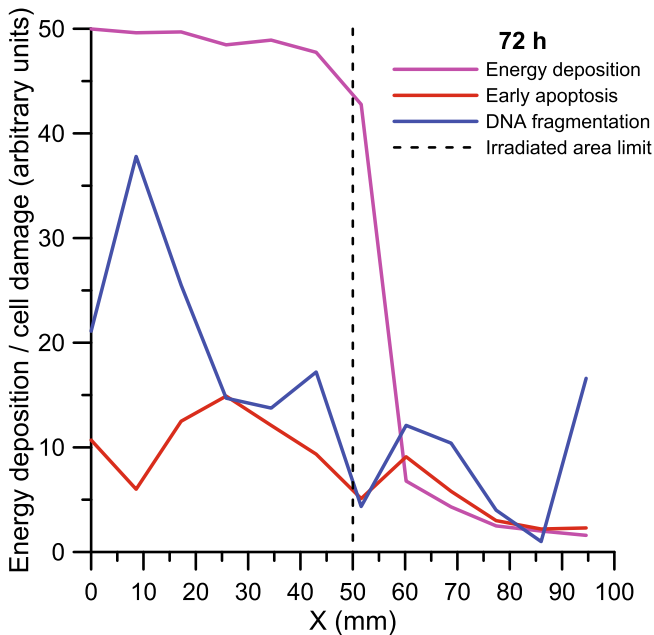


Fig. 14.21 Correlation between the energy deposition and the observed biological damage as a function of the distance from the centre of the irradiated area, 72 h after 2 Gy irradiation

is formed by charged particles. Charged particles gradually lose their energy in the medium, thus having a well-defined range into a water phantom. In the case of a charged particle beam, the radiobiological effectiveness of the radiation could be far from proportional to the absorbed dose, and further radiobiological studies will be needed to establish an appropriate RBE assignment.

Acknowledgements This study has been mainly supported by the EU through the FP7-PEOPLE-2013-ITN programme (project ARGENT-608163). It has also been supported by the Spanish Ministerio de Ciencia, Innovación y Universidades (project FIS2016-80440). We also acknowledge the Hospital Universitario Puerta de Hierro of Madrid for providing the required equipment and services to perform the presented experiments.

References

- Abdoul-Carime H, Golke S, Illenberger E (2004) *Phys Rev Lett* 92:168103
 Abrahan RT, Weiss A (2004) *Nat Rev Immunol* 4:301–308
 Agostinelli S, Allison J, Amako K, Apostolakis J, Araujo H, Arce P, Asai M, Axen D, Banerjee S, Barrand G, Behner F, Bellagamba L, Bourdreau J, Broglia L, Brunengo A, Burkhardt J, Chauvie S, Chuma J, Chytracsek R, Cooperman G, Cosmo G, Degtyarenko P, Dell’Acqua A, Depaola G, Dietrich D, Enami R, Feliciello A, Ferguson C, Fesefeldt H, Folger G, Foppiano F, Forti A, Garelli S, Giani S, Giantrapani R, Gibin D, Gomez Cadenas JJ, Gonzalez I, Gracia Abril G, Greeniaus

- G, Greiner W, Grichine V, Grossheim A, Guatelli S, Gumplinger P, Hamatsu R, Hashimoto K, Hasui H, Heikkinen A, Howard A, Ivanchenko V, Johnson A, Jones FW, Kallenbach J, Kanaya N, Kawabata M, Kawabata Y, Kawagitu M, Kelner S, Kent P, Kimura A, Kodama T, Kokoulin R, Kossov M, Kurashige H, Lamanna E, Lampen T, Lara V, Lefebvre V, Lei F, Liendl M, Lockman W, Longo F, Magni S, Maire M, Medernach E, Minamimoto K, Mora de Freitas P, Morita Y, Murakami K, Nagamatu M, Nartallo R, Nieminen P, Nishimura T, Ohtsubo K, Okamura M, O'Neale S, Oohata Y, Paech K, Perl J, Pfeiffer A, Pia MG, Ranjard F, Rybin A, Sadilov S, Di Salvo E, Santin G, Sasaki T, Savvas N, Sawada, Scherer S, Sei S, Sirotenko V, Smith D, Starkov N, Stoecker H, Sulkimo J, Takahata M, Tanaka S, Tcherniaev E, Safai Tehrani E, Tropeano M, Truscott P, Uno H, Urban L, Urban P, Verderi M, Walkden A, Wander W, Weber H, Wellisch JP, Wenaus T, Williams DC, Wright D, Yamada T, Yoshida H, Zschesche D (2003) *Nucl Instrum Methods Phys Res A* 506:250–303
- Ann ICRP (International Commission on Radiological Protection) 33:1 (2003)
- Battistoni G, Broggi F, Brugger M, Campanella M, Carbone M, Empl A, Fasso A, Gadioli E, Cerutti F, Ferrari A, Ferrari A, Lantz M, Mairani A, Margiotta M, Morone C, Muraro S, Parodi K, Patera V, Pelliccioni M, Pinsky L, Ranft J, Roesler S, Rollet S, Sala P, Santana M, Sarchiapone L, Sioli M, Smirnov G, Sommerer F, Theis C, Trovati S, Villari R, Vincke H, Vincke H, Vlachoudis V, Vollaire J, Zapp N (2011) *Nucl Instrum Methods Phys Res B* 269:2850–2856
- Barth S, Ončák M, Ulrich V, Mucke M, Lischke T, Slavíček P, Hergenhan U (2009) *J Chem Phys A* 113:13519–13527
- Blanco F, Muñoz A, Almeida D, Ferreira da Silva F, Limão-Vieira P, Fuss MC, Sanz AG, García G (2013) *Eur Phys J D* 67(19). Colloquium
- Blanco F, Ellis-Gibbins L, García G (2016) *Chem Phys Lett* 645:71–75
- Boudaïffa B, Cloutier P, Hunting D, Huels MA, Sanche L (2000) *Science* 287:1658–1660
- Champion C, Le Luarec C, Stosic B (2012) *Int Radiat Biol* 88:54–61
- Cullen DE, Hubbell JH, Kissel L (1997) EPDL97: the evaluated photon data library '97 version. UCRL-LR-5400, vol 6 rev 5. Lawrence National Laboratory
- Darzynkiewicz Z, Galkowski D, Zhao H (2008) *Methods* 44:250–254
- Faure A, Gorfinkiel JD, Tennyson J (2004) *J Phys B* 37:801
- Fowler JF (1990) *Int J Radiat Oncol Biol Phys* 18:1261–1269
- Friedland W, Jacob P, Kunderát P (2010) *Radiat Res* 173:677–688
- Fuss M, Muñoz A, Oller JC, Blanco F, Almeida D, Limão-Vieira P, Do TPD, Brunger MJ, García G (2009) *Phys Rev A* 80:052709
- García G, Manero F (1998) *Phys Rev A* 57:1069–1073
- García G, Blanco F (2000) *Phys Rev A* 62:044702
- García Gómez-Tejedor G, Fuss MC (eds) (2012) *Radiation damage in biomolecular systems*. Canopus-Springer, London
- Harb T, Kedzierski W, McConkey JW (2001) *J Chem Phys* 115:5507–5512
- Hishiyama N, Hoshino M, Blanco F, García G, Tanaka H (2017) *J Chem Phys* 147:224308
- Hitchcock AP, Brion CE (1980) *J Electron Spectrosc Relat Phenom* 18:1–21
<http://fismed.ciemat.es/GAMOS/>
- Incerti S, Baldacchino G, Bernal M, Capra R, Champion C, Francis Z, Guèye P, Mantero A, Mascialino B, Moretto P, Nieminen P, Villagrasa C, Zacharatou C (2010) *Int J Model Simul Sci Comput* 1:157–158
- Inokuti M (1971) *Rev Mod Phys* 43:297
- Inokuti M, McDowell MRC (1974) *J Phys B* 7:2382
- Itikawa Y, Mason NJ (2005) *J Phys Chem Ref Data* 34:1–22
- Johns HE, Bates LM, Epp ER, Cormack DV, Fedorux SO, Morrison A, Dixon WR, Garrett C (1951) *Nature* 168:1035–1036
- Journal of the ICRU (International Commission on Radiation Units and Measurements (ICRU) vol 10, no 1, Report 83 (2010)
- Journal of the ICRU vol 11, no 2, Report 86 (2011)
- Kedzierski W, Derbyshire J, Malone C, McConkey JW (1998) *J Phys B* 31:5361–5368

- Kenis H, van Genderen H, Bennaghmouch A, Rinia HA, Frederik P, Narula J, Hofstra L, Reutelingsperger CPM (2004) *J Biol Chem* 279:52623–52629
- Krämer M, Kraft G (1994) *Radiat Environ Biophys* 33:91–109
- Kyrylkova K, Kyryachenko S, Leid M, Kioussi C (2012) Detection of apoptosis by TUNEL assay. In: Kioussi C (eds) *Odontogenesis. Methods in molecular biology (Methods and protocols)*, vol 887
- Lagares JI (2017) Private communication
- Loupas A, Lozano AI, Blanco F, Gorfinkiel JD, García G (2018) *J Chem Phys* 149:034304
- Müller IB, Cederbaum LS (2006) *J Chem Phys* 125:204305
- Muñoz A, Pérez JM, García G, Blanco F (2005) *Ncl Instrum Meth A* 536:176–188
- Muñoz A, Blanco F, Oller JC, Pérez JM, García G (2007a) *Adv Quant Chem* 51:21–57
- Muñoz A, Oller JC, Blanco F, Gorfinkiel JD, Limao-Vieira P, García G (2007b) *Phys Rev A* 76:052707
- Muñoz A, Blanco F, García G, Thorn PA, Brunger MJ, Sullivan JP, Buckman SJ (2008) *Int J Mass Spectrom* 277:175–179
- Muñoz A, Fuss MC, Cortés-Giraldo MA, Incerti S, Ivanchenko V, Ivanchenko A, Quesada JM, Salvat F, Champion C, García G (2012). In: García Gómez-Tejedor G, Fuss MC (eds) *Radiation damage in biomolecular systems*. Canopus-Springer, London
- Nishimura T, Gianturco FA (2004) *Europhys Lett* 65:179–185
- NIST. <https://physics.nist.gov/PhysRefData/Star/Text/ESTAR.html>
- Oubaziz D, Quinto MA, Champion C (2015) *Phys Rev A* 91:0022703
- Perkins ST, Cullen DE, Seltzer SM (1991) *Tables and graphs of electron-interaction cross sections from the LLNL Evaluated electron data library (EEDL), Z=1-100*. UCRL-50400, vol 31. Lawrence National Laboratory
- Polyansky OL, Ovsyannikov RI, Kyuberis AA, Lodi L, Tennyson J, Zobov NF (2013) *J Phys Chem A* 117:9633–9643
- Ptasinska S, Denifl S, Grill V, Märk TD, Illenberger E, Scheier P (2005) *Phys Rev Lett* 95:093201
- Roldán A, Pérez JM, Blanco F, Willart A, García G (2004) *J Appl Phys* 95:5865–5870
- Roldán AM, Krupa K, McEachran RP, White RD, Marjanović S, Lj. Petrović Z, Brunger MJ, Machacek JR, Buckman SJ, Sullivan JP, Chiari L, Limão-Vieira P, García G (2016) *J Phys B* 49:145001
- Rupnow BA, Murtha AD, Alarcon RM, Giaccia AJ, Knox SJ (1998) *Cancer Res* 58:1779–1784
- Salvat F, Fernández-Varea JM, Sempau J (2003) *PENELOPE. a code system for monte carlo simulation of electron and photon transport*. OECD-Nuclear Energy Agency
- Sanz AG, Fuss MC, Blanco F, Sebastianelli F, Gianturco FA, García G (2012) *J Chem Phys* 137:124103
- Sanz AG, Fuss MC, Blanco F, Gorfinkiel JD, Almeida D, Ferreira da Silva F, Limão-Vieira P, Brunger MJ, García G (2013) *J Chem Phys* 139:184310
- Sanz AG, Fuss MC, Masin Z, Gorfinkiel JD, Carelli F, Sebastianelli F, Gianturco FA, García G (2014) *Appl Rad Isot* 83B:148–154
- Santivasi WL, Xia F (2014) *Antioxid Redox Signal* 21:251–259
- Schneider U, Schwenk H, Bornkamm G (1977) *Int J Cancer* 19:621–626
- The Beginning of the Monte Carlo method (1987). Special issue. Los Alamos Science, Los Alamos
- Tennyson J (2010) *Phys. Rep* 491:29–76
- Thwaites DI, Tuohy JB (2006) *Phys Med Biol* 51:R343–362
- Trajmar S, Williams W, Kuppermann A (1973) *J Chem Phys* 58:2521–2531